USE OF THESES

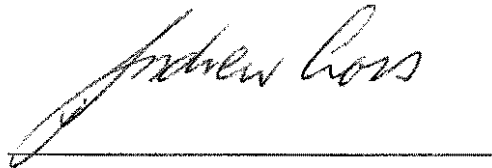# SHRIMP U-Pb xenotime geochronology and its application to dating mineralisation, sediment deposition and metamorphism

Andrew Joseph Cross

A thesis submitted for the degree of Doctor of Philosophy of the Australian National University

June, 2009

I hereby certify that this thesis is my own work except where acknowledged otherwise.

Andrew Cross

ACKNOWLEDGEMENTS

ABSTRACT

Diagenetic and hydrothermal xenotime typically occurs in rocks as tiny crystals (≤ 20 μm), either individually or as outgrowths on a zircon substrate. Currently only large radius ion microprobes such as the SHRIMP or Cameca 1270/1280 have the high sensitivity and spatial resolution necessary to analyse these crystals for U—Th—Pb isotopes. However, such analyses are prone to significant matrix effects (ME) related to the large natural range of U (0 to ~9 wt%) and REE ($\sum$REE: ~12 to 22 wt%) abundances in xenotime. Consequently, the $^{206}Pb/^{238}U$ calibration procedure for xenotime differs significantly from that employed for SIMS dating of zircon.

Contrasts in U, and to a lesser extent $\sum$REE, contents between the primary calibration standard and unknown xenotime can result in SHRIMP $^{206}Pb/^{238}U$-$^{208}Pb/^{232}Th$ ME of up to ~20%. The matrix correction technique developed requires the concurrent analysis of three xenotime standards with a range of U and $\sum$REE concentrations on a session-by-session basis. The $^{206}Pb/^{238}U$-$^{208}Pb/^{232}Th$ ME is monitored by the analysis of two secondary standards, a high $\sum$REE xenotime (BS1) and a high U xenotime (Z6413). Additionally, the chemical composition of each spot is determined by EPMA (WDS) prior to SHRIMP analysis. Each spot is corrected for ME by defining a series of simultaneous linear equations that relate the fractional $^{206}Pb/^{238}U$-$^{208}Pb/^{232}Th$ ME of the secondary standards to their U and $\sum$REE concentration contrasts with the primary calibration standard (MG1). On average, every 1 wt% contrast in U between the primary calibration standard and the unknown results in a ~11.9% difference in the $^{206}Pb/^{238}U$ and $^{208}Pb/^{232}Th$ ratios, whereas a 1 wt% contrast in REE results in a difference in the $^{206}Pb/^{238}U$ and $^{208}Pb/^{232}Th$ ratios of ~0.9%.

SHRIMP RG was used for these experiments because the analyses on that instrument are not prone to the molecular interferences or 'scattered ions' that affect the ^{204}Pb peak when xenotime is analysed on SHRIMP II. Matrix uncorrected $^{206}Pb/^{238}U$ ratios were determined from the raw $^{206}Pb/^{270}(UO_2^+)$ ratios as suggested for zircon analyses by Stern & Amelin (2003). Additionally, matrix uncorrected $^{208}Pb/^{232}Th$ ratios were determined from the raw $^{208}Pb/^{248}(ThO^+)$ ratios, however, this calibration appears to only be effective for xenotime with > ~1000 ppm Th.

The technique developed is broadly similar to the SHRIMP xenotime U—Th—Pb correction procedure proposed by Fletcher et al. (2004). Whereas Fletcher and others related SHRIMP xenotime $^{206}Pb/^{238}U$-$^{208}Pb/^{232}Th$ ME to contrasts in U, Th and $\sum$REE, this study indicates that the effect of Th on the $^{206}Pb/^{238}U$-$^{208}Pb/^{232}Th$ ME is minor to insignificant. It appears likely that for xenotime, it is the matrix sensitivity of the emission of the Pb^+ secondary ions, not U or Th species that is the principal cause of the $^{206}Pb/^{238}U$-$^{208}Pb/^{232}Th$ ME. Using the new matrix correction procedures developed here, it is possible to measure $^{206}Pb/^{238}U$ and $^{28}Pb/^{232}Th$ ages of Phanerozoic xenotime with an accuracy and precision of about 2% (95% confidence).

Three application studies of SHRIMP U—Pb xenotime geochronology using the matrix correction procedures developed were undertaken as a part of this study as well as a SHRIMP U—Pb detrital zircon study of the principal sedimentary units within the Tanami Basin, central Australia.

SHRIMP U—Pb analyses of xenotime that occurs as outgrowths on detrital zircon from a sample of quartzite from the Serra da Mesa Group, central Brazil, has the same Neoproterozoic age within error to that of SHRIMP U—Pb monazite analyses from the same sample, both giving $^{206}Pb/^{238}U$ ages of ~570 Ma. This latest Neoproterozoic age may be related to metamorphism associated with the final stages of the Brasiliano Orogeny. Further U—Pb studies are required on other rocks from this region to establish its regional extent. The identical SHRIMP $^{206}Pb/^{238}U$ ages for both monazite and xenotime in this study lend strong support to the matrix correction protocols developed.

SHRIMP U—Pb analyses of hydrothermal xenotime from the Callie and Coyote Au deposits in the Tanami region has demonstrated that they formed between ~1.81 and ~1.80 Ga. The ~1.81 Ga age for the Callie deposit contrasts with the results from an earlier $^{40}Ar/^{39}Ar$ study of hydrothermal biotite from the Callie deposit by Fraser (2002), which suggested that mineralisation occurred at ~1.72 Ga. Mineralisation between ~1.81 and ~1.80 Ga occurring in the Tanami region is coincident with the ~1.81 to ~1.79 Ga Stafford event which was a period of widespread magmatism across much of the North Australia Craton in which Scrimgeour (2006) suggested was

linked to a long-lived north-dipping subduction system active at the south-east margin of the craton.

A preliminary isotopic dating investigation of the Molyhil scheelite-molybdenite skarn deposit in the north-eastern Arunta region, central Australia has determined that it formed from fluids associated with the crystallisation of the Marshall Granite during the ~1.73 to ~1.72 Ga Strangways Oregeny. Rhenium—Osmium dating of ore stage molybdenite has an age of 1720.7 ± 5.9 Ma which is also coincident with skarn–related hornblende which has an $^{40}Ar/^{40}Ar$ age between ~1.72 and ~1.73 Ga (G. Fraser, unpublished data; Geoscience Australia). Importantly for this study is that one of the xenotime grains has a concordant SHRIMP U-Pb $^{207}Pb/^{206}Pb$ age of 1714 ± 26 Ma which is well within error of the ages determined by the other two isotopic methods adding further support to the SHRIMP U—Pb analytical protocols and $^{206}Pb/^{238}U$ matrix correction techniques developed during this PhD. Younger xenotime components from the Molyhil sample investigated have SHRIMP $^{206}Pb/^{238}U$ ages of ~760 Ma and ~650 Ma and probably crystallised in response to far-field tectonothermal events.

TABLE OF CONTENTS

Index of Figures

Index of Tables

PREFACE

In choosing to focus my PhD on both the analytical aspects of SHRIMP U—Pb xenotime analysis and also its practical application, I had two aims in mind. Firstly, I had identified two projects in the Tanami region of central Australia where SHRIMP U—Pb xenotime analysis could potentially solve some outstanding geological questions. These were, the timing of mineralisation at the Callie Au deposit and also the timing of deposition for two key sedimentary units. I also recognised that the significant SHRIMP $^{206}Pb/^{238}U$ matrix effects that stifle xenotime $^{206}Pb/^{238}U$ determinations had, at that stage, only been addressed in one paper, that of Fletcher et al. (2000). Subsequently, soon after starting my PhD project, researchers at the University of Western Australia improved on their earlier work and published a second paper dealing with SHRIMP $^{206}Pb/^{238}U$ xenotime matrix corrections (Fletcher et al. 2004). However, with the aim of developing my expertise in all aspects of SHRIMP U—Pb xenotime analysis I decided to pursue my interest in xenotime $^{206}Pb/^{238}U$ matrix corrections and hopefully build on the work of Fletcher et al. (2000), and Fletcher et al. (2004). This task turned out to be the most difficult, time consuming but ultimately most rewarding aspect of this project (see Chapter 3).

For my planned SHRIMP U—Pb xenotime dating experiments in the Tanami region, I was only able to undertake work on the Callie Au deposit and also the Coyote Au deposit (see Chapter 5). This was because no diagenetic xenotime was located in either of the two sedimentary units I had chosen to investigate, which were the Mount Charles Formation and the Gardiner Sandstone. It was hoped that diagenetic xenotime SHRIMP U—Pb analysis of the Mount Charles formation would resolve an inconsistency of 100 m.y. that exists between its currently accepted stratigraphic position and the results of SHRIMP U—Pb detrital zircon studies of this unit (see Chapter 1). SHRIMP U—Pb analysis of diagenetic xenotime from the Gardiner Sandstone was planned to test the reproducibility, over a large region, of a previously reported SHRIMP U—Pb diagenetic xenotime age for this unit that was sampled from a region of U mineralisation and reported in Vallini et al. (2007). A field trip to the Tanami region was conducted in 2005 to collect material for both of these projects. Samples of the Gardiner Sandstone were collected from widely dispersed locations across the Tanami, whereas samples of the Mount Charles formation were collected

from diamond drill core. Despite extensive XRF screening for Y, P, U and Th, and also manual, detailed backscattered electron SEM investigation of these samples, the presence of xenotime was neither indicated nor seen. It is for this reason that these proposed projects were abandoned.

Therefore, two alternative projects were chosen. These are SHRIMP U—Pb xenotime case studies of xenotime and monazite from the Serra da Mesa Group, Central Brazil (Chapter 4) and also xenotime and Re-Os molybdenite dating of the Molyhil skarn in the eastern Arunta region of central Australia (Chapter 6). The most significant of these studies is that of the xenotime and monazite from the Serra da Mesa Group where the results of SHRIMP U—Pb monazite analyses were used as a check against the SHRIMP U—Pb xenotime results and therefore the $^{206}Pb/^{238}U$ matrix correction procedures developed in this PhD study.

Chapter 1 of this thesis is presented here in the form of a re-print of a research paper that I had published with my co-worker Andrew Crispe, in Mineralium Deposita (Cross & Crispe 2007). For this Chapter, Andrew Crispe provided some geological background and Figure 3. This Chapter presents the results of SHRIMP U—Pb detrital zircon analyses of 12 sedimentary units and one volcanic unit from the Tanami region, which was subsequently used by me to help interpret the Palaeoproterozoic evolution of the Tanami Basin. It was planned as a pre-curser to the SHRIMP diagenetic xenotime investigation of the Mount Charles Formation and Gardiner Sandstone that, as described above, was unable to be undertaken. Included are eight SHRIMP detrital zircon studies from four major Tanami units undertaken prior to starting this PhD project, while an additional four SHRIMP detrital zircon studies and a SHRIMP U—Pb study of a volcanic unit were conducted during the course of this PhD. The eight samples carried out before beginning this PhD were undertaken by me as a part of a joint Geoscience Australia – Northern Territory Geological Survey geochronology project. A brief interpretation and the individual SHRIMP U—Pb analyses for these samples were presented in Cross et al. (2003). However, in the process of writing this Chapter, the results of the eight samples presented in Cross et al. (2003) were completely re-interpreted and re-written by me and subsequently incorporated with the additional samples from the Tanami region that were analysed in the early stages of this PhD project.

2

The other Chapters in this thesis are arranged in logical order. Chapter 2 deals with xenotime occurrence and geochemistry and is followed by a full analysis of SHRIMP U—Pb xenotime dating detailed in Chapter 3. The next three Chapters are case studies, which apply the SHRIMP $^{206}Pb/^{238}U$ xenotime matrix corrections developed during this study to: dating metamorphism and possibly diagenesis in the Serra da Mesa Group, central Brazil; the timing of mineralisation at the Callie and Coyote Au deposits, central Australia and the timing of skarn formation at the Molyhil skarn, also located in central Australia.

1. SHRIMP U–PB ANALYSES OF DETRITAL ZIRCON: A WINDOW TO UNDERSTANDING THE PALEOPROTEROZOIC DEVELOPMENT OF THE TANAMI REGION, NORTHERN AUSTRALIA.

Reprint of:

ARTICLE

SHRIMP U–Pb analyses of detrital zircon: a window to understanding the Paleoproterozoic development of the Tanami Region, northern Australia

A. J. Cross · A. J. Crispe

Abstract Poorly exposed Paleoproterozoic turbiditic to shallow marine sedimentary rocks of the Tanami Basin, NT, Australia are largely the erosional products of either the ~1.87–1.85 Hooper Orogeny and/or magmatism associated with the ~1.87 Ga Nimbuwah Event. Dating of detrital zircon from six of the principal sedimentary units shows that deposition spanned at least the period ~1.84–1.77 Ga. Collectively, the detrital zircon ages reveal a progression in provenance that is a record of the development of the orogen. The basal Dead Bullock Formation contains only zircon derived from Archean basement and no contemporaneous products of orogeny. Its deposition age is inferred to be ~1.87–1.84 Ga. Orogenic ~1.86 Ga zircon appears in the overlying Killi Killi Formation, deposited between ~1.84–1.82 Ga and persists, probably due to recycling in all overlying units except one, the Mount Charles Formation. The accepted stratigraphic position of this unit might be incorrect.

Keywords Geochronology · SHRIMP · Detrital zircon · Provenance · Tanami · North Australia

A. J. Cross (✉)
Research School of Earth Sciences,
The Australian National University,
Canberra, ACT 0200, Australia
e-mail: andrew.cross@anu.edu.au

A. J. Cross
Geoscience Australia,
GPO Box 378, Canberra, Australia

A. J. Crispe
Northern Territory Geological Survey,
P.O. Box 2655, Alice Springs, Australia

Introduction

The Tanami Region in NW central Australia is one of the richest gold-bearing Proterozoic regions in Australia. Gold production from the major mines (e.g. Callie, Tanami, The Granites) over the last 20 years has exceeded 4.8 Moz, with proven reserves of over 7.7 Moz (Wygralak et al. 2005). The province is a part of the North Australia Craton (NAC; Fig. 1) and has similarities with other north Australian Paleoproterozoic terranes such as the Halls Creek Orogen, the Pine Creek Orogen and the northern Arunta Inlier. However, because much of the Tanami Region is covered by regolith, its geology remains poorly understood.

The stratigraphy of Paleoproterozoic sequences of the Tanami Region has been established principally on the basis of drill core logging and mine exposures. The studied areas are widely scattered, however, and the paucity of intervening surface outcrop has made correlations tenuous. The only direct information about deposition ages has been provided by geochronology of felsic volcanic units that have yielded zircon U–Pb ages of approximately 1.82 Ga (Smith 2001).

Poor knowledge of the stratigraphy and basin architecture has been a major hindrance to effective exploitation of the Tanami Region's mineral potential. Therefore, in 1998, a geochronological study of the region was included in the joint Northern Territory Geological Survey—Australian Geological Survey Organisation (now Geoscience Australia) age determination program. The aims of the study were to document the history of sedimentation and igneous activity in the Tanami Region, providing a time framework for basin development and improved basin-wide correlations.

In this paper, we report the results of a SHRIMP U–Pb isotopic study of detrital zircon from 12 sedimentary rocks representing each of the major stratigraphic units from the

Ⓓ Springer

Fig. 1 Location of the Tanami Region
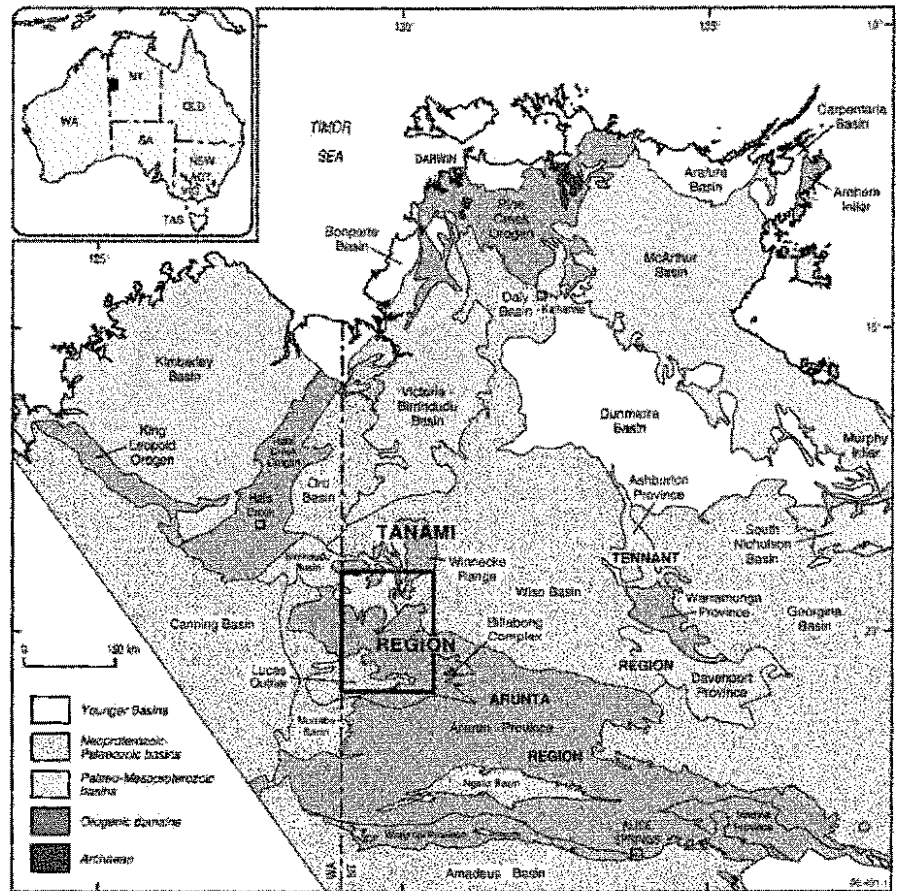
Tanami Region. These age determinations provide direct information both on the provenances of the sediments and their maximum deposition ages. An additional constraint on the deposition age of the Dead Bullock Formation was obtained by dating igneous zircon from an intercalated felsic tuff. This study has established that deposition occurred at least between the period 1.84 to 1.77 Ga, and that the sediments were probably eroded from sources to the north (Pine Creek Orogen) and northwest (Halls Creek Orogen) in response to uplift before ~1.84 Ma.

Geology

The following is a brief summary of the major geological features of the Tanami region. The reader is referred to Crispe et al. (2006) for a more complete discussion. Figure 2 is a generalized geological map of the Tanami region showing SHRIMP U Pb zircon geochronology sample sites discussed in this paper, and Fig. 3 is a generalized time event column for the Tanami region.

The Tanami province consists of a thick sequence of predominantly low grade Paleoproterozoic marine sedimen-

tary rocks and rare volcanic rocks deposited on late Archean granitic gneiss and intruded by granite mostly at ~1.82 1.79 Ga (Hendrickx et al. 2000; Page et al. 1995). Recent unpublished work suggests that the oldest known Paleoproterozoic rocks occur in the Bald Hill sequence in Western Australia. A high level rhyodacite in this unit has an interpreted zircon U Pb SHRIMP crystallization age of ~1,864 Ma (cited in Huston et al. 2006). The sedimentary sequence has been subdivided into six main units. These, from base to top, are: the Dead Bullock Formation (lower sandstone, upper carbonaceous siltstone with lesser iron formation); the Killi Killi Formation (turbidite) of the Tanami Group; the Ware Group (coarse sandstone, felsic volcanic rocks); the Mount Charles Formation (predominantly turbidite, arkosic sedimentary rocks with interlayered basalt); the Pargee Sandstone (sandstone and conglomerate); and the Birrindudu Group (marine to fluvial sandstone, conglomerate, and calcareous sedimentary rocks). There is a progression within the sequence from deeper to shallower water facies. The principal hosts for Au mineralization are the Dead Bullock and Mount Charles Formations.

Rocks of the Tanami Group were intruded by doleritic sills and subsequently deformed by the ~1,830 Ma Tanami

Event (D₁ M₁). This event locally caused meso- and macroscopic disharmonic folds and greenschist facies metamorphism. A second period of compressional deformation (D₂) is broadly synchronous with ~1.82 1.79 Ga granite intrusion and is the first event to affect Ware Group rocks. A further compressional event (D₃) is interpreted to have affected rocks of the Ware Group. An extensional event is interpreted, resulting in the deposition of sediments and basalts of the Mount Charles Formation before D₄, a SSE-directed shortening event. D₅ transpression resulted in the development of shear zones and faults. Many of the Au deposits in the Tanami region are associated with D₅ structures (Huston et al. 2006).

Materials and methods

Zircon separates were obtained using magnetic and density techniques from crushed samples. Detrital zircons were not handpicked, but sprinkled onto the mount surface to ensure an unbiased range of zircon grains. Zircons were mounted in epoxy resin, together with standard zircons SL13 (U abundance zircon) and QGNG (Pb/U age standard). The epoxy mount was polished to reveal zircon interiors and photomicrographs were taken in transmitted and reflected light. Cathodoluminescence (CL) images were taken using a Hitachi S 2250-N SEM at the ANU-RSBS Electron Microscopy Unit.

Fig. 3 Generalised time–event column for the Tanami Region. *Asterisks* denote units hosting significant gold mineralisation
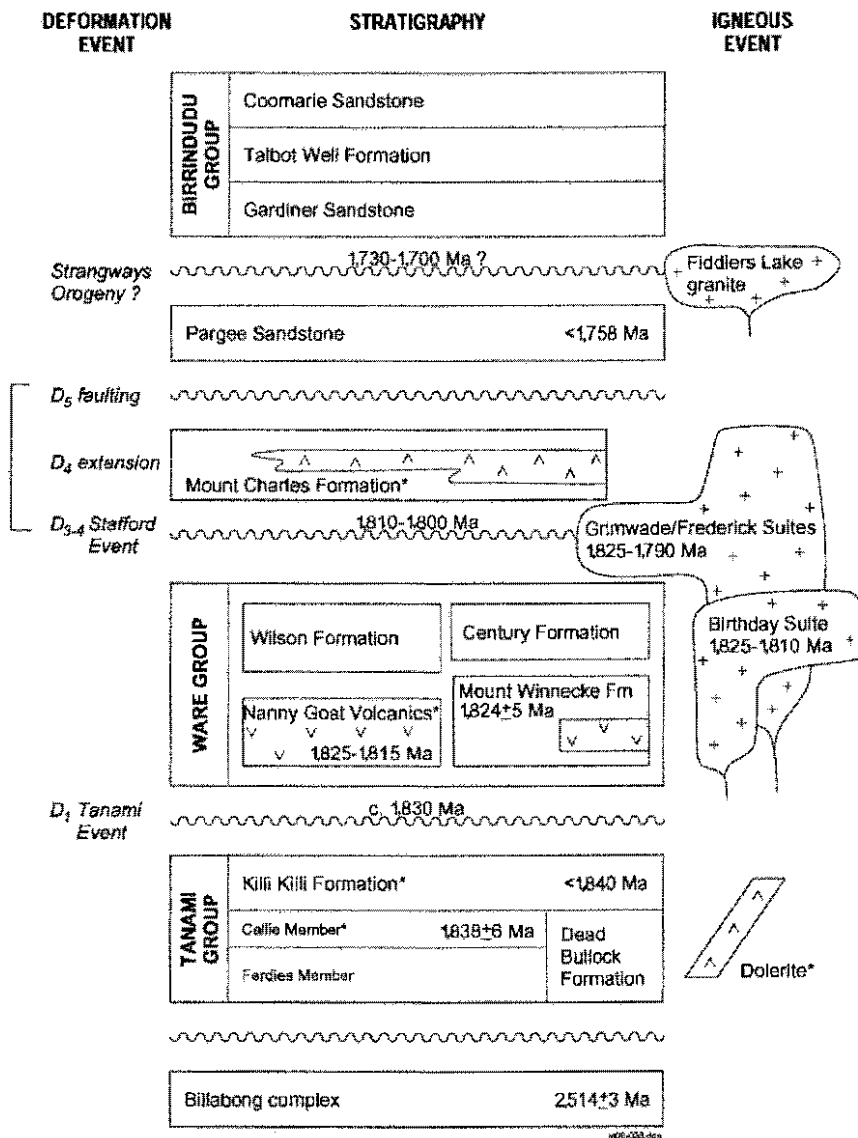
Isotopic analyses reported in this study were carried out on the SHRIMP I, SHRIMP II and SHRIMP-RG ion microprobes at the Australian National University, Canberra and SHRIMP B at the Curtin University of Technology in Perth, Western Australia. Analytical procedures are described in Compston et al. (1984), Williams and Claesson (1987) and Claoué-Long et al. (1995).

The primary oxygen ion beam ranged between ~2 to ~6 nA in intensity for a spot diameter of between ~20 to ~40 μm. Ionized particles were extracted into the mass spectrometer with a 10 kV potential and counted by a single electron multiplier. Ions were focussed into the collector by a cyclic stepping of the magnet. Each analysis represents the average of five to seven scans through the different mass stations.

Calibration of Pb/U ratios was by comparison to the zircon standard QGNG and the power law relationship of Pb^+/U^+ and UO^+/U^+ (Claoué-Long et al. 1995). The Pb/U ratios were normalized to an assumed value for QGNG of 0.3324 (equivalent to 1,850 Ma). Uranium and thorium abundances have been calculated with reference to SL13 (238 ppm U) and are subject to uncertainty of at least ±20%, this being the range of U abundance within that reference material. Common Pb corrections were based on individual measured ^{204}Pb abundances and assuming crustal common Pb of the same age in the zircon as

modelled by Stacey and Kramers (1975). Data reduction was carried out using the SQUID 1 and ISOPLOT 3 Microsoft Excel-based macros of Ludwig (2001, 2003).

Individual analyses reported in this paper have uncertainties listed in the tables and plotted on concordia diagrams as shaded ellipses at the 1σ level; unfilled ellipses represent compositions that are greater than 10% discordant. Final ages are quoted in the text with 95% confidence limits. Analyses of the QGNG standard were interspersed with the unknowns at the rate of approximately one in four.

Detrital zircon maximum deposition age calculation

Detrital zircon U–Pb age studies by either ion microprobe or laser ablation ICPMS routinely provide a large number of age determinations on individual zircon grains recovered from clastic sedimentary rocks. The zircon age distributions generated by these methods can be used to infer sediment provenance, and to make correlations between discontinuous sedimentary sequences. In addition, the youngest zircon(s) can be used to estimate the maximum deposition age of a sedimentary unit. Maximum deposition age estimates obtained in this way have the potential to provide important stratigraphic constraints for siliclastic sequences, especially those from Proterozoic basins where interlayered felsic volcanics are rare and fossil control absent.

There are two broad approaches in estimating a maximum deposition age from the isotopic ages of the youngest detrital zircon grains in a population. These are to use the age determination from the youngest zircon grain analyzed (Cross et al. 2003), or to determine a pooled age from the youngest statistically coherent zircon age population (Williams 2001; Black et al. 2004).

Maximum deposition ages derived from the age of the youngest zircon grain(s) from a detrital population are based on a number of assumptions. First, the analyzed zircon grains are assumed to have experienced no Pb loss. Second, all zircon grains are considered as individuals. Finally, in the absence of any morphological or chemical similarities, no assumption of age-group membership is made. Using this approach, the age and uncertainty of the youngest zircon is used as an estimate for the maximum deposition age. The uncertainty of this age estimate can be improved by calculating a pooled age from the youngest few analyses.

The above approach can involve sampling of individual zircon ages from the younger tail of a Gaussian, near-Gaussian or composite age distribution. Individual ages may be statistically indistinguishable from older members of the population. In addition, when the youngest few apparent ages are pooled to increase the precision of the age estimate, the resulting mean squared weighted deviation (MSWD) can be well below unity, and therefore indicate biased sampling of the detrital zircon population (e.g. Cross et al. 2003).

In the circumstance where the youngest detrital zircon from an age distribution is statistically distinguishable from older grains, multiple analyses will improve the precision of the age and should be performed to ensure that Pb loss has not occurred. Nelson (2001) was able to show that in some situations, the youngest grains can be a reliable estimate of the depositional age of a clastic unit. However, the possibility of contamination during sample processing must be borne in mind when interpreting the significance of a maximum depositional age based on the presence of a single zircon.

Many researchers (e.g. Black et al. 2004; Williams 2001; Smithies et al. 2001; Trendall et al. 2004) establish the age of the youngest detrital zircon component in an age distribution, using the age and uncertainty of the youngest statistically coherent zircon age population. This approach involves an iterative process of culling individual zircon ages (points) from the older analyses in an age distribution, until the age of the youngest grouping of zircon grains has an MSWD value that approaches the upper 95% confidence interval boundary for a given number of points (i.e. degrees of freedom). This method of defining a statistically coherent population from either a Gaussian, near-Gaussian or composite population is treated on a sample-by-sample basis and is an entirely appropriate method to use when a morphological and/or chemical similarity between zircon grains is recognised. However, when no such similarity is observed, the youngest statistically defined population of zircon grains is assumed to have originated from a single crystallization event, even though it could represent a mix of different protolith sources with a range of overlapping zircon crystallization ages. This is an important point to consider, as most detrital zircon analyses on SHRIMP typically use four to five scans. The relatively reduced count rates have lower precisions in comparison to six to seven scan analyses which are typically used for SHRIMP U–Pb dating of igneous rocks.

Maximum deposition age estimates calculated from the youngest zircon(s) on the younger tail of a larger distribution may result in an under-estimation of the true deposition age, whereas maximum deposition age estimates calculated from the youngest statistically coherent population may result in an over-estimation of the true depositional age.

A crucial difference between the two approaches is that by calculating the age of the youngest statistically coherent zircon component, the researcher acknowledges that the age and uncertainties of the analyses on the younger tail of a larger distribution cannot be statistically separated from older zircon in the same distribution. We believe this to be the conservative approach and have adopted it in this contribution.

Sample selection

Samples were selected from the Tanami basin sequence with the aim of constraining the deposition age of each of the major stratigraphic units. To maximize the recovery of detrital heavy minerals, sandstone samples were chosen wherever possible in preference to shale samples. The samples collected included: (1) an arkose and feldspathic arenite from the Ferdies Member of the Dead Bullock Formation, (2) a graywacke, quartz arenite and two quartz wackes from the Killi Killi Formation, (3) a lithic arenite and graywacke from the Ware Group, (4) two arkoses from the Mount Charles Formation, (5) a quartz arenite from the Pargee Sandstone and (6) a quartz arenite from the Gardiner Sandstone. Most of the samples were collected from outcrop or mine exposures; four samples were selected from drill core provided by Newmont Mining. At each outcrop sampled, the material collected was the most coherent, least altered and least weathered available. Particular care was taken to avoid veining and obvious alteration. Veining and mineralization were also avoided when selecting samples from drill core.

Results

Dead Bullock formation—Tanami group

Ferdies Member, arkose (2003082647)

Sample 2003082647 was collected from a massive bed of immature, poorly sorted arkosic conglomerate exposed in the southern extension of the Groundrush Pit on the eastern wall about 60 m below ground level (Table 1). The arkose consists of coarse-grained microcline, quartz and plagioclase in a quartz–biotite matrix. The zircon grains recovered are a mixed population with a range of sizes (30–200 μm diameter), shapes and colours, consistent with derivation from a variety of sources. Most are clear, colourless, relatively equant, subhedral to anhedral grains with few fractures or inclusions. Many are angular crystal fragments and a few have pitted surfaces resulting from sedimentary transport and reworking. Rare grains are more prismatic with sharply euhedral terminations. Some of the more equant grains also have some well-preserved crystal faces, and about 20% of the grains have faint internal zoning visible in transmitted light. CL imaging shows the zoning patterns more clearly, although the luminescence in most cases is dark. Concentric oscillatory and sector zoning predominates. Relatively few grains have obvious textural cores. Some grains have thin, irregular, very weakly luminescent overgrowths.

One hundred and twenty grains were analyzed (S1, Fig. 4). With two exceptions, U contents are moderate to low (28–500 ppm) and Th/U moderate to high (0.2–1.9, median 0.9). Most of the analyzed areas, although appearing clear, glassy and free of fractures or inclusions, contain significant amounts of common Pb. These range from just detectable (~0.15 ppm) to very high (300 ppm), median 2.5 ppm. There is, however, no systematic correlation between the common Pb content and radiogenic $^{207}Pb/^{206}Pb$ or Pb/U. The great majority of ages are concordant or near concordant within analytical uncertainty, although the uncertainties on the analyses with large common Pb corrections are much higher than normal. Four exceptions are more than 20% discordant (A100.1, A63.1, A71.1 and A19.1) and are not considered further in the age assessment (Fig. 4). Five other analyses (A53.1, A42.1,

Table 1 Location and other information for samples analysed as a part of this study

Unit	Lithology	OZCHRON number	Location GDA 94		Analyses >90% concordant
Ferdies Member	Arkose	2003082647	604082	7819984	112
Ferdies Member	Feldspathic arenite[a]	2003082649	571390	7710386	87
Callie Member	Tuff	2001082511	590477	7798371	27[b]
Killi Killi Formation	Quartz wacke[a]	2001082021	599116	7730736	58
Killi Killi Formation	Quartz arenite	2001082505	560827	7767424	55
Killi Killi Formation	Quartz wacke	2001082515	507360	7790816	69
Killi Killi Formation	Greywacke[a]	2001082036	600796	7756265	56
Ware Group	Lithic arenite	2001082519	523028	7782433	82
Ware Group	Greywacke	2001082527	615954	7884346	66
Mount Charles Formation	Arkose	2003082644	564775	7770935	91
Mount Charles Formation	Arkose	2001082507	574953	7792871	32
Pargee Sandstone	Quartz arenite	2001082517	525686	7826720	66
Gardiner Sandstone	Quartz arenite	2003082642	580942	7804774	74

[a]Drill core sample
[b]Magmatic zircon
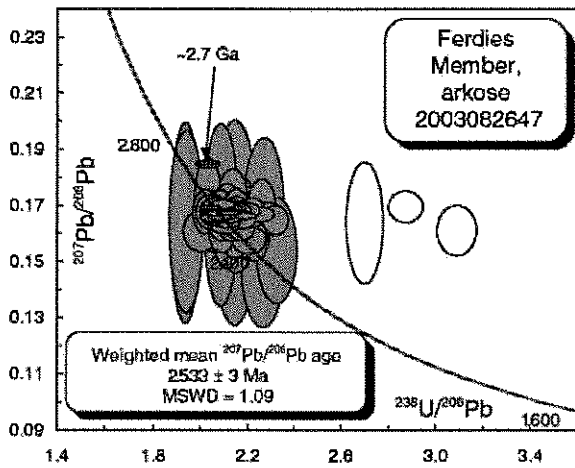
Fig. 4 Concordia plot of detrital zircon U–Pb analyses for arkose sample 2003082647 from the Ferdies Member of the Dead Bullock Formation

A75.1, A119C.1 and A12.1) have very large uncertainties in ^{207}Pb/^{206}Pb (>15%). These are not plotted in Fig. 4 and are not considered further.

The remaining 112 analyses scatter in radiogenic ^{207}Pb/^{206}Pb more than expected from the analytical uncertainties (MSWD=4.6). The entire excess scatter is due to one analysis higher than the rest (A11.1). Omitting this analysis leaves 111 determinations that form a single population (MSWD=1.1). The weighted mean radiogenic ^{207}Pb/^{206}Pb (0.16750±0.00030) is equivalent to an age of 2,533±3 Ma. Taking into account uncertainty in decay constants (Ludwig 2000), the uncertainty in the age is ±7 Ma.

Ferdies Member, feldspathic arenite (2003082649)

Sample 2003082649 was a section of half core from Officer Hill (OHD002, 217.5 225.7 m) (Table 1). The arenite selected is the coarsest unit within an otherwise fine-grained sequence of carbonaceous siltstone. The sample is a fine- to medium-grained, grey green, feldspathic arenite with a pronounced foliation defined by anastomosing chlorite. The zircon grains recovered are a mixed population of sizes (100 400 μm diameter) and shapes consistent with derivation from a variety of sources. The majority of the grains are subhedral, rounded to subrounded, stubby prismatic crystals with few or no preserved crystal faces. Rare grains are euhedral. Most grains are clear and weakly coloured, with relatively few inclusions or fractures. Some larger grains are highly fractured and discoloured. About 20% of the grains have faintly visible internal zoning and/or cores and rims in transmitted light. Some zircons have surface pitting but in most grains, the surfaces are covered

by a thin (<5 μm) layer of younger zircon that partially obscures this texture. There is a wide range in luminescence from dark to light with the average CL much stronger than that seen in the zircon grains from sample 2003082647. Many of the grains (~30%) have little or no obvious growth zoning. Zoning in the remainder ranges from broad banding to fine oscillatory zones. Truncation of the zones by the grain margins shows that most grains are fragments of larger crystals. The thin late overgrowths are dark in CL, a feature often typical of zircon rims.

One hundred and four grains were analyzed, eight in duplicate and two in triplicate (S2, Fig. 5). There is a very wide range in U content (24 2,135 ppm), but low U contents predominate (median 100 ppm). This range is skewed only to a small extent by the decision not to analyse those grains that are in poor crystallographic condition. Th/U is mostly moderate (0.1 1.5) with just a few grains lower (0.01 0.05) and higher (1.8 3.1). In contrast to those from sample 2003082647, the zircon grains have a very wide range of isotopic compositions; many (~20%) are significantly discordant. ^{207}Pb/^{206}Pb apparent ages range from ~3.24 to ~1.57 Ga. The main clusters of ages are at ~3.20 and ~2.70 Ga. There are very few grains with apparent ages less than 2.20 Ga. With four exceptions, the 31 grains in the ~3.20 Ga group are concordant within analytical uncertainty, but there is a significant range in radiogenic ^{207}Pb/^{206}Pb (MSWD=46). The population is broadly bimodal with a main group at ~3.20 Ga and minor group at ~3.05 Ga. Considering only the concordant analyses, the 11 oldest grains have the same radiogenic ^{207}Pb/^{206}Pb within analytical uncertainty yielding a weighted mean age of 3,219±7 Ma. With four exceptions, the 16 younger grains also form a coherent group with a weighted mean age 3,169±10 Ma.
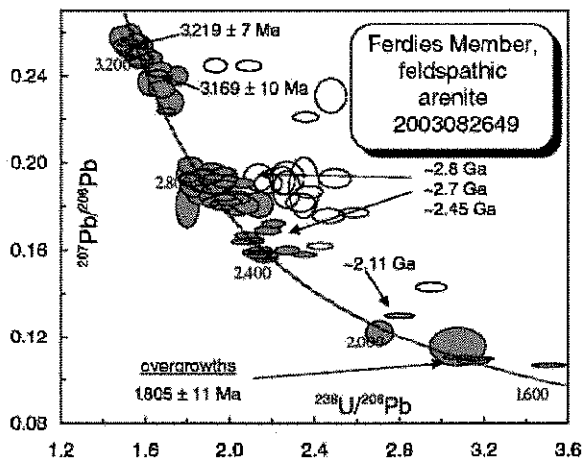
Fig. 5 Concordia plot of detrital zircon U–Pb analyses for feldspathic arenite sample 2003082649 from the Ferdies Member of the Dead Bullock Formation

Twelve of the 50 grains in the ~2.70 Ga group are more than 10% discordant and are not considered further. The remaining 38 grains have a broadly trimodal age distribution, with peaks at ~2.78, ~2.70 and ~2.45 Ga. Each of these groups is composite. There are only four grains with an age similar to that of the 2.53 Ga zircon, which is dominant in sample 2003082647.

Due to their possible importance in placing a limit on the deposition age of the arenite, the six grains on which apparent ages less than ~2.20 Ga were analyzed mostly in duplicate or triplicate. With one exception (grain 82), these crystals are subhedral prisms with distinct cores and euhedrally zoned overgrowths. It is the overgrowths that give the grains their prismatic form and crystal faces. The cores of these grains, in shape and size, closely resemble the bulk of the rounded zircon grains in the rock. It is possible that these overgrowths are the same material that forms a very thin coating on those rounded grains. The overgrowths are rich in U (555 2,135 ppm) and mostly have high to very high (~2 25 ppm) common Pb contents. It is the overgrowths that yield the younger ages but there is no direct correlation between discordance and either U or common Pb contents. Three of the eight overgrowths are less than 5% discordant and combine to give a ^{207}Pb/^{206}Pb age of 1,805±11 Ma. The other two analyses in the younger group both come from cores. One has a large analytical uncertainty (±93 Ma), but the other is relatively precise and, if there has been no Pb loss from the grain, places an upper limit of 2,109±10 Ma on the deposition age of the arenite. Thus, the deposition age for this unit must be between 2,109±10 and 1,805±11 Ma.

Callie Member, tuff (2001082511)

Sample 2001082511 was collected from a thin oxidized, feldspathic layer within a low lying outcrop of more mature sandstone in the Black Hills region, located about 15 km northeast of the Hurricane-Repulse Pit (Table 1). The tuff is friable, fine- to medium-grained, bleached orange, weakly foliated and deeply weathered. It consists of quartz and altered feldspar in a clay-rich matrix. The foliation is defined by weathered chlorite. The zircon grains recovered are a homogeneous population of fine (~40 80 µm diameter), predominantly euhedral, clear, colourless, prismatic grains with aspect ratios of 1 6. Considering the highly weathered state of the rock, the zircon grains are remarkably unaltered, coherent, and free from iron oxide discolouration. Many (~20%) have the irregular axial cavities commonly found in zircons from volcanic rocks (Nutman et al. 1997). Very few have faint visible internal zoning or cores in transmitted light. The grains have a moderate to bright luminescence, which reveal that the population is dominated by broad oscillatory growth

zoning. Texturally discordant cores are very rare. All these features are consistent with the zircon grains being derived from a single igneous source rock.

Thirty-two grains were analyzed (S3, Fig. 6), each selected to be a best possible example of igneous growth. No attempt was made to analyse inherited cores. The analyzed areas have moderate U contents (~70 200 ppm) and Th/U ratios (~0.4 1.15, median 0.55). Two grains have higher Th/U ratios of ~1.71 (A14.1) and ~1.74 (A29.1). Common Pb contents are low (<0.5 ppm) and all but one of the ages are concordant to near concordant. The discordant grain (A6.1) was not included in the pooled age calculation. The remaining 31 grains have the same radiogenic ^{207}Pb/^{206}Pb within analytical uncertainty (MSWD=1.2), yielding a weighted mean age of 1,834.9±6.9 Ma. However, there is a general trend towards grains with higher measured ^{204}Pb having lower radiogenic ^{207}Pb/^{206}Pb, implying a small isobaric interference at mass ^{204}Pb. The four analyses with the highest mass 204 counts are the most affected. Omitting these, the weighted mean ^{207}Pb/^{206}Pb age becomes 1,838.4±6.4 Ma (MSWD=0.99), which is our best estimate of the crystallization age of the tuff.

Killi Killi Formation, quartz wacke (2001082021)

Sample 2001082021 was collected from diamond drill core in the Dead Bullock Soak goldfield (DBD 422, 170.95 178.5; Table 1). The sample was selected from a long section of monotonous nonmineralized mature quartz wacke. It consists of sub-rounded to sub-angular, moderately sorted quartz, and rare feldspar in a sericitised clay matrix. Zircons are a mixed population of sizes, shapes and colours consistent with derivation from a range of sources. Most (~70%) of the grains are of relatively uniform size (80 100 µm diameter).
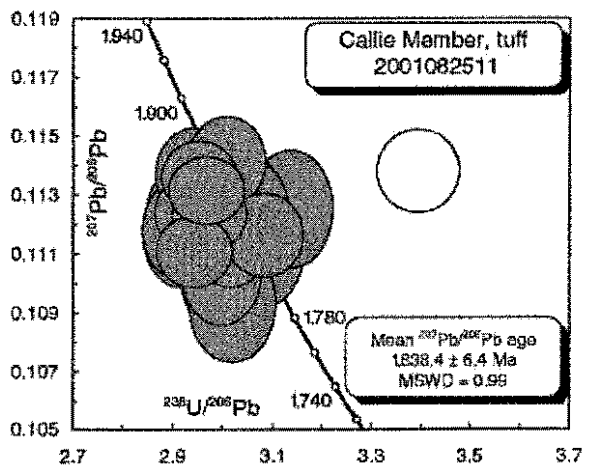
Fig. 6 Concordia plot of zircon U–Pb analyses for tuffaceous rock sample 2001082511 from the Callie Member of the Dead Bullock Formation

The full size range is 40 200 µm in diameter, and equant sub-rounded grains predominate. About 10% of these have surfaces pitted presumably by mechanical sedimentary abrasion. Approximately 5% of the grains are subhedral to euhedral, with some well-preserved crystal faces. The zircon grains are colourless to pale-brown, clear, with relatively few fractures and inclusions. Many of the grains have visible concentric growth zoning in transmitted light. With very few exceptions, the CL is uniformly dark and provides little information on the internal zoning textures.

The 94 zircon grains analyzed have, with few exceptions, a very limited range of U content (100 400 ppm) and normal felsic igneous Th/U (0.2 0.9) (S4, Fig. 7). Common Pb contents are uniformly low, but about 30% of the analyses are moderately to strongly discordant (Fig. 7). Most of the analyses (67%) define a discordance line with an upper concordia intercept of ~1.86 Ga. The remaining analyses have $^{207}Pb/^{206}Pb$ apparent ages in the range 3.2 2.0 Ga, with a cluster at ~2.50 Ga. The discordance line defined by the 63 analyses in the youngest group is moderately well defined MSWD=4, with concordia intercept ages of 1,868.6±6.5 and 99±71 Ma, indicating that most of the Pb loss has taken place very recently. The best estimate of the zircon crystallization age is given by the radiogenic $^{207}Pb/^{206}Pb$ of the least discordant analyses. The 38 analyses that are less than 10% discordant have a range of radiogenic $^{207}Pb/^{206}Pb$ that is slightly greater than expected from the analytical uncertainties (MSWD=2.6). Even omitting the analysis with the lowest $^{207}Pb/^{206}Pb$, which has the highest common Pb correction, some scatter remains (MSWD=2.2). There are, however, no remaining identifiable outliers. The $^{207}Pb/^{206}Pb$ robust median age (Ludwig 2001) of the remaining 37 analyses is 1,865.6+3/−7.5 Ma, with the asymmetric uncertainties reflecting the asymmetric distribution of the data.
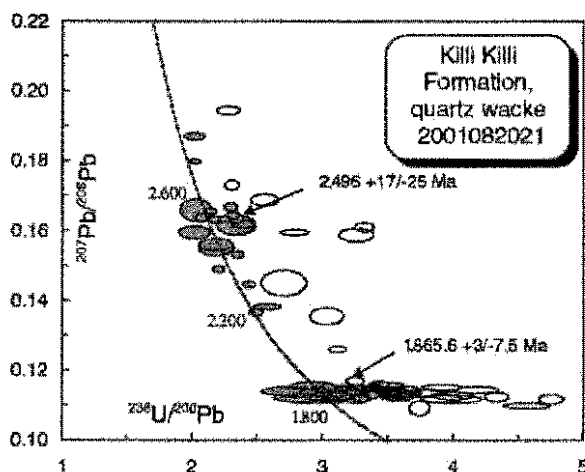
Fig. 7 Concordia plot of detrital zircon U–Pb analyses for quartz wacke sample 2001082021 from the Killi Killi Formation

A loose cluster of 18 analyses dominates the older group at ~2.50 Ga. Five of these are more than 10% discordant. Although there is no correlation between discordance and radiogenic $^{207}Pb/^{206}Pb$ because the age of the Pb loss is not known, these analyses are of no value in assessing the age distribution. The 13 remaining grains have $^{207}Pb/^{206}Pb$ apparent ages in the range ~2.53 2.41 Ga and are dispersed beyond analytical uncertainty (MSWD=10). Most of the analyses (11) cluster at ~2.50 Ga but are still scattered (MSWD=4.8). This scatter can be reduced, but not eliminated, by omitting one other low analysis (MSWD=3.8). No other omissions can be justified. The median age of the remaining grains is 2,496+17/−25 Ma, the large uncertainty reflecting the residual scatter.

Killi Killi Formation, quartz arenite (2001082505)

Sample 2001082505 was collected from outcrop in the Turkey Bore region, approximately 5 km southwest of Jims Pit (Table 1). The sample is a moderately sorted quartz arenite with rounded to sub-rounded quartz grains and sericitised matrix. The zircon grains recovered are a mixture of sizes, shapes and colours consistent with derivation from a range of sources. The grains range in diameter from ~40 to 200 µm and the majority are equant and sub-rounded. Less than 5% of the grains are subhedral with some retaining well preserved crystal faces. Approximately 50% of grains have pitted surfaces indicative of mechanical sedimentary abrasion and ~20% have what is predominantly faintly visible growth zones in transmitted light. The zircon grains are mainly clear, colourless to pale brown and many grains have fractures that are stained by iron oxides. Most grains have a dark to moderate luminescence. Two contrasting types of zoning, finely oscillatory and broadly diffuse, are about equally represented.

The 64 zircon grains analyzed have a limited range of ages. U contents are mostly 100 350 ppm (S5, Fig. 8). The full range is 25 615 ppm. Th/U is 0.14 to 1.8, with most values in the range 0.3 1.0. Common Pb contents are consistently low. Most of the analyses (~80%) are concordant or near concordant. The grains have a wide range of $^{207}Pb/^{206}Pb$ apparent ages. The main cluster is at ~1.85 Ga and there are smaller groups at ~2.50 and ~2.10 1.90 Ga. Most of the discordant grains are included in the youngest group. The 29 analyses in the youngest group plot almost within error on a single discordance line (MSWD=1.8). Omitting one concordant low value (C22.1) reduces the scatter (MSWD=1.5). The resulting line has concordia intercept ages of 1,870.2±6.1 and 210±88 Ma. The 24 analyses that are concordant or near concordant have a range in radiogenic $^{207}Pb/^{206}Pb$ that is barely larger than expected from the analytical uncertainties (MSWD=1.9). Omitting the same low value
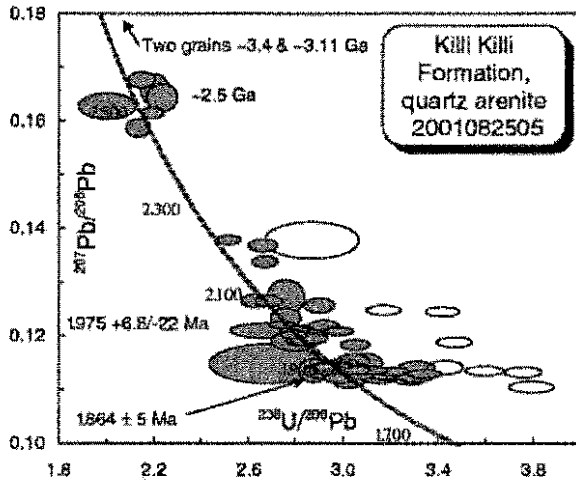
Fig. 8 Concordia plot of detrital zircon U–Pb analyses for quartz arenite sample 2001082505 from the Killi Killi Formation

Fig. 9 Concordia plot of detrital zircon U–Pb analyses for quartz wacke sample 2001082515 from the Killi Killi Formation

that was an outlier in the regression reduces the scatter (MSWD=1.6), yielding a weighted mean $^{207}Pb/^{206}Pb$ age of 1,864.4±5.3 Ma.

The remaining analyses cluster at ~2.50, ~2.0 and ~1.97 Ga. The 1.97 Ga cluster is consists of 14 grains that have a range in $^{207}Pb/^{206}Pb$ ages of ~1.99 to 1.94 Ga. One analysis is significantly discordant and is not included in assessing the age distribution. The remaining 13 analyses are dispersed beyond analytical uncertainty (MSWD=3.4). Omitting the youngest grain reduces the scatter (MSWD=2.3), but does not eliminate it and no other omissions can be justified. The robust median $^{207}Pb/^{206}Pb$ age of the remaining grains is 1,975+6.8/−22 Ma, the large uncertainty reflecting the residual scatter. The ~2.03 Ga group consists of seven analyses with a range of discordance that plot within error (MSWD=1.09) on a single discordance line with concordia intercept ages at 2,050±12 and 174±130 Ma. The lower intercept indicates very recent Pb loss. The ~2.50 Ga group consists of six grains that range in age from ~2.54 to ~2.44 Ga.

Killi Killi Formation, quartz wacke (2001082515)

Sample (2001082515) was collected about 5 km northeast of the Maverick granite. The quartz wacke consists of well sorted, sub-rounded to sub-angular quartz grains in a sericitised, fine-grained matrix. The zircon grains recovered range in size from ~30 to 200 μm in diameter. They are mostly equant, rounded to sub-rounded, clear and colourless. Surface abrasion is common, but a few grains still preserve some crystal faces. Relatively few grains (<5%) have faintly visible growth zoning in transmitted light. Dark CL and faint oscillatory growth zoning predominate. Most grains are

fragments of larger crystals. A few grains (~10%) have stronger CL and in some the zoning is weak or absent.

One hundred and twelve analyses are listed in S6 and plotted in Fig. 9. The zircon grains have mostly low to moderate U contents (50–500 ppm), with a full range of 20–1,000 ppm. Th/U is mostly moderate to high (0.1–3.1), and an unusually large fraction of the grains (50%) have values in the range 1–3. More than 30% of the analyses are greater than 10% discordant. The $^{207}Pb/^{206}Pb$ apparent ages are dispersed over the range ~3.50 to ~1.70 Ga, with prominent groups at ~2.50 and 1.86 Ga. The 58 analyses in the youngest group are very poorly fitted to a discordance line (MSWD=11) consistent with dominantly recent Pb loss. Considering only the 38 least discordant analyses, there is nevertheless a significant range in radiogenic $^{207}Pb/^{206}Pb$ (MSWD=17). The scatter is mainly due to a group of seven analyses with ages significantly higher than the main population. Omitting these, the scatter is not eliminated (MSWD=2.2). Omitting the lowest value (1696±63 Ma) makes little difference because of its large analytical uncertainty (MSWD=2.0) and there are no other obvious outliers. The median $^{207}Pb/^{206}Pb$ age for the remaining 30 values is 1,868+5.3/−6.1 Ma. The seven older grains are dispersed over the range ~1.98–1.90 Ga and do not form a discrete age group.

The 26 analyses in the ~2.50 Ga group do not even loosely define a discordance line. Considering just the 16 least discordant points, there is a significant range in radiogenic $^{207}Pb/^{206}Pb$ (MSWD=16). This group can be divided into three subgroups. Nine of the analyses have equal $^{207}Pb/^{206}Pb$ within error (MSWD=1.3), with a weighted mean age of 2,499±9 Ma. Five of the grains are younger, with a weighted mean age of 2,443±17 Ma (MSWD=2.4) and two grains are older with ages of ~2.55 Ga.

Killi Killi Formation quartz wacke (2001082036)

Sample 2001082036 was a section of half core from the Titania Au prospect (TDH01, 110.6 116.6 m), located about 40 km northwest of The Granites Goldfield (Table 1). The sample was a piece of vein-free quartz wacke from a long section of monotonous non-mineralised quartz wacke. It consists of moderately sorted, sub-rounded to sub-angular quartz grains and minor feldspar in a sericitised, fine-grained matrix. The zircon grains recovered range from 40 to 180 µm in diameter. Most are sub-rounded equant grains, ~5% are elongate prisms with aspect ratios of 2 3. Approximately 5% of the grains are subhedral to euhedral with some preserved crystal faces. The majority (60%) have predominantly well-defined visible growth zones in trans-mitted light and many (~40%) have pitted abraded surfaces. Many of the growth zones are metamict. The zircon grains are clear, colourless to brown and many have fractures that are iron oxide stained. They predominantly show faint oscillatory growth zones in CL.

Seventy-nine analyses are listed in S7 and plotted in Fig. 10. The zircon grains have low to moderate U contents (50 500 ppm) with a full range of 9 2,383 ppm. Th/U ranges from 0.06 1.60, with most values in the range 0.2 1.1. Common Pb contents are mostly low (<0.6 ppm) but about 30% of the isotopic compositions are moderately to strongly discordant. Most analyses cluster at ~1.86 Ga, with smaller groups between ~2.50 and 1.90 Ga. The 37 analyses in the dominant 1.86 Ga group do not define a discordance line. Considering only the 27 concordant and near-concordant analyses, the data are slightly dispersed in radiogenic $^{207}Pb/^{206}Pb$ (MSWD=2.0). This scatter can be reduced, but not eliminated by omitting the two highest values (MSWD=1.7). No other omissions can be justified.
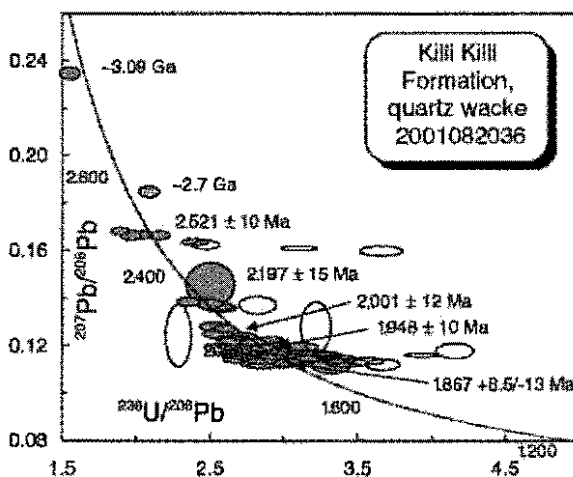
Fig. 10 Concordia plot of detrital zircon U–Pb analyses for quartz wacke sample 2001082036 from the Killi Killi Formation

The median $^{207}Pb/^{206}Pb$ age of the remaining grains is 1,867.2+8.5/−13 Ma.

The other age clusters are at ~2.50, ~2.20, ~2.00 and ~1.95 Ga. The ~1.95 Ga group consists of 15 grains that have a constant $^{207}Pb/^{206}Pb$ within error (MSWD=1.6), giving a weighted mean $^{207}Pb/^{206}Pb$ age of 1,948±10 Ma. The ~2.0 Ga group consists of 10 grains that have a significant range in radiogenic $^{207}Pb/^{206}Pb$ (MSWD=3.2). By omitting two of the highest values, the scatter is eliminated (MSWD=0.57) leaving eight analyses which give a weighted mean $^{207}Pb/^{206}Pb$ age of 2,001±12 Ma. The ~2.20 Ga cluster comprises six analyses that have the same radiogenic $^{207}Pb/^{206}Pb$ within analytical uncertainty (MSWD=0.98) giving a weighted mean age of 2,197±15 Ma. The eight analyses in the ~2.50 Ga group lie within error (MSWD=0.92) on a discordance line, with concordia intercept ages of 2,521±10 and 250±66 Ma.

Ware group

Century Formation, lithic arenite (2001082519)

Sample 2001082519 was collected from a low lying, isolated outcrop of silicified, medium to coarse grained sandstone, located about 15 km southwest of the Pendragon deposits (Table 1). The rock comprises approximately 70% moderately sorted rounded to sub-rounded quartz grains in a matrix of poorly sorted mostly angular lithic fragments. Zircon grains recovered range in diameter from 50 200 µm. They are mostly sub-rounded to rounded equant grains but ~30% are euhedral to subhedral crystals or crystal fragments with some well preserved faces. The zircon grains are clear, colourless to pink with few fractures or inclusions. Less than ~5% have faintly visible growth zones in transmitted light, and ~10% have abraded surfaces. The majority are dull in CL, and well-developed oscillatory growth zones predomi-nate over lesser sector zoning and diffuse banding.

The 99 zircon grains analyzed have uniformly low U contents (14 290 ppm, median 115) and low to moderate Th/U (0.11 1.75, median 0.57, S8, Fig. 11). Common Pb contents are also low, and about 17% of the analyses are more than 10% discordant. The $^{207}Pb/^{206}Pb$ apparent ages are scattered through the range of ~3.50 1.80 Ga. There is a major group at ~1.83 Ga, a secondary group at ~1.88 Ga, and minor clusters at ~2.50 and ~3.40 Ga. Euhedral to subhedral grains and fragments with preserved crystal faces predominate in the ~1.83 Ga group. Two analyses are more than 10% discordant and have not been used in assessing the age distribution. The remaining 38 concordant and near-concordant analyses have the same radiogenic $^{207}Pb/^{206}Pb$ within analytical uncertainty (MSWD=0.96) and yield a weighted mean age of 1,823.2±3.7 Ma. The 1.88 Ga group consists of 20 analyses, six of which are more than 10%
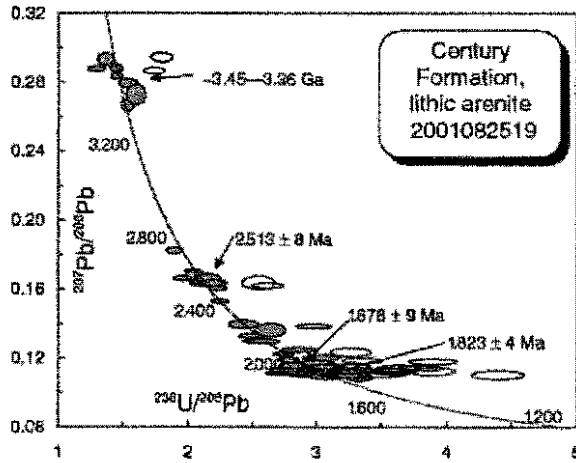
Fig. 11 Concordia plot of detrital zircon U-Pb analyses for lithic arenite sample 2001082519 from the Century Formation
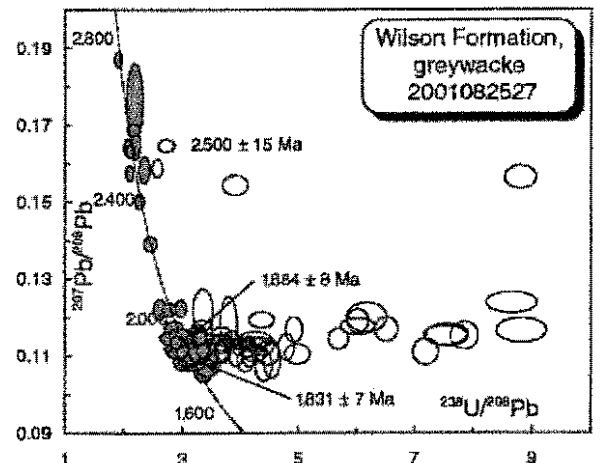
Fig. 12 Concordia plot of detrital zircon U-Pb analyses for graywacke sample 2001082527 from the Wilson Formation

discordant but all have the same radiogenic $^{207}Pb/^{206}Pb$ within error (MSWD=1.4). The weighted mean $^{207}Pb/^{206}Pb$ age of the 14 near-concordant analyses is 1,877.8±9.3 Ma.

The ~2.50 Ga group consists of a loose cluster of 14 analyses. Two of these are more than 15% discordant and are not considered further. The remaining 12 analyses are dispersed in radiogenic $^{207}Pb/^{206}Pb$ beyond analytical error (MSWD=2.4). The scatter is eliminated by removing the two lowest values (MSWD=1.5) leaving 10 that give a weighted mean age of 2,512.6±8.3 Ma. The ~3.40 Ga group consists of seven grains that range in apparent age from ~3.45 to 3.36 Ga.

Wilson Formation, graywacke (2001082527)

Sample 2001082527 was collected from a low lying outcrop of tightly folded, thick-bedded, graded, granular conglomerate and graywacke located about 2 km east of the Crusade Au prospect (Table 1). This graywacke is poorly sorted, consisting of rounded to sub-rounded monocrystalline quartz grains with lesser lithic fragments, polycrystalline quartz and feldspars ~4 mm in diameter, in a matrix of finer grained angular feldspars and quartz grains in a sericitic groundmass. The zircon grains recovered range in diameter from 40 to 150 μm. Most are sub-rounded to rounded, turbid, fractured and metamict with well-defined visible growth zones in transmitted light. Approximately 20% of the grains are subhedral to euhedral, clear and colourless with some well-preserved crystal faces. There is also a minor population (~10%) of rounded to sub-rounded clear, colourless grains that have abraded surfaces.

One hundred and twenty grains were analyzed (S9, Fig. 12). U contents are mostly low to moderate, (60 550 ppm, median 180), with the full range being 29 2,664 ppm. Th/U is moderate to very high (0.3 7, median 1.14). Common Pb contents are moderate to high (~0.05 6 ppm) and ~45% of the grains are moderately to strongly discordant. Most of the grains (~80%) have $^{207}Pb/^{206}Pb$ apparent ages that cluster between ~1.98 and ~1.76 Ga. There is a minor group at 2.50 Ga and scattering of ages between ~2.44 and ~1.99 Ga. Three grains have $^{207}Pb/^{206}Pb$ apparent ages less than 1.72 Ga but none give a reliable estimate on the primary age. Two of the grains (B27.2, B40.1) are U-rich and their ages are extremely discordant (~80%), the third (B42.1) has a high common Pb content.

The dominant grouping consists of 93 analyses that are dispersed beyond analytical uncertainty (MSWD=3.1). This population is bimodal with a dominant cluster at ~1.83 Ga and a minor cluster at ~1.89 Ga. The ~1.83 Ga cluster consists of 57 analyses ~35% of which are greater than 10% discordant. All analyzed compositions in this group, plot within error on a single discordance line (MSWD=0.97) with concordia intercept ages at 1,831.7±6.1 and 3±40 Ma. The lower concordia intercept age indicates that Pb loss has taken place very recently. In that case, the best estimate of the zircon crystallization age can be obtained from the radiogenic $^{207}Pb/^{206}Pb$ of the least discordant analyses. The 36 analyses that are less than 10% discordant are within analytical error (MSWD=1.08) and give a weighted mean age of 1,830.9±6.5 Ma.

The 1.89 Ga cluster comprises of 36 analyses, ~55% of which are greater than 10% discordant. The 16 concordant and near concordant analyses from this group have the same radiogenic $^{207}Pb/^{206}Pb$ within analytical uncertainty (MSWD=0.48) and yield a weighted mean age of 1,883.8±8.4 Ma. The older ~2.50 Ga group consists of four concordant and near concordant analyses that have the same radiogenic $^{207}Pb/^{206}Pb$ (MSWD=0.39) and give a weighted mean age of 2,500±15 Ma.

17

Mount charles formation, arkose (2003082644)

Sample 2003082644 was collected from a massive bed of medium-grained arkose exposed in the western side of Jims Pit located about 30 m below ground level (Table 1). The sample is a dark grey medium-grained arkose with rare rounded chert and/or siltstone intraclasts up to 8 mm in diameter. It is very strongly sericitised, containing a poorly sorted matrix of angular and sub-angular altered feldspars, quartz, lithic grains, rounded polycrystalline quartz and 20 30% opaque Fe Ti oxides.

Zircon grains recovered comprise a range of shapes and sizes, in the range of ~40 to ~200 μm in diameter. The majority are stubby, subhedral to euhedral, clear, colourless prisms and crystal fragments with few fractures or inclusions. About 30% of the grains have abraded surfaces and almost all have some preserved crystal faces. Less than 5% have faintly visible growth zones in transmitted light. Luminescence ranges from dull to bright, but most are moderately luminescent. Fine oscillatory and broadly diffuse growth zones predominate.

One hundred and two grains were analyzed (S10, Fig. 13). U contents are low to moderate (18 250 ppm), with one value higher (B24.2, 390 ppm), and Th/U moderate to high (0.14 2.8, median 0.6). Common Pb contents are uniformly low (<0.01 0.8 ppm) and 10% of the analyses are moderately to strongly discordant. The sample comprises three distinct age clusters, a dominant grouping at ~2.50 Ga and two minor groups at ~3.50 3.32 and ~1.91 Ga. The dominant grouping consists of 80 analyses, nine of which are greater than 10% discordant and are not considered further. The concordant and near-concordant grains scatter in radiogenic ^{207}Pb/^{206}Pb more than expected from the analytical uncertainties (MSWD=2.9). This scatter can be reduced but not eliminated by omitting

Fig. 13 Concordia plot of detrital zircon U–Pb analyses for arkose sample 2003082644 from the Mount Charles Formation

two of the highest values (MSWD=1.8). No other omissions can be justified. The median age for the remaining grains is 2,503.6+4.4/−5.8 Ma. The oldest zircon grains in this sample comprise seven grains that have apparent ^{207}Pb/^{206}Pb ages between 3.50 and 3.32 Ga. Four of these grains are within analytical uncertainty (MSWD=0.66) and have a weighted mean age of 3,421.6±6.4 Ma. The ~1.91 Ga group is made up of euhedral crystals and crystal fragments with preserved faces. Zircon grains from this group generally has Th/U>1. Nine analyses on eight grains have the same radiogenic ^{207}Pb/^{206}Pb within analytical uncertainty (MSWD=1.7), and give a weighted mean age of 1,913±18 Ma.

Mount Charles formation, arkose (2001082507)

Sample 2001082507 was collected from a massive bed of coarse-grained arkose exposed in the western side of the Hurricane-Repulse Pit approximately 20 m below ground level (Table 1). Petrographically, it is similar to sample 2003082644. The sample consists of angular and sub-angular quartz, feldspar and rounded polycrystalline quartz grains in a matrix of strongly sericitised, mostly angular lithic fragments.

Zircon grains recovered comprise a mixed population of shapes with a wide range in size (20 200 μm diameter). The majority (~70%) are sub-rounded, optically turbid, metamict, highly fractured with well-defined visible growth zones in transmitted light and abraded surfaces. Other zircon grains are clear, colourless and subhedral to euhedral, many have preserved crystal faces and only rarely do they show signs of abrasion. The CL response from the turbid, metamict zircon grains is dark and provides little information on the internal zoning characteristics of these grains. The clear, colourless zircon grains however, are dull to brightly luminescent and reveal a predominance of fine concentric growth zoning over sector-zoned crystals.

Sixty analyses were made on zircon grains from this sample (S11, Fig. 14). There is a large range in U content (36 2281, median 150) and, with one exception, moderate to high Th/U (0.42 4.2). Common Pb contents are moderate to high (~0.05 6 ppm) and ~50% of the grains analyzed are moderately to strongly discordant. These analyses show no correlation between radiogenic ^{207}Pb/^{206}Pb and discordance, and because the age of the Pb loss is not known, they have been excluded from the age assessment for this sample. The remaining 30 concordant and near concordant analyses principally cluster at ~3.42 and ~1.91 Ga. The older grouping consists of eight grains that have constant radiogenic ^{207}Pb/^{206}Pb within analytical uncertainty and give a weighted mean age of 3,419.2±3.6 Ma. Zircon grains in the youngest ~1.91 Ga grouping consists of euhedral to subhedral grains with preserved crystal faces and Th/U generally >1. These 10 analyses have the same radiogenic
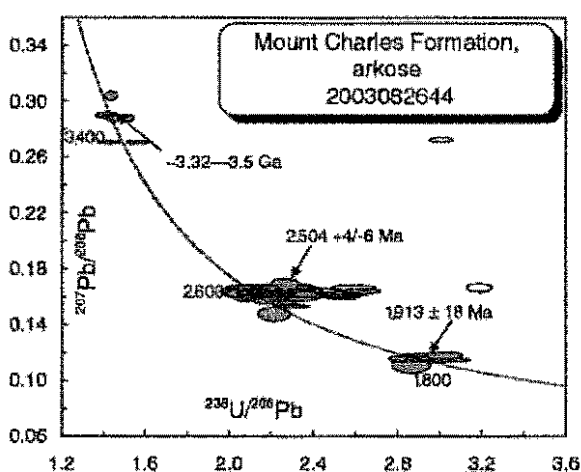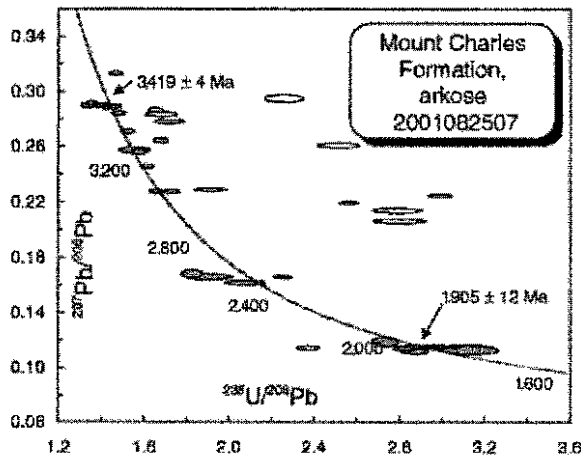
Fig. 14 Concordia plot of detrital zircon U–Pb analyses for arkose sample 2001082507 from the Mount Charles Formation

Fig. 15 Concordia plot of detrital zircon U–Pb analyses for quartz arenite sample 2001082517 from the Pargee Sandstone

^{207}Pb/^{206}Pb within analytical uncertainty (MSWD=1.8) and give a weighted mean age of 1,905±12 Ma.

Pargee Sandstone, quartz arenite (2001082517)

Sample 2001082517 was collected in the Pargee Hills area, from a low lying sequence of thickly bedded medium to coarse grained sandstone and conglomerate, located about 250 m south of the contact with the unconformably overlying Gardiner Sandstone (Table 1). The sample is a red, medium-grained, moderately well-sorted quartz arenite, with rounded to sub-rounded quartz grains and rare sub-rounded lithic fragments. The zircon grains recovered comprise a wide range of shapes, colours and sizes that range from ~50 to 150 μm in diameter. The vast majority are equant, sub-rounded to rounded grains and range from turbid and brown in colour to clear and colourless. Many grains are highly fractured which in the majority of cases made SHRIMP-spot overlaps onto these fractures unavoidable. The zircon grains have well-defined visible growth zones in transmitted light and almost all have abraded surfaces. Most grains have a moderate to bright CL with oscillatory growth zones, and ~20% have rounded cores. Approximately 20% are dull in CL and give little or no information on their internal growth zones.

One hundred and eleven grains were analysed from this sample (S12, Fig. 15). Many of these analyses (~40%) are moderately to strongly discordant which is consistent with the highly fractured nature of many of the zircon grains in this sample. Forty-five analyses that are greater than 10% discordant are not considered further. The remaining 66 analyses have low to moderate U contents (27–250 ppm), moderate Th/U (0.4–1.4), and low to moderate common Pb contents (<0.01–2 ppm). The ^{207}Pb/^{206}Pb apparent ages are scattered between ~3.37 and 1.73 Ga with clusters at ~2.53
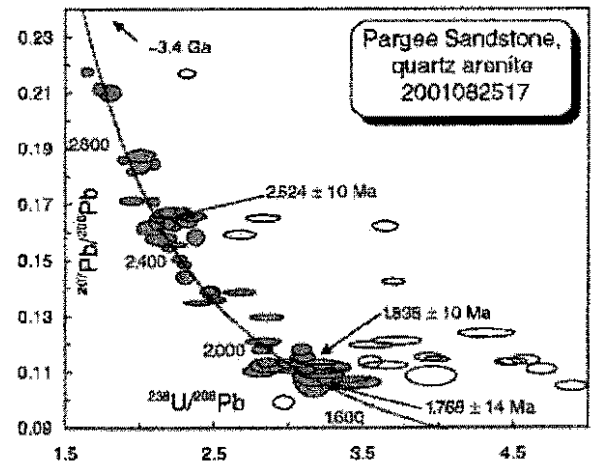
and ~1.80 Ga. The youngest cluster comprises 25 analyses that are dispersed in radiogenic ^{207}Pb/^{206}Pb apparent ages (MSWD=8). This population is bimodal with a dominant grouping at ~1.83 Ga and a minor one at ~1.77 Ga. The dominant grouping consists of 13 analyses that are dispersed in radiogenic ^{207}Pb/^{206}Pb (MSWD=2.1). This scatter can be eliminated by removing the highest value (MSWD=1.3), the remaining analyses combine to give a weighted mean age of 1,835.4±9.8 Ma. The minor group is made up of 12 analyses that all have the same radiogenic ^{207}Pb/^{206}Pb (MSWD=1.7), and combine to yield an age of 1,768±14 Ma. The oldest grouping comprises nine analyses that have the same radiogenic ^{207}Pb/^{206}Pb (MSWD=1.6) and combine to give a weighted mean age of 2,524±10 Ma. There are also minor peaks at ~2.70 and ~2.21 Ga.

Gardiner Sandstone, sublitharenite (2003082642)

Sample 2003082642 was collected from an outcrop of thickly bedded, massive, purple sandstone in the Coomarie Range (Table 1). The sample is well sorted and consists of about 80% sub-angular to sub-rounded quartz and about 15% fine-grained sedimentary and meta-sedimentary lithic clasts. The zircon grains recovered are remarkably uniform in diameter (~70–100 μm). They are clear and colourless, with relatively few fractures or inclusions. The majority are equant, rounded to sub-rounded, and 70–80% have abraded surfaces. Rare grains (<5%) have some preserved crystal faces. CL imaging shows that most grains have fine oscillatory growth zones. There is also a lesser population of crystals that show diffuse banding and sector zoning.

Ninety-three analyses are listed in S13 and plotted in Fig. 16. The analyzed zircon grains have low to moderate U contents (~30–270 ppm, median 130) and Th/U (0.15–1.68, median 0.51). Common Pb contents are uniformly low
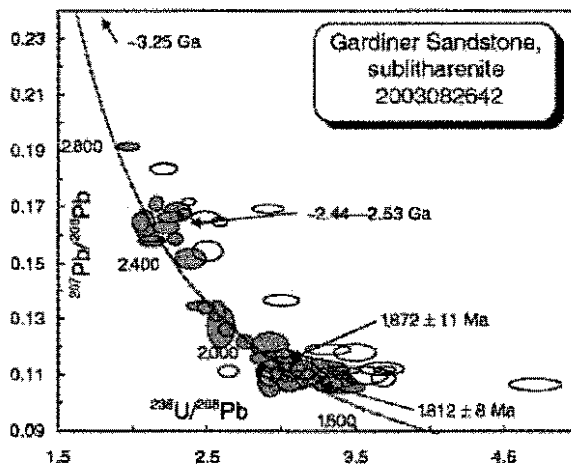
Fig. 16 Concordia plot of detrital zircon U–Pb analyses for sublitharenite sample 2003082642 from the Gardiner Sandstone

(<0.01 0.6 ppm) and approximately 20% of the analyses are moderately discordant. The $^{207}Pb/^{206}Pb$ apparent ages range between ~3.25 and ~1.74 Ga with a dominant cluster at ~1.83 Ga (70%) and a minor cluster at ~2.50 Ga. The 65 analyses in the youngest grouping do not define a single discordance line. Considering only the analyses that are less than 10% discordant, there is significant dispersion in radiogenic $^{207}Pb/^{206}Pb$ (MSWD=4.1). This population is bimodal, forming a dominant group at ~1.81 Ga and a subordinate one at ~1.87 Ga. The dominant group comprises 36 analyses that have equal $^{207}Pb/^{206}Pb$ within error

(MSWD=1.4) and combine to give a weighted mean age of 1,812.2±7.9 Ma. The subordinate group comprises 18 analyses that have the same radiogenic $^{207}Pb/^{206}Pb$ (MSWD= 1.7) and combine to give a weighted mean age of 1,872± 11 Ma. The 2.50 Ga group comprises six analyses that range in apparent $^{207}Pb/^{206}Pb$ age between 2.53 and 2.44 Ga.

Discussion

The detrital zircon age distributions displayed in Fig. 17 comprise 12 samples from the six principal sedimentary units in the Tanami Region, and the depositional age estimates for these units are shown in Table 2. The data in Fig. 17 demonstrate that all units contain zircons with an age mode of ~2.50 Ga. In addition, with the exception of the Mount Charles Formation, all units younger than the Ferdies Member of the Dead Bullock Formation are dominated by Paleoproterozoic detritus with an age mode between ~1.89 and ~1.84 Ga. The Ware Group samples contain a youngest zircon component between ~1.83 and ~1.82 Ga and only in the youngest Pargee and Gardiner Sandstone do ~1.80 Ga zircon components appear. The Ferdies Member contains zircon grains with age groups of ~3.20, ~2.70 and ~2.50 Ga (Fig. 17). These ages contrast markedly with younger sedimentary units in the Tanami Region. The Mount Charles Formation is also dominated by zircons with Archean ages but in addition, contains a youngest detrital component at ~1.91 Ga, which is about 100 Ma older than its depositional age as suggested by Crispe et al. (2006).

Table 2 Depositional age estimates for the principal sedimentary sequences in the Tanami Region

Unit	OZCHRON Number	Max. age (Ma) (detrital zircon)	Max. Age (Ga)	Min. age (Ga)
Ferdies Member	2003082647	2,533±3	~2.11[a]	~1.84 Ga[b]
Ferdies Member	2003082649	2,109±20	~2.11[a]	~1.84 Ga[b]
Killi Killi Formation	2001082021	1,866+3/ 8	~1.84[b]	~1.82 Ga[e]
Killi Killi Formation	2001082505	1,864±5	~1.84[b]	~1.82 Ga[e]
Killi Killi Formation	2001082515	1,868+5/ 6	~1.84[b]	~1.82 Ga[e]
Killi Killi Formation	2001082036	1,867+9/ 13	~1.84[b]	~1.82 Ga[e]
Ware Group	2001082519	1,823±4	~1.82[c]	~1.80 Ga[f]
Ware Group	2001082527	1,831±7	~1.82[c]	~1.80 Ga[f]
Mount Charles Formation	2003082644	1,913±18	~1.82[e]	~1.80 Ga[f]
Mount Charles Formation	2001082507	1,905±12	~1.82[e]	~1.80 Ga[f]
Pargee Sandstone	2001082517	1,768±14	~1.77[d]	~1.64 Ga[g, h]
Gardiner Sandstone	2003082642	1,812±8	~1.77[d]	~1.64 Ga[g, h]

[a] Age of youngest detrital zircon in Ferdies Member sample 2003082649 (this study)
[b] Crystallisation age for sample of tuff in Callie Member (this study)
[c] Contemporaneous felsic volcanism in Ware Group
[d] Age of youngest detrital zircon population from Pargee Sandstone, sample 2001082517 (this study)
[e] Age of cross cutting igneous intrusion (Crispe et al. this volume)
[f] Inference from ages of cross cutting igneous intrusions (Crispe et al. this volume)
[g] SHRIMP U–Pb dating of diagenetic xenotime from Gardiner Sandstone (Vallini et al. this volume)
[h] Correlation of Gardiner Sandstone with rocks in the Victoria River Basin which are overlain by the ~1.64 Ga Limbunya Group (Cutovinos et al. 2002)

Fig. 17 Probability density distribution diagrams comparing detrital zircon U–Pb ages for analyzed samples from this study with data from: Cross et al. (2005b) for the Lander Rock beds (2002082504); Cross et al. (2005c) for the 'Prickle Hill' sandstone (2001082549); Cross et al. (2005a) for the Acacia Gap Quartzite (2001082542) and Beestons Formation (2001082533). *Grey vertical lines* are common major age peaks at ~2.50 and ~1.87 Ga

Tanami

Arunta Region

Pine Creek Orogen
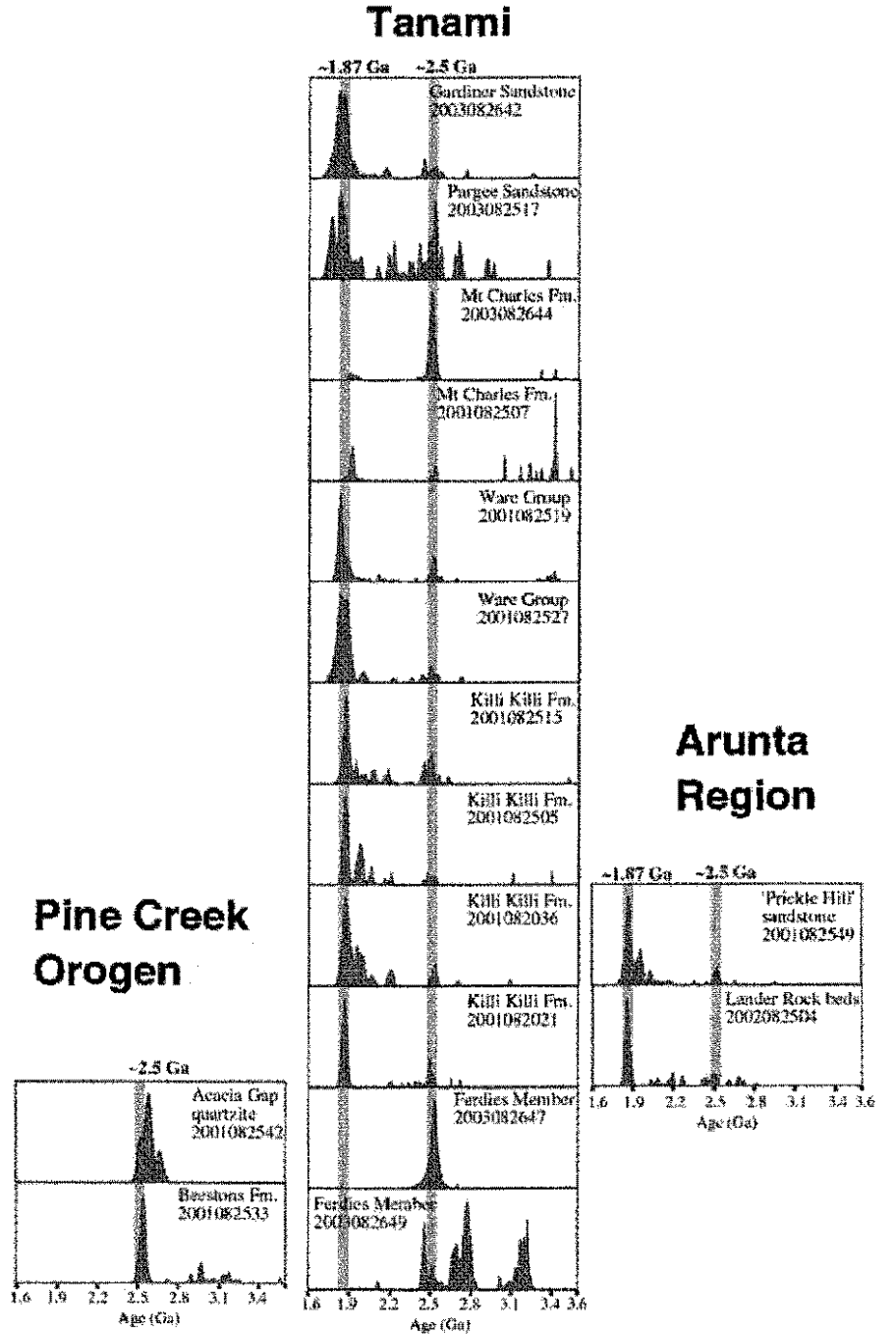
The tuffaceous sample from the Callie Member of the Dead Bullock Formation (2001082511) represents the only volcanic rock to have been isotopically dated from the Tanami Group. Rare angular and euhedral grains of quartz, feldspar and zircon indicate a tuffaceous origin. The zoned zircons strengthen this interpretation. Isotopically, they

record a single U Pb age. Morphologically they are homogenous, pristine, euhedral zircon grains with axial inclusions a feature typical of volcanic zircon. Features that would indicate an intrusive origin for this unit, such as contact metamorphism in local rocks, or chilled margins with adjacent units were not observed at the sample site. It

21

is for the above reasons that we interpret this sample as tuffaceous in origin and likely to have been deposited contemporaneously with sediments of the Callie Member. The SHRIMP U–Pb age for this unit of 1,838±6 Ma provides an important constraint for the depositional chronology of the rocks included in the Tanami Group and early basin development.

Detrital zircon depositional age estimates

Ferdies member of the dead bullock formation

Zircon grains from the Ferdies Member arkose (2003082647) sampled from the Groundrush region define a maximum deposition age of 2,533±3 Ma, whereas a feldspathic arenite (2003082649) from the same unit at Dead Bullock Soak contains zircon grains that imply a deposition age after ~2.11 Ga. A minimum age of sedimentation for the Ferdies Member is provided by the overlying Callie Member felsic tuff (2001082511), which contains zircons that crystallized at 1,838±6 Ma (Table 2).

The timing of deposition for the Ferdies Member is poorly constrained between ~2.11–1.84 Ga. Therefore, estimates of the true age of deposition remain speculative. Two alternatives are possible. Firstly that there may be an extended depositional hiatus (i.e. cryptic unconformity) between the Ferdies and Callie Members of the Dead Bullock Formation lasting up to a maximum of approximately 270 Ma. A similar scenario to this has been detected in the Paleoproterozoic Hurwitz Group in the western Churchill Province of northern Canada. Using U–Pb dates from baddeleyite and detrital zircon, Aspler et al. (2001) detected a previously unrecognized time break of approximately 200 Ma across an internal cryptic unconformity. The second alternative is that the Archean detrital zircons found in the Ferdies Member were derived from the uplift of either Archean basement rocks or sedimentary rocks derived from Archean source rocks. In this scenario, uplift of these sources before ~1.84 Ga, during either the ~1.87–1.85 Hooper Orogeny, the ~1.87 Ga Nimbuwah Event or the early stages of the ~1.83 Ga Tanami Event shed detritus into the proto-Tanami basin. If this model is adopted, Ferdies Member sedimentation would have occurred between ~1.86 and 1.84 Ga. Of the two models presented in this study, we prefer the latter as the most likely as the Dead Bullock and Killi Killi Formations share a similar structural history and have been interpreted as conformable in numerous drill core intersections (see Crispe et al. 2006).

Killi killi formation

The youngest zircon component in all four samples from the Killi Killi Formation, provide a consistent maximum

depositional age estimate of between ~1.87–1.86 Ga. However, this unit is well constrained between the conformably underlying 1,838±6 Ma, Callie tuff (2001082511), and an intrusive contact with the 1.82 Ga Water Tower Tonalite (Crispe et al. 2006). Therefore, the Killi Killi Formation was deposited at least 20 Ma after the age indicated by its youngest detrital zircon component.

Ware group

The youngest detrital zircon component in the Century Formation (Ware Group), lithic arenite (2001082519) indicates a maximum deposition age of 1,823±4 Ma, whereas a graywacke from the Wilson Formation (2001082527) contains a youngest zircon component at 1,831±7 Ma. Similar ages have been measured in felsic volcanic units within the Ware Group. For example, a sample of rhyolite from the Mount Winnecke Formation has a SHRIMP U–Pb age of 1,824±5 Ma (Page 1995) and a dacite and felsic volcanic from the Nanny Goat Volcanic Complex have SHRIMP U–Pb ages of 1,816±7 and 1,821±5 Ma, respectively (Smith 2001). Crispe et al. (2006) suggest that minimum age constraints for sedimentation in the Ware Group can be inferred from the ~1.82–1.79 Ga, age of D_2 deformation, and the intrusion of the 1,815±5 Winnecke Granophyre.

For the two samples of sedimentary units in the Ware Group considered in this study, the youngest zircon grains constitute a minor population of euhedral and unabraded grains. Given their relatively pristine state, we consider them to be first-cycle sediments, and to have probably been derived from either one or a combination of nearby ca. ~1.82 Ga felsic volcanic rocks and granites. This indicates that sedimentation and volcanism associated with this group was broadly contemporaneous. Accordingly, we consider the maximum deposition age estimates for the two Ware Group sedimentary rocks analyzed for this study to be good approximations for their true depositional age.

Mount Charles formation

The ages of the youngest zircon component in both samples from the Mount Charles Formation are indistinguishable. Sample 2003082644 has a youngest component at 1,913± 18 Ma, while the youngest grains analyzed from 2001082507 crystallized at 1,905±12 Ma. Page (1998) obtained similar results to these in another detrital zircon SHRIMP U–Pb study of a sediment from the Mount Charles Formation. In this study, Page (1998) calculated a maximum deposition age of 1,916±8 Ma, (MSWD=1.66) from the youngest 14 grains analyzed.

The ~1.91 Ga detrital zircon from our Mount Charles samples and that of Page (1998) share similar morphological

and chemical characteristics. They all have preserved crystal faces with no signs of sedimentary abrasion and have Th/U> 1. The youngest component from all three samples have the same radiogenic $^{207}Pb/^{206}Pb$ within analytical uncertainty (MSWD=1.16) and combine to give an age of 1,913±6 Ma.

The absence of D_1–D_3 deformation in rocks included in the Mount Charles Formation, aplite dyke intrusions, and also contact metamorphism associated with Grimwade suite granites have led Crispe et al. (2006) to suggest a depositional age for the Mount Charles Formation at ~1.80 Ga. This is 100 Ma younger than the ~1.91 Ga age of the youngest zircon grains in the three samples examined in this study.

Pargee Sandstone and Gardiner Sandstone

The youngest detrital zircon component analyzed from the Pargee Sandstone (2001082517) crystallized at 1,768± 14 Ma. In contrast, the youngest zircons from the unconformably overlying Gardiner Sandstone (2003082644) records an age of 1,812±8 Ma, about 45 Ma older than zircons from the Pargee Sandstone. Clearly, the detrital zircon maximum deposition age estimate for the Gardiner Sandstone does not approximate the true age of sedimentation.

There are no direct minimum age constraints for the deposition of the Pargee Sandstone. Therefore, controls on the timing of sedimentation for the Gardiner Sandstone offer the only geological constraints for the minimum age of deposition for the Pargee Sandstone. The upper limit for sedimentation in the Gardiner Sandstone is constrained by diagenetic xenotime growth at 1,632±3 Ma (Vallini et al. 2006) and the ~1.64 Ga age of Limbunya Group rocks, which were interpreted in drill core by Cutovinos et al. (2002) to overlie Birrindudu rocks in the Victoria River Basin, north of the Tanami Region. Therefore, the timing of sedimentation for both the Pargee Sandstone and Gardiner Sandstone is currently loosely constrained to between ~1.77 and ~1.64 Ga. The depositional age constraints from the six principal sedimentary units from the Tanami Region outlined above show that sedimentation occurred at least between the period ~1.84–1.77 Ga.

The above examples emphasize the importance of isotope studies of intercalated volcanic units to reliably determine the deposition age of non-fossiliferous sedimentary rocks. An alternative to this approach, is to date diagenetic minerals (such as monazite and xenotime) (see Vallini et al. 2006).

Source of detrital zircon

Ferdies member—dead bullock formation

The detrital zircon age distributions in the basal Ferdies Member samples discussed in this study are remarkably

different compared to other Tanami sedimentary units. Ferdies Member samples are almost entirely composed of Archean aged detritus and lack the ~1.86 Ga zircon that is a principal component in most younger samples (Fig. 17).

Detrital zircon grains from the Ferdies Member arkose 2003082647 constitute a unimodal age peak at ~2.53 Ga. This rock is clearly derived from a restricted late Archean source. Known rocks of this age in the NAC occur in the nearby Billabong Complex, where Page et al. (1995) have interpreted an age of 2,514±3 Ma, and in the Rum Jungle Complex where the earliest phase of granite intrusion occurred at ~2.53 Ga (Cross et al. 2005a). The wide range in morphology of these zircon grains (euhedral to rounded and sometimes pitted) probably reflects both proximal and more distal sources. Therefore, we consider it possible that these zircon grains could have been derived from either of the above regions, a combination of both or an exotic source. Detrital zircon SHRIMP studies from two sedimentary rocks from the Pine Creek Orogen share similar zircon age distributions to the Ferdies Member arkose 2003082647. The Acacia gap Quartzite Member of the Wildman Siltstone, and the Beestons Formation which rests unconformably on the Archean Rum Jungle Complex are both dominated by detrital zircon approximately 2.50 Ga old (Fig. 17; Cross et al. 2005a). This could indicate the once widespread occurrence of NeoArchean crust across much of northern Australia.

Feldspathic arenite (2003082649) from the Ferdies Member has age modes at ~3.20, ~2.78, ~2.70 and ~2.45 Ga. It is possible that a large percentage of these zircon grains are derived from the Pilbara Craton in Western Australia. The ~3.20 Ga zircon grains can be correlated with the ~3.27 to 3.23 Ga Cleland Supersuite of the western part of the Pilbara Craton (Van Krandendonk et al. 2004) and the ~2.78 age mode with magmatism associated with the Fortescue Group (Nelson 1999). The ~2.45 Ga age mode may in part be derived from the Pine Creek Orogen, or alternatively from magmatism in the Pilbara region between ~2.60 and 2.45 Ga that was associated with the Hamersley Group (Thorne and Trendall 2001).

Killi killi formation

Detrital zircon age distributions from four samples of Killi Killi Formation are remarkably similar. Each is dominated by a zircon population that crystallized at ~1.87 Ga, with a subordinate age group at ~2.50 Ga (Fig. 17). The dominant zircon component could have been derived from one or a combination of similarly aged rocks in Northern Australia. These include magmatic rocks from the Pine Creek and Litchfield provinces (Worden et al. 2004; Needham et al. 1988), the Halls Creek Orogen (Blake et al. 2000) and Tennant Creek Region (Compston 1995 and Smith 2001).

23

The dominant ~1.87–1.86 Ga zircon grains from the four samples of Killi Killi Formation are likely to represent first-cycle sedimentary components because they are typically equant subrounded prisms with ~5% having retained their crystal faces. Furthermore, when sedimentary pitting on zircon exteriors is present, it is usually faint. This is in contrast to the NeoArchean zircon grains that are typically well rounded and have a marked pitting on grain exteriors, which is indicative of a longer history of sedimentary transport and/or recycling. The Archean zircon grains in the Killi Killi Formation samples were probably recycled from underlying units such as the Ferdies Member, which contain a high percentage of zircons of this age. Alternatively, these zircon grains may have been derived from similarly aged granites and also clastic units that are dominated by late Archean zircon grains from the Pine Creek Orogen (see Cross et al. 2005a).

The detrital zircon age distributions in the four Killi Killi samples (this study) share close similarities to detrital zircons from the Lander Rock beds, southern Arunta (Cross et al. 2005b) and the 'Prickle Hill' sandstone, northern Arunta (Cross et al. 2005c) (Fig. 17). The similarities in the detrital zircon age distributions between these widely separated samples indicates that the Killi Killi Formation may have once been a part of a much larger depositional system.

Ware group

Detrital zircon grains from two samples of sedimentary rocks from the Ware Group have similar age distributions. Both are dominated by ~1.83 Ga detrital zircons, and like other units analyzed in this study, have a minor age population at ~2.50 Ga (Fig. 17). The detrital zircon age distributions for the Ware Group samples 2001082527 and 2001082519 are broadly similar to that of the Killi Killi Formation samples discussed above. Like the samples from the Killi Killi Formation, samples from the Ware Group contain a significant proportion of ~1.86 Ga detrital zircon. These zircon grains are characteristically mature with rounded to well-rounded morphologies. Only the younger, ~1.82 Ga, euhedral, non-abraded zircon grains present in samples from the group can be used to isotopically distinguish between sedimentary rocks in the Killi Killi Formation and Ware Group. We interpret that the similarity of detrital zircon age patterns in these samples indicates that the younger Ware Group may be largely derived from the recycling of the underlying, Tanami Group. The abraded morphology of the ~1.86 Ga, and Archean-aged zircon grains in the samples from the Ware Group supports this interpretation. Therefore, we consider that the Ware Group has mostly been derived from the recycling of sedimentary rocks in the Tanami Group with a relatively minor input of ~1.83–1.82 Ga volcanics and granites derived from local sources.

Mount Charles formation

Detrital zircon age distributions from two samples of arkose from the Mount Charles Formation are distinctive. Both are largely comprised of Archean-aged zircons. Sample 2003082644 is dominated by ~2.50 Ga zircons, while 2001082507 contains only a minor age group at ~2.50 Ga and is dominated by zircons that crystallized at ~3.40 Ga. Both samples also have a youngest component at ~1.91 Ga (Fig. 17). The older Archean-aged zircon grains in these rocks are rounded with pitted surfaces. The ~2.50 Ga zircon grains may have been derived from similarly aged granites in the Pine Creek Orogen or recycled from underlying units such as the Ferdies Member. The well-rounded morphology of Archean zircons from these two samples probably excludes a local granitic protolith such as the Billabong Complex as a source. The ~3.40 Ga zircon grains from sample 2001082507 represents the oldest zircon component measured during this study. These zircon grains may indicate a provenance from similarly aged rocks in the Pilbara Craton (Nelson 1999).

A possible source for the 1.91 Ga zircon component common to all Mount Charles samples examined is the Ding Dong Downs Volcanics. These rocks are comprised of mainly mafic and also felsic volcanics and form the basement to the eastern zone of the Halls Creek Orogen. The Ding Dong Downs Volcanics have a SHRIMP U–Pb age of 1,907±6 Ma and a granophyre from the same unit has a SHRIMP U–Pb age of 1,912±3 Ma (Blake et al. 1999). Zircons from the Ding Dong Downs Volcanics have Th/U ratios that are distinctively high and are often >1. Given that the youngest Mount Charles detrital zircon grains crystallized at ~1.91 Ga and also have Th/U ratios >1, we suggest that they may have been derived from the Ding Dong Downs Volcanics in the Halls Creek Orogen.

In contrast to the rounded and pitted surface textures of the Archean-aged zircon grains in the Mount Charles Formation, zircons from the 1.91 Ga population have retained crystal faces with no signs of sedimentary abrasion. The grains are therefore likely to represent first-cycle sedimentary detritus. Their pristine condition and presence in three samples from the Mount Charles Formation suggests that they may record the true age of sediment deposition, either representing the products of source region uplift and coeval magmatism, or contemporaneous volcanism. In addition, Archean zircon age distributions from the Mount Charles Formation, in particular sample 2003082644, are similar to the basal Ferdies Member arkose (2003082647) (Fig. 17). Significant also is the lack of any ~1.87 Ga zircon component in sedimentary rocks analyzed from the Mount Charles Formation. As pointed out earlier, this component is a major feature of the Killi Killi Formation, Ware Group,

Pargee Sandstone and Gardiner Sandstone. We interpret the presence of ~1.87 Ga zircon in sedimentary rocks younger than the Killi Killi Formation to be the result of reworking of underlying clastic units. Given that Crispe et al. (2006) place the Mount Charles Formation as overlying the Ware group and deposited at ~1.80 Ga, the apparent absence of ~1.87 Ga zircon grains in this unit is puzzling. If the Mount Charles Formation was deposited at ~1.91 Ga, it would require that this unit was in some way partitioned from the effects of three significant deformational events (D_1 to D_3) in the Tanami Region. The inference that the Mount Charles Formation may have been deposited before ~1.88 Ga has obvious implications for exploration. That is, that the Au-rich Mount Charles Formation may in fact underlie either the Callie Member, Killi Killi Formation or Ware Group.

An alternative explanation for the 1.91 Ga detrital zircon component in the Mount Charles samples is that they do not approximate the age of sediment deposition and were derived from a very restricted catchment that only eroded rocks of the Ding Dong Downs Volcanics, or age equivalents, together with older basement endowed with Archean zircons. Clearly further studies of the Mount Charles Formation are required to establish its true depositional age and stratigraphic position.

Pargee Sandstone and Gardiner Sandstone

Principal age groups in samples from the Pargee Sandstone (2001082517) and Gardiner Sandstone (2003082644) occur at ~2.70, ~2.0 and ~1.80 Ga. A younger population at ~1.76 Ga was only detected in the Pargee Sandstone sample. Scrimgeour (2003) has suggested that this component was probably related to magmatic events associated with the Late Strangways Orogeny in the Arunta Region.

Older zircon grains from the Pargee and Gardiner Sandstones are predominantly well rounded with pitted surfaces indicative of a long history of sedimentary transport and reworking. These grains were probably derived from underlying sedimentary rocks in the Tanami Group.

Considered collectively, detrital zircon grains from the Killi Killi Formation, Ware Group, Pargee Sandstone and Gardiner Sandstone are characterized by a high percentage of ~1.86 Ga grains with a minor component at ~2.50 Ga. The ~1.86 Ga component from these samples shows a progression in zircon rounding from their appearance in the Killi Killi Formation to the top of the sequence in the Gardiner Sandstone. Detrital zircons in the Killi Killi Formation is predominantly sub-rounded with rare signs of surface abrasion, whereas zircon grains from the Gardiner Sandstone is predominantly rounded and 70–80% of grains have abraded surfaces. We interpret the presence of the ~1.86 Ga and ~2.50 Ga age populations in all of these units, and the successive rounding of the ~1.86 Ga zircon

component from older to younger units, to indicate that recycling of underlying sediments has played a major role in supplying detritus to younger sequences.

Early development of the Tanami Basin

Reassessment of Browns Range Dome granite sample 88495008

A sample of granite (88495008) from the Browns Range Dome in the north west of the Tanami Region was interpreted from a SHRIMP U Pb zircon study by Page et al. (1995) to have crystallized at 2,510±22 Ma and to have undergone high-grade metamorphism at either ~1.97 or ~1.88 Ga. The latter (~1.88 Ga) age interpretation for this sample has been used by Hendrickx et al. (2000) as evidence for the initial extension associated with the early development of the Tanami Basin. To access the evidence for this proposed ~1.88 Ga metamorphism, the original SHRIMP mount with zircon from the granite sampled from the Browns Range Dome was re-examined using CL imaging, a technique unavailable to the original researchers.

Zircons from this sample have a diverse array of sizes and shapes. They dominantly constitute rounded to well-rounded concentrically and sector-zoned zircon cores that are overgrown by highly metamict, dark luminescence response overgrowths up to 100 μm in thickness. Concordant and near-concordant compositions range in apparent age between ~3.42 to ~1.87 Ga and fall into three loosely defined groups of ~3.15 to 3.04 Ga ($n=6$), ~2.67 to 2.44 Ga ($n=8$) and ~1.99 to 1.87 Ga ($n=9$). There are also two zircon grains at ~2.31 and ~2.26 Ga and two older grains at ~3.42 and ~3.24 Ga (Fig. 18). The nine concordant and near-concordant compositions that range in $^{207}Pb/^{206}Pb$ age
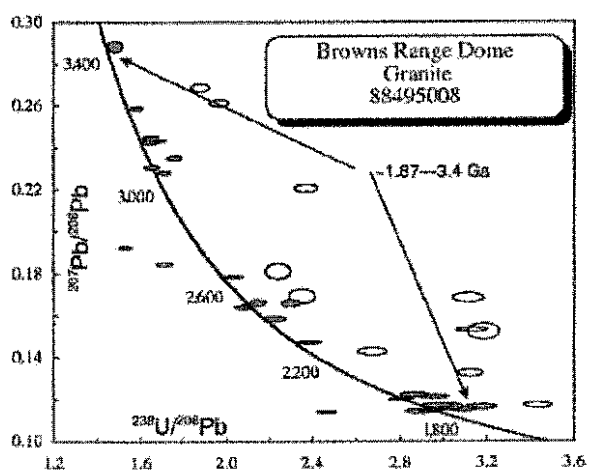
Fig. 18 Concordia plot of zircon U–Pb analyses for Browns range Dome granite sample 88495008

between ~1.99 and ~1.87 Ga (Table 3) were interpreted by Page et al. (1995) as recording the age of metamorphism in Browns Range Dome.

The precise location of each SHRIMP spot for analyses that ranged between ~1.99 and ~1.87 Ga were examined with reference to the new CL images. These images showed that each SHRIMP spot was entirely centred on concentrically or sector zoned, luminescent, rounded to well-rounded zircon cores (for example, Fig. 19). We interpret these internal zoning features and high degree of rounding of these cores to be more characteristic of zircon grains that have crystallized from an igneous melt and later rounded during sedimentary transport, rather than zircon that has grown and/or re-crystallized under metamorphic conditions.

Zircons that have grown or re-crystallized under metamorphic conditions generally has Th/U<1 (Hoskin and Black 2000; Williams 2001) and is often very poorly luminescent. Regions in zircons that have been re-crystallized can appear as lobate, poorly luminescent patches discordant to the primary growth zones (e.g. Hoskin and Black 2000). In contrast, new zircon growth under metamorphic conditions usually forms poorly luminescent new crystals (Williams 2001) or precipitates as an overgrowth onto a protolith zircon core (Williams 2001; Tyler et al. 1999). Although almost all zircon grains from this sample have thick, poorly luminescent overgrowths, these are highly metamict and when targeted with the SHRIMP, yielded grossly discordant ages.

Th/U ratios for the nine analyses between ~1.99–1.88 Ga, are generally low, ranging from 0.19–0.02. Four analyses have Th/U less than 0.1, and the remaining five range between 0.13 and 0.19. Although some of these Th/U ratios are <0.1, by themselves, they cannot be used to diagnose a metamorphic origin. The majority remain within the normal range for zircons from felsic igneous rocks (1–0.1:Williams 2001). Furthermore, Th/U ratios for the older, Archean

zircons in this sample vary widely between 0.04 and 1.66 with no apparent pattern.

The morphological characteristics of these zircon grains, as seen in the CL images, is thought to be diagnostic of their origins. The interpretation of Page et al. (1995) that these zircon grains formed by metamorphic processes within their host granite is inconsistent with these new observations. They are better interpreted to represent inherited components possibly from a meta-sedimentary protolith. By inference therefore, the Archean crystallization age attributed to this granite must also represent an inherited component. The youngest three analyses from this sample combine to give a weighted mean age of 1,874±10 Ma, and can be used as a maximum emplacement age for this rock.

Proposed model for the early evolution of the Tanami Basin

With the removal of the evidence for a ~1.88 Ga event to have affected Tanami rocks in the Browns Range Dome, the model for the early evolution of the Tanami Basin can be revised. To do this, understanding the timing of the earliest sediment deposition of the Ferdies Member is crucial. However, there are no direct constraints on the timing of sedimentation for this unit. The oldest direct constraint for the minimum age of sedimentation for the Ferdies Member is the 1,838±6 Ma age of the overlying Callie tuff (2001082511). Therefore any ideas regarding the true deposition age of this sequence are speculative. However, as previously stated, we believe that the early development of the Tanami basin to have occurred between ~1.87 and 1.84 Ga. This interpretation is partly supported by the ~1,864 Ma age of the Bald Hill sequence in Western Australia (cited in Huston et al. 2006). This unit may represent one of the earliest sedimentary units in the Tanami Region.

Table 3 SHRIMP U–Pb isotopic data for zircons (~1.87–1.99 Ga) from granite in Browns Range Dome (88495008)

Spot name	U (ppm)	Th (ppm)	Th/U	^{206}Pb (ppb)	^{238}U/^{206}Pb (±1σ %)		^{207}Pb/^{206}Pb (±1σ %)		^{207}Pb/^{206}Pb age (Ma±1σ)		Discordance (%)
19.1	240	45	0.19	138	0.3469	0.0043	0.1143	0.0007	1,869	11	−3
14.1	611	106	0.17	352	0.3401	0.0041	0.1145	0.0004	1,871	7	−1
17.1	415	55	0.13	858	0.3245	0.0040	0.1155	0.0008	1,888	12	4
28.1	890	43	0.05	2085	0.3154	0.0047	0.1163	0.0007	1,900	10	7
41.1	211	37	0.18	204	0.3316	0.0051	0.1165	0.0010	1,903	16	3
44.1	200	27	0.14	43	0.3372	0.0052	0.1169	0.0007	1,910	11	2
8.1	800	33	0.04	101	0.3572	0.0043	0.1202	0.0003	1,960	5	0
27.1	979	23	0.02	1074	0.3385	0.0051	0.1213	0.0005	1,975	7	5
31.1	1,003	28	0.03	2846	0.3496	0.0052	0.1222	0.0006	1,988	9	3

Isotope ratios are corrected for common Pb by reference to the measured abundance of ^{204}Pb
^{206}Pb denotes the amount of common ^{206}Pb measured

Fig. 19 Cathodoluminescence images of zircons from sample 88495008, which Page et al. (1995) used to interpret metamorphic events at ~1.99 or ~1.87 Ga. The SHRIMP spot locations are shown to have targeted rounded zircon cores (see text for discussion)
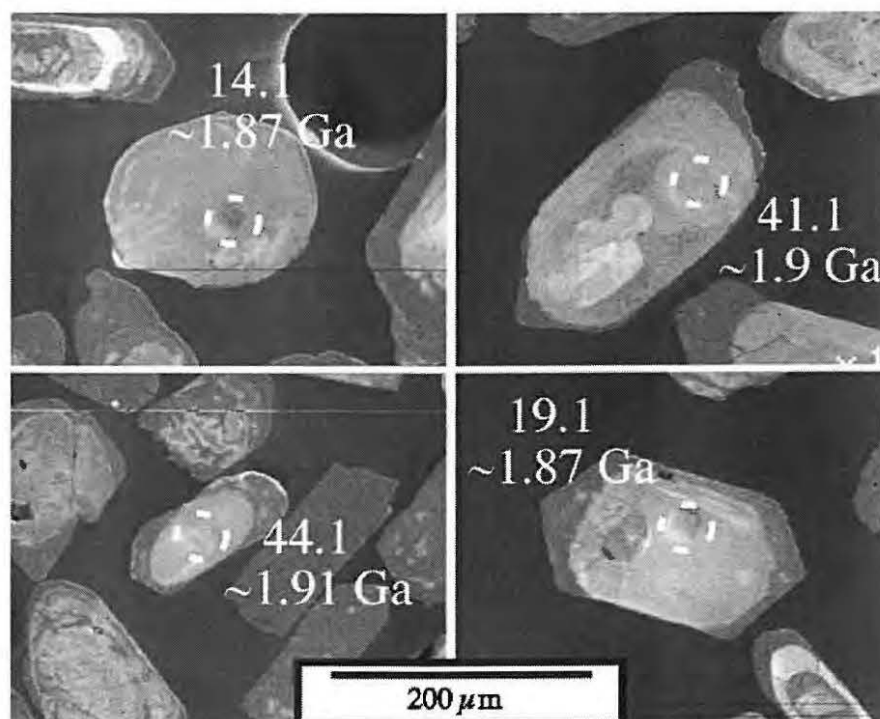
Initial uplift caused by either the ~1.87 1.85 Ga Hooper Orogeny (Halls Creek Orogen) and/or the Nimbuwah Event (Pine Creek Orogen) or alternatively, the very early stages of the ~1.83 Ga Tanami Event caused Archean basement rocks or sedimentary rocks derived from Archean sources to be shed into the Tanami basin forming the basal Ferdies Member of the Dead Bullock Formation. Between ~1.84 1.82 Ga the ~1.86 Ga voluminous products of the Hooper Orogeny and magmatism associated with the Nimbuwah Event were exposed, eroded and transported to form turbidite of the Killi Killi Formation. A similar significant age contrast in detrital zircons between basal and overlying sediments shed from an orogen has been observed by McLennan et al. (2001) in the lower Paleozoic rocks in the New England region of North America. These researchers also reported that the oldest sedimentary sequences do not record contemporaneous orogenic activity, but rather reflected older recycled continental margin rocks. Detrital zircon studies thus suggest that the first sediments shed from an emerging orogen might not record contemporaneous magmatism, but rather represent the eroded products of uplifted basement rocks.

Conclusions

The Paleoproterozoic Tanami basin probably developed between ~1.87 1.84 Ga in response to either the Hooper Orogeny (Halls Creek Orogen), Nimbuwah Event (Pine Creek Orogen) or very early stages of the Tanami Event. Initial uplift and erosion of Archean basement probably occurred between ~1.87 1.84 Ga and produced sediments now represented by the Ferdies Member of the Dead Bullock Formation. Its deposition age is loosely constrained between ~2.11 and 1.84 Ga. The extensive turbiditic sandstone units of the Killi Killi Formation can be correlated with the Lander Rock beds in the adjacent Arunta region. Killi Killi Formation turbidite was largely derived from the erosion of ~1.86 Ga orogenic granites and deposited at ~1.84 Ga. Detrital zircon ~2.50 Ga old, appears in all Tanami sediments investigated and with the possible exception of the Mount Charles Formation, ~1.86 Ga zircon components are present in all sediments younger than the Killi Killi Formation. The persistence of these age modes throughout the various units shows that recycling has played a major role in the development of the sedimentary successions of the Tanami basin.

Based primarily on structural grounds, the Mount Charles Formation is interpreted by Crispe et al. (2006) to have been deposited at ~1.80 Ga. However, this unit lacks the ~1.86 Ga component so prominent in sequences younger than the Killi Killi Formation and is dominated by Archean detritus with a youngest zircon component defining a maximum deposition age of ~1.91 Ga. One possible source for this component is the similarly aged Ding Dong Downs Volcanics in the eastern part of the Halls Creek Orogen. The

unabraded nature and preserved crystal faces of this zircon component indicate that they are first-cycle sediments and may record the timing of contemporaneous volcanism and by inference the depositional age of this unit. Alternatively, the youngest 1.91 Ga detrital zircon component in the Mount Charles Formation may not approximate the timing of sedimentation, but represent a derivation from a restricted catchment, that only eroded rocks endowed with Archean and ~1.91 Ga zircon components.

Detrital zircon grains from the Pargee Sandstone define a maximum deposition age of 1,768±14 Ma, whereas the youngest zircons from the overlying Gardiner Sandstone are ~40 Ma older, and crystallized at 1,812±8 Ma. Therefore, detrital zircons from the Gardiner Sandstone do not approximate its depositional age. There are no minimum age constraints for the deposition of the Pargee Sandstone other than the ~1.64 Ga constraint provided by the Gardiner Sandstone (Vallini et al. 2006; Cutovinos et al. 2002). Hence, timing controls for sedimentation of the Pargee Sandstone currently span ~40 Ma. Without firm minimum age controls for the deposition of this unit, the accuracy of the ~1.77 Ga, detrital zircon max deposition age cannot be determined. Clearly, further isotopic and field studies focussing on locating intercalated volcanic units and/or diagenetic minerals are needed to establish the depositional age and stratigraphic setting of the Mount Charles and Gardiner Sandstone units.

References

Aspler LB, Wisotzek IE, Chiarenzelli JR, Losonczy MJ, Cousens BL, McNicoll VJ, Davis WJ (2001) Palaeoproterozoic breakup of Kenorland to assembly of Laurentia: Hurwitz Basin, Nunavut, Canada. Sediment Geol 141–142:287–318

Black LP, Calver CR, Seymour DB, Reed A (2004) SHRIMP U–Pb detrital zircon ages from Proterozoic and Early Palaeozoic sandstones and their bearing on the early geological evolution of Tasmania. Aust J Earth Sci 51:885–900

Blake DH, Tyler IM, Griffin TJ, Sheppard S, Thorne AM, Warren RG (1999) Geology of the Halls Creek 1:100 000 Sheet area (4461), Western Australia. Australian Geological Survey Organisation, Canberra

Blake DH, Tyler IM, Page RW (2000) Regional geology of the Halls Creek Orogen. In: Hoatson DM, Blake DH (eds) Geology and economic potential of the Palaeoproterozoic layered mafic-ultramafic intrusions in the East Kimberley, Western Australia. Australian Geological Survey Organisation, Canberra, 246:35–62

Claoué-Long JC, Compston W, Roberts J, Fanning CM (1995) Two Carboniferous ages: a comparison of SHRIMP zircon dating with conventional zircon ages and 40Ar/39Ar analysis. In: Berggren WA, Kent DV, Aubrey M-P, Hardenbol J (eds) Geochronology time scales and global stratigraphic correlation. Society for Sedimentary Geology (Special Publication No. 4), pp 3–21

Compston D (1995) Time constraints on the evolution of the Tennant Creek Block, northern Australia. Precambrian Res 71:107–130

Compston W, Williams IS, Meyer C (1984) U-Pb geochronology of zircons from Lunar Breccia 73217 using a sensitive high mass-resolution ion microprobe. Proceedings of the 14th lunar and planetary science conference, part 2. J Geophys Res 89 (Suppl): B525–B534

Crispe AJ, Scrimgeour IR, Vandenberg LC (2006) Geological framework of the Palaeoproterozoic Tanami Region, Northern Territory. Miner Deposita (in press)

Cross AJ, Claoué-Long JC, Crispe AJ (2003) Summary of results. Joint NTGS-GA geochronology project: Tanami Region 2001–2002. Northern Territory Geological Survey, Record 2003-006

Cross AJ, Claoué-Long JC, Scrimgeour IR, Ahmad M, Kruse PD (2005a) Summary of results. Joint NTGS-GA geochronology project: Rum Jungle, basement to southern Georgina Basin and eastern Arunta Region 2001–2003. Northern Territory Geological Survey, Record 2005-006

Cross AJ, Claoné-Long JC, Scrimgeour IR, Close DF, Edgoose CJ (2005b) Summary of results. Joint NTGS-GA geochronology project southern Arunta Region. Northern Territory Geological Survey, Record 2004-003

Cross AJ, Claoné-Long JC, Scrimgeour IR, Crispe AJ, Donnellan N (2005c) Summary of results. Joint NTGS-GA geochronology project: northern Arunta and Tanami regions 2000–2003. Northern Territory Geological Survey, Record 2005-003

Cutovinos A, Beier PR, Kruse PD, Abbott ST, Dunster JN, Brescianini RF (2002) Limbunya, Northern Territory (Second Edition). 1:250 000 geological map series explanatory notes, SE 52–07. Northern Territory Geological Survey, Darwin

Hendrickx MA, Slater KR, Crispe AJ, Dean AA, Vandenberg LC, Smith JB (2000) Paleoproterozoic stratigraphy of the Tanami Region: regional correlations and relation to mineralisation—preliminary results. Northern Territory Geological Survey Record GS2000-13

Hoskin PWO, Black LP (2000) Metamorphic zircon formation by solid-state recrystallisation of protolith igneous zircon. J Metamorph Geol 18 4:423–439

Huston DL, Vandenberg L, Wygralak A, Mernagh T, Bagas L, Crispe A, Lambeck L, Cross A, Fraser G, Williams N, Worden K, Meixner T, Goleby B, Jones L, Lyons P, Maidment D (2006) Lode-gold mineralisation in the Tanami Region northern Australia. Miner Deposita (in press)

Ludwig KR (2000) Decay constant errors in U–Pb concordia-intercept ages. Chem Geol 166:315–318

Ludwig KR (2001) Squid 1.02: a users manual. Berkley Geochronology Centre Special publication No. 2

Ludwig KR (2003) Isoplot 3: a users manual. Berkley Geochronology Centre Special publication No. 4

McLennan SM, Bock B, Compston W, Hemming SR, McDaniel DK (2001) Detrital zircon geochronology of Taconian and Acadian foreland sedimentary rocks in New England. J Sediment Res 71:305–317

Needham RS, Stuart-Smith PG, Page RW (1988) Tectonic evolution of the pine creek inlier, northern territory. Precambrian Res 40/41:543–564

Nelson DR (1999) Chronological correlations between the Pilbara and Kaapvaal cratons. Precambrian Res 97:165–189

Nelson DR (2001) An assessment of the determination of depositional ages for Precambrian clastic sedimentary rocks by U–Pb dating of detrital zircons. Sediment Geol 141–142:37–60

Nutman AP, Bennett VC, Friend CRL, Rosing MT (1997) ~3710 and ≥3790 Ma volcanic sequences in the Isua (Greenland) supracrustal belt: structural and Nd isotope implications. Chem Geol 141:271–287

Page RW (1995) Sample 87495029. Unpublished data in Geoscience Australia OZCHRON database. http://www.ga.gov.au

Page RW (1998) Sample 94495025. Unpublished data in Geoscience Australia OZCHRON database. http://www.ga.gov.au

Page RW, Sun S-s, Blake D (1995) Geochronology of an exposed late Archean basement terrane in The Granite-Tanami region. AGSO Res Newsl 22:19–20

Scrimgeour IR (2003) Developing a revised framework for the Arunta Region. Annual Geoscience Exploration Seminar (AGES) Record of Abstracts, Northern Territory Geological Survey Record 2003–001

Smith JB (2001) Summary of results. Joint NTGS-AGSO age determination program 1999–2001. Northern Territory Geological Survey Record 2001-007

Smithies RH, Nelson DR, Pike G (2001) Development of the Archean Mallina Basin, Pilbara Craton, northwestern Australia; a study of detrital and inherited zircon ages. Sediment Geol 141–142:79–94

Stacey JS, Kramers JD (1975) Approximation of terrestrial lead isotope evolution by a two-stage model. Earth Planet Sci Lett 26:207–221

Thorne AM, Trendall AF (2001) Geology of the Fortesque Group, Pilbara Craton, Western Australia. Geological Survey of Western Australia Bulletin 144

Trendall AF, Compston W, Nelson DR, De Laeter JR, Bennett VC (2004) SHRIMP zircon ages constraining the depositional chronology of the Hamersley Group, Western Australia. Aust J Earth Sci 51:621–644

Tyler IM, Page RW, Griffin TJ (1999) Depositional age and provenance of the Marboo Formation from SHRIMP U–Pb zircon geochronology: implications from the early Palaeoproterozoic tectonic evolution of the Kimberley region, western Australia. Precambrian Res 95:225–243

Vallini DA, Groves DI, McNaughton NJ, Fletcher IR (2006) Uraniferous diagenetic xenotime in northern Australia and its relationship to unconformity-associated uranium mineralisation. Miner Deposita (in press)

Van Kranendonk MJ, Smithies RH, Wickman AH, Baggas L, Williams IR, Farell TR (2004) Event stratigraphy applied to 700 million years of Archean crustal evolution, Pilbara Craton, Western Australia. Geol Surv West Aust Annu Rev 2003–04:49–61

Williams IS (2001) Response of detrital zircon and monazite, and their U–Pb isotopic systems, to regional metamorphism and host rock partial-melting, Cooma complex, southeastern Australia. Aust J Earth Sci 48:557–580

Williams IS, Claesson S (1987) Isotopic evidence for the Precambrian provenance and Caledonian metamorphism of high grade paragneisses from the Seve Nappes. Scandinavian Caledonides. II Ion microprobe zircon U–Th–Pb. Contrib Mineral Petrol 95:205–217

Worden KE, Claoué-Long J, Scrimgeour I, Lally J (2004) Summary of results. Joint NTGS-GA geochronology project: August 2003–December 2003. Northern Territory Geological Survey, Record 2004–04

Wygralak AS, Mernagh TP, Huston DL, Ahmad M (2005) Gold mineral system of the Tanami Region. Northern Territory Geological Survey, Report 18

2. XENOTIME OCCURRENCE AND GEOCHEMISTRY

2.1 Introduction

Xenotime (YPO_4) is a widespread but volumetrically minor mineral that can occur in granites (e.g. Förster 1998; Wark & Miller 1993; Schaltegger et al. 2005), pegmatites (Amli 1975; Demartin et al. 1991), metapelites (Franz et al. 1996; Bea & Montero 1999), hydrothermal quartz veins (Brown et al. 2002; Cross et al. 2005), siliciclastic sedimentary rocks as authigenic overgrowths on detrital zircon (Rasmussen 1996) and also as a detrital mineral in placer deposits (Van Emden et al. 1997). Xenotime preferentially incorporates the HREE which substitute for Y and can also contain appreciable amounts of U, Th, Ca and Si. Xenotime has the zircon-type tetragonal structure and forms solid solutions with tetragonal thorite ($ThSiO_4$), zircon ($ZrSiO_4$), coffinite ($USiO_4$), hafnon ($HfSiO_4$) and pretulite ($ScPO_4$) (Förster 2006).

Xenotime crystals commonly have dipyramidal forms (similar to zircon). They occur as individual crystals or radial intergrowths, fine grained aggregates and also as pyramidal overgrowths on a zircon substrate. Colours range from yellowish, reddish, and brown to greenish. It has a perfect cleavage (100), a hardness of 4 to 5, specific gravity of 4.4 to 5.1 and is moderately paramagnetic. Optically it is uniaxial positive and weakly pleochroic (Vlasov 1966a).

With its low initial Pb concentrations, high U and Th contents, ability to self anneal radiation damage (Harrison et al. 2002) and closure temperature similar to that of zircon and monazite of approximately 900° C (Cherniak 2006), xenotime has many attributes of an excellent geochronometer. Xenotime in metamorphic rocks can also be used as a geothermometer. When xenotime coexists with monazite or garnet, the partitioning of Y is temperature dependant i.e. the monazite-xenotime miscibility gap (Gratz & Heinrich 1997; 1998; Andrehs & Heinrich, 1998; Heinrich et al. 1997) and the YAG–xenotime thermometer (Pyle & Spear 2000).

Recent applications of xenotime geochronology have been focussed on the U–Pb dating of hydrothermal and diagenetic xenotime which typically occur as overgrowths on detrital zircon, aggregates and individual grains < 20 μm in diameter. The minute size of these crystals has meant that the preferred method of in situ U—Pb analysis is

SIMS (Secondary Ion Mass Spectrometry), for which a spatial resolution of ~5 μm can be achieved (Fletcher et al. 2000).

2.2 Xenotime structure and chemistry

Xenotime has a tetragonal symmetry (ditetragonal dipyramidal) with the space group $I4_1/amd$ (identical to zircon). Each Y and/or HREE atom is surrounded by 8 oxygen atoms (Y/REO$_8$ polyhedra). The Y/REO$_8$ polyhedra are separated by an intervening PO$_4$ tetrahedron. Each of the O atoms in this structure is coordinated to two Y/HREE atoms and one P atom. The xenotime unit cell contains four polyhedron-tetrahedron chains which are linked laterally [in (001)] by sharing the edges of adjacent Y/REO$_8$ polyhedra. The xenotime structural unit therefore comprises chains of alternating PO$_4$ tetrahedra with intervening Y/REO$_8$ polyhedra (Fig. 2.1) (Ni et al. 1995). This structure preferentially accommodates Y and the similarly sized HREE (Ni et al. 1995).
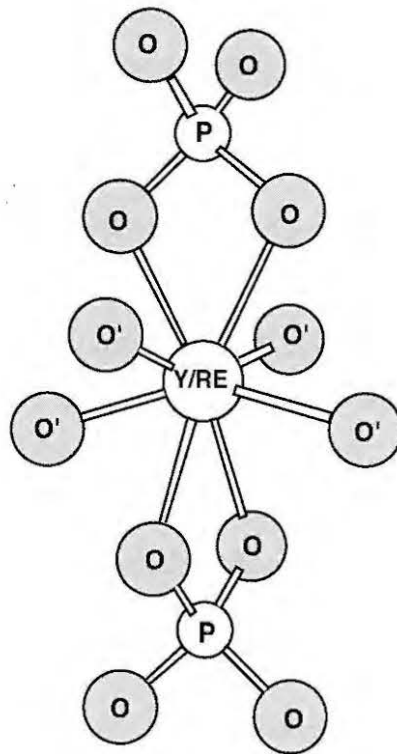
Fig. 2.1. Xenotime polyhedron-tetrahedron chain. Ball and stick depiction rotated about c axis (Ni et al. 1995).

The HREE elements (in particular Gd, Dy, Er, and Yb) substitute for Y owing to their very similar chemical properties. Indeed some authors as recently as the 1960's refer to the HREE Dy–Lu as the yttrium earths and/or the yttrium group lanthanides (see Vlasov 1966b). Electron microprobe analyses of natural xenotime show it to be variable in the relative proportions of Y and the HREE. Y_2O_3 concentrations typically range from ~33 to ~37 wt% and total REE contents between ~14 and ~22 wt%. UO_2 concentrations can range from <0.01 to ~9.4 wt% and ThO_2 from <0.01–3.1 wt%.

The incorporation of Th and U into the xenotime structure is governed by two charge balanced substitution mechanisms involving Si and Ca (van Emden et al. 1997):

$$(Th, U)^{4+} + Si^{4+} = (REE, Y)^{3+} + P^{5+} \qquad \text{(1; Thorite; } ThSiO_4)$$

$$(Th, U)^{4+} + Ca^{2+} = 2(REE, Y)^{3+} \qquad \text{(2; Brabantite; } CaTh(PO_4)_2)$$

Size restrictions imposed by the xenotime structure favour the incorporation of Th and U by substitution mechanism 1 (van Emden et al. 1997). This is because the Si^{4+} ion is smaller than the Ca^{2+} ion and is therefore preferentially partitioned into the lattice where it replaces the P^{5+} ion. Although Förster (1998), in noting the predominance of substitution mechanism 1 over mechanism 2, suggests that factors such as the availability of the charge balancing cations Si^{4+} and Ca^{2+} may also play an important role in controlling the mechanism of actinide incorporation into the xenotime structure. Typically, size restrictions imposed by the xenotime structure favour the incorporation of the U ion over the larger Th ion. Hence U/Th ratios in xenotime are commonly greater than 1 (van Emden et al. 1997; Förster 1998).

2.3 Metamorphic and igneous xenotime

2.3.1 Metamorphic xenotime

Xenotime occurs in greenschist to granulite facies rocks, and is typically relatively abundant in metapelites with low Ca contents (Franz et al. 1996; Spear & Pyle, 2002). However in the garnet zone, xenotime is removed by garnet-forming reactions (Franz et al. 1996; Bea & Montero 1999; Spear & Pyle 2002) but can remain as inclusions within garnet crystals (Spear & Pyle, 2002). Xenotime can reappear in the migmatite zone due to melt crystallisation, and as a result of garnet breakdown reactions

(releasing Y and HREE), can precipitate during retrogression (Spear & Pyle 2002). Xenotime exsolutions have also been reported in monazite (Petersson et al. 2001) and zircon (Spandler et al. 2004).

2.3.2 Igneous xenotime

Xenotime can occur as a minor accessory phase in a wide range of igneous rocks of felsic and alkaline composition. For example, xenotime occurs in the alkaline granites, pegmatites, syenites and nephelinic syenites of the Kola Peninsula, Russia (Belolipetskii & Voloshin 1996) and also carbonatites such as The Hicks Dome carbonatite complex, USA (Mariano 1987, as cited in Wall & Mariano 1996), Mt Weld, Western Australia (Mariano 1984, as cited in Wall & Mariano 1996) and Kangankunde, southern Malawi (Wall & Mariano 1996). Although xenotime can be present in metaluminous (Casillas et al. 1995) and peralkaline igneous rocks (Bea 1996), it is commonly most abundant in peraluminous, Ca–poor fractionated leucogranites (Bea 1996; Casillas et al. 1995; Förster 1998).

The relative abundance of xenotime in peraluminous igneous systems is linked to the increased solubility of apatite at high ASI values (A/CNK = 1.2-1.4) (Pichavant et al. 1992; London 1992; Wolf & London 1994) which contributes P and REE to the melt fraction. The subsequent crystallisation of plagioclase then serves to lower the Ca/P ratio of the melt below that of apatite, which allows for the crystallisation of monazite and/or xenotime (Wolf & London 1995). Xenotime crystals in peraluminous igneous rocks are typically between 10–40 μm in diameter and rarely >100 μm. More typically, xenotime is intergrown with other accessory minerals including biotite, zircon, monazite and rutile (Förster 1998; Wark & Miller 1993; Bea 1996).

Similarities in the HREE pattern in xenotime and its host granite demonstrate that it can be an important repository for the HREE (Förster 1998; Wark & Millar 1993). Bea (1996) in a study of xenotime from granites in Iberia and the Urals, suggested that in low Ca peraluminous granites, xenotime contains between 30 to 50% of the total HREE budget.

2.4 Diagenetic Xenotime

Diagenetic xenotime commonly forms as minute <1 to 20 μm pyramidal outgrowths on zircon with which it is isostructural. It can also occur in voids and cavities. Their tiny size has meant that diagenetic xenotime overgrowths on zircon have only been positively identified since the advent of microanalytical techniques in the latter part of the twentieth century (Rasmussen 2005 and references therein).

2.4.1   Formation of diagenetic phosphate minerals

Diagenetic phosphate minerals are a widespread but volumetrically minor constituent of many sedimentary rock types. These minerals form during early diagenesis, soon after burial within a few metres of the sediment water interface (Rasmussen 1996). Besides xenotime (YPO_4), other significant diagenetic phosphate minerals include Francolite or carbonate flourapatite ($Ca_5(PO_4, CO_3, OH)_3F$), viviannite ($Fe_3(PO_4)_2.8H_2O$), goyazite ($SrAl_3(PO_4)_2(OH)_6$), crandallite ($CaAl_3(PO_4)_2(OH)_6$), rhabdophane ($(REE, Th)PO_4.nH_2O$), monazite ($(REE, Th)PO_4$) and florencite ($(REE)Al_3(PO_4)_2(OH)_6$) (Rasmussen 1996).

Diagenetic phosphate minerals form in regions where the upwelling of deep water supplies nutrients to marine ecosystems (Föllmi 1996; Burnette 1977; Glenn 1990) and also away from upwelling zones such as in near-shore and deltaic environments (Berner 1993; Lucotte et al. 1993; Rasmussen 1996). In these environments, sediment pore-water phosphate is made available primarily through the microbial breakdown of organic debris (Föllmi 1996; Berner et al. 1993; Compton et al. 1993) and to a lesser extent by the desorption of phosphate from iron and manganese oxyhydroxides after burial (Föllmi 1996; Berner 1973; Froelich et al. 1977; Krom & Berner, 1981; O'Brien & Heggie 1988). Rasmussen (1996; 1998) suggests that the Y and REE necessary for xenotime precipitation are probably derived from a number of processes including, decomposition of organic complexes, reduction of iron and manganese oxyhydroxides, release of REE adsorbed onto clay mineral surfaces and surface reactions of REE bearing minerals such as monazite and apatite.

Diagenetic xenotime has principally been found to occur in medium to coarse grained sandstones (Rasmussen 2005) but has also been found in conglomerates (England et

al. 2001; Vallini et al. 2007) and siltstones and shales (Rasmussen 1996; Rasmussen 1998). A post depositional origin for many xenotime outgrowths is strongly supported by petrographic studies that detail xenotime growth textures that clearly predate other diagenetic minerals (Fig. 2.2)
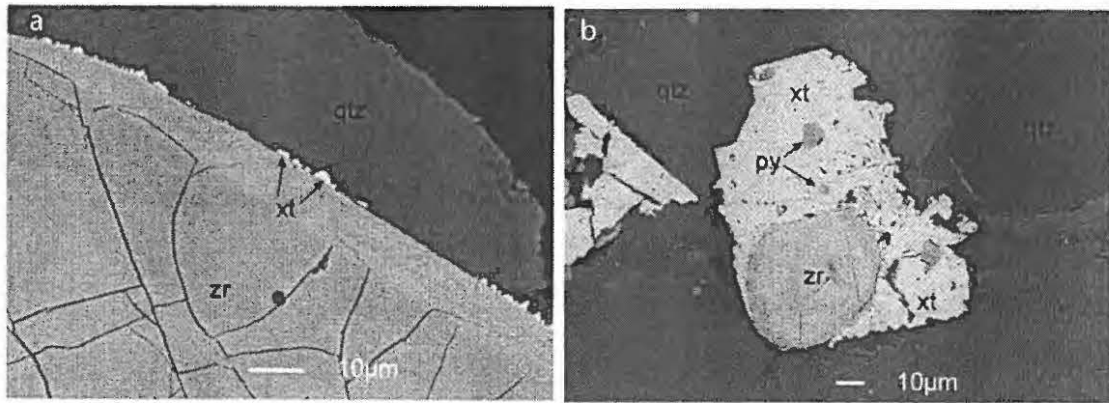
Fig. 2.2. (a) Backscattered electron (BSE) image of minute pyramidal outgrowths of xenotime engulfed by diagenetic quartz. (b) BSE image of xenotime outgrowth containing authigenic pyrite (Rasmussen 2005).

Backscattered electron imaging can also reveal different growth stages of diagenetic xenotime. Figure 2.3 for example, shows a BSE image of xenotime overgrowing zircon from a quartzite sample LIS-34 (see Chapter 4).
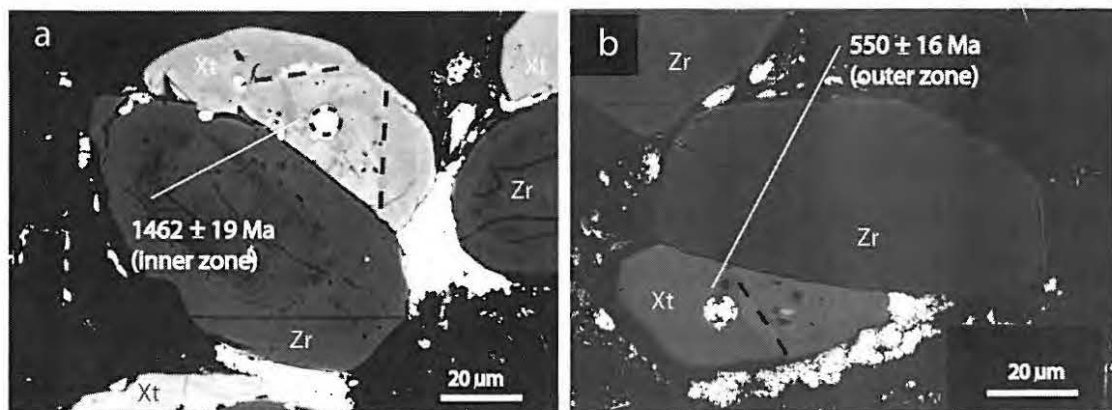
Fig. 2.3. BSE image of xenotime overgrowth on zircon showing SHRIMP U—Pb ages measured in this study (see Chapter 4). The inner pyramidal overgrowth has a pitted texture and is ~900 m.y. older than the outer massive zone. Brighter regions in these two images are due to a residual SHRIMP Au coating.

2.5 Hydrothermal phosphate minerals (xenotime and monazite)

Hydrothermal phosphate minerals can be found in late–stage magmatic–hydrothermal quartz veins (Schaltegger et al. 2005), Cu–Au deposits such as the Carajás belt Brazil (Tallarico et al. 2005), but have commonly been found to occur in orogenic Au deposits where ore-related datable minerals are rare (Vielreicher et al. 2003). In fact the precipitation of hydrothermal phosphate minerals may be commonplace in orogenic gold settings. For example Vielreicher et al. (2003) states that hydrothermal phosphate minerals either in ore veins or associated with alteration minerals have been found in all deposits in the eastern Yilgarn Craton where samples have been examined. Hydrothermal xenotime has also recently been found and dated by SHRIMP (Sensitive High Resolution Ion Microprobe) U–Pb in two spatially separated orogenic Au deposits in the Tanami region of central Australia (Callie and Coyote Au deposits, see Chapter 5). Hydrothermal xenotime and monazite crystals occur in pre- and post-ore rocks as well as in veins and alteration zones and can be intimately associated with gold and ore related minerals (Fig. 2.4a). Hydrothermal xenotime can also form in association with monazite and occur in fractures within altered zircon and as overgrowths (Fig. 2.4b).
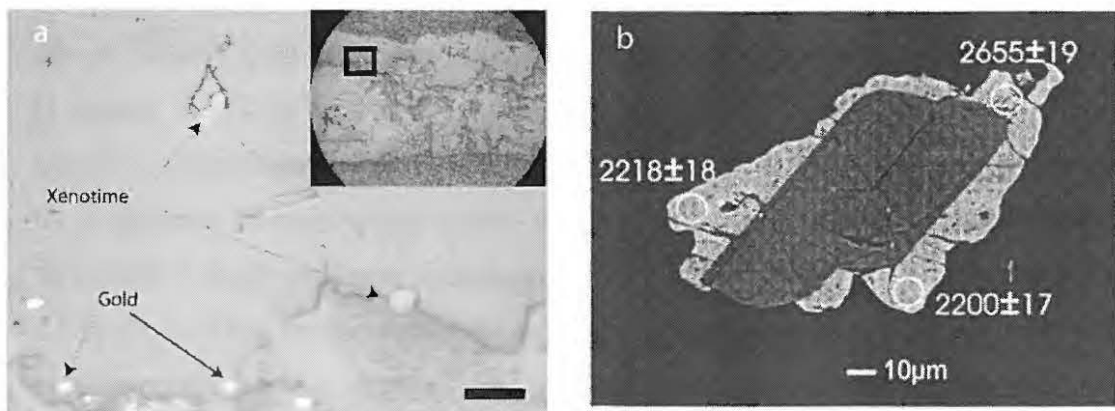
Fig. 2.4. (a) Reflected light photomicrograph of xenotime crystals (~10–25 μm) in auriferous quartz-carbonate-chlorite-biotite vein. Top right inset is smaller scale photomicrograph showing quartz vein and location of xenotime (scale bar is 50 μm). Callie Au deposit, Tanami region, northern Australia (this study, Chapter 5). (b) BSE image of hydrothermal xenotime overgrowing detrital zircon. Witwatersrand Group, South Africa showing $^{207}Pb/^{206}Pb$ ages (Ma) measured by SHRIMP (Kositein et al. 2003).

2.6 Xenotime composition

There have only been a few electron microprobe (EPMA) studies of the chemical composition of xenotime reported in the literature. These include studies of xenotime from igneous rocks (Wark & Miller 1993; Bea 1996; Förster 1998; Casillas et al. 1995, Kositcin et al. 2003; Schaltegger et al. 2005; Amli 1975; Demartin et al. 1991), metamorphic rocks (Franz et al. 1996; Bea & Montero 1999; Suzuki & Adachi 1991; Pan 1997), sedimentary rocks (Forbes 1999, as cited in Rasmussen 2005; Kositcin et al. 2003; Vallini et al. 2005; Vallini et al. 2007) and hydrothermal veins (Kositcin et al. 2003; Kerrich & King 1993; Schaltegger et al. 2005). The ranges in xenotime composition from these studies for different xenotime types are shown in Table 2.1. It is immediately obvious from this table that there are significant compositional overlaps between the xenotime types. Therefore, currently only broad observations can be made regarding the compositional characteristics of the the xenotime types. Furthermore, the data for hydrothermal xenotime in Table 2.1 are derived exclusively from lode Au deposits and therefore probably not representative of hydrothermal xenotime from other mineralisation styles.

2.6.1   U and Th

U contents from all xenotime types show an extremely large range from <0.01 to 9.4 wt% UO_2. Overall the highest U contents seem to be more typical of igneous xenotime, although they too range from below the detection limit (<0.01) to the highest values recorded. Hydrothermal xenotime appears to have the lowest U contents ranging from 0.05 to 0.13 wt% UO_2. Diagenetic and metamorphic xenotime from metapelites and metapsammites share a similar compositional range in U of between ~0.1 to 1.1 wt% UO_2. The data for diagenetic xenotime from Vallini et al. (2007) (i.e. the 'Diagenetic 2' grouping) has a much higher upper limit for UO_2 of 2.7 wt%. This apparently higher concentration of U for diagenetic xenotime is considered anomalous as the xenotime studied by these researchers was taken from the Killi Killi Hills U prospect in the Tanami region of central Australia. It is for this reason that this limited data set appears separately in Table 2.1. A notable feature of this data also is the extreme range in FeO concentrations (0.7 to 0.67 wt% FeO) that the authors attributed to Fe-staining and the highly weathered nature of the rocks sampled.

The concentration of Th in the different xenotime types is in most cases lower than that of U. ThO_2 concentrations in xenotime from igneous rocks range from below the detection limit to 3.1 wt%. A similar range in Th content is shown for diagenetic xenotime. Metamorphic and hydrothermal xenotime appear to contain similarly moderate concentrations of ThO_2 between <0.01 and 0.9 wt%. Th/U ratios from the xenotime compositions in Table 2.1, are generally < 1, reflecting the preference in xenotime for U rather than Th.

Table 2.1. EPMA data for igneous, metamorphic, hydrothermal and diagenetic xenotime.

	Igneous	Metamorphic	Diagenetic 1	Diagenetic 2	Hydrothermal
SiO_2	0.1–1.6	0.1–1.1	0.1–2.15	0.01–0.4	0.1–0.9
P_2O_5	32.2–35.8	30.1–34.7	32.5–36.3	30.2–36.0	30.2–35.1
CaO	<0.01–1.8	0.02–0.19	0.1–0.6	0.1–1.1	~0.1
Y_2O_3	34.8–46.1	38.6–45.9	36.6–47.7	39.5–47.7	34.7–42.3
ThO_2	<0.01–3.1	<0.01–0.9	0.1–2.6	0.1–0.4	0.01–1.48
UO_2	<0.01–9.4	0.1–0.9	0.3–1.1	0.1–2.7	0.05–0.13
La_2O_3	<0.01	<0.01–0.1	<0.01–0.1	n.r.	<0.01
Ce_2O_3	<0.01–0.1	<0.01–0.1	<0.01	n.r.	<0.01
Pr_2O_3	<0.01–0.1	<0.01–0.1	<0.01	n.r.	<0.01
Nd_2O_3	0.1–0.7	0.1–0.5	<0.01–0.1	n.r.	<0.01–0.4
Sm_2O_3	0.1–1.3	<0.01–0.5	0.2–0.8	n.r.	0.2–1.6
Eu_2O_3	0.01–0.02	-	0.1–0.6	n.r.	0.2–1.2
Gd_2O_3	1.6–4.9	1.7–8.6	1.4–7.7	n.r.	1.5–9.7
Tb_2O_3	0.5–1.2	0.5–1.2	0.5–1.5	n.r.	0.5–1.5
Dy_2O_3	4.2–7.0	3.3–6.7	5.4–8.6	n.r.	3.9–8.3
Ho_2O_3	0.9–1.3	0.7–1.3	1.1–1.6	n.r.	1.1–2.3
Er_2O_3	2.0–5.2	3.8–5.6	2.7–4.3	n.r.	1.7–5.9
Tm_2O_3	0.3–0.7	-	0.3–0.7	n.r.	0.3–0.6
Yb_2O_3	0.9–6.5	1.8–7.3	1.8–4.0	n.r.	0.8–4.0
Lu_2O_3	0.1–1.3	0.3–1.5	0.1–0.6	n.r.	<0.01–0.14
FeO	-	-	<0.01–0.3	0.7–6.7	<0.01–1.03

Analyses are weight %. – not analysed. n.r. not reported.

Data sources: Igneous (Förster 1998; Bea 1996; Forbes 1999; Kositcin et al. 2003; Schaltegger et al. 2005; Casillas et al. 1995; Amil 1975), metamorphic (this grouping represents xenotime analysed from regionally metamorphosed metasedimentary rocks by, Franz et al. 1996; Bea & Montero 1999), diagenetic 1 (Kositcin et al. 2003; Forbes 1999; Vallini et al. 2005), diagenetic 2 (Vallini et al., 2007) hydrothermal (Kositcin et al. 2003; Kerrich & King 1993; Schaltegger 2005).

2.6.2   REE

The LREE La–Pr are generally at or below electron microprobe detection limits in xenotime from the different groups and will not be considered further (see Fig. 2.5). The MREE–HREE comprises virtually the entire REE budget in xenotime. The

MREE–HREE which can occur in significant amounts includes Gd, Dy, Er and Yb. In addition Nd, Sm, Eu, Tb, Ho, Tm and Lu are in many cases above detection limits and range up to a maximum level of approximately 1 wt% REE_2O_3. The elements Gd, Dy, Er and Yb in xenotime are present in a wide range of concentrations which overlap among the different groups. Gd contents in metamorphic and diagenetic xenotime are similar and cover a broad range of between ~1.4 to 8.6 wt% Gd_2O_3. Gd contents in hydrothermal xenotime are high (1.5–9.7 wt% Gd_2O_3). Magmatic xenotime has the lowest concentrations of Gd among the different xenotime types, ranging from 1.6 to 4.9 wt% Gd_2O_3. Dy contents range from 3.3 to 8.6 wt% Dy_2O_3 and apparently show the higher levels in the diagenetic grouping. Erbium contents show no differences between the groups, with concentrations ranging between ~1.7 and ~5.9 wt% Er_2O_3. The highest Yb contents apparently occur in igneous and metamorphic xenotime. However, for these xenotime types, Yb concentrations are also widespread ranging from ~0.9 to ~6.5 wt% Yb_2O_3 for igneous xenotime and for metamorphic xenotime there is a similar range from ~1.8 to ~7.3 wt%. In contrast Yb contents in diagenetic xenotime appear to be uniformly low, ranging from ~1.8 to ~4.0 wt% Yb_2O_3, while similarily low Yb concentrations also occur in hydrothermal xenotime (~0.8 to ~4.0 wt%). There also appears to be significant differences in Eu content between the diagenetic and hydrothermal xenotime (~0.1 to ~0.6 wt% and ~0.2 to ~1.2 wt% Eu_2O_3 respectively) and for the igneous–metamorphic xenotime, Eu contents are barely above detection limits.

2.6.2.1   REE patterns

Chondrite-normalised REE patterns for xenotime show a steep rise from La to Gd, and generally a smooth transition to Lu that maybe flat, or show a slightly positive or negative trend. Igneous xenotime has an obvious negative Eu anomaly (Fig. 2.5) reflecting the incorporation of Eu^{2+} in Plagioclase (Förster 1998; Kositcin et al. 2003). Kositcin et al. (2003) demonstrated that chondrite-normalised REE patterns for xenotime can, on a local scale, differ between igneous, diagenetic and hydrothermal types. This research, carried out on rocks from the Witwatersrand Supergroup, showed that in contrast to igneous-derived xenotime (distinguishable by a prominent negative Eu anomaly), diagenetic xenotime is enriched in the MREE Gd, Tb, and Dy compared to the HREE and also has a small to negligible negative Eu anomaly. Similarly, hydrothermal xenotime has a small to negligible negative Eu anomaly and

is enriched in the MREE at the expense of the HREE relative to either igneous or detrital zircon (Fig. 2.5).
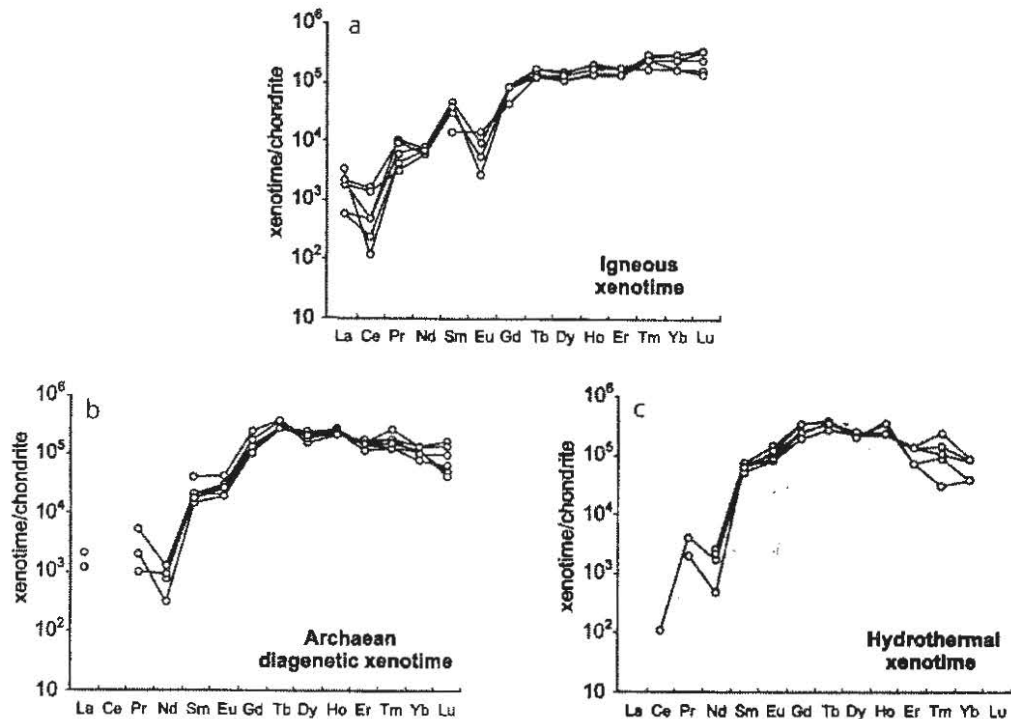
Fig. 2.5. Comparison of chondrite-normalised REE profiles for igneous, diagenetic and hydrothermal xenotime obtained from EPMA. (a) Igneous xenotime (xtc, xeno1 and xeno2). Igneous xenotime is from an Archaean pegmatite in Western Australia (xtc), granite pegmatite in Grenville Province (XENO1) and granite pegmatite from Aust-Agder province Norway (XENO2). (b) Diagenetic xenotime from the Witwatersrand Basin, South Africa (Kositcin et al. 2003). (c) Hydrothermal xenotime from Witwatersrand Basin, South Africa (Kositcin et al. 2003). Source: Rasmussen (2005).

2.6.3   Geochemical characterisation of xenotime

Presently the broad overlap in composition between different xenotime types and limited data precludes any reliable geochemical classification scheme. However, there have been a few case studies which have attempted at a local scale to either link xenotime composition to petrogenesis or, distinguish between different xenotime types. Attempts by Förster (1998) to link the composition of xenotime to the degree of crystal fractionation in peraluminous granites from Erzgebirge Germany generally didn't find any correlations between the concentrations of the REE in xenotime and their granite hosts. Only in the most differentiated S-type Li mica granite group was a trend toward higher concentrations of HREE observed. However the relative proportions of Gd–Ho and Er–Lu could distinguish between the granite types.

41

Although the granite suites studied did not show any changes in U or Th concentrations, a weak correlation in Th/U ratio was noted. The highest Th/U ratios (~1-4) occurred in A-type granites, whereas low Th/U ratios (~0.1–1) occurred in S-type Li-mica granites. This difference was consistent with whole rock Th and U contents.

Wark & Miller (1993) found that systematic changes in the trace element composition of cogenetic granites and aplites from the S-type Sweetwater Wash pluton in south-eastern California were largely controlled by the crystallisation of monazite, xenotime and zircon. These researchers showed that besides monazite and zircon, xenotime compositions can be used to track changes in melt composition as fractional crystallisation proceeds. Xenotime from the more differentiated aplites has a weak trend toward higher Gd/Ho ratios. In contrast to the results of Förster (1998), Wark & Miller (1993) showed that the more differentiated rocks contain xenotime with higher U and Th concentrations.

Two separate studies of xenotime geochemistry in regionally metamorphosed metapelites and metapsammites, by Franz et al. (1996) and Bea & Montero (1999), did not observe any difference in xenotime Y and HREE abundances with increasing metamorphic grade. However, Bea & Montero (1999) did report a minor shift in Th/U ratios from 0.2 to 0.3 in amphibolite grade metapelites to <0.1 in transition-granulite zone rocks.

More recently Kositcin et al. (2003) were able to discriminate chemically between hydrothermal, diagenetic and igneous xenotime in rocks from the Witwatersrand Supergroup which proved useful in interpreting the results of SHRIMP U–Pb analyses. To do this, Kositcin et al. (2003) devised REE discrimination diagrams using combinations of Gd, Yb, Eu and Dy.

Chemical controls placed on xenotime composition from different igneous and metamorphic protoliths and hydrothermal and diagenetic environments will greatly complicate a purely geochemical classification scheme for different xenotime types. Even the negative Eu anomaly observed in igneous derived xenotime when plotted on chondrite-normalised REE plots, is not always diagnostic of an igneous origin. For

example, it is demonstrated in Chapter 6 of this thesis that hydrothermal xenotime can in some circumstances also have a negative Eu anomaly (see Fig. 6.7). In this case, hydrothermal xenotime from the Molyhil deposit, central Australia which had crystallised within a sample of altered granite has probably inherited relatively low Eu concentrations from its protolith.

2.7 Xenotime as a geochronometer

A number of features make xenotime an excellent geochronometer and the diverse range of environments in which it is found enhances its applicability to answering geological questions. Xenotime typically has high U contents and low initial Pb. In fact, Donovan et al. (2003) suggest that xenotime may incorporate less initial Pb than monazite. These researchers have noted that monoclinic LREE (La-Gd) orthophosphates grown in a Pb pyrophosphate flux, incorporate appreciable amounts of Pb, whereas tetragonal HREE orthophosphates incorporate very little. This was attributed by Donovan et al. (2003) to the larger relative size of Pb and the preference of xenotime for small ions. In addition to incorporating low initial Pb contents, xenotime also has a closure temperature for Pb diffusion similar to zircon and monazite. For example, Cherniak (2006) calculated that for a cooling rate of 10 °C/Ma, a xenotime grain of 10 µm radius would have a closure temperature of about 890 °C, which is similar to that for zircon and only about 50 °C lower than for monazite. Similarly, for the same cooling rate, a 50 µm xenotime grain will have a closure temperature of 980 °C which is about 20 °C higher than for zircon and ~30 °C lower than for monazite. Xenotime also has the ability to anneal radiation damage at moderate crustal temperatures despite the high U contents regularly encountered in natural xenotime (Harrison et al. 2002). Indeed there are no reports of metamict xenotime in the literature (Harrison et al. (2002). Like zircon and monazite, individual xenotime crystals can also contain inherited cores (Fig. 2.6).
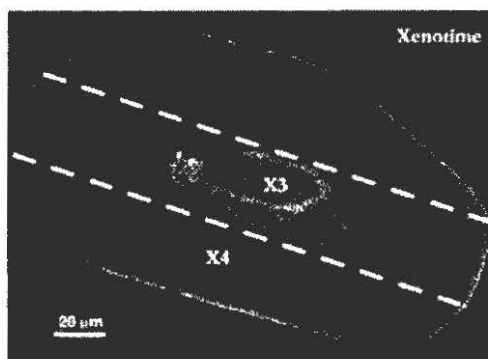
Fig. 2.6. BSE image of an inherited core in xenotime crystal from a Himalayan orthogneiss. The rim yielded a TIMS U–Pb age of ~20 Ma, whereas the core was interpreted to be ~470 Ma. The dashed white lines are where the grain was cut for U—Pb, ID-TIMS analysis (Viskupic & Hodges 2001).

Xenotime has been dated using U—Pb by a range of techniques: isotope dilution (e.g. Schärer et al. 1990; Hawkins & Bowring 1997), electron microprobe (e.g. Suzuki & Adachi 1991, 1994; Asami et al. 2002; Grew et al. 2002) and SIMS (e.g. McNaughton et al. 1999; Petersson et al. 2001; Vallini et al. 2002). Recent work has focussed on the in situ dating of small (usually ~10 to ~50 µm diameter) diagenetic and hydrothermal xenotime crystals.

Microbeam analytical techniques capable of in situ U—Th—Pb dating of single xenotime crystals include, electron microprobe (EPMA), laser ablation (ICP-MS), and SIMS (SHRIMP, Cameca 1270/1280, Nano SIMS 50). Total U—Th—Pb chemical EPMA dating has been successfully applied to monazite (e.g. Montel et al. 1996; Suzuki & Adachi 1991; 1994; Williams et al. 1999) and xenotime studies (Suzuki & Adachi 1991; 1994; Asami et al. 2002). Although EPMA offers the finest spatial resolution of the above techniques (~1-2 µm), isotopic information is unavailable, and therefore assessments of concordance cannot be made. Furthermore, EPMA U—Th—Pb chemical dating of xenotime is restricted to high-U xenotime as the primary Pb peak (Mα) overlaps with the Y (Lγ) peak requiring Pb to be measured on the subordinate Mβ peak which significantly increases the analytical uncertainty. Therefore diagenetic and hydrothermal xenotime, which typically have U concentrations of < 1000 ppm, cannot be dated by this technique.

U—Pb geochronology by Laser-Ablation Inductively Coupled Plasma Mass

Spectrometry (LA-ICP-MS) is now a widely used method with a precision and accuracy similar to that of SIMS instruments (Horn et al. 2000; Kosler et al. 2002). Generally, in situ LA-lCP-MS, U—Th—Pb analyses are limited to spot diameters of 40 μm (40x40x15μm sample volume), precluding their usefulness for the analysis of <20 μm diagenetic and hydrothermal xenotime. Although Simonetti et al. (2006) successfully undertook U—Pb analysis of a high-U monazite sample using a 5 μm spot (5x5x2 μm sample volume), with a laser ablation MC-ICP-MS, this procedure has not been proven for the analysis of low U minerals.

U—Pb analysis of geological materials using the Cameca NanoSIMS 50 ion probe, may also be restricted to high-U minerals. For example, Stern et al. (2005) using a spot diameter of between 3-5 μm, reported a sensitivity for Pb^+ in zircon and zirconolite of 3.0 to 3.5 (cps/ppm/nA), which is about one-third of that obtainable with large-radius ion probes. These researches concluded that geochronology using the Cameca NanoSIMS 50, is presently restricted to high-U minerals where the $^{207}Pb/^{206}Pb$ ratios can be used.

The vast majority of recent U–Pb studies of xenotime have been preformed by SIMS techniques, in particular using SHRIMP II. The success of SHRIMP in dating tiny, typically low-U, hydrothermal and diagenetic xenotime crystals is underpinned by the high mass resolution (~5000), sensitivity and spatial resolution achievable with these instruments. However, significant limitations to SIMS techniques remain, in particular the determination of xenotime $^{206}Pb/^{238}U$ ratios which can show a large chemical fractionation on SIMS instruments. Although correction protocols have been developed for these matrix affects (see Chapter 3; Fletcher et al. 2000; Fletcher et al. 2004) all SIMS dating of diagenetic and hydrothermal xenotime so far has relied primarily on the determination of $^{207}Pb/^{206}Pb$ ratios, for which the instrumental isotope fractionation is very small.

2.8 U–Pb analysis of diagenetic xenotime
Isotopic dating of felsic volcanic rocks intercalated with siliciclastic sedimentary units is commonly the most reliable and simplest means to estimate the age of sediment deposition (e.g. Bowring et al. 1993; Trendall et al. 2004). This approach assumes

that the mineral or whole rock dated by U–Pb, K–Ar, Ar–Ar or Rb–Sr methods crystallised (at least on a geological time scale) at the same time as sediment deposition. However, in Precambrian basins where felsic volcanic intercalations and dateable fossiliferous horizons are rare or non existent, estimates of depositional ages are often equivocal.

In the absence of felsic volcanic intercalations, the timing of sediment deposition can be inferred from the U–Pb age of the youngest detrital zircon recovered from a clastic unit. Such studies are now routinely carried out using either ion microprobe or laser ablation ICP-MS where large numbers of zircon grains can be analysed. In some cases this technique is very reliable (e.g. Nelson 2001) but in the absence of independent geological controls the results can be ambiguous. In an extreme example, Andersen et al. (2002) reported a detrital zircon U–Pb maximum deposition age from a glaciofluvial sediment in Norway that is ~1000 Ma older than its true age of deposition.

In some cases isotopic dating of diagenetic minerals (e.g. glauconite, illite, K-feldspar, apatite and carbonate) has proved useful in determining the depositional ages of some sedimentary units. However, because of the susceptibility of these minerals to isotopic resetting during low grade metamorphism, their usefulness is mostly restricted to Phanerozoic rocks.

Recent studies have indicated that the SIMS U–Pb dating of diagenetic xenotime may prove to be a robust and reliable method to determine the age of sediment deposition isotopically (McNaughton et al. 1999; Vallini et al. 2007; Rasmussen et al. 2004). The attractiveness of this method is underpinned by the qualities of xenotime which make it an excellent geochronometer. U–Pb dating of diagenetic xenotime can be used in conjunction with U–Pb detrital zircon studies to yield both minimum and maximum depositional ages respectively for a sediment. For example, McNaughton et al. (1999) used that technique to determine maximum and minimum ages for the deposition of the Kimberley Group in north-western Australia. Making the first U—Pb isotopic analyses of diagenetic xenotime, McNaughton et al. (1999) established that the Warton Sandstone was deposited between 1786 ± 14 Ma and 1704 ± 7 Ma and constrained deposition of the Pentecost Sandstone to between ~1790 Ma, the age of

the intrusive Hart Dolerite and 1704 ± 4 Ma, the time of diagenetic xenotime growth. Prior to this study it was known only that these units were deposited sometime between ~1790 Ma and ~750 Ma.

In another more recent example, Vallini et al. (2007), based on SHRIMP U–Pb analyses of diagenetic xenotime, established a minimum depositional age of 1632 ± 3 Ma for the Gardiner Sandstone of the Birrindudu Group, northern Australia. This information, coupled with a SHRIMP U–Pb detrital zircon study by Cross & Crispe (2007, see Chapter 1) on the same unit and the disconformably underlying Pargee Sandstone has established that the Gardiner Sandstone was deposited between ~1.77 and 1.63 Ga.

As mentioned above, xenotime can be one of the earliest diagenetic minerals to form. However, several SHRIMP U–Pb studies of diagenetic xenotime have shown that xenotime growth is not restricted to early diagenesis but can continue in a response to hydrothermal fluid events over hundreds of millions of years (e.g. England et al. (2001); Rasmussen et al. (2004), Vallini et al. (2002), Vallini et al. (2007)) (Fig. 2.7). Therefore careful identification of textures diagnostic of early diagenesis and BSE imaging are essential when selecting xenotime overgrowths for in situ U–Pb analysis.
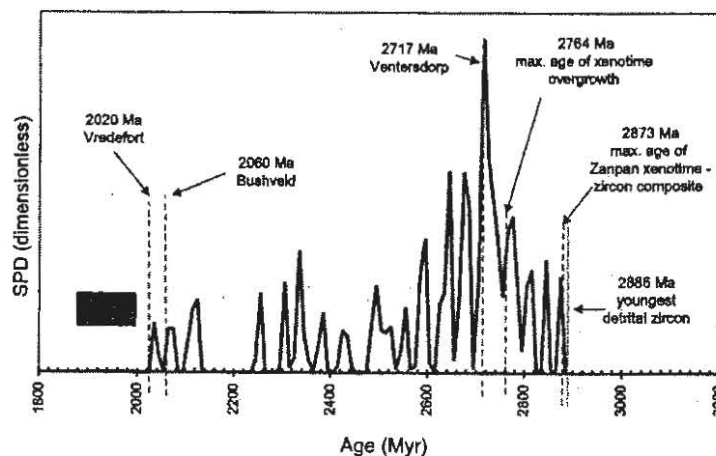
Fig. 2.7. Probability plot of xenotime SHRIMP ^{207}Pb/^{206}Pb ages for sedimentary rocks from the Witwatersrand Supergroup, South Africa. The large spread in xenotime ^{207}Pb/^{206}Pb ages shows that there have been numerous phases of xenotime growth in these rocks (England et al. 2001).

2.8.1 Sampling strategies

The tiny size of most diagenetic overgrowths necessarily restricts U–Pb isotopic studies to SIMS techniques (see above). Rasmussen (2005) estimated that only ~1% of xenotime overgrowths in a typical sample of sedimentary rock are large enough to be dated isotopically by SIMS (i.e. >10 μm diameter). The scarcity of xenotime overgrowths large enough to be analysed by SIMS techniques necessitates the SEM examination of many polished thin sections per sample, which can amount to "exhaustive amounts of SEM examination" (Rasmussen 2005). For example, England et al. (2001), in studying both diagenetic and hydrothermal xenotime from the Witwatersrand Supergroup, examined 73 polished thin sections, whereas Vallini et al. (2002) examined 48 polished thin sections while investigating diagenetic xenotime from Mount Barren Group rocks in south-western Australia. Prior to SIMS analysis, selected xenotime overgrowths are typically cut from the polished thin section and mounted in epoxy resin, thus maintaining the textural integrity of each xenotime overgrowth.

2.9 Hydrothermal phosphate

Hydrothermal phosphate U–Pb geochronology has gained credibility in recent years as a reliable and robust means to date the timing of ore deposition. The high closure temperatures of xenotime and monazite to diffusive Pb-loss means that they are more likely to remain isotopically closed during post ore formation events that may otherwise disturb K-Ar and Ar-Ar isotopic systems. A number of SHRIMP U—Pb studies have been undertaken on hydrothermal xenotime associated with mineralised systems. These studies have been driven by the mining and exploration industry in an effort to constrain evolutionary and exploration models (see Pigois et al. 2003; Sener et al. 2005; Salier et al. 2004; Salier et al. 2005; Brown et al. 2002; Rasmussen et al. 2006; Cross et al. 2005).

Like diagenetic xenotime, the minute size of hydrothermal xenotime (usually <~20 μm) means that their location generally requires extended periods of SEM examination and SIMS analyses are carried out in situ on polished thin sections. As previously mentioned, hydrothermal xenotime appears to be associated with many orogenic lode-Au type deposits (section 2.5) and it is in these deposits where the

majority of SHRIMP U—Pb studies of hydrothermal xenotime have been undertaken (e.g. Brown et al. 2002; Cross et al. 2005; Salier et al. 2004; Compston & Matthai 1994; Pigois et al. 2003; Sener et al. 2005). For example, Pigois et al. (2003) used SHRIMP U—Pb xenotime geochronology to establish an age of 2063 ± 9 Ma for mineralisation at the Damang orogenic lode-Au deposit in Ghana which these authors also suggested is a good age estimate for a regional orogenic lode-Au event that includes the giant Obuasi orogenic Au deposits. In a separate SHRIMP U—Pb xenotime study conducted during this PhD, it was established that orogenic lode-Au mineralisation at the Callie Au deposit (Tanami region, central Australia) occurred at ~1.81 Ga (Cross et al. 2005; see Chapter 5). This age contrasts with an earlier ^{40}Ar-^{39}Ar biotite age for mineralisation at Callie of ~1.72 Ga reported by Fraser et al. (2002), which is now probably better interpreted to represent the timing of a later thermal overprint.

U—Pb dating of hydrothermal and diagenetic xenotime has the potential to solve geological questions that can not be answered by any other means. Currently the most suitable instruments to carry out these measurements are large radius SIMS. The significant ^{206}Pb/^{238}U matrix effects which complicate SHRIMP U—Pb xenotime analyses are fully investigated in the following Chapter.

3. SHRIMP XENOTIME U–Pb–Th DATING

3.1 Introduction

The development of the Sensitive High Resolution Ion Microprobe (SHRIMP) in the late 1970's to mid 1990's revolutionised U–Pb zircon geochronology. These double focusing SIMS instruments are routinely used for the analysis of U–Pb in U–rich trace minerals (particularly zircon) at high mass resolution (~5000) and sensitivity, with a spatial resolution of usually 20 to 40 μm (Compston et al. 1984; Williams & Claesson 1987; Williams 1998; Claoué-Long et al. 1995). The spatial resolution offered by SHRIMP allows for the U–Pb dating of separate domains within a single crystal. Additionally, U–Pb analyses are relatively fast (~10 to 20 minutes) allowing for good sample throughput. Although less precise than U–Pb analyses undertaken by thermal ionisation (TIMS), the excellent spatial resolution, accuracy, precision and high productivity of SHRIMP instruments has meant that they are now routinely used for U–Pb geochronology in a number of research institutions around the world.

Much of the success of the SHRIMP and now Cameca (1270/80) instruments in the application of U—Pb dating is linked to the unique characteristics of zircon as a geochronometer. Zircon ($ZrSiO_4$) is a widespread mineral that crystallises in igneous, metamorphic and hydrothermal environments. Its almost ubiquitous presence as a detrital component in clastic sedimentary rocks is testament to its excellent physical and chemical durability. Nearly all zircon has a composition that is within a few weight percent of the stoichiometric formula for the mineral. The most abundant trace element substitutions are Hf, Y and the REE. Total REE and Y contents are typically <1 wt% and Hf concentrations average ~2 wt% (Hoskin & Schaltegger 2003). Zircon also incorporates trace amounts of U (typically ~50 to 1500 ppm) and Th (~10 to 700 ppm), but rejects Pb during crystallisation. Its closure temperature for Pb diffusion is >900°C (Lee et al. 1997; Cherniak & Watson, 2003, Cherniak 2006). The relatively small range in zircon major element compositions and its generally low and restricted range in U content mean that SIMS analyses of zircon are mostly free of the inter– and intra–grain matrix effects to which SIMS analyses of other minerals are particularly prone. Exceptions are analyses of zircon with U contents >2500 ppm U for which a U dependant matrix correction is required (Williams & Hergt 2000).

In contrast to zircon, xenotime (YPO_4) has a wide range in composition. The heavy REE, which substitute for Y, typically range up to ~10 wt%, whereas U and Th concentrations can range up to as much as ~6 wt%. This range in chemical composition is the source of significant matrix effects which greatly complicate the SIMS analysis of this mineral. These matrix effects cause a breakdown of the U–Pb calibration scheme typically used for zircon, as well as normal SIMS procedures for measuring elemental abundances. Further, the ubiquitous presence of scattered ions on and near the ^{204}Pb peak when xenotime is analysed using SHRIMP II limits the precision of ages measured on xenotime older than ~1.0 Ga for which an accurate measurement of radiogenic $^{207}Pb/^{206}Pb$ and hence the common Pb correction is required. SIMS analyses of xenotime are further complicated by the typically tiny size of xenotime crystals (particularly in sedimentary rocks), which demand the smallest possible primary beam diameter (typically 5 to 7 μm). The consequent reduction in secondary ion count rates further reduces the precision of SIMS xenotime analyses. Overcoming these analytical issues in order to obtain the most accurate and precise SIMS xenotime U–Pb analyses has required close investigation of many factors. The techniques developed here differ significantly from those used for the more 'routine' SHRIMP zircon U–Pb analyses (e.g. Compston et al. 1984; Williams & Claesson 1987; Claoué–Long et al. 1995) and involve; multiple xenotime U–Pb standards, electron microprobe measurement of the major and trace element contents of each dated grain, use of an O⁻ rather than an O_2^- primary beam and the adoption of the SHRIMP RG as the most suitable instrument for SIMS xenotime analysis.

3.1.1   Aims, definitions, background and instrumentation

The aim of this phase of the project was to examine the current limitations of SHRIMP xenotime U–Pb–Th dating, focusing on the effects, causes and possible solutions to age deviations that result from matrix mismatches between the primary calibration standard and unknown. To do this, SHRIMP U–Pb–Th dating experiments were conducted on a number of xenotime samples of contrasting chemical composition that had been accurately dated by U–Pb ID–TIMS.

3.1.2 Definition of the SIMS matrix effect

The SIMS matrix effect refers to differences in relative ionisation efficiency or sensitivity of a given element in crystals of different composition or structural orientation. Therefore, the intensity of a secondary ion beam for a given element or molecule is not only related to its concentration in the target mineral, but also can be influenced by the concentration of other elements in the mineral, its degree of crystallinity and its structural orientation.

3.1.3 SIMS Instrumentation

SHRIMP instrumentation has been described in detail by Clement et al. (1977), Ireland (1995), Williams (1998), De Laeter & Kennedy (1998), Compston (1996) and Ireland et al. (2008) so only a brief description will be given here. The focus is on SHRIMP RG as this instrument was chosen as the best suited to xenotime U–Pb analysis and used for the majority of the experiments undertaken.

SHRIMP instruments are large radius, double focusing mass spectrometers where the generation of secondary ions is achieved by ion-impact sputtering. For U–Pb analysis, a mass filtered, focused, primary beam of usually O_2^- ions is generated in the primary column, accelerated to 10kV and strikes the target at an angle of 45°. Positively charged secondary ions are then accelerated to -10kV where they pass into a mass analyser, which can have either a forward geometry design (electrostatic analyser (ESA) precedes magnet e.g. SHRIMP I and SHRIMP II) or reverse geometry design (magnet precedes ESA, e.g. SHRIMP RG).

The SIMS ion optical designs that encouraged the development of SHRIMP I, SHRIMP II and SHRIMP RG instruments were those of Matsuda (1974) and Matsuda (1990). The approach used in these designs for double focusing SIMS instruments was to treat the image aberrations caused by the sputtering and secondary ion transfer process as an integrated whole, rather than attempting to minimise individual image aberrations arising from separate components. The design of Matsuda (1974) addressed the minimisation of first and second order aberrations. The reverse geometry design of Matsuda (1990) tackled the minimisation of third order ion image aberrations.

The ion optical design of the SHRIMP I and SHRIMP II secondary mass analysers were based on one of the solutions found by Matsuda (1974). In this model the velocity (i.e. energy) spread of the ESA is adjusted to be equal but opposite to that of the magnet (Compston 1996). Furthermore, second order aberrations such as those arising from image curvature caused by fringing magnetic fields were also cancelled out by an electrostatic quadrupole lens between the ESA and magnet (Compston 1996). The SHRIMP RG mass analyser was based on a series of designs published by Matsuda (1990) that were aimed at reducing third order image aberrations. This design, in which the magnet precedes the ESA, ultimately demagnifies the final ion image without an equivalent reduction in the mass dispersion (Compston 1996). This theoretically results in a four-fold increase in mass resolution relative to SHRIMPs I and II, while maintaining high sensitivity.

After exiting the object slit of the SHRIMP RG, the secondary ion beam traverses the QQH chamber, where it passes through two quadrupole lenses and a hexapole lens (which is currently unused) prior to momentum separation in the magnet. The purpose of these two quadrupole lenses is to compress the beam in the Z direction while expanding it in the Y direction for entry into the magnet. Momentum dispersion occurs in a 46° magnet with a 1 metre turning radius and energy dispersion is compensated for by a 0.751 m cylindrical ESA with a turning radius of 88.65^O. There are two further quadrupole lenses, at the entrance and the exit to the ESA respectively, the final quadrupole acting as a projection lens onto the collector slit (Fig. 3.1).

There are advantages and disadvantages inherent in both forward– and reverse–geometry SHRIMP instruments. Analysis by multi–collection is not possible using SHRIMP RG, a feature of the SHRIMP II design which allows for high precision O and S isotopic analysis. Although SHRIMP RG can operate at a much higher mass resolution than SHRIMP II, the sensitivity of SHRIMP RG for U–Pb analysis is currently approximately 75 % of that achieved by SHRIMP II at a mass resolution of ~5500 (Ireland et al. 2008). However, the reverse-geometry of SHRIMP RG allows only a single mass secondary ion beam to pass from the magnet into the ESA and ultimately the collector at any one time. As will be explained below this is a major advantage for xenotime U–Pb analysis as scattered ions with a mass similar to that of

[204]Pb are effectively removed from the secondary ion spectrum.
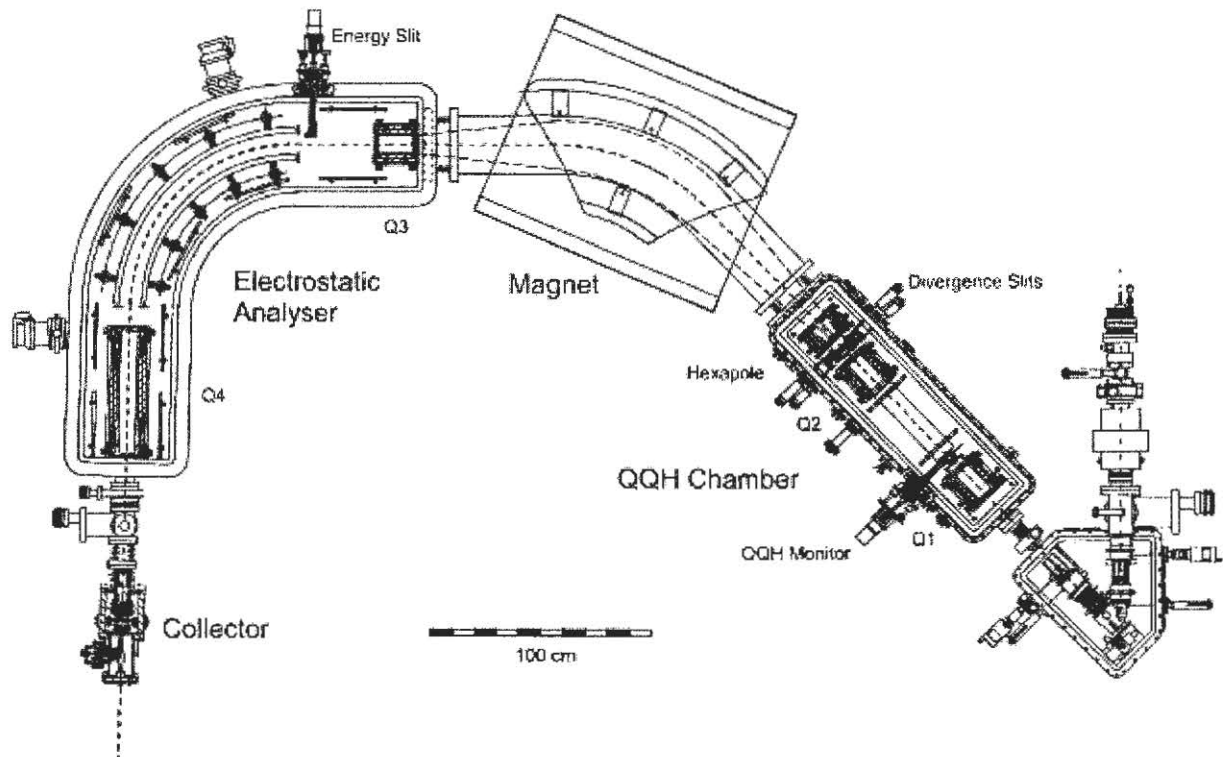
Fig. 3.1. Schematic diagram of the SHRIMP RG ion microprobe. Source: Ireland et al. (2008).

3.1.4 SIMS U–Pb dating

The basis of SIMS zircon U–Pb geochronology is the Pb^+/U^+ versus UO^+/U^+ calibration (Compston et al. 1984). This calibration addresses the two major problems that affect SIMS $^{206}Pb/^{238}U$ determinations, namely that the relative sensitivity factor for Pb^+ is 3 to 4 times higher than that for U^+, and that these two factors change both during and between analyses over an analytical session. The change is, in almost all cases, highly correlated with simultaneous changes in the relative sensitivity factors for UO^+ and U^+. The changes are monitored by interspersing analyses of a reference standard with analyses of the unknown sample. Therefore, with reference to a standard of known age and knowledge of the functional relationship between Pb^+/U^+ and UO^+/U^+, $^{206}Pb/^{238}U$ ratios measured on an unknown sample can be corrected to yield the true $^{206}Pb/^{238}U$. The correlation of Pb^+/U^+ with UO^+/U^+ is the most widely

used for SHRIMP data reduction because it shows the biggest range and therefore has the best leverage for calibration. Other ratio pairs include $Pb^+/UO^+:UO^+/U^+$ e.g. Compston (2000) and $Pb^+/UO^+:UO_2^+/U^+$ (Petersson et al. 2001).

Early attempts to quantify the functional relationship between Pb^+/U^+ and UO^+/U^+ yields from zircon, used a simple linear correlation (Compston et al. 1984). Williams & Claesson (1987) later suggested a quadratic form for the relationship, which is now widely accepted to be better described by a power law (Claoué-Long et al. 1995). Regardless of the form of the relationship between Pb^+/U^+ and UO^+/U^+ ratios, the critical assumption in all methods is that both standard and unknown behave similarly. For example, the commonly used power law function proposed by Claoué-Long et al. (1995) assumes that $Pb^+/U^+ = A(UO^+/U^+)^b$, where b is normally assumed to be 2.

More recently, Stern & Amelin, (2003) suggested that for zircon, $^{206}Pb^+/^{270}(UO_2^+)$ ratios do not show any functional relationship with concurrently measured $^{238}U[O_x]/$ $^{238}U[O_x]$ ratios. The recognition by these researchers that the spot–to–spot variability in $^{206}Pb^+/^{270}(UO_2^+)$ ratios is very small compared to the wide variation associated with Pb^+/U^+ ratios allows the $^{206}Pb^+/^{270}(UO_2^+)$ ratios to be used without normalisation to a specific UO^+/U^+ value. Therefore, they concluded that the calculation of $^{206}Pb/^{238}U$ ages from sputtered $^{206}Pb^+/^{270}(UO_2^+)$ ions in the target, need only be corrected for the overall SHRIMP $^{206}Pb^+/^{270}(UO_2^+)$ bias. Furthermore, concerns regarding any dissimilarities in lnPb/U:lnUO/U gradients between standard and unknown are minimised.

3.1.5   U–Pb calibration and matrix effects

Black et al. (1991) were perhaps the first to recognise an ion–probe instrumental bias in the $^{206}Pb^+/^{238}U^+$ ratios from high U zircons. Working on high U (2830–6760 ppm) zircons from mafic dykes in the Vestfold Hills of East Antarctica, Black et al. (1991) noted ~8% elevations in $^{206}Pb/^{238}U$ ages relative to $^{207}Pb/^{206}Pb$ ages. These researchers attributed the apparent elevations in $^{206}Pb/^{238}U$ to an instrumental bias in the sputtering and ionisation efficiency of the $^{206}Pb^+$ and $^{238}U^+$ ions, between the matrix of the standard zircon, and high U zircons which were presumed to be metamict and

therefore structurally damaged. Black et al. (1991) also suggested that previous ion probe studies of high U zircons by Harrison et al. (1987) and Kinny (1987), which gave reversely discordant results, were better interpreted as indicating instrumental bias in the $^{206}Pb/^{238}U$ ratios, rather than the original interpretation given in these studies, namely U loss.

McLaren et al. (1994) also recognised an ion probe instrumental bias in the measurement of $^{206}Pb/^{238}U$ ratios from a single, high U zircon (SL14). These researchers, like Black et al. (1991), attributed this effect to U–induced structural contrasts with the standard, low U zircon SL13, the effects were amplified when the zircon was heat treated, causing recrstallisation to ZrO_2 and SiO_2. More recently, Williams & Hergt (2000) and Butera et al. (2001), have suggested that the elevated $^{206}Pb/^{238}U$ ratios, typical for ion probe analyses of high U zircon, are better interpreted to be a U–induced instrumental bias rather than a microstructural one resulting from accumulated radiation damage. Butera et al. (2001) suggested that the U–induced matrix effect for zircon occurs only in crystals with over ~2500 ppm U. They suggested that for every ~1000 ppm over this threshold, there is approximately a 2 % increase in the $^{206}Pb^+/^{238}U^+$ ratio.

Although there are many published ion probe U–Pb–Th studies of monazite, only a few report Pb/U—Pb/Th matrix effects. For example, Stern & Sanborn (1998) and Stern & Berman (2000), reported elevations in monazite $^{206}Pb/^{238}U$ and $^{208}Pb/^{232}Th$ ratios of ~6 and ~8 % respectively, which were attributed to Th concentration contrasts between the calibration standard and unknown. Zhu et al. (1998) also reported $^{206}Pb/^{238}U$ ion probe matrix effects which they thought stemmed from Th and/or Si concentration contrasts. More recently, Rasmussen & Fletcher (2002) reported both a Th– and U–related matrix effect for ion probe $^{206}Pb/^{238}U$ determinations of monazite. Crystal orientation can also cause significant U–Pb matrix effects. Wingate & Compston (2000) reported that the crystal orientation of baddeleyite (ZrO_2) can cause as much as a 10 % deviation in $^{206}Pb/^{238}U$ ages.

The increased interest in, and application of, SIMS xenotime U–Pb dating has inspired research that aims to address Pb/U—Pb/Th matrix effects in this mineral. Fletcher et al. (2000) proposed a method of U abundance scaling. This method

attributes all $^{206}Pb/^{238}U$ age deviations to U, and assumes the relationship to be linear. The difference in U abundance between the standard and unknown can then be multiplied by a correction factor. The formula is:

$$Pb/U = Pb/U\text{-raw} * (1\text{-}x*(\ U\ ppm_{unk}\text{-}\ U\ ppm_{std}) \qquad (eq.\ 1)$$

Where Pb/U-raw is the calibrated Pb/U ratio and x is the correction factor = 8.

More recently, Fletcher et al. (2004) suggested that besides U, Th and $\sum$REE concentration contrasts in xenotime also result in Pb/U—Pb/Th age deviations. These researchers calculated correction factors for these elements by concurrently analysing a number of reference xenotime standards with differing compositions and determined the correction factors for each element using a simple least squares routine. The correction factors for U, Th and $\sum$REE were applied to the raw (not matrix corrected) $^{206}Pb/^{238}U$ and $^{208}Pb/^{232}Th$ ratios in a similar fashion to that shown in (1). Using this method, Fletcher et al. (2004), stated an accuracy of ~1 % for $^{206}Pb/^{238}U$ determinations and ~2 % for $^{208}Pb/^{232}Th$ determinations.

3.2 Xenotime reference standards

SHRIMP xenotime U–Pb and Th–Pb experiments, for the present study were mostly conducted on fragments from three single grained specimens, MG1, BS1, and Z6413. These samples were used by Fletcher et al. (2004) in their study of xenotime U–Pb and Th–Pb matrix effects. In addition, some experiments were conducted on multi–grain specimens, NY/PK 6-80 (Aleinikoff & Grauch 1990) and D43764, which is from the Yilgarn Craton, Western Australia.

BS1 and MG1 crystal fragments were obtained from Dr John Aleinikoff, USGS. Both crystals were originally collected by Dr. Miguel Basei, University of Sao Paulo, Brazil. These crystals originated from metamorphic host rocks. BS1 is from Bahia State, and MG1 is from Ouro Preto, Minas Gerais State (pers. comm. Miguel Basei, 2005). Full descriptions of the original crystals are given in Fletcher et al. (2004). BS1 fragments are clear, honey–yellow and homogenous in backscattered electron images. MG1 fragments are honey–yellow often with lobate patches of red iron oxide

staining. Backscattered images of MG1 are homogenous. Fletcher et al. (2004) report ID–TIMS data for BS1 that are concordant with a $^{206}Pb/^{238}U$ age of 508.9 ± 0.3 Ma (1σ) and a $^{207}Pb/^{206}Pb$ age of 505.5 ± 0.6 Ma (1σ) (Table 3.1). A reference $^{206}Pb/^{238}U$ age of 509 Ma has been used in this study. ID–TIMS ages for MG1 are concordant with a $^{206}Pb/^{238}U$ age of 490.0 ± 0.3 Ma (1σ) and a $^{207}Pb/^{206}Pb$ age of 491.8 ± 0.6 Ma (1σ) (Fletcher et al. 2004). A reference $^{206}Pb/^{238}U$ age of 490 Ma for MG1 has been used in this study. For both MG1 and BS1, $^{208}Pb/^{232}Th$ ratios were calculated directly from the $^{206}Pb/^{238}U$ age assuming a closed isotopic system.

Table 3.1. Reference ages for xenotime samples used in this study. Uncertainties are 1σ.

Sample	$^{206}Pb/^{238}U$ age (Ma)	±	$^{207}Pb/^{206}Pb$ age (Ma)	±	$^{208}Pb/^{232}Th$ age (Ma) (assumed)	±
MG1[1]	490.0	0.3	491.8	0.6	490.0	0.3
BS1[1]	508.9	0.3	505.5	0.6	509	0.3
Z6413[2]	994	1	997	1	994	1
Sample	Reference $^{206}Pb/^{238}U$ age (Ma)	±	Reference $^{207}Pb/^{206}Pb$ age (Ma)	±	Reference $^{208}Pb/^{232}Th$ age (Ma)	±
D43764[3]	2625		2625		2625	
NY/PK 6-80[4]	1000		1000		1000	

1. Source: Fletcher et al. (2004).
2. Source: Stern & Rayner (2003).
3. Reference age interpreted from SHRIMP $^{207}Pb/^{206}Pb$ age and EPMA dating.
4. Reference age interpreted from unpublished data (Kamo, 2005), supplied by Dr. John Aleinikoff (USGS), see appendix 3.1.

Z6413 fragments were obtained from Dr. Richard Stern, Geoscience Australia. This crystal is from a pegmatite from the Grenville Province Canada (Stern & Rayner, 2003). Grain fragments are honey-yellow, clear and appear homogenous in backscattered electron images. Stern & Rayner (2003) report an ID–TIMS $^{206}Pb/^{238}U$ age of 994 ± 1 Ma (1σ) and $^{207}Pb/^{206}Pb$ age of 997 ± 1 Ma (1σ) (Table 3.1). A reference $^{206}Pb/^{238}U$ and $^{208}Pb/^{232}Th$ age of 994 Ma for Z6413 has been used in this study.

NY/PK 6-80 xenotime consisted of individual grains from a monazite–xenotime gneiss from the Hudson Highlands of south-eastern New York (Aleinikoff & Grauch, 1990). Individual crystals are mostly anhedral and range from ~50 to 300 µm in diameter. Approximately 70 % are clear and colourless, but ~30 % are frosted and are

pale green to brownish. Backscattered imaging shows that many crystals have distinct cores and rims as well as small monazite inclusions (<1–5 μm) (Fig. 3.2). Age estimations for this sample are complex. Aleinikoff & Grauch (1990), from conventional ID–TIMS analyses, suggest that NY/PK 6-80 xenotime crystallised at ca. 987 Ma but also reported an inherited component at ca. 999 Ma. Recent ID–TIMS analyses of NY/PK 6-80 (Appendix 3.1) were conducted by Sandra Kamo, Royal Ontario Museum (results kindly supplied by Dr. John Aleinikoff, USGS). Thirteen individual analyses of both abraded and un-abraded grains have $^{206}Pb/^{238}U$ ages that range between 970.3 ± 1.9 (2σ) and 1006.4 ± 2.7 Ma (2σ). Even after omitting the youngest analysis (sk17p168) the data are spread beyond analytical uncertainty (MSWD=13), and range between 992.6 ± 4 (2σ) and 1006.4 ± 2.7 Ma (2σ). This age range is probably the result of ID–TIMS analysis of both core and rims. Although the oldest 12 $^{206}Pb/^{238}U$ analyses represent a mixed population, their median age of 1000 +3.2/-5 Ma (95 % confidence) is used in this study as the reference $^{206}Pb/^{238}U$ and $^{208}Pb/^{232}Th$ age for this sample.
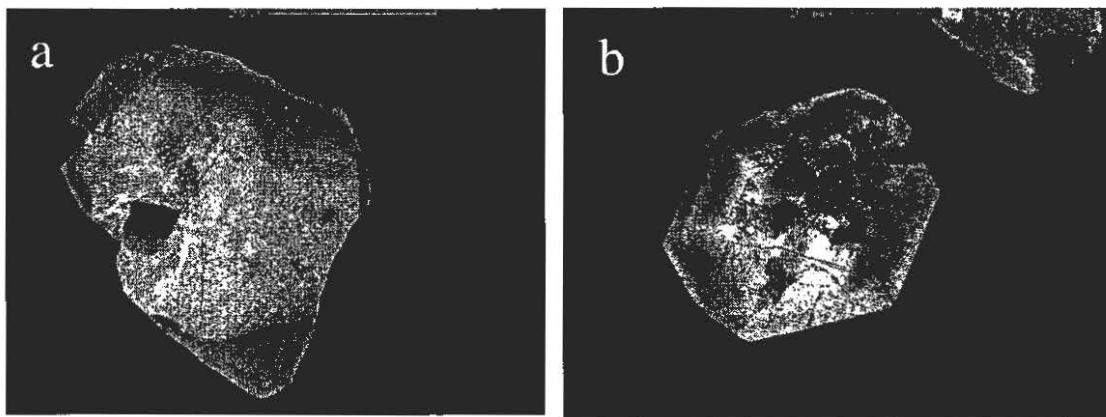
Fig. 3.2. BSE images for NY/PK 6-80 (a) and D43764 (b) xenotimes. Small white blebs are monazite.

Sample D43764 is from a biotite schist from the Holleton region of the eastern Goldfields, Western Australia, and was procured from the Australian Museum. Xenotime crystals recovered from D43764, are yellow, euhedral dipyramids that range in size from ~70 to 400 μm. The crystals are variably cracked and the majority are speckled with <1 to 5 μm monazite inclusions that mainly occur in patches (Fig. 3.2). There are no ID–TIMS data for this sample. However, SHRIMP $^{207}Pb/^{206}Pb$ data

collected during this study have a single age of 2625 ± 5 Ma (95 % confidence). This age has been corroborated by independent EPMA dating (Appendix 3.2). Therefore, the $^{207}Pb/^{206}Pb$ age of 2625 Ma was used as the reference age for both $^{206}Pb/^{238}U$ and $^{208}Pb/^{232}Th$ ratios.

3.3 Analytical and data processing protocols

Xenotime crystal fragments and single crystals were mounted in epoxy resin and polished to reveal the sample interiors. Transmitted and reflected light photomicrographs were taken of the xenotime, followed by backscattered SEM images using a Cambridge 360 SEM at the ANU Electron Microscopy Unit. Electron microprobe analyses were conducted on a Cameca SX100 at RSES.

Isotopic analyses were carried out on the SHRIMP II and SHRIMP RG ion microprobes located at the RSES. Early experiments were carried out on SHRIMP II, however, later experiments showed SHRIMP RG to be more suitable for xenotime analysis as this instrument does not encounter the scattered ions detectable on the mass ^{204}Pb peak and Background that the SHRIMP II instrument detects (see section 3.3.7 and Fletcher et al. 2000).

3.3.1 Electron Probe

Xenotime samples were analysed for Y, P, Si, Ca, Nd, Sm, Eu, Gd, Tb, Dy, Ho, Er, Tm, Yb, Lu, Th, and U by wavelength dispersive spectrometry (WDS). All analyses were preformed with a 25 kV electron beam regulated at 100nA with a beam size of ~5 μm. The REE were calibrated against synthetic REE phosphate standards and U oxide and Th oxide standards were used for U and Th calibration. Analyses were carried out using the analytical peaks as recommended by Pyle et al. (2002). Peak and background positions for each element were carefully chosen from WDS scans of the three xenotime standards MGI, Z6413 and BS1. Appendix 3.3 contains the analytical conditions used for xenotime electron microprobe characterisation and the approximate errors and detection limits for each of the elements analysed.

61

3.3.2 SHRIMP

Experiments conducted on SHRIMP II used a primary O_2^- beam with an ion current that ranged between ~2 to 6.5 nA. Kohler apertures of either 70 or 120 μm yielded spot diameters of ~10 to 30 μm. For some experiments, the energy window was set to exclude ~50–90 % of the low energy ions. This was done in order to remove the scattered ions associated with the ^{204}Pb peak and also to test whether the high energy ion population is less susceptible to ^{206}Pb/^{238}U SHRIMP matrix effects. The majority of experiments conducted on SHRIMP RG were carried out under the analytical conditions needed for the analysis of ~10 to 15 μm diagenetic xenotime overgrowths and hydrothermal xenotime. To achieve this, the primary beam was focussed through a ~30 μm Kohler aperture which resulted in spot diameters of between ~5–7 μm. Initial trials using SHRIMP RG using a ~0.1 nA, O_2^- primary beam yielded a ^{206}Pb count rate of about 100 cps for analyses of the primary calibration standard MG1 (~70 ppm ^{206}Pb; i.e. 14cps/nA/ppm). However, there was a concern that the low primary beam current may be approaching the lower limit of stable analytical conditions and also resulting in poor individual ^{206}Pb$^+$/^{238}U$^+$ spot precisions of ~2%. Because of the higher O$^-$ current achievable with the SHRIMP RG duoplasmatron (O$^-$/O_2^- = 4) an O$^-$ primary beam was trialled which resulted in an increase in the absolute ^{206}Pb count rate for MG1 by a factor of ~3, albeit at a reduced relative count rate (sensitivity) of approximately ~50 %. The stronger primary current and better counting statistics offered by the O$^-$ primary beam was judged to be the best balance between precision, sensitivity and instrument stability. Under these conditions, primary O$^-$ beam strengths focussed through a 30 μm Kohler aperture, ranged between ~0.8 to 1.2 nA. Appendix 3.4 details the SHRIMP instrumental conditions for the 14 SHRIMP xenotime U–Pb sessions discussed in this chapter.

Sets of different mass peaks were tested throughout the various experiments to determine the optimal data acquisition sequence for xenotime U–Pb and Th–Pb analysis. A typical run table consisted of ^{89}Y$_2$^{16}O$^+$ [^{194}(Y$_2$O$^+$)], ^{204}Pb, BG, ^{206}Pb$^+$, ^{207}Pb$^+$, ^{208}Pb$^+$, ^{238}U$^+$, ^{232}Th^{16}O$^+$ [^{248}(ThO$^+$)], ^{238}U^{16}O$^+$ [^{254}(UO$^+$)] and ^{238}U^{16}O$_2$$^+$ [^{270}(UO$_2$$^+$)] (BG=background measured at +0.04 mass units up mass of the ^{204}Pb peak). Some experiments included ^{232}Th$^+$ and ^{232}Th^{16}O$_2$$^+$ [^{264}(ThO$_2$$^+$)] for independent ^{208}Pb/^{232}Th determinations. Additionally, with the aim of monitoring the matrix

effects introduced by the HREE, some experiments included $^{174}Yb^{16}O^+$ [$^{190}(YbO^+)$], $^{161}Dy^{16}O^+$ [$^{177}(DyO^+)$] and $^{165}Ho^{16}O^+$ [$^{181}(HoO^+)$]. Each of the analyses for the various analytical sessions consisted of 5 to 7 scans. Raw isotopic ratios were calculated with PRAWN 6.55. The secondary ion ratios were calculated from the mid point of a linear regression of count rate vs. time from the various scans. Calculated uncertainties consisted of counting statistics augmented, if necessary, by the uncertainties introduced by the scatter about the linear regression. $^{206}Pb/^{238}U$ and $^{208}Pb/^{232}Th$ ages were calculated via a procedure written by the author in EXCEL to calculate $^{206}Pb/^{238}U$ and $^{208}Pb/^{232}Th$ ages from the raw $^{206}Pb^+/^{270}(UO_2^+)$ and $^{208}Pb^+/^{248}(ThO^+)$ ratios (procedure discussed below). The uncertainties for these age calculations used the algorithms from ISOPLOT 3 (Ludwig, 2003). Common Pb corrections were based on individual measured ^{204}Pb abundances and assuming crustal common Pb of the same age as the xenotime, using the model of Stacey & Kramers (1975). However, the very low common Pb contents typical of xenotime result in age corrections that are not sensitive to the choice of common Pb composition.

3.3.3 Electron microprobe characterisation of the reference standards

Representative WDS data for MG1, BS1, Z6413, NY/PK 6-80 and D43764 are shown in Tables 3.2 and 3.3. Table 3.2 shows typical averaged concentrations for each of the samples, whereas Table 3.3 contains the typical concentration ranges for U_2O_3, ThO_2 and $\sum REE$–oxides. Overall, there is a wide range in $\sum REE$ and actinide concentrations among these samples. U_2O_3 contents range from ~0.02–2.8 wt%, ThO_2 from 0.06–1.9 wt% and $\sum REE_2O_3$ from ~15–21 wt%.

Table 3.2. WDS determined average compositions for the reference xenotimes used in this study.

sample oxide	MG1 n=30	BS1 n=28	Z6413 n=32	NY/PK 6-80 core n=22	NY/PK 6-80 rim n=21	D43764 n=25
SiO2	0.15	0.26	0.69	0.58	0.49	0.73
P2O5	35.10	33.24	34.27	34.27	34.38	33.87
CaO	0.02	0.01	0.02	0.09	0.08	0.10
Y2O3	47.07	42.76	43.58	41.89	42.45	39.35
ThO2	0.11	0.35	0.26	0.42	0.38	1.00
U2O3	0.11	0.05	1.46	1.76	1.43	1.62
Nd2O3	0.26	0.16	0.04	0.45	0.44	0.90
Sm2O3	0.63	0.52	0.13	0.59	0.58	0.75
Eu2O3	0.37	0.21	0.03	0.04	0.05	0.02
Gd2O3	3.73	3.08	1.02	2.20	2.25	2.29
Tb2O3	0.67	0.74	0.33	0.58	0.61	0.57
Dy2O3	5.24	6.63	4.30	5.73	5.90	4.79
Ho2O3	1.07	1.46	1.19	1.36	1.36	1.10
Er2O3	2.26	3.99	4.37	4.18	4.05	3.68
Tm2O3	0.24	0.52	0.71	0.60	0.57	0.53
Yb2O3	0.72	2.52	5.30	3.54	3.20	3.83
Lu2O3	0.33	0.58	1.07	0.81	0.77	0.12
total	98.07	97.09	98.78	99.09	98.98	95.25
av. U/Th	0.96	0.15	5.79	4.19	3.76	1.62
total REE oxide	15.51	20.42	18.49	20.09	19.78	18.57

Table 3.3. WDS determined U, Th and $\sum$REE concentration ranges for the reference xenotimes ('c' and 'r' denotes core and rim analyses respectively).

	U_2O_3 wt%	ThO_2 wt%	$\sum REE_2O_3$ wt%
Sample	Range	Range	Range
MG1	~0.075–0.144	~0.0614–0.199	~14.91–16.77
Z6413	~1.088–1.781	~0.20–0.336	~18.15–18.85
BS1	~0.02–0.087	~0.115–0.549	~19.75–21.32
NY/PK 6-80 r	~0.546–1.979	~0.152–0.504	~18.68–20.2
NY/PK 6-80 c	~1.04–2.51	~0.296–0.565	~18.72–20.56
D43764	~0.772–2.778	~0.405–1.916	~17.71–19.48

MG1 is distinguished by relatively low $\sum$REE concentrations (~15 wt% $\sum REE_2O_3$) and also low to moderate U_2O_3 and ThO_2 contents, both of which are ~0.11 wt%. BS1 contains the lowest levels of U among the reference xenotimes (~0.05 wt% U_2O_3) but moderate to high ThO_2 (~0.35 wt%) and high $\sum REE_2O_3$ contents of ~20 %. Three of the xenotime samples, Z6413, NY/PK 6-80 and D43764, have high U_2O_3 concentrations which are generally above ~1.4 wt%. Z6413 typically contains U_2O_3 of ~1.4 wt%, however some fragments were found to have concentrations of ~0.5 wt%. Z6413 is also characterised by moderate to low ThO_2 (0.26 wt%) and moderate

to high $\sum REE_2O_3$ levels of ~18.5 wt%. There appears to be no chemical difference between the cores and rims of NY/PK 6-80. This sample contains high U_2O_3 (~1.5 wt%), moderate to high ThO_2 (0.4 wt%) and high $\sum REE_2O_3$ levels (~20 wt%). Sample D43764 contains the highest ThO_2 concentrations amongst the reference xenotimes (~1 wt%) as well as high U_2O_3 (~1.6 wt%) and moderate to high $\sum REE_2O_3$ (~18.5 wt%). Z6413 and NY/PK 6-80 have the highest U/Th ratios (~6 and ~4 respectively) whereas D43764 has a U/Th ratio of ~1.6. BS1 has the lowest U/Th ratio of ~0.15 and MG1 has a ratio of ~1.

3.3.3.1   *Actinide substitution mechanisms for the reference xenotimes*

Plots of Ca and Si versus Th and U for the reference xenotimes show a strong correlation between the actinide elements and Si but little or no correlation with Ca indicating that the incorporation of Th and U into these samples principally occurs through the thorite substitution mechanism i.e. $(Th, U)^{4+} + Si^{4+} = P^{5+} + (REE, Y)^{3+}$ (Fig. 3.3b, 3.3f, 3.3j, 3.3n, 3.3r). The brabantite substitution seems only to be significant in NY/PK 6-80 where there is a moderate positive correlation between Ca and Th + U (R=0.7; Fig. 3.3e). Of particular interest is the very strong correlation between Si and U in Z6413, NY/PK 6-80 and D43764 (R = 0.99, 0.94 and 0.81 respectively) (Fig. 3.3c; 3.3g; 3.3s). Of note also is the particularly strong correlation between U and Th in the single crystal sample Z6413 (R=0.98), compared with the multi–grain, high U samples D43764 and NY/PK 6-80 (R=0.56) (Fig. 3.4).

The data for the reference xenotimes plotted in Fig. 3.3 (b, f, j, n, r) lie above the idealised thorite substitution vector (Si vs. Th + U), indicating an excess of Si. The zircon substitution i.e. $Zr^{4+} + Si^{4+} = P^{5+} + (REE. Y)^{3+}$ maybe an additional mechanism by which Si enters the xenotime lattice, as has previously been suggested by Spear & Pyle (2002). However, Zr was not analysed in this study, so this suggestion was not tested.

The electron microprobe data for the reference xenotimes show that collectively, they cover a wide range of compositions. They therefore enable an investigation of the role mineral composition plays in xenotime SHRIMP U–Pb and Th–Pb age determinations.
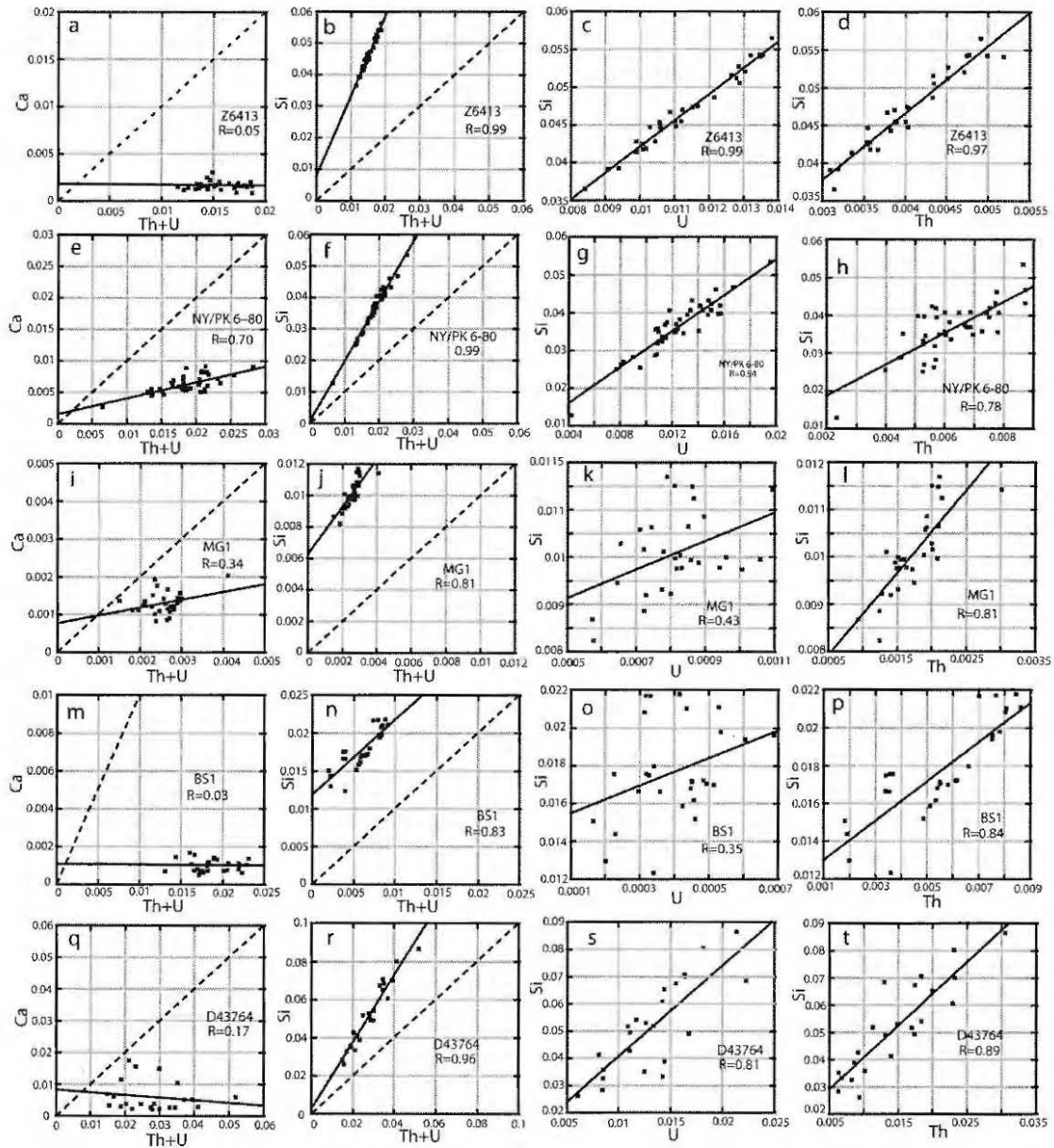
Fig. 3.3. Plots demonstrating the chemical substitutions for the reference xenotimes (axes are cation proportions). Cation proportions (cations/4 oxygens) of Si and Ca vs. Th+U and Si vs. Th and U. Dashed straight line represents the ideal thorite and brabantite substitution vector.
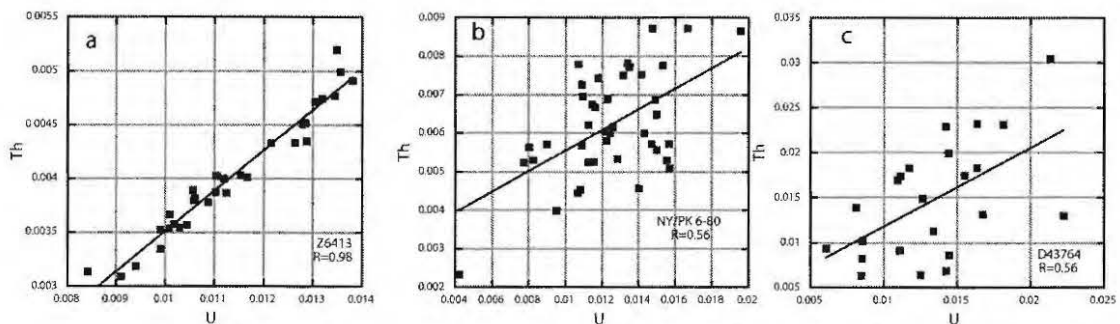
Fig. 3.4. Plots of the cation proportions (cations/4 oxygens) for Th and U for the high U reference xenotimes Z6413 (a), NY/PK 6-80 (b) and D43764 (c). The strong correlation between Th and U for Z6413, contrasts with that for NY/PK 6-80 and D43764. Axes are cation proportions.

3.3.4   SHRIMP U—Pb Calibration

Early xenotime experiments during this study, using SHRIMP II, tested all nine combinations of Pb/U[O_x]:U[O_x] / U[O_x] to determine which ratio pair yielded the best correlation and therefore, the least scatter in calculated ^{206}Pb/^{238}U ratios (see Appendix 3.5). These experiments determined that the ratio pair of Pb/U:UO/U performed best overall for the three xenotime standards MG1, BS1 and Z6413. Fig. 3.5 shows typical lnPb/U:lnUO/U linear regressions for the three xenotime standards obtained with SHRIMP II using a ~6.5 nA primary O_2^- beam. This graph shows that all xenotimes have a similar slope of ~1.4 and highly correlated Pb/U:UO/U ratio pairs. These data show that a power law relationship between Pb$^+$/U$^+$ and UO$^+$/U$^+$ ratios, i.e. $y = ax^b$, as commonly used to calibrate Pb$^+$/U$^+$ ratios in zircon, probably applies for this analytical session. In this case, $b \approx 1.4$.

The excellent correlation and similarity in gradients between Pb$^+$/U$^+$ and UO$^+$/U$^+$ ratios using the analytical conditions described for SHRIMP II above, are in contrast to the xenotime data collected on SHRIMP RG using a ~1 nA, O$^-$ primary beam focussed through a 30 μm Kohler aperture (Fig. 3.6). This figure shows lnPb/U:UO/U plots for two SHRIMP RG sessions, where the gradient of the linear regressions varies significantly between the reference xenotimes. For example, for the SHRIMP session RG-2 (Fig. 3.6b) the high U Z6413 xenotime has a slope of ~3.9, whereas the low to moderate U standard, MG1 has a slope of ~1.5. Contrasts in slope amongst these xenotime standards occurred for all of Pb/U[O_x]:U[O_x]/U[O_x] ratio combinations in each of the SHRIMP RG sessions carried out under the analytical conditions described above. Therefore, it appears that the Pb/U:UO/U correction method cannot be used to correct SHRIMP RG xenotime Pb$^+$/U$^+$ ratios collected under the analytical conditions described above.
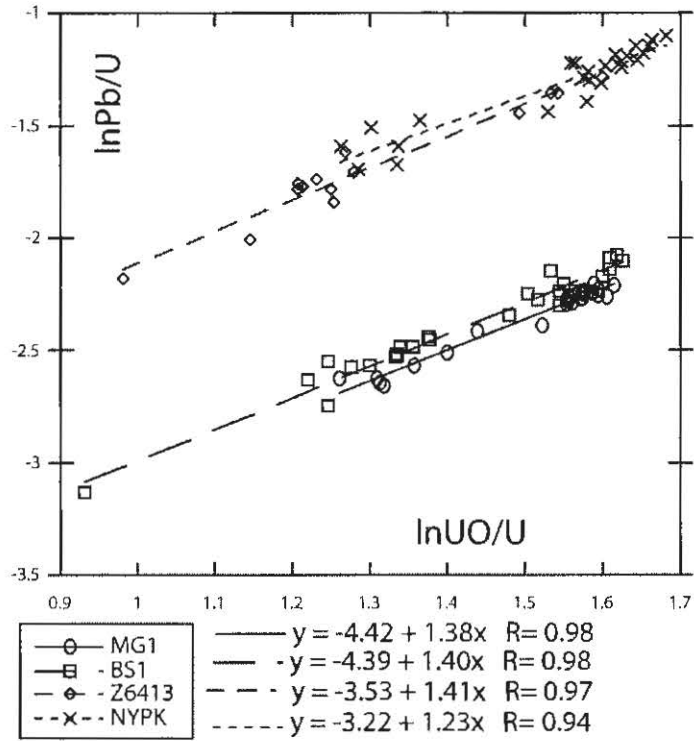
Fig. 3.5. lnPb/U:lnUO/U calibration plot for session SHII-1.
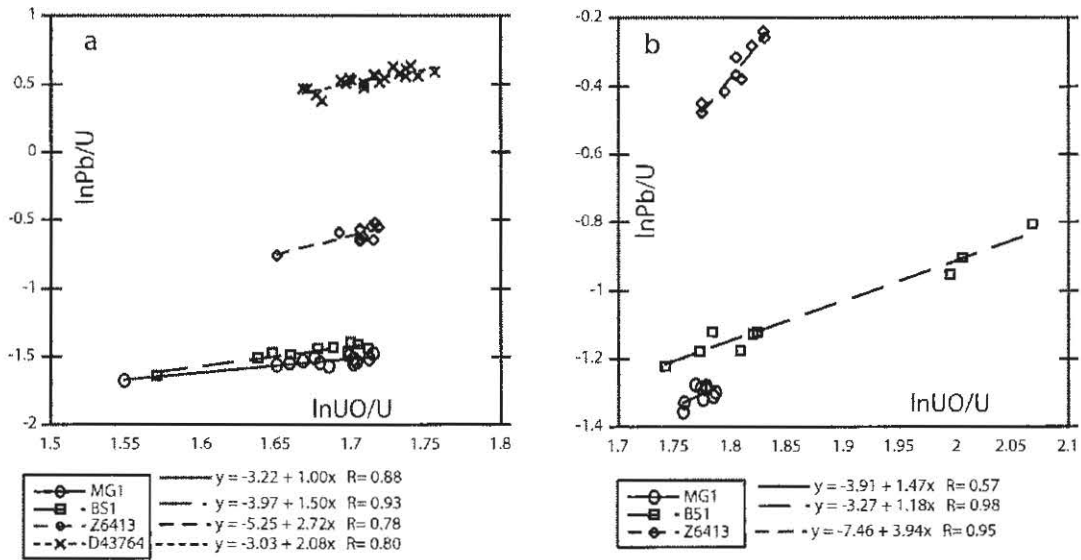
Fig. 3.6. lnPb/U:lnUO/U calibration plots for two representative SHRIMP RG sessions, RG–1 (a) and RG–2 (b), demonstrating the variable calibration slopes between the reference xenotimes.

The scarcity of xenotime Pb/U standards has made it necessary in many case studies to analyse the $^{206}Pb/^{238}U$ standards and unknowns in separate mounts, during the same analytical session (e.g. Kositcin et al. 2003; Pigois et al. 2003; Salier et al. 2004; Vallini et al. 2005 and; Vallini et al. 2006). However, this practise could result in slight variations in analytical conditions, such as charging contrasts between the two mount holders on the sample stage, or slightly different gold coat thicknesses between the mounts. These minor differences may cause variations in Pb/U:UO/U slope between standard and unknown, hence jeopardising the resultant $^{206}Pb/^{238}U$ age calculation. Figure 3.7 shows such a situation from the Curtin University SHRIMP II-B where the Pb/U:UO/U slope for the standards (slope = ~2.3) contrasts with that of the unknown sample (slope = ~1.2) which was analysed from a separate mount, during the same session. For this case, the Pb/U:UO/U calibration method may lead to aberrant $^{206}Pb/^{238}U$ age results for the unknown particularly given that the UO/U for the sample is mostly lower than that for the standard. The failure of the SHRIMP RG xenotime Pb/U:UO/U calibration under the instrumental conditions listed above prompted an investigation of using the raw $^{206}Pb^+/^{270}(UO_2^+)$ ratios to calculate $^{206}Pb/^{238}U$ ages, as has been suggested for zircon by Stern & Amelin (2003).
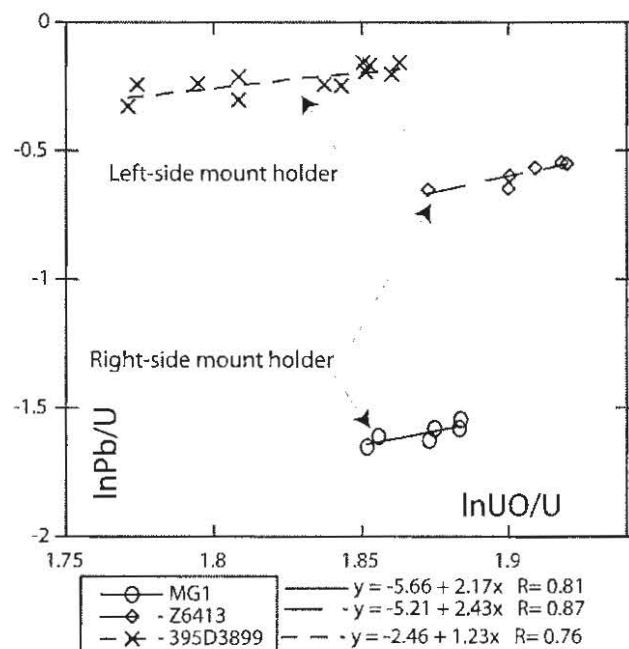
Fig. 3.7. lnPb/U:lnUO/U calibration slope variation between samples analysed concurrently from separate mount holders on the SHRIMP sample stage. Standards MG1 and Z6413 (right–side mount) and sample 395D3899 (left–side mount). (SHRIMP B, Curtin University of Technology, Perth, WA).

An investigation of all the SHRIMP xenotime Pb/U data sets collected during this study shows that xenotime $^{206}Pb^+/^{270}(UO_2^+)$ ratios, regardless of analytical conditions or instrument, are virtually independent of the $U[O_x]/U[O_x]$ ratios. This is similar to findings of Stern & Amelin (2003) for zircon. Figure 3.8a & b, show $^{206}Pb^+/^{270}(UO_2^+):UO^+/U^+$ plots for MG1 data from SHRIMP II and SHRIMP RG. Both of these plots show that the $^{206}Pb^+/^{270}(UO_2^+)$ ratios do not show any relationship with the concurrently measured UO^+/U^+ ratios. Furthermore, the percent standard deviation (coefficient of variation) of the raw $^{206}Pb^+/^{270}(UO_2^+)$ ratios for the calibration standard, is significantly reduced in comparison to the raw $^{206}Pb^+/^{238}U^+$ ratios and indeed comparable to the reproducibility associated with Pb/U:UO/U correction techniques (Table 3.4). The 1σ percent standard deviation of the $^{206}Pb^+/^{270}(UO_2^+)$ ratios for the six SHRIMP analytical sessions shown in Table 3.4, range from 1.4–2.5, which is comparable to the reproducibility associated with the Pb/U:UO/U calibration technique.
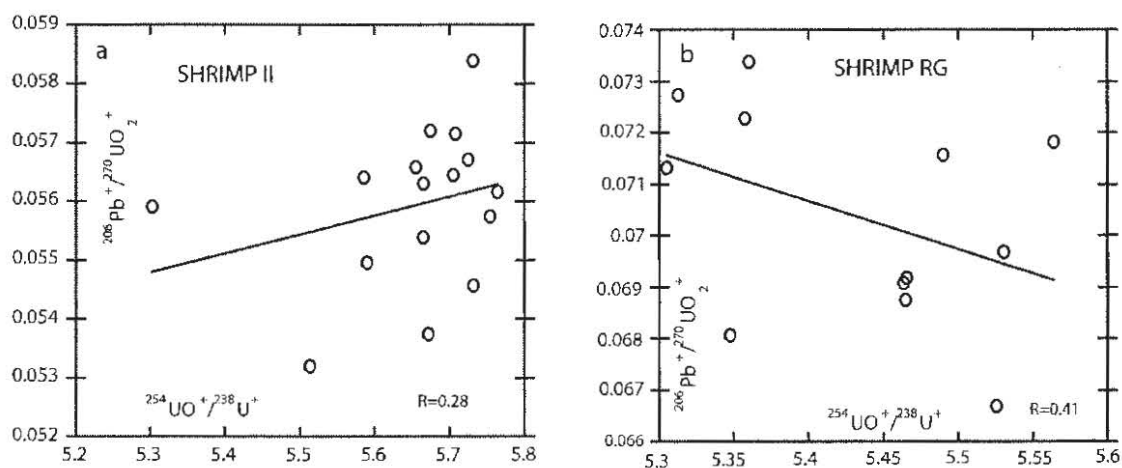
Fig. 3.8. $^{206}Pb^+/^{270}(UO_2^+)$ vs. $^{254}(UO^+)/^{238}U^+$ plots for two SHRIMP sessions SHII–6 (a) and RG–1 (b) demonstrating the poor correlation between these ratios pairs.

Table 3.4. Comparison of the reproducibility of the raw $^{206}Pb^+/^{270}(UO_2^+)$ ratios for the primary calibration standard MG1, with the reproducibility associated with a linear and power law function typically used to correct for the SHRIMP Pb^+/U^+ spot-to–spot variation. 1. Raw $^{206}Pb^+/^{270}(UO_2^+)$ ratios 2. Pb^+/U^+:UO^+/U^+ correction using a simple unweighted linear regression $y = mx + b$ (Stern 1997) and 3. Power law, $y = ax^b$ of Claoué-Long et al. (1995). Error is calculated as the 1σ percent standard deviation. Reproducibility of the raw Pb^+/U^+ ratios is also shown for comparison.

Session	SHRIMP	% EF	1. $^{206}Pb^+/^{270}UO_2^+$	2. Pb/U:UO/U linear	3. Pb/U:UO/U power law	4. $^{206}Pb^+/^{238}U^+$	No.
SH-II-1	II	50	2.3	2.3	2.3	13.3	25
SH-II-6	II	90	2.5	2.1	1.9	3.4	14
SH-II-4	II	-	1.4	1.3	1.6	3.5	12
RG-1	RG	-	2.3	2.9	2.4	4.8	13
RG-4	RG	-	2.2	2.6	2.6	3.2	10
RG-7	RG	-	1.8	2.1	2.2	2.1	9

(% EF = the percent energy filtering of the low energy ions).

The secondary ion energy profiles for $^{206}Pb^+$, $^{238}U^+$, $^{254}(UO^+)$ and $^{270}(UO_2^+)$ also support the calculation of $^{206}Pb/^{238}U$ from the raw $^{206}Pb^+/^{270}(UO_2^+)$ ratios (Fig. 3.9a & 3.9b). Energy distributions for $^{206}Pb^+$ and $U[O_x]$ species, were measured on SHRIMP II and SHRIMP RG and show similar trends to those obtained for monazite (Harrison et al. 1995 and Stern & Berman 2000) and zircon (Stern 2000). Specifically, the energy profile for $^{270}(UO_2^+)$ most closely parallels that of the $^{206}Pb^+$ ion distribution. $^{254}(UO^+)$ ions also show a close but lesser similarity to the $^{206}Pb^+$ profile, and the $^{238}U^+$ ions have a broader energy distribution in comparison to the $^{206}Pb^+$ and $U[O_x]$ ion distributions.
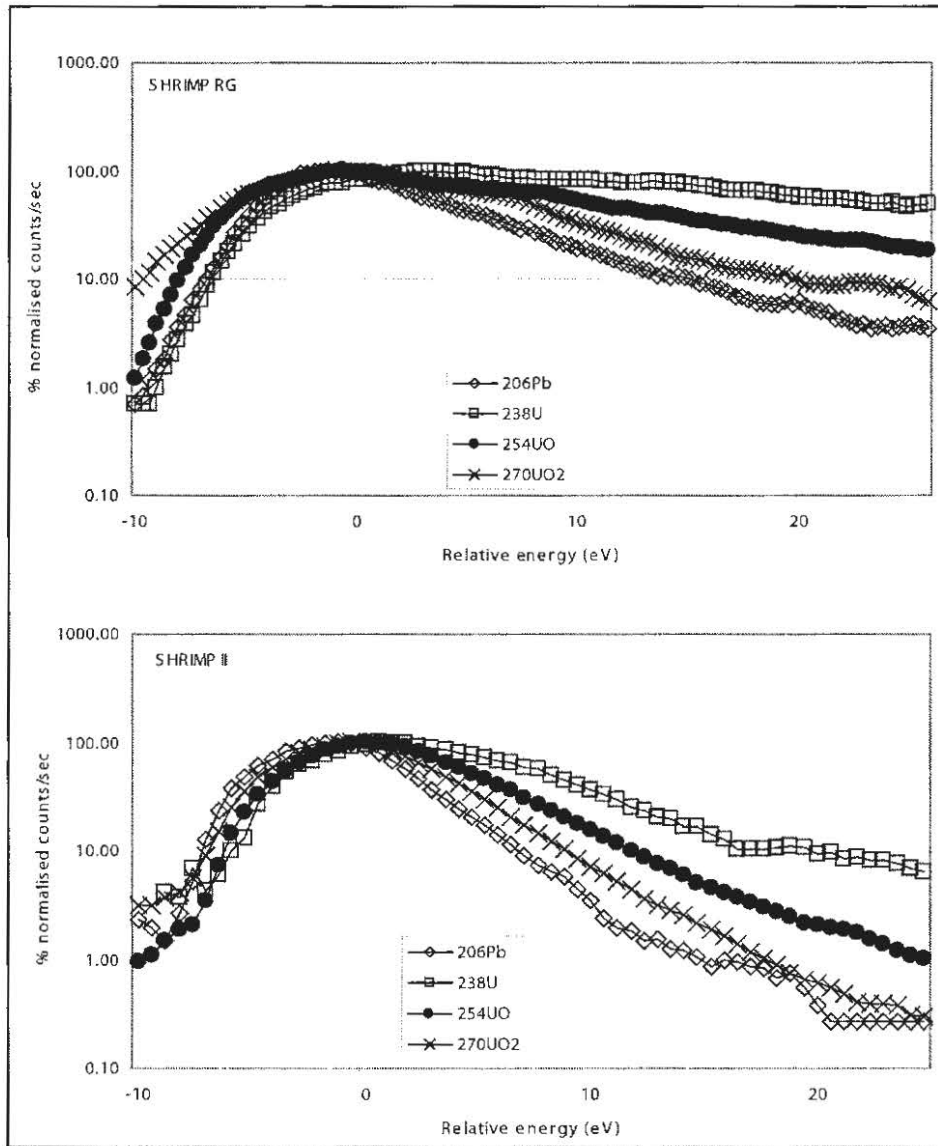
Fig. 3.9. Energy profiles for the reference xenotime MG1, carried out on SHRIMP RG (top) and SHRIMP II (bottom). The zero volts position was taken as the maximum transmission of the 254(UO+) molecule. Each scan is normalised to the maximum count rate to allow for a better comparison between the two instruments.

Calculating $^{206}Pb/^{238}U$ from the raw $^{206}Pb^{+}/^{270}(UO_2^{+})$ ratios may also be an acceptable method for situations where the scarcity of standards dictate that they must be analysed from a separate mount to the unknowns. Figure 3.10a and 3.10b, compares the scatter of the raw $^{206}Pb^{+}/^{270}(UO_2^{+})$ ratios with that of the Pb/U:UO/U regression for two SHRIMP RG sessions, where MG1 was analysed from both the left– and right–side mount holders on the sample stage. Eight analyses of MG1 on the right-side mount and nine analyses on the left-side mount from experiment RG-2 are shown in Fig. 3.10a. These data when plotted on a lnPb/U:lnUO/U plot, lie on a single regression line but can be separated by their contrast in UO^{+}/U^{+} ratios. The Pb^{+}/U^{+}

ratios for this experiment have a standard deviation about the regression line of 1.8 % (1σ). The raw $^{206}Pb^+/^{270}(UO_2^+)$ ratios for the same data points, are uniformly scattered about their mean, with a slightly elevated standard deviation of 2.5 % (1σ) in comparison to the lnPb/U:lnUO/U regression. The lnPb/U:lnUO/U regression line for the data shown in Fig. 3.10b (experiment RG–3) is poorly defined. This may be due in part to the very narrow range of UO^+/U^+ ratios and also the limited data collected for this experiment, which consisted of seven MG1 analyses on the right–side mount, and five on the left–side mount. The scatter of the Pb^+/U^+ ratios about the lnPb/U:lnUO/U regression line for both mounts is 3.2 % (1σ). The relatively poor reproducibility of this data set when considered as a whole may indicate that the MG1 analyses from the left– and right–side mounts form two separate lnPb/U:lnUO/U regression lines. By contrast, the raw $^{206}Pb^+/^{270}(UO_2^+)$ ratios have a standard deviation of 2.6 % (1σ).
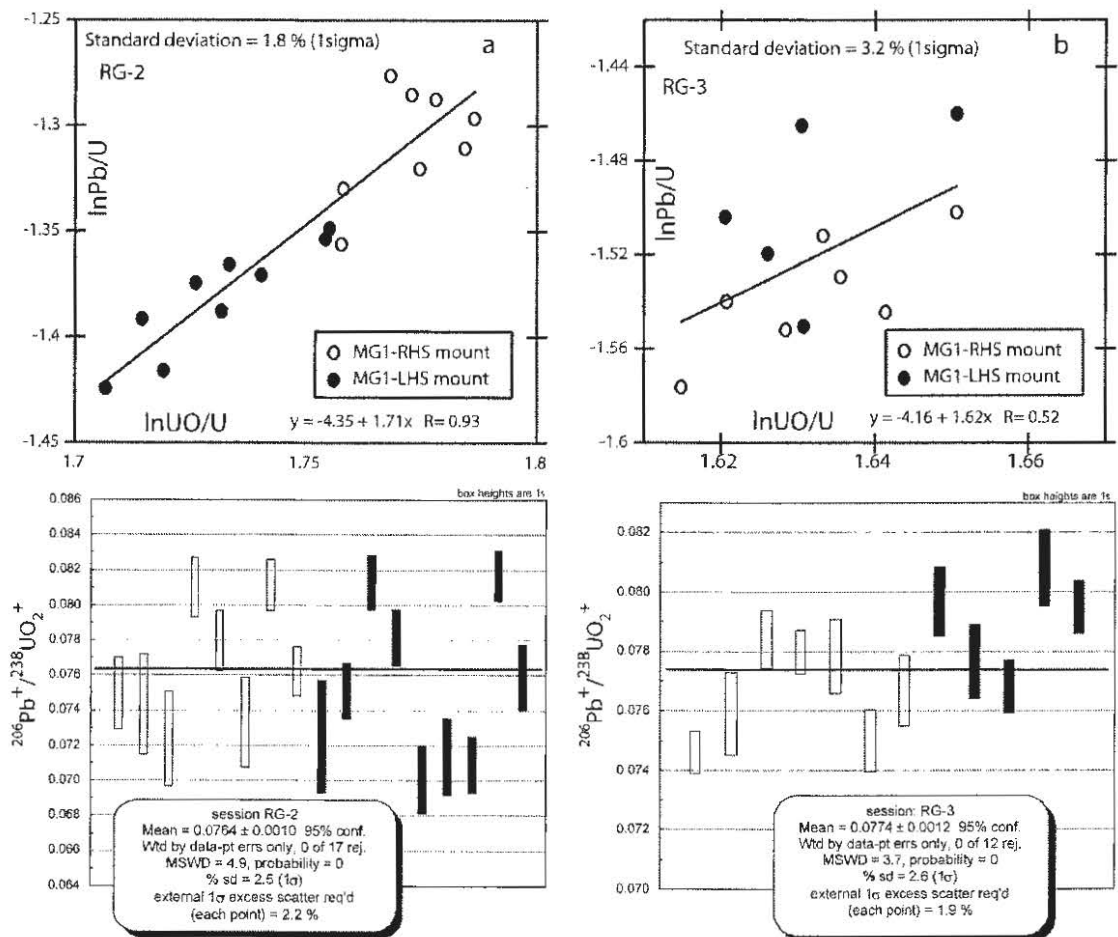
Fig. 3.10. lnPb/U:lnUO/U plots and $^{206}Pb^+/^{270}(UO_2^+)$ for two SHRIMP RG sessions, RG–2,(a) and RG–3,(b) where MG1 was analysed concurrently from both the left– and right–side mount holders.

Although the data from these two experiments are perhaps limited, the scatter of the individual raw $^{206}Pb^+/^{270}(UO_2^+)$ ratios as analysed from separate mounts during the one experiment, suggests an acceptable reproducibility of approximately ~2.5 % (1σ). Additionally, the $^{206}Pb^+/^{270}(UO_2^+)$ calibration technique may also be more resistant to changes in instrumental conditions, which may cause contrasts in the lnPb/U:lnUO/U regression line between different samples. It is considered that this situation is more likely to occur when analysing the Pb/U—Pb/Th standards and unknowns from separate mounts.

Accounting for the variability in SHRIMP Pb^+/U^+ ratios by a regression against the UO^+/U^+ ratios is based on the premise that both $^{206}Pb/^{238}U$ calibration standard and unknown obey the same functional relationship. However, in situations where the above premise is not met, as is the case for all xenotime Pb/U—Pb/Th experiments conducted on SHRIMP RG under the experimental conditions listed above, calculation of $^{206}Pb/^{238}U$ from the raw $^{206}Pb^+/^{270}(UO_2^+)$ ratios appears to be a robust, practical alternative. It is for these reasons that all xenotime $^{206}Pb/^{238}U$ ages reported in this thesis are calculated from the raw $^{206}Pb^+/^{270}(UO_2^+)$ ratios, unless otherwise stated.

Calculating $^{206}Pb/^{238}U$ from $^{206}Pb^+/^{270}(UO_2^+)$ ratios is straightforward. The raw $^{206}Pb^+/^{270}(UO_2^+)$ ratio of the unknown is divided by the average $^{206}Pb^+/^{270}(UO_2^+)$ of the standard, which is in turn multiplied by the $^{206}Pb/^{238}U$ ratio of the standard (equation 2).

$$^{206}Pb/^{238}U_{(unk)} = (^{206}Pb^+/^{270}(UO_2^+))_{unk}/av.(^{206}Pb^+/^{270}(UO_2^+))_{std} * (^{206}Pb/^{238}U)_{std}$$
(eq. 2)

3.3.4.2 Independent $^{208}Pb/^{232}Th$ age calculations

The calculation of $^{208}Pb/^{232}Th$ ages from the sample xenotimes can be used to assess the concordance of the target mineral, and thereby assess the SHRIMP $^{208}Pb/^{232}Th$ xenotime matrix effect. The significant matrix effects of SHRIMP xenotime $^{206}Pb/^{238}U$ ratios preclude the calculation of derivative $^{208}Pb/^{232}Th$ ages that are based

on $^{206}Pb/^{238}U$, $^{208}Pb^{+}/^{206}Pb^{+}$ and $^{248}(ThO^{+})/^{254}(UO^{+})$ ratios as described by Williams et al. (1996). Therefore, independent $^{208}Pb/^{232}Th$ age calculations are necessary.

For the independent $^{208}Pb/^{232}Th$ age calibration, combinations of $^{208}Pb/^{232}Th:^{232}ThO/^{232}Th$ and $^{208}Pb/^{232}ThO:^{232}ThO/^{232}Th$ were trialled. However, variations in slope exist between all of the reference xenotimes and these calibration pairs (Fig. 3.11). This is similar to the findings of Fletcher et al. (2004) who found that the $^{208}Pb/^{232}Th$ calibration is very sensitive to the choice of calibration slope, which subsequently yielded inferior results to the $^{206}Pb/^{238}U$ age calculations and matrix corrections.

The limited range in variability that the $^{206}Pb^{+}/^{270}(UO_2^{+})$ ratios show, compared to the $^{206}Pb^{+}/^{238}U^{+}$ ratios, is also evident between the xenotime $^{208}Pb^{+}/^{232}Th^{+}$ and $^{208}Pb^{+}/^{232}ThO_x^{+}$ ratios (Table 3.5). Table 3.5 shows that the $^{208}Pb^{+}/^{248}(ThO^{+})$ ratios show the least amount of scatter which generally ranges between ~1.5 and 3.5 % (1σ), which is slightly elevated compared with the typical standard deviation of the raw $^{206}Pb^{+}/^{270}(UO_2^{+})$ ratios. Therefore, $^{208}Pb/^{232}Th$ ratios were calculated from the raw $^{208}Pb^{+}/^{248}(ThO^{+})$ in the same way xenotime $^{206}Pb/^{238}U$ ratios were derived from the raw SHRIMP $^{206}Pb^{+}/^{270}(UO_2^{+})$ ratios. However, $^{208}Pb/^{232}Th$ ages calculated by this method were only found to be accurate for xenotimes with Th concentrations > ~1000 ppm. The reasons for this are unknown so this method has limited applicability and may not be able to be used for the calculation of $^{208}Pb/^{232}Th$ ages from hydrothermal and diagenetic xenotime, where Th concentrations are typically in the 100's of ppm.

Table 3.5. Percent standard deviation (1σ) of the raw $^{208}Pb^{+}/^{248}(ThO^{+})$ ratios for MG1 for nine separate SHRIMP sessions. Limited data for $^{208}Pb^{+}/^{232}Th^{+}$ and $^{208}Pb^{+}/^{264}(ThO_2^{+})$ is shown for comparison (EF = energy filtered).

Session	SHRIMP	EF	$^{208}Pb^{+}/^{232}Th^{+}$	$^{208}Pb^{+}/^{248}ThO^{+}$	$^{208}Pb^{+}/^{264}ThO_2^{+}$	n
SH-II-2	II	50	-	2.10	-	16
SH-II-3	II	-	-	2.7	-	8
SH-II-4	II	-	2.7	2.0	21.1	11
SHII-5	II	90	-	2.8	-	14
RG-1	RG	-	-	1.8	-	10
RG-3	RG	-	19.8	3.3	2.9	7
RG-4	RG	-	-	1.31	-	10
RG-5	RG	-	-	3.1	-	8
RG-7	RG	-	-	2.6	-	8
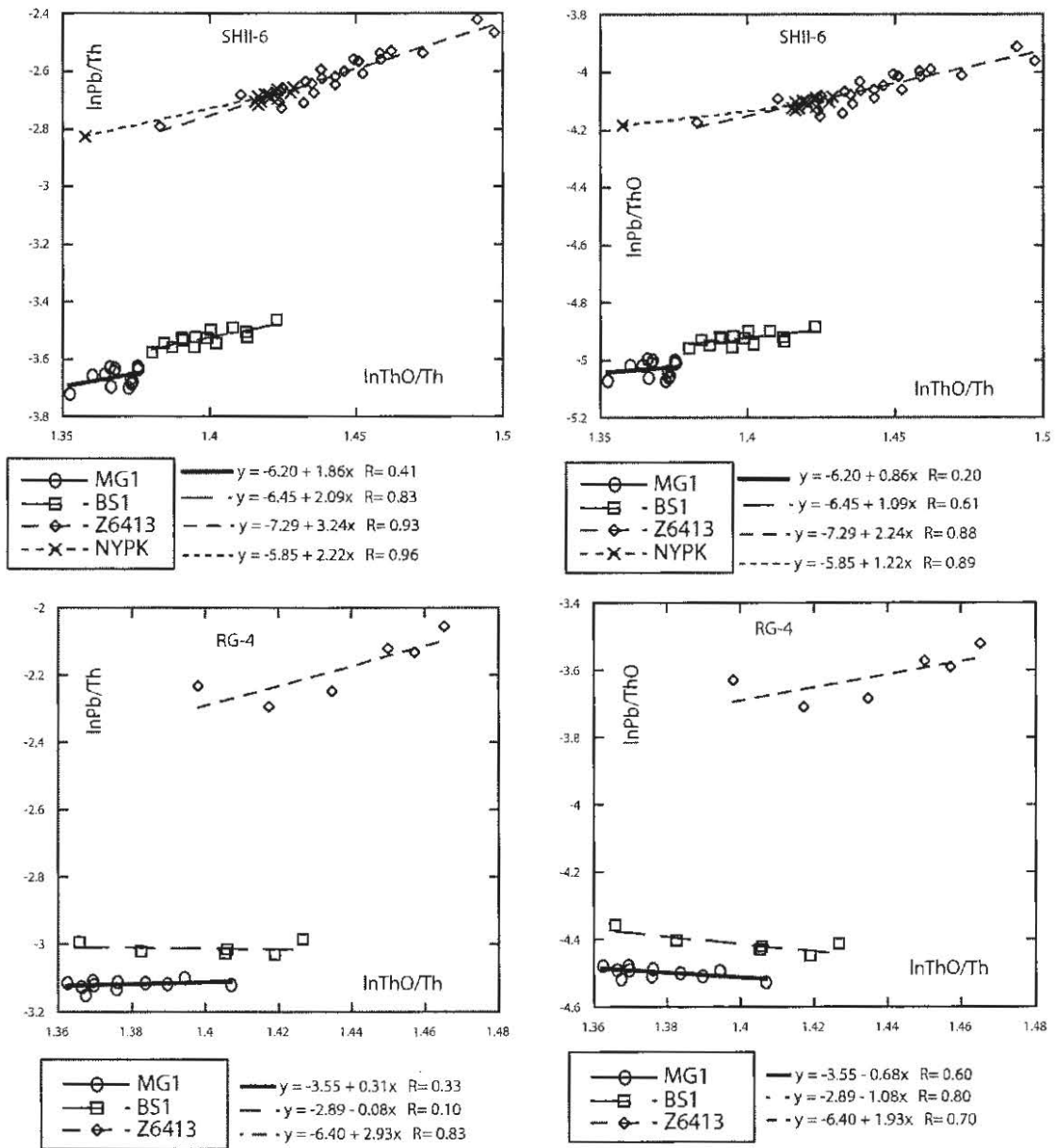
Fig. 3.11. lnPb/Th:lnThO/Th and lnPb/ThO:lnThO/Th for SHRIMP sessions SHII-6 and RG-4.

3.3.4.3 Standard Calibration errors

Initially, the uncertainty in the standard calibration was calculated as the percent standard deviation of the raw $^{206}Pb^+/^{270}(UO_2^+)$ or $^{208}Pb^+/^{248}(ThO^+)$ standard analyses. However, this sometimes resulted in an overestimation of the analytical errors for the calibration standard MG1 which sometimes gave MSWD's of < 0.3. A more realistic approach in accessing the reproducibility of the standard is to incorporate the common Pb correction and elemental counting errors. Using the calibration corrected

76

$^{206}Pb^+/^{270}(UO_2^+)$ and $^{208}Pb^+/^{248}(ThO^+)$ ratios and their counting and common Pb correction errors, the additional error required for the ratio errors to reach unity (MSWD=1) can be determined using an ISOPLOT weighted mean algorithm. It is this error, termed the 'constant external error' which was used as the calibration error for each analytical session. For the sessions where the counting errors and the common Pb correction error entirely accounted for the dispersion in the standard $^{206}Pb^+/^{270}(UO_2^+)$ and/or $^{208}Pb^+/^{232}Th^{16}O^+$ ratios, a minimum calibration error of 1 % was applied, which is a typical minimum value applied to SHRIMP $^{206}Pb/^{238}U$ calibrations. Using this method, the reproducibility of MG1 for both $^{206}Pb^+/^{270}(UO_2^+)$ and $^{208}Pb^+/^{232}Th^{16}O^+$ ratios ranged between 1–3.5 % (1σ).

3.3.5 Quantitative elemental SIMS xenotime analysis

Quantifying the elemental concentrations of geological materials by SIMS is significantly hampered by matrix effects. To overcome this problem both theoretical and empirical models have been used with varying degrees of success. Perhaps the most studied of the theoretical models used to describe the SIMS ionisation process is the local thermal equilibrium (LTE) model of Andersen & Hinthorne (1973). This model hypothesises that a plasma layer exists above the target where atoms, ions, molecules and electrons are in local thermal equilibrium with each other. Using atomic properties such as ionisation energy and electron affinity, Saha–Eggert equations are used to predict relative ionisation yields. However, the LTE model has serious shortcomings as investigations have shown that temperature and electron densities used by this method are inconsistent with the existence of a true thermal equilibrium (Benninghoven et al. 1987; Cristy 2000). Although other theoretical models have been developed in an attempt to quantify SIMS measurements (see Benninghoven et al. 1987), the best results have been obtained by more empirical approaches that use matrix matched standards and relative sensitivity factors (RSF).

The use of RSF to calculate elemental concentrations from SIMS analyses has achieved widespread acceptance. The RSF approach as explained by Benninghoven et al (1987) (pages 290–291) is outlined below. RSF are calculated from the ratio of the practical sensitivity of the elements of interest. Where the practical sensitivity of element 'A' i.e., $[S_p(A)]$ is defined as: cps/nA/concentration (ppm). Therefore the

RSF of element A with respect to element R is $[S_r(A)] = S_p(A)/S_p(R)$. Therefore, the concentration of element 'A' can be calculated from the ratio of the ion currents of elements A and R and the known concentration of the reference element R in the sample (usually measured by EPMA) according to the equation:

$$C(A) = 1/S_r(A) * (A^+/R^+) * R \text{ (ppm)} \qquad \text{(eq. 3)}$$

Where $C(A)$ is the concentration of element A, A^+ and R^+ are the ion currents of elements A and R and R (ppm) is the known concentration of element R. The procedure used for the technique described above involves the determination of RSF from standards of known composition which are then compared to 'unknown' samples that ideally are matrix–matched.

The approach outlined above deviates from that typically used for U abundance determinations for SHRIMP zircon analysis. For this method, a comparison is made between a matrix matched standard zircon of known composition and the 'unknown' zircon. The assumption used in this technique is that the Zr content for the vast majority of zircon is constant within a few wt% and as such can be used as a reference element, without external EPMA analysis. The method involves a calibration between $^{196}(Zr_2O^+)/^{238}U^+$ and $^{248}(UO^+)/^{238}U^+$ which obeys a power law of the form $y = ax^{0.66}$ (Claouè-Long et al. 1995). Ireland & Bukovanska (2003) state for SHRIMP analyses of the standard zircon SL13, U determinations are generally within 10 % of the long term average which approximately equates to the known variation of U in this mineral.

The range of Y abundance and the substituting HREE in xenotime means that there is no element of constant concentration that can be used as a reference from which to calculate elemental abundances. For example, the WDS data displayed in Table 2.1 (Chapter 2) show that Y_2O_3 concentrations can range from ~34 to 46 wt%. Even the reference xenotime samples used as a part of this study have Y concentrations that differ between samples by ~5 wt% Y_2O_3 (Table 3.2). Therefore, SHRIMP based elemental abundance calculations in xenotime using Y as a reference element (without external EPMA analysis) will be biased by the actual Y concentration contrast between the standard and unknown.

With the above considerations in mind, Fletcher et al. (2004) argued that first order U abundance estimates were achievable via a method of U abundance scaling. This method relies on an observed correlation between $^{254}(UO^+)/^{194}(Y_2O^+)$ ratios and WDS U concentrations determined from the same locations (see Fig. 6 from Fletcher, et al. 2004). U abundances are then derived by calculation of a U sensitivity factor, which is simply the average WDS U concentration of the standard, divided by the average $^{254}(UO^+)/^{194}(Y_2O^+)$ of the standard. The U concentration of an unknown is then calculated by multiplying the sensitivity factor by the $^{254}(UO^+)/^{194}(Y_2O^+)$ of the unknown.

3.3.5.1 WDS and SIMS elemental quantification

In an effort to determine the most suitable SIMS elemental quantification method for xenotime, the method of U abundance scaling proposed by Fletcher et al. (2004) was trialled against quantification via relative sensitivity factors as explained above, using either Y or Ho as reference elements. With these methods U concentrations were calculated from SHRIMP analyses of the reference xenotimes and compared to WDS U abundances determined at each spot location prior to SHRIMP analysis.

For determination of U abundance using the scaling method of Fletcher et al. (2004), MG1 was used as the U standard and the $^{270}(UO_2^+)$ molecule as a proxy for U concentration. Nine WDS analyses of fragments from MG1, have an average U concentration of 965 ± 65 ppm (2σ, SDOM; Standard Deviation of the Mean), which was used as the reference U concentration of MG1 for this experiment. The reference U value for MG1 has a 2σ variation of ~6.7 %, therefore U abundance calculations for 'unknown' xenotimes at best can only be expected to be accurate to this amount.

MG1 was also used as the standard for U abundance determinations using RSF, i.e., $RSF_{(U-Y)}$ and $RSF_{(U-Ho)}$. Y was measured as $^{194}(Y_2O^+)$, Ho as $^{181}(HoO^+)$ and U as $^{270}(UO_2^+)$. The average of nine MG1 WDS and SHRIMP analyses was used to determine the RSF, where $RSF_{(U-Y)}$ has a value of 45.96 and $RSF_{(U-Ho)}$ 0.39. Therefore, the $^{270}(UO_2^+)$ molecule is more efficiently ionised than $^{194}(Y_2O^+)$ but not as

efficiently as $^{181}(\text{HoO}^+)$. For the $\text{RSF}_{(U–Y)}$ and $\text{RSF}_{(U–Ho)}$, Y and Ho concentrations were determined by WDS for each of the unknowns prior to SHRIMP analysis.

Table 3.6 shows the comparison between the xenotime WDS U abundance measurements for the reference xenotimes (MG1, BS1, Z6413 and NY/PK 6-80) with the SHRIMP based U determinations. The WDS U xenotime data clearly show the limitations of EPMA of U. Although the xenotime samples with U concentrations greater than ~ 1 wt% have individual uncertainty estimates of ~6–7 % (σ) (i.e. Z6413 and NY/PK 6-80), the xenotime with U concentrations significantly below ~1000 ppm have very imprecise U determinations. For example, WDS U determinations of BS1 range between 150 and 570 ppm, and have individual 1σ precision estimates of ~30 to 114 %.

The three different SHRIMP xenotime U abundance determination methods shown in Table 3.6 are best assessed with reference to the results for Z6413 and NY/PK 6-80. Comparisons between the results of MG1 are excluded as in each of the methods MG1 was used as the calibration standard. The highly imprecise WDS U determinations for BS1 result in all three of the SHRIMP based U abundance methods falling well within the analytical errors of the WDS determinations. Therefore the relative merits of the three SHRIMP based techniques for BS1 cannot be assessed independently. The comparison between the three SHRIMP based methods of U concentration determination for Z6413 and NY/PK 6-80 show that $\text{RSF}_{(U–Ho)}$ performs the best overall, with individual U determinations generally within 5 % of the WDS value. Furthermore, the SHRIMP U abundance determinations using $\text{RSF}_{(U–Y)}$ are generally more accurate than the U abundance scaling method of Fletcher et al. (2004) by approximately 6–7 %.

The better results of $\text{RSF}_{(U–Y)}$ in comparison to the U scaling method of Fletcher et al. (2004) are partly explained by the ca. 3–5 wt% difference in Y concentration that Z6413 and NY/PK 6-80 have with the standard MG1, that is compensated for with $\text{RSF}_{(U–Y)}$. However, the superior results of $\text{RSF}_{(U–Ho)}$ over $\text{RSF}_{(U–Y)}$ are less easily explained. It may be that the ionisation of Y varies in the reference xenotimes, i.e. that the $^{194}(\text{Y}_2\text{O}^+)$ molecule is subject to matrix effects. This may be supported by the

findings of Zinner & Crozaz (1986) who suggest that RSF for major elements are more affected by the matrix than for trace elements. Although the concentration of Ho in xenotime is not in trace proportions (usually about 1 wt%) its low concentration compared to Y may mean that Ho is relatively insensitive to matrix effects.

Table 3.6. Table comparing WDS and SHRIMP-based xenotime U abundance determinations for reference xenotimes analysed in RG-2. Of the three techniques presented, $RSF_{(U-Ho)}$ is superior (see text).

Labels	U ppm (WDS)	U ppm (WDS) %error (σ)	U ppm Fletcher et al. (2004)	% diff. to WDS value	U ppm RSF (U-Y)	% diff. to WDS value	U ppm RSF (U-Ho)	% diff. to WDS value
MG1-1.2	852	22	861	1	865	2	865	1
MG1-1.1	853	22	860	1	865	1	892	5
MG1-1.3	946	20	881	-7	877	-7	854	-10
MG1-1.4	1006	19	1027	2	1012	1	973	-3
MG1-1.5	941	20	922	-2	935	-1	955	1
MG1-1.6	891	21	893	0	903	1	935	5
MG1-1.8	968	20	973	1	981	1	996	3
MG1-1.9	1104	18	1173	6	1173	6	1167	6
MG1-1.10	1125	17	1096	-3	1076	-4	1036	-8
Z6413-1.1	13479	6	16128	16	14858	10	12924	-4
Z6413-1.11	10453	7	12526	17	11500	10	10294	-2
Z6413-1.2	16480	6	21145	22	19345	17	16034	-3
Z6413-1.3	10472	7	12387	15	11338	8	10268	-2
Z6413-1.5	15273	6	19113	20	17392	14	14666	-4
Z6413-1.6	17082	6	22717	25	20663	21	16463	-4
Z6413-1.7	8122	7	9348	13	8539	5	7989	-2
Z6413-1.8	7483	7	8597	13	7961	6	7404	-1
Z6413-1.9	7091	7	7679	8	7177	1	6996	-1
NYPK-1.1	13815	6	18157	24	16097	17	13178	-5
NYPK-1.2	14394	6	18900	24	16744	16	13912	-3
NYPK-2.1	10950	7	13850	21	12526	14	10851	-1
NYPK-3.1	11543	6	15139	24	13571	18	11343	-2
NYPK-4.1	12908	6	16049	20	14379	11	12171	-6
NYPK-5.1	17493	6	23876	27	20869	19	16191	-7
NYPK-6.1	12894	6	15590	17	14069	9	11992	-7
NYPK-6.2	13166	6	16698	21	14930	13	12406	-6
NYPK-9.1	15538	6	18347	15	16286	5	13416	-14
BS1-1.10	225	78	291	23	270	20	249	11
BS1-1.3	360	50	400	10	366	2	325	-10
BS1-1.4	156	114	332	53	304	95	260	67
BS1-1.5	226	79	368	39	338	50	304	35
BS1-1.6	162	109	174	7	161	0	152	-6
BS1-1.7	332	54	539	38	493	49	421	27
BS1-1.8	363	49	440	17	406	12	357	-2
BS1-1.9	262	67	303	14	283	8	263	0
BS1.2	568	32	578	2	534	-6	492	-13

The up to ~10 % variation in Y content between different xenotime grains precludes this element from being used as a reference without knowledge of its actual concentration. Therefore the U scaling method proposed by Fletcher et al. (2004)

should be avoided. SHRIMP elemental quantification using $RSF_{(U-Ho)}$ can reasonably be expected to be within ~5–10 % of the actual value, whereas $RSF_{(U-Y)}$ can be expected to be within 15–20 % of the real concentration.

The SHRIMP U–Pb–Th xenotime matrix correction technique detailed later in this chapter critically depends upon the accurate determination of xenotime chemical composition. As discussed above, the SIMS quantification of elemental abundances in xenotime is best determined with RSF that are normalised to either Ho or Y determined independently by EPMA. The abundance levels of the significant REE in xenotime (i.e. Nd–Lu) and good precision achievable with EPMA for these elements mean that their analysis is most efficiently carried out by this technique prior to SHRIMP analysis. The abundance of U in concentrations of ~1000 ppm or greater can be determined accurately by EPMA. However, for xenotime with significantly lower levels of U the use of $RSF_{(U-Ho)}$ or $RSF_{(U-Y)}$ is preferred. Similarly, EPMA analyses of xenotime with Th abundances less than ~500 ppm are imprecise, and Th concentrations are better determined from SHRIMP derived Th/U ratios (see below for calculation).

Accurately targeting the SHRIMP spot at the same sample location as analysed by the EPMA requires great care in recording the location of the WDS spot. Using an Au coat for EPMA analysis greatly helps this task as the electron probe beam 'welds' the Au onto the sample surface leaving a bright spot which is easily photographed and indeed clearly seen on the SHRIMP video monitor.

A Monte Carlo simulation of the EPMA excitation volume using the Casino program (V 2.4.2) for an average xenotime matrix using a ca. 1 µm diameter, 25 kV electron beam, shows that ~99 % of the electrons penetrate to a depth of ~2.4 µm. By contrast, it is estimated that the SHRIMP primary beam when focussed through a 30µm aperture sputters a region of approximately 5~7 µm in diameter by 0.5–1 µm in depth. Therefore, when using the combined analytical results from the electron probe and SHRIMP to determine elemental abundances and Pb/U—Pb/Th ratios, it is assumed that the xenotime samples are homogenous at the maximum combined sampling scale of both methods, i.e., the analysed xenotimes are homogenous at a scale equivalent to a 7 µm diameter spot that penetrates 2.4 µm into the sample. Modelling the excitation

volume of the electron microprobe analysis as a sphere and the sampled volume of the SHRIMP spot as a cylinder, equates to a total sample volume of ~45 μm^3.

3.3.6   SHRIMP xenotime Th/U ratios

Xenotime Th/U ratios were determined using the known age of MG1 (490 Ma) and the $^{208}Pb^+/^{206}Pb^+$ and $^{248}(ThO^+)/^{254}(UO^+)$ ratios following the method of Williams et al. (1996). This method relies on the strong correlation between $^{208}Pb^+/^{206}Pb^+$ and $^{248}(ThO^+)/^{254}(UO^+)$ to define a calibration factor to correct SHRIMP $^{248}(ThO^+)/^{254}(UO^+)$ ratios to their true $^{232}Th/^{238}U$ ratio (Fig. 3.12). Assuming a closed Th—U—Pb system for MG1, radiogenic $^{208}Pb/^{206}Pb$ and $^{232}Th/^{238}U$ define a Th—U—Pb isochron with a fixed gradient of 0.310 (i.e. 'expected'). To obtain a Th/U calibration factor, the observed gradient for the SHRIMP determined $^{208}Pb^+/^{206}Pb^+$ and $^{248}(ThO^+)/^{254}(UO^+)$ (typically ~0.258, 'observed') is divided by the expected value (i.e. observed/expected). Therefore, the Th/U ratios are simply calculated by equation 4:

$$^{232}Th/^{238}U = {}^{248}(ThO^+)/^{254}(UO^+)\,[0.832] \qquad \text{(eq. 4)}$$

The difference between the expected and observed Th—U—Pb isochrons is attributable to the interelement fractionation between $^{232}ThO^+$ and $^{254}(UO^+)$ (Williams et al. 1996).
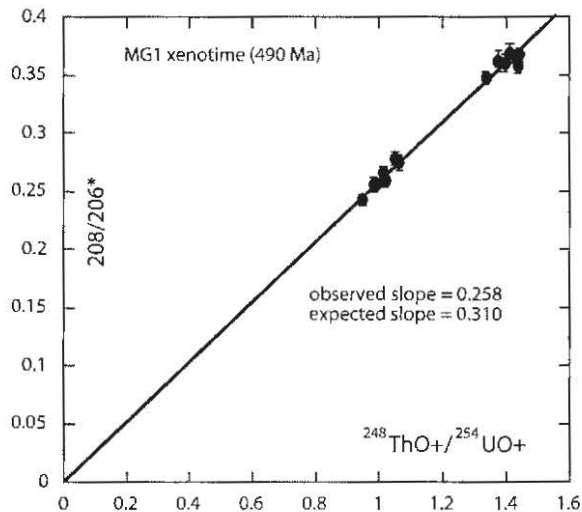
Fig. 3.12. $^{208}Pb^+/^{206}Pb^+$ vs. $^{248}(ThO^+)/^{254}(UO^+)$ isochron.

It is clear that the Th/U calibration factors differ between SHRIMP RG and SHRIMP II. There is also minor variation in the Th/U calibration factors between analytical sessions as is the case for monazite. Table 3.7 shows the Th/U calibration factors for MG1, BS1 and Z6413, for six different analytical sessions using SHRIMP II and SHRIMP RG.

Table 3.7. Representative Th/U calibration factors calculated from MG1, BS1 and Z6413, for both SHRIMP II and SHRIMP RG instruments. (EF = energy filter).

Session	SHRIMP	EF	MG1	BS1	Z6413	average
SHII-6	II	90%	0.831	0.828	0.832	0.830
SHII-4	II	-	0.876	0.862	0.876	0.871
SHII-3	II	-	0.862	0.856	0.866	0.861
RG-1	RG	-	0.938	0.932	0.948	0.939
RG-7	RG	-	0.929	0.928	0.955	0.937
RG-4	RG	-	0.928	0.931	0.955	0.938

For the two SHRIMP II analytical sessions that did not use energy filtering (SHII–3 and SHII-4), the Th/U calibration factors for the xenotime standards vary internally by up to ~1.5 %, and by ~2 % between the sessions. However, the average value of these sessions for the three standards is 0.871 and 0.861, representing only a ~1% difference. The Th/U correction factors for the SHRIMP II energy filtered session (SHII–6), internally varies by only ~0.5 % and has an average value of 0.830 which is ~5 % lower compared to the unfiltered sessions. This is probably due to the different energy ranges of $^{248}ThO^+$ and $^{254}UO^+$ ions that were sampled during the energy filtered session. The average Th/U correction factors for the two unfiltered SHRIMP II sessions of 0.871 and 0.861 are within ~2 % of the calibration factor of 0.883 calculated by Fletcher et al. (2004) using a SHRIMP II instrument and an unfiltered secondary ion beam.

Th/U correction factors calculated from the three SHRIMP RG sessions are significantly elevated compared to the SHRIMP II results, with an average value of 0.938. However, although the Th/U correction factors for BS1 and MG1 are similar to within 0.5 %, for these sessions, the calibration factor for Z6413 is elevated in comparison to MG1 and BS1 by between ~1.7 and 2.8 %. Using the results from

session RG–1, the apparent elevation in the Th/U correction factor for Z6413 may be related to the limited number of analyses used to define the calibration factor (n=7). Figure 3.13 is a diagram showing $^{208}Pb^+/^{206}Pb^+$ vs. $^{248}(ThO^+)/^{254}(UO^+)$ plots for MG1, BS1, Z6413 and D43764 for session RG–1. This diagram shows that the Th/U correction factor for the high U–Th–REE xenotime D43764 is within 0.5 % of the correction factors determined for MG1 and BS1. Therefore, the slightly elevated Th/U correction factor for Z6413 is not representative for this SHRIMP RG session.
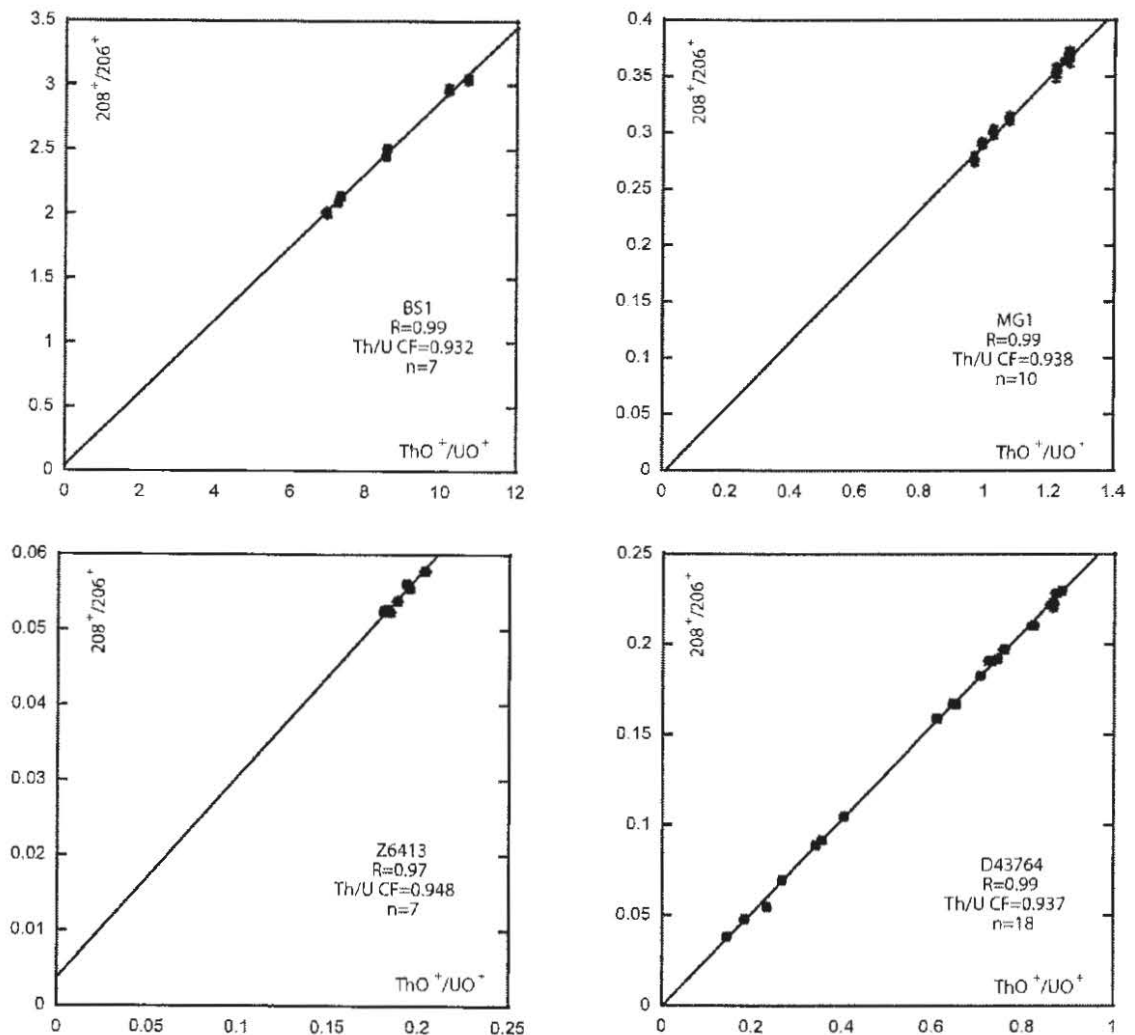
Fig. 3.13. $^{208}Pb^+/^{206}Pb^+$ vs. $^{248}(ThO^+)/^{254}(UO^+)$ isochrons for reference xenotimes analysed in session RG–1. Samples BS1, MG1 and D43764 have Th/U correction factors that are accurate to within 0.5 %, demonstrating that Pb/U—Pb/Th matrix effects do not affect this calibration. Error bars are approximately the same size as the symbols.

The variation in Th/U calibration factors is dependant on the instrument used and the analytical conditions employed. Xenotime Th/U correction factors collected from two separate SHRIMP II instruments from an unfiltered secondary ion beam (i.e. Fletcher

et al. 2004 and this study) are within ~2 % of each other and as such, consistent. However, energy filtering reduced the Th/U calibration factor by ~4 % in the above example. The variation of the xenotime Th/U correction factors between sessions demonstrates that this correction should be routinely determined for each analytical session.

Fletcher et al. (2004) were concerned about a variation of ~3.5 % in the Th/U correction factor determined from different xenotime standards and analytical sessions, which was tentatively attributed to a matrix effect. However, variations in the Th/U calibration factor between analytical sessions also occurs for monazite and varies by ~6 % (Stern & Berman 2000). Interestingly, the Th/U calibration factors for the different xenotime standards analysed in the three SHRIMP II sessions for this study are internally very similar and indicate that the $^{208}Pb^+/^{206}Pb^+$ vs. $^{248}(ThO^+)/^{254}(UO^+)$ calibration is unaffected by matrix contrasts which cause the extreme Pb/U—Pb/Th matrix effects. The consistent Th/U correction factors for MG1, BS1 and D43764 (Fig. 3.13) for the SHRIMP RG session RG–1 also support this.

3.3.7 Scattered ions in the vicinity of mass ^{204}Pb

Excess ion counts at mass ^{204}Pb were reported by Fletcher et al. (2004) to occur in the secondary ion spectrum of xenotime. SHRIMP monazite analysis also encounters excess ion counts at mass ^{204}Pb, the intensity of which was shown by Berman & Stern (2000) to be related to the Th concentration. However, Ireland et al. (1999) suggested that the interference is also related to the monazite REE concentration and identified the doubly charged molecule $^{232}Th^{144}NdO_2^{++}$ as the causal molecular species. Excess counts on the ^{204}Pb peak renders the 204 correction method unusable. This is a serious problem especially for Proterozoic and older rocks which rely on the 204 correction. Energy filtering has been found to remove these excess counts during monazite analysis. First proposed by Stern & Berman (2000) this technique is now common practice for the SHRIMP II analysis of monazite, where it is also used to reduce the size of the ThO^+ secondary ion current. However, energy filtering of the secondary ion beam reduces the total secondary ion current and therefore sensitivity of the analysis.

Fletcher et al. (2004) suggested that like monazite, the intensity of the ^{204}Pb interference in xenotime was related to the Th content. These researchers demonstrated that the 204 correction resulted in over corrected ^{207}Pb/^{206}Pb ratios and that the uncorrected Pb ratios were more accurate. Fletcher et al. (2004) concluded that the excess mass 204 counts were caused by an interference. For xenotime analysis, the 204 interference can be removed by a post-magnet retardation lens (Fletcher et al. 2000), or alternatively, by energy filtering indicating that the interference is a low energy species.

Experiments conducted during this study indicate that the excess counts at mass ^{204}Pb encountered during SHRIMP II xenotime analysis, may not be related to Th concentration. SHRIMP II xenotime experiments showed that for analyses conducted with a ~3 nA, O_2^- primary beam, the count rate at the mass ^{204}Pb and background positions are approximately equal and ranged between 2–3 cps. Figure 3.14 shows that the measured ^{204}Pb counts for MG1, BS1 and Z6413 do not correlate with Th content, contrary to the suggestion by Fletcher et al. (2004). The equal count rates at the mass ^{204}Pb and background positions show that it is not only the ^{204}Pb peak that is affected. For SHRIMP II xenotime analysis, under the analytical conditions mentioned above, the scattered ions can be removed by removing the lowest energy secondary ions, reducing the total secondary beam by ~50%. Alternatively, the scattered ions can be removed by the post collector slit retardation lens, which is the standard procedure used for xenotime analysis carried out at the Curtin University of Technology, Perth, WA (Ian Fletcher pers. comm. 2004).

In contrast to SHRIMP II, the design of SHRIMP RG effectively filters out any scattered ions before they reach the collector. For SHRIMP RG, only a single mass species enters the ESA, prior to entering the collector. However, for SHRIMP II, the entire ion beam passes from the ESA into the magnet where collisions between molecules and the flight tube result in scattering and a loss of energy. Because of the energy loss, the scattered ions can be removed from the mass spectrum by energy filtering. The presence of scattered ions near mass 204 in both monazite and xenotime, both REE rich minerals, suggests that it is the REE ions that are being scattered.

The majority of published SHRIMP xenotime U–Pb analyses have been conducted on tiny overgrowths and hydrothermal crystals, ~5–10 μm spot sizes and primary beams of ~0.5–0.8 nA O_2^- are regularly used. Under these instrumental conditions, the precision of each analysis is significantly reduced in comparison with routine U–Pb zircon analysis. Additionally, the removal of scattered ions with either the retardation lens or by energy filtering during SHRIMP II xenotime analysis removes a significant percentage of the secondary ion spectrum and therefore, further lowers the precision of the analysis. By contrast, xenotime analysis with SHRIMP RG requires no additional energy filtering and hence, no attendant loss of precision. With these considerations in mind, SHRIMP RG was chosen over SHRIMP II as the most suitable for xenotime U–Pb and Th–Pb analysis.
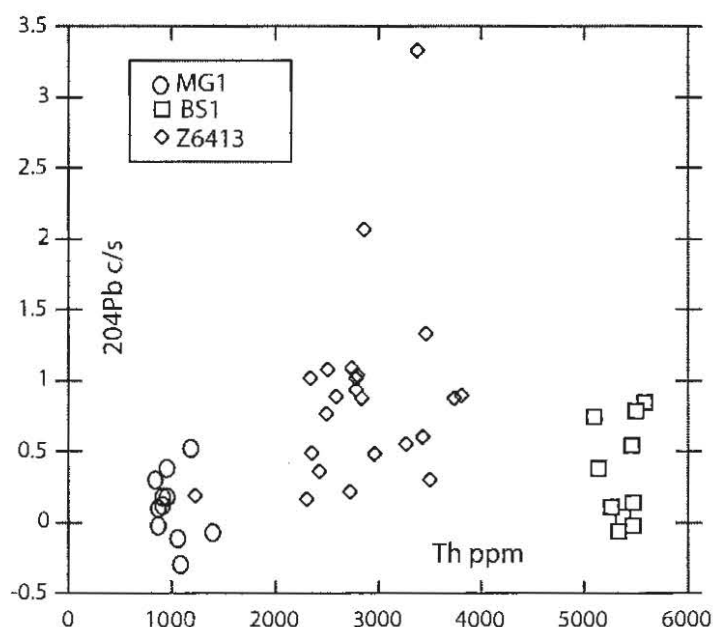
Fig. 3.14. Plot of the individual [204]Pb count rates vs Th concentration for MG1, BS1 and Z6413 session SHII-4. There is no apparent correlation between Th concentration and the [204]Pb count rate.

3.4 Reference xenotime U–Pb and Th–Pb raw age determinations

Chemical contrasts between the reference xenotimes were found to cause significant Pb/U—Pb/Th matrix effects (ME). In general, a high U xenotime, when measured relative to a low to moderate U standard, results in elevated $^{206}Pb/^{238}U$ and $^{208}Pb/^{232}Th$ ratios for the unknown sample, producing reversely discordant compositions (Fig. 3.15a). The opposite occurred when a xenotime with low to moderate U

concentrations was calibrated against a high U standard, that is, the 'unknown' sample appeared normally discordant (Fig. 3.15b).
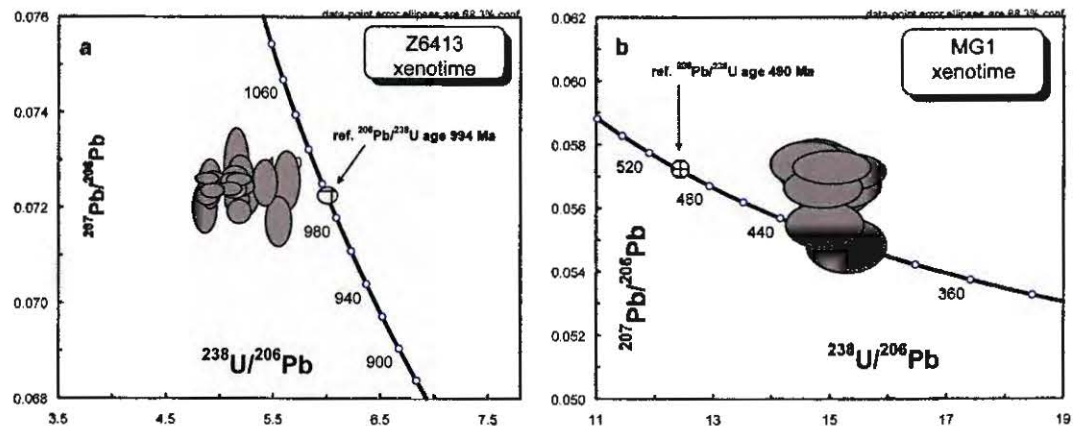
Fig. 3.15. Concordia plot of raw xenotime U–Pb analyses for Z6413 (a) and MG1 (b) (session SHll-4). Fig. 3.15a demonstrates the effect of a U matrix mismatch, which favours the unknown and results in reversely discordant results, and Fig 2.15b, is the opposite situation where a U matrix mismatch favouring the standard, results in normally discordant results.

Figure 3.16 compares the independently calculated raw $^{206}Pb/^{238}U$ and raw $^{208}Pb/^{232}Th$ ages as well as the $^{207}Pb/^{206}Pb$ ages for Z6413 (high U), calibrated against MG1 (low–moderate U) using SHRIMP II. This graph shows that the $^{206}Pb/^{238}U$ and $^{208}Pb/^{232}Th$ ages for Z6413 are highly correlated (R=0.99) and similarly elevated by approximately 14 % relative to the reference age for this sample. Additionally, the $^{207}Pb/^{206}Pb$ ages for Z6413 appear to be unaffected by matrix contrasts or scattered ions and lie within error of the reference age. Xenotime Pb/U—Pb/Th ME are also evident between xenotimes with contrasting Th and/or HREE concentrations. Figure 3.17 shows that the raw Pb/U—Pb/Th ages for BS1 (low U, high Th and HREE) when calibrated against MG1 are elevated by between 5 and 6 %. $^{206}Pb/^{238}U$ and $^{208}Pb/^{232}Th$ xenotime matrix effects are also evident in SHRIMP RG analyses. Figure 3.18 demonstrates that the $^{206}Pb/^{238}U$ and $^{208}Pb/^{232}Th$ ages from the high U xenotime D43764, when calibrated to MG1, are elevated by ~18 % and are also strongly correlated (R= 0.95).

Pb/U and Pb/Th xenotime ME can be minimised when contrasts in U, Th and REE between standard and unknown are minimised. Figure 3.19 demonstrates the contrast in $^{206}Pb/^{238}U$ ages for D43764, after calibration against a low U standard MG1 and the high U standard Z6413. D43764 analyses, when calibrated to MG1, yield $^{206}Pb/^{238}U$ ages that are elevated by ~20 %. However, when the same D43764 analyses are

calibrated to Z6413, which has broadly similar U concentrations, the $^{206}Pb/^{238}U$ ages are closer to the reference age. Therefore, matching xenotime matrix components is the most desirable approach to SHRIMP xenotime Pb/U—Pb/Th dating.
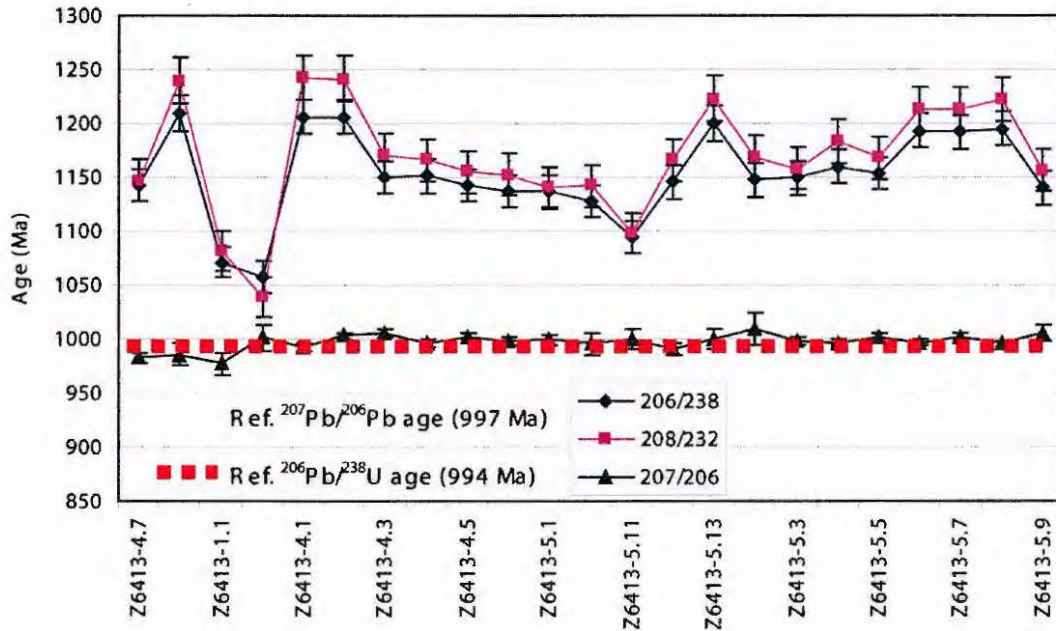
Fig. 3.16. Plot showing the individual SHRIMP results for raw Pb/U—Pb/Th and $^{207}Pb/^{206}Pb$ analyses of Z6413 (session SHII-4). Results for Pb/U—Pb/Th are elevated by ~14%, and strongly correlated (R=0.99). The $^{207}Pb/^{206}Pb$ ratios are within error of their reference age.
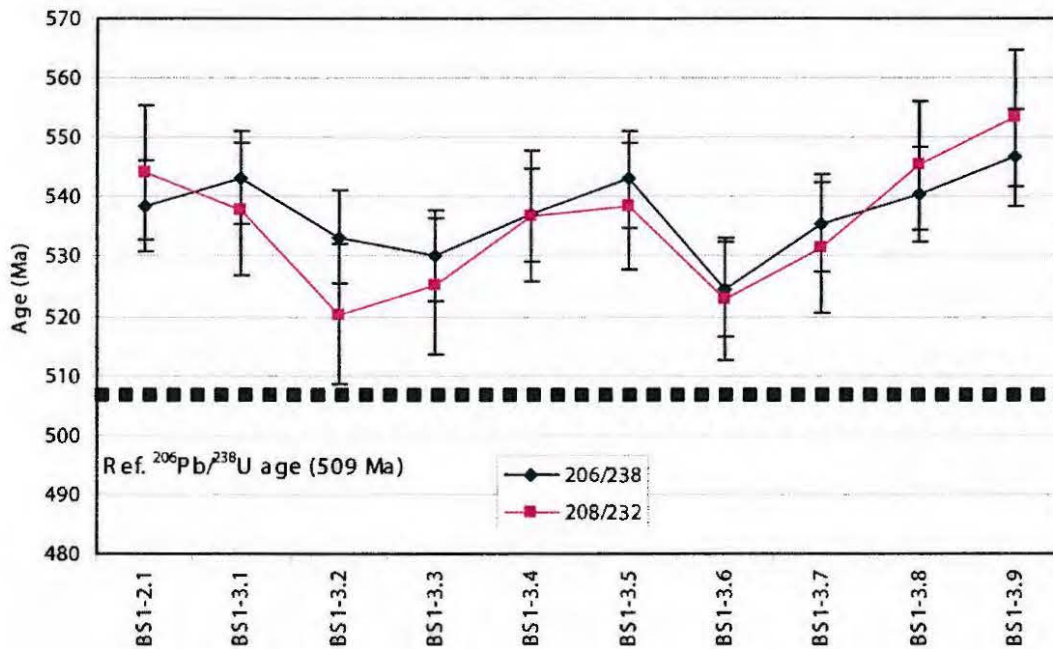
Fig. 3.17. Plot showing the individual SHRIMP results for Pb/U—Pb/Th analyses of BS1 (session SHII–4). The raw Pb/U—Pb/Th ratios are within error of each other, but elevated by ~5 to 6 %.

90
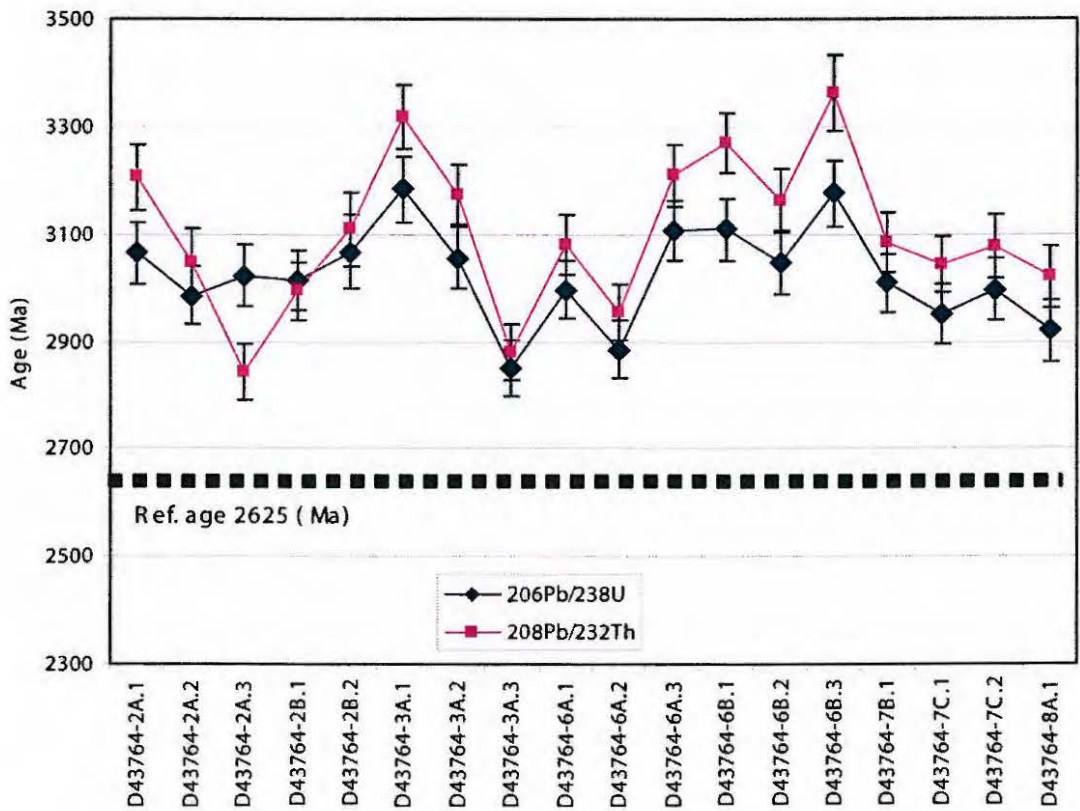
Fig. 3.18. Plot of individual SHRIMP results for Pb/U—Pb/Th analyses of D43764 (session RG–1). The raw Pb/U—Pb/Th ages are within error of each other and strongly correlated (R=0.95).
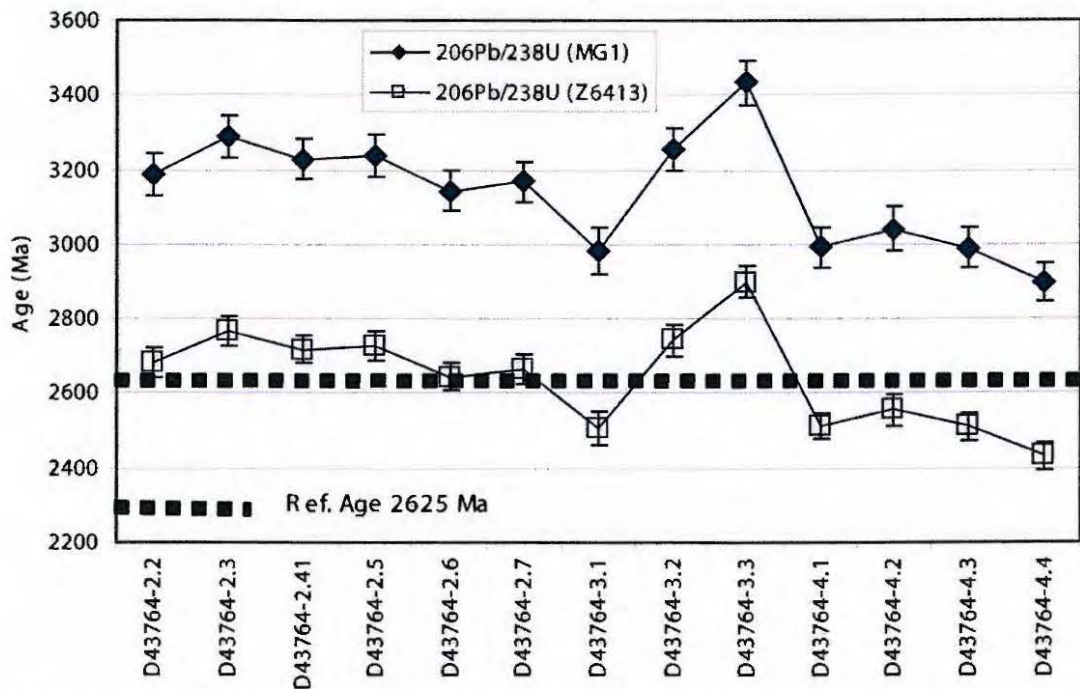
Fig. 3.19. Plot of the individual SHRIMP raw Pb/U—Pb/Th results for the high U reference xenotime, D43764. The most elevated Pb/U—Pb/Th ratios have been calibrated to the low to moderate xenotime MG1. However, the raw Pb/U—Pb/Th ages for D43764, are more reflective of their reference age, when calibrated to the high U xenotime Z6413.

A significant finding of this study has been to demonstrate that both $^{206}Pb/^{238}U$ and $^{208}Pb/^{232}Th$ SHRIMP xenotime determinations are similarly affected by matrix contrasts between calibration standard and unknown. Figures 3.16, 3.17 and 3.18, show the close relationship between the raw $^{206}Pb/^{238}U$ and $^{208}Pb/^{232}Th$ ages. In each of these cases, the independently calculated $^{206}Pb/^{238}U$ and $^{208}Pb/^{232}Th$ ages for Z6413, D43764 and BS1 are all within error of each other. $^{206}Pb/^{238}U-^{208}Pb/^{232}Th$ concordia diagrams also demonstrate this. Figures 3.20a & 3.20b show $^{206}Pb/^{238}U-$ $^{208}Pb/^{232}Th$ concordia diagrams for Z6413 and BS1, and demonstrates that these samples have concordant to near-concordant compositions, that are however, significantly elevated in comparison to their reference ages. Of interest also is the magnitude of the SHRIMP xenotime $^{206}Pb/^{238}U$ ME found in this study, compared to that of Fletcher et al. (2004). For Z6413 analyses calibrated to MG1, this study typically observed the $^{206}Pb/^{238}U$ ratios for Z6413 to be elevated by ~15 %. However, Fletcher et al. (2004) using a SHRIMP II instrument reports Z6413 analyses calibrated to MG1 to be elevated by ~11 %.
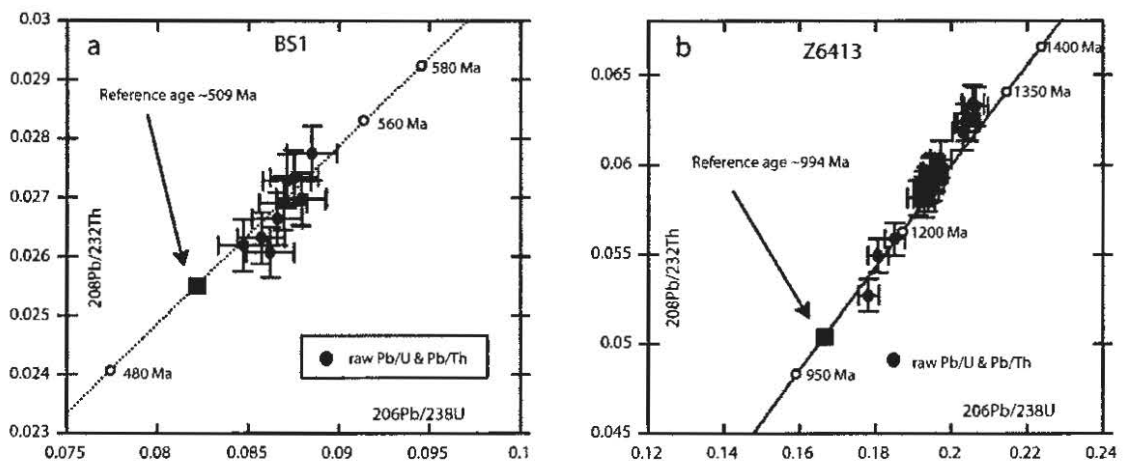
Fig. 3.20. U–Pb–Th concordia plots for BS1 (a) and Z6413 (b) (session SHII-4). Both samples are shown to have elevated but concordant Pb/U—Pb/Th ratios.

3.4.1 Xenotime compositions and Pb/U—Pb/Th matrix effects.

Electron probe analyses of the reference xenotimes allow both generalised comparisons of the xenotime compositions with the SHRIMP U–Pb and Th–Pb ME, and also more detailed spot–to–spot comparisons. Additionally, SHRIMP determinations of $^{177}(DyO^+)$ and $^{190}(YbO^+)$ measured concurrently with the $^{206}Pb^+/^{238}U^+$ and $^{208}Pb^+/^{232}Th^+$ ratios were carried out to determine whether these

species could act as monitors for the U–Pb and Th–Pb matrix–induced fractionations. Typically, the best correlations between xenotime composition and measured SHRIMP Pb/U and Pb/Th were observed in the samples with the biggest compositional range. These are the two multi–grain samples NY/PK 6-80 and D43764, and also fragments of the single crystal Z6413, in which the range of U content is up to 1 wt%.

3.4.2   General observations on the relationship between xenotime composition and Pb/U—Pb/Th matrix effects.

As indicated above, matrix effects are strongly influenced by chemical composition. Table 3.8 shows the averaged contrasts in U, Th and $\sum$REE between the reference xenotimes and the calibration standard MG1, and also their typical SHRIMP Pb/U— Pb/Th fractionations. The xenotimes with the highest observed U–Pb/Th–Pb fractionations are Z6413, NY/PK 6-80 and D43764, which have fractionations between ~15 and 20 % relative to the primary calibration standard MG1. Each of these samples has U contents that are between ~1.1 and 1.4 wt% in excess of the MG1 U concentration. BS1, which has a lower U content than MG1, has typical Pb/U— Pb/Th fractionations of ~5 %. The elevated levels of Th and/or $\sum$REE in BS1 relative to MG1 may also cause Pb/U—Pb/Th ME. From Table 3.8 it appears that contrasts in Th and/or $\sum$REE between xenotime standard and unknown cause Pb/U—Pb/Th ME which, although significant, are subordinate to the more extreme ME caused by contrasts in U content.

Table 3.8. Table showing the typical SHRIMP xenotime Pb/U and Pb/Th fractionations for the reference xenotimes and the contrasts they have in U, Th and $\sum$REE with the Pb/U— Pb/Th calibration standard MG1.

Sample	Typical % Pb/U fractionation	Typical % Pb/Th fractionation	Average U ppm diff. to MG1	Average Th ppm diff. to MG1	Average $\sum$REE wt% diff. to MG1
Z6413	+~15	+~15	12000	1000	2.8
BS1	+~4–6	+~4–6	-500	2500	4.7
NY/PK 6-80	+~20	+~20	14400	2760	4.0
D43764	+~16	+~16	11600	5300	4.0

3.4.3 Within–session spot–to–spot monitors of the SHRIMP xenotime Pb/U and Pb/Th fractionation

Significant positive spot-to-spot correlations exist between the raw ($^{206}Pb^+/^{270}(UO_2^+)$, $^{208}Pb^+/^{248}(ThO^+)$) ratios and $^{254}(UO^+)/^{194}(Y_2O^+)$ ratios in the high–U xenotimes Z6413, NY/PK 6-80 and D43764 (Fig. 3.21). These correlations are due to the strong dependence of the xenotime $^{206}Pb^+/^{270}(UO_2^+)$ and $^{208}Pb^+/^{248}(ThO^+)$ ratios on U abundance.
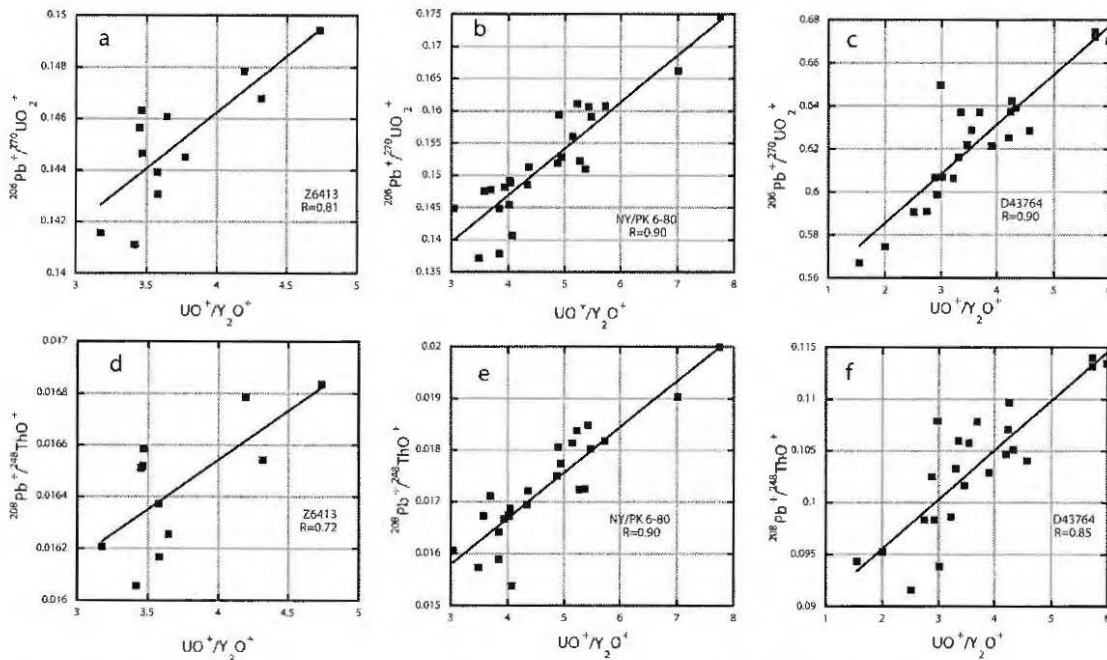
Fig. 3.21. Plots demonstrating the good correlations between $^{254}(UO^+)/^{194}(Y_2O^+)$ ratios and the $^{206}Pb^+/^{270}(UO_2^+)$ and $^{208}Pb^+/^{248}(ThO^+)$ ratios for the high U reference xenotimes, Z6413, NY/PK 6-80 and D43764.

Raw $^{206}Pb^+/^{270}(UO_2^+)$ and $^{208}Pb^+/^{248}(ThO^+)$ ratios from Z6413, NY/PK 6-80 and BS1 are also positively correlated with $^{190}(YbO^+)/^{194}(Y_2O^+)$ and $^{177}(DyO^+)/^{194}(Y_2O^+)$, with R values ranging between 0.78–0.97 (Fig. 3.22). The significant correlation between ($^{190}(YbO^+)$, $^{177}(DyO^+))/^{194}(Y_2O^+)$ and the $^{206}Pb^+/^{270}(UO_2^+)$ and $^{208}Pb^+/^{248}(ThO^+)$ ratios was unexpected as Y and the REE's, Dy and Yb, substitute for each other in the xenotime structure, all occupying the 'A' site. Indeed, WDS–determined Y and Yb concentrations for NY/PK 6-80 demonstrate a strong negative correlation coefficient (R=-0.85) supporting the Y=REE substitution (Fig. 3.23a). However, plots for the SHRIMP–determined count rates for $^{194}(Y_2O^+)$ verses $^{190}(YbO^+)$ show them to be

positively correlated, with R values of up to 0.99 (Fig. 3.23d). The positive correlations between the SHRIMP $^{206}Pb^+/^{270}(UO_2^+)$ and the $(^{190}(YbO^+), {}^{177}(DyO^+))/$ $^{194}(Y_2O^+)$ ratios, suggests that the ionisation of these ratio pairs are similarly influenced by changes in the xenotime matrix.
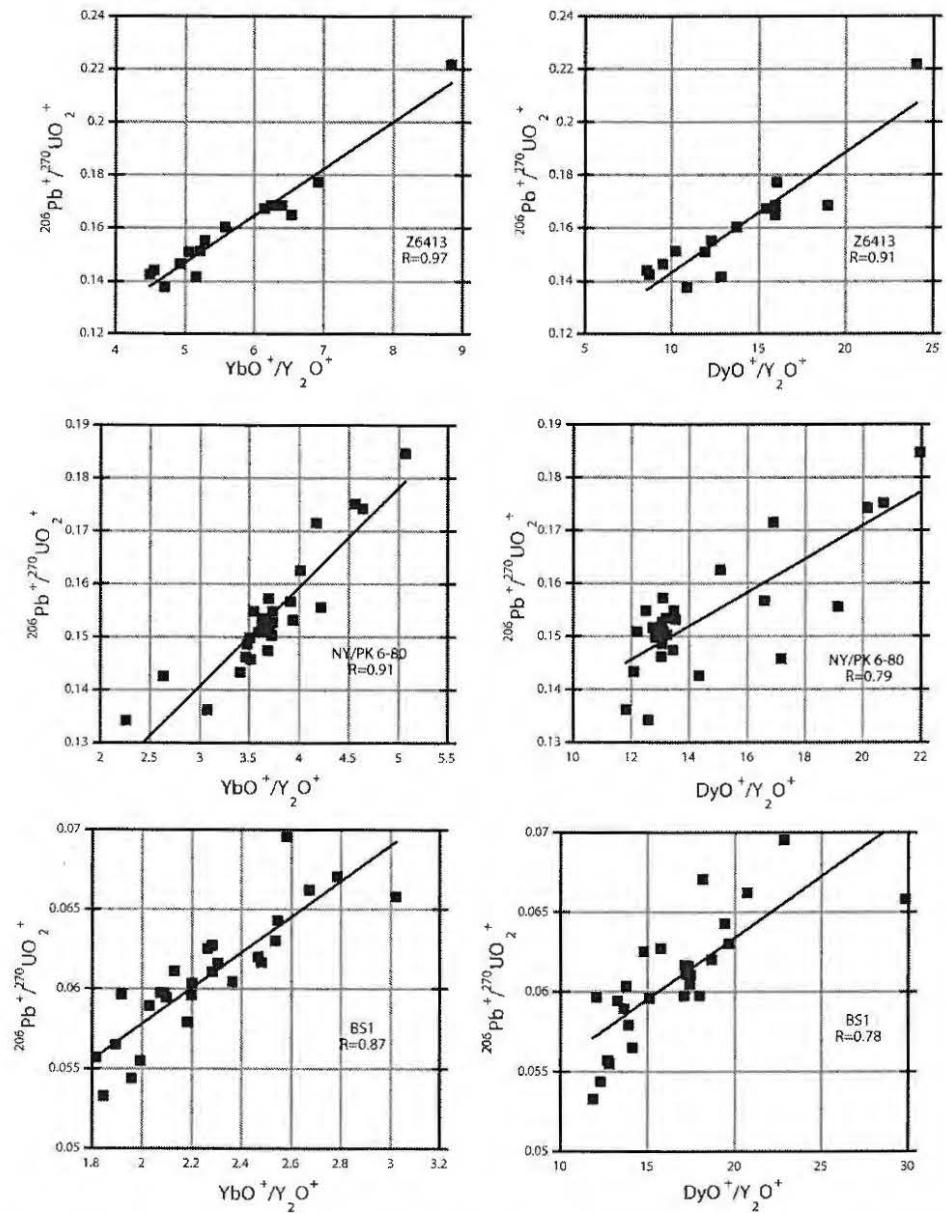
Fig. 3.22. Plots demonstrating the good correlations between $^{190}(YbO^+)/^{194}(Y_2O^+)$ and $^{177}(DyO^+)/^{194}Y_2O^+$ ratios and the $^{206}Pb^+/^{270}(UO_2^+)$ and $^{208}Pb^+/^{248}(ThO^+)$ ratios for the reference xenotimes, Z6413, NY/PK 6-80 and BS1.
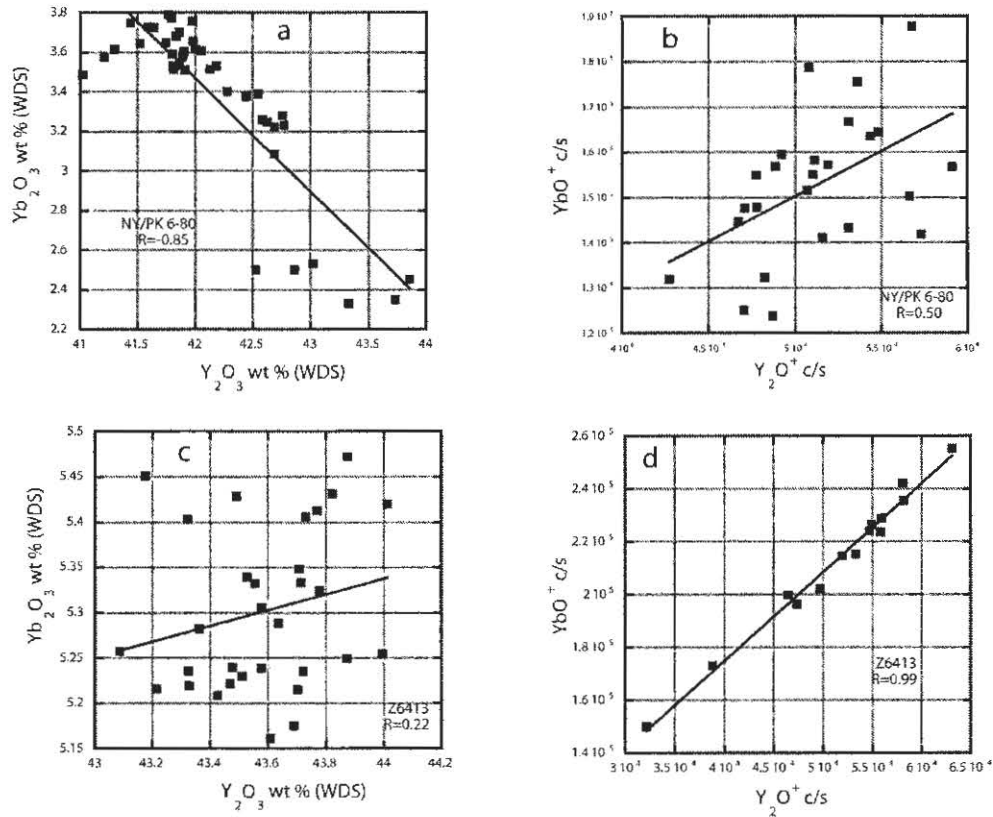
Fig. 3.23. Diagram comparing plots for WDS determined Yb_2O_3 vs Y_2O_3 concentrations (wt%) and SHRIMP determined $^{190}(YbO^+)$ vs. $^{194}(Y_2O^+)$ (counts/sec). The negative correlation for the WDS determined values (3.23a) contrasts with the positive correlation for the SHRIMP determined values (3.23d and 3.23b).

3.4.4 EPMA–WDS analysis as a monitor for SHRIMP xenotime Pb/U and Pb/Th ME.

Independent WDS analyses made prior to, and at the same spot location as the SHRIMP analyses, show a strong positive correlation between U content and the SHRIMP $^{206}Pb^+/^{270}(UO_2^+)$ and $^{208}Pb^+/^{248}(ThO^+)$ ratios in the three high U xenotimes Z6413, NY/PK 6-80 and D43764 (Fig. 3.24). In addition, Th and Si WDS determinations are also shown to positively correlate well with the raw $^{206}Pb^+/^{270}(UO_2^+)$ and $^{208}Pb^+/^{248}(ThO^+)$ ratios in Z6413 (Fig. 3.25a, 3.25d, 3.25g, 3.25j), whereas in NY/PK 6-80, only the Si concentration has a positive correlation with the $^{206}Pb^+/^{270}(UO_2^+)$ and $^{208}Pb^+/^{248}(ThO^+)$ ratios (Fig. 3.25h, 3.25k). However, the correlations between the $^{206}Pb^+/^{270}(UO_2^+)$ and $^{208}Pb^+/^{248}(ThO^+)$ ratios and the Si and Th contents in these samples may simply be a proxy effect, resulting from the positive correlation between Si and U in NY/PK 6-80 (Fig. 3.3h) and Si and Th with U in Z6413 (Fig. 3.3c and 3.3d). Spot–to–spot correlations between the

$^{206}\text{Pb}^+/^{270}(\text{UO}_2^+)$ and $^{208}\text{Pb}^+/^{248}(\text{ThO}^+)$ ratios and WDS–determined $\sum$REE were not observed in any of the reference xenotimes.
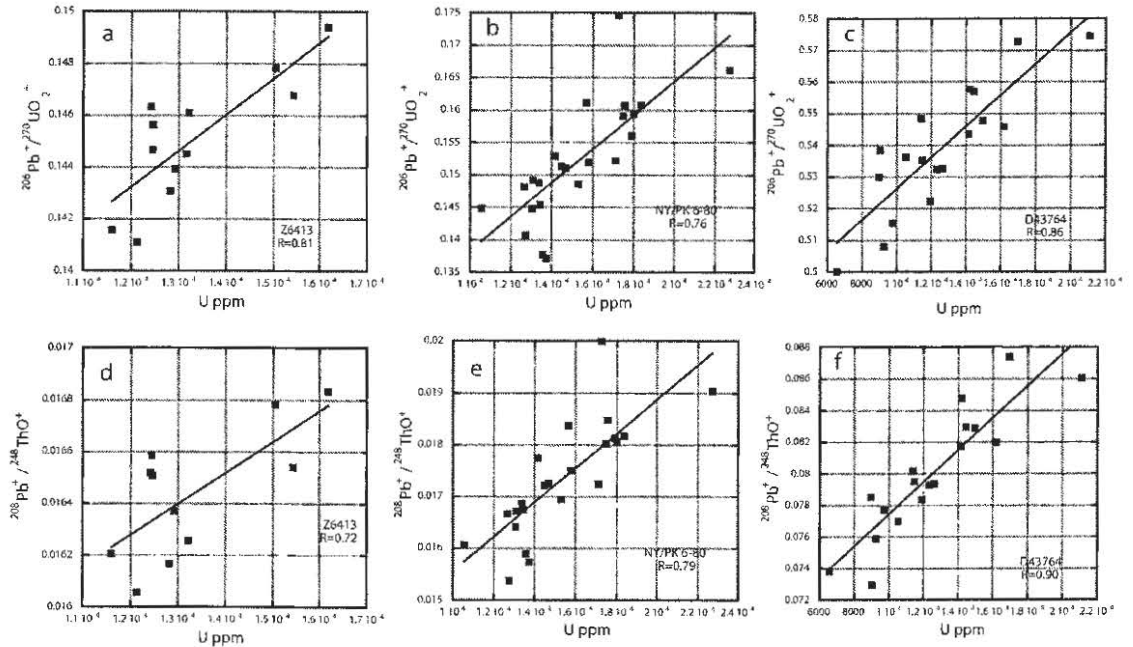
Fig. 3.24. $^{206}\text{Pb}^+/^{270}(\text{UO}_2^+)$ and $^{208}\text{Pb}^+/^{248}(\text{ThO}^+)$ vs U ppm (WDS) plots demonstrating the strong dependence that the $^{206}\text{Pb}^+/^{270}(\text{UO}_2^+)$ and $^{208}\text{Pb}^+/^{248}(\text{ThO}^+)$ ratios have with the U concentration, for the high U reference xenotimes Z6413, NY/PK 6-80 and D43764.

In agreement with previous studies by Fletcher et al. (2000) and Fletcher et al. (2004), xenotime Pb/U determinations were found to be positively correlated to the xenotime U content. This is evident in the high–U xenotime samples Z6413, NY/PK 6-80 and D43764, where both the $^{206}\text{Pb}^+/^{270}(\text{UO}_2^+)$ and $^{208}\text{Pb}^+/^{248}(\text{ThO}^+)$ ratios are positively correlated with the SHRIMP $^{254}(\text{UO}^+)/^{194}(\text{Y}_2\text{O}^+)$ ratios and the WDS–determined U contents. It is likely that the dominant control on the SHRIMP U–Pb/Th–Pb ME is a mismatch in U content between standard and unknown. The dominance of the xenotime U–dependant ME may mask, or dilute, any observable spot–to–spot effect arising from concentration contrasts in Th and/or $\sum$REE. However, the influence on $^{206}\text{Pb}^+/^{270}(\text{UO}_2^+)$ and $^{208}\text{Pb}^+/^{248}(\text{ThO}^+)$ ratios caused by matrix mismatches between Th and/or $\sum$REE concentrations is evident in the elevated $^{206}\text{Pb}/^{238}\text{U}$ and $^{208}\text{Pb}/^{232}\text{Th}$ ratios observed in BS1 analyses calibrated to MG1. Additionally, positive spot-to-spot correlations between $^{206}\text{Pb}^+/^{270}(\text{UO}_2^+)$ and $^{208}\text{Pb}^+/^{248}(\text{ThO}^+)$ ratios, and $^{190}(\text{YbO}^+)/^{194}(\text{Y}_2\text{O}^+)$, $^{177}(\text{DyO}^+)/^{194}(\text{Y}_2\text{O}^+)$ ratios in Z6413, NY/PK 6-80 and BS1, indicate that the matrix effects that cause variations in the $^{206}\text{Pb}^+/^{270}(\text{UO}_2^+)$ and $^{208}\text{Pb}^+/^{248}(\text{ThO}^+)$ ratios, also cause corresponding variations in the xenotime $^{190}(\text{YbO}^+)/^{194}(\text{Y}_2\text{O}^+)$ and $^{177}(\text{DyO}^+)/^{194}(\text{Y}_2\text{O}^+)$ ratios.
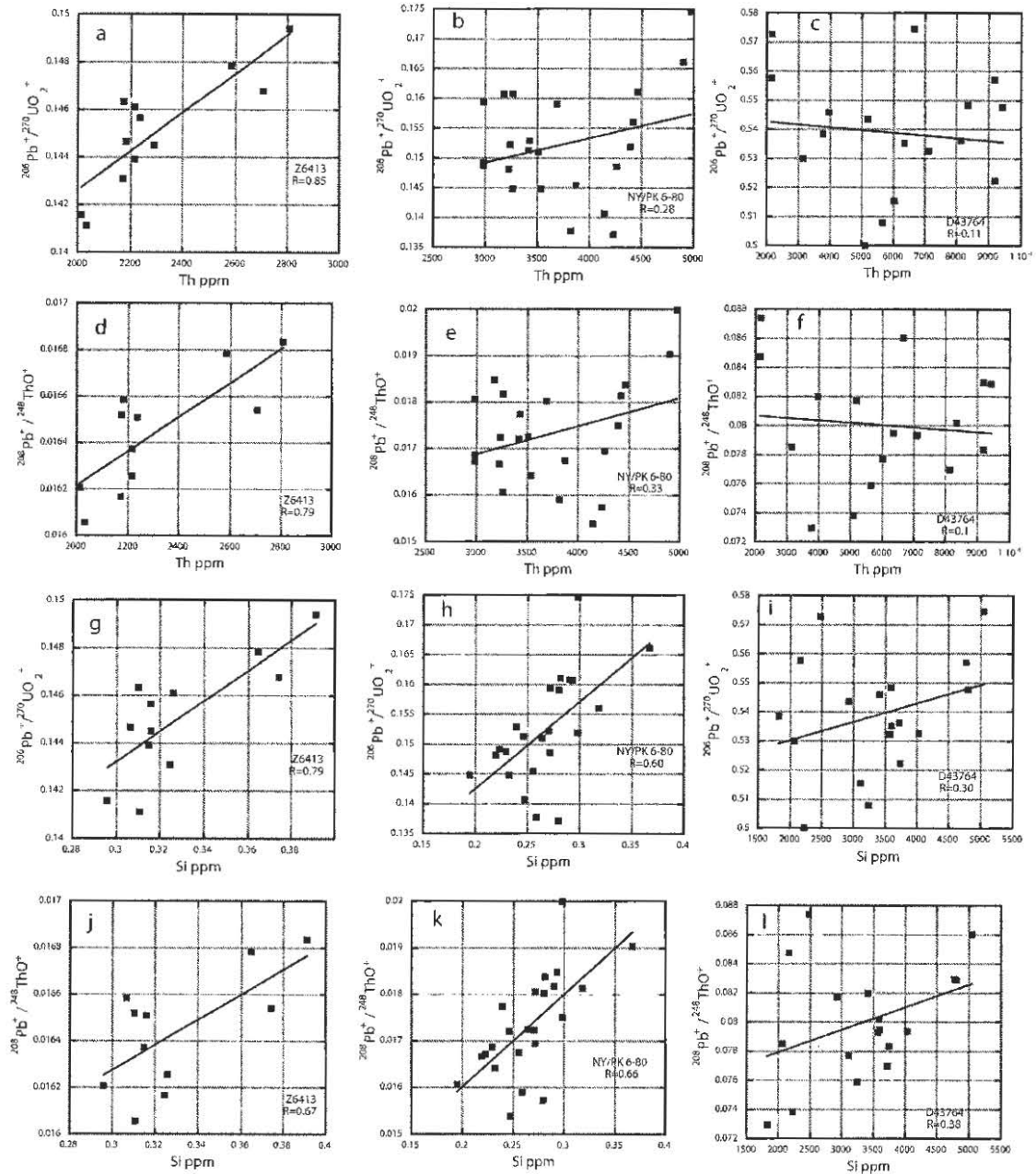
Fig. 3.25. $^{206}Pb^+/^{270}(UO_2^+)$ and $^{208}Pb^+/^{248}(ThO^+)$ vs Si ppm and Th ppm (WDS) plots for the reference xenotimes Z6413, NY/PK 6-80 and D43764.

The wide range of actinide and REE contents in xenotime means that matching concentrations of U and possibly Th and $\sum$REE between Pb/U—Pb/Th standards and unknowns, is virtually impossible. For example, fragments from the Z6413 crystal have a range in U content of up to ~1 wt% which can cause the SHRIMP $^{206}Pb/^{238}U$ ages (calibrated to MG1) to vary by ~15 % during a single analytical session. If synthetic xenotime crystals were to be used as standards, they would need to be chemically matched with the range of compositions in the unknown sample. This

requirement could mean that the impractical situation arises where xenotime standards would need to be synthesised to suit the range of compositions in a single unknown sample. Therefore, for SHRIMP xenotime U–Pb/Th–Pb dating to be effective, alternative SHRIMP analytical conditions or matrix correction procedures need to be adopted that can correct $^{206}Pb/^{238}U$ and/or $^{208}Pb/^{232}Th$ ratios over a wide range of xenotime compositions. Two approaches were used in attempting to remove the SHRIMP U–Pb/Th–Pb ME; energy filtering and empirically based matrix corrections.

3.4.5   Energy Filtering

For SIMS analysis, the isotopic and chemical composition of the secondary ion beam typically differs from that of the target. Fractionation of the secondary ion beam was considered by Shimizu & Hart (1982) to be a basic feature of the SIMS sputtering and ionisation process. Typically, isotopic fractionation favours the lighter isotope. Shimizu & Hart (1982) suggested that the mass dependence of this fractionation is to be expected, as the sputtering and ionisation process involves the transport and transfer of energy and momentum from the primary ion beam to the target. Additionally, the physical constraints that govern the chemical fractionation of the secondary ion beam are complex and include differing elemental ionisation potentials, mass, work functions and binding energies. For example, Shimizu & Hart (1982) suggested that in some cases, low–mass species are preferentially sputtered whereas in other minerals, components with weaker bonds to nearby atoms are more easily removed.

Shimizu & Hart (1982) suggested that both isotopic and chemical fractionation of the secondary ion beam is to a large extent energy dependent, and that this fractionation is less obvious in the high energy ion population. Therefore, they suggested that the chemical and isotopic fractionation of the secondary ion beam could be reduced, or even eliminated, by energy filtering.

With the aim of reducing the Pb/U—Pb/Th ME observed amongst the reference xenotimes, energy filtering of the secondary ion beam was trialled. Energy filtering by removing ~50 % and ~90 % of the total xenotime secondary ion beam was carried

out as described in section 3.3.2. An upper limit of ~90 % reduction of the total secondary ion beam was considered the maximum level at which the energy filtering experiments could be carried out without a prohibitive reduction in ion beam intensity.

3.5 Results

Energy filtering of the secondary ion beam failed to influence the SHRIMP xenotime Pb/U—Pb/Th ME. That is, the relative ionisation yield of Pb^+ and/or U^+ in Z6413, NY/PK 6-80 and BS1 remained elevated compared to that measured in the primary calibration standard MG1. Even after ~90 % of the low energy component of the primary beam was removed, the measured $^{206}Pb/^{238}U$ fractionation for the reference xenotimes showed a similar level of fractionation to the unfiltered data sets (Table 3.9).

Table 3.9. Table comparing xenotime $^{206}Pb/^{238}U$ fractionations of BS1 and Z6413, that were collected using an unfiltered and filtered secondary ion beam.

session	Sample	% Energy filter	% $^{206}Pb/^{238}U$ δ
SHII-6	Z6413	90	~17
SHII-6	BS1	90	~4
SHII-4	Z6413	-	~14
SHII-4	BS1	-	~4

% $^{206}Pb/^{238}U$ δ represents the percent deviation from their reference age

3.5.1 Empirically based U, Th, $\sum$REE, YbO/Y_2O based matrix Pb/U—Pb/Th corrections

It has been shown in section 3.4 that variations in xenotime Pb/U—Pb/Th ratios are strongly correlated with differences in target chemical composition. The approach adopted to correct for xenotime Pb/U—Pb/Th ME was therefore to quantify them by concurrently analysing a number of reference xenotimes with contrasting compositions.

For the initial experiments conducted for this project, it was hoped to monitor and correct the xenotime Pb/U—Pb/Th ME from elemental ratios collected within a SHRIMP xenotime Pb/U—Pb/Th dating experiment. The most promising ratio pair

for this role is $^{190}(YbO^+)/^{194}(Y_2O^+)$, which was shown to correlate well with $^{206}Pb^+/^{270}(UO_2^+)$ ratios in NY/PK 6-80, Z6413 and BS1 (Fig. 3.22). This suggests that this ratio pair, by tracking changes in xenotime Pb/U—Pb/Th fractionation, could also be used to correct the ME via a secondary calibration. Figure 3.26 is a plot of the proportional ME (raw $^{206}Pb/^{238}U$ age/reference $^{206}Pb/^{238}U$ age) for NY/PK 6-80, BS1 and Z6413 calibrated to MG1 for session SHII-1. Although the analyses of BS1 and NY/PK 6-80 lie on similar trajectories, those of Z6413 do not. The data shown in Fig. 3.26 demonstrate that the $^{206}Pb/^{238}U$ ME of BS1 could be used to correct the ME of NY/PK 6-80, but not that of Z6413. The trajectories shown in Figure 3.26 of BS1 and NY/PK 6-80 compared with Z6413 are probably the result of compositional contrasts between these samples. Although the good correlation between the proportional $^{206}Pb/^{238}U$ ME and the $^{190}(YbO^+)/^{194}(Y_2O^+)$ ratios is worth noting, a Pb/U—Pb/Th calibration based solely on this relationship would not be valid.
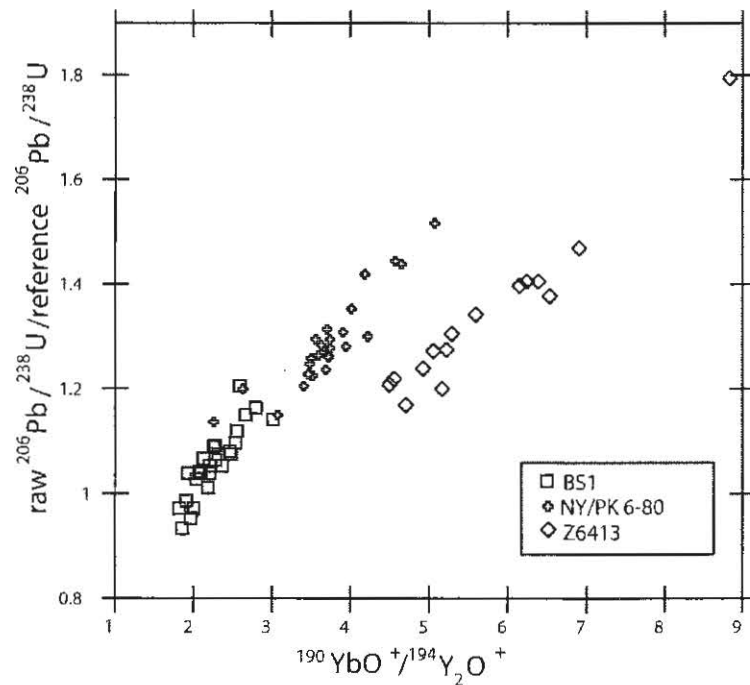
Fig. 3.26. Plot demonstrating the correlation between the relative fractionation of the raw $^{206}Pb/^{238}U$ ratios vs $^{190}(YbO^+)/^{194}(Y_2O^+)$ ratios, for the reference xenotimes BS1, Z6413 and NY/PK 6-80. The correlation between these ratio pairs for BS1 and NY/PK 6-80 is evident, however analyses for Z6413, follow a different trajectory.

3.5.2 Multi-element Pb/U—Pb/Th ME least squares correction

A least squares methodology was developed that can be used to quantify and correct xenotime Pb/U—Pb/Th ME. This method aims to quantify the xenotime Pb/U—Pb/Th ME by a series of simultaneous linear equations that relate the U–Pb/Th–Pb fractionation of xenotimes of a known age (here called secondary standards) to the chemical contrasts they have with the primary calibration standard. This technique allows for more than one variable to be considered simultaneously, which in turn allows for combinations of different elements to be assessed as to their effect on correcting the xenotime Pb/U—Pb/Th ME. The technique is explained below with the example variables of U, Th and $\sum$REE. All experiments that were processed with this technique use MG1 as the primary calibration standard and Z6413 and BS1 as the secondary standards. Additionally, all elemental concentration values were derived by WDS. The simultaneous equation used to model the Pb/U–Pb/Th ME is as follows:

$$\text{Pb/U–Pb/Th ME} = (x * \Delta U) + (y * \Delta Th) + (z * \Delta\textstyle\sum REE) \qquad \text{(eq. 5)}$$

For equation 5, Pb/U–Pb/Th ME is the percent Pb/U–Pb/Th mass fractionation of the given secondary standard referenced to the primary U–Pb/Th–Pb calibration standard. ΔU, ΔTh and $\Delta\sum REE$ represent the difference in the WDS determined elemental concentration of these elements for each of the secondary standard analyses, relative to the average values for the primary calibration standard. The unknown parameters for these equations are given by x, y and z, and are the correction coefficients for ΔU, ΔTh and $\Delta\sum REE$. The numerical values for these correction coefficients can be determined using a simple least squares method, using either the MATLAB program or with Microsoft Excel Solver. Once the correction coefficients are computed, correction factors for U, Th and $\sum$REE can be determined. For example, the U correction factor (U_{CF}) is simply determined by multiplying the U correction coefficient (x) by ΔU, equation 6.

$$U_{CF} = (x*\Delta U) \qquad \text{(eq. 6)}$$

The U, Th and $\sum$REE correction factors for each analysis represent the proportion of the raw Pb/U—Pb/Th ratio that has resulted from concentration mismatches with the primary calibration standard, for a given element. Once the correction factors for each of the U, Th and $\sum$REE are summed, they represent the total U, Th, $\sum$REE correction which is applied to the raw Pb/U—Pb/Th ratios, as shown in equation 7. Once determined, the correction factors can be used to correct for any U, Th or $\sum$REE induced, Pb/U or Pb/Th fractionation for a xenotime of unknown age.

$$^{U,Th,\sum REE}mc\ Pb/U\text{---}Pb/Th = raw\ Pb/U\text{---}Pb/Th*(1-(U_{CF}+Th_{CF}+ \sum REE_{CF}))\ (eq.\ 7)$$

(mc = matrix corrected)

A useful calculation which expresses the relative SHRIMP xenotime Pb/U—Pb/Th ME caused by U, Th and $\sum$REE for a given analytical session, can be defined with knowledge of the U, Th and $\sum$REE correction factors (U_{CF}, Th_{CF}, $\sum REE_{CF}$) and ΔU, ΔTh and $\Delta \sum REE$. The calculation of the relative U correction factor for $^{206}Pb/^{238}U$ (U–% $^{206}Pb/^{238}U$) is shown in equation 8.

$$U\text{--}\%\ ^{206}Pb/^{238}U = U_{CF}\ /\Delta U(ppm)/1000000 \qquad\qquad (eq.\ 8)$$

From equation 8, the relative U correction factor (U–% $^{206}Pb/^{238}U$) represents the percent change in the raw $^{206}Pb/^{238}U$ ratio that results from every 1 wt% difference in U concentration between the secondary standards and the primary calibration standard. By calculating the relative correction factors for U, Th and $\sum$REE, an assessment of the individual contributions that each element has had on the raw Pb/U—Pb/Th ratios can be made for each analytical session. Calculation of this parameter allows comparisons to be made between different sessions and instruments.

The key assumption underpinning the above method is that the function used to quantify the Pb/U—Pb/Th ME is linear. The procedure outlined above is similar to that used by Fletcher at al. (2004) to correct for SHRIMP Pb/U–Pb/Th ME in xenotime. A similar approach was also used by Vielzeuf et al. (2005) to correct for matrix effects associated with SIMS oxygen isotope analysis of Fe–Mg–Ca garnets.

Combinations of U, Th and $\sum$REE were principally trialled as variables in the least squares routine to determine which are the most effective in quantifying and correcting for the xenotime Pb/U—Pb/Th ME. Additionally, Ca and Si concentrations were also trialled, as these elements can occur in concentrations of up to 1000's of ppm, are responsible for actinide substitution into the xenotime lattice, and therefore may themselves impact on the SHRIMP xenotime Pb/U—Pb/Th ME. The best results were obtained using (U, Th, $\sum$REE) and (U, $\sum$REE). Trials which included Ca and Si gave poor results, indicating that these elements have little or no detectable effect on xenotime ME. Additionally, trials which only used U and Th as variables also yielded poor results.

3.5.3   U, Th and $\sum$REE Pb/U—Pb/Th least squares correction

The assumption underpinning this approach is that contrasts in xenotime U, $\sum$REE and Th contents are all responsible for Pb/U—Pb/Th ME. This is also the premise that Fletcher et al. (2004) used in developing their U, Th and $\sum$REE relative correction factors. Although U has been demonstrated to have a major effect on ME, $\sum$REE and Th have not. Th was shown by Stern & Sanborn (1998) and Stern & Berman (2000) to cause SHRIMP $^{206}Pb/^{238}U$ ME in monazite and therefore, by inference, may also cause xenotime ME. Total REE concentrations in xenotime can vary by as much as ~10 wt%, and therefore be a significant cause of matrix contrasts between different xenotimes.

Table 3.10 compares the relative correction factors for U, Th and $\sum$REE derived by the least squares routine for nine xenotime Pb/U—Pb/Th dating sessions conducted during this study, and also the relative correction factors for the same combination of variables published by Fletcher et al. (2004). It is immediately obvious from the results shown in Table 3.10, that the relative correction factors for U, Th and $\sum$REE change for both $^{206}Pb/^{238}U$ and $^{208}Pb/^{232}Th$ ratios, from session to session. Additionally, the relative correction factors derived for U from this study exceed that published by Fletcher et al. (2004) by a factor of two. The contrast in the U correction factor between the results of this study and that of Fletcher et al. (2004) might be

explained by the different methods by which U was calculated. Fletcher et al. (2004) used SHRIMP based calculations based on $^{254}(UO^+)/^{194}(Y_2O^+)$ ratios, which for high U xenotimes such as Z6413 and NY/PK 6-80, overestimate the U concentration by ~25 % (see section 3.3.5 and Table 3.6). A significant over estimation of the U content using $^{194}(Y_2O^+)$ as a reference element will result in an apparent reduction in the U-related Pb/U—Pb/Th ME, and therefore the U relative correction factor.

Table 3.10. Pb/U—Pb/Th relative correction factors for U, Th and $\sum$REE, for nine SHRIMP sessions. Pb/U—Pb/Th correction factors determined by Fletcher et al. (2004) are also shown for comparison.

	$^{206}Pb/^{238}U$			$^{208}Pb/^{232}Th$			
session	U	Th	$\sum$REE	U	Th	$\sum$REE	Shrimp
SHII-6 (Dec-05)	12.48	-5.96	1.36	10.68	-5.53	1.72	II
RG-2 (Sep-06)	11.66	12.58	0.90	11.4	0.37	0.94	RG
RG-3 (Nov-06)	13.03	1.60	1.04	12.14	4.73	1.57	RG
RG-7 (Feb-07)	10.26	22.38	0.37	11.01	26.31	0.66	RG
RG-4 (Oct-06)	11.37	-15.47	1.22	9.46	-10.84	1.28	RG
RG-5 (Oct-06)	14.17	-0.87	1.45	13.41	-10.59	2.67	RG
RG-6 (Nov-06)	11.27	17.48	0.17	9.94	10.41	0.18	RG
RG-1 (Jun-06)	11.39	5.14	0.44	11.17	1.08	0.68	RG
RG-8 (Apr-07)	11.88	3.43	0.55	10.23	15.55	0.96	RG
Fletcher et al. (2004)	6.28	3.01	0.79	2.46	0.63	1.6	Shrimp A

Fletcher et al. (2004) preferred method.

For the SHRIMP xenotime analyses for this study, the Pb/U—Pb/Th relative correction factor for U typically dominates the correction. The U relative correction factors for the $^{206}Pb/^{238}U$ data are all positive and range from 10.26 to 14.17, with an average value of 11.38. Also consistent are the $^{206}Pb/^{238}U$ relative correction factors for $\sum$REE. These are also positive and range from 0.37 to 1.45, with an average value of 0.83. However, the Th relative correction factors for the $^{206}Pb/^{238}U$ data have a range from −15.47 to 22.38. This extreme range in the relative correction factors for Th implies that differences in the SHRIMP instrumental conditions between analytical sessions can cause Th contrasts between the same primary and secondary standards to either increase, or reduce the xenotime $^{206}Pb/^{238}U$ ratio. For example, the relative correction factors for Th in session RG-7 indicate that for every one weight percent difference in the Th concentration between the primary calibration standard and secondary calibration standards, there is a 22.38 % increase in the $^{206}Pb/^{238}U$ ratio. Yet for session RG-4, a negative value for the relative Th correction factor has

been calculated, indicating that for this session, every one weight percent difference in Th concentration, results in a reduction of the $^{206}Pb/^{238}U$ ratio by 15.47 %.

The relative correction factors for U, Th and $\sum$REE for the $^{208}Pb/^{232}Th$ results are similar to those for the $^{206}Pb/^{238}U$ results. The relative correction factor for U ranges between 9.4 and 13.41, and is consistently lower than that of the $^{206}Pb/^{238}U$ data. The $\sum$REE relative correction factors for the $^{208}Pb/^{232}Th$ results are also generally similar to the $^{206}Pb/^{238}U$ data and range between 0.66 and 2.67. For the $^{208}Pb/^{232}Th$ results, the relative correction factor for Th varies from positive to negative values (−10.84 to 26.31).

The least squares matrix correction routine using U, Th and $\sum$REE as variables, implies that Th mismatches can either significantly increase or reduce the $^{206}Pb/^{238}U$ and $^{208}Pb/^{232}Th$ ratios. It is unrealistic to consider that differences in instrumental conditions alone, from session to session, are responsible for this. A better interpretation of these results is that Th plays either an undetectable or insignificant role in SHRIMP xenotime Pb/U—Pb/Th ME. This possibility was explored by omitting Th from the linear equations.

3.5.4   U–$\sum$REE Pb/U—Pb/Th least squares correction

The relative correction factors for U and $\sum$REE derived from the least squares routine from nine separate SHRIMP sessions are shown in Table 3.11. These results show that the relative correction factors for U and $\sum$REE for both the $^{206}Pb/^{238}U$ and $^{208}Pb/^{232}Th$ data are reasonably consistent from session to session and also between different instruments and running conditions. Generally, the relative U correction factors for the $^{206}Pb/^{238}U$ data is slightly elevated compared with the $^{208}Pb/^{232}Th$ data, whereas the relative correction factor for $\sum$REE is reduced in the $^{206}Pb/^{238}U$ compared to the $^{208}Pb/^{232}Th$ data.

Table 3.11. Pb/U—Pb/Th relative correction factors for U and $\sum$REE, for the same SHRIMP sessions shown in Table 3.10.

	^{206}Pb/^{238}U		^{208}Pb/^{232}Th		
session	U	$\sum$REE	U	$\sum$REE	Shrimp
SHI1-6 (Dec-05)	12.52	1.09	10.73	1.47	11
RG-2 (Sep-06)	12.21	1.40	11.41	0.95	RG
RG-3 (Nov-06)	13.09	1.12	12.33	1.81	RG
RG-7 (Feb-07)	11.42	0.93	12.34	1.31	RG
RG-4 (Oct-06)	11.29	0.57	9.4	0.82	RG
RG-5 (Oct-06)	14.13	1.42	12.88	2.29	RG
RG-6 (Nov-06)	10.75	0.71	9.52	0.52	RG
RG-1 (Jun-06)	11.67	0.76	11.54	0.78	RG
RG-8 (Apr-07)	12.13	0.62	11.33	1.28	RG

For the ^{206}Pb/^{238}U data, the U relative correction factor ranges between 10.75 and 14.73 and has an average of 11.89. For the same data, the $\sum$REE relative correction factors range between 0.57 and 1.42, with an average of 0.9. For the ^{208}Pb/^{232}Th data, the U relative correction factor ranges between 9.4 to 12.88, with an average value of 11.49, whereas the relative correction factor for $\sum$REE ranges between 0.95 and 2.29 and an average of 1.33.

Two experiments were conducted to test the effectiveness of the U–$\sum$REE least squares routine in correcting the Pb/U—Pb/Th ME for the reference xenotimes NY/PK 6-80 and D43764, which were treated as 'unknowns'. These were session SHII-6 and session RG-1.

3.5.5   Results Experiment SHII-6 – SHRIMP II

Experiment SHII-6 was designed to test the U–$\sum$REE least squares matrix correction method using MG1, Z6413 and BS1 as the xenotime U–Pb/Th–Pb standards and NY/PK 6-80 as the unknown. To reduce the acquisition time for each analysis, and therefore increase the total number of analyses carried out during the experiment, ^{207}Pb was not measured. WDS analyses to determine the concentrations of U, Th and $\sum$REE were carried out prior to the SHRIMP analyses.

3.5.5.1 Electron microprobe

Table 3.12 shows the averaged WDS determinations for U, Th and $\sum$REE for MG1, as well as the individual determinations for BS1, Z6413, and NY/PK 6-80. This table shows that the U, Th and $\sum$REE concentrations in NY/PK 6-80 are generally similar to the range of these elements measured in the secondary standards Z6413 and BS1.

3.5.5.2 SHRIMP II

Twenty six analyses were carried out on the two secondary standards. The raw U–Pb/Th–Pb ratios for these analyses, calibrated to MG1, show them to be mutually concordant but elevated in comparison to their reference ages (Fig. 3.27a & b). Raw (i.e. no Pb/U—Pb/Th matrix correction) Pb/U—Pb/Th ratios for BS1 are elevated by ~4 % whereas those for Z6413, are elevated by ~17% (Table 3.13a & b). However, once the U, Th and $\sum$REE corrections are applied, the U–Pb/Th–Pb ratios are mutually concordant to near-concordant and corrected to within error of their reference compositions (Fig. 3.27a & b and Table 3.13a & b and 3.14). Fourteen analyses of BS1 combine to give a SHRIMP $^{U-\sum REE}$mc $^{206}Pb/^{238}U$ age of 509 ± 8 Ma (95% conf.) with an MSWD = 0.55, and a near identical independently calculated $^{U-\sum REE}$mc $^{208}Pb/^{232}Th$ age of 508 ± 8 Ma (95% conf.), MSWD = 0.52. For Z6413, 12 analyses combine to give a $^{U-\sum REE}$mc $^{206}Pb/^{238}U$ age of 995 ± 17 Ma (95% conf., MSWD = 0.2) and a $^{U-\sum REE}$mc $^{208}Pb/^{232}Th$ age of 995 ± 19 Ma (95% conf., MSWD = 0.48).

Twenty five analyses were carried out on crystals from NY/PK 6-80. The independently calculated $^{206}Pb/^{238}U$ and $^{208}Pb/^{232}Th$ raw ages are all concordant within experimental error, but on average ~21 % elevated compared to the reference $^{206}Pb/^{238}U$ age of 1000 Ma for this sample (Fig. 3.28, Table 3.13a & b). The dispersion in the Pb/U—Pb/Th ratios is strongly correlated to the U concentrations (R = ~0.77). There is a ~25 % range in the uncorrected $^{206}Pb/^{238}U$ and $^{208}Pb/^{232}Th$ ages. However, once the U and $\sum$REE matrix corrections are applied, the U–Pb/Th–Pb ages correct to within error of the reference age for this sample. All 25 matrix corrected $^{206}Pb/^{238}U$ ages give an age of 993 ± 13 Ma (95% conf.), with a MSWD = 1.31,

whereas the matrix corrected $^{208}Pb/^{232}Th$ ages combine to give an age of 1001 ± 14 Ma (95% conf.) with an MSWD = 1.40 (Fig. 3.28 and Table 3.14).

Table 3.12. Generalised WDS results for session SHII-6. ($\sum$REE = Nd, Sm, Eu, Gd, Tb, Dy, Ho, Er, Tm, Yb, Lu).

Label	U wt%	± U % err.	Th wt%	± Th % err.	ΣREE wt%	± ΣREE % err.
		(1σ)		(1σ)		(1σ)
average MG1 (n=14)	0.0910	6.05	0.0980	8.57	13.43	2.25
BS1-2.8*	0.0230	76.96	0.1109	13.62	17.96	3.55
BS1-2.9*	0.0388	46.65	0.3666	5.37	17.93	3.57
BS1-2.10*	0.0189	96.30	0.1008	18.35	17.81	3.50
BS1-3.1*	0.0363	49.31	0.2026	8.24	17.87	3.57
BS1-3.2*	0.0372	47.85	0.1892	8.72	17.86	3.57
BS1-3.3*	0.0518	35.33	0.3081	6.07	18.02	3.57
BS1-3.4*	0.0515	35.34	0.3028	6.11	17.52	3.56
BS1-3.5*	0.0565	32.39	0.3097	5.97	17.47	3.57
BS1-4.1*	0.0493	37.12	0.4456	4.80	18.64	3.66
BS1-4.2*	0.0611	30.28	0.4372	4.83	18.08	3.57
BS1-4.3*	0.0791	23.51	0.4226	4.92	17.77	3.55
BS1-4.4*	0.0376	48.14	0.3890	5.19	18.49	3.64
BS1-5.1*	0.0604	30.46	0.4822	4.56	18.17	3.60
BS1-5.2*	0.0360	50.56	0.4246	4.95	18.61	3.58
Z6413-5.*1	1.3156	6.64	0.2291	7.46	16.22	3.55
Z6413-5.2*	1.2436	6.67	0.2182	7.70	16.26	3.56
Z6413-5.3*	1.5045	6.58	0.2580	6.82	16.19	3.56
Z6413-5.4*	1.2920	6.64	0.2214	7.63	16.16	3.57
Z6413-6.1*	1.2411	6.66	0.2173	7.73	16.33	3.54
Z6413-6.2*	1.2452	6.66	0.2235	7.56	16.39	3.53
Z6413-6.3*	1.1592	6.70	0.2014	8.19	16.36	3.53
Z6413-6.4*	1.2116	6.68	0.2034	8.16	16.33	3.54
Z6413-6.5*	1.5431	6.57	0.2704	6.62	16.50	3.53
Z6413-6.6*	1.6180	6.55	0.2807	6.45	16.39	3.53
Z6413-7.1*	1.3210	6.63	0.2215	7.63	16.38	3.53
Z6413-7.2*	1.2815	6.65	0.2171	7.74	16.45	3.52
NYPK-3.2	1.2782	6.65	0.3967	5.12	16.99	3.68
NYPK-3.3	1.2442	6.66	0.4425	4.79	17.09	3.67
NYPK-4.10	1.5305	6.72	0.4257	5.03	17.64	3.63
NYPK-4.11	1.3083	7.69	0.3535	5.91	17.21	3.69
NYPK-4.12	1.2738	6.81	0.4142	4.68	17.09	3.69
NYPK-4.1	1.5679	5.40	0.4461	4.60	17.84	3.51
NYPK-4.2	1.7252	6.53	0.4967	4.47	17.97	3.61
NYPK-4.3	1.7492	6.53	0.3683	5.38	17.68	3.61
NYPK-4.4	1.0538	6.76	0.3262	5.79	17.21	3.66
NYPK-4.5	1.2671	6.65	0.3221	5.84	17.51	3.63
NYPK-4.6	1.4494	6.60	0.3413	5.60	17.58	3.60
NYPK-4.7	1.7101	6.54	0.3236	5.81	17.25	3.64
NYPK-4.8	1.3095	6.64	0.2987	6.16	17.56	3.60
NYPK-4.9	1.7983	6.52	0.2984	6.17	17.61	3.61
NYPK-5.1	1.4169	6.61	0.3423	5.64	17.70	3.59
NYPK-5.2	1.3404	6.63	0.2985	6.13	17.56	3.61
NYPK-5.3	2.2728	6.46	0.4898	4.51	17.52	3.64
NYPK-7.1	1.3453	6.63	0.3870	5.19	17.30	3.65
NYPK-7.2	1.7898	6.52	0.4417	4.82	17.97	3.58
NYPK-7.3	1.7553	6.53	0.3174	5.92	17.70	3.59
NYPK-8.1	1.4692	6.59	0.3506	5.50	17.70	3.58
NYPK-8.2	1.3585	6.62	0.3816	5.21	17.38	3.64
NYPK-8.3	1.5783	6.56	0.4391	4.83	17.85	3.58
NYPK-8.4	1.8349	6.51	0.3262	5.79	17.66	3.61
NYPK-8.5	1.3739	6.61	0.4230	4.92	17.30	3.64

* denotes secondary $^{206}Pb/^{238}U$ standard.

109
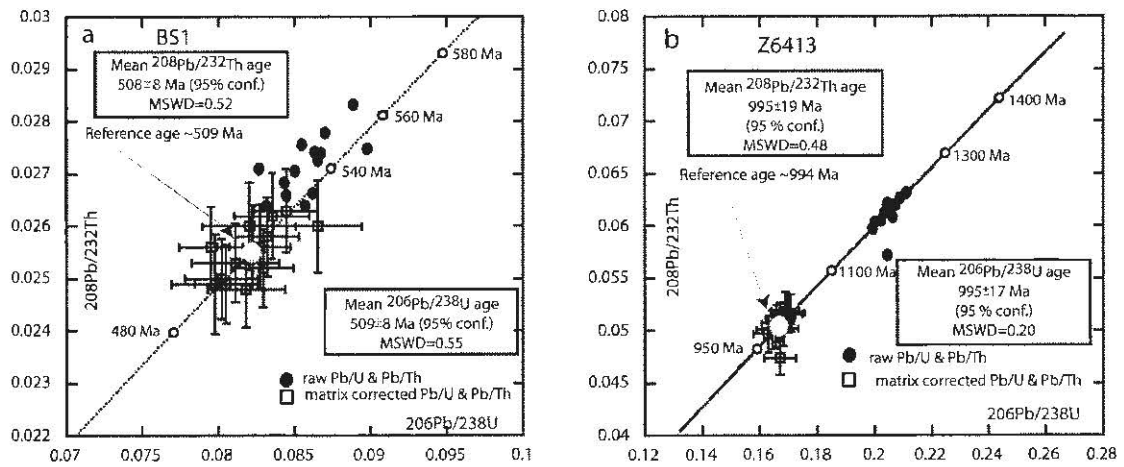
Fig. 3.27. U–Pb–Th concordia plots for BS1 (a) and Z6413 (b) used as secondary standards in session SHII-6. The raw Pb/U—Pb/Th ratios are shown to be significantly elevated prior to the U–∑REE matrix correction, which subsequently corrects these determinations to within error of their reference compositions.
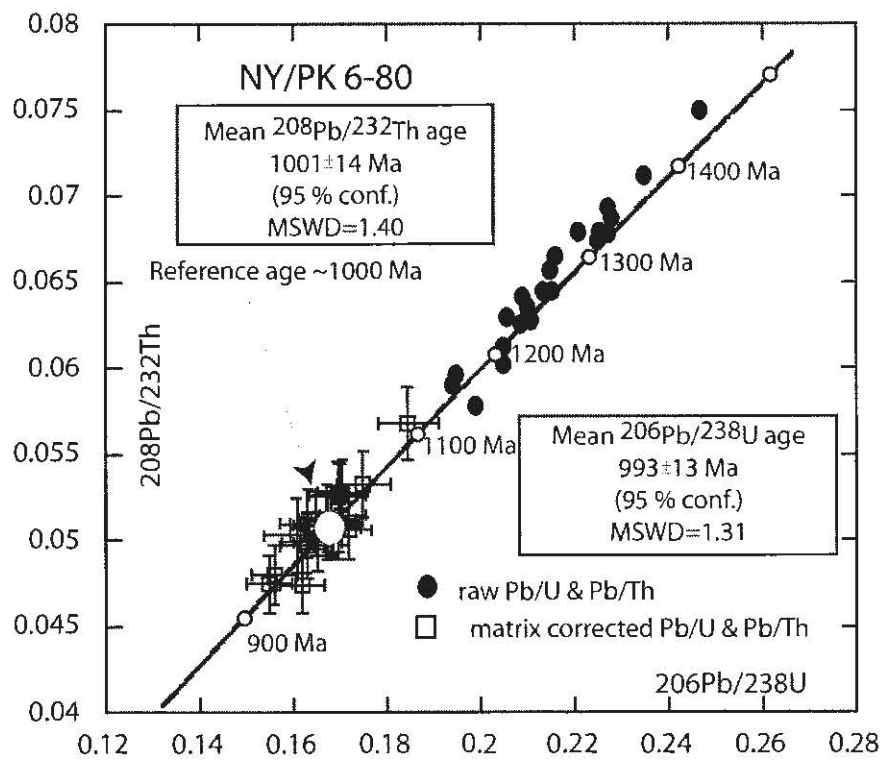
Fig. 3.28. U–Pb–Th concordia plot for NY/PK 6-80, session SHII-6. Both raw Pb/U–Pb-Th and matrix corrected Pb/U—Pb/Th ratios are plotted.

110

Table 3.13a. Table showing the raw and matrix corrected $^{206}Pb/^{238}U$ ratios for session SHII-6.

Spot name	raw $^{206}Pb/^{238}U$ (± 1σ %)		% δ¹	^{U,ΣREE}m.c. $^{206}Pb/^{238}U$ (± 1σ %)		% $^{206}Pb/^{238}U$ correction	% δ²
BS1-2.8*	0.0831	3.4622	1.2	0.0798	3.58	-3.9	-2.9
BS1-2.9*	0.0867	2.4666	5.3	0.0832	2.55	-4.1	1.2
BS1-2.10*	0.0898	3.2345	8.5	0.0865	3.42	-3.7	5.0
BS1-3.1*	0.0855	3.6731	3.9	0.0820	3.73	-4.0	-0.2
BS1-3.2*	0.0870	2.9376	5.6	0.0835	3.01	-4.0	1.6
BS1-3.3*	0.0865	2.4217	5.0	0.0827	2.49	-4.4	0.6
BS1-3.4*	0.0826	2.6067	0.6	0.0795	2.66	-3.8	-3.4
BS1-3.5*	0.0862	2.4571	4.7	0.0829	2.51	-3.8	0.9
BS1-4.1*	0.0889	2.4495	7.6	0.0844	2.54	-5.0	2.7
BS1-4.2*	0.0850	3.5275	3.3	0.0811	3.57	-4.6	-1.3
BS1-4.3*	0.0857	3.0948	4.1	0.0818	3.14	-4.4	-0.4
BS1-4.4*	0.0863	2.6964	4.8	0.0822	2.79	-4.7	0.1
BS1-5.1*	0.0844	2.5385	2.7	0.0805	2.60	-4.6	-2.0
BS1-5.2*	0.0843	2.8665	2.5	0.0802	2.96	-4.8	-2.4
Z6413-5.1*	0.2042	2.5894	18.3	0.1669	3.32	-18.2	0.1
Z6413-5.2*	0.2044	2.1769	18.4	0.1688	2.93	-17.4	1.3
Z6413-5.3*	0.2088	2.1982	20.2	0.1659	3.24	-20.6	-0.5
Z6413-5.4*	0.2033	2.1784	18.0	0.1670	2.98	-17.9	0.2
Z6413-6.1*	0.2068	2.1761	19.4	0.1707	2.92	-17.4	2.3
Z6413-6.2*	0.2058	2.1973	19.0	0.1697	2.94	-17.5	1.7
Z6413-6.3*	0.2000	2.1914	16.7	0.1672	2.85	-16.4	0.3
Z6413-6.4*	0.1993	2.1594	16.4	0.1653	2.88	-17.1	-0.8
Z6413-6.5*	0.2074	2.1773	19.6	0.1630	3.28	-21.4	-2.3
Z6413-6.6*	0.2111	2.1712	21.0	0.1642	3.36	-22.2	-1.5
Z6413-7.1*	0.2064	2.1597	19.2	0.1682	3.00	-18.5	0.9
Z6413-7.2*	0.2021	2.1614	17.5	0.1656	2.96	-18.1	-0.7
NYPK-3.2	0.2088	2.1779	19.6	0.1699	2.98	-18.6	1.3
NYPK-3.3	0.2085	2.1692	19.5	0.1704	2.93	-18.3	1.5
NYPK-4.10	0.2099	2.1709	20.1	0.1627	3.29	-22.5	-3.1
NYPK-4.11	0.2046	2.1788	18.0	0.1652	3.07	-19.2	-1.6
NYPK-4.12	0.1988	2.1824	15.6	0.1617	2.98	-18.7	-3.8
NYPK-4.1	0.2276	2.1726	26.3	0.1749	3.25	-23.1	4.1
NYPK-4.2	0.2467	2.1711	32.0	0.1844	3.52	-25.3	9.0
NYPK-4.3	0.2247	2.2084	25.3	0.1680	3.57	-25.2	0.1
NYPK-4.4	0.2046	2.1707	18.0	0.1718	2.74	-16.0	2.3
NYPK-4.5	0.2094	2.1850	19.9	0.1696	2.98	-19.0	1.0
NYPK-4.6	0.2137	2.1739	21.5	0.1680	3.18	-21.4	0.1
NYPK-4.7	0.2150	2.1880	22.0	0.1628	3.50	-24.3	-3.1
NYPK-4.8	0.2108	2.2056	20.4	0.1694	3.04	-19.6	1.0
NYPK-4.9	0.2252	2.1710	25.5	0.1671	3.61	-25.8	-0.4
NYPK-5.1	0.2160	2.1812	22.3	0.1704	3.15	-21.1	1.5
NYPK-5.2	0.2102	2.2269	20.2	0.1682	3.09	-20.0	0.2
NYPK-5.3	0.2348	2.1656	28.5	0.1605	4.26	-31.6	-4.5
NYPK-7.1	0.2055	2.1820	18.3	0.1649	3.06	-19.8	-1.8
NYPK-7.2	0.2205	2.1711	23.9	0.1630	3.61	-26.1	-3.0
NYPK-7.3	0.2270	2.1710	26.1	0.1695	3.56	-25.3	1.0
NYPK-8.1	0.2133	2.1670	21.3	0.1669	3.20	-21.8	-0.5
NYPK-8.2	0.1947	2.2145	13.8	0.1557	3.10	-20.0	-7.8
NYPK-8.3	0.2147	2.1646	21.8	0.1647	3.33	-23.3	-1.9
NYPK-8.4	0.2271	2.1735	26.1	0.1674	3.66	-26.3	-0.2
NYPK-8.5	0.1938	2.1708	13.4	0.1547	3.08	-20.1	-8.4

δ¹ percent deviation of the raw ratios from their reference age.

δ² percent deviation of the matrix corrected ratios from their reference age.

* denotes secondary $^{206}Pb/^{238}U$ standard.

111

Table 3.13b. Table showing the raw and matrix corrected ^{208}Pb/^{232}Th ratios for session SHII-6.

Spot name	raw ^{208}Pb/^{232}Th (± 1σ %)		% δ[1]	$^{U,\Sigma REE}$m.c. ^{208}Pb/^{232}Th (± 1σ %)		% ^{208}Pb/^{232}Th correction	% δ[2]
BS1-2.8*	0.0266	3.71	4.1	0.0250	3.84	-6.1	-2.1
BS1-2.9*	0.0274	2.86	7.0	0.0257	2.97	-6.2	0.8
BS1-2.10*	0.0283	3.21	9.9	0.0266	3.39	-5.8	4.3
BS1-3.1*	0.0276	3.10	7.5	0.0259	3.21	-6.1	1.5
BS1-3.2*	0.0278	3.03	8.2	0.0261	3.13	-6.1	2.3
BS1-3.3*	0.0274	3.06	7.1	0.0257	3.16	-6.5	0.6
BS1-3.4*	0.0271	2.90	5.9	0.0255	2.99	-5.7	0.2
BS1-3.5*	0.0266	2.89	4.3	0.0251	2.97	-5.7	-1.5
BS1-4.1*	0.0284	2.92	10.2	0.0263	3.05	-7.4	3.1
BS1-4.2*	0.0271	2.85	5.8	0.0253	2.96	-6.7	-1.0
BS1-4.3*	0.0264	2.89	3.4	0.0247	2.98	-6.4	-3.3
BS1-4.4*	0.0274	3.00	7.0	0.0255	3.13	-7.1	-0.1
BS1-5.1*	0.0266	2.91	4.1	0.0248	3.02	-6.8	-2.9
BS1-5.2*	0.0268	2.95	4.9	0.0249	3.09	-7.2	-2.5
Z6413-5.1*	0.0574	2.97	12.2	0.0476	3.47	-17.2	-6.0
Z6413-5.2*	0.0621	2.87	18.9	0.0519	3.34	-16.5	2.8
Z6413-5.3*	0.0627	2.88	19.6	0.0507	3.54	-19.2	0.5
Z6413-5.4*	0.0612	2.84	17.7	0.0509	3.34	-16.9	1.0
Z6413-6.1*	0.0623	2.94	19.1	0.0520	3.39	-16.6	3.0
Z6413-6.2*	0.0621	2.85	18.9	0.0517	3.33	-16.7	2.6
Z6413-6.3*	0.0604	2.86	16.5	0.0508	3.27	-15.7	0.9
Z6413-6.4*	0.0597	3.01	15.5	0.0500	3.44	-16.3	-0.8
Z6413-6.5*	0.0620	2.85	18.7	0.0496	3.56	-20.0	-1.6
Z6413-6.6*	0.0633	2.90	20.4	0.0502	3.65	-20.7	-0.4
Z6413-7.1*	0.0608	2.85	17.1	0.0501	3.38	-17.5	-0.5
Z6413-7.2*	0.0606	2.93	16.8	0.0502	3.42	-17.2	-0.5
NYPK-3.2	0.0642	2.82	21.0	0.0527	3.34	-18.0	3.7
NYPK-3.3	0.0626	2.95	19.0	0.0515	3.43	-17.8	1.5
NYPK-4.10	0.0636	2.88	20.3	0.0499	3.61	-21.7	-1.7
NYPK-4.11	0.0613	2.89	17.2	0.0499	3.46	-18.6	-1.7
NYPK-4.12	0.0578	2.88	12.3	0.0474	3.39	-18.1	-7.0
NYPK-4.1	0.0687	2.85	26.2	0.0533	3.57	-22.4	4.9
NYPK-4.2	0.0750	2.81	32.3	0.0568	3.72	-24.2	10.7
NYPK-4.3	0.0674	2.87	24.8	0.0512	3.77	-24.0	1.0
NYPK-4.4	0.0602	2.91	15.8	0.0506	3.28	-15.9	-0.1
NYPK-4.5	0.0628	2.93	19.2	0.0511	3.44	-18.7	0.7
NYPK-4.6	0.0644	2.93	21.2	0.0510	3.57	-20.7	0.6
NYPK-4.7	0.0645	2.85	21.4	0.0497	3.71	-23.0	-2.1
NYPK-4.8	0.0628	2.94	19.2	0.0507	3.48	-19.2	0.0
NYPK-4.9	0.0679	2.84	25.3	0.0513	3.79	-24.5	1.1
NYPK-5.1	0.0665	2.88	23.7	0.0528	3.51	-20.5	4.0
NYPK-5.2	0.0631	2.93	19.6	0.0508	3.50	-19.5	0.1
NYPK-5.3	0.0712	2.82	28.8	0.0503	4.24	-29.4	-0.8
NYPK-7.1	0.0630	2.87	19.5	0.0509	3.44	-19.2	0.4
NYPK-7.2	0.0679	2.82	25.3	0.0510	3.79	-24.9	0.5
NYPK-7.3	0.0693	2.89	26.8	0.0526	3.80	-24.1	3.6
NYPK-8.1	0.0645	2.83	21.3	0.0509	3.51	-21.1	0.3
NYPK-8.2	0.0596	2.95	14.9	0.0480	3.52	-19.4	-5.6
NYPK-8.3	0.0657	2.82	22.9	0.0510	3.60	-22.5	0.5
NYPK-8.4	0.0678	2.92	25.1	0.0509	3.89	-24.9	0.3
NYPK-8.5	0.0590	2.88	14.0	0.0475	3.47	-19.5	-6.8

δ[1] percent deviation of the raw ratios from their reference age.
δ[2] percent deviation of the matrix corrected ratios from their reference age.
* denotes secondary ^{208}Pb/^{232}Th standard.

Table 3.14. SHRIMP U–Pb–Th isotopic data for xenotime analysed in session SHII-6. Results for the secondary standards BS1 and Z6413 are shown together with the sample treated as the unknown, NY/PK 6-80.

Spot name	Th/U	% Com. [206]Pb	$^{U,\Sigma REE}$m.c. $^{206}Pb/^{238}U$ (± 1σ %)		$^{206}Pb/^{238}U$ age (Ma ± 1σ)		$^{U,\Sigma REE}$m.c. $^{208}Pb/^{232}Th$ (± 1σ %)		$^{208}Pb/^{232}Th$ age (Ma ± 1σ)		Disc. %
BS1-2.8*	1.20	0.14	0.0798	3.58	495	18	0.0250	3.84	499	19	0.7
BS1-2.9*	6.27	0.00	0.0832	2.55	515	13	0.0257	2.97	513	15	-0.4
BS1-2.10*	10.08	0.08	0.0865	3.42	535	18	0.0266	3.39	532	18	-0.6
BS1-3.1*	6.59	0.00	0.0820	3.73	508	19	0.0259	3.21	516	17	1.6
BS1-3.2*	6.92	1.65	0.0835	3.01	517	16	0.0261	3.13	521	16	0.7
BS1-3.3*	6.80	0.58	0.0827	2.49	512	13	0.0257	3.16	512	16	0.0
BS1-3.4*	6.99	0.00	0.0795	2.66	493	13	0.0255	2.99	510	15	3.5
BS1-3.5*	6.78	0.14	0.0829	2.51	513	13	0.0251	2.97	501	15	-2.3
BS1-4.1*	6.74	0.10	0.0844	2.54	523	13	0.0263	3.05	525	16	0.4
BS1-4.2*	10.43	0.00	0.0811	3.57	503	18	0.0253	2.96	504	15	0.3
BS1-4.3*	7.90	0.91	0.0818	3.14	507	16	0.0247	2.98	493	15	-2.8
BS1-4.4*	7.71	0.36	0.0822	2.79	509	14	0.0255	3.13	509	16	-0.1
BS1-5.1*	9.78	0.14	0.0805	2.60	499	13	0.0248	3.02	495	15	-0.9
BS1-5.2*	8.20	0.62	0.0802	2.96	497	15	0.0249	3.09	497	15	-0.1
Z6413-5.1*	10.52	1.07	0.1669	3.32	995	33	0.0476	3.47	939	33	-5.6
Z6413-5.2*	0.19	-0.01	0.1688	2.93	1006	29	0.0519	3.34	1022	34	1.6
Z6413-5.3*	0.18	0.00	0.1659	3.24	989	32	0.0507	3.54	999	35	1.0
Z6413-5.4*	0.18	0.01	0.1670	2.98	995	30	0.0509	3.34	1003	34	0.8
Z6413-6.1*	0.18	0.01	0.1707	2.92	1016	30	0.0520	3.39	1024	35	0.8
Z6413-6.2*	0.18	-0.01	0.1697	2.94	1010	30	0.0517	3.33	1020	34	0.9
Z6413-6.3*	0.18	0.00	0.1672	2.85	996	28	0.0508	3.27	1002	33	0.6
Z6413-6.4*	0.18	0.00	0.1653	2.88	986	28	0.0500	3.44	986	34	-0.1
Z6413-6.5*	0.18	0.02	0.1630	3.28	974	32	0.0496	3.56	978	35	0.5
Z6413-6.6*	0.19	0.00	0.1642	3.36	980	33	0.0502	3.65	991	36	1.0
Z6413-7.1*	0.19	-0.01	0.1682	3.00	1002	30	0.0501	3.38	989	33	-1.3
Z6413-7.2*	0.18	0.01	0.1656	2.96	988	29	0.0502	3.42	989	34	0.2
NYPK-3.2	0.18	0.00	0.1699	2.98	1012	30	0.0527	3.34	1037	35	2.5
NYPK-3.3	0.34	0.00	0.1704	2.93	1014	30	0.0515	3.43	1015	35	0.1
NYPK-4.10	0.34	0.01	0.1627	3.29	972	32	0.0499	3.61	984	36	1.2
NYPK-4.11	0.24	0.00	0.1652	3.07	986	30	0.0499	3.46	983	34	-0.2
NYPK-4.12	0.30	0.02	0.1617	2.98	966	29	0.0474	3.39	936	32	-3.2
NYPK-4.1	0.32	0.00	0.1749	3.25	1039	34	0.0533	3.57	1050	37	1.1
NYPK-4.2	0.25	0.01	0.1844	3.52	1091	38	0.0568	3.72	1117	42	2.3
NYPK-4.3	0.32	0.00	0.1680	3.57	1001	36	0.0512	3.77	1010	38	0.9
NYPK-4.4	0.25	0.01	0.1718	2.74	1022	28	0.0506	3.28	999	33	-2.3
NYPK-4.5	0.31	0.00	0.1696	2.98	1010	30	0.0511	3.44	1007	35	-0.3
NYPK-4.6	0.26	-0.01	0.1680	3.18	1001	32	0.0510	3.57	1006	36	0.5
NYPK-4.7	0.25	0.01	0.1628	3.50	972	34	0.0497	3.71	980	36	0.8
NYPK-4.8	0.19	0.01	0.1694	3.04	1009	31	0.0507	3.48	1000	35	-0.9
NYPK-4.9	0.25	0.00	0.1671	3.61	996	36	0.0513	3.79	1010	38	1.4
NYPK-5.1	0.25	0.00	0.1704	3.15	1014	32	0.0528	3.51	1040	37	2.6
NYPK-5.2	0.24	0.01	0.1682	3.09	1002	31	0.0508	3.50	1001	35	-0.1
NYPK-5.3	0.24	0.01	0.1605	4.26	960	41	0.0503	4.24	992	42	3.4
NYPK-7.1	0.24	0.01	0.1649	3.06	984	30	0.0509	3.44	1004	34	2.0
NYPK-7.2	0.31	-0.01	0.1630	3.61	973	35	0.0510	3.79	1005	38	3.2
NYPK-7.3	0.27	0.01	0.1695	3.56	1009	36	0.0526	3.80	1036	39	2.7
NYPK-8.1	0.17	0.00	0.1669	3.20	995	32	0.0509	3.51	1003	35	0.8
NYPK-8.2	0.20	0.01	0.1557	3.10	933	29	0.0480	3.52	948	33	1.6
NYPK-8.3	0.28	0.00	0.1647	3.33	983	33	0.0510	3.60	1005	36	2.2
NYPK-8.4	0.24	0.00	0.1674	3.66	998	37	0.0509	3.89	1003	39	0.5
NYPK-8.5	0.19	0.02	0.1547	3.08	927	29	0.0475	3.47	938	33	1.1

* denotes secondary $^{206}Pb/^{238}U$ standard.

3.5.6 Results experiment RG-1 – SHRIMP RG

Experiment RG-1 was conducted using SHRIMP RG and designed to test the U–$\sum$REE matrix correction routine using the reference xenotime D43764 as the 'unknown' sample. MG1 was used as the primary calibration standard and BS1 and Z6413, the secondary standards. U, Th and $\sum$REE contents were measured by WDS prior to SHRIMP analysis. Backscattered SEM images and transmitted and reflected light photography guided the choice of analytical sites.

3.5.6.1 _Electron microprobe_

WDS determinations of xenotime from D43764 show it to be broadly similar in compositional range to the two secondary standards. U contents in D43764 range from ~0.65 to 2.1 wt% (average 1.2 wt%), whereas Th concentrations range from ~0.2 to 0.9 wt% (average ~0.6 wt%). These U and Th levels are only slightly elevated compared to the U content of Z6413 (range ~0.6–1.4 wt%, average 1.2 wt%) and the Th content of BS1 (range ~0.1–0.4 wt%, average 0.3 wt%). The average $\sum$REE concentration of D43764 is ~17 wt% which is similar to that determined for BS1 (Table 3.15).

3.5.6.2 _SHRIMP RG_

The U and $\sum$REE xenotime U–Pb/Th–Pb matrix correction factors for this session were determined from eight SHRIMP and WDS analyses on each of the two secondary standards. The uncorrected Pb/U—Pb/Th xenotime ratios for Z6413 and BS1 show these analyses to be mutually concordant, although elevated by ~15 % and ~4 % respectively, compared to their reference ages (Table 3.16a & b). However, the corrected Pb/U—Pb/Th ages are well within error of their reference compositions (Fig. 3.29a & b, Table 3.16a & b).

Table 3.15. Generalised WDS results for session RG–1. ($\sum$REE = Nd, Sm, Eu, Gd, Tb, Dy, Ho, Er, Tm, Yb, Lu).

Label	U wt%	± U % err.	Th wt%	± Th % err.	ΣREE wt%	± ΣREE % err.
average MG1		(1σ)		(1σ)		(1σ)
(n=10)	0.1006	8.00	0.1083	13.72	12.51	1.12
BS1-1.2*	0.0213	81.69	0.1079	13.81	16.99	2.48
BS1-2.1*	0.0548	32.85	0.4196	4.93	16.80	2.61
BS1-2.2*	0.0573	31.59	0.4342	4.84	16.99	2.62
BS1-3.1*	0.0467	38.12	0.2972	6.12	16.82	2.55
BS1-3.2*	0.0558	32.08	0.2949	6.17	16.88	2.56
BS1-4.1*	0.0405	43.95	0.3721	5.29	17.34	2.67
BS1-4.2*	0.0372	47.85	0.4127	4.97	17.46	2.69
Z6413-1.1*	1.3644	6.61	0.2240	7.54	15.53	2.37
Z6413-2.1*	0.6207	7.27	0.1092	13.64	15.54	2.36
Z6413-3.1*	1.3750	6.61	0.2177	7.72	15.70	2.35
Z6413-3.2*	1.3632	6.62	0.2209	7.61	15.76	2.34
Z6413-3.3*	1.4225	6.59	0.2246	7.52	15.84	2.34
Z6413-3.4*	1.4422	6.59	0.2332	7.29	15.70	2.35
Z6413-4.1*	1.0806	6.74	0.1917	8.50	15.72	2.35
Z6413-4.2*	1.0632	6.74	0.1763	9.08	15.73	2.35
D43764-2A.1	1.4957	6.59	0.9431	3.39	16.83	2.50
D43764-2A.2	0.8966	6.87	0.3137	5.96	17.86	2.50
D43764-2A.3	0.9035	6.87	0.3770	5.28	17.85	2.53
D43764-2B.1	1.0509	6.77	0.8140	3.57	17.81	2.49
D43764-2B.2	1.1416	6.71	0.8353	3.54	16.84	2.49
D43764-3A.1	2.1060	6.48	0.6649	3.90	17.32	2.53
D43764-3A.2	1.6161	6.55	0.3963	5.12	17.58	2.51
D43764-3A.3	0.6546	7.21	0.5114	4.42	17.07	2.45
D43764-6A.1	1.2616	6.66	0.7134	3.77	17.13	2.51
D43764-6A.2	0.9234	6.84	0.5638	4.20	16.76	2.48
D43764-6A.3	1.4447	6.60	0.9183	3.43	16.89	2.55
D43764-6B.1	1.4173	6.60	0.2153	7.85	17.65	2.38
D43764-6B.2	1.4134	6.60	0.5186	4.38	17.55	2.38
D43764-6B.3	1.6935	6.54	0.2163	7.77	17.60	2.38
D43764-7B.1	1.1486	6.70	0.6335	3.98	17.21	2.50
D43764-7C.1	1.1914	6.68	0.9184	3.42	17.73	2.58
D43764-7C.2	1.2311	6.67	0.7093	3.79	17.53	2.56
D43764-8A.1	0.9729	6.81	0.6006	4.08	17.46	2.51

* denotes secondary $^{206}Pb/^{238}U$ standard.
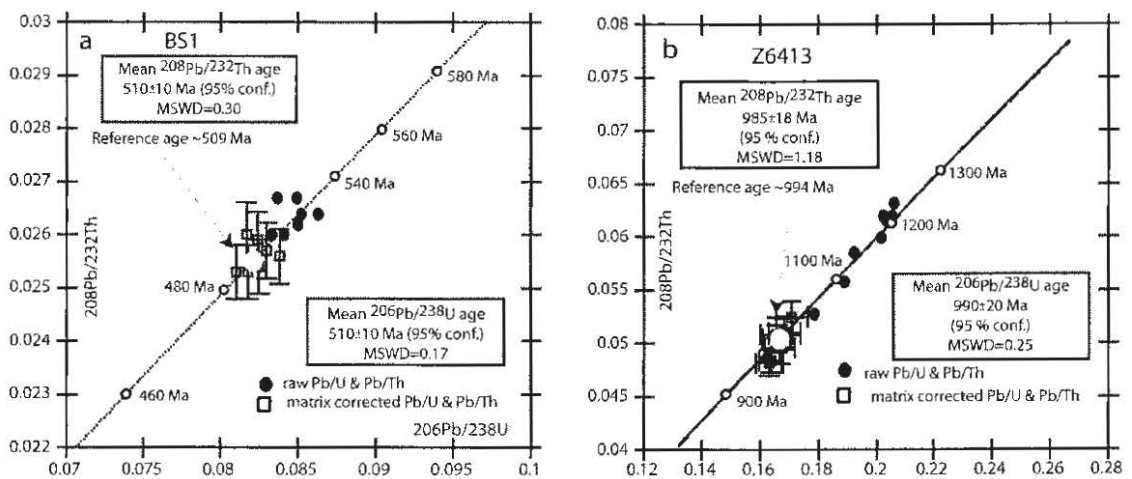
Fig. 3.29. U–Pb–Th concordia plot for the secondary standards BS1 (a) and Z6413 (b) for session RG–1. Both raw and U–$\sum$REE matrix corrected Pb/U–Pb/Th ratios are shown.

Table 3.16a. Table showing the raw and matrix corrected ^{206}Pb/^{238}U ratios for session RG–1.

Spot name	raw ^{206}Pb/^{238}U ($\pm 1\sigma$ %)		% δ^1	$^{U,\Sigma REE}$m.c. ^{206}Pb/^{238}U ($\pm 1\sigma$ %)		% ^{206}Pb/^{238}U correction	% δ^2
BS1-1.2*	0.0837	3.3998	1.9	0.0817	3.50	-2.5	-0.6
BS1-2.1*	0.0841	2.5058	2.3	0.0818	2.53	-2.7	-0.4
BS1-2.2*	0.0863	2.4652	4.8	0.0838	2.49	-2.9	1.9
BS1-3.1*	0.0852	2.4655	3.6	0.0830	2.50	-2.6	1.0
BS1-3.2*	0.0833	2.6112	1.4	0.0810	2.64	-2.8	-1.5
BS1-4.1*	0.0849	2.6670	3.2	0.0824	2.71	-2.9	0.3
BS1-4.2*	0.0850	2.6083	3.4	0.0825	2.66	-3.0	0.4
Z6413-1.1*	0.2057	2.2779	19.0	0.1707	3.13	-17.0	2.3
Z6413-2.1*	0.1784	2.2665	6.5	0.1635	2.45	-8.4	-2.0
Z6413-3.1*	0.2015	2.2586	17.3	0.1667	3.13	-17.3	0.0
Z6413-3.2*	0.2031	2.2698	17.9	0.1682	3.12	-17.2	0.9
Z6413-3.3*	0.2050	2.2796	18.7	0.1682	3.20	-17.9	0.9
Z6413-3.4*	0.2020	2.3264	17.5	0.1655	3.25	-18.1	-0.7
Z6413-4.1*	0.1921	2.2661	13.2	0.1655	2.82	-13.9	-0.7
Z6413-4.2*	0.1888	2.2578	11.7	0.1630	2.80	-13.7	-2.3
D43764-2A.1	0.6086	2.3238	17.4	0.4897	3.32	-19.5	-2.6
D43764-2A.2	0.5888	2.2745	14.6	0.5104	2.68	-13.3	1.5
D43764-2A.3	0.5982	2.3405	16.0	0.5181	2.74	-13.4	3.0
D43764-2B.1	0.5957	2.2852	15.6	0.5059	2.83	-15.1	0.7
D43764-2B.2	0.6092	2.7926	17.5	0.5153	3.32	-15.4	2.5
D43764-3A.1	0.6384	2.4080	21.3	0.4659	4.15	-27.0	-7.9
D43764-3A.2	0.6065	2.2939	17.1	0.4761	3.45	-21.5	-5.6
D43764-3A.3	0.5556	2.2857	9.5	0.5006	2.50	-9.9	-0.4
D43764-6A.1	0.5917	2.2612	15.1	0.4910	3.01	-17.0	-2.4
D43764-6A.2	0.5643	2.2754	10.9	0.4920	2.69	-12.8	-2.2
D43764-6A.3	0.6190	2.2569	18.8	0.5015	3.21	-19.0	-0.2
D43764-6B.1	0.6196	2.3260	18.9	0.5005	3.24	-19.2	-0.4
D43764-6B.2	0.6038	2.3338	16.8	0.4884	3.24	-19.1	-2.9
D43764-6B.3	0.6365	2.4474	21.0	0.4939	3.65	-22.4	-1.8
D43764-7B.1	0.5947	2.2727	15.5	0.5009	2.90	-15.8	-0.3
D43764-7C.1	0.5802	2.2975	13.4	0.4836	2.97	-16.7	-3.9
D43764-7C.2	0.5916	2.4253	15.0	0.4913	3.11	-17.0	-2.3
D43764-8A.1	0.5728	2.4008	12.2	0.4931	2.85	-13.9	-1.9

δ^1 percent deviation of the raw ratios to their reference ages.
δ^2 percent deviation of the matrix corrected ratios to their reference ages.
* denotes secondary ^{206}Pb/^{238}U standard.

Table 3.16b. Table showing the raw and matrix corrected $^{208}Pb/^{232}Th$ ratios for session RG–1.

Spot name	raw $^{208}Pb/^{232Th}$ ($\pm$ 1σ %)		% δ[1]	$^{U, ΣREE}$m.c. $^{208}Pb/^{232}Th$ ($\pm$ 1σ %)		% $^{208}Pb/^{232}Th$ correction	% δ[2]
BS1-1.2*	0.0267	2.26	4.6	0.0260	2.40	-.26	2.4
BS1-2.1*	0.0260	1.99	1.9	0.0253	2.03	-2.8	2.0
BS1-2.2*	0.0264	1.96	3.3	0.0256	2.00	-3.0	2.0
BS1-3.1*	0.0264	2.01	3.74	0.0257	2.06	-2.7	2.1
BS1-3.2*	0.0260	1.95	2.0	0.0253	1.99	-2.9	2.0
BS1-4.1*	0.0267	2.01	4.5	0.0259	2.07	-3.1	2.1
BS1-4.2*	0.0262	1.92	2.7	0.0254	1.99	-3.1	2.0
Z6413-1.1*	0.0632	20.2	20.2	0.0525	2.90	-16.9	2.9
Z6413-2.1*	0.0528	4.5	4.5	0.0484	2.17	-8.4	2.2
Z6413-3.1*	0.0599	15.8	15.8	0.0496	2.91	-17.2	2.9
Z6413-3.2*	0.0616	18.2	18.2	0.0511	2.86	-17.1	2.9
Z6413-3.3*	0.0620	18.7	18.7	0.0509	2.96	-17.8	3.0
Z6413-3.4*	0.0620	18.7	18.7	0.0509	2.98	-18.0	3.0
Z6413-4.1*	0.0585	13.9	13.9	0.0505	2.58	-13.8	2.6
Z6413-4.2*	0.0558	9.7	9.7	0.0482	2.55	-13.6	2.6
D43764-2A.1	0.1719	19.3	19.3	0.1384	3.13	-19.5	3.1
D43764-2A.2	0.1628	14.8	14.8	0.1411	2.55	-13.3	2.5
D43764-2A.3	0.1510	8.1	8.1	0.1307	2.39	-13.4	2.4
D43764-2B.1	0.1597	13.1	13.1	0.1356	2.53	-15.1	2.5
D43764-2B.2	0.1662	16.6	16.6	0.1407	2.94	-15.4	2.9
D43764-3A.1	0.1784	22.3	22.3	0.1305	3.88	-26.9	3.9
D43764-3A.2	0.1699	18.4	18.4	0.1335	3.19	-21.4	3.2
D43764-3A.3	0.1531	9.4	9.4	0.1379	2.15	-9.9	2.2
D43764-6A.1	0.1646	15.7	15.7	0.1366	2.77	-17.0	2.8
D43764-6A.2	0.1573	11.9	11.9	0.1372	2.40	-12.8	2.4
D43764-6A.3	0.1721	19.4	19.4	0.1395	2.98	-18.9	3.0
D43764-6B.1	0.1756	21.0	21.0	0.1419	2.92	-19.2	2.9
D43764-6B.2	0.1694	18.1	18.1	0.1371	2.97	-19.1	3.0
D43764-6B.3	0.1811	23.4	23.4	0.1406	3.51	-22.3	3.5
D43764-7B.1	0.1649	15.9	15.9	0.1389	2.67	-15.7	2.7
D43764-7C.1	0.1625	14.6	14.6	0.1354	2.65	-16.6	2.7
D43764-7C.2	0.1644	15.6	15.6	0.1365	2.86	-16.9	2.9
D43764-8A.1	0.1611	13.9	13.9	0.1387	2.56	-13.9	2.6

δ[1] percent deviation of the raw ratios from their reference age.
δ[2] percent deviation of the matrix corrected ratios from their reference age.
* denotes secondary $^{208}Pb/^{232}Th$ standard.

Eighteen crystals were analysed from D43764. Common Pb contents are uniformly low (<0.01 % common ^{206}Pb). All 18 analyses have the same radiogenic $^{207}Pb/^{206}Pb$ within analytical uncertainty (MSWD = 1.6) and combine to give a weighted mean age of 2625 ± 5 Ma (95 % conf.) which is within error of the EPMA determined chemical U—Th—Pb age for this sample. However, the raw $^{206}Pb/^{238}U$ and $^{208}Pb/^{232}Th$ ages are, on average, elevated by ~16 % compared to the $^{207}Pb/^{206}Pb$ age. When plotted on a $^{208}Pb/^{232}Th$–$^{206}Pb/^{238}U$ concordia, the raw ratios are elevated and systematically displaced to the high $^{208}Pb/^{232}Th$ side of concordia (Fig. 3.30). When plotted on a Tera-Wasserberg concordia, the compositions are also significantly reversely discordant (Fig. 3.31a). Once the matrix corrections are applied, the $^{U-ΣREE}$mc $^{206}Pb/^{238}U$ and $^{208}Pb/^{232}Th$ ratios are both well within error of the $^{207}Pb/^{206}Pb$

age for this sample, resulting in concordant, $^{206}Pb/^{238}U$, $^{208}Pb/^{232}Th$ and $^{207}Pb/^{206}Pb$ ratios (Figs. 3.30 & 3.31b, Table 3.16a &b). All 18 $^{U-\Sigma REE}mc$ $^{206}Pb/^{238}U$ ratios combine to form a single population (MSWD = 0.44) equivalent to a mean age of 2599 ± 36 Ma (95 % conf.). The Th $^{U-\Sigma REE}mc$ $^{208}Pb/^{232}Th$ ratios also form a single population (MSWD = 0.61) and give a near identical mean age of 2598 ± 33 Ma (95 % conf.). Final results are given in Table 3.17.
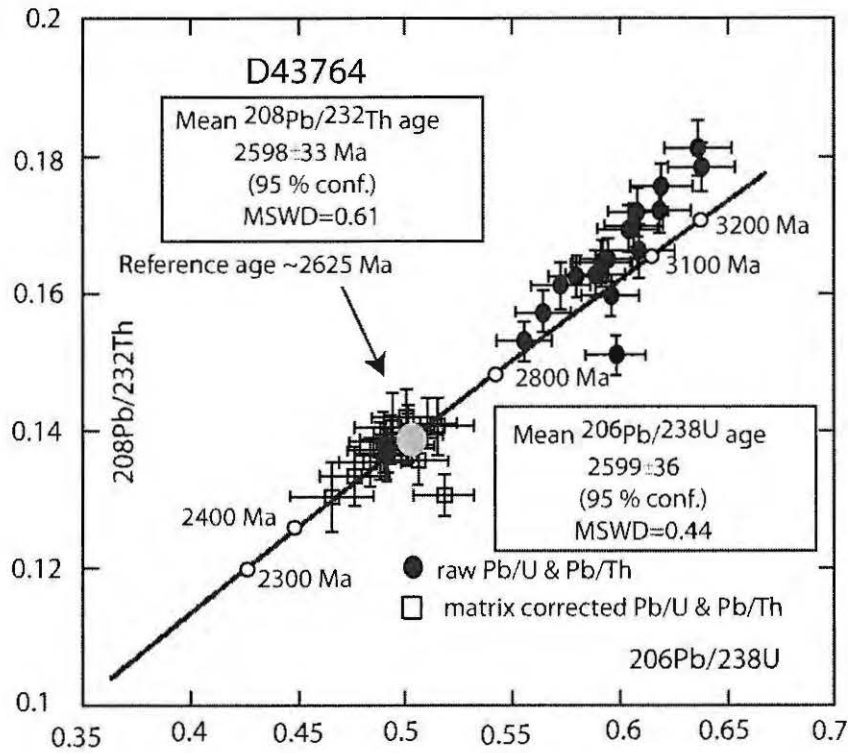
Fig. 3.30. U–Pb–Th concordia plot for D43764, session RG–1. Both raw and U–ΣREE matrix corrected Pb/U–Pb/Th ratios are shown.
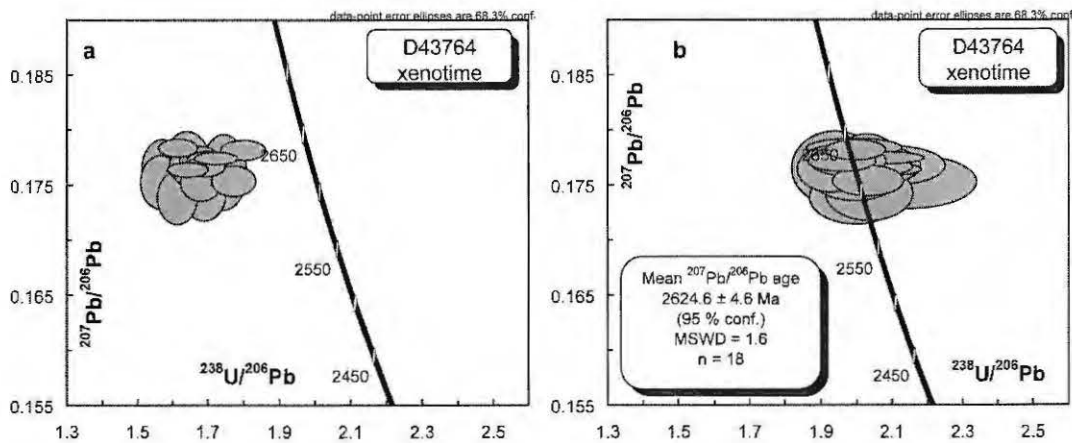
Fig. 3.31a & b. Concordia plots of U–Pb analyses for D43764. 3.31a are the raw $^{206}Pb/^{238}U$ ratios, and 3.31b the U–ΣREE matrix corrected results.

Table 3.17. SHRIMP U–Pb–Th isotopic data for xenotime analysed in session RG–1. Results for the secondary standards BS1 and Z6413 are shown together with the sample treated as the unknown, D43764.

150 name	Th/U	% Com. ^{206}Pb	$^{U,\Sigma REE}$m.c. ^{208}Pb/^{232}Th (± 1σ %)		^{208}Pb/^{232}Th age (Ma ± 1σ)		$^{U,\Sigma REE}$m.c. ^{206}Pb/^{238}U (± 1σ %)		^{206}Pb/^{238}U age (Ma ± 1σ)		^{207}Pb/^{206}Pb (± 1σ %)		^{207}Pb/^{206}Pb age (Ma ± 1σ)		Disc. %
BS1-1.2*	6.52	1.29	0.0260	2.40	520	12	0.0817	3.50	506	18	0.0471	16.12	55	385	1.7
BS1-2.1*	8.03	0.64	0.0253	2.03	504	10	0.0818	2.53	507	13	0.0519	5.17	282	118	-0.1
BS1-2.2*	8.00	0.72	0.0256	2.00	510	10	0.0838	2.49	519	13	0.0530	4.78	330	108	-1.1
BS1-3.1*	6.80	0.39	0.0257	2.06	512	11	0.0830	2.50	514	13	0.0519	3.95	280	90	-0.4
BS1-3.2*	6.89	0.37	0.0253	1.99	504	10	0.0810	2.64	502	13	0.0543	3.74	384	84	0.4
BS1-4.1*	9.56	0.54	0.0259	2.07	517	11	0.0824	2.71	510	14	0.8181	1.57	4954	22	1.4
BS1-4.2*	10.02	0.37	0.0254	1.99	507	10	0.0825	2.66	511	14	0.0548	3.84	403	86	-0.6
Z6413-1.1*	0.18	0.01	0.0525	2.90	1034	30	0.1707	3.13	1016	32	0.0738	0.44	1037	9	2.1
Z6413-2.1*	0.19	0.02	0.0484	2.17	954	21	0.1635	2.45	976	24	0.0730	0.42	1015	9	4.0
Z6413-3.1*	0.17	0.01	0.0496	2.91	978	28	0.1667	3.13	994	31	0.0730	0.25	1014	5	2.1
Z6413-3.2*	0.17	0.00	0.0511	2.86	1006	29	0.1682	3.12	1002	31	0.0717	0.25	979	5	-2.4
Z6413-3.3*	0.17	0.01	0.0509	2.96	1004	30	0.1682	3.20	1002	32	0.0727	0.31	1007	6	0.4
Z6413-3.4*	0.17	0.01	0.0509	2.98	1003	30	0.1655	3.25	987	32	0.0714	0.82	970	17	-1.7
Z6413-4.1*	0.18	0.01	0.0505	2.58	995	26	0.1655	2.82	987	28	0.0720	0.31	985	6	-0.2
Z6413-4.2*	0.18	0.02	0.0482	2.55	952	24	0.1630	2.80	973	27	0.0717	0.34	977	7	0.4
D43764-2A.1	0.68	0.00	0.1384	3.13	2621	82	0.4897	3.32	2569	85	0.1764	0.25	2619	4	1.9
D43764-2A.2	0.32	0.00	0.1411	2.55	2667	68	0.5104	2.68	2658	71	0.1771	0.35	2626	6	-1.2
D43764-2A.3	0.22	0.01	0.1307	2.39	2483	59	0.5181	2.74	2691	74	0.1764	0.79	2620	13	-2.7
D43764-2B.1	0.77	0.00	0.1356	2.53	2570	65	0.5059	2.83	2639	75	0.1771	0.51	2626	8	-0.5
D43764-2B.2	0.81	0.00	0.1407	2.94	2660	78	0.5153	3.32	2679	89	0.1765	1.26	2620	21	-2.2
D43764-3A.1	0.33	0.00	0.1305	3.88	2479	96	0.4659	4.15	2466	102	0.1753	0.92	2609	15	5.8
D43764-3A.2	0.25	0.00	0.1335	3.19	2533	81	0.4761	3.45	2510	87	0.1767	0.67	2622	11	4.5
D43764-3A.3	0.83	0.01	0.1379	2.15	2611	56	0.5006	2.50	2617	65	0.1781	0.35	2636	6	0.7
D43764-6A.1	0.57	0.00	0.1366	2.77	2588	72	0.4910	3.01	2575	78	0.1766	0.33	2621	5	1.8
D43764-6A.2	0.66	0.01	0.1372	2.40	2598	62	0.4920	2.69	2579	69	0.1753	0.51	2609	9	1.2
D43764-6A.3	0.71	0.00	0.1395	2.98	2640	79	0.5015	3.21	2620	84	0.1783	0.30	2637	5	0.7
D43764-6B.1	0.17	0.00	0.1419	2.92	2682	78	0.5005	3.24	2616	85	0.1738	0.92	2595	15	-0.8
D43764-6B.2	0.38	0.00	0.1371	2.97	2597	77	0.4884	3.24	2564	83	0.1767	0.67	2623	11	2.3
D43764-6B.3	0.14	0.00	0.1406	3.51	2659	93	0.4939	3.65	2587	94	0.1764	1.01	2619	17	1.2
D43764-7B.1	0.61	0.00	0.1389	2.67	2629	70	0.5009	2.90	2618	76	0.1752	0.61	2608	10	-0.4
D43764-7C.1	0.82	0.00	0.1354	2.65	2567	68	0.4836	2.97	2543	76	0.1774	0.22	2629	4	3.4
D43764-7C.2	0.61	0.00	0.1365	2.86	2586	74	0.4913	3.11	2576	80	0.1742	0.95	2599	16	0.9
D43764-8A.1	0.69	0.00	0.1387	2.56	2625	67	0.4931	2.85	2584	74	0.1761	1.28	2617	21	1.3

3.6 Discussion

The results of experiments RG-1 and SHII-6 in correcting the Pb/U—Pb/Th ME in NY/PK 6-80 and D43764 demonstrate that the linear least squares routine used to measure and correct for the U and $\sum$REE mismatches with the primary calibration standard works. It is not necessary to include Th in the correction. The additional uncertainties associated with this approach, namely the uncertainty associated with the U and $\sum$REE correction and WDS elemental determinations, result in 95 % confidence precision estimates of approximately 2 %.

An essential part of the success of the SHRIMP Pb/U—Pb/Th xenotime matrix correction procedure is the calculation of $^{206}Pb/^{238}U$ and $^{208}Pb/^{232}Th$ from the raw $^{206}Pb/^{270}(UO_2^+)$ and $^{208}Pb/^{248}(ThO^+)$ ratios. In contrast, when xenotime $^{206}Pb/^{238}U$ and $^{208}Pb/^{232}Th$ ratios were calculated from the Pb^+/U^+ versus UO^+/U^+ calibration (or any combination of $Pb/U[O_x]:U[O_x]/U[O_x]$ and/or $Pb/Th[O_x]:Th[O_x]/Th[O_x]$), the matrix correction routine performed poorly. The better results obtained by the xenotime Pb/U—Pb/Th matrix correction procedure when using the raw $^{206}Pb/^{270}(UO_2^+)$ and $^{208}Pb/^{248}(ThO^+)$ ratios is very likely because they are independent of the variations in slope that commonly exist between the various combinations of xenotime $Pb/U[O_x]:U[O_x]/U[O_x]$ calibrations (see section 3.3.4).

Although U and $\sum$REE are presented above as the most plausible causes of Pb/U—Pb/Th ME in xenotime, it is important to note that the combination of U, Th and $\sum$REE used by Fletcher et al. (2004) produces comparable results (Table 3.18). However, the extreme variations in the relative correction factors for Th indicate that for the typical ~2000–3000 ppm contrast in Th between the secondary standard BS1 and the primary calibration standard MG1, there is seemingly no consistent Th-related Pb/U—Pb/Th ME. Additionally, the success of the linear least squares routine using U and $\sum$REE as variables is able to correct the Pb/U—Pb/Th ME of D43764, even though the Th concentration of this sample exceeds that of the primary calibration standard by up to ~8000 ppm. These results do not exclude Th as potential cause of Pb/U—Pb/Th ME in xenotime. Rather they suggest that Th contrasts between the primary calibration standard and unknown of approximately 1 wt% appear to have no effect on the Pb/U—Pb/Th ME. However, the majority of published xenotime EPMA

analyses record Th concentrations of < 1 wt% which therefore will have little to no effect on the SHRIMP xenotime Pb/U—Pb/Th ME.

The strong inference that a mismatch in xenotime U and $\sum$REE contents between the calibration standard and unknown causes SHRIMP xenotime Pb/U—Pb/Th ME explains the ~5 % ME of the Pb/U—Pb/Th ratios measured on BS1. The low concentrations of U in this crystal (~400 ppm) exclude U as a factor causing $^{206}Pb/^{238}U$ or $^{208}Pb/^{232}Th$ fractionation. The Pb/U—Pb/Th ME in BS1 is better interpreted to be the ~4–5 wt% contrast in $\sum$REE it has with the primary calibration standard MG1, rather than its ~3000–4000 ppm contrast in Th.

Table 3.18. Comparison between the U–Th–$\sum$REE and U–$\sum$REE based Pb/U—Pb/Th xenotime matrix correction.

Sample	Session	Variables	$^{206}Pb/^{238}$ U (Ma)	mswd	$^{208}Pb/^{232}$Th (Ma)	mswd	Ref. Age (Ma)
D43764	RG-1 (Jun-06)	U, $\sum$REE	2599±36	0.44	2598± 33	0.61	2625
D43764	RG-1 (Jun-06)	U, Th, $\sum$REE	2540±37	0.96	2572±32	0.71	2625
NY/PK 6-80	SHII-6 (Dec-05)	U, $\sum$REE	993±13	1.31	1001±14	1.40	1000
NY/PK 6-80	SHII-6 (Dec-05)	U, Th, $\sum$REE	999±13	0.97	1011±14	1.01	1000

Excel Solver proved to be an efficient means to calculate the correction factors for a range of variable combinations and thereby determine the best combination that corrects for the SHRIMP xenotime Pb/U–Pb/Th ME. For the experiments carried out in this study the best combination of variables for the simultaneous equations used to model the Pb/U–Pb/Th ME were found to be U and $\sum$REE. That is:

$$\text{Pb/U–Pb/Th ME} = (x * \Delta U) + (y * \Delta\textstyle\sum REE) \qquad \text{(eq. 9)}$$

To determine the correction coefficients for ΔU and $\Delta\sum REE$, Excel Solver iteratively calculates the values of the correction coefficients that minimise the sum of squares between the measured fPb/U–Pb/Th ME for the secondary standards and the linear function used to model it (i.e. equation 9). A worked example demonstrating how

Excel Solver was used to determine the correction coefficients for ΔU and $\Delta \sum REE$ as well as the assignment of errors for this procedure is shown in Appendix 3.6.

3.6.1 Comparison of the xenotime Pb/U—Pb/Th ME correction procedures developed in this study to that of Fletcher et al. (2004).

The processing protocols developed in this study to measure and account for the xenotime Pb/U—Pb/Th ME differs from that of Fletcher et al. (2004) in a number of areas. Although both methodologies use a linear least squares approach, Fletcher et al. (2004) use as variables U, Th and $\sum REE$. Whereas this study, for the reasons given above, has shown that Th probably does not play a significant role in xenotime Pb/U—Pb/Th ME.

The methods by which xenotime U concentrations are determined also differ between this study and that of Fletcher et al. (2004). Those researchers determined U and Th concentrations from the U concentration of MG1 and the SHRIMP $^{254}(UO^+)/^{194}(Y_2O^+)$ ratios. When this approach was used in this study, U contents for the high–U xenotimes NY/PK 6-80 and Z6413 were over estimated by ~25 %. Two factors preclude elemental concentrations being calculated in this way. Firstly, the up to ~10 wt% difference in Y concentrations between different xenotimes means that Y cannot be used as a reference element. More importantly, the ionisation of the $^{194}(Y_2O^+)$ molecule in high–U xenotime appears to decrease with increasing U content. Therefore, although time consuming, WDS analysis is the preferred method to determine elemental concentrations in xenotime.

The Pb/U—Pb/Th ME corrections developed by Fletcher et al. (2004) were determined from four samples (Z6413, Z6412, BS1 and XTC) calibrated against MG1 in one SHRIMP analytical session. The results from this study suggest that BS1 and Z6413 are adequate secondary standards for measuring xenotime U and $\sum REE$ Pb/U—Pb/Th ME. Additionally, the Pb/U—Pb/Th ME corrections determined by Fletcher et al. (2004) were assumed to be reasonably consistent between analytical sessions and instruments. The U, Th and $\sum REE$ Pb/U—Pb/Th ME corrections determined by Fletcher et al. (2004) have subsequently been used in a number of SHRIMP xenotime application studies, which for the most part report concordant

$^{206}Pb/^{238}U$ and $^{207}Pb/^{206}Pb$ xenotime analyses (e.g., Vallini et al. 2005; Kositcin et al. 2003; Salier et al. 2004; Pigois et al. 2003 and; Vallini et al. 2006). However, these application studies have all been carried out on hydrothermal and diagenetic xenotimes where the U concentrations are typically within the 100's of ppm rather than in weight percent proportions. Therefore the dominant U–related $^{206}Pb/^{238}U$ ME correction is minor, meaning that fluctuations in the real U, Th and $\sum REE$ $^{206}Pb/^{238}U$ ME have gone unnoticed. In comparison, the results of this study clearly demonstrate that the Pb/U—Pb/Th ME caused by U and $\sum REE$ change from session to session, and indicate that for the best results, the Pb/U—Pb/Th ME should be determined for each analytical session. This is particularly the case for high U and $\sum REE$ xenotimes where the Pb/U—Pb/Th ME will be significant. This requirement, although cumbersome, requires that at least three standards need to be analysed for each analytical SHRIMP session; a primary calibration standard and at least two secondary standards of contrasting U and REE content.

The primary calibration standard should be as much as possible chemically homogenous in U and $\sum REE$, ensuring minimal internal chemically induced Pb/U—Pb/Th ME. A single crystal standard therefore is most likely the best candidate for this role. The secondary standards must differ in composition from the primary calibration standard, and therefore expose the Pb/U—Pb/Th ME. It is not necessary for the secondary standards to be chemically homogenous, however they must have concordant U–Pb/Th–Pb compositions. For the analytical sessions carried out during this study, the chemical homogeneity of MG1 made it an excellent choice as the primary calibration standard. The high and variable U content of Z6413 (U ~0.5–1.5 wt%) made it a good monitor of the SHRIMP xenotime U–related Pb/U—Pb/Th ME, whereas BS1 being characterised by low U (~0.3–0.5 wt%) and high $\sum REE$ (~19 wt%), rendered this sample a monitor of the $\sum REE$–related Pb/U—Pb/Th ME.

3.6.2   Origins/causes of SHRIMP xenotime Pb/U—Pb/Th ME

The relative correction factors for U and $\sum REE$ shown in Table 3.11 for nine separate SHRIMP sessions, although internally variable, show a consistent pattern. For both the $^{206}Pb/^{238}U$ and $^{208}Pb/^{232}Th$ results, U is the dominant cause of ME, whereas $\sum REE$

plays a subordinate role. For both the $^{206}Pb/^{238}U$ and $^{208}Pb/^{232}Th$ data, the relative correction factors for U and $\sum$REE appear to be reasonably consistent across the different instruments and operating conditions. For example, the relative correction factors for the SHRIMP II session, SHII-6, are typical for the entire data set, even though this session was run under very different instrumental conditions compared to the eight other SHRIMP RG sessions. Even the energy filtering of ~90 % of the secondary ion beam during this session failed to reduce the $^{206}Pb/^{238}U$ ME, or to shift the U and $\sum$REE relative correction factors significantly towards those determined for the SHRIMP RG sessions. The inference from this observation and the general consistency of the relative U and $\sum$REE correction factors is that xenotime Pb/U—Pb/Th ME are probably caused at the site of sputtering and ionisation, which is consistent with a suggestion made by Williams (1998) concerning SIMS ME.

The consistency of the relative correction factors for U and $\sum$REE observed between different instruments and operating conditions used in this study is probably a function of the identical primary column and secondary ion extraction configuration used in both instruments. Therefore, xenotime U and $\sum$REE related Pb/U—Pb/Th ME can be expected to behave similarly between different SHRIMP II and SHRIMP RG instruments. Generally, it is expected that the average relative correction factors for U and $\sum$REE in Table 3.11 will broadly apply between different instruments. However, a tenet of this study has been that the U and $\sum$REE related xenotime Pb/U—Pb/Th ME should be determined and corrected for each analytical session in the same manner as the $^{206}Pb/^{238}U$ calibration is routinely established for each SHRIMP U—Pb session.

A number of lines of evidence suggest that it is the relative ionisation of the Pb^{+} ion between xenotimes with contrasting U and $\sum$REE concentrations that results in the Pb/U—Pb/Th ME. Strong support for this is given in section 3.3.6 where it was demonstrated that the Th/U correction factor is unaffected by matrix contrasts. If it is relative ionisation of the UO_x^{+} and/or ThO^{+} molecules which results in xenotime Pb/U—Pb/Th ME, then the Th/U calibration factors for these three minerals would be significantly different. However, a relative increase or decrease in the ionisation of the Pb^{+} isotopes does not result in any noticeable isotopic ME as ions of all Pb isotopes

are equally effected. The relative change in the ionisation of the Pb^+ ions has no noticeable effect on the $^{207}Pb/^{206}Pb$ ratios.

Further evidence suggesting that it is the ionisation of the Pb^+ ion that is affected by U and $\sum$REE concentrations in xenotime is the remarkable respective similarity in the uncorrected $^{206}Pb/^{238}U$ and $^{208}Pb/^{232}Th$ ages of Z6413, BS1, NY/PK 6-80 and D43764. The concordance between independently calculated $^{206}Pb/^{238}U$ and $^{208}Pb/^{232}Th$ is striking. It appears that for each of the above samples, both the $^{248}(ThO^+)$ and $^{270}(UO_2^+)$ ions would have to be fractionated to almost exactly the same extent.

3.6.3   Matrix effects in xenotime, zircon and monazite

The chemically-induced xenotime Pb/U—Pb/Th SHRIMP fractionations of up to ~25% observed in this study exceed the Pb/U ME that have been reported for monazite and zircon, which range between ~1 and ~5% (see 3.1.5 introduction). The magnitude of the Pb/U—Pb/Th fractionations in xenotime is directly related to the high U concentrations often associated with this mineral. Xenotime U concentrations measured from samples used in this study range from ~0.04 to 2 wt%, whereas the range reported in the literature is from <0.01 to ~9 wt%. Additionally, U concentrations can differ significantly within a single crystal and also within a crystal population. For example, fragments from the single crystal standard Z6413 have a U range of ~ 1 wt%, whereas in NY/PK 6-80 U concentrations were found to differ by ~1.5 wt%. The internal range of U concentration in Z6413 alone will result, on average, in a ~11.89 % range in measured SHRIMP $^{206}Pb/^{238}U$ ratios. By contrast, the U concentrations in zircon and monazite are considerably lower. For monazite, U concentrations rarely exceed 0.5 wt% (Overstreet 1967) and are more commonly <1000 ppm, whereas for zircon, U concentrations are typically <1500 ppm. Therefore, U–induced SHRIMP Pb/U—Pb/Th ME fractionations are less likely and generally will be minor in monazite and zircon, compared to xenotime.

The role of the REE's in SHRIMP Pb/U—Pb/Th fractionation is less straightforward. Monazites typically have $\sum$REE concentrations of between ~35 to 55 wt%. The dominant component is the LREE, in particular La, Ce and Nd. For the few studies

that have recognised SHRIMP Pb/U—Pb/Th matrix effects in this mineral, the causal element was thought to be U and/or Th (Rasmussen & Fletcher 2002; Stern & Berman 2000), REE were not considered.

Like xenotime, zircon is typically enriched in the HREE, with the total concentration rarely exceeding 0.5 wt% (from Table 1 in: Hoskin & Schaltegger, 2003). For zircon, only one study has examined a possible link between $^{206}Pb/^{238}U$ matrix effects and REE concentrations. This study, by Black et al. (2004), suggested that $^{206}Pb/^{238}U$ matrix effects of ~1 % were caused by matrix mismatches in the trace elements Y, P and REE between the calibration standard and unknown. An interesting finding of this research was that the zircons with the highest concentration of trace elements had reduced not elevated $^{206}Pb/^{238}U$ ratios. However, for xenotime, where the $\sum$REE concentration typically ranges between ~13 and 22 wt% (dominated by the HREE, Gd, Dy, Er and Yb), it is the crystals with the higher HREE concentrations which have elevated Pb/U—Pb/Th ratios. The results of this study suggest that, on average, a 1 wt% increase in the $\sum$REE between the calibration standard and unknown results in a $^{206}Pb/^{238}U$ increase of ~0.9 %.

Although the $\sum$REE concentrations in monazite typically exceed those in xenotime by a factor of two, only in xenotime has a REE-related Pb/U—Pb/Th matrix effect been noted in both this study and that of Fletcher et al. (2004). The reasons for this are probably related to the structural and elemental contrasts between these two minerals. Namely, for xenotime the tetragonal symmetry, and the incorporation of the smaller, heavier HREE, may result in differing sputtering and ionisation characteristics between these two minerals. The end result of this is a HREE–induced Pb/U—Pb/Th matrix effect when HREE mismatches occur between the calibration standard and unknown. The very low REE concentrations in zircon mean that the HREE–induced Pb/U—Pb/Th matrix effect in this mineral is probably mostly insignificant.

3.6.4   Future SHRIMP xenotime Pb/U—Pb/Th studies

An accurate knowledge of xenotime composition is crucial when correcting for the significant Pb/U—Pb/Th ME associated with SHRIMP xenotime analysis. However, two factors complicate any SIMS-based elemental quantification of xenotime. Firstly

there is no element in xenotime with a relatively consistent concentration that can be used as a reference to normalise SIMS-based estimates of the concentrations of other elements. Also it appears that xenotime chemical matrix contrasts which influence the ionisation and emission of the Pb^+ ions, also affect the ionisation of Y and some REE. This was demonstrated by the strong positive correlations between SHRIMP xenotime $^{206}Pb^+/^{270}(UO_2^+)$ and $^{208}Pb^+$ $/^{232}ThO^+$ ratios with $^{190}(YbO^+)/^{194}(Y_2O^+)$, $^{177}(DyO^+)/^{194}(Y_2O^+)$ ratios (section 3.4.4). These limitations of the SIMS elemental quantification of xenotime supports xenotime elemental quantification by WDS or WDS-assisted procedures such as via relative sensitivity factors (RSF) as explained in section 3.3.5.

WDS results from this study show that $\sum$REE concentrations can be accurately estimated from the four major REE constituents of xenotime (Gd, Dy, Er and Yb). Figure 3.32 demonstrates the excellent correlation between Gd + Dy + Er + Yb and $\sum$REE in xenotime for igneous, metamorphic, diagenetic and hydrothermal xenotime analysed in this study. The $\sum$GdDyErYb concentrations for the xenotime plotted in Fig. 3.32 are accurate to within a range of $\pm$ 3 % of their $\sum$REE concentrations and hence can serve as an excellent proxy. Therefore, the WDS REE quantification for xenotime necessary to carry out SHRIMP $^{206}Pb/^{238}U$ matrix corrections could be reduced to analysing Gd, Dy, Er and Yb. Additionally, it is recommended that Ho is also analysed by WDS to serve as a reference for the determination of xenotime U concentration via $RSF_{(U-Ho)}$ (section 3.3.5).
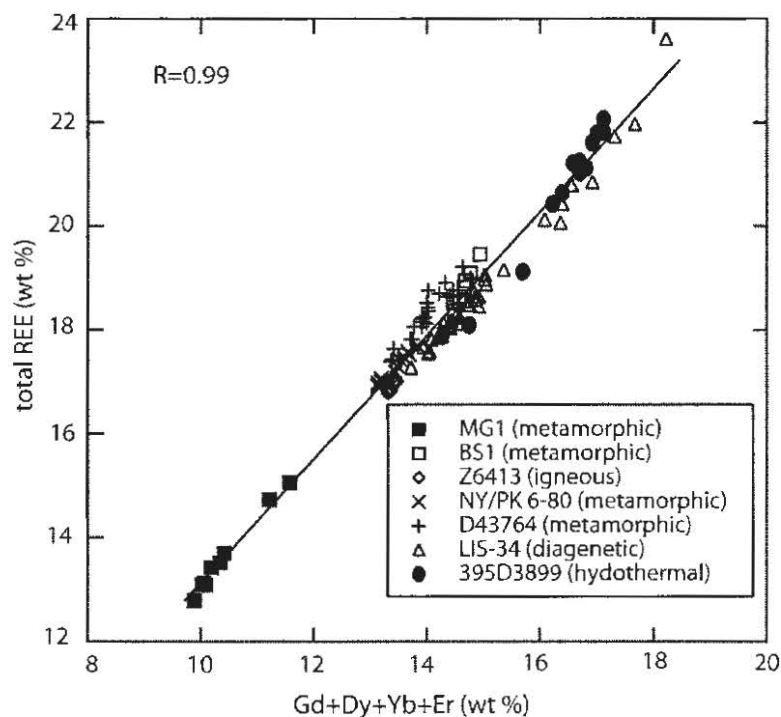
Fig. 3.32. Plot showing the excellent correlation (R=0.99) between the xenotime $\sum$REE concentration (Nd, Sm, Eu, Gd, Tb, Dy, Ho, Er, Tm, Yb, Lu) and $\sum$Gd, Dy, Er, Yb, for the different types of xenotime analysed in this study.

3.7 Conclusions

The wide range in chemical composition of xenotime, particularly in Y, $\sum$REE and U, results in significant difficulties for SIMS analysis for both the determination of $^{206}Pb/^{238}U$ ratios and quantitative elemental analysis.

For SHRIMP U—Pb xenotime analysis, chemical contrasts in U, and to a lesser extent $\sum$REE, between the primary calibration standard and unknown can result in Pb/U—Pb/Th ME of up to ~25%. It appears that for xenotime, it is the secondary emission of the Pb$^+$ ions that causes the Pb/U—Pb/Th ME. Therefore, the emission and transmission of the Pb$^+$ ions during SHRIMP analysis is not only a function of the Pb concentration in the target, but also the concentration of U and $\sum$REE. Additionally, the ionisation and emission of Y, Yb and Dy also appears to be affected by the xenotime matrix. To correct for the SHRIMP $^{206}Pb/^{238}U$ xenotime matrix effects, a detailed knowledge of the chemistry of the xenotime standards and unknowns at each analytical spot is required. For this task, WDS analysis is

128

recommended. In addition, accurate U abundance estimates can be determined using $RSF_{(U-Ho)}$.

The SHRIMP Pb/U—Pb/Th matrix correction technique developed here requires the concurrent analysis of three xenotime standards of variable U and ΣREE concentration on a session-by-session basis. The Pb/U—Pb/Th ME is monitored by the analysis of two secondary standards. During this study, a high ΣREE xenotime (BS1) and a high U xenotime (Z6413) proved to be adequate monitors of the Pb/U—Pb/Th ME. The Pb/U—Pb/Th ME is corrected for by a series of simultaneous linear equations that relate the fractional Pb/U—Pb/Th ME of the secondary standards to their U and ΣREE concentration contrasts with the primary calibration standard according to the equation:

$$f\,^{206}Pb/^{238}U\,ME = (\Delta U * x) + (\Delta\Sigma REE * y)$$

Where ΔU and $\Delta\Sigma REE$ represent the difference in elemental concentration of each analysis with the primary calibration standard, and x and y are the unknown parameters or correction coefficients that are determined using a simple least squares routine (see Appendix 3.6). An underlying assumption of this technique is that the SHRIMP xenotime Pb/U—Pb/Th ME is linear.

A number of SHRIMP xenotime analytical procedures and $^{206}Pb/^{238}U$ processing protocols were also determined. During some sessions, significant contrasts in lnPb/U : lnUO/U gradients between the different reference xenotimes, forced the calculation of the raw $^{206}Pb/^{238}U$ ratios from the raw $^{206}Pb^+/^{270}(UO_2^+)$ ratios, which proved to be a robust method for SHRIMP xenotime $^{206}Pb/^{238}U$ calibration. Similarly, raw $^{208}Pb^+/^{232}Th^{16}O^+$ ratios were used to calibrate independent $^{208}Pb/^{232}Th$ xenotime ages. However, this method was only found to be effective for xenotime with Th concentrations greater than ~1000 ppm. The SHRIMP RG is also recommended as the most suitable for SHRIMP U—Pb xenotime analysis as there are no detectable molecular interferences or 'scattered ions' associated with the ^{204}Pb peak. The presence of scattered ions associated with the ^{204}Pb peak renders the ^{204}Pb common Pb correction unusable. Although the scattered ions can be removed by energy

filtering or by the insertion of the retardation lens, both of these techniques result in a loss of sensitivity. This is a significant consideration as the SHRIMP analysis of tiny (~5-10 μm) xenotime crystals demands SHRIMP spot diameters of between ~5-7 μm, which therefore results in significantly reduced primary and secondary ion currents. Furthermore, the adoption of an O^- rather than O_2^- primary beam (typically used for SHRIMP U—Pb zircon analysis) when analysing xenotime with a small ~5-8μm SHRIMP spot, increased the precision of individual analyses.

The optimal data acquisition sequence for SHRIMP U—Pb-Th analysis should comprise $^{181}(HoO^+)$, $^{194}(Y_2O^+)$, ^{204}Pb, BG, $^{206}Pb^+$, $^{207}Pb^+$, $^{208}Pb^+$, $^{238}U^+$, $^{248}(ThO^+)$, $^{254}(UO^+)$ and $^{270}(UO_2^+)$ (BG=background measured at +0.04 mass units away from the ^{204}Pb peak). The $^{181}(HoO^+)$ and $^{270}(UO_2^+)$ molecules can be used as an alternative to WDS analysis for the calculation of U and Th abundances. Furthermore, the addition of the $^{270}(UO_2^+)$ molecule can be used as an alternative means to calibrate SHRIMP $^{206}Pb/^{238}U$ ratios. The various analytical sessions conducted in this study demonstrate that SHRIMP Th/U calibration factor can vary by a few percent between sessions, and therefore, like the Pb/U—Pb/Th matrix corrections, should be determined for each session.

The SHRIMP xenotime Pb/U—Pb/Th matrix correction technique developed here is broadly similar to that proposed by Fletcher et al. (2004). Both the technique determined in this study and that of Fletcher et al. (2004) relate the SHRIMP Pb/U—Pb/Th ME to chemical contrasts between the $^{206}Pb/^{238}U$ calibration standard and 'unknown' xenotime. Additionally, both techniques assume that the Pb/U—Pb/Th ME effect is linear and can be modeled by a series of simultaneous equations whose solutions can be found using a simple least squares method. Whereas Fletcher et al. (2004) related SHRIMP xenotime Pb/U—Pb/Th ME to contrasts in U, Th, and ΣREE, this study indicates that the effect Th has on the Pb/U—Pb/Th ME is insignificant and that only U and ΣREE play an important role in SHRIMP xenotime Pb/U—Pb/Th matrix effects. However, Fletcher et al. (2004) suggested their Pb/U—Pb/Th matrix correction factors could apply to all SHRIMP U—Pb dating experiments. This study has shown the need to determine SHRIMP xenotime Pb/U—Pb/Th matrix correction factors on a session-by-session basis. Slight differences in instrumental conditions between analytical sessions are likely to be responsible for this. Having to determine

Pb/U—Pb/Th matrix correction factors for each SHRIMP U—Pb dating experiment necessarily requires that all standards and unknown xenotimes be analysed by WDS prior to the SHRIMP U—Pb dating experiment.

The results of this study show that the SHRIMP U—Pb xenotime analyses of Phanerozoic samples using the Pb/U—Pb/Th xenotime matrix correction technique developed here can be expected to result in $^{206}Pb/^{238}U$ and $^{208}Pb/^{232}Th$ analyses accurate to within approximately 2%.

4. THE TIMING OF METAMORPHISM, PROVENANCE AND DEPOSITIONAL CONSTRAINTS FOR THE SERRA DA MESA GROUP, CENTRAL BRAZIL: A SHRIMP U–Pb XENOTIME, MONAZITE AND ZIRCON STUDY.

4.1 Introduction

The Serra da Mesa Group is an extensive metasedimentary sequence located within the Neoproterozoic Brasília Fold Belt of the Tocantins Province, central Brazil. Very little is known about the timing of sediment deposition or metamorphism of this unit. Additionally, it does not appear to contain any felsic volcanics, and geological relationships with nearby units are either faulted or controversial. In order to gain a better understanding of the provenance and depositional history of this unit, a SHRIMP U–Pb detrital zircon study was carried out on a sample of quartzite by Dr. Richard Armstrong (Research School of Earth Sciences, ANU). During this study, Dr. Armstrong noticed that many of the zircon grains have xenotime outgrowths and suggested to me that I use the SHRIMP $^{206}Pb/^{238}U$ xenotime matrix correction procedures that I had recently developed to determine the age of the xenotime outgrowths. 1 accepted the project and on SEM examination of the zircons on the sample mount, noticed a population of discrete monazite grains. Therefore, SHRIMP U—Pb monazite analysis of this sample would provide the perfect opportunity for me to test the accuracy of the SHRIMP U—Pb xenotime matrix correction procedures that I had developed during my PhD study. Additionally, the U—Pb isotopic results for the zircon, monazite and xenotime from this sample may be able to help establish depositional constraints for this unit, as well as provide some information regarding its post depositional thermal history.

4.2 Regional Geology

The Tocantins province in central Brazil is a large Neoproterozoic Orogen that was formed by the collision of the Amazon, São Francisco and Paraná cratons, during the Neoproterozoic Brasiliano Orogeny resulting in the juxtaposition of Archaean, Proterozoic and Neoproterozoic terranes (Marini et al. 1984, as cited in Soares et al. 2006; Fuck et al. 1994, as cited in Soares et al. 2006; Pimentel et al. 2000). Three separate fold belts comprise the Tocantins Province. These are the Araguaia and Paraguay fold belts, located at the eastern limit of the Amazon Craton, and the Brasília Fold Belt at the western margin of the São Francisco Craton (Fig. 4.1).

Phanerozoic cover

Araguaia Belt

Folded supracrustal rocks

Basement

Brasília Belt

Golás Magmatic Arc

Volcano-sedimentary sequences

Orthogneiss

Goias Massif

Orthogneiss/greenstone Belts

Serra da Mesa Group

Layered complexes +
volcano-sedimentary sequences

Ⅰ Cana Brava

Ⅱ Niquelandia

Ⅲ Barra Alto

Metamorphic core

Granulite/orthogneiss
(Anápolis-Itaucu Complex)

External zone

Passive margin sequence

Araxá and Andrelândia groups

Rift sequence (Arai Group)

Orthogneiss / supracrustal belts

São Francisco Craton

Sedimentary cover (Bambuí Group)

Orthogneiss / greenstone belts

Faults

① Transbrasiliano Lineament

② Rio dos Bois Fault- Mandinópolis Shear Zone

③ Rio Maranhao Fault System

④ Paranã Fault

Fig. 4.1. Generalised geology map of the Tocantins Province, central Brazil. From east to west, the map shows the São Francisco Craton, the Brasília Belt (external zone, Goiás Massif, and Goiás magmatic arc) and Araguaia Belt. Inset shows location of study area (see Fig. 4.2). Location map shows the position of the Tocantins Province (d) and adjacent geological regions: a, Rio Branco; b, Tapajós; c, São Francisco Craton; e, Mantiqueira; f, Borborema; g, Parnaíba Basin; h, Amazon Basin; I, Paraná Basin. Regions a, b and h form the Amazon Craton (note the Paraná craton is now concealed under the Paraná Basin). Adapted from Soares et al. (2006).

4.2.1   The Brasília Fold Belt

The Brasília Fold Belt extends for over 1100 km in a N–S direction from western Minas Gerais, through Goiás to southern Tocantins. It principally consists of (1) a thick and extensive Palaeo– to Mesoproterozoic metasedimentary sequence along the western margin of the São Francisco Craton, termed the External zone by Soares et al. (2006); (2) a large Neoproterozoic (~900 to 630 Ma) juvenile magmatic arc in the west (Goiás Magmatic Arc); (3) exposed older Archaean greenstones and associated granite gneiss complexes as well as Palaeoproterozoic to Mesoproterozic metasedimentary units (Goiás Massif) and (4) the Neoproterozoic Anápolis–Itaucu Complex which is a NW–SE elongate region comprising granulites, granites and layered mafic–ultramafic intrusions (Fig. 4.1) (Moraes et al. 2006; Pimentel et al. 2006; Piuzana et al. 2003; Soares et al. 2006). Most of the geological contacts are thrust and reverse faults which indicate tectonic transport toward the east (Strieder & Nilson 1992, as cited in Dardenne 2000; Fuck et al. 1994, as cited in Soares et al. 2006).

The principal geological elements in the area surrounding the sample site include, (i) Palaeoproterozoic metasedimentary rocks of the Araí Group and associated volcanics and granitoids; (ii) ?Palaeo– to ?Mesoproterozoic metasedimentary rocks of the Serra da Mesa Group as well as the Mesoproterozoic Cana Brava layered mafic-ultramafic complex and its associated 'Palmeirópolis' volcano-sedimentary sequence (Goiás Massif) and; (iii) the Neoproterozoic Goiás Magmatic Arc.

4.2.2   Palaeoproterozoic metasedimentary rocks of the Araí Group

The Araí Group consists of a thick (1500m) sequence of pelitic and clastic metasedimentary rocks that outcrop over large areas of the Tocantins and Goiás States in central Brazil (Fig. 4.1). It unconformably overlies the Ticunzal Formation (>1.77

Ga) and ~2.27 to ~2.02 Ga, granitic–gneissic basement (Dardenne 2000; Pimentel et al. 1997). It is overlain by the late Proterozoic platform sedimentary rocks of the Paranoá and Bambuí Groups (Dardenne 2000) and is spatially associated with ~1.77 Ga A–type, anorogenic tin-bearing granites of the Rio Paranã Sub-province (RPS). The Araí Group consists of thick quartzite units associated with intraformational conglomeratic units and interlayered metasiltstones as well as felsic to mafic volcanics (Dardenne 2000). The evidence for alluvial fan and lacustrine environments suggests deposition in a continental setting (Pimentel et al. 1991a). The unit is well dated by an ID-TIMS U–Pb zircon age of 1771 ± 2 Ma from a rhyolite lava from the lower parts of the group (Pimentel et al. 1991a).

4.2.3   Goiás Massif

The Goiás Massif is exposed in the central part of the Brasília Fold Belt and comprises Archaean, Palaeoproterozoic and Mesoproterozoic rocks. Its western border is marked by the Rio dos Bois fault, which separates it from the Neoproterozoic rocks of the Goiás Magmatic Arc. The southern part of the massif is dominated by Archaean greenstone belts, whereas in the study area, Goiás Massif rocks are represented by the metasedimentary rocks of Serra da Mesa Group as well as the Cana Brava layered mafic-ultramafic complex and associated Palmeirópolis volcano-sedimentary sequence on its western margin (Fig. 4.2).

4.2.3.1   Serra da Mesa Group

The Serra da Mesa Group consists of an extensive and thick (~1850m) sequence of folded and deformed metasedimentary rocks dominated by quartzite and mica schist (Dardenne 2000). The presence of garnet, staurolite and kyanite within micaceous and fine–grained quartzite beds implies that it has undergone amphibolite facies metamorphism (Dardenne 2000). Serra da Mesa Group rocks unconformably overlie ~2.20 Ga orthogneisses of the Goiás Massif (Pimentel et al. 1997) and is spatially associated with ~1.61 to 1.57 Ga, Mesoproterozoic A–type, anorogenic tin-bearing granitoids of the Rio Tocantins Sub-province (RTS) (Fig. 4.2). It is intruded by the 1.50 Ga Peixe Alkaline Complex (Kitajima et al. 2001) which is a N-S orientated elongate body approximately 30 by 7 km, located ~60 km north of the sample site. The Groups western margins are bounded by the Rio dos Bios Fault separating it from

Goiás Arc rocks, and to the east of the sample site, it is in faulted contact with the Araí Group and the Mesproterozoic Palmeirópolis volcano-sedimentary sequence (Fig. 4.2).

LEGEND

Neoproterozoic granite		Serra do Encosto Granite	
Goiás Magmatic Arc, supracrustal rocks		Serra Dourada Granite	
Goiás Magmatic Arc, orthogneiss		Serra da Mesa Granite	
Cana Brava layered complex		Serra da Mesa Group, quartzite	
Palmeirópolis sequence, felsic volcanics		Serra da Mesa Group, biotite gneiss	
Palmeirópolis sequence, metasedimentary rocks		Serra da Mesa Group, mica schist	
Palaeoproterozoic Basement			

Fig. 4.2. Solid geology map of the Serra Dourada region, showing the LIS-34 sample location site.

4.2.3.2   Mesoproterozoic layered mafic-ultramafic complexes

To the east of the sample site are the rocks of the Palmeirópolis volcano-sedimentary sequence and associated Cana Brava layered mafic ultra-mafic complex (Fig. 4.2). These rocks are related to two other layered mafic ultra-mafic complexes and their associated volcano-sedimentary sequences to the south, the Niquelândia and Barra Alto layered mafic-ultramafic complexes. Although now separated, they form a ~350

137

km long, roughly linear belt which was originally part of the same unit (Ferreira Filho 1998). It is generally accepted that the Cana Brava, Niquelândia and Barro Alto complexes are coeval with their associated volcano-sedimentary sequences and were formed during a Mesoproterozoic rifting event between about ~1.36 and ~1.26 Ga (Pimentel et al. 2004; Pimentel et al. 2006; Moraes et al. 2006).

4.2.4   Goiás Magmatic Arc

Approximately 10 km to the west of the sample site is the NE-SW trending Rio dos Bois Fault, which separates the Serra da Mesa Group from rocks of the Goiás Magmatic Arc (Fig. 4.1). The metavolcano-sedimentary and plutonic rocks of the Goiás Magmatic arc are separated by Archaean rocks of the Goiás Massif into the northern Mara Rosa and the southern Arenópolis . The rocks of the Goiás Magmatic are generally juvenile and consist of meta-igneous and metasedimentary rocks that have geochemical and isotopic characteristics similar to those found in modern day island arcs and continental margins (Dardenne 2000; Pimentel et al. 2000 and Laux et al. 2005). The volcano-sedimentary sequences form linear belts with NNW and NNE orientations and are associated with calcic to calc-alkaline tonalite/granodiorite gneisses (Laux et al. 2005). Isotopic ages of rocks in the Goiás Magmatic Arc fall into two broad ranges, a ~890 to ~790 Ma period related to the early stages of arc development, and a later Brasiliano Orogeny between ~670 to ~630 Ma which was associated with widespread greenschist to amphibolite facies metamorphism, deformation and magmatism throughout the arc (Pimentel et al. 2000).

4.2.5   Tectonic Evolution

Present knowledge of this region of the Tocantins province suggests that continental rifting of ~2.2 to ~2.0 Ga granitic to gneissic basement at about ~1.77 Ga was associated with the deposition of the Araí Group, contemporaneous bimodal volcanism and intrusion of the anorogenic RPS granitoids (Dardenne 2000). A later second period of rifting during the Mesoproterozoic was associated with the intrusion of the ~1.61 to 1.57 Ga RTS granitoids, the Peixe Alkaline Complex and the layered mafic ultramafic complexes of the Goiás Massif. During the early Neoproterozoic at about ~890 Ma, subduction of an ocean basin separating the Saõ Francisco, Paraná and Amazon cratons led to the development of the Goiás Magmatic Arc (Pimentel et al. 2000). Evolution of the arc is thought to consist of an early ~890 to 850 Ma stage

of development, followed by a ~790 Ma period of magmatism and metamorphism interpreted to have resulted from an early Brasiliano collisional event between the São Francisco craton and the now concealed Paraná craton (Pimentel et al. 2000; Dardenne 2000). Closure of the ocean basin is interpreted to have occurred during the ~670 to 630 Ma Brasiliano Orogeny when the Paraná/Saõ Francisco craton collided with the Amazon craton (Fuck et al. 1994, as cited in Soares et al. 2006; Dardenne 2000; Pimentel et al. 2000; Piuzana et al. 2003). Soon after or during the final stages of the Brasiliano Orogeny, post-orogenic, ~590 to ~560 Ma mafic to felsic plutonic rocks were emplaced into both the Mara Rosa and Arenópolis arcs (Pimentel et al. 2000). This period of crustal melting and post-orogenic bimodal magma generation, has been interpreted by Pimentel et al. (2000) and Soares et al. (2006) to have resulted from the emplacement and/or underplating of mafic magma into the crust and final arc amalgamation.

4.2.6 Current Age Controls for the Serra da Mesa Group

The timing of sedimentation for the Serra da Mesa Group is currently unknown. No intercalated volcanic units have been identified for isotopic dating however, an unpublished Sm–Nd analysis of a sample of Serra da Mesa Group quartzite has a model T_{DM} age of ~2.67 Ga, indicating an average late Archaean to early Proterozoic detrital component for this unit (pers. comm. Professor Reinhardt Fuck 2007; University of Brasilia). Furthermore, field relationships with the nearby ~1.61 to ~1.57 Ga, A–type anorogenic granitoids of the RTS are controversial For example, Macambira (1983, as cited in Pimentel 1991a) and Pimentel et al. (1991a) claim that field evidence supports an intrusive relationship, whereas Marini & Bothelo (1986, as cited in Dardenne 2000) and Dardenne (2000) argue against any field evidence suggestive of an intrusive relationship. Although a correlation with the Araí Group has been made by Marini et al. (1984, as cited in Soares et al. 2006) which if true would mean sedimentation of the group at about 1.77 Ga, this has not been proven.

The only robust age control for the Serra da Mesa Group is that provided by the Peixe Alkaline Complex which intrudes it. A nepheline syenite from this complex has an ID-TIMS U—Pb zircon upper intercept age of 1503 ± 3 Ma and a lower intercept of 577 ± 26 Ma. The upper intercept age can be used to constrain a minimum age estimate for Serra da Mesa Group. The lower intercept 577 ± 26 Ma age was

suggested by Kitajima et al. (2001) to be associated with metamorphism and deformation related to the late Brasiliano Orogeny.

4.3 LIS-34 sample description

A sample of quartzite from the Serra da Mesa Group (LIS-34) was collected from the Taboquinha Creek in the Serra Dourada area, northern Goiás State (UTM: 763663E, 8500572N; WGS84) by Professor Reinhardt Fuck (Fig. 4.2). Serra da Mesa Group rocks in this area dominantly consist of mica schist containing garnet, staurolite and kyanite indicating that these rocks have undergone amphibolite facies metamorphism. The quartzite unit where the sample was collected from is a few 10's of metres thick that also contains some lenses of conglomerate. It is surrounded by thick units of mica schist that in-turn, surround the Serra Dourada Granite (written communication, Professor Reinhardt Fuck). It is assumed that the quartzite unit sampled has experienced the same degree of metamorphism as the enclosing mica schists.

LIS-34 is a weakly foliated quartzite. It contains ~98–99% recrystallised quartz with ~1% muscovite. Accessory minerals include zircon, monazite, xenotime, tourmaline, rutile, ilmenite and magnetite. The muscovite is clear to colourless and sometimes altered to a brownish colour. In places the muscovite encloses the matrix quartz. It is the muscovite which defines the weak foliation associated with this sample, and is best observed in hand specimen. Monazite was observed to occur either as inclusions within the muscovite or along quartz grain boundaries (Fig. 4.3). Only a few zircon grains observed in thin section have xenotime outgrowths, which were typically < 5 μm thick. The few zircons observed in the thin section occur along quartz grain boundaries. The close association of monazite with muscovite in this sample suggests that the monazite probably crystallised contemporaneously with the muscovite during the amphibolite facies metamorphic event which has affected the rocks surrounding the sample site.
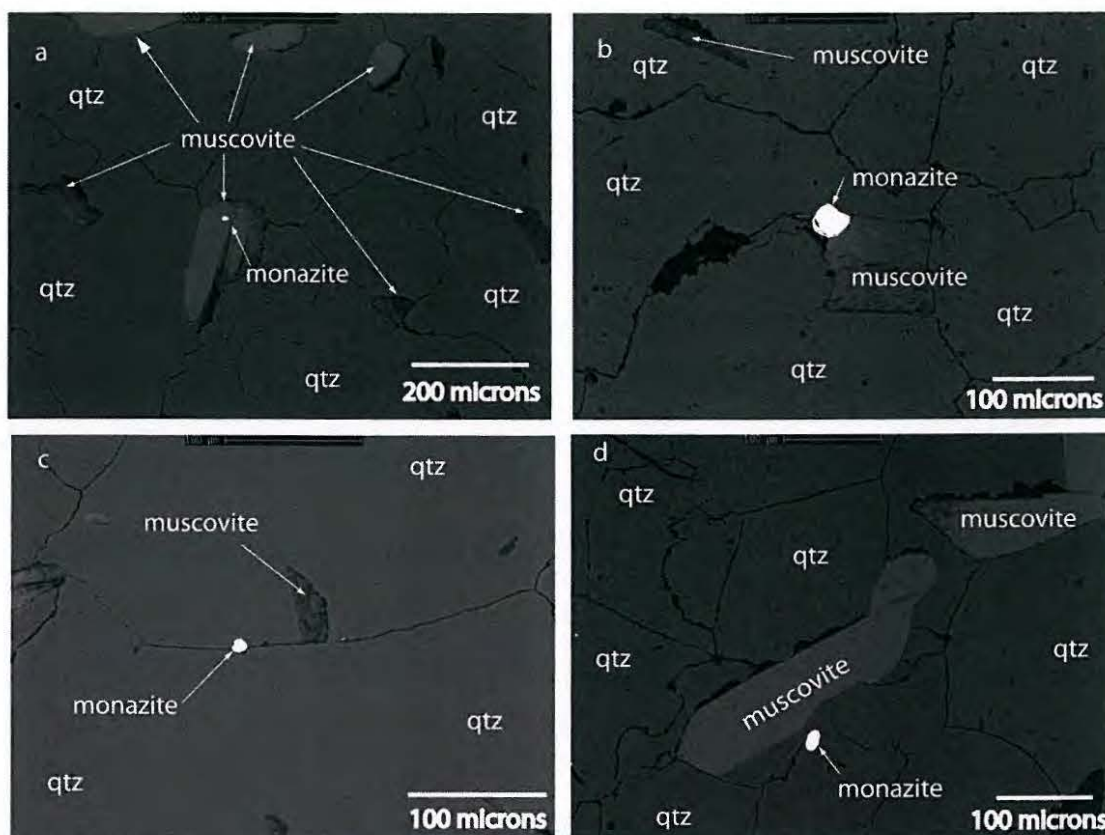
Fig. 4.3a-d. BSE images showing the textural setting of monazite from LIS-34. BSE images (a-b) are examples where monozite has precipitated within muscovite and (c-d) examples where monazite occurs along quartz grain boundaries.

4.4 Methods

4.4.1 Sample preparation

Sample crushing and heavy mineral separation were carried out at the Institute of Geosciences, University of Brasilia. This involved sample crushing followed by panning of the heavy mineral concentrate, which was then passed through 500, 300 and 100 micron sieves before magnetic separation. The heavy mineral concentrate, which comprised zircon (many with xenotime outgrowths), monazite, tourmaline and rutile, was sprinkled onto the mount surface to ensure an unbiased range of mineral grains and then polished to reveal the mineral interiors. Also mounted with the LIS-34 sample were the $^{206}Pb/^{238}U$ standards FC1 (zircon; 1099 Ma; Paces & Miller 1993), 44069 (monazite; 425 Ma; Aleinikoff et al. 2006), MG1 (xenotime; 490 Ma; Fletcher et al. 2004); BS1 (xenotime; 509 Ma; Fletcher et al. 2004) and Z6413 (xenotime; 994 Ma; Stern & Rayner 2003). Prior to analysis, all grains were photographed in transmitted and reflected light. Zircon was imaged by cathodoluminescence (CL), and

141

monazite and xenotime by back-scattered electron (BSE) imaging to choose the most pristine areas for electron probe and SHRIMP U—Pb analysis, and also to determine the presence of different age regions formed during different geological events. CL images were taken using a Hitachi S2250–N scanning electron microscope. BSE images were taken using a Cambridge S360 scanning electron microscope using a voltage of 15 kV, a current of ~2 nA and working distance of ~20 mm. Both the Hitachi S2250–N and Cambridge S360 are located at the Australian National University (ANU).

4.4.2 Electron probe

Electron microprobe wavelength dispersive spectrometry (WDS) analyses were undertaken on xenotime and monazite grains before SHRIMP U—Pb analysis using a Cameca SX100 located at the ANU. WDS characterisation of the chemical composition of each xenotime spot location to be analysed by SHRIMP is needed to correct the SHRIMP $^{206}Pb/^{238}U$ ratios for instrumental interelement fractionation (as described in Chapter 3). Additionally, WDS analyses of the 'unknown' xenotime were also used to determine compositional differences between the different xenotime growth zones. The xenotime Pb/U standards and xenotime outgrowths from the Serra da Mesa Group sample (LIS-34) were analysed for Y, P, Si, Ca, Nd, Sm, Eu, Gd, Tb, Dy, Ho, Er, Tm, Yb, Lu, Th, and U under the operating conditions described in Chapter 3 and Appendix 3.3.

WDS analyses were also undertaken on the monazite from LIS-34 and the Pb/U standard 44069. LIS–34 monazite WDS analyses were done in order to determine the compositional differences between different growth zones. WDS analyses on 44069 were carried out to compare the chemical composition of this mineral with the LIS–34 monazite, thereby assessing its suitability as a Pb/U calibration standard. Monazite grains were analysed for Si, Ca, P, Y, La, Ce, Pr, Nd, Sm, Eu, Gd, Dy, Th and U. Operating conditions included a 15 kV electron beam regulated at 100nA with a beam diameter of 10 μm. The REE were calibrated against synthetic REE phosphate standards and U oxide and Th oxide standards were used for U and Th calibration. Analyses were done with the analytical peaks recommended by Pyle et al. (2002). A correction was also applied to Dy (Lα) for a minor Eu (Lβ) interference as

recommended by Pyle et al. (2002). Final WDS results include matrix effect corrections using standard ZAF procedures. Appendix 4.1 shows the analytical settings used for the monazite WDS analysis as well as approximate detection limits and relative errors for the elements analysed.

4.4.3 SHRIMP

SHRIMP analyses were carried out using SHRIMP RG and SHRIMP II located at the ANU. Zircons were analysed using SHRIMP RG by Dr. Richard Armstrong. Analytical procedures followed the methodology described by Compston (1984), Williams and Claesson (1987) and Claoué–Long et al. (1995). The primary O_2^- beam had an intensity of ~4 nA, and was focussed through a 70 μm Kohler aperture which resulted in a spot diameter of ~10μm. The sputtered secondary ions were extracted into the mass spectrometer with a 10 kV potential and counted with a single electron multiplier. Each analysis represents six scans through the different mass stations and the Pb/U calibration standard was measured every fourth analysis. Calibration of the Pb/U ratios was by comparison to the zircon standard FC1 and used the power law relationship between $^{206}Pb^+/^{238}U^+$ and $^{254}UO^+/^{238}U^+$ (Claoué–Long et al. 1995). U abundances were calculated with reference to SL13 (238 ppm) and are subject to an uncertainty of at least ±20%, this being the range of U abundance within that reference material. Th/U ratios were calculated using the linear relationship $^{232}Th/^{238}U$ = $^{232}ThO^+/^{238}UO^+ * [0.03446(UO^+/U^+)+0.868]$. Data reduction was carried out using SQUID 1 and ISOPLOT 3 Microsoft Excel–based macros of Ludwig (2001; 2003).

Monazite analyses were carried out on SHRIMP II. Analytical procedures followed those described by Williams et al. (1996) and Rubatto et al. (2001). The primary O_2^- beam had an intensity of ~3.5 nA, and was focussed through a 120 μm Kohler aperture which resulted in a spot diameter of ~30 μm. Energy filtering of the low energy primary ions was used to remove an isobaric interference at mass 204 (Ireland et al. 1999). The monazite $^{254}UO^+$ count rate was reduced by ~60% by setting the energy window to remove the lowest energy ions. Each analysis represents six scans through the different mass stations and the Pb/U calibration standard was analysed every fourth analysis. Pb/U ratios were calibrated to the monazite standard 44069 and the power law relationship of $^{206}Pb^+/^{238}U$ and $^{238}UO^+/^{238}U^+$ (Claoué–Long et al. 1995).

Monazite U abundance determinations were based on 44069. A reference U concentration for 44069 was determined from sixteen WDS analyses which yielded an average U concentration of 3857 ± 630 ppm (2σ, SDOM; Standard Deviation of Mean; see Appendix 4.2). However, the relatively few WDS analyses used to determine this value render it as preliminary only. Furthermore, contrasts in Ce concentration between 44069 and the monazite rims of ~3 wt% Ce_2O_3, will result in commensurate contrasts in the secondary ion intensity of the $^{140}CePO_2^+$ signal, which is used as a reference species for U abundance determinations. With the above in mind, the SHRIMP-based U determinations reported here for the LIS-34 monazite could be in error by up to 50% of their true value. Data reduction for the SHRIMP U–Pb monazite analyses was carried out using PRAWN 6.55 and LEAD 6.55.

Xenotime was dated using SHRIMP RG in three separate sessions using the analytical procedures and Pb/U matrix correction techniques described in Chapter 3. For these analytical sessions, the primary O⁻ beam ranged between ~0.8–1 nA, was focussed through a 30 μm Kohler aperture which gave a spot diameter that ranged between ~6 to ~8 μm. Each analysis represents six scans through the different mass stations. The primary calibration standard (MG1) was analysed one in every four analyses, whereas the secondary standards (Z6413 and BS1) one in every eight. Th/U ratios for all monazite and xenotime SHRIMP analyses were corrected by a factor determined from the correlation between $^{232}ThO^+$ and $^{238}UO^+$ and radiogenic ^{208}Pb and ^{206}Pb and the known age of the Pb/U calibration standard, as described by Williams et al. (1996).

Ages were calculated using the constants recommended by the IUGS Sub commission on Geochronology (Steiger & Jäger 1977). Common Pb corrections for all zircon, monazite and xenotime analyses are based on individual measured ^{204}Pb abundances and assuming crustal common Pb of the same age as modelled by Stacey & Kramers (1975). Individual analyses are listed in tables and plotted on concordia diagrams as shaded ellipses at the 1σ level, unfilled ellipses represent compositions that are greater than 10% discordant. Final ages are quoted in the text with 95% confidence limits.

4.5 Results

4.5.1 Mineral description

4.5.1.1 Zircon

The zircon grains recovered from LIS-34 have a variety of sizes and shapes consistent with a derivation from a range of sources. All grains are rounded to subrounded and are variably pitted which is a surface texture typical of detrital zircon. Almost all of the grains (99%) have xenotime outgrowths which range from < 1 to ~60 μm in thickness. In some cases xenotime almost totally encloses the zircon crystal. The association of the pitted texture of the zircons in this sample overgrown by xenotime is strong evidence that the xenotime outgrowths grew on the zircon substrate in-situ.

4.5.1.2 Monazite

Most of monazite crystals recovered from LIS-34 have a generally amoeboid shape with embayed crystal margins. They range in size from ~40 to ~100 μm in diameter and are clear and colourless in transmitted light. Approximately 20% of the monazite grains have aspect ratios of between 1 and 3 and of these, ~5% have some well defined crystal faces. BSE images of the monazite shows that ~90% of the grains have a faintly visible core which progressively grades toward the margins of the crystals to a featureless zone with a stronger BSE response. Only a few crystals have a completely uniform BSE response, the intensity of which is similar to the outer margins of the crystals with cores (Fig. 4.4).
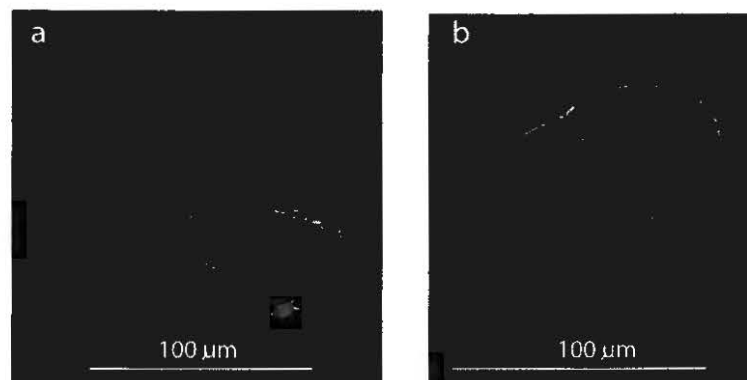
Fig. 4.4a-b. BSE image of monazite from LIS-34. Note the distinctive core of the monazite on the left hand side in (a), whereas the grain to the right, has a uniform BSE response. (b) An amoeboid shaped LIS-34 monazite, with a faint core.

4.5.1.3 Xenotime

Xenotime from LIS-34 occurs as <1 to 60 μm outgrowths on rounded to sub-rounded zircon. The large size of these outgrowths must have contributed to their survival through the crushing, mounting and polishing process. Two texturally distinct phases of xenotime growth are apparent and consist of an inner zone which is pitted, and in most places has a pyramidal outline and an outer, lobate xenotime outgrowth (Fig. 4.5). The two phases are often separated by a thin < ~1–4 μm, irregular zone which has a stronger BSE response compared to the inner and outer zones. The texturally oldest phase is the inner xenotime growth zone, which ranges in apparent thickness from < ~5–40 μm and is everywhere associated with an outer more massive, lobate zone. The outer xenotime zone typically has a uniform BSE response, is massive with a typically lobate shape and ranges in apparent thickness from ~1 to ~60 μm. Most of the xenotime outgrowths consist solely of the younger massive lobate generation, whereas ~30% of outgrowths consist of both generations. However, this may not be representative of the total proportion of xenotime outgrowths in the rock that contain both generations of outgrowth but rather a bias introduced during the crushing process.
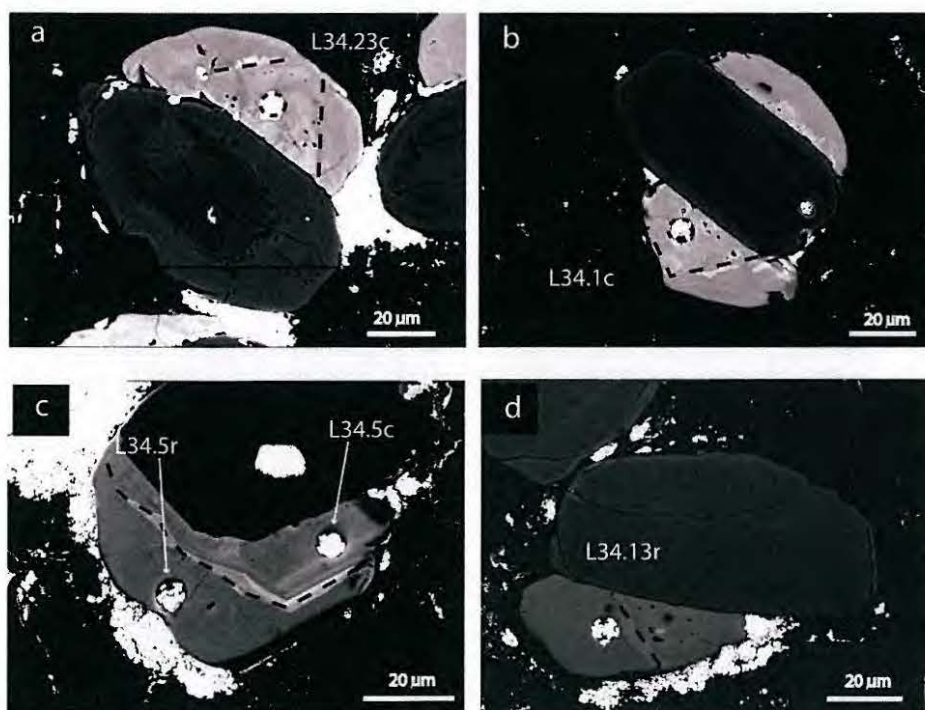
Fig. 4.5a-d. BSE images of xenotime outgrowths on sub-rounded to rounded zircon from LIS-34. All xenotime outgrowths shown have two separate growth zones, the boundary of which has been marked with a dashed line. Note the typically pitted texture of the inner zone xenotime and more uniform outer zone xenotime. Also shown is the location and sample number of the SHRIMP analytical pits. The brighter regions are caused by a residual Au coat.

4.5.2 Electron microprobe Results

4.5.2.1 Monazite chemistry

Electron microprobe analyses of the LIS-34 monazite show distinct differences between the cores and rims (Table 4.1). The cores have elevated concentrations of Nd, Sm and Eu relative to the rims, whereas the rims are generally enriched in La, Dy and Y. In addition, the cores have variable concentrations of La, Nd, Sm and Eu relative to the rims. Neodymium in the cores ranges from ~11 to ~21 wt% Nd_2O_3, whereas the rims have a more limited range of between ~10 and ~13 wt% Nd_2O_3. Similarly, La_2O_3 in the cores ranges from ~6 to ~15 wt%, whereas in the rims La concentrations range between ~12 and ~14 wt% La_2O_3. Figure 4.6 shows a plot of Nd verses La concentration for monazite cores and rims and demonstrates the heterogeneity of the cores relative to the rims. ThO_2 and U_2O_3 concentrations in the rims are ~2 wt% and ~0.1 to ~0.68 wt% respectively. For the cores ThO_2 concentrations are more variable than the rims and range from ~0.2 to ~3 wt%, whereas the rims range in U_2O_3 concentration between <0.02 to ~0.33 wt%.

The variable element concentrations of in particular La and Nd in the range of monazite cores indicate that they have probably crystallised from a range of different rocks and therefore are likely to represent detrital components of this rock. In contrast, the relatively homogenous composition of the rims suggests that they crystallised during a single event.

Table 4.1. Electron microprobe (WDS) analyses of monazite from LIS-34

LIS-34 monazite (core) WDS analyses

Label	m3.1c	m5.5.2	m5.5.3	m5.3.1b	m5.3.2	m5.3.3	m5.6.3	m6.1.2	m6.2.1	m12.1c	m12.3.1	m13.2.3	m13.2.4	m14.2	m14.3.2	m14.4.2
oxide wt%																
SiO2	0.03	0.09	0.04	0.07	0.10	0.03	0.01	0.03	0.01	0.05	0.02	0.07	0.11	0.12	0.02	0.07
CaO	0.95	0.45	0.72	0.74	0.89	0.95	0.80	0.76	0.48	0.75	0.79	0.36	0.55	0.52	1.42	0.66
P2O5	29.32	29.72	29.68	29.42	29.82	29.28	29.78	29.67	29.60	29.87	29.35	29.74	29.83	29.47	29.31	29.61
Y2O3	0.93	1.01	0.66	0.93	1.42	0.81	0.54	0.74	0.56	1.15	0.51	0.83	1.42	0.71	0.53	1.41
La2O3	8.59	13.60	9.74	7.73	12.45	5.89	8.49	13.20	13.99	13.96	6.91	14.60	13.53	11.47	7.12	10.28
Ce2O3	28.79	29.54	29.88	27.69	27.72	25.94	30.93	32.87	32.17	31.31	29.11	31.12	29.91	29.21	28.36	27.79
Pr2O3	4.94	3.99	4.77	4.93	3.90	5.10	5.07	4.22	4.08	3.97	5.27	3.84	3.98	4.27	4.76	4.24
Nd2O3	18.12	13.00	16.82	19.44	13.74	21.58	18.36	12.58	13.36	11.85	20.13	12.86	12.62	14.95	18.15	16.11
Sm2O3	2.98	2.17	2.68	3.62	2.71	4.44	2.82	1.52	1.86	1.65	3.31	1.90	1.95	2.38	2.87	3.07
Eu2O3	0.33	0.41	0.36	0.57	0.44	0.71	0.40	0.12	0.17	0.26	0.40	0.31	0.23	0.34	0.38	0.43
Gd2O3	1.28	1.62	1.19	1.42	1.37	1.67	0.92	0.81	0.83	0.99	1.04	1.35	1.59	1.41	0.95	1.65
Dy2O3	0.22	0.31	0.13	0.05	0.32	0.03	0.12	0.16	0.15	0.25	0.04	0.25	0.40	0.26	0.07	0.38
ThO2	0.69	1.65	1.29	1.15	3.11	0.66	0.20	0.62	0.19	1.61	0.07	1.28	1.59	1.96	2.81	1.49
U2O3	0.10	0.24	0.10	0.10	0.36	0.11	<0.02	0.15	0.05	0.27	<0.02	0.10	0.33	0.09	0.04	0.24
Total	97.45	97.95	98.18	98.01	98.58	97.38	98.56	97.64	97.67	98.14	97.08	98.86	98.29	97.39	96.91	97.68

LIS-34 monazite (rim) WDS analyses

Label	m3.1b	m5.1b	m5.1c	m5.4	m5.4c	m5.3.4	m5.3.5	m5.6.1	m5.6.2	m6.1.1	m6.2.2	m10.1b	m10.1c	m10.1d	m11.4.1
oxide wt%															
SiO2	0.07	0.06	0.14	0.12	0.09	0.08	0.06	0.20	0.14	0.13	0.06	0.09	0.15	0.13	0.45
CaO	0.61	0.61	0.49	0.78	0.75	0.84	0.84	0.50	0.69	0.64	0.74	0.69	0.71	0.69	1.11
P2O5	29.80	29.98	29.85	29.93	29.92	29.90	29.83	29.58	29.63	29.75	29.78	29.58	29.74	29.96	29.57
Y2O3	1.72	0.98	0.94	1.72	1.72	1.74	1.67	0.79	1.73	1.74	1.69	1.69	1.75	1.66	2.21
La2O3	13.31	13.82	12.73	13.77	14.04	13.38	13.67	13.73	13.23	12.89	12.83	13.35	12.81	12.79	12.56
Ce2O3	29.48	29.77	29.34	28.86	28.85	28.75	29.00	29.98	29.47	29.45	29.25	29.78	29.37	29.50	27.38
Pr2O3	4.03	3.98	4.10	3.68	3.81	3.72	3.66	3.83	3.97	3.99	3.86	3.80	3.83	3.79	3.09
Nd2O3	12.74	12.61	13.89	12.34	12.06	12.31	12.12	13.02	12.57	12.74	12.46	12.23	12.70	12.88	10.34
Sm2O3	2.05	2.04	2.13	1.94	1.94	2.06	2.14	2.09	2.00	2.10	2.01	1.94	2.07	2.04	1.71
Eu2O3	0.32	0.30	0.36	0.31	0.31	0.36	0.34	0.25	0.31	0.35	0.29	0.31	0.31	0.28	0.18
Gd2O3	1.70	1.60	1.72	1.18	1.29	1.33	1.26	1.36	1.41	1.30	1.37	1.43	1.50	1.52	1.65
Dy2O3	0.52	0.34	0.30	0.41	0.43	0.46	0.40	0.27	0.46	0.40	0.46	0.46	0.46	0.48	0.67
ThO2	1.53	1.94	2.23	2.56	2.31	2.65	2.62	2.51	2.10	2.06	2.24	1.79	2.32	2.20	6.19
U2O3	0.31	0.44	0.12	0.38	0.39	0.41	0.38	0.08	0.31	0.31	0.41	0.32	0.35	0.34	0.66
Total	98.52	98.69	98.61	98.38	98.22	98.22	98.31	98.38	98.27	98.05	97.68	97.72	98.41	98.61	98.10

LIS-34 monazite (rim) WDS analyses (cont.)

Label	m11.4.2	m12.1b	m12.3.2	m12.3.3	m12.4.1	m12.4.2	m13.1b	m13.1c	m13.2.1	m13.2.2	m14.1.1	m14.1.2	m14.1.3	m14.3.1	m14.4.1
oxide wt%															
SiO2	0.44	0.19	0.09	0.10	0.09	0.07	0.20	0.14	0.05	0.05	0.07	0.07	0.07	0.14	0.10
CaO	1.09	0.52	0.61	0.69	0.77	0.76	0.76	0.57	0.52	0.48	0.77	0.77	0.77	0.63	0.58
P2O5	29.57	29.37	29.53	29.61	29.71	29.50	29.65	29.85	29.77	29.70	29.44	29.62	29.45	29.41	29.37
Y2O3	2.21	0.69	0.95	1.64	1.66	1.70	1.70	1.70	1.24	0.95	1.73	1.76	1.73	1.75	1.65
La2O3	12.52	13.33	13.73	13.23	12.93	12.65	13.44	13.75	14.37	14.50	12.64	12.43	12.64	13.37	12.64
Ce2O3	27.75	29.77	29.90	29.45	28.96	28.67	30.77	31.08	30.48	30.54	28.82	28.65	28.75	29.57	29.13
Pr2O3	3.19	3.92	3.94	3.77	3.71	3.80	3.58	3.62	3.85	3.87	3.75	3.66	3.74	3.69	3.99
Nd2O3	10.23	13.08	12.38	12.45	12.27	12.31	10.64	10.86	12.35	12.36	12.81	12.43	12.64	12.06	13.08
Sm2O3	1.75	2.08	1.92	1.95	2.02	2.06	1.74	1.76	1.79	1.81	1.95	2.01	1.97	1.91	2.08
Eu2O3	0.18	0.40	0.15	0.19	0.32	0.34	0.26	0.35	0.26	0.22	0.33	0.37	0.31	0.21	0.25
Gd2O3	1.61	1.33	1.44	1.35	1.70	1.69	1.24	1.19	1.44	1.36	1.76	1.89	1.86	1.80	1.58
Dy2O3	0.71	0.21	0.41	0.44	0.45	0.54	0.37	0.40	0.38	0.34	0.54	0.51	0.57	0.57	0.55
ThO2	6.23	2.85	2.34	2.08	2.38	2.33	3.74	2.74	1.25	1.48	2.36	2.31	2.28	2.03	1.62
U2O3	0.68	0.09	0.36	0.33	0.37	0.37	0.43	0.38	0.36	0.30	0.44	0.42	0.40	0.33	0.40
Total	98.50	98.03	97.93	97.50	97.62	97.07	98.82	98.69	98.33	98.16	97.79	97.20	97.57	97.77	97.39
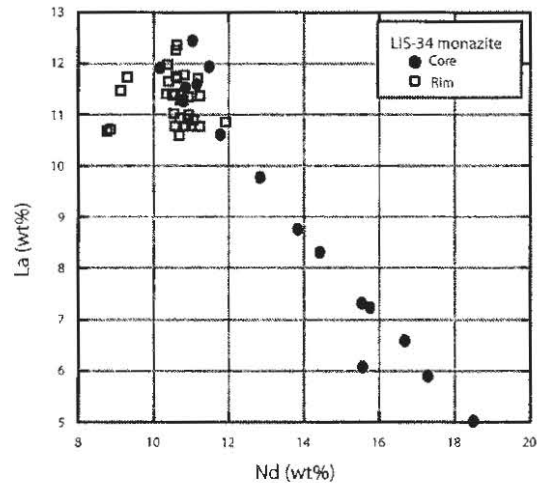
Fig. 4.6. Plot of electron microprobe (WDS) analyses of La and Nd concentrations in monazite cores and rims from LIS-34. The variation in La and Nd concentrations in the cores is interpreted to represent crystallisation from a range of different source rocks supporting a detrital origin.

4.5.2.2   *Xenotime chemistry*

Electron microprobe analyses of the LIS-34 xenotime outgrowths reveal a distinct contrast between the inner zones and the outer massive outgrowths. In general, the inner xenotime has elevated concentrations of MREE (Sm–Dy) and lower concentrations of HREE (Er–Lu) relative to the outer outgrowths (Table 4.2). This is seen in Figure 4.7, which compares the average chondrite normalised REE profiles for the inner and outer xenotime growth zones. For the MREE, (Eu_2O_3, Gd_2O_3, Tb_2O_3 and Dy_2O_3) concentrations of the inner zones are typically ~0.5 wt%, ~4.8 wt%, ~1.0 wt% and ~7.5 wt% respectively, whereas the outer growth zones have lower concentrations of ~0.27 wt%, ~2.7 wt%, ~0.6 wt% and ~6.0 wt% respectively. Conversely, the HREE (Er_2O_3 and Yb_2O_3) concentrations in the inner zones are typically ~3.5 wt% and ~2.2 wt% respectively, whereas the outer growth zones have concentrations of ~4.2 wt% and ~3.4 wt% respectively. Average U_2O_3 and ThO_2 concentrations for the inner zones are ~0.2 wt% and 0.3 wt% respectively, whereas the outer zones are ~0.3 wt% and 0.1 wt% respectively. This results in a distinctive contrast in Th/U ratio between the inner and outer xenotime outgrowths. The inner zones have Th/U ratios that are > 1 and range from 1 to 5, whereas in the outer xenotime outgrowths, Th/U ratios are more uniform and are typically ~0.30 or less (Table 4.3).

149

Table 4.2. Electron microprobe (WDS) analyses of xenotime from LIS-34

LIS-34 inner pyramidal xenotime outgrowth WDS analyses

oxide wt%	L34.5c	L34.7c	L34.23c	L34.56c	L34.50c	L34.38c	L34.47c	L34.46c	L34.1c	L34.29c	L34.34c	L34.48c	L34.30c	L34.66.1	L34.66.2	L34.66.3	L34.66.4	L34.66.5	L34.64.1	L34.64.2	Mean	95% conf.
SiO2	0.21	0.14	1.20	0.11	0.11	0.13	0.43	0.11	2.20	0.09	0.18	0.11	0.11	0.01	0.03	0.33	0.01	0.02	0.25	0.68	0.32	0.23
CaO	0.22	0.04	0.83	0.04	0.07	0.33	0.40	0.33	0.26	0.17	0.26	0.02	0.13	0.26	0.27	0.30	0.21	0.20	0.17	0.61	0.26	0.09
P2O5	34.26	34.55	32.72	34.81	34.53	34.08	34.40	34.16	33.69	33.02	33.96	34.74	33.73	33.21	36.03	33.66	33.62	33.99	34.17	32.52	33.99	0.35
Y2O3	38.49	40.37	37.48	41.25	38.80	37.89	39.34	38.26	37.10	36.20	38.45	40.99	39.35	37.93	40.35	39.33	36.62	36.63	38.80	38.64	38.61	0.63
Nd2O3	0.00	0.21	0.14	0.15	0.12	0.03	0.04	0.00	0.03	0.03	0.02	0.16	0.15	0.01	0.02	0.02	0.01	0.02	0.05	0.07	0.06	0.03
Sm2O3	0.25	0.43	0.59	0.37	0.62	0.50	0.26	0.44	0.42	0.65	0.30	0.33	0.34	0.50	0.57	0.35	0.77	0.68	0.60	0.48	0.47	0.06
Eu2O3	0.47	0.21	0.25	0.22	0.52	0.51	0.33	0.59	0.57	0.66	0.52	0.23	0.24	0.64	0.67	0.52	0.79	0.80	0.56	0.28	0.48	0.08
Gd2O3	4.08	3.25	3.16	2.73	5.50	5.08	4.00	5.39	5.17	6.44	4.72	2.33	2.25	5.70	6.32	4.92	7.91	7.97	5.40	3.57	4.79	0.72
Tb2O3	1.01	0.75	0.88	0.72	0.99	1.12	0.96	1.13	0.69	1.21	1.08	0.61	0.63	1.18	1.23	1.10	1.27	1.39	1.11	0.74	0.99	0.10
Dy2O3	7.50	6.58	7.44	6.30	6.57	7.74	7.33	8.02	8.09	7.73	7.64	6.16	5.85	8.25	8.30	7.87	8.14	8.23	7.88	7.61	7.46	0.33
Ho2O3	1.42	1.43	1.46	1.41	1.30	1.36	1.40	1.40	1.42	1.29	1.40	1.43	1.34	1.45	1.44	1.44	1.37	1.35	1.42	1.43	1.40	0.02
Er2O3	3.44	3.93	3.72	4.07	3.76	3.28	3.48	3.21	3.28	3.00	3.41	4.19	4.32	3.33	3.27	3.34	3.16	3.15	3.23	3.42	3.50	0.16
Tm2O3	0.58	0.67	0.65	0.71	0.69	0.56	0.56	0.55	0.57	0.54	0.57	0.72	0.79	0.58	0.59	0.56	0.60	0.59	0.58	0.60	0.61	0.03
Yb2O3	1.91	3.00	2.28	3.29	2.91	1.76	1.95	1.69	1.80	1.52	1.82	3.41	4.04	1.84	1.84	1.83	1.75	1.78	1.82	2.03	2.21	0.31
Lu2O3	0.74	0.96	0.82	1.00	0.92	0.70	0.75	0.70	0.73	0.68	0.76	1.00	1.05	0.75	0.73	0.73	0.73	0.72	0.71	0.75	0.80	0.05
ThO2	0.35	0.08	0.87	0.06	0.11	0.78	1.02	0.54	0.53	0.27	0.30	0.05	0.03	0.08	0.06	0.21	0.03	0.04	0.47	0.69	0.33	0.14
U2O3	0.10	0.38	0.42	0.30	0.27	0.14	0.15	0.10	0.11	0.15	0.08	0.27	0.45	0.03	0.03	0.07	0.02	0.02	0.16	0.30	0.18	0.06
ΣREE	21.40	21.42	21.39	20.98	23.91	22.65	21.05	23.12	22.77	23.73	22.25	20.56	20.99	24.24	24.97	22.67	26.49	26.68	23.36	20.97	22.78	0.79
Total	95.09	97.02	95.10	97.66	97.86	96.08	96.92	96.73	96.91	93.69	95.54	96.76	94.86	95.84	101.81	96.66	97.07	97.63	97.48	94.84	96.58	0.74

LIS-34 outer xenotime outgrowth WDS analyses

oxide wt%	L34.2r	L34.3r	L34.5r	L34.8r	L34.21r	L34.20r	L34.55r	L34.38r	L34.39r	L34.49r	L34.13r	L34.12r	L34.14r	L34.15r	L34.25r	L34.27r	L34.57r	L34.53r	L34.54r	L34.32r	Mean	95% conf.
SiO2	0.09	0.13	0.36	0.19	0.11	0.11	0.10	0.12	0.13	0.15	0.13	0.13	0.10	0.17	0.11	0.15	0.17	0.12	0.12	0.10	0.14	0.03
CaO	0.04	0.03	0.04	0.14	0.02	0.02	0.01	0.04	0.03	0.02	0.03	0.04	0.02	0.02	0.02	0.05	0.03	0.06	0.02	0.03	0.04	0.01
P2O5	34.25	33.80	32.83	34.32	34.54	33.98	34.64	34.08	33.84	34.83	33.29	34.37	34.15	33.50	32.98	34.07	34.36	33.88	33.77	33.08	33.93	0.24
Y2O3	40.35	39.98	34.23	39.80	41.45	40.57	41.96	39.74	40.36	41.26	39.33	41.23	40.45	40.09	39.43	40.90	41.25	40.27	40.32	39.57	40.13	0.68
Nd2O3	0.28	0.18	0.05	0.13	0.16	0.15	0.13	0.22	0.22	0.15	0.20	0.22	0.18	0.28	0.17	0.23	0.18	0.24	0.17	0.17	0.19	0.02
Sm2O3	0.43	0.34	1.32	0.37	0.35	0.35	0.34	0.38	0.40	0.41	0.34	0.44	0.37	0.37	0.33	0.41	0.37	0.46	0.36	0.35	0.42	0.09
Eu2O3	0.22	0.19	1.03	0.36	0.25	0.21	0.19	0.26	0.16	0.24	0.21	0.25	0.21	0.24	0.26	0.25	0.18	0.25	0.21	0.18	0.27	0.08
Gd2O3	2.41	1.80	7.63	3.73	2.32	1.93	2.35	3.02	1.64	2.36	1.89	3.47	2.27	2.27	2.09	2.30	1.87	3.29	2.34	2.10	2.65	0.57
Tb2O3	0.62	0.48	1.01	0.91	0.64	0.53	0.67	0.76	0.39	0.62	0.28	0.73	0.58	0.59	0.38	0.52	0.47	0.77	0.61	0.55	0.61	0.08
Dy2O3	6.19	5.50	6.54	6.77	6.22	5.70	6.44	6.51	5.09	6.36	5.47	6.54	5.98	5.97	5.72	5.55	5.28	6.50	6.00	5.88	6.01	0.21
Ho2O3	1.39	1.44	1.25	1.39	1.43	1.39	1.43	1.43	1.38	1.44	1.37	1.38	1.35	1.34	1.32	1.33	1.29	1.35	1.38	1.37	1.37	0.02
Er2O3	4.08	4.48	3.39	3.79	4.20	4.45	4.06	4.03	4.63	4.14	4.42	3.84	4.19	4.03	4.28	4.20	4.34	3.86	4.21	4.33	4.15	0.12
Tm2O3	0.72	0.81	0.67	0.63	0.73	0.77	0.67	0.71	0.87	0.69	0.80	0.67	0.72	0.67	0.72	0.75	0.76	0.67	0.73	0.77	0.73	0.03
Yb2O3	3.26	4.40	2.16	2.58	3.44	3.99	3.01	3.20	4.77	3.24	4.16	2.84	3.36	3.02	3.55	3.72	3.95	2.90	3.48	3.81	3.44	0.28
Lu2O3	0.98	1.20	0.75	0.83	1.07	1.11	0.95	1.02	1.27	1.00	1.14	0.96	1.14	0.95	1.13	1.11	1.15	0.97	1.08	1.12	1.05	0.05
ThO2	0.03	0.05	0.49	0.31	0.06	0.03	0.04	0.05	0.04	0.08	0.03	0.16	0.05	0.04	0.06	0.10	0.09	0.10	0.06	0.03	0.10	0.05
U2O3	0.27	0.41	0.05	0.25	0.22	0.23	0.18	0.34	0.41	0.30	0.39	0.29	0.25	0.44	0.20	0.35	0.50	0.30	0.25	0.27	0.30	0.04
ΣREE	20.59	20.81	25.81	21.50	20.79	20.59	20.24	21.56	20.81	20.64	20.29	21.35	20.35	19.73	19.95	20.37	19.85	21.27	20.57	20.64	20.89	0.56
Total	95.64	95.26	93.89	96.57	97.23	95.59	97.21	95.97	95.70	97.34	93.69	97.69	95.41	94.05	92.90	96.08	96.32	96.03	95.16	93.74	95.57	0.59

Table 4.3. SHRIMP U–P isotopic data for xenotime from LIS-34.

Spot name	U (wt%) (WDS)	ΣREE (wt%) (WDS)	Th/U (SHRIMP)	% Comm $^{206}Pb_c$	$^{206}Pb/^{238}U$ (± 1σ %)		$^{207}Pb/^{206}Pb$ (± 1σ %)		$^{207}Pb/^{206}Pb$ (Ma ± 1σ)		$^{206}Pb/^{238}U$ age (Ma ± 1σ)		Discordance %
outer xenotime outgrowth													
L34.13R	0.3532	17.74	0.28	0.22	0.0891	2.92	0.0597	3.58	593	78	550	16	8
L34.8R	0.2246	18.78	0.36	0.08	0.0892	2.44	0.0590	1.88	566	41	551	13	3
L34.12R	0.2647	18.65	0.28	0.11	0.0893	4.75	0.0589	6.53	564	142	551	26	2
L34.39R	0.3699	18.21	0.28	0.20	0.0916	2.48	0.0580	3.59	532	79	565	14	-6
L34.27R	0.3178	17.82	0.34	0.00	0.0921	2.33	0.0593	1.53	579	33	568	13	2
L34.54R	0.2315	17.98	0.28	0.09	0.0926	2.35	0.0588	1.55	558	34	571	13	-2
L34.55R	0.1666	17.69	0.21	0.10	0.0928	2.61	0.0583	2.73	541	60	572	15	-6
L34.14R	0.2295	17.79	0.17	0.11	0.0931	2.48	0.0577	1.96	520	43	574	14	-9
L34.57R	0.4542	17.36	0.3	0.08	0.0957	2.56	0.0609	3.11	634	67	589	15	8
L34.49R	0.2749	18.04	0.21	0.11	0.0959	3.28	0.0605	2.78	620	60	590	19	5
L34.32R	0.2427	18.04	0.13	0.15	0.0974	3.51	0.0586	2.64	552	58	599	21	-8
L34.3R	0.3716	18.20	0.13	0.04	0.0985	2.41	0.0603	2.47	613	53	605	15	1
inner pyramidal xenotime outgrowth													
L34.38C	0.1248	19.78	3.25	0.70	0.1351	2.79	0.0740	3.79	1042	76	817	23	28
L34.30C	0.4046	18.35	1.92	0.21	0.1419	3.00	0.0809	3.69	1219	73	856	26	42
L34.1C	0.1005	19.88	2.39	0.07	0.1462	2.42	0.0771	1.88	1124	37	879	21	28
L34.48C	0.2421	17.97	2.33	0.08	0.1587	2.83	0.0788	1.70	1167	34	949	27	23
L34.66.2B	0.0312	21.80	0.95	0.12	0.1665	3.52	0.0910	2.95	1447	56	993	35	46
L34.56C	0.2721	18.34	3.64	-0.03	0.1698	3.05	0.0863	2.24	1344	43	1011	31	33
L34.66.1	0.0312	21.17	2.46	0.78	0.1786	2.84	0.0797	3.15	1190	62	1059	30	12
L34.66.5	0.0204	23.30	2.67	-0.02	0.1901	2.77	0.0882	2.45	1386	47	1122	31	24
L34.64.1	0.1457	20.40	2.32	0.09	0.1966	2.52	0.0912	1.66	1452	32	1157	29	25
L34.66.3	0.0648	19.79	2.83	0.03	0.1993	3.19	0.0875	3.92	1371	76	1172	37	17
L34.46C	0.0906	20.17	3.46	0.06	0.1995	2.41	0.0826	1.55	1259	30	1173	28	7
L34.5C	0.0909	18.68	4.31	0.47	0.2008	3.11	0.0822	4.31	1250	84	1179	37	6
L34.50C	0.2466	20.89	4.62	0.26	0.2017	2.87	0.0839	2.76	1290	54	1184	34	9
L34.34C	0.0708	19.43	3.84	0.10	0.2065	2.76	0.0887	2.19	1397	42	1210	33	15
L34.7C	0.3434	18.71	5.43	0.13	0.2066	2.70	0.0891	2.75	1407	53	1211	33	16
L34.29C	0.1375	20.72	1.91	0.02	0.2073	2.53	0.0851	1.48	1318	29	1214	31	9
L34.47C	0.136	18.38	5.05	0.30	0.2123	2.53	0.0911	1.47	1449	28	1241	31	17
L34.66.4	0.021	23.13	2.51	-0.08	0.2133	3.06	0.0873	2.64	1366	51	1247	38	10
L34.64.2	0.2741	18.32	2.79	0.07	0.2143	2.51	0.0876	1.24	1375	24	1252	31	10
L34.66.2	0.0312	21.80	3.88	0.08	0.2145	2.44	0.0865	2.04	1349	39	1253	31	8
L34.23C	0.3847	18.69	2.49	0.02	0.2342	2.48	0.0918	1.01	1462	19	1356	34	8
outer xenotime outgrowth greater than 10% discordant													
L34.38R	0.306	18.84	0.33	0.93	0.0756	2.87	0.0506	7.45	225	172	470	13	-52
L34.21R	0.1985	18.17	0.40	0.06	0.0792	2.41	0.0600	2.28	603	49	491	12	23
L34.53R	0.2712	18.59	0.71	0.00	0.0899	2.66	0.0614	2.62	655	56	555	15	18
L34.15R	0.4022	17.24	0.24	0.01	0.0946	3.11	0.0574	3.25	507	71	583	18	-13
L34.25R	0.1838	17.44	0.10	0.11	0.0987	2.22	0.0582	1.17	536	26	607	13	-12
L34.5R	0.0471	22.57	0.67	0.41	0.0989	3.06	0.0582	3.38	536	74	608	19	-12
L34.20R	0.2112	18.00	0.19	0.22	0.0995	2.86	0.0582	2.22	537	49	611	17	-12
L34.2R	0.2447	18.00	0.48	0.26	0.1021	4.16	0.0587	4.06	557	88	627	26	-11
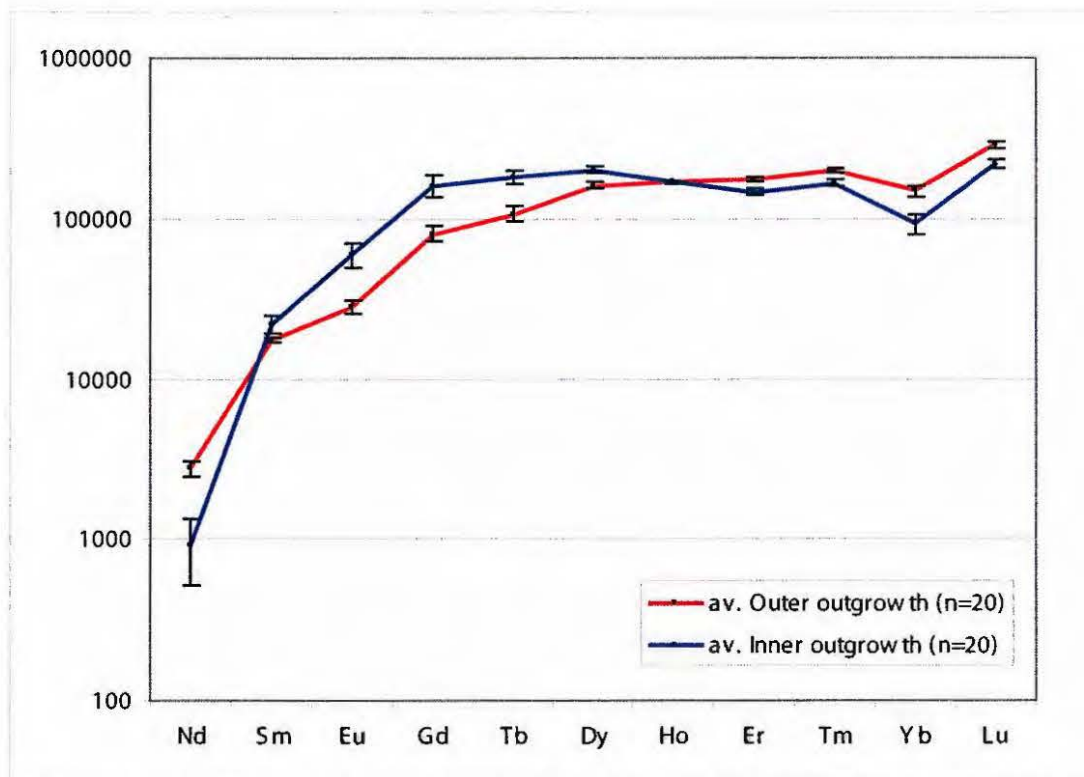
Fig. 4.7. Chondrite normalised (WDS) REE patterns for the inner xenotime and outer, massive xenotime outgrowths. The inner xenotime outgrowths have elevated concentrations of the MREE (Sm–Dy) and lower concentrations of the HREE (Er–Lu) in comparison to the outer, massive xenotime outgrowths. Note the slight negative dip in Yb and positive rise for Lu probably represents a calibration problem with these elements. Error bars are 95% confidence (standard deviation of the mean).

4.5.3 SHRIMP U–Pb geochronology

4.5.3.1 Zircon

Nineteen SHRIMP analyses were carried out on the zircon from LIS–34 by Dr. Richard Armstrong (RSES) (Fig. 4.8 and Table 4.4). U contents range from ~300 to ~700 ppm and Th/U ratios from ~0.3 to ~0.8, indicating that most of the zircon was probably derived from felsic igneous sources (Williams 2001). Common ^{206}Pb contents are mostly below 1%. One spot (7.1) which has a relatively high proportion of common ^{206}Pb (1.19%), also has the highest U concentration (~700 ppm). This grain (not plotted) is grossly discordant and omitted from further consideration. Three additional grains (4.1, 15.1, and 17.1) are more than 10% discordant and are not discussed further. The remaining 16 grains have ^{207}Pb/^{206}Pb ages that range from ~2.7 to 1.96 Ga. There are two small clusters of ages at ~2.08 Ga (n=4, MSWD = 0.64) and ~2.15 Ga (n=3, MSWD = 0.24) and two grains with similar ages of ~2.12 Ga. There are also older individuals at ~2.39 Ga, ~2.48 Ga, ~2.6 Ga and 2.7 Ga. The

youngest grain analysed from this sample is concordant and has a $^{207}Pb/^{206}Pb$ apparent age of 1957 ± 20 Ma (2σ).
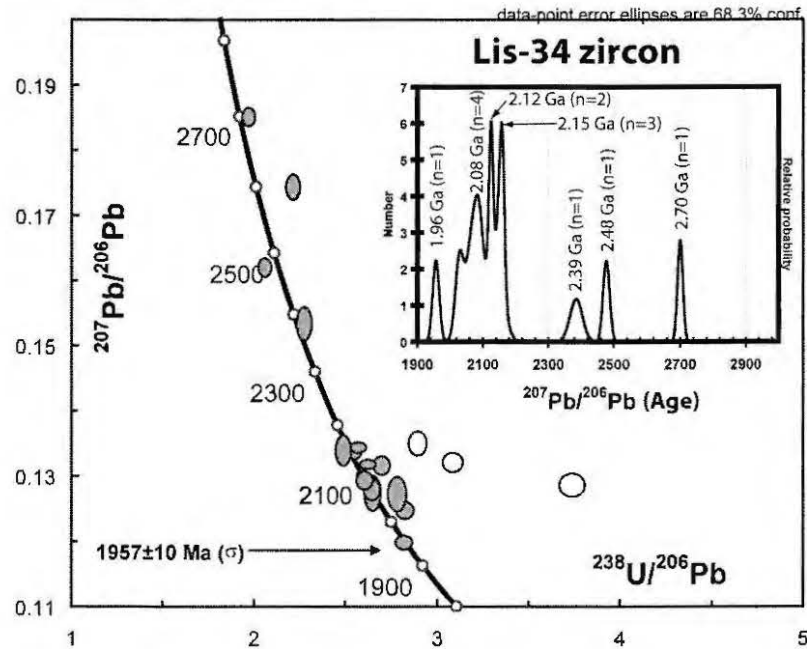
Fig. 4.8. Concordia plot for SHRIMP RG zircon analyses from LIS-34.

Table 4.4. SHRIMP U–P isotopic data for zircon from LIS-34.

Spot name	U (ppm)	Th (ppm)	Th/U	% Comm $^{206}Pb_c$	$^{238}U/^{206}Pb$ ($\pm1\sigma$ %)		$^{207}Pb/^{206}Pb$ ($\pm1\sigma$ %)		$^{207}Pb/^{206}Pb$ age (Ma $\pm 1\sigma$)		Discordance (%)
1.1	134	76	0.58	-0.09	0.5087	1.2	0.18517	0.51	2700	8	2
2.1	338	174	0.53	-0.03	0.3706	1.1	0.13185	0.73	2123	13	4
4.1	135	57	0.44	-0.11	0.3241	1.2	0.13234	0.75	2129	13	15
5.1	196	189	1.00	-0.13	0.384	1.1	0.12955	0.71	2092	12	0
6.1	495	120	0.25	-0.03	0.3814	1	0.13202	0.36	2125	6	2
7.1	738	140	0.20	1.19	0.1397	1	0.1159	0.84	1894	15	56
8.1	250	270	1.11	-0.12	0.3544	1.1	0.12497	0.7	2028	12	4
9.1	368	141	0.40	-0.06	0.3893	1.1	0.13461	0.4	2159	7	2
10.1	126	47	0.38	-0.11	0.4863	1.2	0.16209	0.58	2478	10	-3
11.1	143	75	0.54	-0.22	0.4405	1.2	0.1536	1.1	2386	19	1
12.1	205	128	0.64	-0.19	0.3776	1.1	0.1276	1.4	2066	25	0
13.1	263	142	0.56	-0.13	0.3785	1.1	0.1282	0.87	2074	15	0
14.1	192	106	0.57	-0.17	0.4522	1.1	0.1744	0.73	2600	12	8
15.1	256	50	0.20	0.29	0.346	1.1	0.1352	0.9	2167	16	12
16.1	418	55	0.14	-0.07	0.3923	1	0.13398	0.56	2151	10	1
17.1	111	38	0.35	0.03	0.2672	1.3	0.1289	0.89	2082	16	27
18.1	173	84	0.50	-0.22	0.4017	1.2	0.1341	1.1	2152	20	-1
19.1	233	180	0.80	-0.07	0.3553	1.1	0.12009	0.57	1957	10	0
20.1	237	113	0.49	-0.19	0.3598	1.1	0.1275	1.4	2064	24	4

4.5.3.2 *Monazite*

The tiny monazite cores with their characteristic diffuse margins meant that only the rims were able to be wholly targeted with confidence by the ~30 μm SHRIMP spot. It is for this reason that only the monazite rims were analysed by SHRIMP. Forty-seven monazite rims were analysed on SHRIMPII from LIS-34 (Fig. 4.9, Table 4.5). Of these, eleven SHRIMP spots overlapped both core and rim monazite growth zones (the SHRIMP was operating in auto-run mode) and are not considered further as they represent mixed analyses. The remaining thirty-six analyses sampled the monazite rims. Four of the monazite analyses are more than 10% discordant and omitted from the age calculations. The remaining 32 analyses have a range in $^{206}Pb/^{238}U$ ratios that is slightly larger than that expected from their analytical uncertainties (MSWD=1.5). Omitting the analysis with the highest $^{206}Pb/^{238}U$ (m17.2) removes the excess scatter, leaving 31 analyses that combine to give a weighted mean $^{206}Pb/^{238}U$ age of 570 ± 5 Ma (MSWD = 1.3).
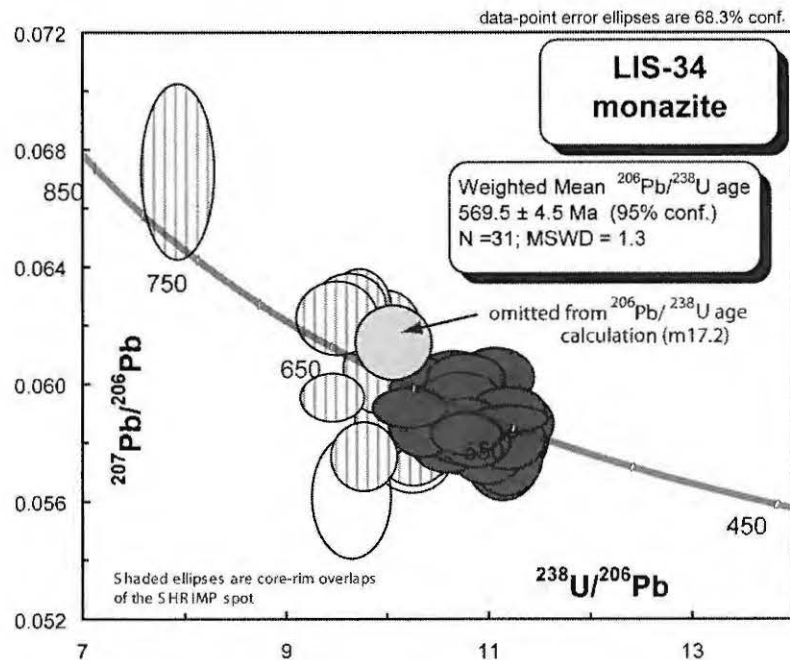
Fig. 4.9. Concordia plot for SHRIMP II, monazite analyses from LIS-34.

4.5.3.3 Xenotime

Forty–one SHRIMP analyses were undertaken on xenotime from LIS-34 (Fig. 4.10 and Table 4.3). Twenty spots were analysed on the outer massive growth zones, and 21

analyses were carried out on the inner xenotime zones. All 41 analyses can be combined to give a loosely defined discordance line (MSWD=2.6) with concordia intercept ages of ~1470 Ma and ~580 Ma. Two analyses (L34.38R and L34.21R) have significantly younger $^{206}Pb/^{238}U$ ratios than other xenotime in this sample and are also greater than 10% discordant. These xenotime may have lost radiogenic Pb and have been omitted from the regression. A third analysis (L34.66.2B) is 46% discordant and plots away from the general Pb-loss trend defined by the other inner xenotime growth zones. It is interpreted as having a mixed or disturbed U—Pb composition and has been removed from the interpretation. Omitting these three analyses from the regression reduces the scatter about the line (MSWD=1.8) but does not eliminate it. No further omissions are justified. The moderately well defined discordance line has concordia intercept ages of 1469 ± 47 Ma and 587 ± 20 Ma (tσ). It is the inner pitted zones which give the older ages. The massive lobate shaped xenotime is considerably younger than the inner xenotime and has a range in $^{206}Pb/^{238}U$ age of ~550–630 Ma. The 12 analyses that are less than 10% discordant combine to give a weighted mean $^{206}Pb/^{238}U$ age of 573 ± 10 Ma (MSWD = 1.3), the same as the monazite rim age within analytical uncertainties.

Table 4.5. SHRIMP U–P isotopic data for monazite from LIS-34.

Spot name	U (ppm)	Th/U	% Comm 206Pb	206Pb/238U (±1 %)		207Pb/206Pb (±1 %)		207Pb/206Pb age (Ma ± 1)		206Pb/238U age (Ma ± 1)		Discordance (%)
monazite rims												
m12.1	2983	4.96	0.03	0.0891	2.37	0.0587	1.24	556	28	550	13	1
m12.5	2757	7.13	0.105	0.0894	2.11	0.0592	0.81	575	18	552	11	4
m12.2	4170	6.05	0.068	0.0894	2.24	0.0589	0.51	562	11	552	12	2
m19.2	3316	5	0.159	0.0895	2.14	0.0582	1.17	536	26	552	11	-3
m5.7	5675	22.64	0.247	0.0895	2.39	0.0582	1.56	538	35	553	13	-3
m5.3	12517	7.43	0.114	0.0896	2.16	0.0576	1.56	516	35	553	11	-7
m6.2	7014	12.3	0.204	0.0899	2.21	0.0576	1.68	514	37	555	12	-7
m14.3	3231	5.12	-0.028	0.0905	2.29	0.0603	1.11	613	24	558	12	10
m16.2	2782	6.67	0.069	0.0908	2.25	0.0590	1.07	568	24	560	12	1
m16.3	2187	5.2	0.18	0.0912	2.20	0.0577	1.26	520	28	562	12	-8
m18.1	2082	5.92	0.123	0.0912	2.22	0.0584	1.28	545	28	563	12	-3
m16.1	3077	6.1	0.105	0.0922	2.11	0.0581	1.02	534	22	568	11	-6
m16.5	4401	5.44	0.101	0.0925	2.23	0.0585	0.74	547	16	570	12	-4
m3.1	6143	5.29	0.163	0.0926	2.43	0.0587	1.29	557	28	571	13	-2
m13.2	2833	10.51	0.087	0.0929	2.13	0.0583	0.79	542	18	572	12	-5
m17.1	4317	9.2	0.138	0.0929	2.18	0.0588	0.83	560	18	573	12	-2
m12.4	2799	5.6	0.081	0.0929	3.09	0.0586	1.13	554	25	573	17	-3
m14.2	2832	6.3	0.051	0.0930	2.32	0.0602	0.90	612	19	573	13	7
m10.1	7343	7.75	0.105	0.0930	2.27	0.0595	1.11	584	24	573	12	2
m11.2	3463	6.46	0.173	0.0932	2.26	0.0583	1.15	541	25	574	12	-6
m13.3	2238	11.51	0.057	0.0932	2.28	0.0599	1.04	598	22	575	13	4
m16.4	3187	6.7	0.11	0.0934	2.30	0.0597	0.85	591	18	576	13	3
m19.1	1544	12.97	0.157	0.0935	2.19	0.0595	1.43	584	31	576	12	1
m18.2	974	18.79	0.21	0.0935	2.23	0.0584	1.61	546	35	576	12	-5
m14.1	1828	12.01	0.17	0.0940	3.18	0.0597	1.68	591	37	579	18	2
m13.1	1638	8.59	0.094	0.0945	2.28	0.0581	1.21	533	27	582	13	-8
m9.2	3253	7.32	0.077	0.0946	3.00	0.0587	1.36	557	30	583	17	-4
m7.1	3947	9.11	0.096	0.0963	2.33	0.0589	1.21	564	26	593	13	-5
m10.2	1019	15.42	0.231	0.0965	2.29	0.0596	1.49	589	33	594	13	-1
m7.2	2887	6.22	0.105	0.0968	2.13	0.0587	1.26	556	28	596	12	-7
m13.4	2622	4.41	0.097	0.0980	2.33	0.0592	0.76	576	17	603	13	-4
m17.2	1197	14.94	-0.053	0.0994	2.40	0.0614	1.33	655	29	611	14	7
monazite analyses greater than 10 % discordant												
m11.1	3047	6.79	0.123	0.0970	2.22	0.0577	0.95	516	21	597	13	-13
m15.1	3199	10.52	0.148	0.0977	2.51	0.0576	1.37	513	31	601	14	-15
m6.1	3731	5.61	0.167	0.0994	2.22	0.0583	1.00	540	22	611	13	-12
m9.5	504	25.13	0.381	0.1039	2.70	0.0562	2.47	462	56	637	16	-28
SHRIMP spot overlap onto monazite cores and rims												
m6.4	2317	13.98	0.107	0.0976	2.42	0.0580	1.54	528	34	600	14	-12
m5.2	9918	23.94	0.05	0.0996	2.59	0.0597	1.94	593	43	612	15	-3
m9.3	17104	6.98	0.129	0.0999	2.30	0.0588	1.22	560	27	614	13	-9
m11.3	1319	7.74	-0.057	0.1002	2.36	0.0618	1.50	667	33	616	14	8
m5.1	30241	9.97	0.19	0.1013	2.21	0.0606	1.60	623	35	622	13	0
m9.4	3621	4.22	0.092	0.1025	2.25	0.0576	1.34	514	30	629	13	-18
m5.5	3989	7.47	0.12	0.1030	2.22	0.0625	1.55	691	34	632	13	9
m12.3	1861	15.55	-0.017	0.1040	2.45	0.0628	1.08	700	23	638	15	10
m7.3	4373	9.31	0.112	0.1055	2.80	0.0623	1.33	684	29	646	17	6
m6.3	3599	6.34	0.019	0.1060	2.24	0.0596	0.91	589	20	650	14	-9
m5.6	2641	37.44	0.628	0.1265	2.96	0.0673	2.93	846	62	768	21	10
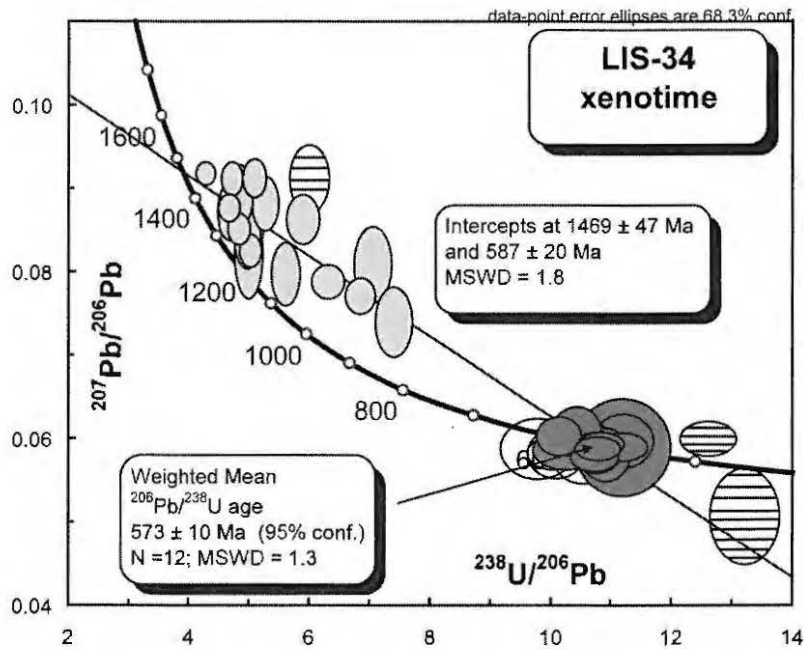
Fig. 4.10. Concordia plot for SHRIMP RG, xenotime analyses from LIS-34. Striped ellipses are outliers and have been omitted from the regression.

4.6 Discussion

Xenotime outgrowths on detrital zircon from LIS-34 occur as two generations distinguishable by their distinctive texture, chemical composition and U–Pb isotopic composition. The discordance trend shown by the inner xenotime outgrowths (Fig. 4.10) indicates that this xenotime formed during one event at ~1.47 Ga and later lost some radiogenic Pb at ~570 Ma, coincident with the precipitation of the outer xenotime outgrowths. The monazite rims have a consistent U–Pb and minor element composition, whereas the cores are chemically heterogeneous, particularly for La and Nd, indicating that they are probably derived from a range of different source rocks and therefore detrital in origin. The monazite rims and outer xenotime outgrowths have mutually indistinguishable $^{206}Pb/^{238}U$ ages of 570 ± 5 Ma and 573 ± 10 Ma respectively, demonstrating that they precipitated during the same geological event.

4.6.1 Depositional age constraints for the Serra da Mesa Group

SHRIMP U–Pb detrital zircon analyses of LIS-34 demonstrate a provenance from Palaeoproterozoic to late Archaean sources. These data corroborate a Sm–Nd model T_{DM} age of ~2.67 Ga (pers. comm. Reinhardt Fuck) from the same sample. Very minor detrital zircon groups in LIS-34 occur at ~2.05 Ga and ~2.15 Ga, and may have

been derived from similarly–aged local Palaeoproterozoic basement granitoids and gneisses. The Late Archaean zircon ranges in age from ~2.70 to ~2.47 Ga, which is similar to the ages of some metavolcanic units and granite-gneiss bodies of the Goiás Massif reported by Pimentel et al. (2000). The youngest zircon has a $^{207}Pb/^{206}Pb$ age of 1957 ± 20 Ma (2σ) and assuming no later radiogenic Pb-loss, can be used to define a maximum deposition age for the Serra da Mesa Group in this region. The inner xenotime outgrowths crystallised at ~1.47 Ga which defines a minimum age for this unit. However a more precise minimum age estimate for the group is the 1503 ± 3 Ma age of the Peixe Alkaline Complex, which intrudes Serra da Mesa Group rocks further to the north of the sample site. Additionally, the minimum age defined by the inner xenotime outgrowths of 1469 ± 47 Ma is probably not to related to the timing of diagenesis but rather the intrusion of the Peixe Alkaline Complex. Therefore, this attempt to isotopically constrain the timing of sedimentation for the Serra da Mesa Group has yielded very limited new information. The ~1.96 Ga maximum deposition age defined by the youngest zircon although ~200 m.y. younger than the ~2.2 Ga basement, nevertheless still leaves a ~500 million year interval (i.e. ~1.96 to 1.50 Ga) in which the Serra da Mesa Group could have been deposited.

Further field and geochronological studies are clearly required to better constrain the depositional age of the Serra da Mesa Group. Detailed field studies could also be used to establish whether an intrusive relationship exists between the Serra da Mesa Group and nearby ~1.61 to ~1.57 Ga, Serra do Encosto, Serra Dourada and Serra da Mesa Granitoids of the RTS. Further work could also be carried out on the LIS-34 sample itself. Only sixteen zircon grains analysed by SHRIMP have concordant U–Pb ages. An additional SHRIMP U–Pb zircon dating session could be devoted to substantially increasing this number to better investigate whether zircon younger than ~1.96 Ga is present in this sample. Additionally, a number SHRIMP U—Pb detrital zircon studies could be carried out on other samples from the Serra da Mesa Group and also samples from the Araí Group. These studies could also better constrain a maximum deposition age as well as provide the opportunity to compare the detrital zircon spectra from each of the units and thereby test the possible extent to which the Araí Group and Serra da Mesa Group can be correlated.

4.6.2 Late Neoproterozoic metamorphism of the Serra da Mesa Group

The outer xenotime outgrowths and monazite rims have identical ages of ~570 Ma, The most precise age for this event is given by the SHRIMP U–Pb analyses of the monazite rims of 570 ± 5 Ma. Given that the muscovite in LIS-34 defines the foliation in this rock and that there is a close association between monazite and muscovite, it is likely that the U—Pb isotopes in the monazite rims represent the timing of the host fabric. However, a thorough petrogenetic study combined with in-situ SHRIMP U—Pb analyses of the monazite particularly from the surrounding mica shist unit is needed to confirm this.

The ~570 Ma ages for the xenotime outgrowths and monazite rims are within error of the ID-TIMS U—Pb zircon lower intercept age of 577 ± 26 Ma for a nepheline syenite within the Peixe Alkaline Complex which intrudes the Serra da Mesa Group (Kitajima et al. 2001). This age was interpreted by these workers as probably related to a metamorphic event associated with the very late stages of the Brasiliano Orogeny. These ~570 Ma ages from phosphate minerals in the Serra da Mesa Group and zircons from the Peixe Alkaline Complex record the same event and are similar in age to the post-orogenic, ~590 to ~560 Ma mafic to felsic plutonic rocks in the Mara Rosa and Arenópolis arcs.

The extent to which this ~570 Ma event affected rocks east of the Rio dos Bois fault should be investigated further. Crucial to this study would be petrogenetical studies coupled with in-situ geochronology. However, the results of this study and also that of Kitajima et al. (2001) opens up the possibility that in this region, the final effects of the Brasiliano Orogeny may have occurred at about ~570 Ma. Interestingly, the effects of the ~670 to ~630 Ma Brasiliano Orogeny appear to be significant only in the arc rocks, west of the Rio dos Bois Fault. East of the fault, isotopic evidence for the main ~670 to ~630 Ma phase of the Brasiliano Orogeny is scarce. For example, mylonites associated with the Rio Maranhâo thrust system have whole rock Rb–Sr ages of ~640 Ma (Girardi et al. 1978, as cited in Pimentel et al. 2000). Ferreira Filho (1994, as cited in Pimentel et al. 2006) has also reported $^{207}Pb/^{206}Pb$ ages for rutile fractions from Niquelândia Complex rocks of between ~660 Ma and ~690 Ma. These 'Brasiliano' ages are further corroborated by a Sm–Nd mineral isochron age of approximately 610 Ma on a Niquelândia Complex garnet-rich band (Ferreira Filho &

Pimentel 2000). Additionally, Pimentel et al. (1991a) report an ID–TIMS, U–Pb zircon lower intercept age of ~660 Ma for the ~1770 Ma, RPS, Soledale Granite.

4.7 Conclusions

SHRIMP U–Pb xenotime, monazite and zircon analyses from a sample of quartzite from the Serra da Mesa Group, Brasilia Fold Belt were undertaken in an attempt to isotopically constrain the timing of sediment deposition and amphibolite grade metamorphism of the Serra da Mesa Group. Two texturally, chemically and isotopically distinct generations of xenotime occur as outgrowths on detrital zircon. It was originally hoped that the inner pyramidal xenotime growth zone may have formed during diagenesis and thereby establish the timing of sedimentation for the Serra da Mesa Group. However, the 1469 ± 39 Ma age determined from this xenotime zone probably grew in a response to the intrusion of the 1503 ± 3 Ma, Peixe Alkaline Complex which intrudes rocks of the Serra da Mesa Group and is located approximately 60 km north of the sample site. Additionally, the youngest zircon analysed from just 16 concordant compositions, gives a $^{207}Pb/^{206}Pb$ age of ~1.96 Ga. Therefore deposition of the Serra da Mesa Group is constrained between ~1.96 Ga and 1.50 Ga, which in practical terms is only a relatively minor improvement on the existing maximum age constraint provided by the 2.20 Ga gneissic basement. Further SHRIMP U—Pb detrital zircons studies of other Serra da Mesa Group sedimentary rocks may be useful in better establishing a maximum deposition age for this unit.

The monazite rims and outer xenotime outgrowths have indistinguishable $^{206}Pb/^{238}U$ ages of 570 ± 5 Ma and 573 ± 10 Ma respectively. These phases from the Serra da Mesa Group are identical within error of a ID-TIMS U—Pb zircon lower intercept age recorded in the Peixe Alkaline Complex of 577 ± 26 Ma (Kitajima et al. 2001), which probably records the same event. This ~570 Ma age was interpreted by Kitajima et al. (2001) to be related to metamorphism associated with the final stages of the Brasiliano Orogeny. Further U—Pb studies on other metamorphic rocks in this region are needed to investigate this and establish its regional extent.

This SHRIMP U–Pb xenotime dating exercise is the first example where $^{206}Pb/^{238}U$ ages have been used to accurately determine the crystallisation age of xenotime

occurring as outgrowths on zircon. The identical ages of the outer xenotime outgrowths and monazite rims support the accuracy of the SHRIMP U–Pb xenotime analytical protocols, ^{206}Pb/^{238}U calibration technique and ^{206}Pb/^{238}U matrix correction techniques developed during this PhD project.

5. IN SITU SHRIMP U–Pb DATING OF HYDROTHERMAL XENOTIME FROM THE CALLIE AND COYOTE AU DEPOSITS: ESTABLISHING TEMPORAL LINKS BETWEEN GRANITE INTRUSION AND LODE-AU MINERALISATION IN THE TANAMI REGION AND PINE CREEK OROGEN, NORTHERN TERRITORY

5.1 Introduction

Preface

During the early stages of this PhD project a SHRIMP U–Pb xenotime experiment was conducted on hydrothermal xenotime from the Callie Au deposit in the Northern Territory. This was undertaken using SHRIMP IIB at the Curtin University of Technology in Perth, Western Australia under the guidance of Dr. Ian Fletcher (Curtin University of Technology). The U–Pb matrix correction procedures followed those of Fletcher et al. (2000) and the analysed xenotime crystals gave a $^{207}Pb/^{206}Pb$ age of 1803 ± 19 Ma (95% confidence, MSWD = 0.57). This was interpreted to be the age of mineralisation for the Callie deposit and was reported in an extended abstract in Cross et al. (2005), (Appendix 5.1). This age for the Callie xenotime has since been cited and incorporated into the results of six peer reviewed scientific journal articles (Huston et al. 2007; Crispe et al. 2007; Williams 2007; Rasmussen et al. 2006; Bagas et al. 2007; Tunks & Cooke 2007). With the aim of improving the precision of the Callie xenotime age, and also applying the U–Pb matrix correction techniques developed in this study, the xenotime from the Callie Au mine was re-analysed and is fully reported here. SHRIMP U–Pb analyses were also undertaken on hydrothermal xenotime from the Coyote deposit in the western Tanami region. Xenotime from this sample had also been analysed previously using SHRIMP by Dr. Richard Armstrong (Australian National University) and reported confidentially to Anglogold Australia Ltd. in 2002. That SHRIMP experiment did not use any U–Pb matrix correction procedures necessary for SHRIMP U–Pb xenotime determinations and an interpreted $^{207}Pb/^{206}Pb$ age from these data of 1791 ± 8 Ma has been reported by Bagas et al. (2007). Therefore, a second SHRIMP U–Pb dating experiment was conducted on this sample using the techniques and U–Pb matrix correction procedures developed in this study. Together the new SHRIMP U–Pb xenotime results for the Callie and Coyote Au deposits place the timing of mineralisation in these mines on a firmer grounding to be incorporated into exploration and tectonic models for the genesis of lode-Au

deposits in northern Australia. The temporal relationships between lode–Au mineralisation in the Tanami Region and Pine Creek Orogen were also investigated. To do this, a SHRIMP U–Pb monazite age used to infer the timing of mineralisation at the Goodall Deposit by Sener et al. (2005), which was reinterpreted by Rasmussen et al. (2006), was further examined here.

5.1.2 Regional Geology

The geology and evolution of the Tanami region have recently been discussed by Crispe et al. (2007) and Cross & Crispe (2007, i.e. Chapter 1) and only a brief synopsis is given here. The region consists of a thick sequence of variably deformed, dominantly marine, sedimentary rocks and rare volcanics that was deposited on a late Archaean substrate and intruded by granite mostly between ~1.82 and 1.79 Ga. Deposition of the sedimentary units probably spanned the time period between ~1.87 and ~1.64 Ga. Recent unpublished geochronology suggests that the oldest known rocks in the Tanami region occur in the Bald Hill sequence in Western Australia. A rhyodacite from this unit has a SHRIMP zircon U–Pb age of ~1.86 Ga (Data of D. Maidment, cited in Huston et al. 2007). The sedimentary rocks have been subdivided into six main units. From base to top these are: the Dead Bullock Formation (lower sandstone, upper carbonaceous siltstone with lesser iron formation) and the Killi Killi Formation (widespread turbidite), which comprise the Tanami Group; the Ware Group (coarse sandstone, felsic volcanic rocks); the Mount Charles Formation (predominantly turbidite, arkosic sedimentary rocks with interlayered basalt); the Pargee Sandstone (sandstone and conglomerate); and the Birrindudu Group (marine to fluvial sandstone, conglomerate and calcareous sedimentary rocks). There is a progression within the sequence from deeper to shallower water facies. The principal hosts for Au mineralisation are the Dead Bullock and Mount Charles Formations, however mineralisation also occurs in the Killi Killi Formation in the Coyote and Bald Hill regions in the western Tanami (Fig. 5.1).

The Tanami basin was interpreted by Cross & Crispe (2007; see Chapter 1) to have developed between ~1.87 and 1.84 Ga in response to the Hooper Orogeny (Halls Creek Orogen), the Nimbuwah Event (Pine Creek Orogen) or very early stages of the Tanami Event. The initial uplift of Archaean basement rocks caused sedimentary

detritus to be shed into the early Tanami Basin forming the Ferdies Member of the Dead Bullock Formation, which is dominated by ~2.50 Ga detrital zircon. The extensive turbiditic sandstone units of the Killi Killi Formation were largely derived from the erosion of ~1.86 Ga orogenic granitoids and deposited at ~1.84 Ga (Cross & Crispe 2007). Crispe et al. (2007) suggest that deposition of the Killi Killi Formation was probably halted by the ~1.84–1.82 Ga collision of the North Australia Craton (NAC) with the Kimberley Craton (Myers et al. 1996; Sheppard et al. 1999; Bodorkos et al. 2002). This event also caused deformation and predominantly greenschist facies metamorphism (D_1–M_1) in the Tanami region. Two further periods of compressional deformation (D_2 and D_3) were broadly synchronous with intrusion of ~1.82–1.79 Ga granitoids that might be related to the similarly aged Stafford event in the Arunta region to the south-east. In the Arunta region, the ~1.81-1.79 Ga Stafford event is recorded by bimodal volcanism, high-temperature, low pressure metamorphism and also the emplacement of voluminous granitic and minor mafic magmas (Scrimgeour 2006). Scrimgeour (2006) suggests that during this time, tectonism in the NAC shifted to the southern margin of the craton in what is now the Aileron province of the Arunta region where a long-lived north-dipping subduction system was active between ~1.81 and 1.69 Ga. Closely following D_3, but before another compressional event (D_4), is an interpreted extensional event which resulted in the deposition of the sedimentary rocks and eruption of the Mount Charles basalts. D_5 transpression resulted in the development of faults and shear zones that are interpreted to have had a significant control on Au mineralisation in the Tanami and to have been active between ~1.81 and 1.79 Ga. Late thrust faults, many of which postdate ~1.70 Ga, may be related to the King Leopold and Alice Springs Orogenies and are grouped as D_{6+}. A generalised time-event diagram for the Tanami region is shown in Fig. 3 of Chapter 1.
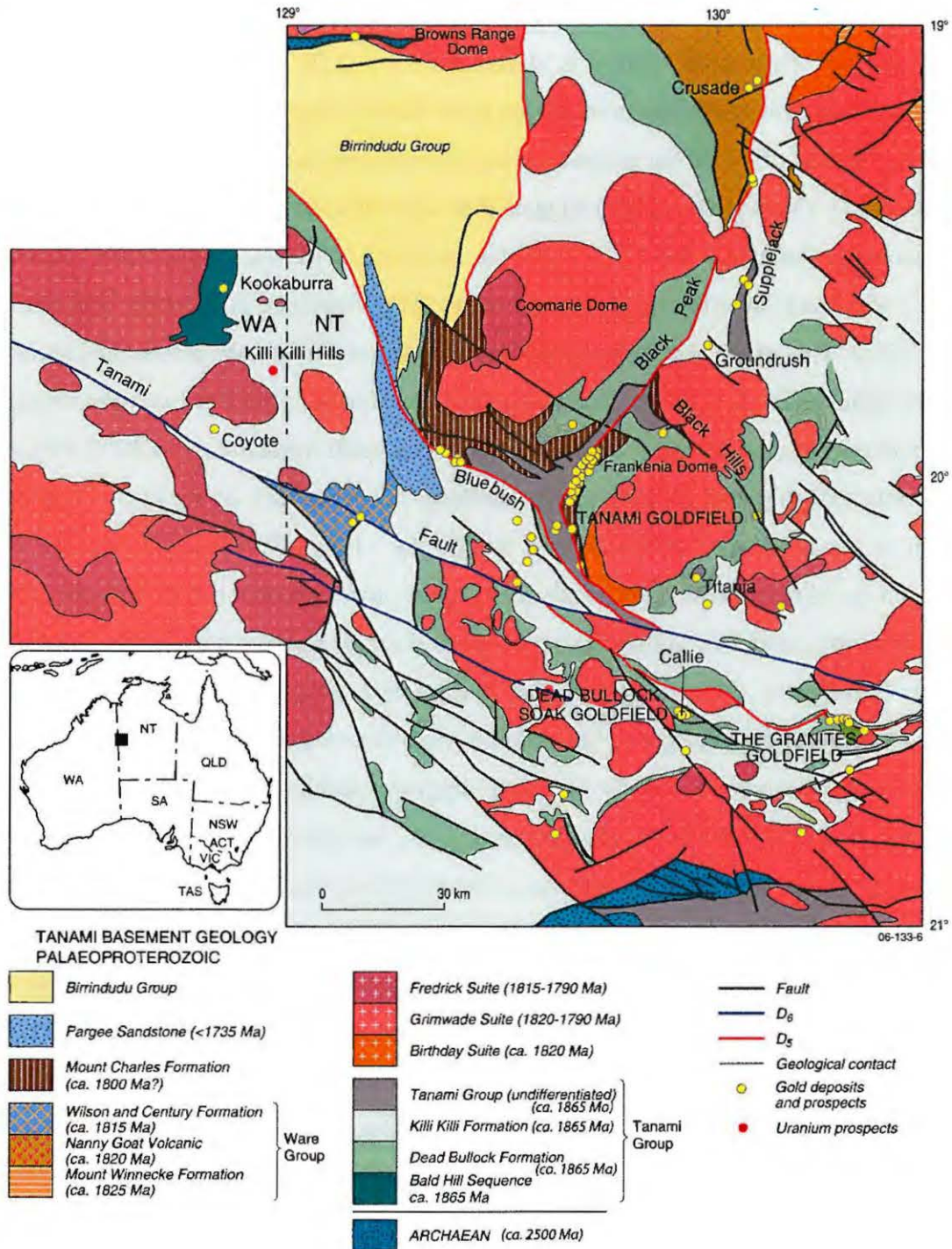
Fig. 5.1. Generalised geology map of the Tanami Region.
Adapted from Huston et al. (2007).

5.2 Mineralisation

The Tanami region is host to significant lode-Au mineralisation. Over the past 20 years production has exceeded 4.8 Moz, with proven reserves of over 7.7 Moz (Wygralak et al. 2005). Mineralisation is concentrated in three principal regions, Dead Bullock Soak, The Granites and Tanami Goldfields. Significant Au deposits also

166

occur in the western Tanami at the Coyote deposit and in the Bald Hill area (Fig. 5.1). Reactive carbonaceous and iron rich units of the Dead Bullock Formation are the host to major mineralisation at the world class Callie deposit (Dead Bullock Soak goldfield) and at The Granites. Mineralisation at the Coyote deposit predominantly occurs in finer grained siltstone units of the Killi Killi Formation. Mernagh & Wygralak (2007) have suggested that Au deposition in the Tanami mainly occurred at depths ranging from ~1.5 to 11 km, from low to moderate salinity carbonic fluids with temperatures between ~200 and 400°C. These fluids are thought by Huston et al. (2007) to have resulted from metamorphic dewatering related to elevated crustal temperatures or alternatively, from coeval granite intrusion.

5.2.1   The timing of Tanami lode-Au mineralisation

Lode-Au mineralisation in the Tanami Region is interpreted to have occurred during two phases, an early phase associated with 1.84–1.82 Ga, D_1–M_1 structures such as at The Granites (Adams et al. 2007) and the Bald Hill deposits (Bagas et al. 2007), and a later phase associated with ~1.82–1.79 Ga, D_5 structures at Callie (Smith et al. 1998), Tanami Goldfields (Adams et al. 2007) and Coyote (Bagas et al. 2007). These interpretations imply that mineralisation was associated with two separate tectonic events marginal to the NAC. Firstly, the collision between the NAC and Kimberley Craton to the north-east between ~1.84 and 1.82 Ga (D_1–M_1), and secondly the ~1.81–1.79 Ga Stafford event (D_5) to the south-east (Scrimgeour 2006).

The timing of the major D_5 mineralising event has been somewhat loosely constrained by recent SHRIMP U–Pb xenotime geochronology by Cross et al. (2005) and also a SHRIMP xenotime $^{207}Pb/^{206}Pb$ age mentioned but not fully reported in Bagas et al. (2007). Cross et al. (2005) reported a relatively imprecise SHRIMP xenotime $^{207}Pb/^{206}Pb$ age of 1803 ± 19 Ma for the Callie deposit. This age range allows for mineralisation at this deposit to have occurred as early as ~1.82 Ga and as late as ~1.78 Ga, associated with the very latest stage of granite generation. The xenotime $^{207}Pb/^{206}Pb$ age reported by Bagas et al. (2007) of 1791 ± 8 Ma for hydrothermal xenotime from the Coyote deposit was based on an unpublished SHRIMP xenotime age interpretation based on five xenotime analyses undertaken by Richard Armstrong (RSES) without the necessary U–Pb xenotime matrix corrections. A relatively recent

$^{40}Ar/^{39}Ar$ study of hydrothermal biotite from the Callie deposit by Fraser (2002), which suggested mineralisation occurred at ~1.72 Ga, is now in the light of the 1.80 Ga SHRIMP U—Pb xenotime result of Cross et al. (2005) to more likely represent a later thermal overprint possibly related to the ~1.74–1.69 Ga Strangways Orogeny which was a major thermal and fluid flow event that principally affected the rocks in the Arunta region (Scrimgeour 2006).

The timing of the earliest phase of mineralisation interpreted to be associated with ~1.84–1.82 Ga, D_1–M_1 structures has not yet been properly established. However, a preliminary $^{40}Ar/^{39}Ar$ muscovite age from an ore-stage vein of ~1.80 Ga has been reported by Fraser et al. (2006) for the Sandpiper deposit, which is interpreted by Bagas et al. (2007) to have formed during D_1–M_1. The significance of this relatively young age in relation to the suggested timing of D_1 by (Crispe et al. 2007) has yet to be resolved.

5.3 The Callie Au deposit

The Callie deposit has an estimated resource of 6.6 Moz of Au and is the largest in the Tanami region. It is located in the Dead Bullock Soak goldfield approximately 550 km north-west of Alice Springs in the Northern Territory. Mineralisation at this deposit has been recently reviewed by Williams (2007) and also discussed by Smith et al. (1998), Voulgaris & Emslie (2004) and Huston et al. (2007). There are four types of quartz veins at Callie. The earliest are pre-ore, bedding parallel with minor chlorite and biotite and were folded by the major D_1 deformation. Ore-stage quartz veins are coincident with D_5 regional deformation, planar, with variable chlorite, biotite, apatite, carbonate, feldspar, pyrrhotite, chalcopyrite, gold, ilmenite, arsenopyrite, marcasite and anatase (Huston et al. 2007). There are also two post-ore vein types, one comprising of carbonate-quartz with accessory sphalerite, galena and pyrite and a later stage of calcite-quartz and ankerite-quartz veins which cut previous fabrics and faults including D_6 structures (Huston et al. 2007). The auriferous ore-stage veins are localised within a series of east-west trending structural corridors of up to 180 metres wide which intersect the D_1 anticlinal closures (Smith et al. 1998; Williams 2007; Voulgaris & Emslie 2004)

The host unit is the informally named Blake beds of Smith et al. (1998) which is broadly equivalent to the Callie Member of the Dead Bullock Formation described by Crispe et al. (2007). The Blake beds consist of over 350 m of graphitic turbidites and mudstones that have undergone greenschist facies metamorphism during the ~1.84 to 1.82 (D_1-M_1) event (Crispe et al. 2007). Hydrothermal alteration at Callie during the D_5 event is associated with bleaching (decarbonisation) of the graphitic host rocks and growth of bedding parallel hydrothermal biotite (Williams 2007).

A xenotime-bearing ore-stage quartz vein was sampled from diamond drill core of the Callie deposit (DBD395D3, 899.0 m) and supplied by Nick Williams (Geoscience Australia) for SHRIMP U–Pb analysis. A thin section of a ~2 mm wide vein containing a quartz-chlorite-apatite-titanite-Au assemblage with associated xenotime was cut and mounted in epoxy resin. Xenotime in the quartz veins occurs as small (~5 to 20 μm) equant, euhedral to anhedral pale yellow-green crystals (Fig. 5.2 and 5.3). No xenotime was observed outside of the quartz vein. The mineral assemblage observed in the thin section clearly identifies it as a typical D_5 auriferous vein.
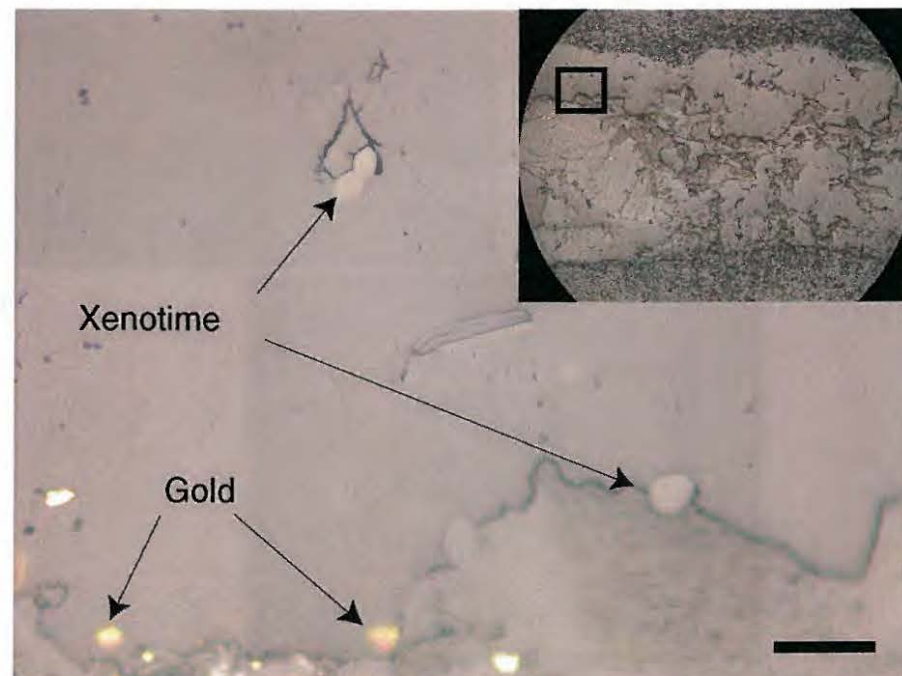
Fig. 5.2. Reflected light photomicrograph of xenotime and gold in an ore-stage, quartz-chlorite-apatite-gold-(xenotime) vein from the Callie deposit (sample: DBD395D3, 899m). Scale bar is 100 microns.
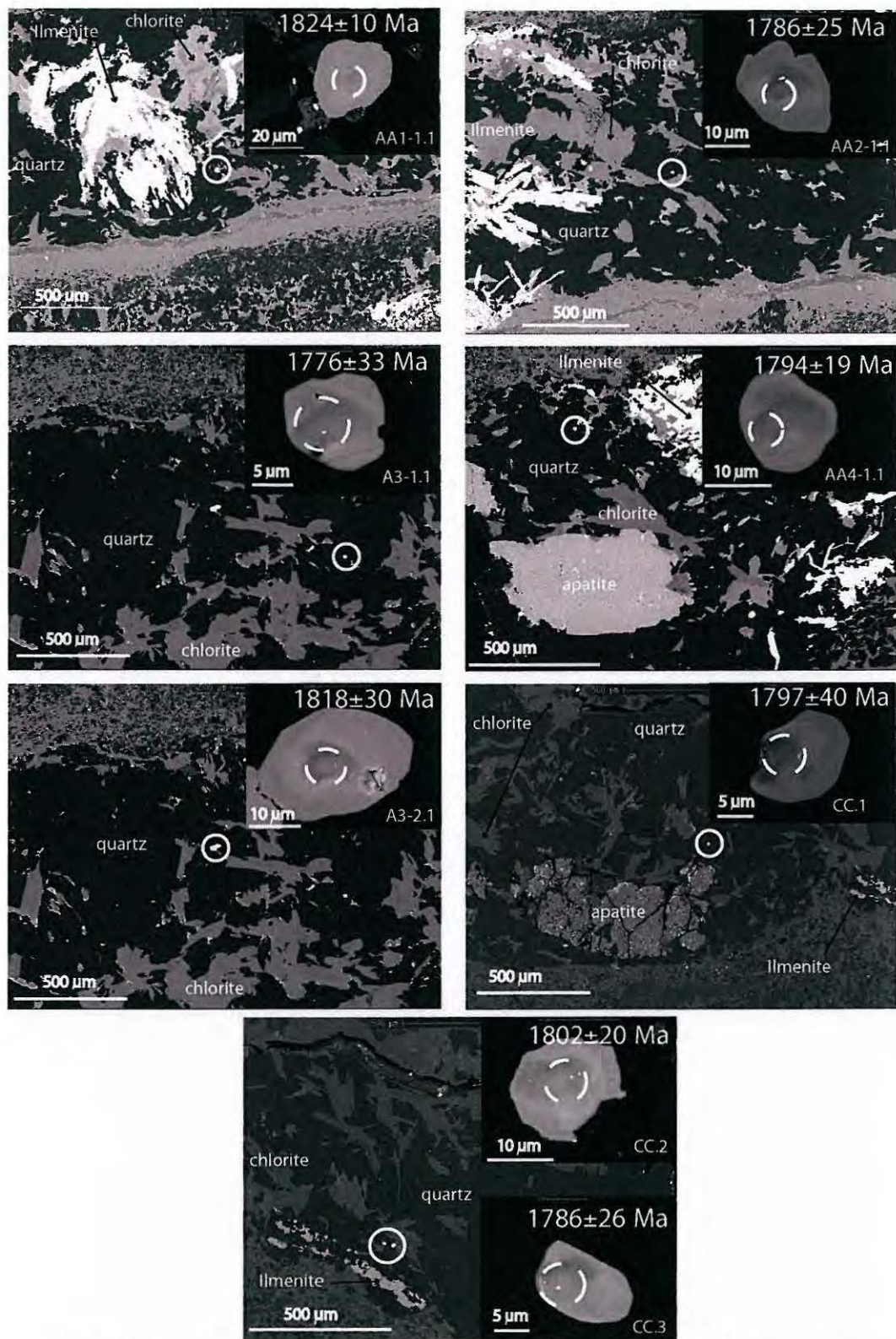
Fig. 5.3. Backscattered scanning electron microscope images (BSE) of ore-related hydrothermal xenotime from the Callie Au deposit (sample: DBD395D3, 899m). Images shown are of a ~1–2 mm wide quartz-chlorite-ilmenite-apatite-gold-(xenotime) vein. The textural setting for each xenotime and SHRIMP spot location is shown for all analyses. Ages are calculated from $^{207}Pb/^{206}Pb$ and uncertainties are 1σ.

5.4 The Coyote Au Deposit

The Coyote Au deposit has an estimated resource of 0.447 Moz of Au (Huston et al. 2007). It is located in Western Australia in the west of the Tanami region approximately 650 km north-west of Alice Springs. The geology and mineralisation at Coyote have recently been described by Bagas et al. (2007). This deposit lies under ~40 m of transported regolith and is hosted mainly in finer siltstone units of Killi Killi Formation. Mineralisation is hosted along the sheared southern limb of the D_1 Coyote anticline and is interpreted to have occurred during deformation associated with D_5 deformation (Bagas et al. 2007). Quartz veins at Coyote comprise pre-, syn- and post-ore types. Pre-ore quartz veins are layer parallel with chlorite and dolomite, are commonly located near anticlinal hinge zones and are interpreted by Bagas et al. (2007) to have formed during the regional D_1 deformation event. These veins are in turn cut by two types of syn-ore veins, a plannar auriferous type and a laminated quartz-chlorite one. Ore stage Au veins at Coyote consist of the assemblage quartz-chlorite-pyrite-(arsenopyrite-galena-sphalerite-xenotime) and are interpreted to be associated with granite-related metamorphic-metasomatic assemblages (Bagas et al. 2007).

An ore-stage quartz vein containing xenotime from the Coyote deposit was kindly supplied by Dr. Richard Armstrong (ANU) for SHRIMP U–Pb analysis. The sample consists of a thin section of a ~10 mm wide quartz-K-feldspar-biotite-apatite-pyrite-(xenotime-monazite) vein mounted in epoxy resin. The xenotime grains are euhedral to anhedral, equant, pale green and are ~20–40 μm in diameter (Fig. 5.4). No xenotime was observed in the wall rock.
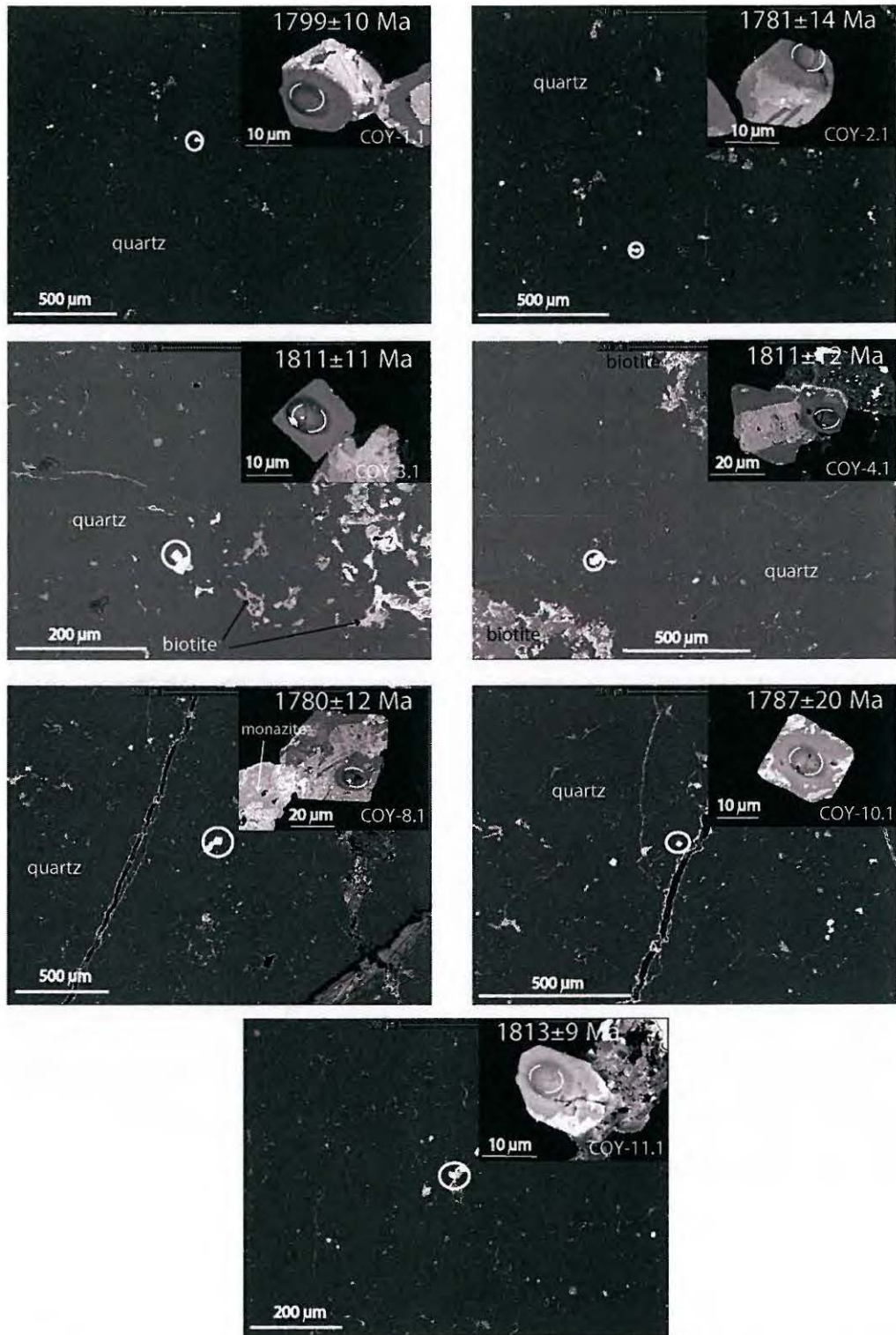
Fig. 5.4. BSE images of ore-related xenotime from the Coyote Au deposit. Images shown are of a ~10 mm wide quartz-biotite-apatite-pyrite-(xenotime-monazite) vein. The textural setting for each xenotime and SHRIMP spot location for each analysis included in the pooled age calculation is shown. Ages are calculated from [207]Pb/[206]Pb and uncertainties are 1σ. Brighter regions on the xenotime crystals themselves and in the thin section are due to a residual SHRIMP Au coating. Cracking of the thin section within the epoxy resin permitted only a light cleaning of the sample prior to further Au coating and post SHRIMP SEM imaging.

5.5 Analytical methods

The analytical conditions and xenotime U–Pb matrix corrections under which the xenotime SHRIMP U–Pb data and electron microprobe analyses were undertaken and processed follow those described in Chapter 3. Xenotime from the Callie and Coyote deposits were analysed in separate SHRIMP RG sessions. For these sessions, a primary O$^-$ beam was focussed through a 30 µm Kohler aperture which produced a ~7 µm spot. Xenotime from Coyote was analysed using a primary beam current of ~0.9 nA in late December 2006, whereas xenotime from the Callie deposit was analysed with an ~0.7 nA primary beam in February 2007. For both of these SHRIMP sessions the primary calibration standard MG1 and secondary calibration standards Z6413 and BS1 were analysed concurrently from a separate mount. Xenotime crystals from the Callie and Coyote deposits were identified and imaged using a Cambridge 360 scanning electron microscope located at the ANU electron microscopy unit.

5.6 Results

5.6.1   Electron Probe

Electron microprobe (WDS) analyses of eight Callie xenotime crystals from DBD395D3 show them to be similar in composition (Table 5.1a). U and Th concentrations are low and average ~400 ppm for U and ~200-300 ppm Th. Th/U ratios are also typically low and have an average ratio of ~0.5 (Table 5.2a). The REE concentrations are elevated compared to the typical levels observed in xenotime (see Table 2.1, Chapter 2). Relatively high concentrations of Gd, Dy, Er and Yb contribute to a $\sum REE_2O_3$ of ~24 wt%, which is approximately 10 wt% higher than that measured in the primary calibration standard MG1. The nine xenotime grains analysed by WDS from the Coyote deposit also have generally similar compositions (Table 5.1b). U concentration is much higher than that observed in the Callie xenotime, with an average of ~2500 ppm. Th concentrations are generally below the detection limit (< 150 ppm). The relatively high U and very low Th levels in the Coyote xenotime result in Th/U of ~0.05 which is an order of magnitude lower than that measured in the Callie xenotime (Table 5.2b). Relative to the Callie xenotime, the Coyote crystals have lower concentrations of Gd, Dy, Er and Yb, which are the main components of

173

the $\sum REE_2O_3$ which is ~19 wt%. This is ~4 wt% higher than that in the primary xenotime calibration standard MG1.

Table 5.1a. Electron microprobe (WDS) analyses of hydrothermal xenotime from the Callie Au deposit.

oxide wt%	A3.1	A3.2.1	AA1.1	AA2.2	AA4.4	CC.1	CC.2	CC.3
SiO2	0.23	0.12	0.18	0.14	0.26	0.24	0.16	0.27
CaO	0.02	0.01	0.02	0.01	0.02	0.03	0.03	0.03
P2O5	32.49	32.36	32.27	32.76	32.43	32.57	32.11	32.66
Y2O3	37.53	37.25	40.74	39.72	37.05	38.34	36.88	38.42
Nd2O3	0.18	0.13	0.05	0.05	0.18	0.12	0.16	0.14
Sm2O3	0.59	0.63	0.13	0.17	0.90	0.44	0.60	0.46
Eu2O3	0.48	0.52	0.05	0.06	0.59	0.44	0.49	0.44
Gd2O3	3.11	3.41	0.92	2.37	4.36	2.98	3.21	2.67
Tb2O3	0.77	0.77	0.13	0.49	0.89	0.70	0.34	0.47
Dy2O3	7.14	7.50	4.84	7.11	7.74	7.36	7.20	7.11
Ho2O3	1.57	1.61	1.50	1.74	1.60	1.60	1.60	1.64
Er2O3	4.25	4.16	5.02	4.47	3.89	4.40	4.26	4.46
Tm2O3	0.84	0.79	0.94	0.79	0.76	0.83	0.82	0.85
Yb2O3	4.27	4.05	5.95	3.83	3.47	4.36	4.15	4.54
Lu2O3	1.10	1.12	1.38	0.97	0.96	1.13	1.13	1.16
ThO2	0.01	0.01	0.05	0.02	0.07	0.01	0.02	0.01
U2O3	0.03	0.02	0.05	0.04	0.08	0.03	0.02	0.03
ΣREE	24.29	24.69	20.89	22.07	25.34	24.35	23.96	23.94
Total	94.67	94.59	94.41	95.06	95.34	95.69	93.72	95.75

Table 5.1b. Electron microprobe (WDS) analyses of hydrothermal xenotime from the Coyote Au deposit.

oxide wt%	COY-1.1	COY-3.1	COY-4.1	COY-7.1	COY-10.1	COY-11.1	COY-2.1	COY-8.1	COY-9.1
SiO2	0.91	0.59	0.52	0.59	0.81	0.37	0.28	0.30	0.42
CaO	0.02	0.02	0.02	0.03	0.02	0.02	0.24	0.02	0.00
P2O5	34.40	33.80	33.76	34.69	33.51	34.45	34.01	34.02	33.64
Y2O3	42.94	43.19	42.12	43.31	41.56	42.85	42.61	42.20	41.65
Nd2O3	0.15	0.36	0.37	0.17	0.69	0.14	0.14	0.25	0.18
Sm2O3	0.52	0.64	0.63	0.50	0.95	0.52	0.47	0.62	0.57
Eu2O3	0.58	0.39	0.33	0.58	0.62	0.55	0.49	0.67	0.58
Gd2O3	2.69	2.46	2.38	2.65	3.01	2.68	2.53	2.90	2.75
Tb2O3	0.60	0.51	0.35	0.55	0.60	0.60	0.59	0.63	0.59
Dy2O3	5.63	5.52	5.35	5.59	5.61	5.63	5.67	5.70	5.71
Ho2O3	1.27	1.22	1.23	1.23	1.20	1.33	1.26	1.18	1.30
Er2O3	3.59	3.53	3.61	3.45	3.29	3.56	3.61	3.44	3.58
Tm2O3	0.62	0.62	0.67	0.62	0.68	0.63	0.64	0.63	0.64
Yb2O3	2.88	2.58	3.07	2.67	2.79	2.83	2.86	2.80	2.93
Lu2O3	0.87	0.73	0.82	0.80	0.83	0.87	0.83	0.88	0.83
ThO2	0.02	<0.01	<0.01	0.01	<0.01	0.02	<0.01	0.01	<0.01
U2O3	0.30	0.07	0.11	0.36	0.20	0.32	0.11	0.52	0.38
ΣREE	19.40	18.56	18.82	18.80	20.27	19.35	19.07	19.69	19.66
Total	98.06	96.31	95.57	97.93	96.49	97.52	96.34	96.88	95.85

The Callie and Coyote xenotimes have similar chondrite normalised REE profiles (Fig. 5.5). Both samples show a steep rise from Nd to Gd and a flat transition to Lu. There is only a very minor negative Eu anomaly seen in two of the Callie xenotime grains, all other crystals show a smooth transition through to Lu. For comparison, chondrite normalised REE profiles of two igneous xenotime samples (Z6413 and XTC) show a distinctive negative Eu anomaly, a characteristic typical for igneous derived xenotime which reflects feldspar fractionation of the source rocks (Kositcin et al. 2003; Förster 1998). The REE profiles for the Callie and Coyote xenotime do not support an igneous origin but are more typical of those observed for hydrothermal or diagenetic xenotime (see Kositcin et al. 2003; Rasmussen 2005).
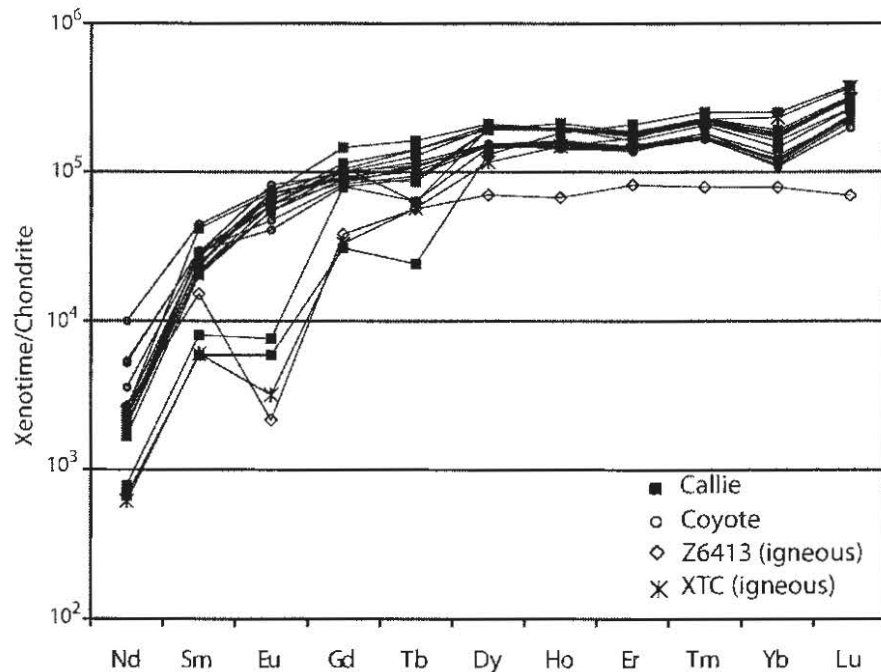
Fig. 5.5. Chondrite normalised REE patterns of xenotime from the Callie and Coyote Au deposits. REE patterns of two igneous xenotime SHRIMP standards (Z6413 and XTC) are shown for comparison. Chondrite data from Boynton (1984). XTC data is from Kositcin et al. (2003).

5.6.2 SHRIMP U–Pb Results

Eight SHRIMP RG analyses were carried out on eight xenotime crystals from Callie sample DBD395D3 (Fig. 5.6, Table 5.2a.). These crystals have concordant to slightly discordant compositions that are interpreted to reflect recent Pb-loss. All analyses are less than 10% discordant and combine to yield a weighted mean $^{207}Pb/^{206}Pb$ age of

1809 ± 13 Ma (95% confidence, MSWD = 0.85). This age determination is well within error of the previous age estimate for this sample by Cross et al. (2005) of 1803 ± 19 Ma.
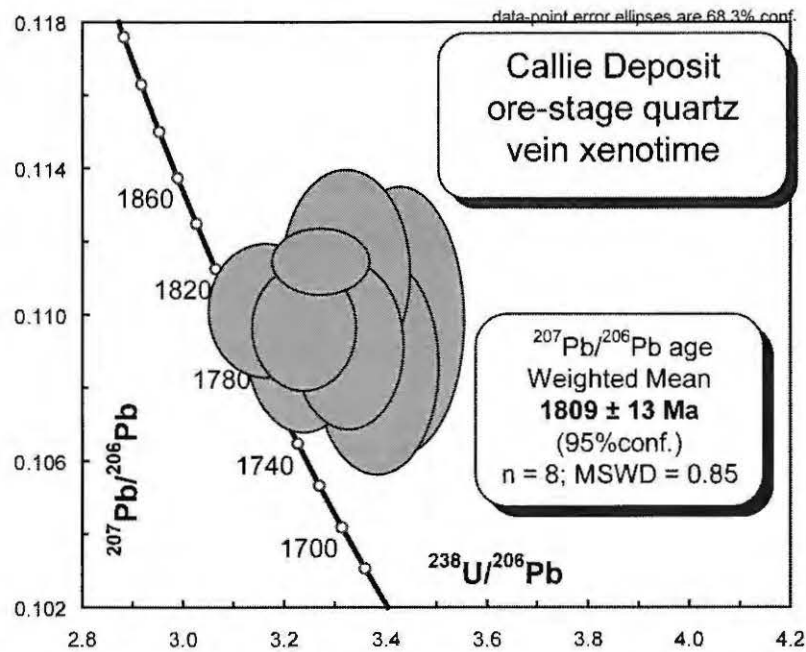
Fig. 5.6. Concordia plot of SHRIMP RG U–Pb xenotime analyses from the Callie Au deposit.

SHRIMP RG data for the Coyote sample consists of nine analyses on nine crystals (Fig. 5.7 and Table 5.2b.). The xenotime has generally concordant to near concordant compositions, however one analysis is more than 10% discordant and is not included in the pooled age calculation. The remaining eight analyses combine to yield a weighted mean $^{207}Pb/^{206}Pb$ age of 1800 ± 8 Ma (95% confidence, MSWD = 1.2). This age measurement is identical within error to the previous $^{207}Pb/^{206}Pb$ age measured for this sample of 1791 ± 8 Ma reported in Bagas et al. (2007).
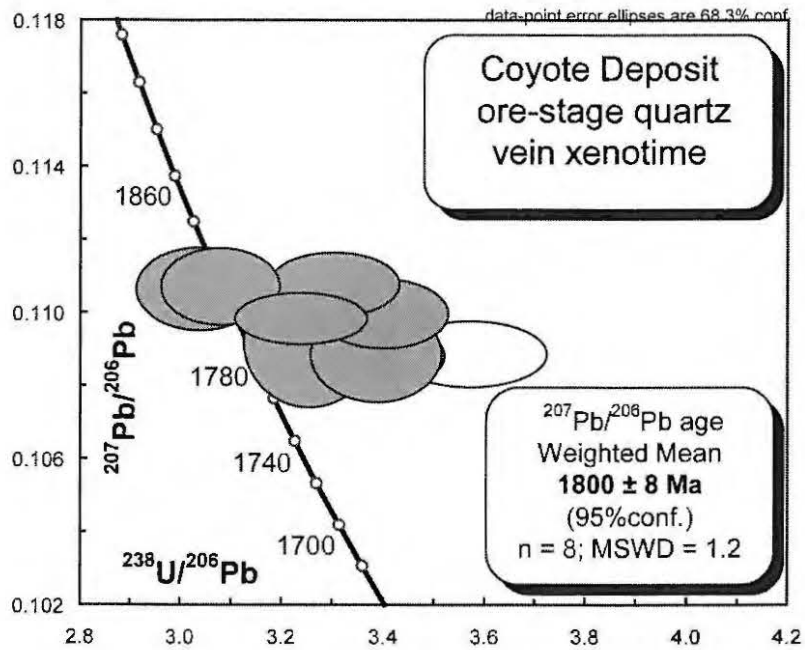
Fig. 5.7. Concordia plot of SHRIMP RG U–Pb xenotime analyses from the Coyote Au deposit.

5.7 Discussion

Convincing textural and chemical criteria strongly support a hydrothermal origin for the Callie and Coyote xenotime analysed in this study. Texturally the xenotime grains are confined within Au-stage quartz veins. For the Callie xenotime found in sample DBD395D3, Williams (2007) cites strong arguments for its hydrothermal origins, including a close association with vein apatite, ilmenite and Au (typical for Au-bearing veins at Callie) as well as the absence of xenotime in the wall rocks. The xenotimes from both deposits also have chemical signatures that point toward a hydrothermal origin. Typical chemical features of hydrothermal xenotime include low concentrations of U and Th, Th/U ratios generally < ~0.5 and the absence of an Eu anomaly (Kositcin et al. 2003; Rasmussen 2005). The chemical properties of the Callie xenotime seen in Tables 5.1a and 5.2a and Figure 5.5 are consistent with a hydrothermal origin for these crystals. The relatively high concentration of U (~2500 ppm) in the Coyote xenotime is the highest yet recorded for hydrothermal xenotime reported in the literature. Regardless of the relatively high U concentration for this xenotime, the extremely low Th/U ratio (~0.05) and absence of a negative Eu anomaly are chemical indicators suggestive of a hydrothermal origin for these grains. Considered together, the textural setting and chemical characteristics for both the Callie and Coyote xenotime strongly suggest that they are hydrothermal in origin.

Table 5.2a. SHRIMP U-Pb isotopic data for hydrothermal xenotime from the Callie Au deposit.

Spot name	U (wt%) (WDS)	ΣREE (wt%) (WDS)	Th/U (SHRIMP)	% Comm ^{206}Pb	^{206}Pb/^{238}U (± 1σ %)		^{207}Pb/^{206}Pb (± 1σ %)		^{206}Pb/^{238}U age (Ma ± 1σ)		^{207}Pb/^{206}Pb (Ma ± 1σ)		Discordance %
A3-1.1	0.0232	21.24	0.48	0.33	0.2968	2.39	0.1086	1.80	1675	40	1776	33	6
A3-2.1	0.0178	21.59	0.43	0.31	0.3023	2.52	0.1111	1.67	1703	43	1818	30	7
AA1-1.1	0.0444	18.28	2.00	0.05	0.3069	1.93	0.1115	0.53	1725	33	1824	10	6
AA2-1.1	0.0386	19.28	0.71	0.21	0.3017	2.15	0.1092	1.38	1700	37	1786	25	5
AA4-1.1	0.0682	22.15	0.40	0.19	0.3099	2.09	0.1097	1.03	1740	36	1794	19	3
CC.1	0.0278	21.29	0.38	0.30	0.2928	2.48	0.1099	2.19	1656	41	1797	40	9
CC.2	0.0195	20.95	0.42	-0.06	0.3174	2.36	0.1101	1.09	1777	42	1802	20	1
CC.3	0.0263	20.94	0.45	0.19	0.3101	2.29	0.1092	1.43	1741	40	1786	26	3

Table 5.2b. SHRIMP U-Pb isotopic data for hydrothermal xenotime from the Coyote Au deposit.

Spot name	U (wt%) (WDS)	ΣREE (wt%) (WDS)	Th/U (SHRIMP)	% Comm ^{206}Pb	^{206}Pb/^{238}U (± 1σ %)		^{207}Pb/^{206}Pb (± 1σ %)		^{206}Pb/^{238}U age (Ma ± 1σ)		^{207}Pb/^{206}Pb (Ma ± 1σ)		Discordance %
COY-1.1	0.2698	16.97	0.02	0.01	0.2943	2.49	0.1100	0.57	1663	41	1799	10	8
COY-3.1	0.0628	16.23	0.08	0.01	0.3249	2.52	0.1107	0.62	1814	46	1811	11	0
COY-4.1	0.0994	16.46	0.03	0.01	0.3294	2.78	0.1107	0.67	1836	51	1811	12	-1
COY-10.1	0.1809	17.74	0.08	0.01	0.3075	2.62	0.1092	1.08	1728	45	1787	20	3
COY-11.1	0.2950	16.92	0.05	0.00	0.3029	2.56	0.1108	0.52	1706	44	1813	9	6
COY-2.1	0.1009	16.68	0.06	0.01	0.2954	2.49	0.1089	0.79	1668	42	1781	14	7
COY-8.1	0.4757	17.22	0.02	0.01	0.3009	3.89	0.1088	0.65	1696	66	1780	12	5
discordant													
COY-7.1	0.3230	16.44	0.02	0.00	0.2801	2.80	0.1089	0.55	1592	45	1781	10	12

The SHRIMP $^{207}Pb/^{206}Pb$ xenotime age determinations reported here are considered to likely represent the ages of their host Au-stage veins and by inference the age of mineralisation in these two deposits. The new and preferred age of mineralisation for the Callie deposit is 1809 ± 13 Ma, whereas the preferred age of mineralisation for the Coyote deposit is 1800 ± 8 Ma.

Considered together these ages constrain the D_5 mineralising event in the Tanami region to between ~1.82 and ~1.79 Ga, coincident with the main period of granite intrusion. A broadly similar age is also inferred for mineralisation at the Tanami Goldfields which is also associated with D_5 structures. The ages presented here support the suggestion made by Scrimgeour (2006) that the ~1.81–1.79 Ga Stafford event is principally responsible for lode-Au mineralisation in the Tanami. The determination of the timing of the D_1–M_1 event is yet to be firmly established. The Granites deposit is interpreted by Adams et al. (2007) to have formed during D_1–M_1. This deposit has not been dated radiometrically, however a possible candidate mineral for this task at The Granites deposit is titanite, which was identified by Scrimgeour and Sandiford (1993) in the alteration assemblages of ore stage veins. The results of this study confirm a strong temporal and spatial link between granite generation and mineralisation in the Tanami Region.

5.7.1   Lode-Au mineralisation in the Pine Creek Orogen

The application of SIMS U–Pb dating of hydrothermal phosphate has achieved particular success in constraining the timing of lode-Au mineralisation in many parts of the world (Pigois et al. 2003; Sener et al. 2005; Salier et al. 2004; Salier et al. 2005; Brown et al. 2002; Rasmussen et al. 2006; Cross et al. 2005). These age determinations are able to be used in both local and regional exploration and ore genesis models. As described above, a convincing spatial and temporal link between granite generation and Au mineralisation occurring between ~1.81 and 1.79 Ga, exists in the Tanami region. However, in the Pine Creek Orogen (PCO) to the north of the Tanami region, a spatial and temporal relationship between significant Au mineralisation and Palaeoproterozoic granites that has been proposed in a number of studies (see below), has been questioned in recent years. Sener et al. (2005) and Rasmussen et al. (2006), based on the results of SHRIMP U—Pb analyses of

hydrothermal monazite and xenotime from mineralised PCO Au systems, have argued that Au mineralisation in this region is significantly younger than the local granites and therefore not temporally related. With the aim of investigating the possibility of a regional temporal link between Au mineralisation across northern Australia, the SHRIMP U—Pb monazite analyses presented in Sener et al. (2005) were reinvestigated and compared with the SHRIMP U—Pb measurements of xenotime from the Callie and Coyote deposits.

5.7.2   Generalised Geology of the Pine Creek Orogen

The central domain of the PCO consists of variably deformed and intruded Palaeoproterozoic metasedimentary rocks and metavolcanics that have been deposited on a rifted late Archaean granitic basement. Recent geochronology has constrained two periods of Palaeoproterozoic sedimentation, an early phase which probably ceased between ~2.02–2.05 Ga, and following a hiatus of ~160 m.y., a later period of sedimentation at about 1.86 Ga (Worden 2006). Between 1.86 and 1.85 Ga, rocks of the PCO were deformed and underwent low-grade regional metamorphism during the Nimbuwah event (Stuart-Smith et al. 1993; Worden 2006). This was closely followed by an extensional event characterised by felsic volcanism and the intrusion of voluminous, post orogenic granites of the Cullen Batholith. The Cullen Batholith is spatially associated with significant Au and base metal mineralisation; it consists predominantly of fractionated I–type granitic rocks exposed over an area of approximately 3,300 km^2 (Fig. 5.8). Crystallisation ages for granites of the Cullen Batholith range from ~1.84 to ~1.80 Ga (Stuart–Smith et al. 1993).

Gold deposits in the Cullen mineral field have been interpreted to have resulted from the interplay between structure, host rock and degree of fractionation of the nearby granites (Budd et al. 2001). For example, Budd et al. (2001) suggested that Au, Ag, Pb, Cu, Sn, W and Fe mineralisation appear to be associated with fractionated leucogranites. By contrast, the Saunders suite is the least fractionated of the Cullen batholith and is unmineralised (Budd et al. 2001). Attesting to the close spatial association between mineralisation and granite emplacement are the Au deposits of Goodall, Cosmopolitan Howley, Enterprise, Mount Todd and Golden Dyke, which all occur in the contact aureole of the Cullen Batholith. Field relationships, structural

investigations, geochemical and stable isotope studies of Au mineralisation in the Cullen Mineral field suggest that mineralisation was synchronous with emplacement of the Cullen Batholith (Sheppard 1996; Matthai 1995; Stuart-Smith et al. 1993; Ewers and Scott 1977; Wall and Taylor 1990; Budd et al. 2001; Wygralak and Ahmad 1990).
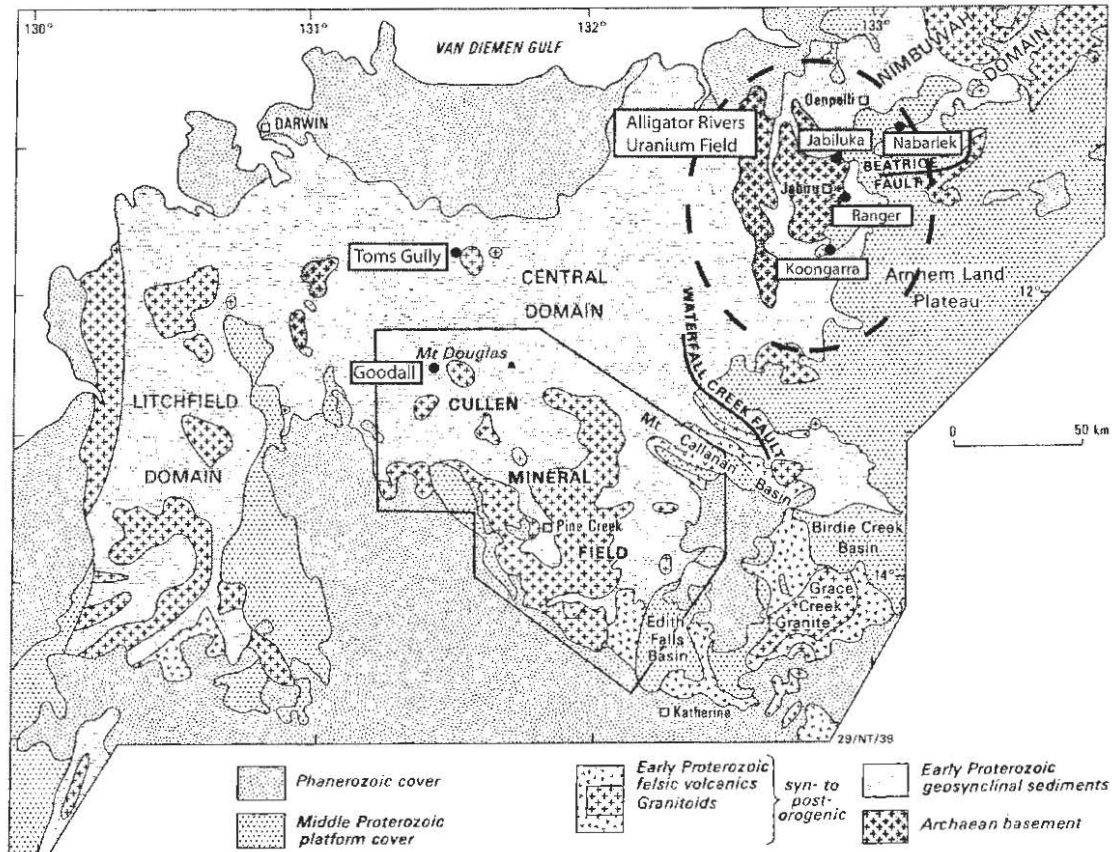
Fig. 5.8. Generalised regional geology map of the Pine Creek Orogen showing the location of the Cullen Mineral Field and Alligator Rivers Uranium Field (after Stuart-Smith et al. 1993).

U–Pb isotopic evidence in support of the strong temporal link between the Cullen granites and Au mineralisation was provided by Compston & Matthai (1994) who reported a $^{207}Pb/^{206}Pb$ age of 1810 ± 10 Ma from SHRIMP U–Pb analyses of xenotime and monazite sampled from auriferous veins from the Goodall Au deposit. This age linked Au mineralisation at the Cullen Mineral Field with the younger phases of the Cullen Batholith. However, more recently Sener et al. (2005) reported a SHRIMP $^{207}Pb/^{206}Pb$ age of 1727 ± 13 Ma from ore-related monazite also sampled from the Goodall deposit, almost ~100 m.y. younger than the younger Cullen

Batholith granites. Rasmussen et al. (2006) reinterpreted the SHRIMP data of Sener et al. (2005), suggesting that mineralisation at the Goodall deposit was related to an older generation of sixteen monazite crystals that were analysed by Sener et al. (2005) but not included in their age calculation. The sixteen older SHRIMP monazite analyses give a weighted mean $^{207}Pb/^{206}Pb$ age of 1776 ± 13 Ma, which was interpreted by Rasmussen et al. (2006) to better represent the age of mineralisation at this deposit. Rasmussen et al. (2006) also reported a similar SHRIMP $^{207}Pb/^{206}Pb$ age of 1780 ± 10 Ma for monazite from the Toms Gully Au mine, located ~50 km to the north of the Cullen mineral field (Fig. 5.8). These ~1.78 Ga age interpretations led Rasmussen et al. (2006) to conclude that hydrothermal Au mineralisation in the PCO was not temporally related to the intrusion of granites, but more likely related to a younger period of minor magmatism, deformation and metamorphism associated with the Shoebridge event which affected rocks across the PCO and adjacent Litchfield province at ~1.78 Ga (Stuart-Smith et al. 1993).

Surprisingly, neither Sener et al. (2005) nor Rasmussen et al. (2006) gave reasons as to why the previous age interpretation of Compston & Matthai (1994) of 1810 ± 10 Ma should be superseded by their significantly younger age interpretations. Indeed, my reinterpretation of all of the SHRIMP monazite data presented for the Goodall deposit by Sener et al. (2005) suggests an age that approximates the original ~1.81 Ga age interpretation of Compston & Matthai (1994). The SHRIMP analyses of monazite from the Goodall deposit presented in Table 1 of Sener et al. (2005) (see Appendix 5.2) were re-examined as a part of this study to properly assess the differences in age interpretations between the results of Compston & Matthai (1994) and those of Rasmussen et al. (2006) and Sener et al. (2005) and thereby establish whether a temporal link exists between mineralisation and the emplacement of the Cullen Batholith. All of the SHRIMP monazite analyses presented in Table 1 of Sener et al. (2005) (excluding two crystals, H.1-3 and H.1-4 which have very high common Pb contents between 5 and 9% common ^{206}Pb) form a moderately well defined discordance line (MSWD = 2.5, n=44). This can be improved by rejecting two of the most discordant analyses (H.2-6 and H.5.1), the oldest and most imprecise analysis (H.2-2, 1909 ± 101 Ma) and the youngest concordant analysis (H.5-4, 1593 ± 37 Ma); no further rejections are justified. The remaining 40 SHRIMP analyses form a moderately well defined discordance line with an MSWD of 1.6, which is slightly

greater than the upper 95% confidence interval for this number of points (Fig. 5.9). This discordance trend does however indicate an upper intercept at 1822 ± 37 Ma which is consistent with the ~1810 ± 10 Ma age of mineralisation at the Goodall deposit reported by Compston & Matthai (1994). The lower intercept shown on Fig. (5.9) has an imprecise intercept age of 780 ± 140 Ma. This age corresponds to a late period of U mineralisation between ~800–950 Ma, recorded in all of the major U deposits of the Alligator Rivers Uranium Field, located approximately 100–150 km north-east of the Cullen Mineral Field. (Gulson & Mizon 1980; Polito et al. 2005; Hills & Richards 1976). Furthermore, it is also within error of a ~760 Ma population of SHRIMP U–Pb xenotime analyses from the Molyhil scheelite–molybdenite skarn, located approximately 1000 km south of the PCO in the northeast Arunta Region (see Chapter 6).
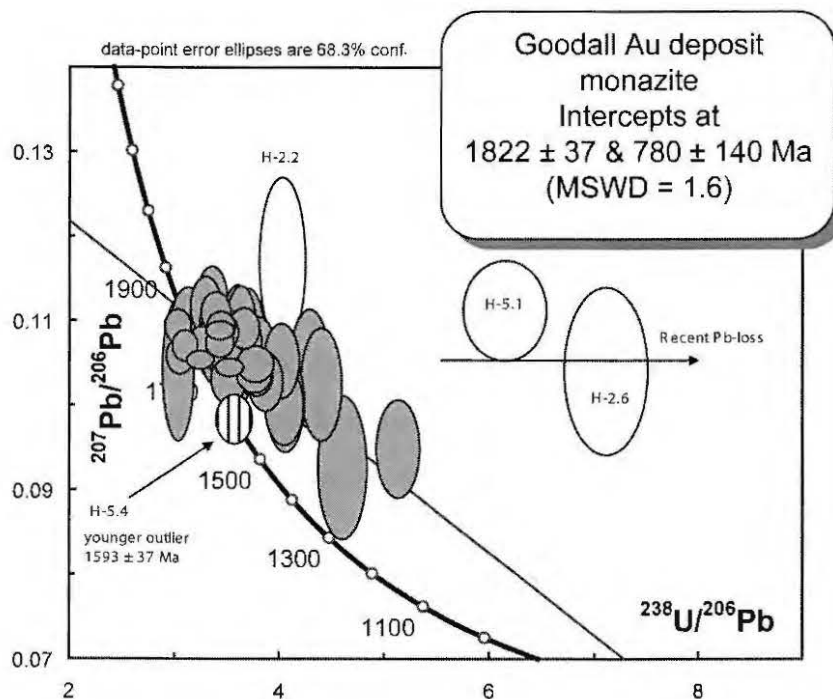
Fig. 5.9. Concordia plot of SHRIMP monazite analyses for the Goodall Au deposit reported by Sener et al. (2005).

The SHRIMP U–Pb monazite age interpretations of Sener et al. (2005) and Rasmussen et al. (2006) for the timing of mineralisation at the Goodall deposit of ~1.73 Ga and ~1.77 Ga respectively, are interpreted here to more likely represent monazite compositions that have experienced a period of ancient Pb-loss. Therefore,

individual $^{207}Pb/^{206}Pb$ determinations from these crystals cannot be used to establish original crystallisation ages. Collectively the data of Sener et al. (2005) support an earlier age interpretation for this deposit of 1810 ± 10 Ma, reported in Compston & Matthai (1994). This age supports a temporal link between the emplacement of the youngest phases of the Cullen Batholith and mineralisation at the Goodall Au deposit. However, the SHRIMP U–Pb monazite age of 1780 ± 10 Ma by Rasmussen et al. (2006) for the timing of mineralisation at the Toms Gully Au deposit, does not appear to be temporally associated with Cullen Batholith granites. This implies that there may be two phases of Au mineralisation in the central PCO, an early phase related to the intrusion of the Cullen Batholith and a latter phase associated with the ~1.78 Ga Shoebridge event. Further work is needed to establish whether these two mineralisation events can be associated with particular structures or regions throughout the central PCO.

The period between ~1.81 and ~1.78 Ga marks a period of significant Au mineralisation in the Tanami Region and PCO. Additionally, similarly aged minor occurrences of VAMS and lOCG style mineralisation occur in the Aileron Province, central Australia (Hussey et al. 2006) and as minor Ag–Pb veins in the Tennant Creek Province, central Australia (D. Huston pers. comm.). These data imply that a major widespread mineralising event occurred across much of the NAC between about 1.81 to 1.79 Ga. This event may be related to convergent tectonics that occurred along the southern margin of the North Australia Craton, where Scrimgeour (2006) suggested a north–dipping subduction system was active from ~1.81 to ~1.69 Ga.

5.8 Conclusions

In the Tanami Region, SHRIMP U–Pb xenotime ages constrain the timing of Au mineralisation at the Callie deposit to 1809 ± 13 Ma and at the Coyote deposit to 1800 ± 8 Ma. These ages coincide with the main phase of granite intrusion between ~1.82 and 1.79 Ga and by inference, also constrain the timing of D_5 structures associated with significant Au mineralisation at the Callie deposit (Smith et al. 1998), Coyote deposit (Bagas et al. 2007) and at the Tanami Goldfields (Adams et al. 2007). This time period is coincident with the ~1.81-1.79 Ga Stafford event which may be linked

to a long–lived, north–dipping subduction system active at the south-east margin of the NAC (Scrimgeour 2006).

Re-interpretation of SHRIMP U–Pb monazite data for the Goodall Au deposit, PCO presented in Sener et al. (2005) supports a previously reported SHRIMP monazite-xenotime $^{207}Pb/^{206}Pb$ age for this deposit of 1810 ± 10 Ma by Compston & Matthai (1994). This age coincides with the intrusion age of the youngest phases of the Cullen Batholith and demonstrates a temporal link between the two events. This finding in part contradicts a suggestion made by Rasmussen et al. (2006) that Au mineralisation in the PCO is not temporally associated with granite emplacement. An age interpretation of ~1.78 Ga for the Toms Gully Au deposit by Rasmussen et al. (2006) suggests that there may be two stages of Au mineralisation in the PCO, an early phase associated with the emplacement of the Cullen Batholith and a younger event associated with the ~1.78 Ga Shoebridge event. The SHRIMP $^{207}Pb/^{206}Pb$ xenotime ages reported here for the timing of mineralisation in the Tanami Region and also the age for mineralisation reported for the Goodall deposit by Compston & Matthai (1994) confirm the temporal link between the significant Au mineralisation in these two regions and granite intrusion. These results also show that the time period between ~1.81 to ~1.79 Ga marks a period of mineralisation widespread across much of the NAC.

6. SHRIMP U—Pb XENOTIME AND RE-OS MOLYBDENITE DATING OF THE MOLYHIL SKARN, NORTHERN AUSTRALIA.

6.1 Introduction

The Eastern Arunta region has a complex, prolonged and polyphase history extending from the Palaeoproterozoic to the mid-Palaeozoic (Mawby et al. 1999; Hand et al. 1999; Buick et al. 2005; Scrimgeour & Raith 2001; Huston et al. 2006). Mineral deposits in this region are typically small but cover a diverse range including lode-Au, VHMS, carbonate replacement Zn–Cu, Cu–Au (IOCG), skarn W–(Mo–Cu-Au) as well as the industrial minerals vermiculite and garnet (Huston et al. 2006). Establishing which time periods are the most favourable for mineralisation in this complex region is of fundamental importance in the exploration for mineral resources. The Molyhil scheelite-molybdenite skarn is the largest intrusion-related deposit in the Eatern Arunta region (Huston et al. 2006). Located in the northern margins of the East Arunta (north-east Arunta) (Fig. 6.1), it has previously been mined for W and Mo during the 1970's and early 1980's.

This study was primarily designed as a geochronological investigation and undertaken to test the accuracy of the SHRIMP U—Pb xenotime matrix correction procedures developed in Chapter 3 of this thesis. To do this, molybdemite separated from mineralised skarn was sent to the University of Alberta and analysed for Re-Os by Dr. Robert Creaser. These results would then allow a comparison to be made between the dates obtained from the Re-Os analysis of molybdenite and SHRIMP U—Pb analysis of xenotime. Additionally, it was also hoped that this study would provide preliminary isotopic constraints for the timing of mineralisation at the Molyhil Skarn.

187
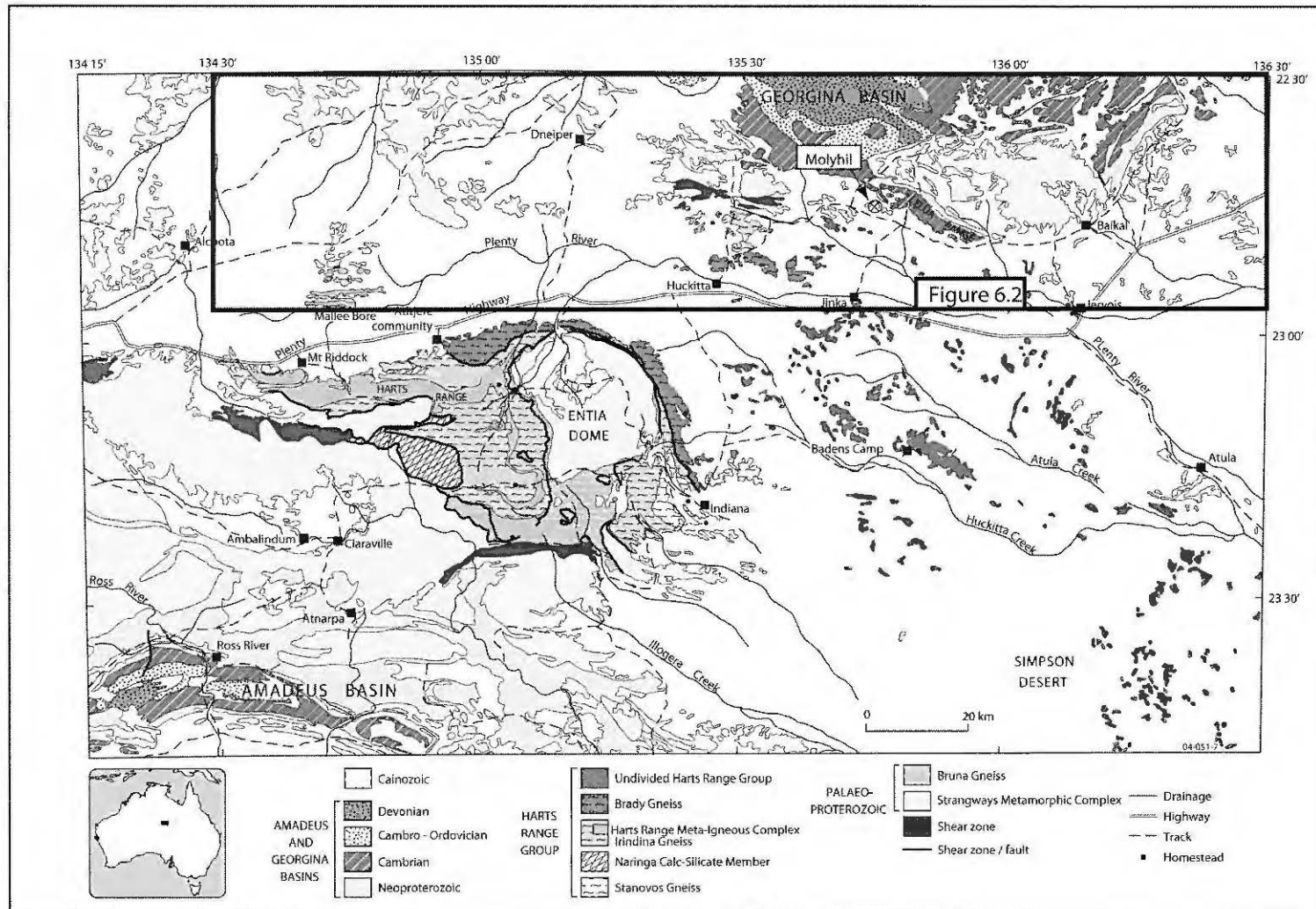
Fig. 6.1. Generalised geology map of the East Arunta region. Also shown is the northeast Arunta region as shown in Fig. 6.2 together with the location of the Molyhil W-Mo skarn deposit, adapted from Maidment (2005).

6.2 Regional Geology

The north-east Arunta area consists of Palaeoproterozoic to early Palaeozoic rocks which have undergone periods of magmatism, metamorphism and deformation from the Proterozoic to the Late Devonian (Scrimgeour & Raith 2001). It is unconformably overlain by Neoproterozoic to Palaeozoic sedimentary rocks of the Georgina and Amadeus Basins to the north and south-east Arunta, respectively. The principal terranes of the north-east Arunta region consist of: Palaeoproterozoic high grade (upper amphibolite to granulite facies) rocks of the Strangways Metamorphic Complex (Kanandra Granulite), the informally named Jinka region, consisting of Palaeoproterozoic amphibolite to granulite facies metasedimentary rocks that have been intruded by Palaeoproterozoic granites (Scrimgeour & Raith 2001), and the Palaeozoic amphibolite to granulite facies metasedimentary rocks of the Harts Range Group. These terranes are separated by two major west trending shear zones. In the south of the region, the Entire Point Shear Zone (EPSZ) partitions rocks of the Harts Range Group from the Kanandra Granulite, and the Delny Shear Zone (DSZ) separates the Kanandra Granulite from the northern Jinka region rocks (Fig. 6.2).
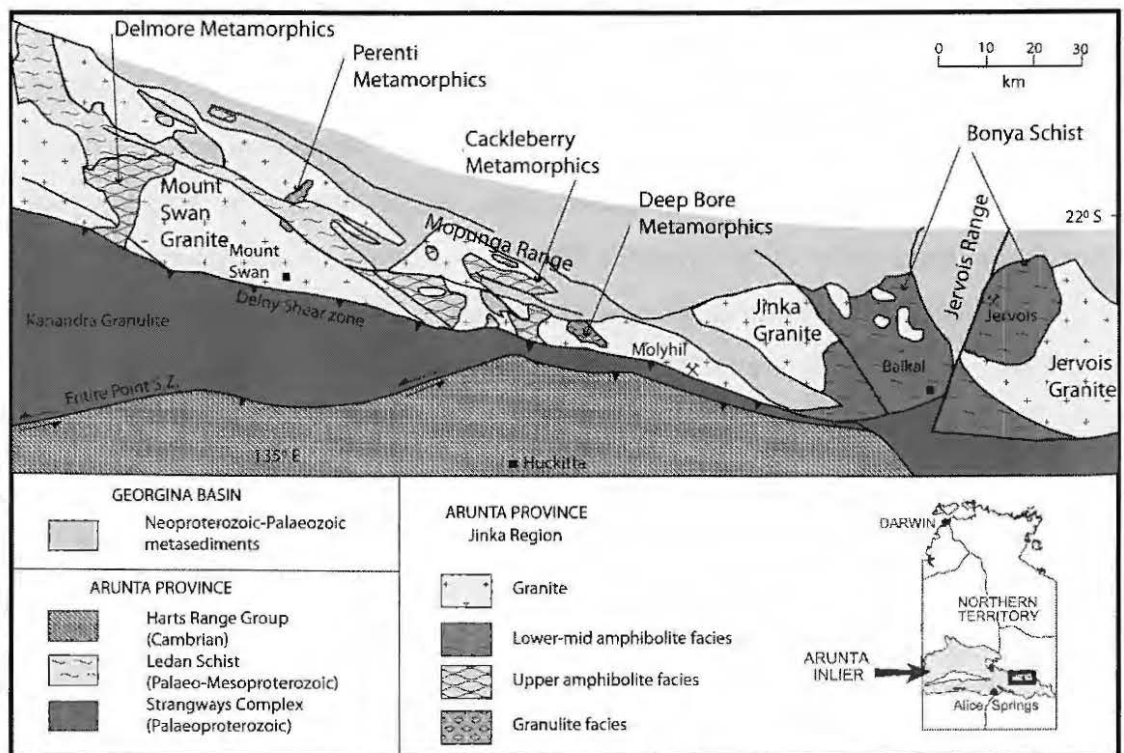
Fig. 6.2. Generalised solid geology map of the north-east Arunta region, adapted from Scrimgeour & Raith (2001).

The Kanandra Granulite outcrops south of the Mopunga Range region and north of Huckitta (Fig. 6.2). It is a part of the Strangways Metamorphic Complex which principally occurs in the Strangways and Harts Ranges (Shaw & Warren 1975). The Kanandra Granulite forms a 150-200 km west trending belt of intermittently outcropping pelitic granulite, mafic granulite, garnet biotite migmatite, with rare calc-silicates and small ultramafic units (Scrimgeour & Raith 2001). Rocks of the Strangways Metamorphic Complex experienced high grade metamorphism (upper amphibolite to granulite) and granite intrusion during two Palaeoproterozoic Orogenies. These events consisted of two cycles of burial and exhumation, termed the Yambah Event (~1.78–1.77 Ga) and Strangways Event (~1.73–1.71 Ga) that Maidment et al. (2005) suggested took place in a broadly convergent setting at the southern margin of the North Australia Craton (NAC). Granite intrusion during the Yambah Event was widespread across the Arunta region (Zhao & Bennett 1995) and, on geochemical grounds, interpreted by Zhao & McCulloch (1995) to be related to subduction. Strangways plutonism was also widespread and occurred across much of the northern Arunta and also the southern Davenport province.

The informally named Jinka region of Scrimgeour & Raith (2001) is a narrow (5–25 km) belt of low-pressure amphibolite to granulite facies metasedimentary rocks that have been intruded by granites and extend for over 100 km from the Perenti Metamorphics in the west to the Jervois region in the east (Scrimgeour & Raith 2001) (Fig. 6.2). Metamorphic units in the central Jinka region outcrop in the Mopunga Range region and consist of the granulite facies felsic granulites and gneisses of the Perenti and Deep Bore Metamorphics and the amphibolite facies metapelite and amphibolite of the Cackleberry Metamorphics (Freeman 1986; Scrimgeour & Raith 2001). Further to the west, lower amphibolite facies schists of the Ledan Schist unconformably overlie upper greenschist to lower amphibolite facies rocks of the Delmore Metamorphics (Freeman 1986; Scrimgeour & Raith 2001). The amphibolite facies Bonya Schist outcrops in the east of the Jinka region at Bonya Hills and east of the Jervois Range. This unit consists mostly of schist, amphibolite, calc-silicates and quartzite (Freeman 1986). The Jinka region is dominated by granitic intrusive rocks that were intruded during the Yambah and Strangways events. SHRIMP U–Pb zircon dating by Zhao & Bennett (1995) has constrained the Dneiper and Mount Swan Granites of the central Jinka region to have crystallised at 1762 ± 14 Ma and 1713 ± 7

190

Ma respectively, whereas the Jervois granite in the east of the region has an age of 1771 ± 6 Ma.

The oldest rocks in the north-east Arunta were the sedimentary and volcanic protoliths of the Deep Bore Metamorphics, Cackleberry Metamorphics and the Kanandra Granulite. SHRIMP U–Pb dating of zircons from the Deep Bore Metamorphics and Kanandra Granulite defines a maximum deposition age of ~1.80 Ga (Scrimgeour & Raith 2001). These units were intruded by granites during the ~1.78–1.77 Ga, Yambah Event. The subsequent ~1.73–1.71 Ga, Strangways Event resulted in granulite to amphibolite facies metamorphism, deformation and granite intrusion throughout the region. This event is recorded by the intrusion of the Mount Swan Granite and SHRIMP U–Pb zircon ages of ~1.73–1.72 Ga that are interpreted to record metamorphism in the Deep Bore Metamorphics and Kanandra Granulite (Scrimgeour & Raith 2001).

Harts Range Group lithologies in the Huckitta area are similar to those observed elsewhere in the Eastern Arunta and are dominated by migmatitic metapelite, metabasite, garnet–biotite gneiss and lesser calc-silicate, marble and quartzite (Scrimgeour & Raith 2001). The protoliths of these units were deposited during a period of extension and associated mafic magmatism during the early Cambrian (~520–500 Ma) into the Irindina sub-basin (Buick et al. 2005). These rocks later underwent granulite facies metamorphism which peaked at >800°C, 8–12 kbar during the ~480–460 Ma, Larapinta Event (Mawby et al. 1999; Hand et al. 1999; Buick et al. 2001).

A period of protracted exhumation and metamorphism during the intracratonic Alice Springs Orogeny between ~450 and 300 Ma, affected much of central Australia (Collins & Shaw 1995). The earliest expression of this Orogeny may have occurred in the Harts Range region where at about 450 Ma the tectonic regime switched from extension to compression, which resulted in southward directed thrusting in the Harts Range (Mawby et al. 1999). During this time sinistral transpression along the EPSZ, resulting in the juxtaposition of the Harts Range Group and Kanandra Granulite is interpreted to have occurred at 445 ± 5 Ma, as recorded by SHRIMP U–Pb monazite dating of an EPSZ mylonite (Scrimgeour & Raith 2001). Later during the Alice

Springs Orogeny between ~400 and 360 Ma, north-vergent movement associated with the DSZ initially resulted in mid amphibolite metamorphism and later, exhumation and cooling of the Harts Range Group and Kanandra Granulite (Scrimgeour & Raith 2001). Carboniferous felsic magmatism and high grade metamorphism at about 330 Ma recorded in the Harts Range region to the south (Hand et al. 1999; Maidment et al. 2005) does not appear to have affected rocks in the north-east Arunta region (Scrimgeour & Raith 2001).

6.3 The Molyhil Skarn deposit

The Molyhil scheelite-molybdenite skarn is located ~225 km north-east of Alice Springs within the informally named Jinka region of Scrimgeour & Raith (2001) at lat. 22°45' S, long. 135°45' E, on the Huckitta 1:250 000 sheet and is ~1 km north of the DSZ and ~5km north of the EPSZ (Fig. 6.2). Additionally, north-west trending splay faults associated with the DSZ occur north of the deposit (Freeman 1990). Mining at Molyhil between 1974 and 1976 produced 20,000 tonnes of ore that yielded 100 tonnes of concentrate at 70% WO_3 (Freeman 1990). Thor Mining PLC has more recently defined a JORC-compliant mineral resource at Molyhil of 2.4 Mt at 0.54% WO_3 and 0.26% MoS_2. It is interpreted to have developed from hydrothermal fluids associated with the intrusion of the Marshall Granite and contains typical features normally associated with skarn-type mineralisation including a common association of minerals, close spatial association with a large plutonic body and the presence of receptive calcareous host rocks (Barraclough 1979).

Mineralisation at Molyhil occurs in two adjacent orebodies, termed the Yacht Club and Southern orebodies (Fig. 6.3). These orebodies occur in skarn that formed within rafts of metasediment in the Marshall Granite (Freeman 1990; Shaw et al. 1984). The leucogranite in the pit has two distinct alteration assemblages. Along the southern walls is a chlorite altered biotite granite, described as a "green granite", whereas on the north and western walls it is described as a K-feldspar altered pink granite (Huston et al. 2006).

Three types of metasomatic rocks were defined at the Molyhil deposit by Barraclough (1979). These are endoskarn, unmineralised calc-silicate exoskarns and ore-zone calc-

silicate exoskarns. The endoskarn is grey, coarse grained, often foliated and is dominated by K-feldspar and hornblende, with variable concentrations of quartz, calcite, biotite, molybdenite, magnetite and scheelite (Barraclough 1979; Huston et al. 2006). Unmineralised calc-silicate exoskarn separates granitoid rocks from the mineralised ore-zone calc-silicate exoskarn. It has been catagorised by Barraclough (1979) as either a "banded" or "mixed" type. The banded variety consists of alternating diopside and garnet rich bands with accessory garnet, quartz, biotite, and epidote. Additionally, this unit contains minor magnetite, pyrite and rare molybdenite and scheelite (Barraclough 1979; Huston et al. 2006). By comparison, the mixed variety contains rare magnetite and sulfide, and is a mixture of garnet, pyroxene, epidote and calcite (Barraclough 1979). Ore-zone calc-silicate exoskarn is dark coloured and consists of magnetite, pyrite, pyroxene, garnet, amphibole, scheelite, molybdenite, chalcopyrite and quartz (Barraclough 1979; Huston et al. 2006).
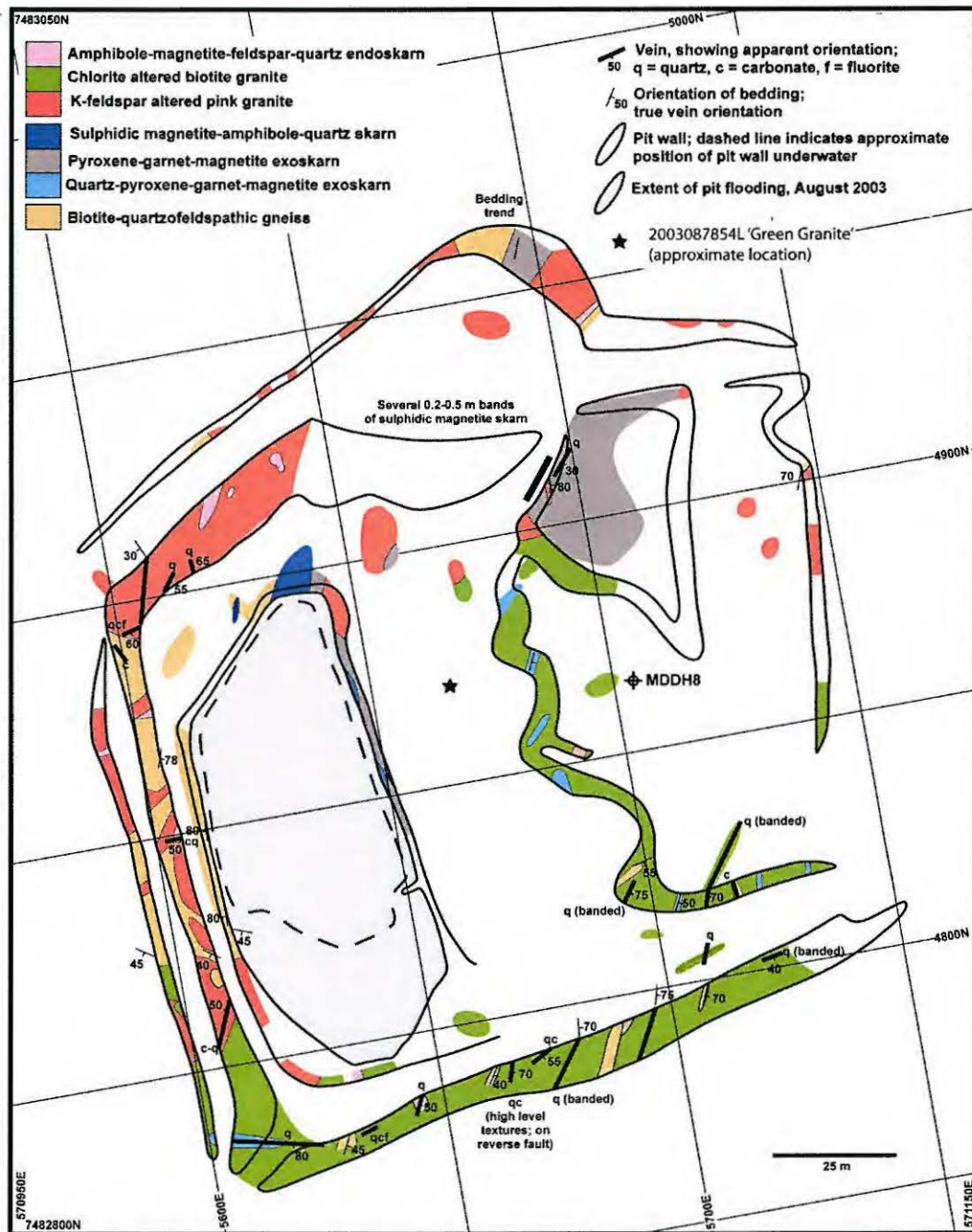
Fig. 6.3. Geological pit map of the Molyhil deposit, adapted from Huston et al. (2006). Map grid is AGD66.

Hornblende from exoskarn associated with the Molyhil deposit has an $^{40}Ar/Ar^{39}$ age of between ~1.72 and 1.70 Ga (G. Fraser, unpub. data; Geoscience Australia). This age is similar to the 1713 ± 7 Ma crystallisation age of the Mount Swan Granite (Zhao & Bennett 1995) which outcrops about 80 km to the west of the Molyhil skarn.

194

Rhenium—Osmium analyses of molybdenite from a sample of exoskarn as well as SHRIMP U—Pb xenotime analyses fom a sample of endoskarn were carried out as a preliminary step toward constraining the age of mineralisation at Molyhil. This dating exercise was undertaken with the assumption that the skarn mineralisation at molyhil has resulted from the same hydrothermal system over a relatively short time. The samples were supplied by David Huston (Geoscience Australia) and consist of a sample of endoskarn which is a chlorite altered xenotime bearing "green granite" and a sample of ore-zone exoskarn containing molybdenite. The exoskarn sample was collected from the Molyhil waste dump and is a magnetite-amphibole skarn rock. The sample consists of amphibole, magnetite, garnet, quartz, molybdenite and pyrite. The garnet is fine to medium grained (0.2 to 1.5 mm) and appears to be the earliest phase. Garnets are light brown, euhedral, strongly fractured and usually embayed. The embayments and fractures are commonly infilled with either quartz, magnetite or amphibole. Some of the garnets are completely or partially replaced by amphibole which occurs as fine to course grained aggregates (~0.1 to 6mm) and clearly post dates the garnet in the sample. The molybedentie is texturally the youngest phase. It is medium grained (~0.5 to ~3mm), homogenous, free of inclusions and occurs in veins intergrown with magnetite and lesser pyrite. In some cases magnetite is found entirely or partially replacing earlier formed amphibole.

Sample 2003087854L is a sample of intensely altered "green granite". It was sampled from diamond drill core of the Molyhil deposit (MDDH8, 85.5-85.9m). The sample consists of >95% of massive intergrown chloritised biotite up to ~2 mm in diameter with lesser sericite, actinolite and quartz. Accessory minerals include titanium oxide, zircon, xenotime, apatite, titanite and molybdenite. TiO_2 crystals (probably rutile or anatase) are up to ~70 μm in diameter and occur along the cleavage planes of the chlorite. Zircon is clearly identifiable in transmitted light by dark brown pleochroic haloes and xenotime occurs as overgrowths on zircon as well as single, irregular crystals (see below). Rare relict apatite and titanite crystals are irregular and embayed.

6.3.1   Xenotime description

Xenotime in sample 2003087854L occurs either as <1–20 μm overgrowths on euhedral zircon crystals or as single irregular crystals with a diameter of up to ~80

μm. Both the xenotime overgrowths and single crystals have internally slightly variable BSE responses, which appear as lighter and darker, patchy and streaked zones (see Fig. 6.4 and Fig. 6.6-MH3-8.1). The xenotime overgrowths either partially or more rarely wholly surround their zircon substrates. Nearly all overgrowths are variably cracked and embayed to some degree. Planar crystal margins when present are often very finely serrated. All are characterised by a pitted and/or porous surface texture, with some pits measuring up ~2 μm in diameter (Fig. 6.5 a-g). The majority of the single irregularly shaped xenotime crystals have embayed edges and also pitted/porous surface textures. One large grain (MH1-9.1, MH1-9.2, Fig. 6.6a) is intergrown with variably orientated TiO_2 laths. In one location irregular xenotime is in close association with relict apatite suggesting that some xenotime crystallisation may be associated with the dissolution of apatite (Fig. 6.6b). One small crystal appears to be texturally unique. This grain (MH3-8.2) has a uniform BSE response and does not have the pitted surface texture observed in other single xenotime grains and overgrowths in this sample. Interestingly, it is within ~50 μm of another single xenotime crystal that has a pitted surface texture and variable BSE response, typical for xenotime in this sample (Fig. 6.6b).
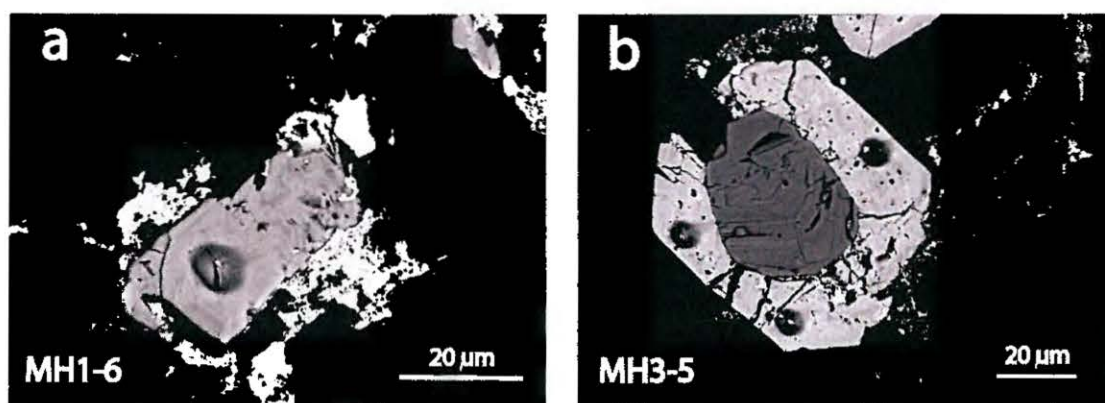
Fig. 6. 4. BSE images of an irregular shaped xenotime crystal (a) and a xenotime overgrowth on zircon (b). Note the slight variability in BSE response in both crystals which show patches and streaks of lighter and darker zones. Both xenotime grains also show a pitted surface texture. Brighter regions are due to residual SHRIMP Au-coating. Dark coloured ellipses are SHRIMP spot locations (see Fig. 6.5). Sample 2003087854L.

The association of the xenotime overgrowths with euhedral zircon crystals indicates that they post date crystallisation of what is likely to be magmatic zircon. Subsequent later periods of fluid dissolution have resulted in embayments and irregular crystal margins for both the xenotime overgrowths and single crystals. There is no apparent

textural setting which favours either the single xenotime crystals or xenotime overgrowths. Both types occur within the chlorite, sericite and quartz in the sample studied (Fig. 6.5 and 6.6). It is likely that the distribution of the xenotime overgrowths were governed by the location of the precursor magmatic zircon substrates and the discrete xenotime grains by the dissolution of apatite (see Fig. 6.6b).
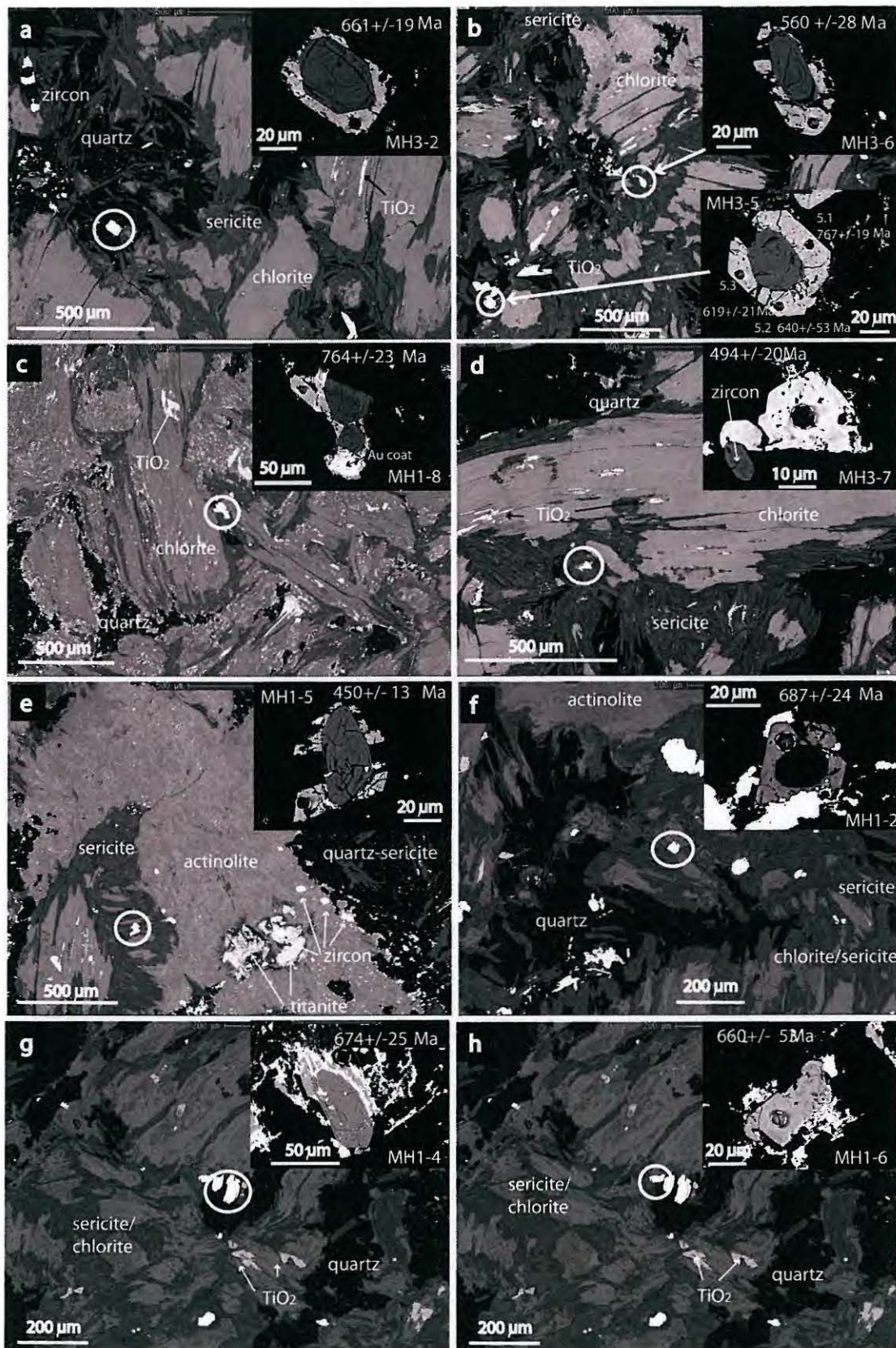
Fig. 6.5(a-h). BSEM images of xenotime overgrowths on zircon (a-g) and single xenotime crystal (h), with their textural settings. SHRIMP spot locations are shown as well as the $^{206}Pb/^{238}U$ ages and 1σ errors. Some of the brightest regions are caused by residual SHRIMP Au coat and is particularly evident in (g). Sample 2003087854L.

198
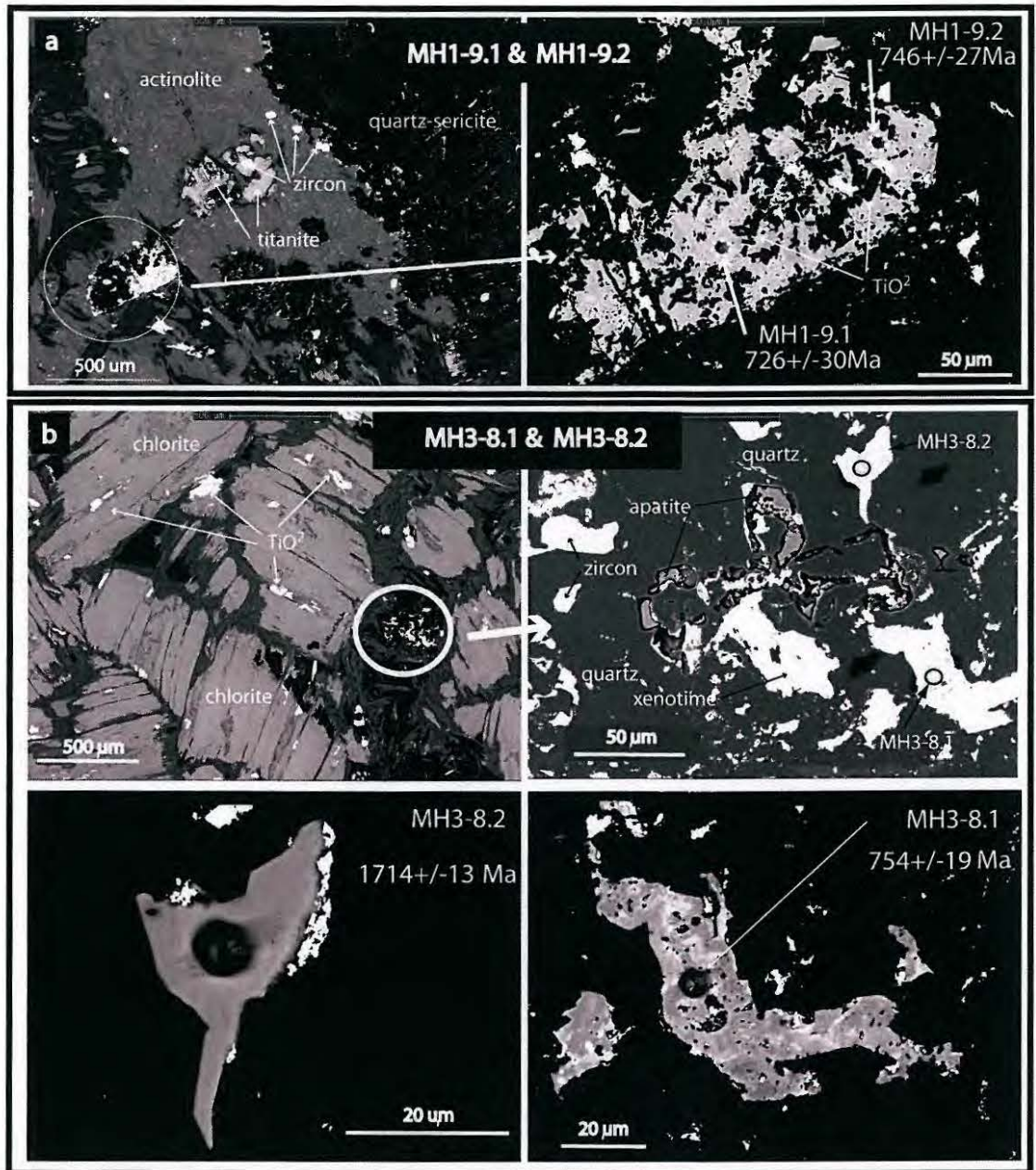
Fig. 6.6(a-b). BSEM images of single irregularly shaped xenotime crystals MH1-9 (a) and MH3-8 (b) with textural settings. SHRIMP spot locations are shown as well as the $^{206}Pb/^{238}U$ ages and 1σ errors for MH1-9.1, 9.2 and MH3-8.1, and $^{207}Pb/^{206}Pb$ age and 1σ error for MH3-8.2. The brightest regions are caused by residual SHRIMP Au coat. Sample 2003087854L.

6.4 Analytical Methods

The SHRIMP and electron microprobe analytical conditions and xenotime SHRIMP U–Pb matrix correction procedures are fully described in Chapter 3 of this thesis. The xenotime was analysed using SHRIMP RG, employing an O⁻ primary beam focussed through a 30 μm Kohler aperture which yielded a spot diameter of ~6 μm. A polished thin section from sample 2003087854L was cut into a number of sections and

mounted in epoxy resin within a standard sized 2.5 cm diameter SHRIMP mount. The primary calibration standard MG1 and secondary standards Z6413 and BS1 were analysed concurrently with the unknown sample from a separate mount. All mounts used during the SHRIMP analytical session were gold coated together. Electron microprobe (WDS) analyses were carried out on the unknown xenotime as well as the primary and secondary xenotime standards before SHRIMP analysis. Prior to the SHRIMP session, all xenotime were photographed in transmitted and reflected light and BSE imaged on a Cambridge 360 scanning electron microscope located at the ANU electron microscopy unit. Molybdenite analyses were carried out at the University of Alberta Radiogenic Isotope Facility by Dr. Robert Creaser. The molybdenite Re and Os concentrations were determined by isotope dilution mass spectrometry following the analytical protocols detailed in Selby and Creaser (2001; 2004). The ^{187}Re decay constant used was 1.666×10^{-11} yr^{-1} (Smoliar et al. 1996).

6.5 Results

6.5.1   Electron Microprobe (WDS)

WDS results for the Molyhil xenotime grains show them to have broadly similar compositions (Table 6.1). U_2O_3 concentrations range from ~700 to 3000 ppm with an average of ~1600 ppm, whereas ThO_2 levels range between ~1300 and 9000 ppm and have an average of ~4800 ppm. This results in Th/U > 1, which is uncommon in xenotime (Table 6.2). The HREE concentrations from Dy through to Lu are remarkably similar and only vary amongst these xenotime grains by about 5%. Of note also are the low to very low concentrations of Tb which range from <0.01 to ~3000 ppm Tb_2O_3. Total REE (oxide) concentrations average ~18.40 wt% which is ~2.5 wt% higher than that in the primary calibration standard MG1.

Chondrite normalised REE profiles for the Molyhil xenotime WDS analysis are generally similar and are plotted together with the pattern from igneous xenotime Z6413 for comparison (Fig. 6.7). Molyhil xenotime shows a gradual rise from Nd to Dy and flat profile from Dy to Lu. Significantly, these xenotime grains have a distinctive negative Eu anomaly, which is typical of igneous derived xenotime and reflects the incorporation of Eu^{2+} in plagioclase (Kositcin et al. 2003; Förster 1998).

Table 6.1. Electron microprobe (WDS) analyses for xenotime from the Molyhil deposit. Sample 2003087854L.

oxide wt %	MH1-1	MH1-2	MH1-3	MH1-4	MH1-5	MH1-6	MH1-8	MH1-9.1	MH1-9.2	MH3-1	MH3-2	MH3-3	MH3-5.1	MH3-5.2	MH3-5.3	MH3-6	MH3-7	MH3-8.1	MH3-8.2
SiO2	0.71	1.08	0.38	2.08	0.86	0.52	0.98	0.96	1.07	0.48	1.02	1.39	2.10	1.52	0.77	1.11	0.79	1.46	0.85
CaO	0.03	0.03	0.01	0.10	0.05	0.02	0.04	0.06	0.08	0.03	0.05	0.05	0.07	0.12	0.05	0.06	0.06	0.09	0.03
P2O5	34.00	32.96	34.52	30.44	32.51	32.25	32.24	31.24	31.63	31.88	30.68	29.89	32.01	32.40	33.09	32.01	33.91	30.29	33.11
Y2O3	43.55	43.41	43.42	38.41	43.69	41.97	41.13	42.20	41.39	43.25	40.83	40.54	41.16	43.58	41.73	41.90	41.84	39.78	41.78
Nd2O3	0.03	0.04	<0.01	0.09	0.09	0.02	0.10	0.08	0.17	<0.01	0.11	0.03	0.04	0.02	0.06	0.07	0.02	0.24	0.11
Sm2O3	0.20	0.23	0.26	0.20	0.25	0.23	0.28	0.20	0.46	0.20	0.25	0.22	0.19	0.17	0.17	0.23	0.24	0.63	0.34
Eu2O3	0.04	0.07	0.04	-0.01	0.15	0.01	0.09	0.05	0.17	0.05	0.10	0.03	0.02	0.08	0.05	0.05	0.04	0.22	0.10
Gd2O3	1.69	1.62	1.87	1.62	1.58	1.78	1.86	1.81	2.35	1.78	1.78	1.56	1.62	1.59	1.74	1.62	1.83	3.24	2.27
Tb2O3	<0.01	<0.01	<0.01	<0.01	<0.01	<0.01	0.06	0.23	0.46	<0.01	0.03	<0.01	<0.01	0.13	<0.01	0.23	<0.01	0.36	0.32
Dy2O3	5.81	5.76	5.80	5.42	5.18	5.87	5.95	5.94	6.07	6.06	5.85	5.62	5.17	5.44	5.71	5.78	6.04	6.65	5.60
Ho2O3	1.45	1.35	1.31	1.30	1.28	1.45	1.40	1.41	1.36	1.43	1.43	1.37	1.31	1.27	1.44	1.39	1.37	1.37	1.26
Er2O3	4.29	4.00	4.16	4.02	4.08	4.25	4.21	4.32	4.04	4.30	4.28	4.20	4.05	4.18	4.24	4.27	4.25	4.03	3.87
Tm2O3	0.51	0.48	0.50	0.49	0.50	0.52	0.49	0.52	0.53	0.52	0.54	0.51	0.49	0.52	0.49	0.52	0.51	0.55	0.48
Yb2O3	3.44	3.14	3.35	3.24	3.74	3.32	3.39	3.58	3.65	3.44	3.68	3.45	3.33	3.63	3.39	3.55	3.34	3.65	3.49
Lu2O3	0.95	0.88	0.97	0.92	1.05	0.99	0.95	0.95	1.03	0.93	0.96	0.92	0.99	0.98	0.93	1.00	0.95	1.09	0.97
ThO2	0.29	0.28	0.30	0.61	0.13	0.47	0.54	0.53	0.24	0.43	0.74	0.65	0.38	0.55	0.54	0.71	0.90	1.21	0.31
U2O3	0.16	0.20	0.07	0.17	0.21	0.15	0.14	0.19	0.20	0.10	0.15	0.15	0.11	0.18	0.13	0.16	0.11	0.37	0.27
ΣREE	18.41	17.56	18.27	17.28	17.90	18.45	18.77	19.09	20.30	19.25	19.01	17.90	17.20	18.01	18.20	18.70	18.60	22.05	18.84
Total	97.71	96.24	97.49	89.74	95.78	94.62	94.30	94.56	95.16	95.46	92.96	91.41	93.92	96.69	95.02	94.96	96.73	95.62	95.44

Spot name	U (wt%) (WDS)	ΣREE (wt%) (WDS)	Th/U (SHRIMP)	% Comm ^{206}Pb	^{206}Pb/^{238}U	($\pm 1\sigma$ %)	^{207}Pb/^{206}Pb	($\pm 1\sigma$ %)	^{207}Pb/^{206}Pb (Ma $\pm 1\sigma$)		^{206}Pb/^{238}U age (Ma $\pm 1\sigma$)		Discordance %
MH3-8.2	0.2454	16.46	1.31	0.05	0.2945	2.49	0.1050	0.73	1714	13	1664	41	3
MH3-5.1	0.1021	14.43	0.90	0.08	0.1263	2.49	0.0651	1.53	778	32	767	19	1
MH1-8	0.1292	16.41	2.09	0.07	0.1257	2.99	0.0651	2.14	778	45	764	23	2
MH3-8.1	0.3335	19.27	2.16	0.27	0.1241	2.52	0.0644	1.53	754	32	754	19	0
MH1-9.2	0.18	17.74	0.81	0.09	0.1227	3.65	0.0630	2.52	707	54	746	27	-5
MH1-9.1	0.1693	16.68	2.29	0.11	0.1193	4.14	0.0642	6.12	747	129	726	30	3
MH1-2	0.1823	14.98	2.85	0.39	0.1125	3.54	0.0622	3.84	682	82	687	24	-1
MH1-4	0.1515	14.91	2.45	0.90	0.1103	3.75	0.0581	7.39	533	162	674	25	-21
MH3-2	0.1372	16.62	4.57	0.48	0.1080	2.82	0.0618	5.86	667	125	661	19	1
MH1-6	0.1394	15.82	3.41	0.00	0.1078	7.97	0.0623	7.68	686	164	660	53	4
MH3-5.2	0.1605	15.75	3.78	0.45	0.1044	8.28	0.0599	12.05	600	261	640	53	-6
MH3-5.3	0.1212	15.81	3.48	0.20	0.1008	3.36	0.0602	2.40	611	52	619	21	-1
MH1-1	0.1462	15.95	2.22	0.03	0.0988	3.68	0.0633	3.11	717	66	607	22	18
Pb-loss													
MH3-6	0.142	16.35	5.43	0.37	0.0908	4.94	0.0583	5.53	539	121	560	28	-4
MH3-3	0.1328	15.20	5.59	1.84	0.0850	2.96	0.0498	8.79	185	205	526	16	-65
MH3-1	0.091	16.26	6.20	0.43	0.0836	3.07	0.0531	4.99	335	113	518	16	-35
MH3-7	0.1004	16.19	7.34	0.02	0.0797	4.03	0.0595	3.79	585	82	494	20	18
MH1-5	0.1876	15.60	2.82	1.57	0.0722	2.92	0.0563	7.44	466	165	450	13	4
MH1-3	0.0631	15.91	5.20	0.25	0.0647	4.74	0.0585	5.01	547	109	404	19	35

Table 6.2. SHRIMP U–Pb isotopic data for xenotime from the Molyhil deposit. Sample 2003087854L.
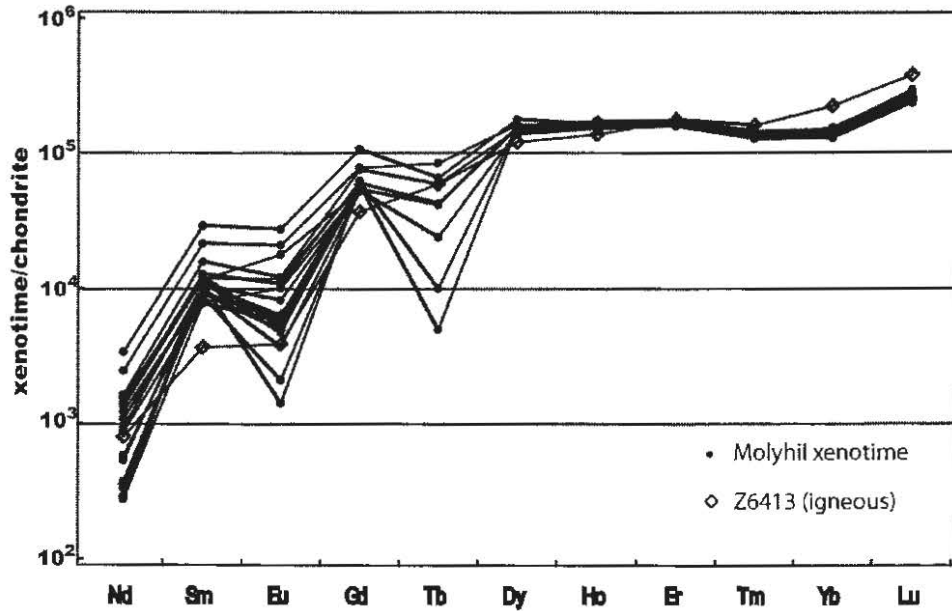
Fig. 6.7. Chondrite normalised REE patterns of xenotime from the Molyhil altered green granite sample 2003087854L. REE pattern for igneous derived xenotime standard Z6413 is shown for comparison. Chondrite data from Boynton (1984).

6.5.2 Molybdenite Re–Os results

The molybdenite analysis of the ore-zone skarn rock gave a ^{187}Re–^{187}Os model age of 1720.7 ± 5.9 Ma (95 % confidence, Table 6.3).

Table 6.3. Results of Re–Os analysis of molybdenite.

sample	Sample weight (milligrams)	Re (ppm)	^{187}Re (ppb)	^{187}Os (ppb)	Model Age (Ma)	Age uncertainty (2s)	Age uncertainty with 0.31% decay constant uncertaint'
Molybdenite (ore-zone skarn)	0.04286	13.45	8.455	245.9	1720.7	5.9	8

203

6.5.3 SHRIMP U–Pb Results

Nineteen SHRIMP U–Pb xenotime analyses were undertaken on Molyhil sample 2003087854L (Fig. 6.8, Table 6.2). U–Pb isotopic compositions in this sample range over ~1.20 Ga. The oldest grain (MH3-8.2) has a $^{207}Pb/^{206}Pb$ age of 1714 ± 26 Ma (2σ). There are also two significantly younger xenotime groupings with $^{206}Pb/^{238}U$ ages at ~760 Ma and ~650 Ma, as well as six individual grains at ~560 Ma, 525 Ma, 520 Ma, 490 Ma, 450 Ma and 405 Ma. The oldest xenotime grouping consists of five analyses which combine to give an age of 755 ± 20 Ma (95% confidence, MSWD = 0.39). The ~650 Ma grouping is made up of seven analyses which all contribute to an age of 648 ± 29 Ma (95% confidence, MSWD = 1.6).
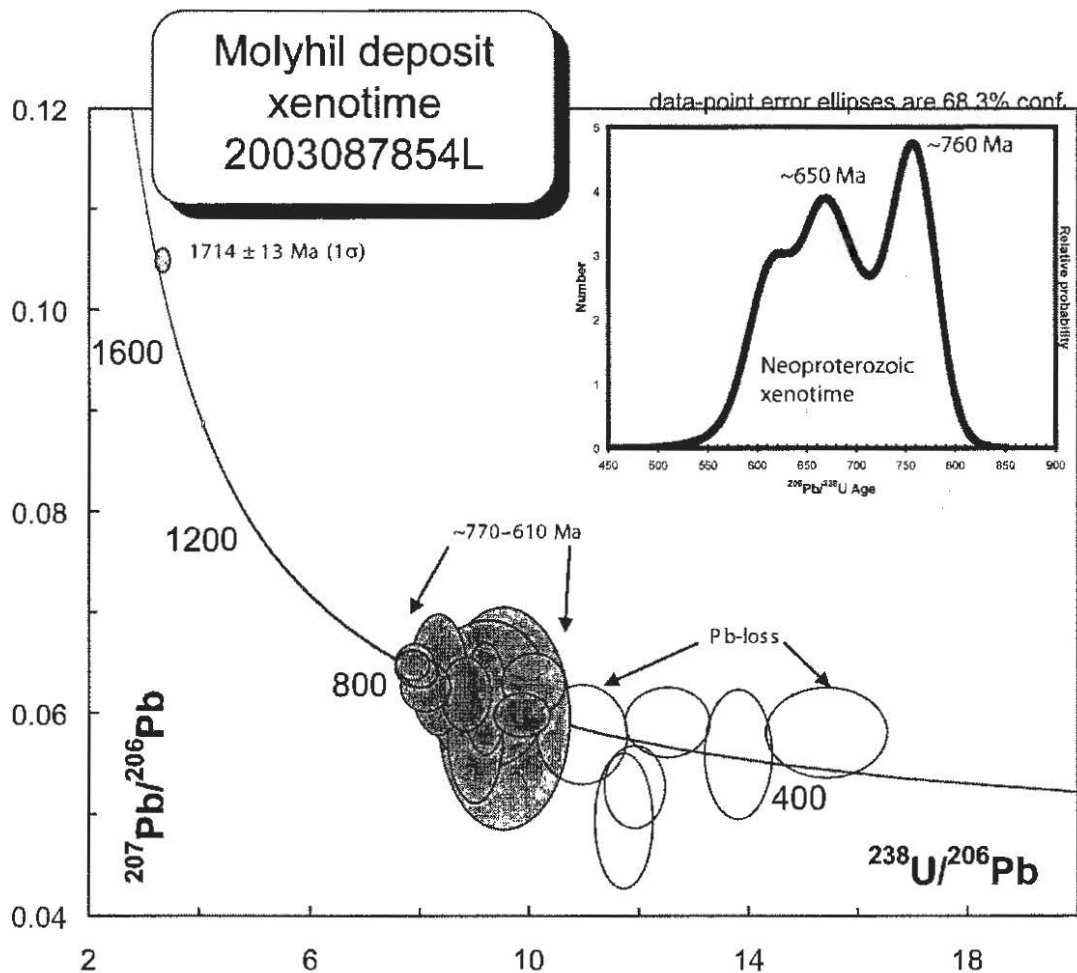
Fig. 6.8. Concordia plot for SHRIMP RG U–Pb xenotime analyses for the Molyhil green granite sample 2003087854L. Unfilled ellipses are interpreted to have undergone Pb-loss. Also shown is a probability density distribution plot of the Neoproterozoic U—Pb xenotime analyses.

6.6 Discussion

Rhenium-Osmium analysis of molybdenite from ore-zone exoskarn constrain the formation of the Molyhil skarn to have occurred at 1720.7 ± 5.9 Ma. This age is similar to an ^{40}Ar/Ar^{39} age of between ~1.72 and 1.70 Ga measured on hornblende from mineralised exoskarn (G. Fraser, unpub. Data; Geoscience Australia) and also the age of the oldest SHRIMP U–Pb dated xenotime, 1714 ± 26 Ma (2σ) (MH3-8.2). However, the U—Pb isotopes, chemistry and textures of xenotime in the sample (2003087854L) also show that this deposit has probably experienced two younger tectonothermal events which have caused xenotime dissolution and reprecipitation during the Neoproterozoic. The six individual xenotime grains between ~560 and ~405 Ma are interpreted to have experienced partial Pb-loss in a response to for example, the ~450 to 300 Ma Alice Springs Orogeny.

Experimental and U–Pb isotopic studies have shown xenotime to be very resistant to diffusive Pb loss. Closure temperatures for xenotime appear to be similar to those for zircon and monazite (Cherniak 2006). U–Pb studies of natural xenotime also support this. Xenotime interpreted to be diagenetic in origin from metasedimentary rocks of the Palaeoproterozoic Mount Barren Group in south Western Australia, record diagenesis at 1.7 Ga despite having undergone amphibolite grade metamorphism at ~1.20 Ga (Dawson et al. 2003). However, studies by Rainbird et al. (2006) and this study (Chapter 4) show that like monazite and zircon, xenotime can also undergo Pb-loss. Therefore, caution is warranted when interpreting U—Pb xenotime systematics especially with Phanerozoic samples where imprecise ^{207}Pb/^{206}Pb determinations make assessments of U–Pb concordance ambiguous. It is for this reason that the interpretation of the SHRIMP xenotime ^{206}Pb/^{238}U ages in this sample is weighted in favour of the xenotime age clusters over individual xenotime ^{206}Pb/^{238}U age measurements.

There is seemingly no relationship between xenotime type, textural setting and xenotime U–Pb ages in sample 2003087854L. Both the ~760 Ma and ~650 Ma xenotime occurs as both zircon outgrowths and distinct crystals associated with either quartz, sericite or chlorite. Interestingly the oldest xenotime analysed (MH3-8.2, ~1.71 Ga) is located ~50 μm from another irregularly shaped crystal (MH3-8.1) that

is about one billion years younger. Both are situated within quartz with nearby relict apatite (Fig. 6.6b). Additionally, the chemical compositions of these two xenotime crystals are very similar, indeed both share near identical chondrite normalised REE patterns (Fig. 6.9). However, these two xenotime grains are texturally distinguishable. Xenotime MH3-8.2 has a smooth surface texture and uniform BSE response, whereas MH3-8.1 has a pitted surface texture and variable BSE response which is similar to all other xenotime analysed from this sample (see Figs. 6.6 and 6.5). The textural contrast between the oldest xenotime (MH3-8.2) and other younger xenotime in this sample is intriguing and may provide clues as to the origins of xenotime MH3-8.2. It may be that xenotime MH3-8.2 is magmatic in origin and crystallised as a part of the Marshall Granite prior to skarn development. By contrast, the younger xenotime in this sample is likely to be associated with compositionally different fluids which co-precipitated xenotime as well as other alteration minerals such as quartz that have subsequently been plucked during preparation of the polished thin section and have resulted in their pitted surface textures.
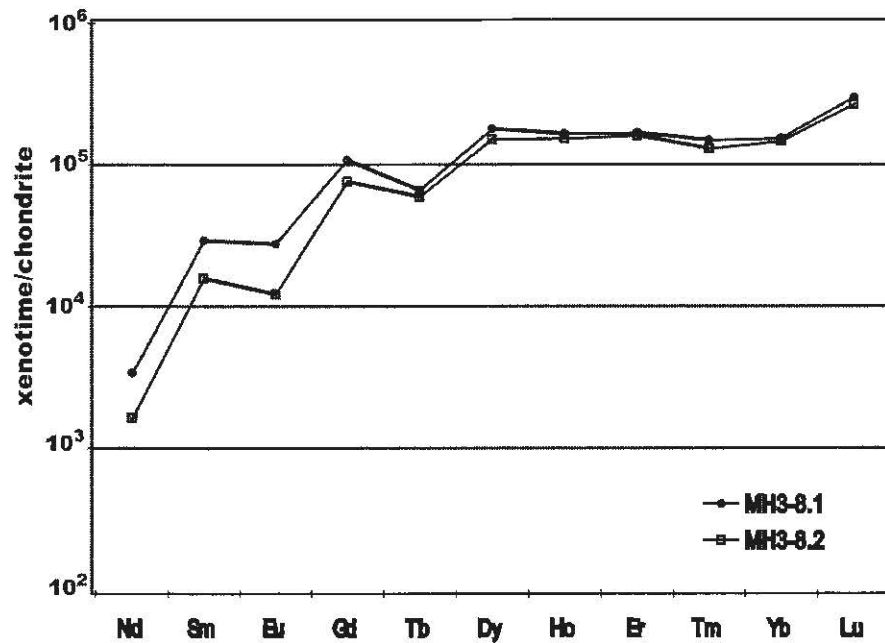
Fig. 6.9. Chondrite normalised REE patterns of xenotime MH3-8.1 and MH-8.2. Chondrite data from Boynton (1984).

The oldest cluster of Neoproterozoic SHRIMP xenotime in this sample forms a distinct grouping at 755 ± 20 Ma. Xenotime in this group occurs as both zircon overgrowths and irregularly shaped crystals. Two analyses on one large irregularly

shaped grain (MH1-9.1 & -9.2, Fig. 6.6b) combine to give an age of 737 ± 40 Ma (2σ), indicating that this crystal grew during one event. However, on one xenotime overgrowth (MH3-5, Fig 6.5b) two distinct SHRIMP $^{206}Pb/^{238}U$ ages are recorded at 767 ± 19 Ma (σ) (MH3-5.1) and 619 ± 21 Ma (σ) (MH3-5.3). These different ages probably indicate that this xenotime has undergone a phase of dissolution and re-precipitation at ~620 Ma following a prior crystallisation at ~760 Ma. Multiple age domains in xenotime overgrowths and single crystals are not unusual and have also been reported by Kositcin et al. (2003); Vallini et al. (2002) and Rasmussen et al. (2007).

The similar chemical composition and chondrite normalised REE patterns for xenotime in this sample suggest they crystallised from a compositionally similar fluid. The distinctive negative Eu anomaly common to the xenotime as well as their textural location within a sample of altered granite, supports a magmatic origin. However, it is the U–Pb isotopes that reveal that these xenotime grains have crystallised episodically during the Neoproterozoic. Therefore, the similar chemical composition and REE profiles for these xenotime grains suggests that they probably developed during various stages of dissolution and reprecipitation of pre-existing xenotime rather than the influx of distinct, successive Y and HREE bearing fluids. This process clearly proceeded at the local scale and involved the dissolution of xenotime resulting in embayed crystal margins, closely followed by xenotime reprecipitation which in some cases must have infilled pre-existing embayments.

6.6.1 Tectonic implications

Skarn formation at Molyhil was synchronous with the crystallisation of the Marshall Granite during the Strangways Orogeny. Younger xenotime $^{206}Pb/^{238}U$ ages in this sample record later Neoproterozoic thermotectonic events. The older of the two xenotime Neoproterozoic age groupings at 755 ± 20 Ma, is within error of the 732 ± 5 Ma U–Pb zircon crystallisation age of the Mud Tank Carbonatite, located approximately 100 km south-east of the Molyhil deposit (Black & Gulson 1978). This is the first instance where a thermotectonic event with an age similar to the Mud Tank Carbonatite has been detected within the NAC. Alternatively, the ~760 Ma Molyhil xenotime may have crystallised in response to far-field tectonic events recorded in the

Adelaide Geosyncline and/or Pilbara Craton. In the Adelaide Geosyncline, a phase of crustal extension with associated bimodal volcanism and normal faulting is recorded by the Boucaut Volcanics which have a SHRIMP U—Pb zircon age of 777 ± 7 Ma (Preiss 2000). This age is similar to ~760–780 Ma granite intrusion in the north-west of Tasmania and on King Island (Turner et al. 1998). Additionally, dolerite dykes in the Pilbara Craton of Western Australia record a similar age. The intrusion of the extensive Mundine Well dyke swarm was constrained by SHRIMP U–Pb zircon and baddeleyite dating to have occurred at 755 ± 3 Ma (Wingate & Giddings 2000). Finally, the ~760 Ma event recorded in xenotime from Molyhil, Boucaut Volcanics (Adelaide Geosyncline) and Mundine Well dyke swarm (Pilbara Craton) all correspond with the ~750 Ma age for the separation of the western half of Rodinia as suggested by Li et al. (2008).

The xenotime $^{206}Pb/^{238}U$ age grouping at 648 ± 29 Ma is less easy to reconcile with the known event chronology of central Australia. This age may however, relate to a period of felsic magmatism that occurred in the Paterson Province in Western Australia between ~650 to 640 Ma as recorded by Dunphy and McNaughton (1998). Alternatively, the 650 Ma xenotime group may correlate with the very loosely defined ~0.8–0.6 Ga, Areyonga Movement of Wells et al. (1970), which resulted in the unconformity between the Bitter Springs and Areyonga Formations of the Amadeus Basin.

6.7 Conclusions

The Molyhil scheelite-molybdenite skarn formed from fluids associated with the crystallisation of the Marshall Granite during the Strangways Event which in the north-east Arunta was associated with granulite to amphibolite facies metamorphism, granite intrusion and deformation in the Jinka region and Kanandra Granulite of the Strangways Metamorphic Complex. This preliminary study suggests that currently the best estimate for the timing of this event is a Re–Os analysis of molybdenite from an ore-zone skarn rock which gave a model age of 1720.7 ± 5.9 Ma. This is similar to an $^{40}Ar/^{39}Ar$ hornblende age of ~1.72–1.70 Ga for this deposit (G. Fraser, unpub. data; Geoscience Australia) and is well within error of the oldest xenotime grain analysed by SHRIMP RG which has a $^{207}Pb/^{206}Pb$ age of 1714 ± 26 Ma (2σ). The fact that one

of the xenotime grains analysed has a concordant U—Pb age within error of the ages determined by two other different isotopic systems on different samples from this deposit, gives credibility to the SHRIMP U—Pb analytical protocols and $^{206}Pb/^{238}U$ matrix correction techniques employed during this study. However, the majority of the xenotime in the sample of green granite analysed by SHRIMP crystallised more than 1000 million years after the formation of the Molyhil Skarn and record the effects of far-field thermotectonic events which up until now have gone undated in this region. These younger xenotime record two previously unrecognised Neoproterozoic tectonothermal events at 755 ± 20 Ma and at 657 ± 21 Ma. The older of these events may be related to the ~730 Ma intrusion of the Mud Tank Carbonatite or events further-afield such as extension in the Adelaide Geosyncline at ~770 Ma and also the ~760 Ma intrusion of the Mundine Well dyke swarm in the Pilbara Craton. The Molyhil xenotime growth at 755 ± 20 Ma is also coincident with the break-up of Rodinia, which Li et al. (2008) suggest occurred at about 750 Ma. Evidence for a tectonothermal event occurring at ~660 Ma in central Australia is presently more cryptic. However, the ~660 Ma xenotime may be related to granitoid intrusion in the Paterson Province of Western Australia between ~650 to ~640 Ma.

Also shown by this study is the tendency for xenotime to form by dissolution and re-precipitation which could mean that in some environments the earliest formed xenotime could, over time, be completely removed or become volumetrically minor. This scenario has probably occurred at the Molyhil deposit where only one of the xenotime crystals analysed has a $^{207}Pb/^{206}Pb$ age that is synchronous with the time of skarn formation.

7. CONCLUSIONS

This study has shown that for SHRIMP U—Pb xenotime analysis, chemical contrasts of U and $\sum$REE between the $^{206}Pb/^{238}U$ calibration standard and unknown sample can cause significant $^{206}Pb/^{238}U$ fraction of the unknown relative to the standard. Experiments conducted on SHRIMP II and SHRIMP RG demonstrate that on average, a 1 wt% contrast in U causes an ~11.9% difference in the $^{206}Pb/^{238}U$ ratio whereas a $\sum$REE contrast of 1 wt% results in a $^{206}Pb/^{238}U$ contrast of on average ~0.9%. In some experiments matrix effects principally caused by elevated U concentrations, resulted in individual SHRIMP $^{206}Pb/^{238}U$ xenotime determinations which were elevated by up to 25% relative to their known age.

For SHRIMP U—Pb xenotime analysis, a number of lines of evidence suggest that it is the ionisation and emission of the Pb^+ ions that are influenced by U and $\sum$REE matrix mismatches. Firstly, the independently calculated SHRIMP $^{206}Pb/^{238}U$ and $^{208}Pb/^{232}Th$ ratios in each sample are equally affected by matrix contrasts (see Figs. 3.16-3.18). Also, the increased emission of the Pb^+ ions must equally affect all Pb isotopes as there is no detectable matrix influence on xenotime $^{207}Pb/^{206}Pb$ ratios. Equally, there is no significant and/or consistent difference in Th/U calibration factors between reference xenotime samples even though they have markedly contrasting chemical compositions indicating again that the xenotime $^{208}Pb/^{206}Pb$ ratios are likely to be equally affected by matrix contrasts (see section 3.36).

Previous investigations of SIMS matrix effects have demonstrated that energy filtering of the low energy secondary ion population can significantly reduce or eliminate matrix effects (e.g. Shimizu & Hart 1982). However, for SHRIMP U–Pb analysis even energy filtering of ~90% of the low energy secondary ion population does not reduce the SHRIMP $^{206}Pb/^{238}U$ ME. Therefore, an empirical xenotime $^{206}Pb/^{238}U$ matrix correction procedure was adopted. This technique requires the concurrent analysis of three xenotime standards that are used to monitor and correct the SHRIMP xenotime $^{206}Pb/^{238}U$ ME. Correction factors for the SHRIMP $^{206}Pb/^{238}U$ xenotime, U and $\sum$REE induced matrix effects are determined using a simple linear least squares routine, which is fully described in Chapter 3 and Appendix 3.6. The results from eight SHRIMP analytical sessions demonstrate that these correction

factors change from session to session, and should be determined for each analytical session in the same way for example that the SHRIMP $^{206}Pb/^{238}U$ zircon calibration is routinely determined.

For the SHRIMP U—Pb xenotime analyses conducted in this study, the most effective means to calculate xenotime $^{206}Pb/^{238}U$ ratios was via raw $^{206}Pb^+/^{270}(UO_2^+)$ ratios as described in Chapter 3.3.4.1 and as suggested for SHRIMP zircon $^{206}Pb/^{238}U$ calibration by Stern & Amelin (2003). Of particular note also is the finding made during this study that for some xenotime, independent SHRIMP $^{208}Pb/^{232}Th$ ratios can be calculated from the raw $^{208}Pb+/^{248}(ThO^+)$ ratios with a reproducibility only slightly worse than that achieved using $^{206}Pb^+/^{270}(UO_2^+)$ to calculate $^{206}Pb/^{238}U$. However, this calibration may only be effective for xenotime with $\geq$ ~1000 ppm Th. Further investigation of this calibration is needed to determine its usefulness.

Additionally, the SHRIMP RG was identified as ideal for xenotime U—Pb analysis as this instrument effectively filters out the scattered ions associated with the mass 204 peak that SHRIMP II instruments routinely detect. The analytical and matrix correction protocols developed and described here can serve as a basis for further future SIMS U—Pb studies of xenotime matrix effects and indeed may also assist with studies of SIMS matrix effects in other minerals such as monazite and uraninite.

Future studies should initially be concentrated on the search for and characterisation of new xenotime Pb/U standards. Currently the single-crystal xenotime MG1 (490 Ma) is a good standard. It is relatively homogenous and typically yields a 1σ Pb/U reproducibility of between 1 to 2%. A major advantage of using MG1 as the primary xenotime $^{206}Pb/^{238}U$ calibration standard is its low U concentration of ~1000 ppm. Diagenetic and hydrothermal xenotime typically contain similar U concentrations, therefore the major U-induced matrix effect associated with SHRIMP $^{206}Pb/^{238}U$ xenotime analyses when using MG1 will be minor. Stocks of MG1 crystal fragments are becoming increasingly limited, therefore the characterisation of a new low U xenotime is of key importance to SIMS U—Pb xenotime dating. Also, the ID-TIMS characterisation of xenotime standards with a wide range of compositions will further increase our knowledge of SHRIMP $^{206}Pb/^{238}U$ matrix effects and how to better correct for them.

212

Crucial to the SHRIMP $^{206}Pb/^{238}U$ matrix correction technique developed is the accurate determination of U and REE xenotime concentrations. This is best carried out using EMPA (WDS) analysis or relative sensitivity factors ($RSF_{(U-Ho)}$) as explained in Chapter 3.3.5. The wide range in the concentration of Y and the REE in natural xenotime, means that there is no element that has a constant or near-constant concentration which can be used as a reference from which to calculate elemental abundances in the same way that for example, Zr is often used as a reference element for SIMS elemental quantification of zircon (see section 3.3.5.1 and Claouè-Long et al. 1995). Furthermore, a comparison of U concentrations determined in different xenotimes using WDS, $RSF_{(U-Ho)}$ and $RSF_{(U-Y)}$ (see Table 3.6) showed that $RSF_{(U-Y)}$ can lead to U abundance determinations that are significantly elevated compared to WDS and $RSF_{(U-Ho)}$ determinations, indicating that the ionisation of the $^{194}(Y_2O^+)$ molecule may also be affected by contrasts in xenotime matrix.

Besides being necessary for SHRIMP U—Pb xenotime matrix corrections, WDS analyses of xenotime combined with SHRIMP U—Pb studies can provide an important 'fingerprint' of the xenotime type and hence greatly assist the interpretation of the U—Pb isotopic results (e.g. Kositcin et al. 2003). For example, for the case study of hydrothermal xenotime from the Callie and Coyote deposits in the Tanami region (Chapter 5), strong support for the hydrothermal origins of the analysed xenotime grains are given by their WDS analyses. The xenotime from the two different deposits has similar chondrite normalised REE patterns that are typical for hydrothermal xenotime. This xenotime typically does not have the negative Eu anomaly that is more normally associated with igneous xenotime. It also has a steep rise from Nd to Gd and a flat transition through to Lu (see Fig. 5.5). The WDS results for the two different types of xenotime outgrowth from the Serra da Mesa Group (Chapter 4) show them to have crystallised from chemically different fluids. Chondrite normalised REE patterns for the inner ~1.47 Ga xenotime have elevated concentrations of MREE (Sm-Dy) and lower concentrations of the HREE (Er-Lu) relative to the outer ~570 Ma xenotime (see Fig. 4.6). In contrast to these results are those for the xenotime from the Molyhil scheelite-molybdenite skarn in the north-east Arunta region where similarities of the chondrite normalised REE profiles between

213

xenotime of markedly different age are near-identical, indicating that xenotime growth probably proceeded by dissolution and re-precipitation (see Fig 6.9).

Interpretation of the results of a SHRIMP U—Pb isotopic study of detrital zircons from 12 sedimentary rocks representing the principal units of the Tanami Basin (Chapter 1) demonstrates the potential for U—Pb detrital zircon studies to provide important clues for basin development and regional tectonic reconstructions. However, major questions concerning the actual timing of sedimentation were left mostly unanswered or only very loosely constrained for some of the units. Therefore this study also highlighted a major and very typical frustration associated with the significance that should placed on maximum deposition ages derived from the U—Pb dating of detrital zircons and how closely they represent the true timing of sedimentation. Typical of other Palaeoproterozoic basins throughout the world, in the Tanami Basin, dateable intercalated felsic volcanic rocks which can be used in combination with detrital zircon U—Pb studies to bracket the timing of sediment deposition are rare. It is in these circumstances where SHRIMP U—Pb dating of diagenetic xenotime can provide either a direct age measurement of sedimentation and/or establish a minimum age, if suitable material can be found. Maximum and minimum depositional constraints for sedimentary units can be obtained by a combination of U—Pb dating of both detrital zircon and diagenetic xenotime. The timing of sedimentation for the Gardiner Sandstone has been bracketed in this way to have occurred between ~1.77 and ~1.64 Ga by the results of a SHRIMP U—Pb study conducted during this study and a SHRIMP U—Pb xenotime age reported in Vallini et al. (2007).

An outstanding question identified by the SHRIMP U—Pb detrital zircon study of the Tanami Basin is that of the true depositional age of the Mount Charles Formation. Based on structural grounds, Crispe et al. (2006) interpreted this unit to have been deposited at ~1.80 Ga. However, three SHRIMP U—Pb detrital zircon studies from separate samples of the Mount Charles Formation conflict with this. The youngest zircon component from all three samples analysed has preserved crystal faces with no signs of abrasion and a SHRIMP ^{207}Pb/^{206}Pb age of ~1.91 Ga, 100 m.y. older than the interpretation of Crispe et al. (2006). It was hoped that if diagenetic xenotime could be found in samples from this unit, their SHRIMP U—Pb analysis could potentially

resolve this 100 m.y. discrepancy. However, even though an extensive geochemical and SEM investigation was conducted, no xenotime was found associated with the Mount Charles Formation samples investigated. This outcome is well worth noting as significant time and resources can be spent on what may ultimately be a null result.

The centrepiece of this study is the results for the SHRIMP U—Pb analysis of xenotime outgrowths from the Serra da Mesa Group, central Brazil. Analyses of the massive outer outgrowths gave a SHRIMP $^{206}Pb/^{238}U$ matrix corrected age of ~570 Ma which is identical within error to a SHRIMP $^{206}Pb/^{238}U$ monazite age measured on the same sample. Both minerals are interpreted to possibly record a period of amphibolite facies metamorphism related to the final stages of the Brasiliano Orgeny. SHRIMP U—Pb analyses of the inner, pyramidal and pitted outgrowths are texturally, chemically and isotopically different from the outer ~570 Ma outgrowths. Collectively, their $^{207}Pb/^{206}Pb$ ratios and matrix corrected $^{206}Pb/^{238}U$ ratios define a Pb-loss trend that has an upper intercept age of ~1.47 Ga which is probably related to the intrusion of the Peixe Alkaline Complex that intrudes rocks of the Serra da Mesa Group to the north of the sample site. Additionally, the youngest detrital zircon analysed from just 16 concordant compositions, gives a $^{207}Pb/^{206}Pb$ age of ~1.96 Ga. Therefore deposition of the Serra da Mesa Group is constrained between ~1.96 Ga and 1.50 Ga, which is only a minor improvement on previous depositional constraints for this unit.

The importance of xenotime as a geochronometer of hydrothermal orogenic Au mineralisation has again been demonstrated by this study. SHRIMP U—Pb analyses of xenotime from the Callie and Coyote Au deposits mark the period between ~1.81 to ~1.79 Ga as significant for Au mineralisation in the Tanami region (Chapter 5). This time period also appears to be important in the Pine Creek region to the north of the Tanami. Re-interpretation of SHRIMP U—Pb monazite data for the Goodall Au deposit presented in Sener et al. (2005) supports a previously reported SHRIMP monazite and xenotime age for the Goodall deposit of 1810 ± 10 Ma by Compston & Matthai (1994) and also suggests that the time period between ~1.81 to ~1.79 Ga is important for mineralisation across much of the North Australia Craton.

215

Mineralisation at the Molyhil scheelite-molybdenite skarn deposit in the north-eastern Arunta region was shown to be coincident with nearby ~1.73 Ga Strangways-aged granites. Rhenium—Osmium dating of ore-stage molybdenite constrains the timing of mineralisation to 1727 ± 5.9 Ma. This age is coincident with skarn–related hornblende which has an $^{40}Ar/^{40}Ar$ age of between 1.72 and 1.73 Ga (Fraser, unpublished data). Significantly for this project is that the oldest xenotime analysed by SHRIMP RG has a $^{207}Pb/^{206}Pb$ age of 1714 ± 26 Ma and therefore coincident with the minerals dated by the other two isotopic methods. This result adds further support to the SHRIMP U—Pb analytical protocols and $^{206}Pb/^{238}U$ matrix correction techniques developed during this study. The agreement of three independent isotopic systems is indeed a notable result.

The majority of xenotime from the Molyhil skarn sample crystallised more than 1000 m.y. after the formation of the skarn and record events that were previously unrecognised in the north-east Arunta. In particular is the major Neoproterozoic age component in the sample at 755 ± 20 Ma which most likely crystallised during the same thermotectonic event as the ~730 Ma Mud Tank Carbonatite, located ~100km south-east of the Molyhil skarn. This is the first example where an event with a similar age to the Mud Tank Carbonatite has been recorded in the North Australia Craton.

The ability of xenotime to form during low temperature events has advantages and disadvantages. If host rocks remain permeable, xenotime crystallisation can occur at low temperatures in a response to far-field thermotectonic events and thus record events that no other isotopic system can. The attractiveness of xenotime as a U—Pb geochronometer of low temperature events is enhanced by the high temperatures (~900° C) which xenotime remains closed to diffusive Pb-loss. However, as demonstrated by this study, the oldest xenotime analysed from the Molyhil skarn formed at ~1.71 Ga and represents a very minor component of this sample relative to the Neoproterozoic xenotime. Therefore it is quite conceivable that in some environments, the earliest formed xenotime could over time become a very minor component of the rock either by the successive influx of Y, REE and P bearing fluids that precipitate new xenotime, or as is the case at the Molyhil skarn, by xenotime dissolution and re-precipitation.

Xenotime has a remarkable potential as a U—Pb geochronometer. It can occur in igneous, metamorphic and hydrothermal environments and form as an authigenic component of sedimentary rocks. During diagenesis it can form within a few metres of the sediment-water interface (Rasmussen 2005) yet has been shown to be resistant to diffusive Pb-loss even at amphibolite grade metamorphism (e.g. Dawson et al. 2003 and Chapter 4). The dating of diagenetic xenotime, especially from Precambrian or non-fossiliferous sedimentary units, can provide a direct measure of the deposition age that cannot be obtained by any other method. Additionally, dating of hydrothermal xenotime associated with mineralisation can provide invaluable support for exploration models. The generally tiny size of diagenetic and hydrothermal xenotime grains, (typically <1 to 20 μm) has meant that up until recently their presence has remained largely unnoticed. Furthermore, xenotime from these environments generally has low concentrations of U and therefore, radiogenic Pb. Together these factors mean that only large radius SIMS instruments such as SHRIMP or the Cameca 1270/1280 have the mass resolution, sensitivity and spatial resolution that is required for xenotime U–Pb analysis. However, chemical contrasts between different xenotime in U and ΣREE results in significant $^{206}Pb/^{238}U$ matrix effects that have meant that most applications of SHRIMP U–Pb xenotime dating have been carried out on rocks older than ~1000 Ma, where $^{207}Pb/^{206}Pb$ ages can be relied upon. The main emphasis of this PhD study has been to develop SHRIMP U—Pb analytical and processing protocols for xenotime $^{206}Pb/^{238}U$ analysis. The correction procedures developed here enable the accurate determination of SHRIMP xenotime $^{206}Pb/^{238}U$ and $^{208}Pb/^{233}Th$ ratios from Phanerozoic rocks with an accuracy of approximately 2%.

REFERENCES

Adams, G.J., Both, R.A. & James, P., 2007. The Granites gold deposits, Northern Territory, Australia: evidence for an early syn-tectonic ore genesis. *Mineralium Deposita*, **42**, 89-105.

Aleinikoff, J.N. & Grauch, R.I., 1990. U–Pb Geochronologic constraints on the origin of a unique monazite-xenotime gneiss, Hudson Highlands, New York. *American Journal of Science*, **290**, 522-546.

Aleinikoff, J.N., Schenck, W.S., Plank, M.O., Srogi, L., Fanning, M.C., Kamo, S.L. & Bosbyshell, H., 2006. Deciphering igneous and metamorphic events in high-grade rocks of the Wilmington Complex, Delaware: Morphology, cathodoluminescence, and backscattered electron zoning, and SHRIMP U–Pb geochronology of zircon and monazite. *Geological Society of America Bulletin*, **118**, 39-64.

Amli, R., 1975. Mineralogy and rare earth geochemistry of apatite and xenotime from the Gloserheia Pegmatite, Froland, southern Norway. *American Mineralogist*, **60**, 607–620.

Andersen, C.A. & Hinthorne, J.R., 1973. Thermodynamic approach to the quantitative interpretation of sputtered ions in mass spectra. *Analytical Chemistry*, **45**, 1421-1438.

Andrehs, G. & Heinnrich, W., 1998. Experimental determination of REE distributions between monazite and xenotime: potential for temperature–calibrated geochronology. *Chemical Geology*, **149**, 83–96.

Asami, M., Suzuki, K. & Grew, E.S., 2002. Chemical Th–U–total Pb dating by electron microprobe analysis of monazite, xenotime and zircon from the Napier Complex, East Antarctica: evidence for ultra–high-temperature metamorphism at 2400 Ma. *Precambrian Research*, **114**, 249–275.

Bagas, L., Huston, D.L., Anderson, J. & Mernagh, T.P., 2007. Paleoproterozoic gold deposits in the Bald Hill and Coyote area, Western Tanami, Western Australia. . *Mineralium Deposita*, **42**, 127-144.

Barraclough, D., 1979. Geological investigations at the Molyhil scheelite mine, central Australia. *Northern Territory Geological Survey Report*, GS 79/016.

Bea, F., 1996. Residence of REE, Y, Th and U in granites and crustal protoliths: implications for the chemistry of crustal melts. *Journal of Petrology*, **37**, 521–552.

Bea, F. & Montero, P., 1999. Behaviour of accessory phases and redistribution of Zr, REE, Y, Th and U during metamorphism and partial melting of metapelites in the lower crust: an example from the Kinzigate Formation of Ivrea–Verbano, NW Italy. *Geochimica et Cosmochimica Acta*, **63**, 1133–1153.

Belolipetskii, A.P. & Voloshin, A.V., 1996. Yttrium and rare earth element minerals of the Kola Peninsula, Russia. In: Jones, A.P., Wall, F. & Williams C.T., (Eds), *Rare*

Earth Minerals, chemistry, origin and ore deposits, The Mineralogical Society Series, **7**, 193-226.

Benninghoven, A., Rüdenauer, F.G. & Werner, H.W., 1987. Secondary ion mass spectrometry: Chemical analysis, **86**, 1227p.

Berner, R.A., 1973. Phosphate removal from sea water by adsorption on volcanogenic ferric oxides . *Earth and Planetary Science Letters*, **18**, 84–86.

Berner, R.A., Ruttenburg, K.C., Ingall, E.D. & Rao, J.L., 1993. The nature of phosphorous burial in modern marine sediments. In: Wollast, R., Mackenzie, F.T., Chou, L. (Eds), Interactions of C, N, P and S Biogeochemical Cycles and Global Change. NATO ASI series, vol 14. Springer–Verlag, Berlin, pp. 365–378.

Black, L.P. & Gulson, B.L., 1978. The age of the Mud Tank Carbonatite, Strangways Range Northern Territory. *Bureau of Mineral Resources, Journal of Geology and Geophysics*, **3**, 227-232.

Black, L.P., Kamo, S.L., Allen, C.M., Davis, D.W., Aleinikoff, J.N., Valley, J.W., Mundil, R., Campbell, I.H., Korsch, R.J., Williams, I.S. & Foudoulis, C. 2004. Improved $^{206}Pb/^{238}U$ microprobe geochronology by the monitoring of a trace-element-related matrix effect; SHRIMP, ID–TIMS, ELA–ICP–MS and oxygen isotope documentation for a series of zircon standards. *Chemical Geology*, **205**, 115-140.

Black, L.P., Kinny, P.D. & Sheraton, J.W., 1991. The difficulties of dating mafic dykes: An Antarctic example. *Contributions to Mineralogy and Petrology*, **109**, 183-194.

Bodorkos, S., Sandiford, M., Oliver, N.H.S. & Cawood, P.A., 2002. High-T, low-P metamorphism in the Paleoproterozoic Halls Creek Orogen, northern Australia: the middle crustal response to a mantle-related transient thermal pulse . *Journal of Metamorphic Petrology*, **20**, 217-237.

Bowring, S.A., Grotzinger, J.P., Isachsen, C.E., Knoll, A.H., Pelechaty, S.M. & Kolosov, P., 1993. Calibrating rates of early Cambrian evolution. *Science*, **261**, 1293–1298.

Boynton, W.V., 1984. Cosmochemistry of the rare earth elements: meteorite studies. In: *Rare Earth Element Geochemistry*. Elsevier, Amsterdam, p. 63-114.

Brown, S.M., Fletcher, I.R., Stein, H.J., Snee, L.W. & Grooves, D.I., 2002. Geochronological constraints on pre–, post–mineralization events at the world–class Cleo gold deposit, eastern goldfields province, Western Australia. *Economic Geology*, **97**, 541–559.

Budd, A.R., Wyborn, L.A.I. & Bastrakova, I.V. 2001. The Metallogenic Potential of Australian Proterozoic Granites. *Australian Geological Survey Organistaion* Record, **2001/12**.

Buick, I.S., Hand, M., Williams, I.S., Mawby, J., Millar, J.A. & Nicoll, R.S., 2005. Detrital zircon provenance constraints on the evolution of the Harts Range Metamorphic Complex (central Australia): links to the Centralian Superbasin. *Journal of the Geological Society of London,* **162,** 777-787.

Burnette, W.C., 1977. Geochemistry and origin of phosphate deposits from off Peru and Chile. *Bulletin of the Geological Society of South America,* **88,** 813–823.

Butera, K.M., Williams, I.S., Blevin, P.L. & Simpson, C.J. 2001. Zircon U–Pb dating of Early Palaeozoic monzonitic intrusives from the Goonumbla area, New South Wales. *Australian Journal of Earth Sciences,* **48,** 457–464.

Casillas, R., Nagy, G., Panto, G., Brandle, J. & Forizs, I., 1995. Occurrence of Th, U, Y, Zr, and REE–bearing accessory minerals in late Variscan granitic rocks from the Sierra de Guadarrama (Spain). *European Journal of Mineralogy,* **7,** 98–1006.

Cherniak, D.J. & Watson, B.E., 2003. Diffusion in zircon. In: Hanchar, J.M. & Hoskin, P.W.O. (Eds). *Zircon.* Mineralogical Society of America. Reviews in Mineralogy and Geochemistry, **53,** 113-143.

Cherniak, D.J., 2006. Pb and rare earth element diffusion in xenotime. *Lithos,* **88,** 1–14.

Claoue-Long, J.C., Compston, W., Roberts, J. & Fanning, M.M., 1995. Two Carboniferous ages: a comparison of SHRIMP zircon dating with conventional zircon ages and 40Ar/39Ar analysis. *Geochronology Time Scales and Global Stratigraphic Correlation,* SEPM Special Publication No. 54.

Clement, S., Compston, W. & Newstead, G., 1977. Design of a large, high resolution ion microprobe, SIMS, Münster. Germany.

Collins, W.J. & Shaw, R.D., 1995. Geochronological constraints on orogenic events in the Arunta Inlier: a review. *Precambrian Research,* **71,** 315-346.

Compston, D.M. & Matthai, S.K., 1994. Age constraints on early Proterozoic gold deposits, Pine Creek Inlier and Tennant Creek Inlier, northern Australia: *Geological Society of Australia Abstracts,* **37,** 70.

Compston W., 2000. Interpretations of SHRIMP and isotope dilution zircon ages for the geological time-scale: I. The early Ordovician and late Cambrian. *Mineralogical Magazine,* **64(1),** 43-57.

Compston, W., 1996. SHRIMP: Origins, impact and continuing evolution. *Journal of the Royal Society of Western Australia,* **79,** 109-117.

Compston, W., Williams, I.S. & Meyer, C., 1984. U-Pb geochronology of zircons from lunar breccia 73217 using a sensitive high resolution ion microprobe. *Journal of Geophysical Research Supplement* **89,** B525-B534.

Compton, J.S., Snyder, S.W. & Hodell, D.A., 1990. Phosphogenesis and weathering of shelf sediments from the southeastern United States: Implications for Miocene ∂^{13} excursions and global cooling. *Geology*, **18**, 1227–1230.

Crispe, A.J., Vandenberg, L.C. & Scrimgeour, I.R., 2007. Geological framework of the Archaean and Paleoproterozoic Tanami Region, Northern Territory. *Mineralium Deposita*, **42**, 3-26.

Cristy, S.S., 2000. Secondary Ion Mass Spectrometry. In: Barshick, C.M., Duckworth, D.C., Smith, D.H., (Eds), *Inorganic Mass Spectrometry: Fundamentals and applications*. Practical Spectroscopy Series Volume 23, 159-222.

Cross, A.J. & Crispe, A.J., 2007. SHRIMP U-Pb analyses of detrital zircon: a window to understanding the Paleoproterozoic development of the Tanami Region, northern Australia. *Mineralium Deposita*, **42**, 27-50.

Cross, A.J., Fletcher, I.R., Crispe, A.J., Huston, D.L. & Williams, N., 2005. New constraints on the timing of deposition and mineralisation in the Tanami Group. *Annual Geoscience Exploration Seminar (AGES) Record of Abstracts, Northern Territory Geological Survey Record* **2005-001**.

Dardenne, M.A., 2000. The Brasília Fold Belt. In: Cordani, U.G., Milani, E.J., Thomaz, Filho, A., Campos, D.A. (Eds). Proceedings of the 31st International geological Congress on the Tectonic Evolution of South America. Rio de Janeiro, 231-263.

Dawson, G.C., Krapez, B., Fletcher, I.R., McNaughton, N.J. & Rasmussen, B., 2003. 1.2 Ga thermal metamorphism in the Albany-Fraser Orogen of Western Australia: consequence of collision or regional heating by dyke swarn? *Journal of the Geological Society (London)*. **160**, 29-37.

De Laeter, J.R. & Kennedy, A.K. 1998. A double focusing mass spectrometer for geochronology. *International Journal of Mass Spectrometry*, **178**, 43-50.

Demartin, F., Pilati, T., Diella, V., Donzelli, S. & Gentile, O., Gramaccioli, C.M., 1991. The chemical composition of xenotime from fissures and pegmatites in the Alps. *Canadian Mineralogist*, **29**, 69–75.

Donovan, J.J., Hanchar, J.M., Picolli, P.M., Schrier, M.D., Boatner, L.A. & Jarosewich, E., 2003. A re-examination of the rare–earth element orthophosphate standards in use for electron microprobe analysis. *Canadian Mineralogist*, **41**, 221–232.

Dunphy, J.M. & McNaughton, N.J., 1998. Geochronology of the Telfer granitoids: zircon and titanite U-Pb SHRIMP data. *Geological Society of Australia Abstracts*, **49**, 127.

England, G.L., Rasmussen, B., McNaughton, N.J., Fletcher, I.R., Groves, D.I. & Krapez, B., 2001. SHRIMP U–Pb ages of diagenetic and hydrothermal xenotime from the Witswatersrand Supergroup of South Africa. *Terra Nova*, **13**, 360–367.

Ewers, G.R. & Scott, P.A., 1977. Geochemistry of the Cullen Granite, Northern Territory: *BMR Journal of Australian Geology and Geophysics*, **2**, 165-176.

Ferreira Filho, C.F. & Pimentel, M.M., 2000. Sm–Nd isotope systematics and REE-Hf-Ta-Th data of troctolites and their amphibolitized equivalents of the Niquelândia Complex Upper Layered Series, central Brazil: further constraints for the timing of magmatism and high-grade metamorphism. *Journal of South American earth Sciences*, **13** (7), 647-659.

Ferreira Filho, C.F. 1998. Geology and petrology of the large layered intrusions of central Brazil: implications for PGE mineralisation. In: Platinum Symposium, Rustenburg, South Africa, Extended Abstracts, 107-110.

Fletcher, I.R., McNaughton, N.J., Aleinikoff, J.A., Rasmussen, B. & Kamo, S.L., 2004. Improved calibration procedures and new standards for U–Pb and Th–Pb dating of Phanerozoic xenotime by ion microprobe. *Chemical Geology*, **209**, 295–314.

Fletcher, I.R., Rasmussen B. & McNaughton, N.J., 2000. SHRIMP U–Pb geochronology of authigenic xenotime and its potential for dating sedimentary basins. *Australian Journal of Earth Sciences*, **47**, 845–860.

Fölmi, K.B., 1996. The phosphorous cycle, phosphogenesis and marine phosphate-rich deposts. *Earth–Science Reviews*, **40**, 55–124.

Förster, H.-J., 1998. The chemical composition of REE–Y–Th–U rich accessory minerals in peraluminous granites of the Erzgebirge–Fichtelgebirge region, Germany. Part II. Xenotime. *American Mineralogist*, **83**, 1302–1315.

Förster, H.-J., 2006. Composition and origin of intermediate solid solutions in the system thorite—xenotime—zircon—coffinite. *Lithos*, **88**, 35-55.

Franz, G., Andrehs, G. & Rhede, D., 1996. Crystal chemistry of monazite from Saxothuringian-Moldanubian metapelites, NE Bavaria, Germany. *European Journal of Mineralogy*, **8**, 1097–1118.

Fraser, G. (2002). Timing of regional tectonism and Au-mineralisation in The Tanami Region: 40Ar/39Ar geochronological constraints. *Annual Exploration Geoscience Seminar (AGES) Record of Abstracts, Northern Territory Geological Survey Record* **2002-003**.

Fraser, G., Huston, D., Bagas, L., Hussey, K., Claoué-Long, J., Cross, A., Vandenburg, L., Wygralak, A., Donnellan, N. & Crispe, A., 2006. $^{40}Ar/^{39}Ar$ constraints on the episodic history of mineralisation and tectonism in the southern North Australia Craton. In: Lyons, P. & Huston, D.L., (Eds). *Evolution and metallogenesis of the North Australian Craton, Conference Abstracts*. Geoscience Australia Record 2006/16.

Freeman, M.J., 1986. Huckitta, Northern Territory. 1:250 000 geological Map Series. *Northern Territory Geological Survey, Explanatory Notes*, SF53-11.

Freeman, M.J., 1990. Molyhil scheelite-molybdenite deposit. *Australian Institute of Mining Engineers Monograph*, **16**, 875-877.

Froelich, P.N., Bender, M.L., Heath, G.R., 1977. Phosphorous accumulation rates in metalliferous sediments on the East Pacific Rise. *Earth and Planetary Science Letters*, **34**, 351–359.

Glenn, C.R., 1990. Pore water, petrologic and stable carbon isotopic data bearing on the origin of modern Peru margin phosphorites and associated authigenic phases. In: Burnett, W.C., Riggs, S.R. (Eds). *Phosphate deposits of the world*. Vol. 3, Genesis of Neogene to Modern Phosphorites. International geological Correlation Program, Project 156: Phosphorites. Cambridge University Press, Cambridge, pp. 46–61.

Gratz, R. & Heinrich, W., 1997. Monazite-xenotime thermobarometry: experimental calibration of the miscibility gap in the binary system $CePO_4$–YPO_4. *American Mineralogist*, **82**, 772–780.

Gratz, R. & Heinrich, W., 1998. Monazite–xenotime thermometry: III. Experimental calibration of the partitioning of gadolinium between monazite and xenotime. *European Journal of Mineralogy*, **10**, 579–588.

Grew, E.S., Kazuhiro, S. & Masao, A., 2002. CHIME ages of xenotime, monazite and zircon from beryllium pegmatites in the Napier Complex, Khmara Bay, Enderby Land, East Antarctica. *Polar Geoscience*, **14**, 99–118.

Gulson, B.L. & Mizon, K.J., 1980. Lead isotope studies at Jabiluka. In: Furguson, J. & Goleby, A.B., (Eds) *Uranium in the Pine Creek Geosyncline*. International Atomic Energy Agency, Vienna, 439-456.

Hand, M, Mawby J., Kinny, P. & Foden, J., 1999. U–Pb ages from the Harts Range, central Australia: Evidence for early Ordovician extension and constraints on Carboniferous metamorphism. *Journal of the Geological Society of London*, **156**, 715-730.

Harrison, M.T., Catlos, E.J. & Montel, J.M., 2002. U-Th-Pb dating of Phosphate Minerals. In: Kohn, M.J., Rakovan, J., Hughs, J.M., (Eds) *Phosphates Geochemical, Geobiological, and Materials Importance*. Mineralogical Society of America. Reviews in Mineralogy and Geochemistry, 523–558.

Harrison, T.M., Aleinikoff, J.N. & Compston W., 1987. Observations and controls on the occurrence of inherited zircon in Concord-type granitoids, New Hampshire. *Geochimica Cosmochimica Acta*, **52**, 2549-2558.

Harrison, T.M., McKeegan, K.D. & LeFort, P., 1995. Detection of inherited monazite in the Manaslu leucogranite by $^{208}Pb/^{232}Th$ ion microprobe dating: crystallisation age and tectonic implications. *Earth and Planetary Science Letters*, **133**, 271-282.

Hawkins, D.P. & Bowring, S.A., 1997. U–Pb systematics of monazite and xenotime: case studies from the Palaeoproterozoic of the Grand Canyon, Arizona. *Contributions to Mineralogy and Petrology*, **127**, 87–103.

Heinrich, W., Andrehs, G. & Franz., G., 1997. Monazite–xenotime miscibility gap thermometry: I. An empirical calibration. Journal of Metamorphic Geology, 15, 3–16. Hills, J.H. & Richards, J.R., 1976. Pitchblende and galena ages in the Alligator Rivers region, Northern Territory, Australia. *Mineralium Deposita*, **11**, 133-154.

Horn, I., Rudnick, R.L. & McDoough, W.F., 2000. Precise elemental and isotope ratio determination by simultaneous solution nebulization and laser ablation–ICP–MS: application to U–Pb geochronology. *Chemical Geology*, **164**, 281–300.

Hoskin, P.W.O. & Schaltegger, U., 2003. The composition of Zircon in Igneous and Metamorphic Petrogenesis. In: Hanchar, J.M. & Hoskin, P.W.O. (Eds). *Zircon*. Mineralogical Society of America. Reviews in Mineralogy and Geochemistry, **53**, 27-62.

Hussey, K.J., Huston, D.L. & Claoué–Long, J.C., 2006. Geology and origin of some Cu-Pb-Zn (Au-Ag) deposits in the Strangways Metamorphic Complex, Arunta Region, Northern Territory. *Northern Territory Geological Survey, Report* 17.

Huston, D.L., Maidment, D. & Hussey, K., 2006. Regional geology and Metallogeny of the eastern Aileron and Irindina Provinces: a field guide. *Geoscience Australia, Record,* **2006/13**.

Huston, D.L., Vandenberg, L.C., Wygralak, A.S., Mernagh, T.P., Bagos, L., Crispe, A.J., Cross, A.J., Fraser, G., Williams, N., Wordon, K., Meixner, T., Goleby, B., Jones, L., Lyons, P. & Maidment, D., 2007. Lode-gold mineralisation in the Tanami region, northern Australia. . *Mineralium Deposita*, **42**, 175-204.

Ireland, T.R. & Bukovanská, M. 2003. Initial $^{182}Hf/^{180}Hf$ in meteoritic zircons. *Geochimica Cosmochimica Acta*, **67**, 4849-4856.

Ireland, T.R., 1995. Ion microprobe mass spectrometry: techniques and applications in cosmochemistry, geochemistry, and geochronology. In: Hyman M. & Rowe, M.W., (Eds). Advances in Analytical Geochemisrty, Greenwich, JAI Press, V. 2, 1-118.

Ireland, T.R., Clement, S., Conıpston, W., Foster, J.J., Holden, P., Jenkins, B., Lanc, P., Schram, M. & Williams, I.S., 2008. Development of SHRIMP. *Australian Journal of Earth Sciences*, **55**, 937-954.

Ireland, T.R., Wooden, J.L., Persing, H.M. & Ito, B. 1999. Geological applications and analytical development of the SHRIMP-RG. *EOS (Transactions of the American Geophysical Union)*, vol. 80, no 46, Supplement, p. F1117.

Kerrich, R. & King, R., 1993. Hydrothermal zircon and baddeleyite in Val–d'Or Archaean mesothermal gold deposits: characteristics, compositions, and fluid inclusion properties, with implications for timing of primary gold mineralisation. *Canadian Journal of Earth Science*, **30**, 2334–2351.

Kinny, P.D., 1987. An ion microprobe study of uranium-lead and hafnium isotopes in natural zircon. PhD thesis, Australian National University (unpublished).

Kitajima, L.F.W., Ruiz, J., Gehrels, G., & Gaspar, J.C., 2001. Uranium-lead ages of zircon megacrysts and zircon included in corundum from Peixe alkaline complex (Brazil) (abstract). Simposio Sul Americano de Geologia de Isotopes, 3 (III SSAGI), Pucón, Chile, Extended Abstracts on CD ROM.

Kositcin, N., McNaughton, N.J., Griffen, N.J., Fletcher, I.R., Grover, D.I. & Rasmussen, B., 2003. Textural and geochemical discrimination between xenotime of different origin in the Archaean Witswatersrand Basin, South Africa. *Geochimica et Cosmochimica Acta*, **67**, 709–731.

Kosler, J. & Sylvester, P.J. 2003. Present trends and the future of zircon in geochronology: laser ablation 1CP–MS. In: Hanchar, J.M., Hoskin, P.W.O., (Eds), *Zircon*. Mineralogical Society of America. Reviews in Mineralogy and Geochemistry, vol. 53, pp. 43–275.

Krom, M.D. & Berner, R.A., 1981. the diagenesis of phosphorous in a nearshore marine sediment. *Geochimica et Cosmochimica Acta*, **45**, 207–216.

Laux, J.H., Pimentel, M.M., Dantas, E.L., Armstrong, R.A. & Junges, S.L., 2005. Two neoproterozoic crustal accretion events in the Brasília belt, central Brazil. *Journal of South American Earth Sciences*, **18**, 183-198.

Lee, J.K.W., Williams, I.S. & Ellis, D.J. 1997. Pb, U and Th diffusion in natural zircon. *Nature*, **390**, 159-162.

Li, Z.X., Bogdanova, S.V., Collins, A.S., Davidson, A., De Waele, B., Ernst, R.E., Fitzsimons, I.C.W., Fuck, R.A., Gladkochub, D.P., Jacobs, J., Karlstrom, K.E., Lu, S., Natapov, L.M., Pease, V., Pisarevsky, S.A., Thrane, K. & Vernikovsky, V., 2008. Assembly, configuration, and break-up history of Rodinia: A synthesis. *Precambrian Research*, **160**, 179-210.

London, D. 1992. The Application of Experimental Petrology to the genesis and crystallization of Granitic Pegmatites. *Canadian Mineralogist*, **30**, 499-540.

Lucotte, M., Mucci, A., Hilaire–Marcel, C. & Trans, S., 1994. Early diagenetic processes in deep Labrador sea sediments: reactive and non reactive iron and phosphorous. *Canadian Journal of Earth Sciences*, **31**, 14–27.

Maidment, D.W., Hand, M. & Williams, I.S., 2005. Tectonic cycles in the Strangways Metamorphic Complex, Arunta Inlier, central Australia: geochronological evidence for exhumation and basin formation between two high-grade metamorphic events. *Australian Journal of Earth Sciences*, **52**, 205-215.

Maidment, D.W., 2005. High-grade metamorphism within the Centralian Superbasin, Harts Range region, central Australia. PhD thesis (unpubl.) Australian National University.

Matsuda H., 1990. Double-focusing mass spectrometers of third order. *Nuclear Instruments and Methods in Physics Research A***298**, 199-204.

Matsuda, H., 1974. Double focusing mass spectrometers of second order. *International Journal of Mass Spectrometry and Ion Physics,* **14**, 219-233.

Matthai, S.K., Henley, R.W., Bacigalupo-Rose, S., Binns, R.A., Andrew, A.S., Carr, G.R., French, D.H., McAndrew, J. & Kananagh, M.E. 1995. Intrusion-related, high-Temperature Gold Quartz Veining in the Cosmopolitan Howley Metasedimentary Rock-Hosted Gold Deposi, Northern Territory, Australia. *Economic Geology,* **90**, 1012-1045.

Mawby, J., Hand, M. & Foden J., 1999. Sm-Nd evidence for high-grade Ordovician metamorphism in the Arunta Block, central Australia. *Journal of metamorphic Geology,* **17**, 653-668.

McLaren, A.C., Fitzgerald, J.D. & Williams, I.S., 1994. The microstructure of zircon and its influence on the age determination from Pb/U ratios measured by the ion microprobe. *Geochimica Cosmochimica Acta,* **58**, 993-1005.

McNaughton, N.J., Rasmussen, B. & Fletcher, I.R., 1999. SHRIMP Uranium–lead dating of diagenetic xenotime in siliciclastic sedimentary rocks. Science, 285, 78–80.

Mernagh, T.P. & Wygralak, 2007. Gold ore-forming fluids in the Tanami region, Northern Australia. *Mineralium Deposita,* **42**, 145-173.

Montel, J-.M., Foret, S., Veschambre, M., Nicollet, C. & Provost, A. 1996. Electron microprobe dating of monazite. *Chemical Geology,* **131**, 37–53.

Moraes, R., Fuck, R.A., Oimentel, M.M., Gioia, S.M.C.L. & Figueiredo, A.M.G., 2003. Geochemistry and Sm–Nd isotopic characteristics of bimodal volcanic rocks of Juscelândia, Goias, Brazil: Mesoproterozoic transition from continental rift to ocean basin. *Precambrian Research,* **125**, 317-336.

Moraes, R., Fuck, R.A., Pimentel, M.M., Gioia, S.M.C.L., Hollanda, M.H.B.M. & Armstrong, R.A. 2006. The bimodal rift-related Juscelândia Volcanosedimentary sequence in central Brazil: Mesoproterozoic extension and Neoproterozoic metamorphism. *Journal of South American Earth Sciences,* **20**, 287-301.

Myers, J.S., Shaw, R.D. & Tyler, I.M., 1996. Tectonic evolution of Proterozoic Australia. *Tectonics,* **15**, 1431-1446.

Nelson D.R., 2001. An assessment of the determination of depositional ages for Precambrian clastic sedimentary rocks by U-Pb dating of detrital zircons. *Sedimentary Geology,* **141-142**, 37-60.

Ni. Y., Hughs, J.M. & Mariano, A.N., 1995. Crystal chemistry of the monazite and xenotime structures. *American Mineralogist,* **80**, 21–26.

O'Brien, G.W., Heggie, D., 1988. East Australian continental phosphorites. *Eos, Transactions of the American Geophysical Union*, **69**, 2.

Oliveira, C.G., Pimentel, M.M., Melo, L.V. & Fuck, R.A., 2004. the copper-gold and gold deposits of the Neoproterozoic Mara Rosa magmatic arc, central Brazil. *Ore Geology Reviews*, **25**, 285-299.

Overstreet, W.C., 1967. The geological occurrence of monazite. *United States Geological Survey, professional Paper*, **530**.

Paces, J.B. & Miller, J.D., Jr., 1993. Precise U-Pb ages of Duluth Complex and related mafic intrusions, north-eastern Minnesota; geochronological insights to physical, petrogenetic, paleomagnetic, and tectonomagnetic processes associated with the 1.1 Ga Midcontinent Rift System. *Journal of Geophysical Research, Ser.B, Solid Earth and Planets*, **98**, 13,997-14013.

Pan, Y., 1997. Zircon– and monazite-forming metamorphic reactions at Manitouwadge, Ontario. *Canadian Mineralogist*, **35**, 15–118.

Petersson, J., Whitehouse, M.J. & Eliason, T., 2001. Ion microprobe U–Pb dating of hydrothermal xenotime from an episyenite: evidence for rift–related reactivation. *Chemical Geology*, **175**, 703–712.

Pichavant, M., Montel, J.-M. & Richard, L.R., 1992. Apatite solubility in peraluminous liquids: Experimental data and an extension of the Harrison-Watson model. *Geochimica et Cosmochimica Acta*, **56**, 3855-3861.

Pigois, J.-P., Groves, D.I., Fletcher, I.R., McNaughton, N.J. & Snee, L.W., 2003. Age constraints on Tarkwaian palaeoplacer and lode gold forming in the Tarkwa–Damang district, SW Ghana. *Mineralium Deposita*, **38**, 695–714.

Pimentel, M.M., Ferreira Filho, C.F. & Armele, A., 2006. Neoproterozoic age of the Niquelândia Complex, central Brazil: Further ID–TIMS and Sm–Nd isotopic evidence. *Journal of South American earth Sciences*, **21**, 228-238.

Pimentel, M.M., Ferreira Filho, C.F. & Armstrong, R.A., 2004. SHRIMP U–Pb and Sm–Nd ages of the Niquelândia layered complex: Meso- (1.25 Ga) and Neoproterozoic (0.79 Ga) extensional events in central Brazil. *Precambrian Research*, **132**, 133-153.

Pimentel, M.M., Fuck, R.A. & Alvarenga, C.J.S., 1996. Post Brasiliano (Pan-African) high-K granitic magmatism in central Brazil: the role of the late Precambrian Early Palaeozoic extension. *Precambrian Research*, **80**, 217-238.

Pimentel, M.M., Fuck, R.A., Jost, H., Ferreira Filho, C.F. & Araújo, S.M., 2000. the basement of the Brasilia Fold Belt and the Goiás Magmatic Arc. In: Cordani, U.G., Milani, E.J., Thomaz, Filho, A., Campos, D.A. (Eds). Proceedings of the 31st International geological Congress on the Tectonic Evolution of South America. Rio de Janeiro, 195-229.

Pimentel, M.M., Heaman, L., Fuck, R.A. & Marini, O.J., 1991a. U–Pb zircon geochronology of Precambrian tin-bearing continental-type acid magmatism in central Brazil. *Precambrian Resarch*, **52**, 321-335.

Pimentel, M.M., Heaman, L. & Fuck, R.A., 1991b. Zircon and sphene U–Pb geochronology of Upper Proterozoic volcanic-arc rock units from southwestern Goiás, central Brazil. *Journal of South American Erath Sciences*, **4 (4)**, 295-305.

Pimentel, M.M., Whitehouse, M.J., Viana, M.d.G., Fuck, R.A. & Machado, N., 1997. The Mara Rosa Arc in the Tocantins Province: further evidence for Neoproterozoic crustal accretion in central Brazil. *Precambrian Research*, **81**, 299-310.

Piuzana, D., Pimentel, M.M., Fuck, R.A. & Armstrong, R.A., 2003. Neoproterozoic granulite facies metamorphism and coeval granitic magmatism in the Brasilia Belt, central Brazil: regional implications of new SHRIMP U–Pb and Sm–Nd data. *Precambrian Research*, **125**, 245-273.

Polito, P.A., Kyser, T.K., Thomas, D., Marlatt, J. & Drever, G., 2005. Re-evaluation of the petrogenesis of the Proterozpoic Jabiluka unconformity-related uranium deposit, Northern Territory, Australia. *Mineralium Deposita*, **40**, 257–288.

Preiss, W.V., 2000. The Adelaide Geosyncline of South Australia and its significance in Neoproterozoic continental reconstruction. *Precambrian Research*, **100**, 21-63.

Pyle, J.M., Spear, F.S., 2000. An empirical garnet (YAG)-xenotime thermometer. Contributions to Mineralogy and Petrology, **138**, 51–58.

Pyle, J.M., Spear, M.S., 1999. Yttrium zoning in garnet: coupling of major and accessory phases during metamorphic reactions. *Geological Material Research*, **1**, 1–49.

Pyle, J.M., Spear, F.S. & Wark, D.A., 2002. Electron Microprobe Analysis of REE in Apatite, Monazite and Xenotime: Protocols and Pitfalls. In: Kohn, M.J., Rakovan, J., Hughs, J.M., (Eds) *Phosphates Geochemical, Geobiological, and Materials Importance*. Mineralogical Society of America. Reviews in Mineralogy and Geochemistry, 337-362.

Rainbird, R.H., Davis, W.J., Stern, R.A., Peterson, T.D., Smith, S.R., Parrish, R.R. & Hadlari, T., 2006. Ar-Ar and U–Pb Geochronology of Late Palaeoproterozoic Rift Basin: Support for a Genetic Link with Hudsonian Orogenesis, Western Churchill Province, Nanavut, Canada. *The Journal of Geology*, **114**, 1-17.

Rasmussen, B., 1996. Early-diagenetic REE-phosphate minerals (Florencite, Gorceixite, Crandallite, and Xenotime) in marine sandstones: a major sink for oceanic phosphorous. *American Journal of Science*, **296**, 601–632.

Rasmussen, B., 2005. Radiometric dating of sedimentary rocks: the application of diagenetic xenotime geochronology. *Earth-Science Reviews*, **68**, 197–243.

Rasmussen, B., Buick, R. & Taylor, W.R., 1998. Removal of oceanic REE by authigenic precipitation of phosphatic minerals. *Earth and Planetary Science Letters,* **164**, 135–149.

Rasmussen, B., Fletcher, I.R., Bengtson, S. & McNaughton, N.J. 2004. SHRIMP U–Pb dating of diagenetic xenotime in the Stirling Range Formation, Western Australia: 1.8 billion-year minimum age for Stirling Biota. *Precambrian Research,* **133**, 133–339.

Rasmussen, B., Fletcher, I.R., Muhling, J.R., Thorne, W.S. & Broadbent, G.C., 2007. Prolonged history of episodic fluid flow in giant hematite ore bodies. Evidence from in situ U–Pb geochronology of hydrothermal xenotime. *Earth and Planetary Science Letters,* **258**, 249-259.

Rasmussen, B., Sheppard, S. & Fletcher, I.R., 2006. Testing of ore deposit models using in situ U-Pb geochronology of hydrothermal monazite: Paleoproterozoic gold mineralisation in northern Australia. *Geology,* **34**, 77-80.

Rassmussen, B. & Fletcher, I.R., 2002. Indirect dating of mafic intrusions by SHRIMP U–Pb analysis of monazite in contact metamorphosed shale: an example from the Palaeoproterozoic Capricorn Orogen, Western Australia. *Earth and Planetary Science Letters,* **197**, 287-299.

Rubatto, D., Williams, I.S. & Buick I.S., 2001. Zircon and monazite response to prograde metamorphism in the Reynolds Range, central Australia. *Contributions to Mineralogy and Petrology,* **140**, 458-468.

Salier, B., Groves, D.I., McNaughton, N.J. & Fletcher, I.R., 2004. The world-class Wallaby gold deposit, Laverton, Western Australia: An orogenic-style overprint on magmatic-hydrothermal magnetite-calcite alteration pipe? *Mineralium Deposita,* **39**, 473–494.

Salier, B., Groves, D.I., McNaughton, N.J. & Fletcher, I.R., 2005. Geochronological and stable isotope evidence for widespread orogenic gold mineralisation from a deep-seated fluid source at ca. 2.65 Ga in the Laverton gold province, Western Australia. *Economic Geology,* **100**, 1363–1388.

Salier, B., Groves, D.I., McNaughton, N.J. & Fletcher, I.R., 2004. The world-class Wallaby gold deposit, Laverton, Western Australia: An orogenic-style overprint on magmatic-hydrothermal magnetite-calcite alteration pipe? *Mineralium Deposita,* **39**, 473–494.

Schaltegger, U., Pettke, T., Audétat, A., Reusses, E. & Heinrich, A., 2005. Magmatic to hydrothermal crystallisation in the W–Sn mineralised Mole Granite (NSW, Australia) Part I: Crystallisation of zircon and REE phosphates over three million years a geochemical and U–Pb geochronological study. *Chemical Geology,* **220**, 215–235.

Schärer, U., Tapponier, P., Lacassin, R., Leloup, P.H., Dalai, Z. & Shaocheng, J., 1990. Intraplate tectonics in Asia: a precise age for large–scale Miocene movement

along the Ailao Shan–Red River shear zone, China. *Earth and Planetary Science Letters*, **142**, 331–351.

Scrimgeour, I & Raith, J. 2001 Tectonic and thermal events in the northeastern Arunta Province. *Northern Territory Geological Survey, Report* **12**.

Scrimgeour, I.R. & Saniford, M., 1993. Early Proterozoic metamorphism at the granites gold mine, Northern Territory: implications for the timing of fluid production in high-temperature, low-pressure terranes. *Economic Geology*, **88**, 1099-1113.

Scrimgeour, I.R., 2006. The Arunta Region: Links between tectonics and mineralisation. *Annual Geoscience Exploration Seminar (AGES) Record of Abstracts, Northern Territory Geological Survey Record* **2006-001**.

Selby, D. & Creaser, R.A., 2001. Re-Os geochronology and systematics in molybdenite from the Endako porphyry molybdenum deposit, British Columbia, Canada. *Economic Geology,* **96**, 197-204.

Selby, D. & Creaser, R.A., 2004. Macroscale NTIMS and microscale LA-MC-ICP-MS Re-Os isotopic analysis of molybdenite: testing spatial restrictions for reliable Re-Os age determinations, and implications for the decoupling of Re and Os within molybdenite. *Geochimica et Cosmochimica Acta*, **68**, 3897-3908.

Sener, A.K., Young, C., Groves, D.I., Krapez, B. & Fletcher, I.R. 2005. Major orogenic gold episode associated with Cordilleran-style tectonics related to the assembly of Paleoproterozoic Australia?: *Geology*, **33**, 225-228.

Shaw, R.D. & Warren, R.G., 1975. Alcoota, Northern Territory, 1;250 000 geological sheet and explanatory notes. *Bureau of Mineral Resource, Australia.*

Shaw, R.D., Warren, R.G., Offe, L.A., Freeman, M.J. & Horsfall, C.L. 1984. Geology of the Arunta Block in the southern part of the Huckitta 1:250 000 sheet area-Preliminary data 1980 Survey. *Bureau of Mineral Resources, Record,* **1984/3**.

Sheppard, S, Tyler, I.M., Griffin, T.J. & Taylor, W.R., 1999. Palaeoproterozoic subduction-related and passive margin basalts in the Halls Creek Orogen, northwest *Australian Journal of Earth Sciences*, **46**, 679-690.

Sheppard, S., 1996. Thrust-controlled, gold quartz vein mineralisation at the Tom's Gully mine, Northern Territory: *Mineralium Deposita*, **31**, 59-70.

Shimizu, N. & Hart, S.R., 1982. Applications of the ion microprobe to geochemistry and cosmochemistry: *Annual Reviews of Earth and Planetary Science*, **10**, 483-526.

Simonetti, A., Heaman, L.M., Chacko, T. & Banerjee, N.R., 2006. In situ petrographic thin section U–Pb dating of zircon, monazite, and titanate using laser ablation–MC–ICP–MS. *International Journal of Mass Spectrometry*, 253, **87-97**.

Smith, M.E.H., Lovett, D.R., Pring, P.I. & Sando, B.G., 1998. Dead Bullock Soak gold deposits, in Geology of Australian and Papuan New Guinean Mineral Deposits.

Berkman, D.A. & Mackenzie, D.H. (Eds). The Australasian Institute of Mining and Metallurgy, Melbourne, 449-460.

Smoliar, M.I., Walker, R.J. & Morgan J.W., 1996. Re-Os ages of Group IIA, IIIA, IVA and IVB iron meteorites. *Nature*, **271**, 1099-1102.

Soares, J.E., Berrocal, J., Fuck, R.A., Mooney, W.D. & Ventura, D.B.R. 2006. Seismic characteristics of central Brazil crust and upper mantle:A deep seismic refraction study. *Journal of Geophysical Research*, **111**, 12302.

Spandler, C., Hermann, J. & Rubatto, D., 2004. Exsolution of thortveitite, yttrialite and xenotime during low-temperature recrystallisation of zircon from New Caledonia, and their significance for trace element incorporation into zircon. *American Mineralogist*, **89**, 1795–1806.

Spear, F.S., Pyle, J.M., 2002. Apatite, monazite and xenotime in metamorphic rocks. . In: Kohn, M.J., Rakovan, J., Hughs, J.M., (Eds) *Phosphates Geochemical, Geobiological, and Materials Importance*. Mineralogical Society of America. Reviews in Mineralogy and Geochemistry, 293-331.

Stacey, J.S. & Kramers, J.D., 1975. Approximation of terrestrial lead isotope evolution by a two-stage model. *Earth and Planetary Science Letters*, **26**, 207-221.

Steiger, R.H. & Jäger, E. 1977. Subcommision on geochronology convention on the use of decay constants in geo- and cosmochronology. *Earth and Planetary Science Letters*, **36**, 359-362.

Stern, R.A., Fletcher, I.R., Rasmussen, B., McNaughton, N.J. & Griffin, B.J. 2005. Ion microprobe (NanoSIMS 50) Pb-isotope geochronology at <5 μm scale. *International Journal of Mass Spectrometry*, **244**, 125-134.

Stern, R.A. & Amelin, Y. 2003. Assessment of errors in SIMS zircon U–Pb geochronology using a natural standard and NIST SRM 610 glass. *Chemical Geology*, **197**, 111-142.

Stern, R.A. & Berman, R.G. 2000. Monazite U-Pb and Th-Pb geochronology by ion microprobe, with an application to in situ dating of an Archean metasedimentary rock. *Chemical Geology*, **172**, 113-130.

Stern, R.A. & Sanborn, N., 1998. Monazite U-Pb and Th-Pb geochronology by high-resolution secondary ion mass spectrometry. Radiogenic Age and Isotopic Studies: Report 11. Geological Survey of Canada, Current Research, 1-18, 1998-F.

Stern, R.A. 2000. The significance of secondary ion energy profiles for understanding inter-element calibration curve in SIMS analysis of zircon and monazite. In: Woodhead, J.D., Hergt, J.M. and Noble, W.P. (Eds). Beyond 2000: *New Frontiers in Isotope Geoscience, Lorne, 2000 Abstracts and Proceedings*, pp. 167–170. University of Melbourne, Melbourne.

Stern, R.A. and Rayner, N. (2003). Ages of several xenotime megacrysts by ID–TIMS: potential reference materials for ion probe U–Pb geochronology. Geological Survey of Canada, Current Research 2003–F1; Radiogenic age and isotope studies, report 16. 1–7.

Stuart-Smith, P.G., Needham, R.S., Page, R.W., & Wyborn, L.A.I. 1993. Geology and Mineral deposits of the Cullen Mineral Field, Northern Territory: *Australian Geological Survey Organisation Bulletin*, **229**, 145.

Suita, M.T.F., Kamo, S., Kroght, T.E., Fyfe, W.S. & Hatmann, L.A., 1994. U–Pb ages from the high-grade Barro Alto mafic-ultramafic complex (Goiás, central Brazil): middle Proterozoic continental mafic magmatism and upper Proterozoic continental collision. In: International Conference on Geochronology, Cosmochronology and Isotope Geology. ICOG, Abstracts, vol. 8., Berkeley, USGS, p.309.

Suzuki, K. & Adachi, M., 1991. Precambrian provenance and Silurian metamorphism of the Tsubonnsawa paragneissin the South Kitakami terrane, Northeast Japan, revealed by the chemical Th–U–total–Pb isochron ages of monazite, zircon and xenotime. *Geochemical Journal*, **25**, 357–376.

Suzuki, K. & Adachi, M., 1994. Middle Precambrian detrital monazite and zircon from the Hida gneiss on Oki–Dogo Island, Japan: their origin and implications for the correlation of basement gneiss of southwest Japan and Korea. *Tectonophysics*, **235**, 277–292.

Tallarico, F.H.B., McNaughton, N.J., Groves, D.I., Fletcher, I.R., Figueiredo, B.R., Carvalol, J.B., Rego, J.L. & Nunes, A.R., 2004. Geological and SHRIMP II U–Pb constraints on the age and origin of the Breves Cu–Au–(W–Bi–Sn)deposit, Carajás, Brasil. *Mineralium Deposita*, **39**, 68-86.

Trendall, A.F., Compston, W., Nelson, D.R., De Laeter, J.R. & Bennett, V.C., 2004. SHRIMP zircon ages constraining the depositional chronology of the Hamersley Group, Western Australia. *Australian Journal of Earth Sciences*, **51**, 621–644.

Tunks, A.J., & Cooke, D.R., 2007. Geological and structural controls on gold mineralisation in the Tanami District, Northern Territory. *Mineralium Deposita*, **42**, 107-126.

Turner, N.J., Black, L.P. & Kamperman, M., 1998. Dating of Neoproterozoic and Cambrian orogenies in Tasmania. *Australian Journal of earth Sciences*, **45**, 789-806.

Vallini, D., Rasmussen, B., Krapez, B., Fletcher, I.R. & McNaughton, N.J., 2002. Obtaining diagenetic ages from metamorphosed sedimentary rocks: U–Pb dating of unusually coarse xenotime cement in phosphatic sandstone. *Geology*, **30**, 1083–1086.

Vallini, D.A., Cannon, W.F. & Schultz, K.J., 2006. Age constraints for the Palaeoproterozoic glaciation in the Lake Superior region: detrital zircon and hydrothermal xenotime ages from the Chocolay Group, Marquette Range Supergroup. *Canadian Journal of Earth Sciences*, **43**, 571–591.

Vallini, D.A., Groves, D.I., McNaughton, N.J. & Fletcher, I.R., (2007) Uraniferous diagenetic xenotime in northern Australia and its relationship to unconformity-associated uranium mineralisation. *Mineralium Deposita*, **42**, 51-64.

Vallini, D.A., Rasmussen , B., Kraez, B., Fletcher, I.R. & McNaughton, N.J., 2005. Microtextures geochemistry and geochronology of authigenic xenotime: constraining the cementation history of a Palaeoproterozoic metasedimentary sequence. *Sedimentology*, **52**, 101–122.

van Emden, B., Thomber, M.R., Graham, J. & Lincoln, F.J., 1997. The incorporation of actinides in monazite and xenotime from placer deposits in Western Australia. *Canadian Mineralogist*, **35**, 95–104.

Vaslov, K., 1966a. Geochemistry and mineralogy of rare elements and genetic types of their deposits. Volume I Mineralogy of rare elements . Academy of the Sciences USSR. State Geological committee of the USSR. Israel Program for Scientific Translation, pp. 945.

Vaslov, K., 1966b. Geochemistry and mineralogy of rare elements and genetic types of their deposits. Volume II Geochemistry of rare elements. Academy of the Sciences USSR. State Geological committee of the USSR. Israel Program for Scientific Translation, pp. 688.

Vielreicher, N.M., Groves, D.I., Fletcher, I.R., McNaughton, N.J & Rasmussen, B., 2003. Hydrothermal Monazite and Xenotime Geochronology: A New Direction for Precise Dating of Orogenic Gold Mineralisation. Society of Economic Geologists, Newsletter, 53, 1, 10–16.

Vielzeuf, D., Champenois, M., Valley, J.W., Brunet, F. & Devidal, J.L. SIMS analysis of oxygen isotopes: Matrix effects in Fe-Mg-Ca garnets. *Chemical Geology*, **223**, 208-226.

Viskupic, K. & Hodges, K.V., 2001. Monazite–xenotime thermochronometry: methodology and an example from the Nepalese Himalaya. Contributions to *Mineralogy and Petrology*, **141**, 233–247.

Voulgaris, P., & Emslie, J., 2004. Geology and ore estimation at the Callie underground gold mine, Tanami, NT. *Australasian Inst. Min. Metall. Bull.*, **2**, 71-78.

Wall, F. & Mariano, A.N., 1996. Rare earth minerals in carbonatites: a discussion centred on the Kangankunde Carbonatite, Malawi. In: Jones, A.P., Wall, F. & Williams C.T., (Eds), *Rare Earth Minerals, chemistry, origin and ore deposits*, The Mineralogical Society Series, 7, 193-226.

Wall, V.J. & Taylor, J.R., 1990. Granite emplacement and temporally related gold mineralisation. *Geological Society of Australia, Abstracts*, **25**, 264-265.

Wark, D.A. & Miller, C.F., 1993. Accessory mineral behaviour during differentiation of a granite suite: monazite, xenotime and zircon in the Sweetwater Wash pluton, southeastern California, USA. *Chemical Geology*, **110**, 49–67.

Wells, A.T., Forman, D.J., Ranford, L.C. & Cook P.J., 1970. Geology of the Amadeus Basin, central Australia. *Bureau of Mineral Resources, Australia, Bulletin*, **100**.

Williams, I.S. & Cleason, S. 1987. Isotopic evidence for the Precambrian provenance and Caledonian metamorphism of hih-grade paragneisses from the Seve Nappes. Scandinavian Caledonides:II. Ion microprobe zircon U-Th-Pb. *Contributions to Mineralogy and Petrology*, **97**, 205-217.

Williams, I.S. & Hergt, J.M., 2000. U–Pb dating of Tasmanian dolerites: a cautionary tale of SHRIMP analysis of high–U zircon. In: Woodhead, J.D., Hergt, J.M. and Noble, W.P. (Eds). Beyond 2000: *New Frontiers in Isotope Geoscience, Lorne, 2000 Abstracts and Proceedings*, pp. 185–188. University of Melbourne, Melbourne.

Williams, I.S., 2001. Response of detrital zircon and monazite, and their U-Pb isotopic systems, to regional metamorphism and host-rock partial melting, Cooma Complex, southeastern Australia. *Australian Journal of Earth Science*, **48**, 557-580.

Williams, I.S., 1998. U–Th–Pb geochronology by ion microprobe. In: McKibben, M.A., Shanks, III, W.C., Ridley, W.I. (Eds.), *Applications of microanalytical Techniques to Understanding Mineralisation Processes*. Rev. Econ. Geol., vol. **7**. Society of Economic Geologists, El Paso, Texas, 1–35.

Williams, I.S., Buick, I.S. & Cartwright, I. 1996. An extended episode of early Mesoproterozoic metamorphic fluid flow in the Reynolds range, central Australia. *Journal of Metamorphic Petrology*, **14**, 29-47.

Williams, N.C., 2007. The role of decarbonization and structure in the Callie gold deposit, Tanami Region of northern Australia. . *Mineralium Deposita*, **42**, 65-87.

Wingate, M.T.D. & Compston, W., 2000. Crystal orientation effects during ion microprobe U-Pb analysis of baddeleyite. *Chemical Geology*, **165**, 75-97.

Wingate, M.T.D. & Giddings, J.W., 2000. Age and Palaeomagnetism of the Mundine Well dyke swarm, Western Australia. *Precambrian Research*, **100**, 335-357.

Wolf, M.B. & London, D., 1994. Apatite dissolution into peraluminous haplogranitic melts: an experimental study of solubilities and mechanisms. Geochim Cosmochim Acta, **58**, 4127-4145.

Wolf, M.B. & London, D., 1995. Incongruent dissolution of REE- and Sr-rich apatite in peraluminous granite liquids: differential apatite, monazite, and xenotime solubilities during anatexis. *American Mineralogist*, **80**, 765-775.

Wordon, K.E. 2006. Geology and Geochronology of the Palaeoproterozoic Pine Creek Orogen. In: Lyons, P. & Huston, D.L., (Eds). *Evolution and metallogenesis of*

the North Australian Craton, Conference Abstracts. Geoscience Australia Record 2006/16.

Wygralak, A.S. & Ahmad, M., 1990. Fluid inclusions and stable isotope studies of Au-quartz vein deposits in the Pine Creek Geosyncline, Northern Territory. *Geological Society of Australia, Abstracts,* **25**, 157.

Wygralak, A.S., Mernagh, T.P., Huston, D.L., & Ahmad, M., 2005. Gold mineral system of the Tanami region: *Northern Territory Geological Survey Report* **18**, CD-ROM.

Zhao, J & McCulloch, M.T. 1995. Geochemical and Nd isotopic systematics of granites from the Arunta Inlier: implications for Proterozoic crustal evolution. *Precambrian Research,* **71**, 265-299.

Zhao, J. & Bennett, V.C. 1995. SHRIMP U–Pb zircon geochronology of granites in the Arunta Inlier, central Australia: implications for Proterozoic crustal evolution. *Precambrian Research,* **71**, 17-43.

Zhu, X.K., O'Nions, R.K. & Gibb, A.J., 1998. SIMS analysis of U-Pb isotopes in monazite: matrix effects. *Chemical Geology,* **144**, 305-312.

Zinner, E.K. & Croaz, G. 1986. A method for the quantitative measurement of rare earth elements in the ion microprobe. *International Journal of mass spectrometry and Ion Physics,* **69**, 17-38.

APPENDIX 1.1- SHRIMP U-Pb data tables for Chapter 1

Table S1 SHRIMP U-Pb isotopic data for zircons from arkose in the Ferdies Member (2003082647).

Spot name	U (ppm)	Th (ppm)	Th/U	^{206}Pbc (ppm)	^{238}U/^{206}Pb (±1σ %)		^{207}Pb/^{206}Pb (±1σ %)		^{207}Pb/^{206}Pb age (Ma ± 1σ)		Discordance (%)
A86.1	41	52	1.31	1.5	2.26	2.69	0.1497	9.88	2342	169	-1
A111.1	36	31	0.89	1.2	2.32	2.56	0.1545	7.99	2396	136	4
A7.1	53	74	1.43	0.4	2.20	2.18	0.1586	2.24	2441	38	1
A118.1	49	49	1.03	0.3	2.21	2.19	0.1597	2.41	2452	41	2
A99.1	145	148	1.05	2.2	2.11	1.89	0.1602	4.98	2458	84	-2
A21.1	77	128	1.73	1.2	2.14	2.06	0.1604	3.45	2460	58	0
A110.1	191	154	0.83	4.3	2.23	1.74	0.1611	4.18	2467	71	3
A48.1	168	283	1.74	2.4	2.09	1.76	0.1612	2.98	2468	50	-2
A3.2	56	60	1.11	1.4	2.15	2.30	0.1613	6.05	2470	102	0
A97.1	32	45	1.46	0.2	2.00	2.51	0.1614	2.97	2470	50	-6
A52.1	67	30	0.46	1.4	2.20	2.08	0.1626	4.63	2483	78	3
A103.1	132	73	0.57	0.2	2.10	1.78	0.1630	0.91	2487	15	-1
A20.1	116	88	0.78	1.0	2.17	1.86	0.1631	2.06	2488	35	2
A37.1	53	83	1.61	0.4	2.11	2.22	0.1633	2.81	2490	47	-1
A87.1	28	35	1.28	0.2	2.08	2.63	0.1635	3.66	2492	62	-1
A36.1	89	89	1.04	0.9	2.13	1.94	0.1638	2.33	2495	39	1
A113.1	97	99	1.06	1.0	2.20	1.89	0.1641	2.51	2499	42	4
A114.1	44	70	1.64	0.2	2.15	2.26	0.1642	1.92	2499	32	1
A115.1	44	70	1.64	0.2	2.15	2.26	0.1642	1.92	2499	32	1
A116.1	44	70	1.64	0.2	2.15	2.26	0.1642	1.92	2499	32	1
A65.1	145	126	0.90	3.8	2.20	1.84	0.1643	5.24	2500	88	4
A107.1	196	134	0.70	16.2	1.93	2.23	0.1643	14.26	2501	240	-7
A17.1	48	85	1.82	3.7	2.14	2.95	0.1644	14.62	2501	246	1
A45.1	96	139	1.50	1.7	2.13	1.95	0.1645	3.73	2502	63	1
A104.1	95	114	1.24	5.4	1.93	2.49	0.1648	12.92	2506	217	-7
A84.1	140	124	0.91	2.9	2.04	1.85	0.1649	4.32	2506	73	-2
A78.1	252	261	1.07	0.7	2.11	1.64	0.1650	0.95	2508	16	0
A44.1	127	74	0.60	1.8	2.09	1.82	0.1650	2.83	2508	48	-1
A85.1	133	121	0.94	0.7	2.09	1.77	0.1651	1.42	2509	24	0
A105.1	136	132	1.00	0.3	2.10	1.76	0.1652	1.03	2510	17	0
A34.1	69	65	0.97	1.7	2.17	2.22	0.1653	5.94	2510	100	3
A59.1	258	230	0.92	2.3	2.32	1.64	0.1654	2.07	2512	35	9
A60.1	258	230	0.92	2.3	2.32	1.64	0.1654	2.07	2512	35	9
A120.1	181	190	1.09	0.5	2.09	1.70	0.1655	1.04	2513	17	0
A1.1	130	86	0.69	0.3	2.17	1.80	0.1656	1.11	2514	19	3
A39.1	197	150	0.79	0.9	2.17	1.69	0.1656	1.26	2514	21	3
A29.1	167	166	1.03	1.5	2.16	1.78	0.1656	2.43	2514	41	2
A3.1	100	119	1.22	0.3	2.13	1.87	0.1659	1.11	2517	19	1
A56.1	43	46	1.09	2.8	2.26	2.60	0.1659	11.36	2517	191	7
A15.1	414	210	0.53	1.1	2.12	1.58	0.1660	0.67	2517	11	1
A4.1	128	123	0.99	0.4	2.09	1.79	0.1660	1.02	2518	17	0
A24.1	291	376	1.34	1.3	2.12	1.64	0.1662	1.10	2519	18	1
A35.1	186	138	0.77	1.5	2.28	1.72	0.1662	2.10	2520	35	8
A79.1	88	162	1.92	0.4	2.08	1.90	0.1663	1.50	2520	25	-1
A49.1	180	189	1.08	0.4	2.07	1.70	0.1663	0.78	2520	13	-1
A96.1	249	100	0.41	0.2	2.04	1.64	0.1663	0.50	2520	8	-2
A68.1	303	94	0.32	2.6	2.11	1.61	0.1663	1.66	2520	28	1
A16.1	189	249	1.36	1.3	2.17	1.72	0.1664	2.19	2522	37	3
A112.1	397	388	1.01	0.3	2.08	1.58	0.1664	0.39	2522	7	-1
A64.1	298	331	1.15	0.3	2.10	1.61	0.1664	0.47	2522	8	0
A69.1	116	107	0.95	1.0	2.11	1.80	0.1666	2.12	2524	36	1
A13.1	240	150	0.65	0.2	2.16	1.66	0.1667	0.57	2524	10	3
A109.1	95	96	1.03	0.2	2.09	1.88	0.1667	1.02	2524	17	0
A41.1	250	140	0.58	2.0	2.15	1.65	0.1667	1.78	2525	30	3
A74.1	185	204	1.14	2.1	2.08	1.70	0.1667	2.24	2525	38	0
A93.1	102	108	1.10	0.2	2.07	1.86	0.1668	1.07	2525	18	-1
A94.1	102	108	1.10	0.2	2.07	1.86	0.1668	1.07	2525	18	-1

Table S1 SHRIMP U-Pb isotopic data for zircons from arkose in the Ferdies Member (2003082647) continued.

Spot name	U (ppm)	Th (ppm)	Th/U	^{206}Pbc (ppm)	^{238}U/^{206}Pb ($\pm 1\sigma$ %)		^{207}Pb/^{206}Pb ($\pm 1\sigma$ %)		^{207}Pb/^{206}Pb age (Ma $\pm$ 1σ)		Discordance (%)
A95.1	102	108	1.10	0.2	2.07	1.86	0.1668	1.07	2525	18	-1
A89.1	402	289	0.74	1.2	2.11	1.58	0.1668	0.71	2526	12	1
A70.1	160	250	1.61	0.2	2.09	1.70	0.1668	0.81	2526	14	0
A25.1	456	141	0.32	0.4	2.18	1.58	0.1668	0.45	2526	7	4
A88.1	317	304	0.99	1.9	2.07	1.61	0.1669	1.34	2527	22	-1
A106.1	144	106	0.76	0.8	2.05	1.76	0.1670	1.50	2527	25	-1
A2.1	171	182	1.10	0.1	2.14	1.71	0.1670	0.64	2527	11	2
A51.1	173	169	1.01	3.6	2.08	1.74	0.1670	3.57	2528	60	0
A90.1	127	79	0.64	0.1	2.09	1.77	0.1670	0.75	2528	13	0
A91.1	127	79	0.64	0.1	2.09	1.77	0.1670	0.75	2528	13	0
A92.1	127	79	0.64	0.1	2.09	1.77	0.1670	0.75	2528	13	0
A10.1	205	182	0.92	2.8	2.15	1.73	0.1671	2.58	2529	43	3
A77.1	151	77	0.53	0.3	2.08	1.72	0.1672	0.83	2529	14	0
A30.1	105	139	1.37	0.3	2.14	1.88	0.1672	1.14	2530	19	2
A47.1	491	148	0.31	2.1	2.09	1.56	0.1672	0.85	2530	14	0
A101.1	93	113	1.26	7.8	2.08	2.33	0.1672	12.80	2530	215	0
A73.1	189	182	1.00	0.3	2.15	1.67	0.1672	0.71	2530	12	3
A98.1	260	167	0.67	0.3	2.14	1.64	0.1673	0.63	2531	11	3
A9.1	144	128	0.92	0.4	2.25	1.77	0.1673	1.05	2531	18	7
A117.1	188	127	0.70	0.5	2.14	1.69	0.1673	1.47	2531	25	3
A40.1	164	153	0.96	0.2	2.12	1.73	0.1674	0.94	2532	16	2
A6.1	332	114	0.36	0.4	2.14	1.61	0.1674	0.52	2532	9	2
A33.1	77	43	0.57	0.2	2.09	1.99	0.1674	1.27	2532	21	1
A72.1	183	164	0.93	0.7	2.08	1.69	0.1676	1.50	2534	25	0
A32.1	161	133	0.86	0.5	2.11	1.75	0.1676	0.97	2534	16	1
A38.1	141	177	1.30	2.6	2.15	1.82	0.1677	3.43	2535	58	3
A67.1	404	226	0.58	0.2	2.07	1.57	0.1678	0.37	2536	6	0
A31.1	1017	386	0.39	0.2	2.12	1.52	0.1678	0.24	2536	4	2
A66.1	170	197	1.20	1.7	2.06	1.72	0.1679	2.31	2537	39	-1
A5.1	177	196	1.14	1.6	2.21	1.73	0.1680	2.05	2537	34	6
A43.1	499	310	0.64	0.4	2.11	1.56	0.1682	0.39	2540	7	1
A57.1	188	164	0.91	1.9	2.03	1.72	0.1683	2.31	2540	39	-2
A58.1	188	164	0.91	1.9	2.03	1.72	0.1683	2.31	2540	39	-2
A80.1	104	95	0.94	2.3	2.11	1.88	0.1683	3.94	2541	66	2
A81.1	104	95	0.94	2.3	2.11	1.88	0.1683	3.94	2541	66	2
A82.1	104	95	0.94	2.3	2.11	1.88	0.1683	3.94	2541	66	2
A76.1	173	107	0.64	2.8	2.02	1.74	0.1683	3.10	2541	52	-2
A54.1	57	41	0.75	0.2	2.06	2.08	0.1684	1.35	2542	23	0
A8.1	219	183	0.86	0.2	2.11	1.68	0.1684	0.50	2542	8	2
A46.1	132	71	0.56	1.5	2.05	1.79	0.1685	2.32	2542	39	-1
A26.1	151	137	0.93	3.5	2.25	1.83	0.1686	4.40	2544	74	7
A27.1	213	186	0.91	0.9	2.19	1.69	0.1688	1.06	2546	18	5
A28.1	125	96	0.79	0.4	2.16	1.82	0.1688	1.13	2546	19	4
A18.1	230	357	1.60	0.2	2.13	1.68	0.1689	0.67	2547	11	3
A102.1	150	147	1.02	0.7	2.10	1.74	0.1690	1.26	2548	21	2
A22.1	291	234	0.83	0.4	2.16	1.64	0.1691	0.74	2549	12	4
A83.1	191	134	0.73	0.5	2.15	1.68	0.1694	0.83	2551	14	4
A50.1	64	70	1.12	0.0	2.12	2.03	0.1694	1.28	2552	21	2
A14.1	115	101	0.90	0.7	2.06	1.85	0.1694	1.46	2552	25	0
A62.1	225	172	0.79	1.0	2.13	1.65	0.1696	1.04	2554	17	3

239

Table S1 SHRIMP U-Pb isotopic data for zircons from arkose in the Ferdies Member (2003082647) continued.

Spot name	U (ppm)	Th (ppm)	Th/U	^{206}Pbc (ppm)	^{238}U/^{206}Pb (±1σ %)		^{207}Pb/^{206}Pb (±1σ %)		^{207}Pb/^{206}Pb age (Ma ± 1σ)		Discordance (%)
A108.1	847	169	0.21	0.3	2.04	1.52	0.1699	0.25	2557	4	-1
A61.1	329	183	0.58	0.7	2.09	1.63	0.1709	0.60	2567	10	2
A23.1	88	142	1.67	1.9	2.13	2.00	0.1723	4.28	2580	71	4
A55.1	146	99	0.70	5.5	2.03	1.86	0.1723	5.85	2580	98	0
A11.1	286	199	0.72	0.3	2.03	1.63	0.1852	0.48	2700	8	4
Analyses greater than 10% discordant and/or with uncertainties greater than 15%											
A100.1	195	56	0.30	7.8	2.70	1.91	0.1643	8.64	2501	145	23
A63.1	308	640	2.15	76.2	2.86	4.46	0.1671	38.72	2529	650	31
A71.1	188	102	0.56	1.5	2.87	1.70	0.1701	2.16	2558	36	33
A19.1	163	260	1.65	1.7	3.09	1.80	0.1617	3.63	2474	61	37
A42.1	28	30	1.10	3.5	2.00	3.94	0.1886	17.95	2730	296	5
A75.1	143	99	0.71	11.5	2.38	2.82	0.1491	20.65	2335	353	3
A53.1	61	32	0.54	5.7	2.09	2.86	0.1605	16.37	2460	277	-2
A119C.1	72	84	1.20	11.7	1.99	3.84	0.1417	32.79	2248	567	-15
A12.1	267	139	0.54	138.9	1.63	8.03	0.1860	52.76	2707	871	-12
Isotope ratios are corrected for common Pb by reference to the measured abundance of ^{204}Pb											
^{206}Pbc denotes the amount of common ^{206}Pb measured (the common Pb contents are quoted in ppm)											

240

Table S2 SHRIMP U-Pb isotopic data for zircons from feldspathic arenite in the Ferdies Member (2003082649).

Spot name	U (ppm)	Th (ppm)	Th/U	^{206}Pbc (ppb)	^{238}U/^{206}Pb (±1σ %)		^{207}Pb/^{206}Pb (±1σ %)		^{207}Pb/^{206}Pb age (Ma ± 1σ)		Discordance (%)
B82.1	25	0	0.01	148	3.07	2.84	0.1163	5.19	1900	93	5
B75.1	209	155	0.77	0	2.80	1.66	0.1308	0.58	2109	10	7
B40.1	90	273	3.11	0	2.16	1.88	0.1581	1.10	2435	19	-1
B91.1	547	71	0.13	1043	2.13	1.59	0.1583	0.55	2438	9	-2
B73.2	232	176	0.78	405	2.16	1.65	0.1588	0.81	2443	14	0
B63.2	915	590	0.67	1623	2.35	1.53	0.1590	0.50	2445	8	7
B22.1	378	174	0.48	107	2.13	1.58	0.1598	0.38	2454	6	-1
B23.1	748	124	0.17	130	2.14	1.53	0.1599	0.26	2454	4	-1
B42.1	194	228	1.21	126	2.11	1.68	0.1599	0.61	2455	10	-2
B34.1	216	120	0.57	103	2.14	1.66	0.1603	0.53	2459	9	-1
B49.1	162	87	0.56	158	2.26	1.73	0.1610	0.78	2466	13	5
B89.1	247	39	0.16	101	2.14	1.64	0.1614	0.50	2470	8	0
B21.1	270	193	0.74	102	2.05	1.62	0.1648	0.41	2506	7	-2
B69.1	152	112	0.76	93	2.10	1.71	0.1651	0.59	2508	10	0
B90.1	504	400	0.82	278	2.11	1.56	0.1659	0.35	2517	6	1
B4.1	216	150	0.71	167	2.07	1.66	0.1677	0.56	2535	9	0
B43.1	126	28	0.23	67	2.17	1.79	0.1699	0.72	2557	12	5
B48.2	229	99	0.45	378	2.20	1.66	0.1730	0.65	2587	11	7
B26.1	314	723	2.38	167	1.96	1.61	0.1804	0.40	2657	7	0
B5.1	44	49	1.17	161	2.03	2.25	0.1811	1.57	2663	26	3
B102.1	101	48	0.49	1544	1.79	2.02	0.1812	3.61	2664	60	-7
B11.1	123	89	0.75	488	2.07	1.81	0.1813	1.37	2665	23	5
B57.1	51	42	0.86	410	2.13	2.18	0.1818	2.10	2669	35	8
B47.1	129	57	0.45	217	1.95	1.78	0.1821	0.75	2672	12	0
B104.1	67	65	0.99	22	1.92	2.04	0.1828	0.83	2678	14	-1
B30.1	136	101	0.77	55	1.99	1.77	0.1832	0.65	2682	11	2
B78.1	47	59	1.31	126	1.93	2.21	0.1840	1.30	2690	21	0
B27.1	140	112	0.82	115	2.03	1.75	0.1844	0.86	2693	14	4
B81.1	237	189	0.82	112	1.97	1.65	0.1851	0.46	2699	8	2
B15.1	61	53	0.91	224	1.91	2.06	0.1858	1.48	2706	24	0
B70.1	101	17	0.18	134	2.03	1.82	0.1859	0.78	2706	13	5
B14.2	208	120	0.60	2132	1.93	1.86	0.1883	2.53	2727	42	2
B51.1	108	58	0.56	250	1.92	1.83	0.1892	0.87	2736	14	1
B8.1	32	25	0.81	212	1.85	2.46	0.1898	2.71	2740	45	-2
B38.1	43	40	0.96	133	1.93	2.26	0.1900	1.53	2742	25	2
B37.1	84	57	0.69	204	1.94	1.92	0.1900	1.08	2742	18	2
B74.1	49	67	1.41	81	1.87	2.15	0.1905	1.09	2746	18	-1
B31.1	44	54	1.27	344	1.89	2.36	0.1906	3.15	2747	52	0
B29.1	77	90	1.21	134	1.88	1.94	0.1908	0.95	2749	16	0
B63.1	225	219	1.01	404	1.97	1.65	0.1913	0.57	2754	9	4
B93.1	124	31	0.26	219	2.05	1.81	0.1918	0.77	2757	13	8
B66.1	37	30	0.83	241	1.82	2.35	0.1919	2.30	2759	38	-2
B80.1	83	60	0.74	41	2.02	1.93	0.1921	0.73	2760	12	6
B84.1	85	147	1.80	51	1.82	1.92	0.1928	0.78	2766	13	-2
B96.1	82	74	0.94	74	1.88	1.94	0.1930	0.80	2768	13	1
B103.1	40	39	1.00	60	1.86	2.34	0.1930	1.25	2768	21	0
B53.2	191	79	0.43	242	1.89	1.68	0.1935	0.63	2772	10	1
B14.1	293	109	0.38	763	1.98	1.61	0.1935	0.62	2772	10	5
B61.1	154	111	0.74	177	1.80	1.73	0.1940	0.62	2776	10	-3
B20.1	53	48	0.93	24	1.85	2.10	0.1940	1.01	2777	16	0
B9.1	54	56	1.07	83	1.91	2.09	0.1941	1.41	2777	23	2
B88.1	61	55	0.93	70	1.81	2.06	0.1944	0.84	2780	14	-2
B13.1	245	13	0.05	181	1.92	1.64	0.1946	0.45	2781	7	3
B62.1	35	31	0.91	75	1.96	2.40	0.1946	1.53	2782	25	5
B77.1	55	45	0.85	69	1.80	2.14	0.1958	1.43	2791	23	-2
B33.1	115	77	0.69	102	1.86	1.81	0.1958	0.65	2792	11	1
B65.1	111	78	0.73	0	1.87	1.80	0.1967	0.57	2799	9	1

Table S2 SHRIMP U-Pb isotopic data for zircons from feldspathic arenite in the Ferdies Member (2003082649) continued.

Spot name	U (ppm)	Th (ppm)	Th/U	^{206}Pbc (ppb)	^{238}U/^{206}Pb (±1σ %)		^{207}Pb/^{206}Pb (±1σ %)		^{207}Pb/^{206}Pb age (Ma ± 1σ)		Discordance (%)
B85.1	160	159	1.02	158	1.97	1.73	0.1971	0.58	2802	9	6
B46.1	47	55	1.21	44	1.91	2.21	0.1979	1.04	2809	17	3
B49.2	55	79	1.47	123	1.81	2.12	0.2000	1.26	2826	21	0
B79.1	219	101	0.48	76	1.69	1.65	0.2250	0.41	3017	7	1
B73.1	36	26	0.74	44	1.71	2.29	0.2291	1.74	3045	28	3
B32.1	34	22	0.67	31	1.67	2.43	0.2352	1.08	3088	17	2
B54.1	27	18	0.69	138	1.62	2.59	0.2383	1.72	3108	27	0
B16.1	79	46	0.60	168	1.74	1.94	0.2411	1.16	3127	19	7
B76.1	152	98	0.67	74	1.65	1.71	0.2422	0.45	3134	7	3
B10.1	52	35	0.69	25	1.66	2.11	0.2444	0.76	3149	12	4
B6.1	51	43	0.86	116	1.62	2.12	0.2464	0.86	3162	14	2
B44.1	95	59	0.64	83	1.56	1.88	0.2469	0.60	3165	10	-1
B12.1	143	76	0.55	110	1.55	1.73	0.2475	0.45	3169	7	-1
B24.1	57	47	0.86	102	1.58	2.08	0.2487	0.81	3177	13	0
B58.1	81	67	0.85	130	1.57	1.91	0.2490	0.67	3178	11	0
B19.1	50	43	0.89	32	1.62	2.14	0.2494	0.80	3181	13	2
B3.1	38	30	0.81	191	1.59	2.32	0.2497	1.22	3183	19	1
B52.2	47	28	0.62	143	1.58	2.22	0.2507	0.94	3189	15	1
B60.1	53	38	0.75	180	1.54	2.12	0.2510	1.16	3191	18	-1
B95.1	103	69	0.70	104	1.54	1.86	0.2522	0.58	3199	9	-1
B35.1	236	197	0.86	161	1.56	1.64	0.2522	0.51	3199	8	0
B64.1	65	39	0.61	62	1.50	2.00	0.2536	0.65	3207	10	-3
B101.1	50	42	0.87	82	1.50	2.19	0.2545	1.16	3213	18	-2
B98.1	111	60	0.55	76	1.48	1.89	0.2552	0.68	3217	11	-3
B1.1	32	23	0.74	89	1.57	2.44	0.2552	1.12	3217	18	1
B45.2	770	438	0.59	29	1.49	1.53	0.2559	0.21	3222	3	-2
B45.1	327	241	0.76	108	1.52	1.60	0.2567	0.30	3227	5	-1
B97.1	73	41	0.59	0	1.55	1.99	0.2578	0.66	3233	10	1
B18.1	35	23	0.67	366	1.52	2.40	0.2581	1.74	3235	27	-1
B36.1	24	16	0.71	39	1.48	2.70	0.2585	1.39	3238	22	-3
Overgrowths											
B75.2	1874	1979	1.09	5591	4.03	1.57	0.0972	2.24	1571	42	10
B53.1	2134	588	0.28	2003	4.27	1.50	0.1000	0.67	1624	12	20
B48.1	1123	352	0.32	3751	4.55	1.53	0.1018	2.18	1657	40	29
B2.2	1004	193	0.20	382	3.51	1.53	0.1072	0.50	1752	9	8
B2.3	670	150	0.23	918	3.15	1.54	0.1092	0.85	1786	15	0
B2.1	648	88	0.14	64	3.17	1.54	0.1102	0.42	1803	8	2
B52.1	822	116	0.15	436	3.08	1.53	0.1109	0.48	1814	9	0
B52.3	557	72	0.13	5165	2.70	1.63	0.1225	3.21	1993	57	-2
Greater than 10% discordant											
B50.1	251	203	0.84	63	2.42	1.64	0.1628	0.60	2485	10	11
B55.1	73	59	0.83	303	2.13	2.11	0.1943	2.11	2779	35	12
B39.1	66	58	0.91	279	2.17	2.05	0.1916	1.60	2756	26	13
B7.1	91	61	0.69	1279	2.26	1.95	0.1887	2.97	2731	49	16
B100.1	84	120	1.48	288	2.33	1.94	0.1828	1.53	2679	25	16
B41.1	170	148	0.90	2151	2.24	1.74	0.1928	2.19	2767	36	16
B99.1	109	81	0.77	449	1.93	1.84	0.2459	0.84	3158	13	17
B67.1	38	40	1.09	289	2.26	2.38	0.1942	2.54	2778	42	18

Table S2 SHRIMP U-Pb isotopic data for zircons from feldspathic arenite in the Ferdies Member (2003082649) continued.

Spot name	U (ppm)	Th (ppm)	Th/U	^{206}Pbc (ppb)	^{238}U/^{206}Pb ($\pm1\sigma$ %)		^{207}Pb/^{206}Pb ($\pm1\sigma$ %)		^{207}Pb/^{206}Pb age (Ma $\pm$ 1σ)		Discordance (%)
Greater than 10% discordant											
B68.1	65	33	0.53	77	2.46	2.02	0.1767	1.19	2622	20	19
B94.1	85	59	0.71	2147	2.34	2.05	0.1896	4.93	2739	81	20
B86.1	108	68	0.65	243	2.37	1.84	0.1877	0.97	2722	16	20
B83.1	287	98	0.35	349	2.95	1.63	0.1438	0.97	2273	17	21
B28.1	154	112	0.75	192	2.58	1.74	0.1780	0.79	2634	13	25
B87.1	84	86	1.06	39	2.08	1.93	0.2459	0.67	3158	11	25
B25.1	77	29	0.39	371	2.49	1.97	0.1939	1.51	2775	25	28
B92.1	196	218	1.15	389	2.35	1.70	0.2222	0.66	2997	11	31
B59.1	103	111	1.12	1243	2.47	1.94	0.2321	2.25	3066	36	40
B56.1	781	290	0.38	1877	3.81	1.55	0.1402	1.37	2230	24	48
B72.1	152	97	0.66	151	3.74	1.74	0.1665	0.96	2523	16	65
Isotope ratios are corrected for common Pb by reference to the measured abundance of ^{204}Pb											
^{206}Pbc denotes the amount of common ^{206}Pb measured											

Table S3 SHRIMP U-Pb isotopic data for zircons from tuff in the Callie Member (2001082511).

Spot name	U (ppm)	Th (ppm)	Th/U	^{206}Pbc (ppb)	^{238}U/^{206}Pb (±1σ %)		^{207}Pb/^{206}Pb (±1σ %)		^{207}Pb/^{206}Pb age (Ma ± 1σ)		Discordance (%)
A1.1	88	44	0.52	38	3.14	1.80	0.1125	1.16	1841	21	3
A2.1	132	70	0.55	93	2.97	1.73	0.1127	1.09	1844	20	-1
A3.1	95	52	0.57	71	2.92	1.80	0.1118	1.01	1830	18	-4
A4.1	92	48	0.54	50	2.93	1.83	0.1121	1.13	1834	20	-3
A5.1	181	109	0.62	57	2.95	1.68	0.1136	0.71	1858	13	-1
A7.1	103	55	0.55	104	3.08	1.78	0.1113	1.22	1821	22	1
A8.1	118	81	0.71	63	2.92	1.75	0.1117	1.10	1828	20	-4
A9.1	175	139	0.82	97	3.05	1.67	0.1126	0.93	1842	17	1
A10.1	163	100	0.64	47	3.08	1.70	0.1117	0.83	1827	15	1
A11.1	111	60	0.56	64	2.97	1.76	0.1118	1.10	1829	20	-2
A12.1	76	39	0.54	69	3.00	1.84	0.1124	1.18	1838	21	-1
A13.1	124	77	0.64	101	3.00	1.73	0.1104	1.05	1806	19	-3
A14.1	84	139	1.71	105	2.95	1.88	0.1130	1.23	1849	22	-2
A15.1	88	36	0.42	24	2.98	1.81	0.1131	0.98	1851	18	-1
A16.1	166	107	0.67	49	2.94	1.68	0.1124	0.74	1839	13	-3
A17.1	98	37	0.39	50	3.00	1.78	0.1126	1.20	1842	22	-1
A19.1	166	141	0.88	91	3.02	1.69	0.1115	0.95	1824	17	-1
A20.1	141	71	0.52	82	2.96	1.71	0.1126	0.92	1842	17	-2
A23.1	91	48	0.55	80	3.00	1.83	0.1105	1.25	1807	23	-3
A24.1	157	96	0.64	29	3.01	1.69	0.1141	0.88	1866	16	1
A25.1	109	61	0.58	11	3.03	1.77	0.1129	1.01	1847	18	0
A26.1	139	70	0.52	67	3.00	1.73	0.1136	0.94	1858	17	0
A27	204	125	0.63	45	2.97	1.65	0.1124	0.72	1838	13	-2
A28.1	70	61	0.90	65	3.02	1.89	0.1094	1.21	1789	22	-3
A30.1	98	48	0.51	35	2.95	1.78	0.1137	0.90	1860	16	-1
A31.1	170	104	0.63	3	2.97	1.68	0.1132	0.67	1851	12	-1
A32.1	156	81	0.53	51	2.94	1.70	0.1111	0.72	1817	13	-4
High mass 204 counts											
A29.1	159	268	1.74	112	3.00	1.73	0.1106	0.90	1810	16	-2
A21.1	159	179	1.16	115	3.15	1.69	0.1097	0.93	1795	17	1
A22.1	131	84	0.66	118	3.02	1.73	0.1109	1.04	1814	19	-2
A18.1	131	71	0.56	125	3.05	1.75	0.1116	1.09	1826	20	0
discordant											
A6.1	224	191	0.88	121	3.39	1.65	0.1138	0.81	1861	15	12
Isotope ratios are corrected for common Pb by reference to the measured abundance of ^{204}Pb											
^{206}Pbc denotes the amount of common ^{206}Pb measured											

Table S4 SHRIMP U-Pb isotopic data for zircons from quartz wacke in the Killi Killi Formation (2001082021).

Spot name	U (ppm)	Th (ppm)	Th/U	^{206}Pbc (ppb)	^{238}U/^{206}Pb (±1σ %)		^{207}Pb/^{206}Pb (±1σ %)		^{207}Pb/^{206}Pb age (Ma ± 1σ)		Discordance (%)
D25.1	573	277	0.50	138	3.26	1.69	0.1118	0.48	1829	9	6
D30.1	396	117	0.30	269	3.31	1.33	0.1124	0.51	1838	9	7
D12.1	276	93	0.35	32	2.96	1.46	0.1126	0.43	1842	8	-2
D48.1	221	94	0.44	29	3.12	2.58	0.1127	0.44	1843	8	3
D91.1	191	80	0.43	60	3.05	3.96	0.1128	0.92	1845	17	1
D81.1	230	80	0.36	110	2.80	3.93	0.1128	0.78	1845	14	-7
D88.1	126	67	0.55	55	2.88	3.98	0.1129	1.04	1846	19	-4
D39.1	213	115	0.56	12	3.06	1.38	0.1129	0.49	1847	9	1
D7.1	284	140	0.51	39	3.08	1.34	0.1129	0.45	1847	8	2
D87.1	223	87	0.40	29	2.82	3.93	0.1133	0.72	1853	13	-6
D28.1	159	65	0.43	19	3.07	1.41	0.1133	0.63	1853	11	2
D26.1	438	58	0.14	68	3.13	1.32	0.1135	0.37	1856	7	4
D52.1	183	143	0.81	113	3.31	2.61	0.1135	0.77	1856	14	8
D37.1	300	130	0.45	42	3.01	1.37	0.1136	0.42	1858	8	1
D9.1	308	110	0.37	25	2.99	1.33	0.1136	0.39	1858	7	0
D46.1	235	98	0.43	31	3.21	2.58	0.1138	0.50	1862	9	6
D80.1	220	141	0.66	0	2.83	3.93	0.1139	0.68	1862	12	-5
D32.1	284	122	0.44	41	3.11	1.35	0.1141	0.44	1865	8	4
D69.1	253	112	0.46	28	3.23	2.58	0.1141	0.43	1865	8	7
D50.1	319	96	0.31	40	3.14	2.57	0.1141	0.37	1866	7	4
D94.1	192	96	0.52	147	3.24	3.97	0.1141	1.21	1866	22	7
D27.1	496	162	0.34	131	3.24	1.32	0.1141	0.38	1866	7	7
D47.1	133	47	0.37	41	3.04	2.63	0.1142	0.70	1867	13	2
D77.1	288	90	0.32	95	2.80	3.92	0.1142	0.76	1867	14	-5
D24.1	188	83	0.46	7	3.13	1.39	0.1142	0.54	1868	10	4
D6.1	250	54	0.22	39	2.90	1.35	0.1143	0.43	1868	8	-2
D90.1	277	128	0.48	80	2.70	3.90	0.1144	0.62	1870	11	-9
D21.1	209	110	0.54	20	3.16	1.38	0.1146	0.57	1873	10	5
D13.1	234	80	0.36	22	2.98	1.36	0.1146	0.44	1873	8	0
D85.1	180	90	0.52	16	2.96	3.93	0.1147	0.75	1875	13	0
D82.1	245	70	0.30	0	3.05	3.99	0.1148	0.79	1876	14	3
D83.1	301	159	0.54	131	3.29	3.91	0.1148	0.75	1876	13	9
D17.1	139	152	1.13	26	3.10	1.42	0.1150	0.60	1880	11	4
D53.1	301	82	0.28	23	3.14	2.61	0.1150	0.38	1881	7	5
D51.1	191	86	0.46	151	3.19	2.59	0.1152	0.63	1883	11	7
D54.1	292	151	0.54	34	3.15	2.57	0.1152	0.39	1883	7	6
D36.1	237	139	0.60	0	3.06	1.37	0.1157	0.46	1891	8	3
D92.1	251	78	0.32	41	2.92	3.93	0.1159	0.73	1894	13	0
D33.1	168	124	0.76	31	2.49	1.40	0.1370	0.49	2190	8	1
D55.1	189	69	0.38	0	2.58	2.59	0.1385	0.43	2209	7	4
D34.1	232	57	0.26	2	2.44	1.39	0.1450	0.40	2287	7	3
D4.1	215	90	0.43	35	2.20	1.36	0.1493	0.41	2338	7	-3
D29.1	232	106	0.47	14	2.35	1.37	0.1534	0.39	2384	7	4
D78.1	94	80	0.87	48	2.18	4.07	0.1555	1.02	2408	17	-1
D76.1	219	78	0.37	53	2.18	3.95	0.1563	0.69	2417	12	-1
D86.1	94	58	0.64	146	2.02	4.03	0.1598	0.75	2453	13	-6
D89.1	41	43	1.09	0	2.34	4.25	0.1620	1.15	2476	19	7
D59.1	225	196	0.90	271	2.40	2.58	0.1622	0.42	2479	7	9
D10.1	187	97	0.53	34	2.17	1.37	0.1636	0.38	2493	6	2
D44.1	171	101	0.61	11	2.26	2.59	0.1637	0.38	2494	6	5
D2.1	98	47	0.50	0	2.34	1.45	0.1638	0.55	2495	9	8
D1.1	130	91	0.72	45	2.07	1.41	0.1640	0.46	2497	8	-2
D22.1	184	108	0.61	39	2.31	1.39	0.1647	0.45	2504	8	8
D14.1	231	91	0.41	75	2.14	1.35	0.1659	0.35	2516	6	2
D79.1	399	86	0.22	78	2.02	3.91	0.1663	1.26	2520	21	-3

Table S4 SHRIMP U-Pb isotopic data for zircons from quartz wacke in the Killi Killi Formation (2001082021) continued.

Spot name	U (ppm)	Th (ppm)	Th/U	^{206}Pbc (ppb)	^{238}U/^{206}Pb (±1σ %)		^{207}Pb/^{206}Pb (±1σ %)		^{207}Pb/^{206}Pb age (Ma ± 1σ)		Discordance (%)
D23.1	276	99	0.37	49	2.29	1.43	0.1670	0.47	2528	8	8
D8.1	401	178	0.46	11	2.02	1.32	0.1800	0.24	2653	4	2
D57.1	211	166	0.82	31	2.01	2.62	0.1872	0.36	2718	6	4
Greater than 10% discordant				0							
D43.1	249	82	0.34	41	3.37	1.41	0.1133	0.59	1853	11	10
D38.1	228	168	0.76	91	3.25	1.37	0.1174	0.62	1917	11	10
D41.1	137	57	0.43	3	2.31	1.47	0.1734	0.52	2590	9	10
D63.1	300	80	0.28	43	3.38	2.58	0.1152	0.50	1883	9	11
D93.1	73	62	0.88	151	2.71	4.23	0.1453	1.66	2292	29	12
D67.1	317	71	0.23	46	3.43	2.57	0.1151	0.39	1881	7	12
D66.1	287	147	0.53	92	3.44	2.58	0.1150	0.48	1880	9	12
D31.1	234	116	0.51	73	3.12	1.37	0.1265	0.49	2049	9	12
D16.1	340	149	0.45	32	3.53	1.35	0.1128	0.43	1846	8	13
D19.1	585	89	0.16	0	3.52	1.31	0.1131	0.31	1850	6	13
D60.1	324	208	0.66	0	3.46	2.58	0.1152	0.37	1883	7	13
D18.1	399	177	0.46	66	3.55	1.33	0.1126	0.41	1842	7	13
D20.1	192	129	0.70	78	3.43	1.40	0.1162	0.66	1899	12	13
D70.1	199	65	0.34	42	3.50	2.60	0.1147	0.59	1876	11	14
D65.1	197	145	0.76	26	3.49	2.60	0.1158	0.57	1893	10	14
D3.1	618	208	0.35	964	3.74	1.36	0.1096	1.29	1792	24	15
D42.1	302	130	0.45	154	3.62	1.41	0.1132	0.69	1851	13	15
D68.1	209	149	0.74	22	3.61	2.64	0.1138	0.48	1861	9	15
D61.1	253	158	0.65	375	3.03	2.79	0.1359	1.17	2175	20	16
D62.1	179	71	0.41	93	2.28	2.60	0.1947	0.40	2782	6	16
D58.1	266	207	0.80	214	3.60	2.58	0.1147	0.65	1875	12	16
D64.1	95	52	0.57	63	2.56	2.67	0.1690	0.65	2548	11	17
D15.1	228	186	0.84	190	1.92	1.35	0.2580	0.29	3235	5	17
D56.1	308	175	0.59	305	3.79	2.58	0.1139	0.56	1863	10	19
D71.1	564	332	0.61	15	2.79	2.56	0.1597	0.32	2453	5	19
D72.1	258	179	0.72	86	3.90	2.58	0.1123	0.59	1837	11	20
D84.1	353	160	0.47	47	3.98	3.90	0.1122	0.67	1835	12	21
D75.1	238	141	0.61	59	3.99	2.59	0.1132	0.65	1851	12	22
D74.1	327	163	0.51	35	3.91	2.58	0.1155	0.45	1888	8	22
D45.1	509	133	0.27	222	4.18	2.56	0.1148	0.53	1877	10	26
D40.1	479	377	0.81	489	4.32	1.38	0.1128	0.76	1845	14	27
D49.1	391	256	0.67	125	4.56	2.57	0.1104	0.48	1805	9	29
D73.1	96	84	0.91	45	3.26	2.66	0.1591	0.79	2446	13	29
D11.1	159	104	0.67	68	3.32	1.40	0.1612	0.53	2468	9	31
D35.1	386	368	0.98	374	4.74	1.35	0.1121	0.76	1834	14	33
D5.1	679	351	0.53	264	6.44	3.67	0.1215	1.14	1978	20	53
Isotope ratios are corrected for common Pb by reference to the measured abundance of ^{204}Pb											
^{206}Pbc denotes the amount of common ^{206}Pb measured											

Table S5 SHRIMP U-Pb isotopic data for zircons from quartz arenite in the Killi Killi Formation (2001082505).

Spot name	U (ppm)	Th (ppm)	Th/U	^{206}Pbc (ppb)	^{238}U/^{206}Pb (±1σ %)		^{207}Pb/^{206}Pb (±1σ %)		^{207}Pb/^{206}Pb age (Ma ± 1σ)		Discordance (%)
C22.1	143	101	0.73	28	3.02	1.44	0.1119	0.62	1831	11	-1
C58.1	145	111	0.79	24	3.28	1.41	0.1126	0.70	1842	13	7
C52.1	128	78	0.63	14	3.15	1.46	0.1127	0.62	1844	11	4
C16.1	126	66	0.54	24	2.98	1.42	0.1128	0.63	1845	11	-1
C51.1	193	114	0.61	37	3.31	1.37	0.1129	0.57	1846	10	8
C39.1	185	113	0.63	28	3.16	1.39	0.1133	0.50	1852	9	4
C47.1	145	90	0.64	42	3.19	1.41	0.1133	0.62	1853	11	5
C60.1	197	131	0.69	12	3.07	1.37	0.1133	0.48	1853	9	2
C50.1	617	428	0.72	78	3.34	1.34	0.1135	0.47	1855	8	9
C18.1	167	98	0.61	0	3.10	1.50	0.1138	0.54	1861	10	3
C54.1	308	112	0.38	27	3.21	1.34	0.1139	0.41	1863	7	6
C14.1	98	40	0.42	25	2.90	1.46	0.1139	0.73	1863	13	-3
C35.1	290	120	0.43	13	3.13	1.34	0.1141	0.40	1865	7	4
C29.1	192	97	0.52	24	3.05	1.38	0.1141	0.47	1866	9	2
C46.1	111	121	1.12	122	2.87	1.47	0.1141	1.28	1866	23	-3
C11.1	214	127	0.61	23	2.93	1.36	0.1141	0.51	1866	9	-1
C30.1	103	45	0.45	6	2.93	1.47	0.1142	0.92	1867	17	-1
C23.1	192	119	0.64	0	3.05	1.37	0.1145	0.48	1872	9	2
C49.1	109	44	0.42	7	3.31	1.48	0.1145	0.71	1872	13	9
C13.1	255	106	0.43	25	2.93	1.35	0.1147	0.42	1874	8	-1
C8.1	215	108	0.52	16	2.96	1.36	0.1148	0.45	1877	8	0
C20.1	293	125	0.44	14	2.98	1.34	0.1150	0.39	1880	7	1
C62.1	29	10	0.36	56	2.67	5.92	0.1152	2.07	1883	37	-9
C27.1	184	104	0.58	0	3.00	1.37	0.1154	0.48	1886	9	2
C5.1	63	66	1.08	44	3.09	1.61	0.1154	1.07	1887	19	4
C44.1	70	67	0.98	22	3.04	1.55	0.1157	0.85	1891	15	3
C41.1	211	60	0.29	64	3.05	1.36	0.1188	0.51	1938	9	6
C4.1	44	22	0.52	0	2.79	2.39	0.1195	0.97	1949	17	-1
C12.1	130	40	0.32	49	2.82	1.42	0.1196	0.62	1951	11	0
C19.1	187	39	0.21	91	2.83	1.38	0.1198	0.64	1954	11	0
C17.1	361	56	0.16	240	2.87	1.33	0.1200	0.56	1956	10	2
C25.1	234	59	0.26	0	2.79	1.35	0.1207	0.42	1966	8	0
C37.1	107	25	0.25	36	2.84	1.49	0.1213	0.61	1975	11	2
C48.1	297	155	0.54	57	2.98	1.34	0.1213	0.41	1976	7	6
C43.1	159	48	0.31	20	2.79	1.43	0.1214	0.51	1976	9	0
C63.1	217	42	0.20	7	2.69	4.35	0.1214	0.82	1977	15	-3
C57.1	136	42	0.32	46	2.91	1.42	0.1218	0.63	1982	11	4
C53.1	142	97	0.71	5	2.92	1.41	0.1223	0.54	1990	10	5
C1.1	273	37	0.14	8	2.74	1.34	0.1225	0.37	1993	7	-1
C21.1	58	52	0.93	35	2.75	1.58	0.1238	0.98	2011	17	1
C55.1	129	73	0.58	9	2.90	1.42	0.1261	0.74	2044	13	7
C7.1	129	40	0.32	40	2.62	1.41	0.1269	0.59	2055	10	-1
C2.1	144	59	0.42	37	2.68	1.40	0.1269	0.54	2055	9	1
C34.1	46	65	1.44	113	2.76	1.94	0.1276	1.67	2066	29	3
C6.1	206	145	0.73	73	2.66	1.38	0.1342	0.50	2154	9	5
C59.1	141	68	0.50	17	2.66	1.54	0.1371	0.52	2191	9	6
C3.2	221	91	0.43	0	2.51	1.35	0.1381	0.38	2204	7	2
C45.1	54	74	1.42	20	2.12	1.58	0.1588	0.70	2443	12	-2
C42.1	161	238	1.53	26	2.18	1.39	0.1617	0.43	2473	7	2
C64.1	121	93	0.79	105	1.99	4.04	0.1629	0.96	2486	16	-5
C40.1	24	32	1.38	16	2.23	1.89	0.1645	1.03	2502	17	4
C36.1	29	50	1.79	0	2.20	1.81	0.1660	1.14	2518	19	4
C24.1	71	55	0.80	0	2.14	1.71	0.1678	0.58	2536	10	3
C9.1	136	76	0.57	0	1.56	1.39	0.2383	0.32	3109	5	-3

Table S5 SHRIMP U-Pb isotopic data for zircons from quartz arenite in the Killi Killi Formation (2001082505) continued.

Spot name	U (ppm)	Th (ppm)	Th/U	^{206}Pbc (ppb)	^{238}U/^{206}Pb ($\pm 1\sigma$ %)		^{207}Pb/^{206}Pb ($\pm 1\sigma$ %)		^{207}Pb/^{206}Pb age (Ma $\pm$ 1σ)		Discordance (%)
C56.1	219	121	0.57	23	1.61	1.35	0.2863	0.25	3398	4	8
Grains greater than 10% discordant											
C28.1	136	60	0.46	59	3.43	1.43	0.1146	0.74	1874	13	12
C61.1	45	46	1.06	0	2.87	4.63	0.1381	1.58	2204	27	12
C33.1	201	75	0.39	48	3.17	1.51	0.1252	0.49	2032	9	13
C38.1	214	212	1.02	0	3.60	1.52	0.1140	0.52	1864	9	15
C32.1	223	79	0.37	34	3.47	1.36	0.1193	0.52	1945	9	16
C26.1	295	189	0.66	188	3.79	1.62	0.1110	0.62	1815	11	17
C15.1	291	200	0.71	136	3.76	1.34	0.1137	0.55	1860	10	18
C10.1	441	317	0.74	146	3.42	1.33	0.1250	0.47	2028	8	18
C31.1	208	184	0.92	76	4.45	1.50	0.1107	0.83	1810	15	28
Isotope ratios are corrected for common Pb by reference to the measured abundance of ^{204}Pb											
^{206}Pbc denotes the amount of common ^{206}Pb measured											

248

Table S6 SHRIMP U-Pb isotopic data for zircons from quartz wacke in the Killi Killi Formation (2001082515).

Spot name	U (ppm)	Th (ppm)	Th/U	^{206}Pbc (ppb)	^{238}U/^{206}Pb (±1σ %)		^{207}Pb/^{206}Pb (±1σ %)		^{207}Pb/^{206}Pb age (Ma ± 1σ)		Discordance (%)
B94.1	22	21	0.98	86	3.16	5.24	0.1040	3.42	1696	63	-4
B67.1	287	78	0.28	190	2.98	3.97	0.1118	0.97	1830	18	-2
B39.1	188	86	0.47	14	3.07	1.36	0.1123	0.47	1837	8	1
B14.1	78	70	0.93	23	2.97	1.53	0.1127	0.98	1843	18	-1
B66.1	190	103	0.56	123	3.27	4.06	0.1127	1.16	1843	21	7
B50.1	195	176	0.93	79	3.21	1.37	0.1128	0.63	1846	11	5
B3.1	44	59	1.40	40	3.30	1.67	0.1128	1.38	1846	25	7
B25.1	998	121	0.13	579	3.29	1.29	0.1134	0.27	1855	5	8
B33.1	184	182	1.02	156	3.24	1.38	0.1135	0.76	1856	14	7
B46.1	134	43	0.33	28	2.83	1.74	0.1135	0.62	1857	11	-5
B18.1	275	171	0.64	13	3.04	1.33	0.1139	0.38	1862	7	2
B13.1	186	52	0.29	29	2.88	1.36	0.1140	0.52	1865	9	-3
B47.1	203	158	0.80	100	2.87	1.37	0.1141	0.55	1865	10	-3
B31.1	226	49	0.23	32	2.94	1.36	0.1141	0.49	1865	9	-1
B76.1	241	171	0.73	249	3.04	3.97	0.1141	1.16	1866	21	2
B53.1	233	79	0.35	71	3.05	1.35	0.1142	0.47	1867	8	2
B74.1	360	169	0.49	385	3.20	3.93	0.1143	1.13	1869	20	6
B85.1	545	361	0.68	225	2.92	3.90	0.1143	0.63	1870	11	-1
B86.1	194	83	0.44	36	3.06	3.99	0.1144	0.83	1871	15	3
B56.1	76	63	0.86	8	3.09	1.49	0.1145	0.79	1872	14	3
B12.1	220	110	0.52	410	3.25	2.20	0.1145	4.15	1873	75	8
B96.1	396	137	0.36	85	2.89	3.94	0.1146	0.67	1873	12	-2
B44.1	194	66	0.35	23	2.88	1.37	0.1146	0.49	1874	9	-2
B69.1	194	59	0.31	93	2.83	4.01	0.1149	0.89	1879	16	-4
B54.1	272	137	0.52	63	3.14	1.33	0.1149	0.43	1879	8	5
B41.1	131	43	0.34	20	3.02	1.40	0.1149	0.57	1879	10	2
B28.1	202	61	0.31	10	2.93	1.36	0.1150	0.45	1880	8	-1
B95.1	155	130	0.87	28	3.04	4.10	0.1153	0.99	1885	18	3
B65.1	415	66	0.17	97	3.20	1.32	0.1158	0.39	1892	7	7
B71.1	222	141	0.65	108	3.07	3.98	0.1161	1.14	1897	20	4
B89.1	170	92	0.56	0	2.82	4.01	0.1161	0.98	1897	18	-3
B99.1	433	54	0.13	0	2.91	3.95	0.1167	0.66	1906	12	0
B108.1	166	65	0.40	0	2.82	3.98	0.1177	0.93	1921	17	-2
B62.1	449	119	0.27	78	3.06	1.31	0.1185	0.37	1934	7	6
B23.1	860	74	0.09	331	3.00	1.29	0.1192	0.24	1944	4	5
B35.1	240	58	0.25	0	2.85	1.43	0.1198	0.40	1953	7	1
B90.1	83	105	1.30	72	2.52	4.21	0.1209	1.87	1970	33	-9
B10.1	219	84	0.39	71	2.79	1.35	0.1215	0.47	1978	8	0
B43.1	239	250	1.08	98	3.04	1.34	0.1233	0.47	2005	8	9
B104.1	265	157	0.61	310	2.72	3.99	0.1243	1.15	2018	20	0
B22.1	157	101	0.66	119	2.82	1.53	0.1274	0.58	2062	10	5
B19.1	62	69	1.15	29	2.61	1.53	0.1278	0.96	2068	17	-1
B107.2	148	29	0.20	31	2.57	4.05	0.1284	0.87	2076	15	-2
B81.1	236	129	0.57	212	2.62	3.95	0.1288	0.82	2081	14	0
B4.1	108	41	0.40	35	2.53	1.43	0.1336	0.59	2146	10	0
B38.1	76	30	0.41	0	2.55	1.50	0.1345	0.68	2158	12	1
B9.1	176	96	0.56	21	2.58	1.37	0.1359	0.42	2176	7	3
B5.1	121	75	0.64	25	2.46	1.54	0.1364	0.50	2182	9	-1
B83.1	77	73	0.98	3	2.43	4.24	0.1391	1.19	2216	21	0
B68.1	93	105	1.16	9	2.35	4.20	0.1495	1.12	2341	19	2
B45.1	81	97	1.24	35	2.23	1.46	0.1564	0.61	2417	10	1
B109.1	127	21	0.17	47	2.02	4.02	0.1578	0.75	2433	13	-7
B40.1	85	61	0.75	15	2.20	1.45	0.1591	0.53	2446	9	1
B32.1	145	148	1.06	53	2.33	1.38	0.1592	0.44	2447	7	6
B17.1	116	121	1.07	52	2.24	1.41	0.1599	0.48	2455	8	3
B88.1	79	33	0.42	81	2.04	4.17	0.1620	1.11	2477	19	-4
B93.1	254	138	0.56	471	2.29	4.01	0.1624	0.81	2480	14	6

Table S6 SHRIMP U-Pb isotopic data for zircons from quartz wacke in the Killi Killi Formation (2001082515) continued.

Spot name	U (ppm)	Th (ppm)	Th/U	^{206}Pbc (ppb)	^{238}U/^{206}Pb (±1σ %)		^{207}Pb/^{206}Pb (±1σ %)		^{207}Pb/^{206}Pb age (Ma ± 1σ)		Discordance (%)
B24.1	108	139	1.33	97	2.24	1.41	0.1629	0.56	2486	9	4
B77.1	196	153	0.81	0	2.18	4.10	0.1633	0.60	2490	10	2
B72.1	130	167	1.32	109	2.03	4.15	0.1636	1.10	2493	19	-3
B34.1	71	56	0.81	31	2.22	1.50	0.1643	0.61	2500	10	4
B49.1	133	161	1.25	50	2.21	1.39	0.1647	0.45	2505	8	4
B48.1	111	140	1.30	18	2.03	1.42	0.1649	0.45	2507	8	-3
B30.1	81	72	0.93	21	2.13	1.46	0.1656	0.55	2513	9	1
B70.1	58	39	0.69	122	2.05	4.34	0.1684	1.55	2542	26	-1
B2.1	125	55	0.45	36	2.10	1.40	0.1699	0.45	2557	8	2
B105.1	49	64	1.35	3	1.81	4.49	0.1763	1.24	2619	21	-8
B84.1	159	138	0.90	17	1.91	4.06	0.1774	0.69	2629	12	-3
B97.1	152	125	0.85	239	1.28	4.07	0.3108	0.61	3525	9	-6
Grains greater than 10% discordant											
B73.1	252	404	1.66	509	3.41	3.97	0.1133	1.76	1852	32	11
B79.1	323	179	0.57	1466	2.81	3.93	0.1377	1.40	2198	24	11
B82.1	45	21	0.48	0	2.21	4.45	0.1847	1.45	2696	24	11
B106.1	109	127	1.20	88	2.38	4.16	0.1680	1.21	2538	20	11
B110.1	221	272	1.27	396	2.46	3.97	0.1623	0.86	2480	15	11
B60.1	255	166	0.67	321	2.68	1.37	0.1464	0.52	2304	9	11
B7.1	238	234	1.02	315	3.43	1.35	0.1141	0.70	1866	13	12
B59.1	149	240	1.67	202	2.50	1.44	0.1642	0.66	2500	11	13
B26.1	195	153	0.81	151	3.49	1.38	0.1158	0.63	1892	11	14
B8.1	164	234	1.47	164	3.54	1.37	0.1147	0.75	1875	14	14
B11.1	114	273	2.48	139	2.60	1.55	0.1633	0.61	2490	10	16
B1.1	227	211	0.96	296	3.72	1.53	0.1140	0.74	1864	13	18
B78.1	287	181	0.65	140	3.66	3.94	0.1163	0.94	1901	17	18
B27.1	251	124	0.51	497	3.70	1.35	0.1162	0.77	1899	14	19
B42.1	247	192	0.81	271	2.48	1.34	0.1850	0.36	2698	6	19
B21.1	19	33	1.82	473	2.53	2.12	0.1885	3.64	2729	60	21
B36.1	206	613	3.08	269	2.83	1.36	0.1646	0.49	2504	8	22
B107.1	55	66	1.24	258	3.83	4.38	0.1205	4.67	1964	83	24
B63.1	361	457	1.31	1609	4.12	1.55	0.1158	1.63	1892	29	26
B91.1	305	270	0.91	618	3.26	3.94	0.1490	0.96	2335	16	26
B16.1	195	216	1.15	376	2.93	1.39	0.1719	0.56	2576	9	26
B80.1	345	599	1.79	1564	4.03	3.97	0.1195	2.34	1948	42	27
B58.1	383	615	1.66	964	4.19	1.35	0.1171	0.83	1913	15	28
B37.1	221	172	0.80	599	4.42	1.43	0.1124	1.26	1838	23	29
B15.1	836	1177	1.45	5627	4.64	1.37	0.1132	0.85	1852	15	32
B64.1	303	859	2.93	869	4.98	1.35	0.1148	1.23	1877	22	37
B61.1	22	59	2.75	37	4.34	2.60	0.1367	2.41	2186	42	39
B103.1	347	452	1.35	1310	4.19	4.41	0.1616	1.44	2472	24	44
B87.1	313	357	1.18	1166	4.98	3.96	0.1379	2.11	2202	37	46
B29.1	372	852	2.37	1658	6.24	1.34	0.1118	1.67	1828	30	48
B55.1	235	300	1.32	464	4.60	1.37	0.1592	0.73	2447	12	48
B20.1	376	448	1.23	1663	6.25	1.53	0.1145	1.40	1871	25	49
B100.1	832	1717	2.13	10325	5.46	4.62	0.1357	3.83	2173	67	50
B51.1	327	854	2.70	1602	4.99	1.35	0.1579	0.86	2434	15	52
B57.1	311	753	2.50	1314	5.52	1.35	0.1472	1.17	2314	20	54
B6.1	353	995	2.91	1372	6.26	1.35	0.1500	1.01	2346	17	59
B92.1	977	1114	1.18	9909	12.60	4.04	0.1195	4.41	1948	79	75
B52.1	893	1341	1.55	5690	13.51	1.35	0.1144	2.96	1871	53	75
B101.1	77	79	1.07	239	1.70	4.32	0.1590	1.44	2445	24	-22
B102.1	100	110	1.13	400	2.24	4.28	0.1216	3.05	1980	54	-20
B98.1	160	185	1.19	220	2.67	4.12	0.1116	2.06	1826	37	-12
Isotope ratios are corrected for common Pb by reference to the measured abundance of ^{204}Pb											
206Pbc denotes the amount of common 206Pb measured											

Table S7 SHRIMP U-Pb isotopic data for zircons from quartz wacke in the Killi Killi Formation (2001082036).

Spot name	U (ppm)	Th (ppm)	Th/U	^{206}Pbc (ppb)	^{238}U/^{206}Pb (±1σ %)		^{207}Pb/^{206}Pb (±1σ %)		^{207}Pb/^{206}Pb age (Ma ± 1σ)		Discordance (%)
C69.1	128	88	0.71	91	2.85	2.45	0.1117	0.87	1828	16	-6
C26.1	54	36	0.68	44	3.31	2.60	0.1118	2.10	1829	38	7
C77.1	133	57	0.45	64	2.96	2.47	0.1121	0.74	1834	13	-2
C51.1	126	64	0.52	23	2.80	2.53	0.1126	1.02	1842	19	-7
C10.1	159	77	0.50	53	2.99	2.18	0.1131	1.01	1850	18	-1
C64.1	114	76	0.69	1	3.04	2.53	0.1133	0.88	1853	16	1
C35.1	245	120	0.51	48	2.84	2.25	0.1133	0.75	1854	14	-5
C46.1	205	84	0.42	8	2.91	2.38	0.1134	0.48	1854	9	-3
C8.1	136	69	0.52	86	2.97	2.24	0.1135	1.06	1856	19	-1
C7.1	237	132	0.57	109	3.11	2.05	0.1136	0.76	1857	14	3
C67.1	133	100	0.78	28	2.88	2.53	0.1137	0.84	1859	15	-3
C45.1	166	77	0.48	0	3.13	2.40	0.1140	0.50	1864	9	4
C65.1	183	82	0.46	28	2.92	2.42	0.1142	0.77	1867	14	-2
C60.1	136	61	0.47	24	2.96	2.48	0.1142	0.86	1868	16	0
C78.1	167	89	0.55	22	2.81	2.46	0.1144	0.71	1870	13	-5
C42.1	148	82	0.57	18	3.05	2.40	0.1145	0.76	1872	14	2
C31.1	164	112	0.71	0	2.90	2.32	0.1147	0.81	1874	15	-2
C30.1	371	53	0.15	167	3.16	1.97	0.1147	0.73	1876	13	5
C6.1	242	109	0.47	0	2.91	2.22	0.1151	0.69	1882	13	-1
C1.1	152	68	0.46	130	2.91	2.23	0.1152	1.66	1882	30	-1
C19.1	247	202	0.84	116	3.13	2.75	0.1154	0.92	1885	17	5
C75.1	285	102	0.37	203	3.21	2.38	0.1156	0.75	1889	14	7
C38.1	114	52	0.47	21	2.69	3.01	0.1157	0.73	1891	13	-8
C43.1	179	89	0.52	0	3.04	2.39	0.1158	0.49	1892	9	3
C16.1	146	74	0.52	0	2.92	2.16	0.1159	1.19	1894	21	0
C62.1	217	120	0.57	0	2.87	2.52	0.1167	0.91	1906	16	-1
C24.1	143	104	0.75	0	3.21	2.12	0.1167	0.90	1907	16	8
C49.1	312	316	1.05	143	3.13	2.36	0.1174	0.56	1917	10	7
C73.1	48	38	0.82	0	2.78	2.72	0.1183	1.08	1930	19	-3
C3.1	250	42	0.17	122	2.84	2.05	0.1190	0.91	1941	16	0
C57.1	554	202	0.38	59	2.93	2.36	0.1194	0.39	1948	7	3
C56.1	133	77	0.60	62	3.10	2.49	0.1196	1.04	1950	19	8
C72.1	138	48	0.36	0	2.84	2.43	0.1202	0.71	1959	13	1
C70.1	101	37	0.38	0	2.71	2.48	0.1206	1.03	1965	18	-3
C37.1	285	75	0.27	64	2.61	2.18	0.1209	1.38	1970	25	-6
C20.1	91	42	0.48	62	2.89	2.26	0.1211	1.14	1972	20	3
C4.1	316	130	0.43	150	2.68	2.50	0.1212	1.28	1974	23	-4
C22.1	216	50	0.24	0	2.78	2.05	0.1214	0.77	1977	14	0
C11.1	264	104	0.41	86	2.90	2.02	0.1225	0.68	1992	12	4
C15.1	51	67	1.37	29	2.71	2.63	0.1226	1.47	1994	26	-1
C66.1	184	87	0.49	0	2.62	2.47	0.1230	0.57	2000	10	-4
C76.1	103	38	0.38	43	2.54	2.51	0.1251	1.00	2030	18	-6
C32.1	180	70	0.40	0	2.58	2.08	0.1271	0.80	2058	14	-3
C79.1	89	69	0.81	33	2.51	2.59	0.1281	0.98	2072	17	-4
C61.1	93	47	0.53	68	2.55	2.84	0.1361	0.94	2178	16	2
C55.1	56	43	0.79	0	2.53	2.75	0.1367	0.98	2186	17	2
C68.1	111	101	0.94	100	2.48	2.47	0.1379	0.89	2201	16	1
C29.1	133	69	0.54	0	2.33	2.14	0.1386	0.77	2210	13	-4
C54.1	9	4	0.45	90	2.49	4.49	0.1458	4.14	2298	71	5
C74.1	157	111	0.73	55	2.38	2.48	0.1639	0.55	2496	9	9
C5.1	150	107	0.74	57	2.14	2.13	0.1666	0.71	2524	12	2
C52.1	142	65	0.47	125	2.01	2.48	0.1669	0.72	2526	12	-3

Table S7 SHRIMP U-Pb isotopic data for zircons from quartz wacke in the Killi Killi Formation (2001082036) continued.

Spot name	U (ppm)	Th (ppm)	Th/U	^{206}Pbc (ppb)	^{238}U/^{206}Pb ($\pm 1\sigma$ %)		^{207}Pb/^{206}Pb ($\pm 1\sigma$ %)		^{207}Pb/^{206}Pb age (Ma $\pm 1\sigma$)		Discordance (%)
C27.1	72	30	0.44	0	1.94	2.32	0.1669	0.86	2527	14	-6
C34.1	176	118	0.69	68	1.87	2.07	0.1685	0.59	2543	10	-8
C2.1	101	92	0.94	64	2.07	2.24	0.1851	0.87	2699	14	6
C41.1	21	8	0.39	24	1.53	2.74	0.2352	0.79	3088	13	-5
Grains greater than 10% discordant											
C36.1	827	49	0.06	2232	3.28	1.95	0.1160	0.71	1896	13	10
C53.1	176	104	0.61	21	3.36	2.45	0.1143	1.00	1869	18	10
C71.1	146	145	1.03	11	3.41	2.80	0.1129	0.98	1847	18	10
C48.1	15	14	1.00	6	2.81	2.96	0.1371	1.73	2191	30	10
C39.1	112	53	0.49	171	2.45	2.52	0.1628	0.74	2484	13	11
C58.1	149	78	0.54	28	3.53	2.54	0.1135	0.90	1857	16	13
C33.1	244	270	1.14	467	3.66	2.04	0.1120	1.37	1833	25	15
C23.1	184	52	0.29	0	3.20	2.15	0.1280	5.48	2070	97	15
C9.1	2383	1339	0.58	1033	3.92	1.92	0.1161	0.38	1896	7	23
C44.1	256	102	0.41	157	3.09	2.55	0.1614	0.41	2470	7	27
C18.1	509	233	0.47	1739	4.15	2.02	0.1178	1.75	1923	31	28
C59.1	266	214	0.83	121	3.65	2.63	0.1601	0.95	2457	16	37
C47.1	67	73	1.13	130	4.91	2.77	0.1240	2.01	2015	36	41
C50.1	166	212	1.32	205	5.39	2.43	0.1183	1.42	1931	25	43
C40.1	419	253	0.62	2007	5.32	2.37	0.1205	1.25	1963	22	43
C12.1	371	141	0.39	989	6.54	2.14	0.1146	2.08	1873	37	51
C13.1	411	83	0.21	126	6.14	2.02	0.1227	0.95	1995	17	51
C14.1	833	498	0.62	3104	16.27	2.06	0.1128	4.11	1845	74	79
C25.1	117	36	0.32	47533	1.04	2.76	0.1758	14.33	2613	239	-66
C17.1	181	91	0.52	67	2.23	2.61	0.1127	0.90	1844	16	-29
C63.1	234	364	1.60	372	2.27	2.52	0.1242	7.01	2017	124	-17
C21.1	179	28	0.16	92	2.54	2.30	0.1189	0.95	1940	17	-10
C28.1	212	125	0.61	24	2.66	2.18	0.1143	0.78	1869	14	-10
Isotope ratios are corrected for common Pb by reference to the measured abundance of ^{204}Pb											
^{206}Pbc denotes the amount of common ^{206}Pb measured											

Table S8 SHRIMP U-Pb isotopic data for zircons from lithic arenite in the Century Formation (2001082519).

Spot name	U (ppm)	Th (ppm)	Th/U	^{206}Pbc (ppb)	^{238}U/^{206}Pb (±1σ %)		^{207}Pb/^{206}Pb (±1σ %)		^{207}Pb/^{206}Pb age (Ma ± 1σ)		Discordance (%)
B89.1	103	62	0.62	106	3.32	2.01	0.1092	1.10	1786	20	5
B74.1	104	42	0.41	48	3.04	2.00	0.1100	0.78	1799	14	-2
B11.1	202	140	0.72	11	3.09	3.15	0.1100	0.63	1800	11	0
B88.1	70	40	0.59	2	3.05	2.05	0.1101	0.76	1801	14	-1
B93.1	213	73	0.36	39	3.13	1.95	0.1106	0.67	1809	12	1
B40.1	174	75	0.44	57	3.09	3.04	0.1106	1.35	1809	25	0
B22.1	116	58	0.52	32	3.28	3.04	0.1106	0.91	1810	16	5
B19.1	162	74	0.47	10	2.93	3.01	0.1107	0.67	1811	12	-4
B85.1	126	47	0.38	14	3.13	1.98	0.1109	0.59	1814	11	2
B81.1	126	65	0.54	40	3.13	2.01	0.1109	0.67	1814	12	2
B86.1	146	92	0.65	29	3.24	1.98	0.1109	0.68	1814	12	5
B14.1	144	41	0.30	33	2.93	3.03	0.1111	0.51	1817	9	-4
B63.1	114	42	0.38	5	3.04	1.99	0.1111	0.58	1818	11	-1
B77.1	182	42	0.24	0	3.06	1.96	0.1112	0.48	1819	9	0
B95.1	199	51	0.27	15	3.08	1.95	0.1113	0.45	1820	8	0
B49.1	112	53	0.49	0	3.18	3.05	0.1114	1.01	1822	18	3
B61.1	94	53	0.58	13	3.08	2.02	0.1114	0.70	1822	13	0
B55.1	147	59	0.42	34	3.07	1.98	0.1115	0.61	1824	11	0
B37.1	148	47	0.33	24	2.88	3.03	0.1115	0.75	1825	14	-5
B66.1	207	76	0.38	35	3.11	1.96	0.1116	0.56	1825	10	2
B9.1	243	57	0.24	32	2.73	3.34	0.1116	0.43	1825	8	-9
B2.1	209	49	0.24	16	3.08	3.00	0.1116	0.52	1826	9	1
B18.1	233	66	0.29	27	2.87	3.00	0.1117	0.42	1828	8	-5
B57.1	133	60	0.47	12	3.00	2.01	0.1118	0.59	1828	11	-1
B7.1	134	63	0.48	4	2.80	3.31	0.1118	0.53	1828	10	-7
B82.1	49	32	0.68	0	3.01	2.11	0.1118	0.86	1829	16	-1
B78.1	136	51	0.39	0	3.03	2.00	0.1119	0.57	1831	10	0
B23.1	282	180	0.66	23	3.19	3.00	0.1120	0.51	1832	9	4
B94.1	91	105	1.19	14	3.06	2.02	0.1121	0.68	1834	12	1
B73.1	119	44	0.38	0	3.03	1.99	0.1122	0.57	1835	10	0
B60.1	116	46	0.41	5	3.06	2.00	0.1122	0.69	1835	13	1
B54.1	170	52	0.32	25	2.84	3.30	0.1122	0.74	1836	13	-5
B92.1	42	46	1.14	16	3.10	2.16	0.1124	1.19	1838	22	2
B65.1	121	64	0.55	21	2.93	2.02	0.1125	0.61	1840	11	-3
B43.1	86	95	1.14	25	2.77	3.08	0.1128	1.02	1845	18	-7
B46.1	229	65	0.29	52	3.22	3.02	0.1129	0.70	1847	13	6
B66.2	58	36	0.64	35	3.13	2.09	0.1134	1.05	1854	19	4
B52.1	192	105	0.56	68	2.76	3.02	0.1134	0.71	1855	13	-7
B44.1	153	57	0.39	6	2.78	3.05	0.1139	0.93	1862	17	-6
B79.1	101	68	0.70	0	2.96	2.12	0.1139	0.62	1862	11	-1
B83.1	109	47	0.44	5	2.97	1.99	0.1139	0.87	1862	16	-1
B51.1	103	34	0.34	48	2.84	3.06	0.1140	1.27	1865	23	-4
B64.1	135	52	0.40	0	2.95	1.98	0.1151	0.54	1881	10	0
B29.1	178	155	0.90	35	2.81	3.03	0.1152	0.69	1882	12	-4
B56.1	47	26	0.57	0	2.98	2.13	0.1152	0.97	1883	17	1
B67.1	185	132	0.74	7	3.07	1.95	0.1153	0.47	1884	8	4
B10.1	116	66	0.59	12	3.07	3.17	0.1157	0.60	1890	11	4
B50.1	107	79	0.76	7	2.87	3.52	0.1163	1.01	1900	18	-1
B38.1	122	56	0.47	0	2.84	3.07	0.1168	0.84	1908	15	-2
B15.1	69	35	0.52	0	2.99	3.08	0.1175	0.74	1918	13	3
B72.1	78	9	0.11	8	2.78	2.09	0.1197	0.75	1951	13	-2
B27.1	93	38	0.42	0	3.03	3.08	0.1208	0.95	1968	17	7
B70.1	121	108	0.92	36	2.74	1.98	0.1228	0.57	1997	10	-1
B6.1	92	140	1.58	25	2.85	3.06	0.1254	0.67	2034	12	5
B35.1	229	105	0.47	28	2.53	3.01	0.1304	0.52	2103	9	-2
B36.1	145	60	0.43	6	2.58	3.03	0.1304	0.63	2104	11	0
B97.1	64	55	0.89	0	2.49	2.70	0.1332	0.71	2141	12	-2

Table S8 SHRIMP U-Pb isotopic data for zircons from lithic arenite in the Century Formation (2001082519) continued.

Spot name	U (ppm)	Th (ppm)	Th/U	^{206}Pbc (ppb)	^{238}U/^{206}Pb (±1σ %)		^{207}Pb/^{206}Pb (±1σ %)		^{207}Pb/^{206}Pb age (Ma ± 1σ)		Discordance (%)
B80.1	14	13	0.95	18	2.63	3.08	0.1368	1.92	2187	33	5
B25.1	47	23	0.50	32	2.42	3.13	0.1402	1.12	2230	19	0
B58.1	75	48	0.67	0	2.23	2.04	0.1534	0.55	2384	9	0
B59.1	72	44	0.62	16	2.22	2.04	0.1612	0.56	2468	9	3
B68.1	56	27	0.49	5	2.14	2.12	0.1631	0.63	2488	11	1
B90.1	33	28	0.88	26	2.07	2.20	0.1642	0.81	2499	14	-2
B20.1	90	48	0.55	6	2.19	3.08	0.1642	0.66	2499	11	3
B24.1	165	243	1.52	11	2.11	3.01	0.1648	0.47	2506	8	0
B91.1	122	80	0.68	3	2.10	2.15	0.1657	0.41	2515	7	0
B99.1	89	75	0.87	46	2.11	2.01	0.1659	0.52	2517	9	1
B75.1	92	54	0.60	0	2.12	2.01	0.1663	0.49	2521	8	1
B84.1	55	50	0.94	0	2.05	2.09	0.1664	0.61	2521	10	-1
B45.1	130	79	0.63	29	2.14	3.04	0.1666	1.04	2524	17	2
B42.1	118	89	0.78	27	1.97	3.16	0.1670	0.58	2527	10	-5
B71.1	141	185	1.35	6	2.11	1.99	0.1680	0.45	2538	7	1
B96.1	84	73	0.90	19	2.04	2.22	0.1691	1.18	2549	20	-1
B76.1	79	71	0.93	2	2.02	2.03	0.1713	0.53	2570	9	-1
B62.1	41	28	0.72	26	1.88	2.15	0.1832	0.69	2682	11	-3
B69.1	111	34	0.32	8	1.52	1.98	0.2678	0.88	3293	14	1
B33.1	70	28	0.42	12	1.58	3.07	0.2739	1.45	3328	23	5
B41.1	71	63	0.91	20	1.52	3.12	0.2805	0.53	3365	8	3
B98.1	118	69	0.60	10	1.43	1.98	0.2846	0.39	3388	6	-1
B8.1	88	49	0.57	0	1.28	3.36	0.2887	0.36	3411	6	-8
B87.1	48	27	0.60	2	1.42	2.11	0.2891	0.49	3413	8	-1
B30.1	95	163	1.77	0	1.35	3.06	0.2943	0.81	3441	13	-4
Analyses greater than 10% discordant											
B1.1	201	87	0.45	35	3.27	3.00	0.1158	0.48	1892	9	10
B34.1	104	34	0.34	15	3.49	3.36	0.1110	0.95	1816	17	12
B16.1	127	78	0.64	0	3.51	3.05	0.1133	0.62	1854	11	15
B12.1	155	61	0.41	18	3.35	3.05	0.1191	0.80	1942	14	15
B5.1	102	84	0.85	24	1.72	3.07	0.2876	0.42	3405	7	15
B28.1	62	88	1.45	0	3.26	3.15	0.1240	1.30	2014	23	17
B48.1	33	20	0.63	14	2.54	3.30	0.1643	1.54	2500	26	17
B17.1	90	48	0.56	17	3.59	3.07	0.1130	1.15	1849	21	17
B26.1	287	162	0.58	228	3.60	3.00	0.1131	0.80	1849	15	17
B4.1	141	96	0.70	0	2.97	3.04	0.1389	0.50	2214	9	18
B3.1	98	106	1.12	39	2.61	3.14	0.1625	0.70	2482	12	19
B21.1	136	87	0.66	0	3.63	3.07	0.1146	1.05	1874	19	19
B31.1	67	48	0.74	59	1.78	3.13	0.2956	0.61	3448	10	20
B47.1	160	144	0.93	0	3.80	3.06	0.1148	0.85	1876	15	24
B39.1	133	45	0.35	63	3.89	3.07	0.1129	1.27	1847	23	25
B13.1	96	56	0.61	10	3.89	3.08	0.1184	0.90	1932	16	31
B32.1	146	120	0.85	55	4.40	3.08	0.1107	1.41	1811	26	37
Isotope ratios are corrected for common Pb by reference to the measured abundance of ^{204}Pb											
^{206}Pbc denotes the amount of common ^{206}Pb measured											

254

Table S9 SHRIMP U-Pb isotopic data for zircons from graywacke in the Wilson Formation (2001082527).

Spot name	U (ppm)	Th (ppm)	Th/U	^{206}Pbc (ppb)	^{238}U/^{206}Pb (±1σ %)		^{207}Pb/^{206}Pb (±1σ %)		^{207}Pb/^{206}Pb age (Ma ± 1σ)		Discordance (%)
B12.1	188	133	0.73	317	3.33	3.54	0.1079	2.68	1764	49	4
B97.2	166	183	1.14	377	3.39	4.19	0.1082	2.05	1769	37	6
B48.2	125	78	0.65	100	3.15	4.08	0.1087	1.46	1777	27	0
B63.2	106	71	0.69	252	2.99	3.98	0.1095	1.80	1791	33	-4
B97.1	116	104	0.92	45	3.08	2.22	0.1099	1.80	1798	33	-1
B69.1	137	72	0.54	37	3.10	2.16	0.1100	1.28	1799	23	0
B50.1	125	69	0.57	62	3.03	3.10	0.1101	1.51	1800	27	-2
B88.1	72	70	1.00	92	3.04	2.52	0.1103	2.13	1804	39	-2
B87.2	150	216	1.48	202	3.21	4.27	0.1103	1.40	1805	25	3
B38.1	137	69	0.52	65	3.22	3.35	0.1108	1.21	1812	22	4
B87.1	138	102	0.76	71	3.18	2.15	0.1108	1.17	1813	21	3
B69.2	147	87	0.61	65	2.88	3.79	0.1109	0.75	1815	14	-6
B50.2	134	95	0.73	66	3.16	3.81	0.1110	1.02	1816	18	2
B21.1	179	217	1.25	169	2.91	3.31	0.1112	1.04	1819	19	-5
B83.2	128	147	1.18	68	3.22	3.89	0.1113	1.13	1821	21	4
B46.2	162	88	0.56	91	3.09	3.77	0.1114	0.72	1823	13	1
B63.1	106	74	0.71	0	2.98	2.23	0.1116	1.68	1826	30	-2
B79.1	225	242	1.11	196	3.31	2.06	0.1116	1.08	1826	20	7
B96.1	120	47	0.41	76	3.11	2.44	0.1117	1.36	1827	25	2
B15.2	150	108	0.75	139	3.01	3.82	0.1118	1.18	1829	21	-1
B41.2	211	132	0.65	73	3.11	3.75	0.1119	0.67	1830	12	2
B83.1	149	90	0.62	105	2.96	2.16	0.1119	1.16	1830	21	-3
B96.2	188	75	0.41	53	2.84	3.77	0.1120	0.83	1833	15	-6
B41.1	155	47	0.31	29	3.33	3.74	0.1123	1.31	1836	24	8
B46.1	188	101	0.56	31	3.27	3.35	0.1123	1.17	1838	21	6
B38.2	135	70	0.53	16	3.19	3.79	0.1124	0.90	1838	16	4
B48.1	115	62	0.56	102	3.12	2.23	0.1129	1.51	1847	27	3
B39.1	158	94	0.62	70	3.01	3.32	0.1130	0.88	1849	16	0
B75.2	119	85	0.74	0	3.02	3.83	0.1131	0.85	1849	15	0
B75.1	101	85	0.87	27	3.16	2.27	0.1132	1.87	1851	34	4
B39.2	164	90	0.57	107	3.06	3.80	0.1132	0.82	1852	15	1
B6.1	173	181	1.08	304	3.18	3.29	0.1134	1.26	1855	23	5
B15.1	103	43	0.43	0	3.03	3.35	0.1137	0.96	1859	17	1
B71.1	131	75	0.59	45	2.86	2.16	0.1138	0.92	1860	17	-4
B67.1	123	75	0.63	79	2.99	2.48	0.1141	1.23	1866	22	0
B27.1	80	70	0.90	0	3.16	3.34	0.1142	1.32	1867	24	5
B61.1	181	143	0.81	23	2.96	2.09	0.1146	0.91	1873	16	0
B100.1	244	656	2.78	740	3.26	2.28	0.1147	2.20	1875	40	8
B82.1	136	53	0.40	46	3.02	2.23	0.1148	1.02	1876	18	2
B13.1	127	82	0.67	10	3.02	3.32	0.1148	0.91	1876	16	2
B26.1	282	654	2.39	404	3.22	3.27	0.1148	1.10	1876	20	7
B24.1	180	443	2.55	173	3.06	3.35	0.1148	1.29	1877	23	3
B5.1	176	110	0.65	0	3.20	3.33	0.1149	0.66	1878	12	7
B71.2	158	145	0.95	5	2.76	3.80	0.1150	0.95	1880	17	-6
B36.1	150	83	0.57	22	3.04	3.26	0.1150	0.65	1880	12	2
B30.1	119	85	0.74	28	3.04	3.29	0.1151	0.94	1882	17	3
B88.2	126	189	1.55	167	3.09	3.95	0.1151	1.21	1882	22	4
B54.1	181	173	0.98	99	3.26	2.09	0.1153	1.20	1885	22	9
B33.1	85	48	0.58	0	2.89	3.32	0.1157	0.97	1891	17	-1
B86.1	152	85	0.58	0	2.96	2.19	0.1159	0.86	1893	15	1
B22.1	231	556	2.48	328	3.20	3.28	0.1159	1.06	1894	19	7
B17.1	182	217	1.23	53	2.82	3.59	0.1176	0.93	1921	17	-2
B91.1	65	25	0.40	32	2.58	2.53	0.1224	1.43	1991	25	-6
B98.1	170	68	0.41	31	2.74	2.59	0.1224	0.91	1992	16	-1
B68.1	146	73	0.52	0	2.94	2.15	0.1226	1.19	1995	21	5
B51.1	126	49	0.40	75	2.42	2.80	0.1395	0.87	2221	15	0
B99.1	143	68	0.49	54	2.25	2.15	0.1506	0.84	2352	14	-1

Table S9 SHRIMP U-Pb isotopic data for zircons from graywacke in the Wilson Formation (2001082527) continued.

Spot name	U (ppm)	Th (ppm)	Th/U	^{206}Pbc (ppb)	^{238}U/^{206}Pb	(±1σ %)	^{207}Pb/^{206}Pb	(±1σ %)	^{207}Pb/^{206}Pb age (Ma ± 1σ)		Discordance (%)
B85.1	97	41	0.44	74	2.07	2.27	0.1579	0.84	2433	14	-4
B52.1	60	90	1.56	53	2.33	2.44	0.1587	1.44	2442	24	6
B78.1	153	96	0.65	54	2.09	2.19	0.1635	0.66	2492	11	-1
B76.1	84	68	0.84	40	2.17	2.27	0.1643	1.11	2500	19	2
B81.1	120	170	1.46	93	2.05	2.23	0.1646	0.94	2503	16	-2
B74.1	70	56	0.83	13	2.18	2.37	0.1657	1.09	2515	18	3
B10.1	154	111	0.74	0	2.14	3.30	0.1693	0.61	2550	10	3
B43.1	29	19	0.67	0	2.16	4.16	0.1766	3.69	2622	61	6
B58.1	118	61	0.54	22	1.88	2.18	0.1875	0.72	2721	12	-1
Ambiguous analses with High U and/or high ^{204}Pb											
B27.2	2664	7325	2.84	6267	25.64	3.74	0.0946	3.37	1520	64	84
B42.1	176	518	3.04	859	3.41	3.55	0.1039	4.37	1695	81	2
B40.1	1055	5576	5.46	2627	18.69	3.26	0.1054	3.09	1721	57	80
Discordant analyses											
B23.1	268	626	2.41	55	3.30	3.37	0.1182	0.71	1929	13	12
B79.2	249	297	1.23	81	3.42	3.74	0.1147	0.74	1876	13	12
B44.1	159	233	1.51	141	3.56	3.39	0.1109	1.41	1815	26	12
B47.1	161	396	2.55	115	2.54	2.16	0.1593	0.98	2448	17	13
B89.1	209	325	1.61	504	3.66	2.07	0.1112	1.56	1818	28	14
B14.1	226	197	0.90	338	3.32	3.34	0.1220	3.01	1986	53	14
B66.1	151	435	2.97	239	3.68	2.16	0.1117	1.85	1827	34	15
B45.1	210	281	1.38	124	3.63	3.38	0.1134	1.41	1854	25	15
B61.2	209	522	2.57	301	3.63	3.79	0.1138	1.23	1862	22	16
B9.1	185	246	1.38	138	3.63	3.28	0.1159	1.13	1893	20	17
B94.1	213	193	0.94	413	3.89	2.08	0.1105	1.78	1808	32	18
B11.1	287	1529	5.50	253	2.69	3.27	0.1651	0.62	2509	10	19
B57.1	277	372	1.39	228	3.81	2.04	0.1146	1.36	1873	24	20
B92.1	186	355	1.97	379	4.05	2.17	0.1091	1.77	1785	32	20
B77.1	228	302	1.37	337	3.94	2.07	0.1129	1.43	1847	26	21
B53.1	70	237	3.52	333	3.77	2.50	0.1188	3.84	1938	69	22
B19.1	217	447	2.13	41	3.99	3.26	0.1133	0.74	1853	13	22
B65.1	187	1063	5.88	428	4.11	2.13	0.1115	2.35	1824	43	23
B90.1	258	758	3.03	256	4.09	2.05	0.1125	1.49	1840	27	23
B34.1	289	694	2.48	680	4.20	3.26	0.1110	1.40	1816	25	24
B84.1	225	718	3.30	649	4.37	2.14	0.1077	2.40	1761	44	25
B35.1	234	231	1.02	302	4.19	3.31	0.1134	0.99	1855	18	26
B100.2	246	570	2.40	141	4.22	4.56	0.1145	1.21	1872	22	27

256

Table S9 SHRIMP U-Pb isotopic data for zircons from graywacke in the Wilson Formation (2001082527) continued.

Spot name	U (ppm)	Th (ppm)	Th/U	^{206}Pbc (ppb)	^{238}U/^{206}Pb (±1σ %)		^{207}Pb/^{206}Pb (±1σ %)		^{207}Pb/^{206}Pb age (Ma ± 1σ)		Discordance (%)
Discordant analyses cont.											
B16.1	324	1225	3.90	547	4.32	3.29	0.1128	1.39	1844	25	27
B60.1	221	486	2.27	380	4.44	2.83	0.1110	1.91	1816	35	28
B95.1	212	301	1.47	466	4.51	2.19	0.1095	3.01	1791	55	28
B18.1	284	581	2.12	451	4.33	3.36	0.1196	1.12	1950	20	31
B72.1	259	1063	4.24	536	4.76	2.06	0.1126	2.00	1842	36	33
B73.1	243	551	2.34	298	4.95	2.93	0.1107	1.56	1812	28	35
B59.1	280	800	2.95	702	4.89	2.10	0.1171	1.85	1912	33	37
B2.1	279	772	2.86	624	3.88	3.69	0.1548	1.12	2399	19	38
B55.1	423	929	2.27	631	5.67	2.00	0.1147	1.51	1875	27	44
B28.1	374	851	2.35	527	6.00	3.25	0.1179	1.17	1925	21	48
B49.1	409	1228	3.10	638	6.01	2.06	0.1193	1.70	1946	30	49
B6.2	475	747	1.62	3248	6.16	3.75	0.1203	2.10	1961	37	51
B64.1	544	1344	2.56	1172	6.50	2.00	0.1172	1.76	1914	32	52
B80.1	458	1573	3.55	523	7.17	2.04	0.1113	1.98	1821	36	54
B25.1	383	1223	3.30	501	7.51	3.24	0.1157	1.42	1890	26	57
B37.1	423	846	2.07	1303	7.55	3.23	0.1156	1.69	1890	30	58
B56.1	472	1166	2.55	758	7.84	2.00	0.1155	2.02	1887	36	59
B32.1	468	1088	2.40	1180	8.82	3.23	0.1168	1.80	1908	32	64
B20.1	577	855	1.53	1515	8.65	3.30	0.1241	1.45	2016	26	65
B62.1	664	2020	3.14	2939	10.41	2.02	0.1270	2.57	2057	45	71
B93.1	329	1504	4.72	389	8.80	2.02	0.1568	1.25	2421	21	71
B70.1	645	1859	2.98	1911	11.41	2.01	0.1176	2.85	1920	51	72
B29.1	384	1384	3.72	403	11.15	3.25	0.1311	1.44	2112	25	74
B3.1	771	2633	3.53	2795	12.39	3.26	0.1391	1.70	2216	30	77
B7.1	1000	6681	6.90	2808	13.15	3.24	0.1340	1.59	2151	28	78
B101.1	831	3075	3.82	2091	16.26	2.14	0.1119	3.15	1831	57	79
B1.1	488	1015	2.15	1236	21.37	3.30	0.1167	3.13	1907	56	85
B4.1	1555	3325	2.21	4163	25.04	11.66	0.1537	42.80	2387	729	89

Isotope ratios are corrected for common Pb by reference to the measured abundance of ^{204}Pb

^{206}Pbc denotes the amount of common ^{206}Pb measured

Table S10 SHRIMP U-Pb isotopic data for zircons from arkose in the Mount Charles Formation (2003082644).

Spot name	U (ppm)	Th (ppm)	Th/U	^{206}Pbc (ppb)	^{238}U/^{206}Pb (±1σ %)		^{207}Pb/^{206}Pb (±1σ %)		^{207}Pb/^{206}Pb age (Ma ± 1σ)		Discordance (%)
B104.1	23	24	1.06	70	2.86	2.06	0.1128	3.47	1845	63	-4
B27.2	123	98	0.83	97	2.87	2.43	0.1159	0.88	1893	16	-2
B3.1	113	196	1.79	47	2.98	2.48	0.1160	0.79	1895	14	2
B26.1	137	225	1.70	60	3.03	2.41	0.1162	0.73	1898	13	3
B93.1	106	161	1.56	67	2.90	1.37	0.1171	1.01	1913	18	0
B107.1	72	42	0.59	24	2.82	1.47	0.1174	1.14	1916	20	-2
B27.1	64	35	0.56	21	2.92	2.52	0.1191	1.08	1943	19	2
B6.1	116	187	1.66	45	2.95	2.48	0.1192	0.93	1945	17	3
B76.1	26	29	1.12	2	3.02	1.93	0.1196	1.41	1950	25	6
B108.1	22	20	0.93	80	2.21	2.29	0.1493	2.24	2337	38	-3
B4.1	151	58	0.39	0	2.30	2.42	0.1547	0.47	2399	8	3
B84.1	126	64	0.52	53	2.27	1.33	0.1575	0.62	2429	11	3
B68.1	56	27	0.50	111	2.16	1.57	0.1591	1.06	2446	18	0
B74.1	50	36	0.76	99	2.08	2.01	0.1609	1.15	2465	19	-3
B42.1	73	34	0.48	69	2.19	2.55	0.1612	0.90	2469	15	2
B16.1	98	40	0.42	46	2.16	2.45	0.1615	0.57	2472	10	1
B9.1	49	40	0.84	69	2.10	2.65	0.1622	1.29	2478	22	-1
B39.1	78	30	0.40	28	2.16	2.51	0.1623	0.80	2480	14	1
B103.1	46	20	0.45	92	2.14	1.63	0.1624	1.19	2481	20	0
B1.1	62	31	0.51	62	2.11	2.54	0.1624	0.87	2481	15	-1
B91.1	74	42	0.59	65	2.08	1.50	0.1624	0.82	2481	14	-2
B21.1	40	68	1.74	78	2.19	2.68	0.1627	1.22	2484	21	3
B29.1	136	54	0.41	51	2.33	2.49	0.1627	0.52	2484	9	8
B71.1	46	72	1.62	59	2.11	1.67	0.1631	1.07	2488	18	0
B73.1	107	43	0.42	104	2.16	1.35	0.1632	0.66	2489	11	1
B43.1	53	56	1.10	90	2.05	2.56	0.1635	1.05	2492	18	-3
B67.1	233	64	0.28	150	2.15	1.26	0.1635	0.45	2492	8	1
B30.1	62	26	0.42	63	2.17	2.52	0.1635	1.17	2492	20	2
B73.1	58	51	0.91	0	2.36	1.58	0.1635	0.86	2492	14	9
B94.1	140	71	0.52	40	2.12	1.31	0.1635	0.49	2492	8	0
B90.1	25	35	1.44	69	2.08	2.02	0.1636	1.71	2493	29	-2
B25.1	94	43	0.47	95	2.23	2.44	0.1636	0.69	2494	12	4
B82.1	70	29	0.43	112	2.11	1.58	0.1636	0.97	2494	16	0
B98.1	155	71	0.47	87	2.11	1.28	0.1637	0.58	2494	10	0
B40.1	56	58	1.08	84	2.19	2.57	0.1638	0.90	2495	15	3
B83.1	152	78	0.53	68	2.12	1.33	0.1638	0.48	2496	8	0
B100.1	266	108	0.42	65	2.07	1.21	0.1640	0.39	2497	7	-2
B24.1	96	49	0.52	102	2.04	2.48	0.1640	0.66	2497	11	-3
B37.1	122	55	0.47	77	2.19	2.43	0.1640	0.66	2498	11	3
B78.1	114	55	0.50	106	2.16	1.35	0.1640	0.64	2498	11	2
B31.1	18	26	1.54	21	2.34	2.95	0.1641	2.19	2498	37	9
B51.1	170	77	0.47	54	2.13	2.53	0.1642	0.48	2500	8	1
B45.1	76	51	0.69	48	2.30	2.51	0.1643	0.63	2500	11	7
B88.1	47	34	0.74	127	2.04	1.63	0.1643	1.24	2500	21	-3
B95.1	108	53	0.51	66	2.12	1.36	0.1643	0.61	2501	10	1
B87.1	172	73	0.44	54	2.11	1.26	0.1644	0.42	2501	7	0
B80.1	133	104	0.81	15	2.09	1.32	0.1644	0.48	2502	8	-1
B34.1	201	149	0.77	6	2.10	2.39	0.1646	0.36	2504	6	0
B49.1	27	34	1.30	116	2.17	2.82	0.1646	1.82	2504	31	2
B20.1	64	33	0.52	6	2.23	3.21	0.1647	0.75	2505	13	5
B35.1	135	84	0.64	94	2.07	2.53	0.1647	0.58	2505	10	-1
B92.1	185	72	0.40	80	2.14	1.36	0.1648	0.43	2505	7	1
B46.1	207	101	0.50	72	2.25	2.38	0.1648	0.42	2506	7	6
B32.1	94	68	0.75	79	2.13	2.63	0.1650	0.69	2507	12	1
B89.1	123	61	0.51	85	2.13	1.35	0.1650	0.65	2508	11	1
B97.1	67	183	2.80	35	2.07	1.49	0.1650	0.87	2508	15	-1
B99.1	97	45	0.48	46	2.08	1.38	0.1651	0.66	2508	11	-1

Table S10 SHRIMP U-Pb isotopic data for zircons from arkose in the Mount Charles Formation (2003082644) continued.

Spot name	U (ppm)	Th (ppm)	Th/U	^{206}Pbc (ppb)	^{238}U/^{206}Pb (±1σ %)		^{207}Pb/^{206}Pb (±1σ %)		^{207}Pb/^{206}Pb age (Ma ± 1σ)		Discordance (%)
B72.1	241	74	0.32	58	2.11	1.24	0.1651	0.38	2509	6	0
B101.1	203	85	0.44	70	2.26	1.24	0.1652	0.42	2509	7	6
B50.1	104	97	0.96	170	2.10	2.53	0.1653	0.70	2510	12	0
B2.1	63	32	0.52	32	2.24	2.52	0.1653	0.81	2511	14	5
B36.1	89	44	0.51	69	2.09	2.46	0.1654	0.63	2511	11	0
B14.1	213	100	0.49	51	2.14	2.40	0.1657	0.48	2515	8	2
B11.1	107	55	0.54	0	2.26	2.48	0.1658	0.54	2515	9	7
B8.1	34	42	1.25	7	2.19	2.67	0.1658	0.89	2516	15	4
B96.1	172	129	0.78	76	2.13	1.27	0.1659	0.47	2516	8	1
B22.1	71	44	0.65	0	2.02	2.50	0.1659	0.63	2517	11	-3
B47.1	68	34	0.52	72	2.13	2.50	0.1660	0.92	2517	15	1
B31.2	181	78	0.45	40	2.14	2.40	0.1661	0.42	2518	7	2
B10.1	222	84	0.39	90	2.31	2.49	0.1661	0.46	2519	8	8
B70.1	80	33	0.42	78	2.11	1.44	0.1661	0.83	2519	14	1
B85.1	20	35	1.83	57	2.27	4.71	0.1662	1.90	2520	32	7
B106.1	159	368	2.39	41	2.10	1.32	0.1662	0.43	2520	7	0
B72.2	45	35	0.80	10	2.22	2.80	0.1662	0.92	2520	15	5
B105.1	97	85	0.91	53	2.07	1.57	0.1664	0.69	2522	12	-1
B86.1	85	57	0.69	75	2.09	1.42	0.1667	0.68	2525	11	0
B38.1	24	58	2.52	78	2.30	2.78	0.1667	1.72	2525	29	9
B110.1	109	89	0.84	55	2.07	1.35	0.1676	0.57	2534	10	0
B77.1	126	93	0.76	43	2.19	1.32	0.1677	0.55	2534	9	5
B33.1	75	48	0.66	34	2.07	2.96	0.1677	0.63	2535	11	0
B79.1	49	39	0.82	50	2.10	1.60	0.1678	0.91	2536	15	1
B5.1	140	86	0.63	0	2.06	2.42	0.1684	0.43	2542	7	0
B7.1	184	136	0.76	2	2.21	2.54	0.1694	0.38	2552	6	6
B102.1	27	37	1.43	31	2.26	1.92	0.1704	1.55	2562	26	9
B41.1	199	90	0.47	71	1.56	2.38	0.2723	0.29	3319	5	4
B44.1	198	58	0.30	54	1.42	2.59	0.2725	0.26	3320	4	-3
B81.1	78	95	1.25	78	1.44	1.77	0.2895	0.44	3415	7	0
B75.1	69	56	0.84	38	1.51	1.56	0.2899	0.60	3417	9	4
B48.2	136	18	0.14	102	1.44	2.43	0.2911	0.30	3424	5	0
B48.1	51	48	0.96	52	1.41	2.54	0.2919	0.50	3428	8	-1
B109.1	99	58	0.61	37	1.43	1.36	0.3058	0.73	3500	11	2
Analyses greater than 10% discordant											
B13.1	193	76	0.41	72	2.31	2.39	0.1680	0.48	2538	8	10
B15.1	132	102	0.80	37	2.41	2.44	0.1662	0.59	2520	10	13
B17.1	246	69	0.29	66	2.52	2.38	0.1620	0.50	2477	8	15
B23.1	60	29	0.51	58	2.53	2.52	0.1626	1.00	2483	17	16
B19.1	86	60	0.72	91	2.53	2.71	0.1635	0.78	2492	13	16
B18.1	186	162	0.90	27	2.58	2.39	0.1647	0.78	2505	13	19
B28.1	108	59	0.57	61	2.62	2.44	0.1657	0.77	2514	13	20
B12.1	87	132	1.56	2	2.59	2.64	0.1683	0.64	2541	11	21
B69.1	237	487	2.12	767	3.19	1.25	0.1681	1.11	2539	19	44
B75.2	257	196	0.79	323	3.01	1.23	0.2742	0.43	3330	7	80
B24.2	390	223	0.59	840	5.46	2.42	0.1427	1.39	2260	24	108
Isotope ratios are corrected for common Pb by reference to the measured abundance of ^{204}Pb											
^{206}Pbc denotes the amount of common ^{206}Pb measured											

Table S11 SHRIMP U-Pb isotopic data for zircons from arkose in the Mount Charles Formation (2001082507).

Spot name	U (ppm)	Th (ppm)	Th/U	^{206}Pbc (ppb)	^{238}U/^{206}Pb (±1σ %)		^{207}Pb/^{206}Pb (±1σ %)		^{207}Pb/^{206}Pb age (Ma ± 1σ)		Discordance (%)
B40.1	82	65	0.81	54	2.87	1.45	0.1136	1.02	1858	18	-4
B40.2	88	85	0.99	151	3.13	2.85	0.1146	1.77	1874	32	4
B58.1	139	105	0.78	47	2.82	1.30	0.1156	0.63	1889	11	-4
B40.3	82	57	0.72	52	3.10	2.88	0.1157	1.63	1891	29	5
B51.1	113	142	1.30	99	2.36	1.42	0.1162	0.96	1899	17	-20
B35.1	182	200	1.13	26	2.91	1.31	0.1164	0.53	1902	10	0
B59.1	122	112	0.94	75	2.96	1.30	0.1170	0.82	1911	15	2
B32.1	106	72	0.70	0	2.85	1.97	0.1171	0.68	1912	12	-1
B57.1	151	71	0.49	11	3.03	1.27	0.1171	0.52	1913	9	4
B52.1	145	105	0.75	8	2.87	1.29	0.1173	0.49	1915	9	-1
B33.1	109	115	1.09	91	2.73	1.48	0.1205	1.81	1964	32	-3
B25.1	48	55	1.18	0	2.06	3.11	0.1632	0.73	2489	12	-2
B43.1	91	45	0.51	12	1.90	3.78	0.1669	0.74	2527	12	-8
B38.1	143	155	1.12	31	2.25	1.31	0.1671	0.45	2529	8	6
B61.1	36	56	1.59	27	1.81	1.81	0.1694	1.02	2552	17	-11
B39.1	105	91	0.90	0	1.72	1.55	0.2284	0.38	3041	6	3
B44.1	161	87	0.55	51	1.65	1.28	0.2284	0.32	3041	5	-1
B47.1	120	86	0.74	2	1.60	1.31	0.2462	0.33	3160	5	1
B53.1	61	78	1.32	0	1.56	1.43	0.2568	0.47	3227	7	1
B26.1	133	163	1.26	107	1.54	2.96	0.2581	0.51	3235	8	0
B50.1	98	79	0.84	177	1.67	1.38	0.2651	0.46	3277	7	8
B41.1	86	65	0.77	0	1.51	1.39	0.2717	0.41	3316	6	1
B56.1	80	1	0.01	7	1.47	1.38	0.2846	0.36	3389	6	1
B37.1	89	61	0.71	0	1.44	1.48	0.2894	0.38	3414	6	0
B45.1	90	66	0.75	15	1.41	1.38	0.2896	0.52	3415	8	-1
B48.1	119	123	1.07	30	1.45	1.32	0.2897	0.31	3416	5	1
B46.1	93	64	0.71	16	1.38	1.38	0.2902	0.34	3418	5	-3
B29.1	135	124	0.95	0	1.38	2.94	0.2903	0.31	3419	5	-3
B42.1	111	139	1.30	29	1.32	1.49	0.2903	0.38	3419	6	-6
B60.1	165	147	0.92	24	1.40	1.25	0.2904	0.24	3420	4	-1
B36.1	125	125	1.03	0	1.34	1.36	0.2919	0.32	3428	5	-5
B54.1	87	62	0.74	13	1.46	1.35	0.3134	0.33	3538	5	5
Analyses greater than 10% discordant											
B55.1	110	130	1.22	44	1.64	1.31	0.2869	0.40	3401	6	10
B30.1	145	105	0.75	144	1.67	2.95	0.2839	0.38	3385	6	11
B16.1	478	226	0.49	274	1.90	2.66	0.2296	0.24	3050	4	11
B17.1	230	126	0.57	0	1.71	2.63	0.2786	0.32	3355	5	11
B34.1	804	351	0.45	928	2.56	1.17	0.2201	0.23	2981	4	29
B5.1	155	396	2.63	147	2.25	2.69	0.2956	0.58	3447	9	31
B27.1	248	691	2.88	329	2.79	2.91	0.2070	0.47	2882	8	32
B18.1	213	500	2.43	104	2.78	2.66	0.2146	0.45	2941	7	33
B15.1	279	327	1.21	510	2.51	2.63	0.2614	0.41	3255	6	34
B49.1	307	1248	4.20	310	2.99	1.22	0.2253	0.34	3019	6	38
B7.1	475	462	1.01	807	4.23	2.62	0.2011	0.52	2835	8	52
B2.1	373	661	1.83	894	3.79	2.69	0.2431	0.60	3141	10	52
B28.1	1321	1315	1.03	6045	7.51	2.87	0.1279	0.91	2070	16	61
B14.1	1040	824	0.82	5673	6.12	2.61	0.1745	0.71	2601	12	62
B11.1	1888	2065	1.13	2792	10.07	2.60	0.1336	0.67	2146	12	72
B22.1	650	2499	3.97	956	8.08	2.61	0.1843	0.68	2692	11	72
B9.1	1724	1181	0.71	3244	9.63	2.61	0.1654	0.64	2511	11	75
B10.1	554	1434	2.67	674	7.68	2.62	0.2607	0.50	3251	8	76
B19.1	1085	1407	1.34	2110	9.61	2.61	0.1999	0.66	2826	11	77

Table S11 SHRIMP U-Pb isotopic data for zircons from arkose in the Mount Charles Formation (2001082507) continued.

Spot name	U (ppm)	Th (ppm)	Th/U	^{206}Pbc (ppb)	^{238}U/^{206}Pb ($\pm1\sigma$ %)		^{207}Pb/^{206}Pb ($\pm1\sigma$ %)		^{207}Pb/^{206}Pb age (Ma $\pm$ 1σ)		Discordance (%)
B21.1	860	1146	1.38	1468	10.08	2.63	0.1940	0.86	2777	14	78
B20.1	1203	1677	1.44	2422	11.35	2.65	0.1905	0.70	2747	12	80
B13.1	1535	2079	1.40	1275	18.70	2.62	0.1686	0.99	2544	17	87
B12.1	1484	603	0.42	935	20.38	2.61	0.1675	0.92	2533	15	88
B3.1	1558	1385	0.92	1363	24.58	2.64	0.1806	1.16	2658	19	90
B4.1	2281	4042	1.83	1861	26.68	2.62	0.1627	1.19	2484	20	90
B6.1	787	1222	1.60	548	26.66	3.01	0.2583	5.62	3236	89	93
B1.1	1991	1448	0.75	710	34.70	2.78	0.1797	1.11	2650	18	93
B8.1	2184	1741	0.82	1389	34.97	2.61	0.1805	1.02	2658	17	93
Isotope ratios are corrected for common Pb by reference to the measured abundance of ^{204}Pb											
^{206}Pbc denotes the amount of common ^{206}Pb measured											

Table S12 SHRIMP U-Pb isotopic data for zircon from quartz arenite in the Pargee Sandstone (2001082517).

Spot name	U (ppm)	Th (ppm)	Th/U	^{206}Pbc (ppb)	^{238}U/^{206}Pb (±1σ %)		^{207}Pb/^{206}Pb (±1σ %)		^{207}Pb/^{206}Pb age (Ma ± 1σ)		Discordance (%)
A100.1	163	67	0.42	120	3.22	2.99	0.1062	1.06	1734	19	0
A100.3	168	70	0.43	49	3.37	3.03	0.1062	0.89	1735	16	3
A1.3	136	126	0.96	48	3.45	2.96	0.1072	1.18	1752	22	6
A22.2	171	84	0.51	41	3.16	2.67	0.1076	0.81	1759	15	-1
A1.1	108	83	0.80	0	3.23	1.65	0.1080	0.74	1766	14	2
A70.2	200	80	0.41	12	3.39	2.71	0.1082	0.56	1769	10	6
A1.2	132	121	0.94	27	3.22	2.71	0.1083	0.90	1770	16	1
A22.3	165	80	0.50	25	3.17	2.71	0.1084	0.93	1773	17	0
A44.2	106	54	0.52	69	3.16	2.76	0.1085	3.93	1774	72	0
A88.1	38	31	0.83	32	3.17	2.93	0.1098	2.40	1795	44	1
A100.2	167	72	0.44	17	3.22	2.97	0.1098	0.81	1796	15	3
A55.2	188	86	0.47	77	2.80	2.68	0.1111	1.05	1817	19	-8
A27.2	186	64	0.36	6	3.02	2.66	0.1112	0.56	1819	10	-1
A101.1	223	80	0.37	26	3.19	2.95	0.1113	0.69	1820	12	3
A96.1	136	103	0.78	25	3.23	2.67	0.1114	0.72	1823	13	5
A116.1	163	89	0.57	42	3.28	1.34	0.1115	0.63	1824	11	6
A38.1	325	310	0.98	472	3.10	1.41	0.1117	1.04	1828	19	1
A48.1	241	149	0.64	95	3.33	1.49	0.1121	0.73	1833	13	8
A117.1	240	72	0.31	0	3.34	1.28	0.1126	0.65	1842	12	8
A111.1	240	184	0.79	43	3.22	1.37	0.1128	0.60	1844	11	5
A28.2	67	45	0.70	51	2.85	2.77	0.1130	1.48	1848	27	-5
A123.1	104	67	0.66	18	2.99	1.41	0.1136	0.94	1858	17	0
A4.1	172	230	1.38	52	3.07	1.49	0.1137	0.76	1859	14	2
A18.1	209	64	0.32	40	2.84	1.39	0.1140	0.95	1864	17	-4
A54.2	277	146	0.55	61	3.19	2.88	0.1141	0.48	1866	9	6
A106.1	122	89	0.75	0	3.08	1.56	0.1160	0.82	1895	15	4
A109.1	105	40	0.40	0	3.10	1.51	0.1161	1.02	1897	18	5
A13.1	102	66	0.67	0	2.81	1.61	0.1186	0.75	1936	13	-1
A108.1	168	93	0.57	0	3.08	1.40	0.1188	1.06	1938	19	7
A118.1	150	94	0.65	0	2.83	1.56	0.1209	0.68	1969	12	1
A26.2	198	57	0.30	76	2.82	2.66	0.1216	0.63	1980	11	1
A67.2	189	89	0.49	52	2.84	2.66	0.1303	0.56	2102	10	8
A59.2	207	139	0.69	6	2.39	2.64	0.1356	0.38	2171	7	-4
A124.1	212	98	0.48	0	2.52	1.27	0.1366	0.41	2185	7	1
A57.1	190	150	0.82	100	2.47	1.53	0.1390	1.06	2215	18	1
A72.2	141	40	0.29	0	2.66	2.66	0.1393	0.49	2218	8	7
A122.1	89	49	0.56	11	2.45	1.45	0.1396	0.62	2223	11	1
A115.1	60	30	0.52	26	2.30	1.70	0.1446	1.07	2283	18	-2
A119.1	182	43	0.25	61	2.29	1.30	0.1491	0.47	2335	8	0
A14.1	176	163	0.96	21	2.26	1.40	0.1511	0.45	2359	8	0
A24.1	292	172	0.61	29	2.19	1.32	0.1551	0.52	2403	9	-1
A24.2	256	145	0.59	0	2.21	2.64	0.1561	0.35	2413	6	0
A91.1	45	37	0.85	18	2.13	3.29	0.1583	0.97	2438	16	-2
A104.1	74	66	0.92	40	2.37	1.57	0.1588	1.18	2443	20	7
A94.1	27	24	0.92	16	2.06	2.98	0.1620	1.09	2477	18	-3
A110.1	140	165	1.22	0	2.22	1.41	0.1627	0.53	2483	9	3
A2.1	302	87	0.30	47	2.19	1.34	0.1637	0.71	2494	12	3
A29.1	123	137	1.15	283	2.10	1.72	0.1646	1.26	2504	21	0
A49.1	66	61	0.96	69	2.31	2.05	0.1653	1.11	2511	19	8
A120.1	61	31	0.52	35	2.11	1.64	0.1659	0.75	2517	13	1
A19.2	113	82	0.75	21	2.34	2.70	0.1663	0.61	2521	10	9
A99.1	207	155	0.78	0	2.25	2.96	0.1669	0.49	2526	8	6
A107.1	145	138	0.98	28	2.13	1.47	0.1673	0.56	2531	9	2
A98.1	110	73	0.68	32	2.22	3.14	0.1677	0.68	2535	11	5
A36.1	141	87	0.64	42	2.28	1.43	0.1681	0.50	2538	8	8
A112.1	151	59	0.40	12	2.07	1.39	0.1715	0.50	2572	8	1
A42.2	101	47	0.48	10	1.93	2.72	0.1717	0.52	2574	9	-4

Table S12 SHRIMP U-Pb isotopic data for zircon from quartz arenite in the Pargee Sandstone (2001082517) continued.

Spot name	U (ppm)	Th (ppm)	Th/U	^{206}Pbc (ppb)	^{238}U/^{206}Pb ($\pm 1\sigma$ %)		^{207}Pb/^{206}Pb ($\pm 1\sigma$ %)		^{207}Pb/^{206}Pb age (Ma $\pm 1\sigma$)		Discordance (%)
A103.1	170	147	0.89	0	1.94	1.37	0.1822	0.42	2673	7	0
A6.1	167	79	0.49	35	2.08	1.42	0.1848	0.64	2697	11	6
A8.1	29	17	0.60	25	1.99	2.15	0.1850	1.22	2698	20	3
A121.1	153	78	0.52	39	1.88	1.33	0.1862	0.44	2709	7	-2
A97.1	96	42	0.45	116	1.99	3.11	0.1876	0.79	2722	13	4
A20.2	66	44	0.69	16	1.78	2.76	0.2102	0.86	2907	14	1
A20.1	85	71	0.86	121	1.72	1.56	0.2114	0.65	2917	11	-2
A31.1	87	130	1.54	0	1.64	1.56	0.2176	0.47	2963	8	-4
A105.1	116	81	0.72	5	1.47	1.44	0.2816	0.45	3372	7	1
Greater than 10% discordant											
A10.1	200	78	0.40	239	3.54	1.44	0.1144	1.30	1870	24	14
A3.3	285	103	0.38	132	3.65	2.64	0.1131	0.68	1850	12	16
A62.2	116	93	0.83	65	2.66	2.69	0.1597	0.68	2453	12	16
A89.1	355	110	0.32	229	3.55	2.68	0.1204	0.54	1962	10	18
A58.2	73	100	1.42	98	3.95	2.78	0.1093	2.07	1788	38	19
A43.1	125	42	0.35	36	2.30	1.47	0.2169	0.46	2958	7	21
A90.1	218	162	0.77	47	2.82	2.69	0.1657	0.46	2515	8	22
A101.2	311	50	0.17	29	3.72	2.92	0.1218	0.71	1983	13	23
A51.1	329	94	0.29	75	3.93	1.44	0.1160	0.82	1895	15	23
A32.1	301	157	0.54	78	3.98	1.37	0.1153	0.56	1885	10	23
A113.1	331	129	0.40	185	4.46	1.27	0.1140	0.69	1865	12	30
A22.1	282	169	0.62	342	4.88	1.45	0.1058	1.03	1728	19	30
A3.1	355	132	0.38	164	4.49	1.33	0.1144	0.71	1870	13	31
A30.1	326	159	0.50	342	4.68	1.39	0.1117	1.06	1827	19	32
A23.1	360	171	0.49	278	3.69	1.31	0.1429	0.51	2263	9	32
A33.1	396	159	0.41	509	4.58	1.34	0.1150	1.03	1879	19	32
A102.1	370	99	0.28	277	4.31	2.90	0.1243	0.77	2019	14	33
A50.1	266	182	0.71	136	3.64	1.51	0.1628	0.71	2484	12	37
A53.2	270	60	0.23	182	4.97	2.64	0.1264	1.24	2048	22	42
A25.2	594	57	0.10	706	5.70	2.62	0.1133	0.71	1854	13	44
A5.1	384	341	0.92	332	5.20	1.33	0.1265	0.78	2050	14	45
A46.1	376	226	0.62	531	5.84	1.33	0.1132	0.95	1851	17	45
A3.2	431	128	0.31	465	6.08	2.71	0.1148	1.03	1876	19	48
A40.2	308	136	0.46	325	6.55	2.64	0.1138	1.19	1861	21	51
A15.1	649	221	0.35	1426	8.20	1.30	0.1186	1.50	1936	27	62
A21.1	817	96	0.12	1135	8.57	1.28	0.1142	0.86	1867	16	62
A11.2	662	313	0.49	559	8.92	2.76	0.1129	1.00	1847	18	63
A87.1	817	242	0.31	1278	9.60	2.62	0.1086	1.14	1776	21	64
A12.2	568	350	0.64	697	8.85	2.64	0.1183	1.07	1931	19	64
A93.1	738	183	0.26	970	9.89	2.62	0.1088	1.16	1779	21	65
A47.1	718	263	0.38	718	9.07	1.39	0.1215	1.83	1978	33	66
A34.1	962	674	0.72	1739	10.75	1.32	0.1157	2.45	1891	44	70
A45.1	831	249	0.31	822	11.54	1.33	0.1160	1.50	1896	27	72
A92.1	799	1219	1.58	1671	11.65	2.62	0.1259	1.22	2041	22	74
A17.1	868	285	0.34	1224	8.91	1.27	0.1863	0.57	2710	9	75
A35.1	1229	456	0.38	2360	12.11	1.30	0.1248	1.85	2025	33	75
A37.1	1136	594	0.54	2134	11.53	1.33	0.1404	1.72	2232	30	76
A69.2	1143	741	0.67	1580	12.07	2.69	0.1342	1.05	2154	18	76
A95.1	1027	570	0.57	1783	14.68	2.61	0.1104	1.37	1805	25	76
A39.2	1177	219	0.19	926	15.04	2.62	0.1104	1.13	1806	21	77
A41.2	1179	239	0.21	1578	17.57	2.62	0.1150	1.45	1880	26	81
A7.1	1833	1558	0.88	4819	27.06	1.32	0.0966	2.75	1560	52	85
A9.1	1468	582	0.41	1833	23.02	1.29	0.1215	1.62	1978	29	86
A16.1	2469	1946	0.81	3320	56.48	1.34	0.1303	2.61	2102	46	95
A56.1	162	82	0.52	46	2.96	1.60	0.1001	1.58	1625	29	-16

Isotope ratios are corrected for common Pb by reference to the measured abundance of ^{204}Pb

^{206}Pbc denotes the amount of common ^{206}Pb measured

Table S13 SHRIMP U-Pb isotopic data for zircons from sublitharenite in the Gardiner Sandstone (2003082642).

Spot name	U (ppm)	Th (ppm)	Th/U	^{206}Pbc (ppb)	^{238}U/^{206}Pb (±1σ %)		^{207}Pb/^{206}Pb (±1σ %)		^{207}Pb/^{206}Pb age (Ma ± 1σ)		Discordance (%)
C60.1	80	78	1.01	0	3.42	2.61	0.1066	1.39	1742	25	5
C53.1	149	140	0.97	8	3.08	2.53	0.1076	0.97	1760	18	-3
C7.1	150	73	0.50	74	3.34	1.39	0.1076	1.43	1760	26	4
C42.1	63	56	0.92	32	3.05	1.76	0.1081	1.85	1767	34	-3
C75.1	150	90	0.62	44	3.37	2.52	0.1083	0.89	1772	16	6
C90.1	57	30	0.54	24	3.34	2.75	0.1084	2.46	1772	45	5
C26.1	60	22	0.39	165	2.91	1.84	0.1087	3.36	1777	61	-7
C31.1	88	102	1.20	72	3.17	1.58	0.1096	1.81	1794	33	2
C84.1	153	61	0.41	9	2.96	2.53	0.1098	0.76	1796	14	-4
C59.1	134	65	0.50	92	3.05	2.52	0.1101	1.11	1801	20	-1
C93.1	213	79	0.38	63	3.25	2.49	0.1102	0.83	1803	15	4
C24.1	172	114	0.69	6	3.05	1.37	0.1106	1.05	1810	19	-1
C80.1	160	75	0.48	67	3.32	2.57	0.1107	0.93	1810	17	7
C52.1	160	58	0.38	48	3.19	2.51	0.1108	1.00	1812	18	3
C65.1	103	76	0.76	0	3.07	2.58	0.1109	0.83	1813	15	0
C50.1	129	54	0.43	35	3.12	2.53	0.1109	0.88	1814	16	1
C92.1	250	37	0.15	13	3.09	2.50	0.1111	0.57	1818	10	0
C34.1	174	84	0.50	0	3.07	1.34	0.1111	0.86	1818	16	0
C91.1	129	76	0.61	45	3.09	2.54	0.1112	0.97	1819	18	1
C33.1	75	33	0.45	57	2.92	1.67	0.1113	2.66	1820	48	-4
C18.1	178	94	0.54	74	3.15	1.32	0.1113	1.07	1821	19	3
C41.1	57	20	0.37	88	2.91	1.85	0.1113	2.56	1822	46	-4
C2.1	165	44	0.27	34	3.13	1.35	0.1114	1.09	1822	20	2
C15.1	128	77	0.62	118	3.00	1.45	0.1114	1.46	1822	27	-2
C25.1	146	92	0.65	78	2.98	1.40	0.1114	1.20	1822	22	-2
C45.1	105	94	0.92	58	3.04	2.59	0.1114	1.35	1822	25	-1
C12.1	49	19	0.41	51	2.99	1.98	0.1114	2.13	1823	39	-2
C23.1	84	38	0.47	52	2.92	1.61	0.1117	1.15	1827	21	-4
C44.1	131	55	0.44	74	2.95	1.49	0.1120	1.58	1832	29	-3
C36.1	130	81	0.64	108	3.04	1.47	0.1122	1.57	1836	28	0
C56.1	193	52	0.28	79	2.98	2.48	0.1123	0.74	1836	13	-2
C17.1	107	155	1.49	0	3.17	1.53	0.1123	1.82	1837	33	4
C74.1	137	76	0.58	1	2.93	2.54	0.1125	0.79	1839	14	-3
C68.1	179	101	0.58	46	3.33	2.53	0.1126	1.29	1842	23	9
C37.1	143	66	0.48	24	2.97	1.41	0.1131	1.25	1849	23	-1
C5.1	138	112	0.84	110	3.24	1.41	0.1133	2.05	1852	37	7
C83.1	159	72	0.47	0	3.18	2.52	0.1134	0.86	1855	16	5
C32.1	126	62	0.51	53	2.94	1.48	0.1134	1.26	1855	23	-2
C28.1	266	114	0.44	1	3.04	1.26	0.1135	0.81	1856	15	1
C4.1	271	237	0.90	34	3.11	1.24	0.1135	0.67	1857	12	3
C77.1	161	64	0.41	21	3.12	2.52	0.1136	0.68	1859	12	4
C72.1	69	34	0.51	7	3.07	2.71	0.1137	1.02	1859	18	2
C29.1	193	75	0.40	0	3.05	1.33	0.1137	0.91	1860	16	2
C47.1	33	19	0.59	12	3.09	2.93	0.1138	1.59	1860	29	3
C27.1	143	57	0.41	0	2.97	1.42	0.1141	0.83	1865	15	0
C6.1	174	80	0.47	0	3.14	1.35	0.1142	1.10	1867	20	5
C51.1	214	83	0.40	17	3.29	2.48	0.1144	0.72	1871	13	9
C67.1	114	43	0.39	0	3.04	2.57	0.1144	1.05	1871	19	2
C11.1	160	125	0.81	0	2.93	1.37	0.1146	0.78	1874	14	-1
C59.2	95	44	0.48	0	3.04	2.59	0.1151	1.06	1882	19	3
C1.1	94	40	0.44	0	3.01	1.56	0.1155	1.26	1888	23	2
C79.1	111	39	0.36	0	3.10	2.57	0.1158	1.02	1893	18	5
C46.1	48	7	0.15	23	2.93	3.26	0.1167	1.39	1906	25	1
C57.1	148	132	0.92	13	3.01	2.55	0.1179	0.69	1925	12	4
C21.1	163	79	0.50	0	3.01	1.38	0.1184	0.79	1931	14	4
C30.1	16	20	1.28	0	2.91	2.96	0.1211	2.56	1972	46	4
C38.1	146	42	0.30	25	2.74	1.40	0.1224	1.30	1992	23	-1

Table S13 SHRIMP U-Pb isotopic data for zircons from sublitharenite in the Gardiner Sandstone (2003082642) continued.

Spot name	U (ppm)	Th (ppm)	Th/U	^{206}Pbc (ppb)	^{238}U/^{206}Pb (±1σ %)		^{207}Pb/^{206}Pb (±1σ %)		^{207}Pb/^{206}Pb age (Ma ± 1σ)		Discordance (%)
C40.1	129	81	0.65	80	2.62	1.46	0.1268	1.22	2055	22	-1
C20.1	31	23	0.79	47	2.58	2.31	0.1279	3.86	2069	68	-2
C16.1	210	85	0.42	0	2.55	1.38	0.1333	1.78	2142	31	1
C13.1	128	84	0.68	33	2.48	1.44	0.1345	1.10	2158	19	-1
C89.1	93	50	0.56	47	2.45	2.60	0.1352	0.83	2166	15	-2
C62.1	40	38	0.99	0	2.37	2.88	0.1524	1.56	2373	27	5
C49.1	111	87	0.81	50	2.11	2.77	0.1586	0.68	2440	12	-2
C58.1	175	33	0.20	0	2.11	2.49	0.1591	0.45	2446	8	-2
C14.1	105	104	1.02	3	2.27	1.53	0.1591	0.83	2446	14	4
C70.1	68	52	0.79	10	2.21	2.62	0.1632	0.88	2489	15	3
C9.1	38	29	0.78	62	2.07	2.09	0.1641	2.06	2499	35	-2
C43.1	60	50	0.86	29	2.04	1.78	0.1650	1.30	2508	22	-2
C73.1	109	50	0.47	103	2.24	2.53	0.1670	0.71	2527	12	6
C76.1	69	66	0.99	95	2.28	2.68	0.1687	1.26	2545	21	9
C22.1	152	52	0.36	82	2.14	1.39	0.1715	0.95	2573	16	4
C63.1	173	25	0.15	91	1.95	2.54	0.1917	0.48	2757	8	4
C61.1	98	31	0.33	27	1.61	2.62	0.2606	0.97	3250	15	5
Greater than 10% discordant											
C78.1	601	568	0.98	642	10.21	2.47	0.1045	2.25	1705	41	183
C64.1	205	178	0.90	111	4.71	2.49	0.1073	1.30	1755	24	41
C8.1	139	226	1.68	125	3.68	1.41	0.1097	1.77	1795	32	16
C86.1	49	21	0.46	27	3.56	2.82	0.1108	1.88	1813	34	13
C39.1	175	107	0.63	106	2.63	1.65	0.1120	1.18	1832	21	-12
C54.1	182	82	0.47	14	3.39	2.49	0.1123	0.84	1837	15	10
C3.1	259	186	0.74	0	3.69	1.27	0.1127	0.69	1843	12	19
C85.1	391	332	0.88	271	7.02	2.48	0.1128	1.28	1845	23	115
C88.1	104	51	0.51	74	3.67	2.63	0.1130	1.33	1848	24	19
C69.1	71	96	1.39	17	3.49	2.63	0.1188	1.65	1938	29	19
C66.1	189	90	0.49	0	3.31	3.02	0.1198	1.04	1953	19	15
C81.1	57	61	1.10	0	2.99	2.70	0.1372	0.98	2192	17	18
C82.1	55	38	0.72	43	2.49	2.74	0.1549	1.42	2401	24	10
C35.1	225	191	0.88	0	2.57	1.27	0.1652	0.64	2509	11	18
C55.1	110	109	1.03	106	2.47	2.56	0.1667	0.86	2525	14	15
C10.1	167	110	0.68	0	2.33	1.35	0.1682	0.63	2540	11	10
C48.1	244	222	0.94	125	2.90	2.47	0.1697	0.56	2555	9	34
C19.1	234	246	1.09	0	2.36	1.26	0.1722	0.47	2580	8	13
C71.1	76	22	0.30	0	2.19	2.60	0.1839	0.72	2689	12	11
Isotope ratios are corrected for common Pb by reference to the measured abundance of ^{204}Pb											
^{206}Pbc denotes the amount of common ^{206}Pb measured											

APPENDIX 3.1- ID TIMS results for NY/PK 6-80 (NYPK)

ID TIMS results for NY/PK 6-80 (NYPK)

Analyst: Dr. Sandra Kamo
Royal Ontario Museum

U-Pb data for single xenotime crystal fragments from NY/PK6-80.

Analysis No.	Fraction		Weight (mg)	U (ppm)	Pb (ppm)	Th/U	Pbtot (pg)	PbCom (pg)	206/204	207/204	206/238	2 Sig	207/235	2 Sig	207/206	2 Sig	206/238 Age (Ma)	2 Sig	207/235 Age (Ma)	2 Sig	207/206 Age (Ma)	2 Sig	% Disc	Corr Coeff
sk17p90	1	not abraded	0.0020	21355	3518	0.24	7037	10.7	43025	3141	0.16732	0.00070	1.6763	0.0072	0.072663	0.000094	997.3	3.9	999.8	2.7	1004.6	2.6	0.8	0.954
sk17p120	2	not abraded	0.0036	6942	1148	0.23	4131	6.8	39854	2912	0.16829	0.00044	1.6870	0.0043	0.072707	0.000068	1002.7	2.4	1003.6	1.6	1005.8	1.9	0.3	0.934
sk17p121	3	not abraded	0.0022	5469	902	0.24	1984	3.2	40769	2966	0.16748	0.00061	1.6717	0.0063	0.072392	0.000102	998.2	3.4	997.8	2.4	997.0	2.9	-0.1	0.928
sk17p116	4	abraded	0.0050	4293	714	0.27	3571	2.7	85254	6207	0.16744	0.00039	1.6769	0.0041	0.072636	0.000096	998.0	2.2	999.8	1.6	1003.8	2.7	0.6	0.849
sk17p118	5	not abraded	0.0058	4289	722	0.29	4188	3.4	80425	5867	0.16888	0.00038	1.6942	0.0043	0.072760	0.000068	1005.9	2.1	1006.4	1.6	1007.3	1.9	0.1	0.930
sk17p119	6	not abraded	0.0044	7575	1248	0.22	5492	3.6	99866	7277	0.16819	0.00041	1.6863	0.0045	0.072716	0.000072	1002.1	2.2	1003.4	1.7	1006.0	2.0	0.4	0.930
sk17p117	7	abraded	0.0022	5558	908	0.19	1997	3.2	41413	3025	0.16815	0.00042	1.6854	0.0047	0.072696	0.000066	1001.9	2.3	1003.0	1.8	1005.5	1.8	0.4	0.947
sk17p166	8	abraded*	0.0100	18734	2742	0.24	27417	9.1	197021	14374	0.16648	0.00072	1.6727	0.0075	0.072879	0.000068	992.6	4.0	998.2	2.9	1010.6	1.9	1.9	0.978
sk17p167	9	abraded*	0.0040	11142	1840	0.26	7361	4.8	100141	7274	0.16692	0.00037	1.6683	0.0043	0.072485	0.000058	995.1	2.1	996.5	1.6	999.6	1.6	0.5	0.956
sk17p168	10	abraded*	0.0040	7883	1280	0.30	5120	8.9	36986	2664	0.16243	0.00035	1.6042	0.0039	0.071626	0.000078	970.3	1.9	971.8	1.5	975.3	2.2	0.6	0.894
sk17p169	11	abraded*	0.0040	12695	2113	0.24	8452	5.7	97235	7099	0.16897	0.00046	1.6974	0.0051	0.072860	0.000062	1006.4	2.5	1007.6	1.9	1010.1	1.7	0.4	0.960
sk17p170	12	abraded*	0.0040	7899	1285	0.17	5139	9.1	37421	2735	0.16839	0.00037	1.6880	0.0043	0.072703	0.000064	1003.2	2.0	1004.0	1.6	1005.7	1.8	0.3	0.941
sk17p171	13	abraded*	0.0040	8000	1327	0.27	5308	6.8	50124	3650	0.16693	0.00042	1.6691	0.0045	0.072517	0.000082	995.2	2.3	996.8	1.7	1000.5	2.3	0.6	0.909

Notes:
not abraded=large fragments were broken apart and small internal fragments were selected for analysis
abraded*-extensively abraded (significant volume reduction)
Pbtot - Total amount of Pb in excess of blank
PbCom - Common Pb, assuming all has blank isotopic composition
Th/U calculated from radiogenic 208Pb/206Pb ratio and 207Pb/206Pb age
Pb/U corrected for spike, fractionation, blank; 206/204 and 207Pb/204Pb corrected for spike and fractionation.
%Disc - per cent discordance for the given 207Pb/206Pb age
Uranium decay constants are from Jaffey et al. (1971).
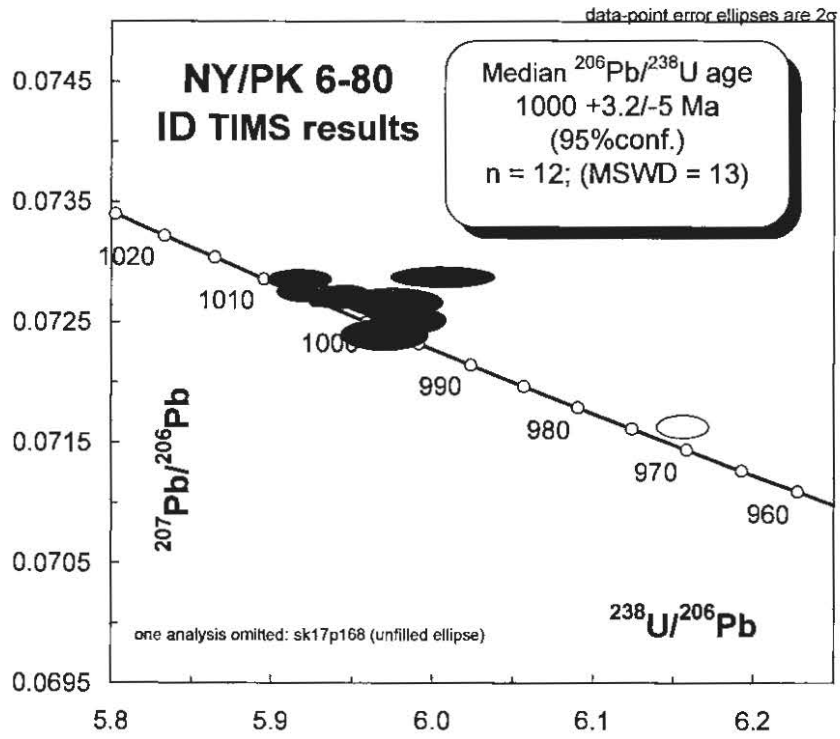
Concordia plot for NY/PK 6-80 analyses

APPENDIX 3.2- Electron microprobe chemical U–Th–Pb dating of reference xenotime D43764

Electron microprobe chemical U–Th–Pb dating was carried out on a single xenotime crystal of D43764 using a Cameca sx100 electron microprobe at the RSES. This experiment was undertaken as a means to independently determine the age of D43764 and therefore provide a check for the SHRIMP determined $^{207}Pb/^{206}Pb$ age of 2625 ± 5 Ma (95% confidence). D43764 xenotime is a good candidate for electron probe U–Th–Pb dating having a high U concentration (~1.5 wt%) and Archaean age. This experiment was conducted under the basic assumptions that underpin electron microprobe chemical U–Th–Pb dating. These are (1) common Pb is negligible and, (2) there has been no modification of the U/Th/Pb ratios except by radioactive decay (Montel et al. 1996). Before analysis, BSE imaging of the xenotime was carried out to determine whether different growth domains exist and also to identify the most pristine areas for analysis. The xenotime was analysed for U, Th, Pb and Y, using a 15 kV electron beam regulated at 200 nA. The X–ray lines were Pb$M\beta$, Th$M\alpha$, U$M\beta$ and Y$L\alpha$. Counting times for Pb, Th and U were 200 s and 90 s for Y. Background count times were done at half of the peak time. Prior to analysis, a WDS scan of xenotime D43764 was carried out in order to select background positions for the analysed elements. The background intensity under the U, Th, Pb and Y peaks was then calculated by an exponential regression of the background regions. Under these operating conditions the detection limit (2σ) is 150 ppm, 215 ppm and 130 ppm for Pb, Th and U respectively. Single–point xenotime age calculations were done with the EPMA dating excel add–in of Pommier et al. (2002) which uses the U–Th–Pb age calculation equation of Montel et al. (1996). Thirty–two analyses were undertaken on a single crystal of D43764 (Fig. 1 and Table 1). All analyses have the same weighted mean U–Th–Pb chemical age within analytical error and combine to give an age of **2637 ± 22 Ma** (MSWD=0.11; 95% confidence). Alternatively, the precision of this age measurement can be calculated by the standard error of the mean (Williams & Jercinovic 2002). Using this technique the age is 2637 ± 8 Ma (95% confidence). Both of the U–Th–Pb chemical age calculations are within error of the SHRIMP $^{207}Pb/^{206}Pb$ age of 2625 ± 5 Ma for this sample, and support it being used as reference age for D43764 xenotime.

References

Montel, J.-M., Foret, S., Veschambre, M.C.N., Provost, A., 1996. Electron microprobe dating of monazite. *Chemical Geology*, **131**, 37–53.

Pommier, A., Cocherie, A. & Legendre, O., 2002. EPMA Dating User's Manual: Age calculation from Electron Probe Microanalyser Measurements of U–Th–Pb. BRGM, 9 pp.

Williams, M.L. & Jercinovic, M.J., 2002. Age dating and mapping of monazite on the electron probe: Deconvoluting multistage tectonic histories. *Geology* **27**, 1023–1026.
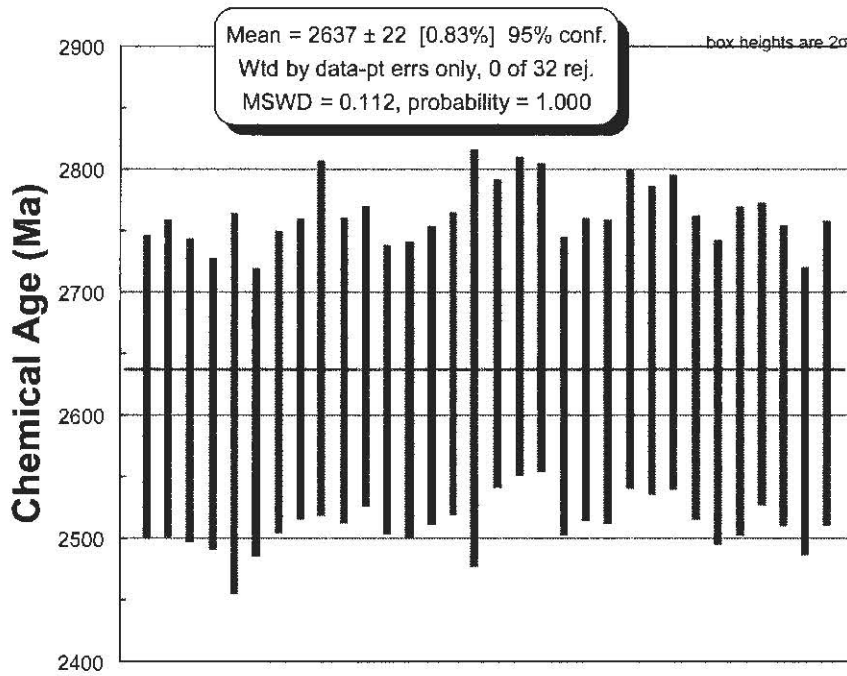
Fig. 1. Diagram showing EPMA chemical U—Th—Pb ages for xenotime standard D42764.

Table 1. EPMA chemical U—Th—Pb ages and results for D43764.

Spot name	Th (ppm)	Pb (ppm)	U (ppm)	Th/U	Chemical age (±2σ %)	
1 / 1.	3788	8003	14796	0.26	2623	124
2 / 1.	4407	7151	12921	0.34	2630	130
3 / 1.	3699	7939	14714	0.25	2621	124
4 / 1.	6047	8934	16205	0.37	2610	119
5 / 1.	7202	5800	9719	0.74	2610	155
6 / 1.	5528	10323	19158	0.29	2603	117
7 / 1.	3923	8196	15102	0.26	2628	123
8 / 1.	3919	8974	16530	0.24	2638	122
9 / 1.	2190	6576	12104	0.18	2663	145
10 / 1.	3234	8216	15226	0.21	2637	124
11 / 1.	4413	9181	16709	0.26	2649	122
12 / 1.	4320	11051	20675	0.21	2622	118
13 / 1.	3191	9859	18610	0.17	2621	120
14 / 1.	2930	9722	18282	0.16	2633	122
15 / 1.	2664	9204	17240	0.15	2643	123
16 / 1.	3749	5506	9765	0.38	2647	170
17 / 1.	3274	8521	15543	0.21	2667	125
18 / 1.	2352	7737	14151	0.17	2681	129
19 / 1.	3319	8639	15646	0.21	2680	126
20 / 1.	3729	9173	17101	0.22	2624	121
21 / 1.	3180	8882	16532	0.19	2638	123
22 / 1.	3426	8421	15592	0.22	2636	124
23 / 1.	2756	7577	13834	0.20	2670	130
24 / 1.	3277	8418	15395	0.21	2662	125
25 / 1.	2785	7716	14110	0.20	2668	128
26 / 1.	3185	8585	15937	0.20	2640	124
27 / 1.	3087	8107	15208	0.20	2619	124
28 / 1.	2571	7067	13157	0.20	2636	133
29 / 1.	3624	8977	16491	0.22	2650	123
30 / 1.	3237	8959	16720	0.19	2633	123
31 / 1.	4842	10969	20600	0.24	2604	117
32 / 1.	3745	8126	14952	0.25	2634	124

APPENDIX 3.3- Electron microprobe settings used for xenotime analysis

Detection Limits and relative errors are 1σ.
HV: 25kV
Current: 100nA
Beam focus: focussed 5μm
Cameca SX100:Research School of Earth Sciences, ANU

Element	Line	Standard	Crystal	Position	Bg 1	Bg 2	Time (s)	Det. Lim. (ppm)	% relative error
Si	Ka	Quartz	TAP	27741	-1000	1500	150	33	1.7
P	Ka	YP_5O_{14}	PET	70526	-400	400	10	430	2.4
Ca	Ka	$CaAl_2O_4$	PET	38375	-521	400	20	77	13.9
Y	La	YP_5O_{14}	PET	73913	-1600	1500	10	528	5.5
Nd	La	NdP_5O_{14}	PET	27084	290	880	30	230	14
Sm	La	SmP_5O_{14}	PET	25140	315	738	30	262	9
Eu	La	EuP_5O_{15}	PET	24243	-505	-190	30	342	9.4
Gd	La	GdP_5O_{14}	PET	23398	-385	400	30	552	7.2
Tb	La	TbP_5O_{14}	PET	22593	-365	430	30	610	10.9
Dy	La	DyP_5O_{14}	LLIF	47391	-885	826	30	200	2.3
Ho	Lb	HoP_5O_{14}	LLIF	40895	-2495	5610	30	407	4.6
Er	La	ErP_5O_{14}	LLIF	44318	-5918	2200	30	203	2.7
Tm	La	TmP_5O_{14}	LLIF	42868	-4468	3637	30	184	4.1
Yb	La	YbP_5O_{14}	LLIF	41502	-3102	4950	30	209	1.6
Lu	Lb	LuP_5O_{14}	LLIF	35336	-2008	3064	30	399	5.4
U	Mb	UO_2	LPET	42463	-1060	550	60	210	7-60
Th	Ma	ThO_2	LPET	47294	-1170	560	60	161	6-15

APPENDIX 3.4- SHRIMP instrumental conditions for the 14 experiments discussed in Chapter 2

Date	Session	Samples	Energy Filter	Primary Beam	n.A.	Kohler	EPMA (WDS)
Feb-05	SHII-1	M, B, Z, N	50 %	O_2^-	6.5	70	No
Mar-05	SHII-2	M, B, Z	50 %	O_2^-	1.8	70	No
Mar-05	SHII-3	M, B, Z	No	O_2^-	1.8	120	No
Apr-05	SHII-4	M, B, Z, D	No	O_2^-	3.1	70	No
Sept-05	SHII-5	M, B, Z	50%	O_2^-	3	120	No
Dec-05	SHII-6	M, B, Z, N	90%	O_2^-	2	120	yes
Jun-06	RG-1	M, B, Z, D	No	O^-	1.3	30	yes
Sep-06	RG-2	M, B, Z, N	No	O^-	0.9	30	yes
Nov-06	RG-3	M, B, Z, N	No	O^-	1.2	30	yes
Oct-06	RG-4	M,B,Z,L	No	O^-	1.4	30	yes
Oct-06	RG-5	M, B, Z, L	No	O^-	0.9	30	yes
Nov-06	RG-6	M, B, Z, L	No	O^-	1	30	yes
Feb-07	RG-7	M, B, Z, C	No	O^-	0.8	30	yes
Apr-07	RG-8	M, B, Z, MH	No	O^-	1	30	yes

M=MG1, B=BS1, Z=Z6413, N=NY/PK 6-80, D=D43764, L=LIS-34, MH=Molyhil, C=Callie.
SHII = SHRIMP II
RG = SHRIMP RG

APPENDIX 3.5- Comparison of SHRIMP xenotime $Pb/U_x/U_xU_x$ ratio pairs for xenotime standards MG1, BS1 and Z6413 (session SHII-1)
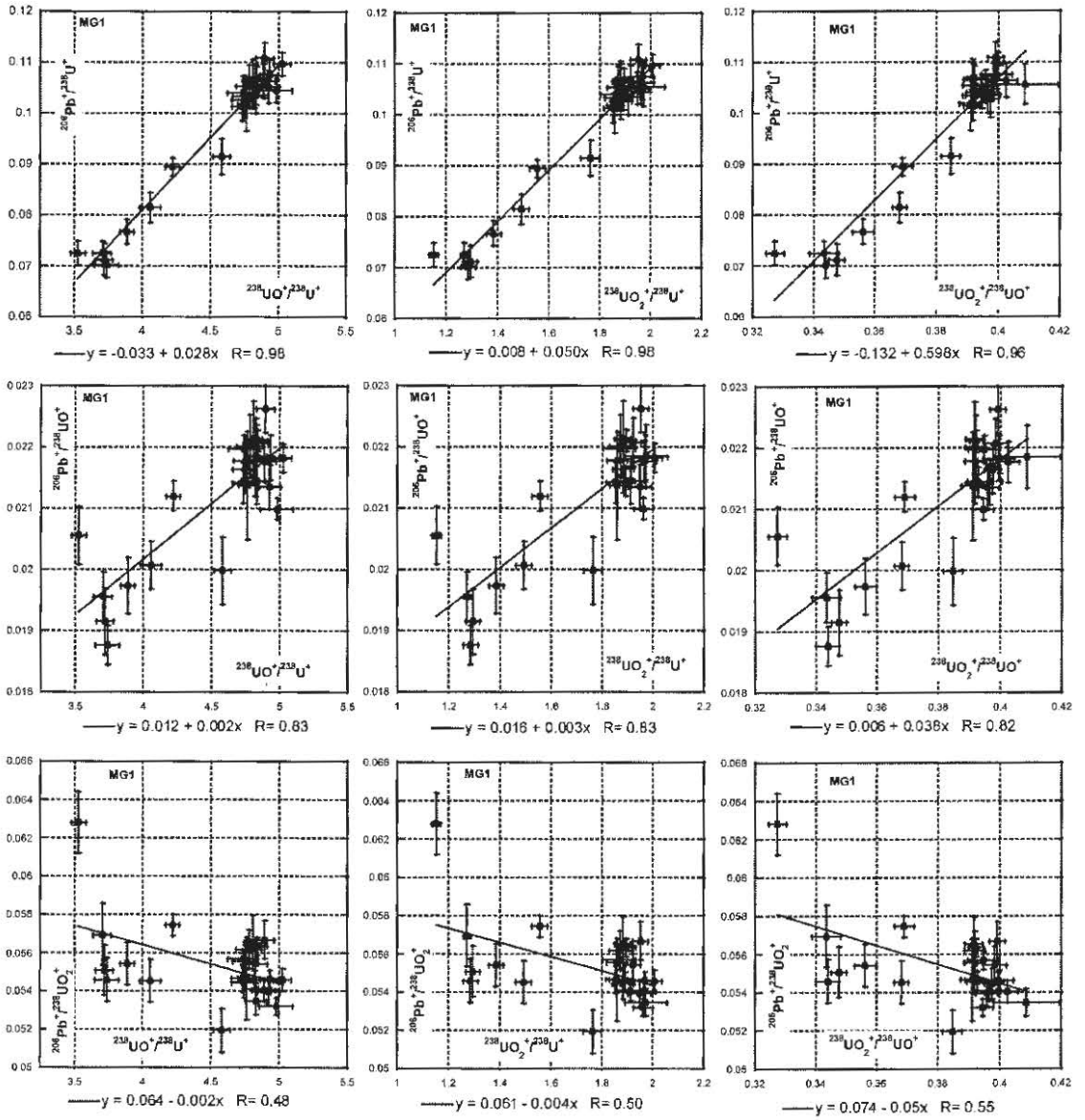
$^{206}Pb^+/^{238}U_x^+$ vs. $^{238}U_x^+/^{238}U_x^+$ plots for MG1.
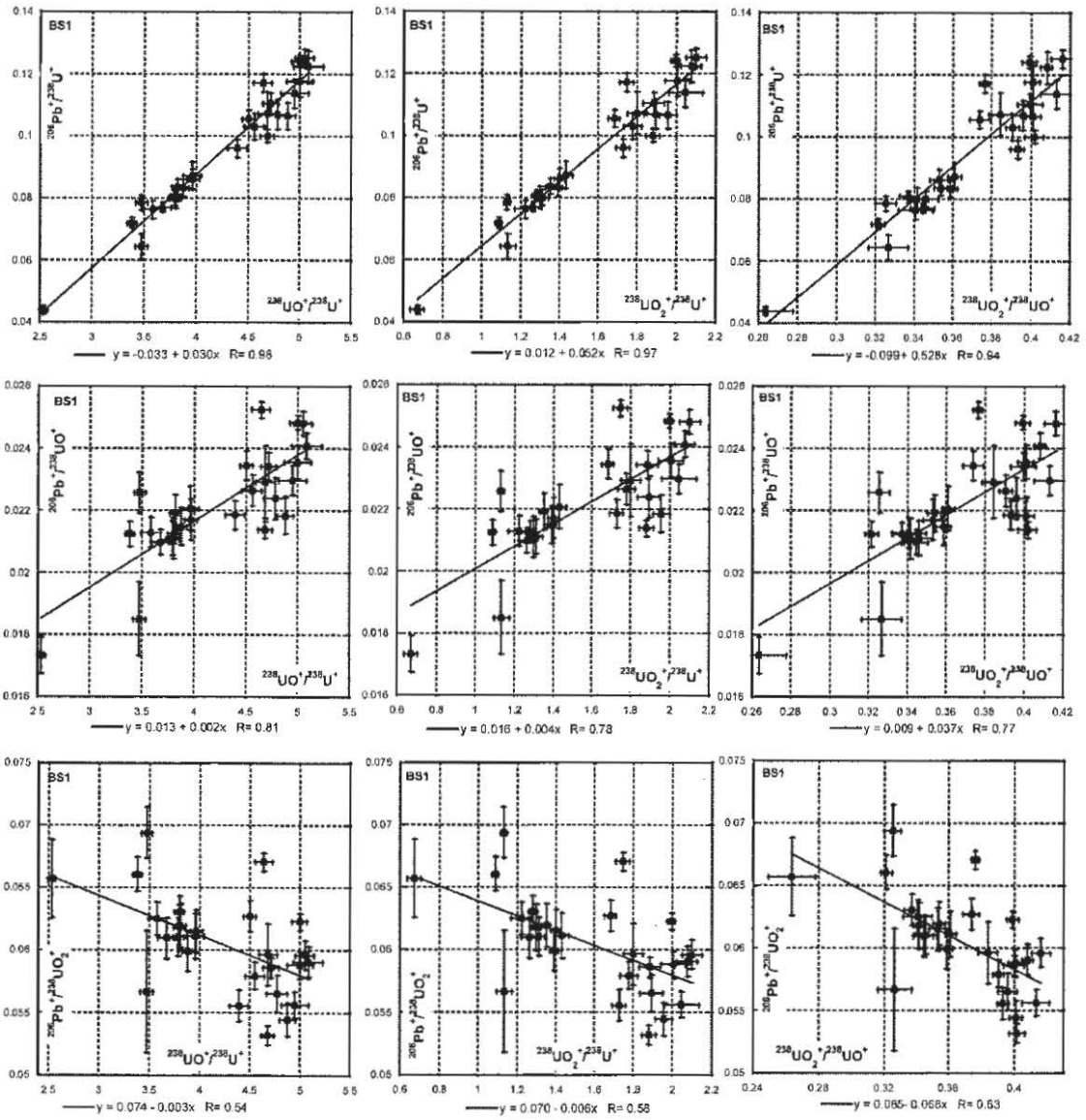
$^{206}\text{Pb}^+/^{238}\text{U}_x^+$ vs. $^{238}\text{U}_x^+/^{238}\text{U}_x^+$ plots for BS1.

276

$^{206}Pb^+/^{238}U_x^+$ vs. $^{238}U_x^+/^{238}U_x^+$ plots for Z6413.

lnPb/U_x/U_xU_x plots for xenotime standards MG1, BS1 and Z6413.
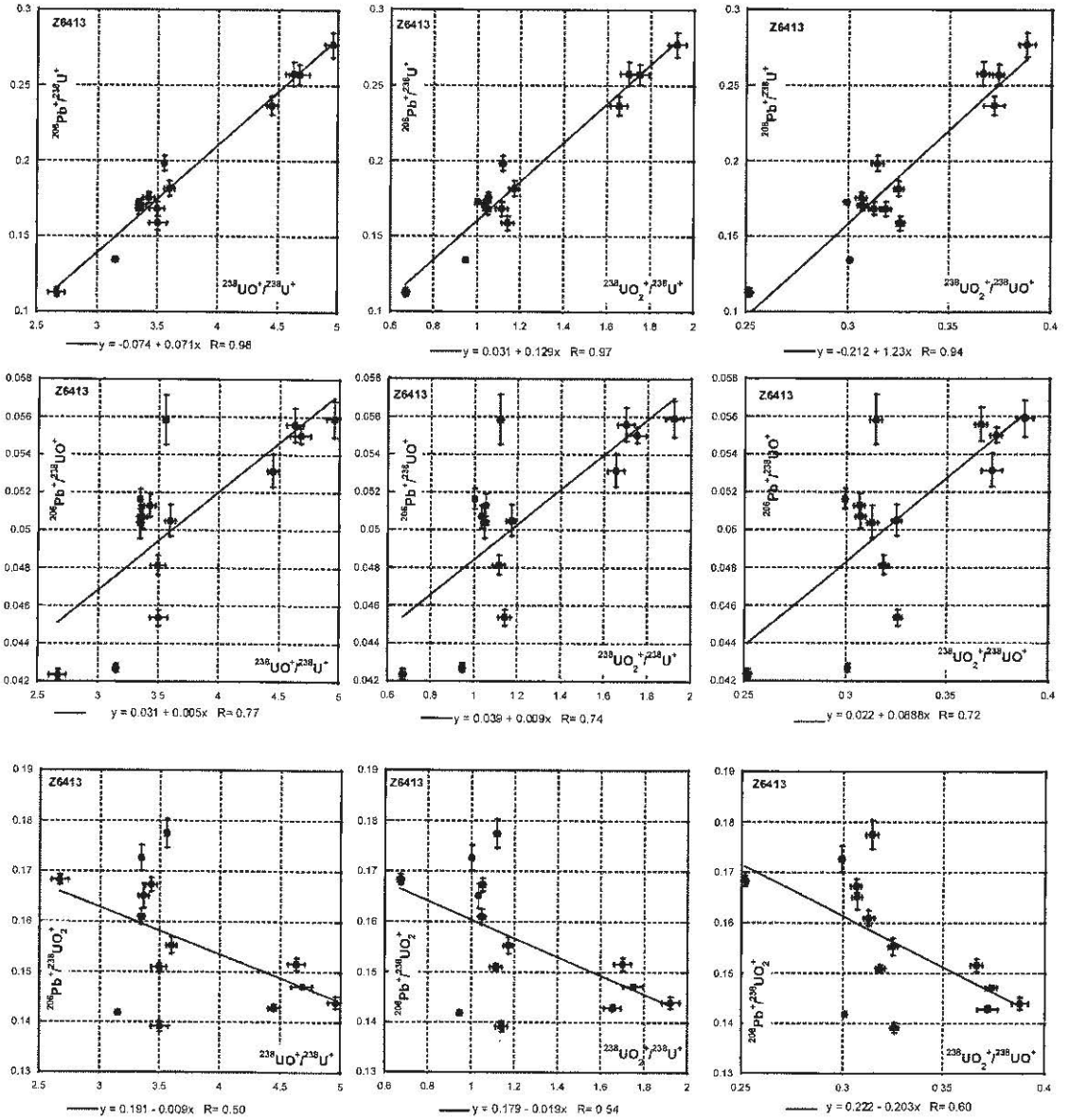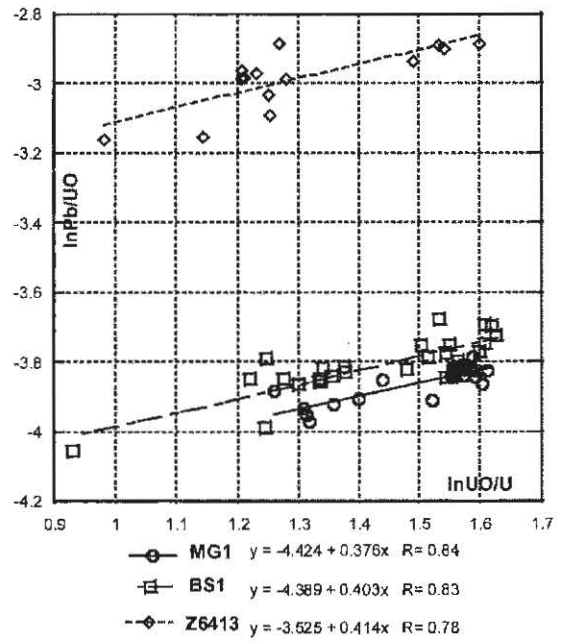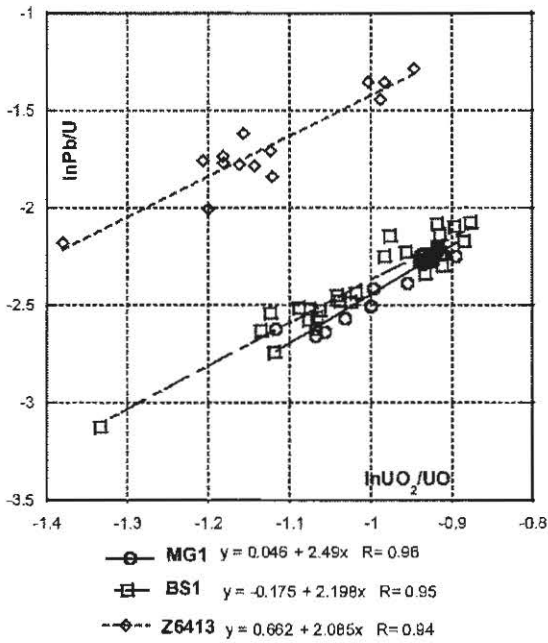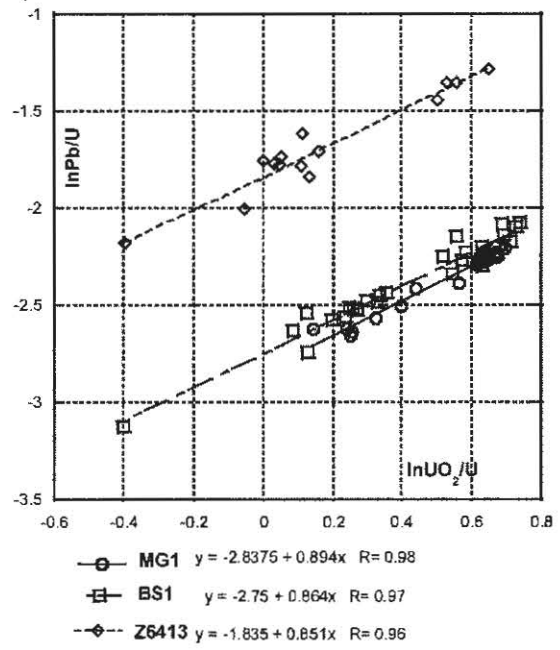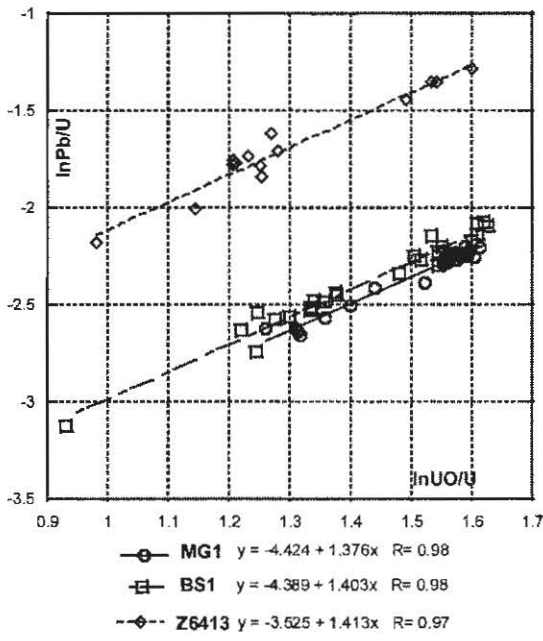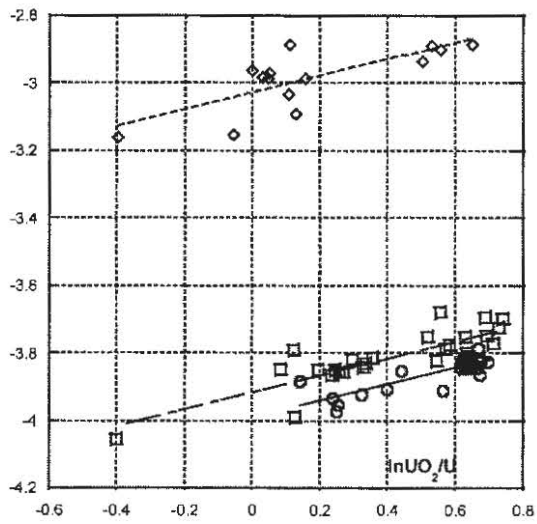
Top-left plot legend:
MG1 — y = -3.990 + 0.244x R= 0.83
BS1 — y = -3.917 + 0.246x R= 0.81
Z6413 — y = -3.03 + 0.245x R= 0.76
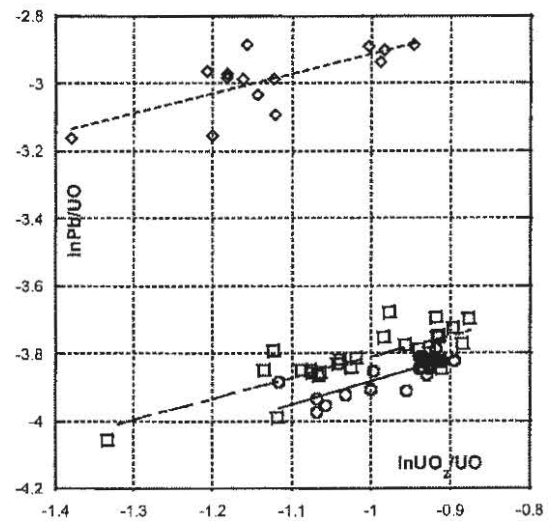
Top-right plot legend:
MG1 — y = -3.21 + 0.678x R= 0.81
BS1 — y = -3.192 + 0.618x R= 0.79
Z6413 — y = -2.326 + 0.587x R= 0.72
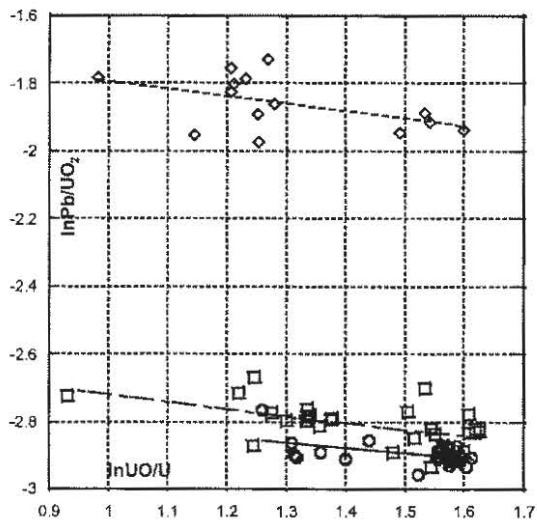
Bottom-left plot legend:
MG1 — y = -2.662 - 0.155x R= 0.49
BS1 — y = -2.511 - 0.207x R= 0.54
Z6413 — y = -1.567 - 0.226x R= 0.50
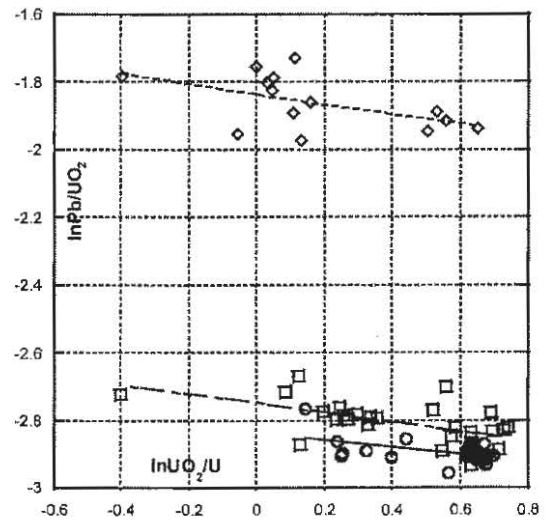
Bottom-right plot legend:
MG1 — y = -2.838 - 0.106x R= 0.52
BS1 — y = -2.75 - 0.136x R= 0.58
Z6413 — y = -1.835 - 0.149x R= 0.54

$lnPb/U_x/U_xU_x$ plots for xenotime standards MG1, BS1 and Z6413.

279
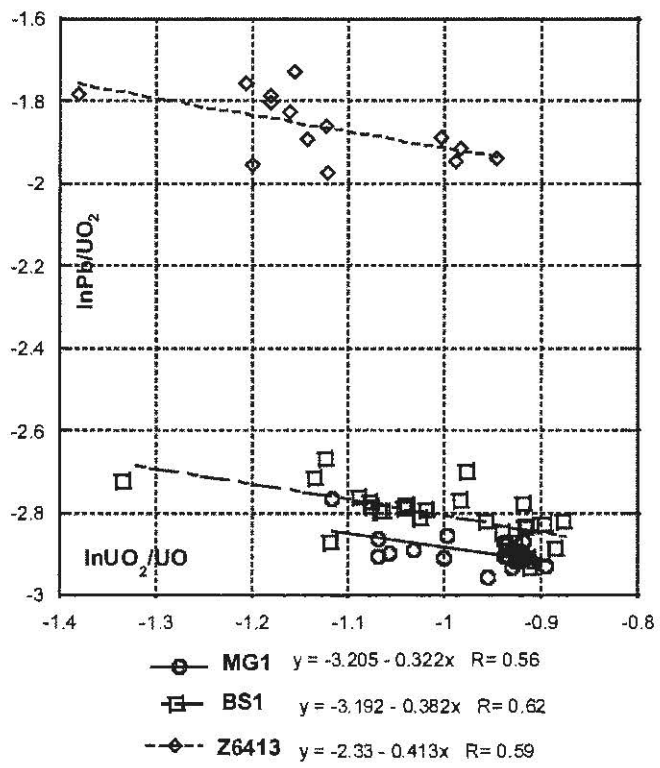
lnPb/U$_x$/U$_x$U$_x$ plots for xenotime standards MG1, BS1 and Z6413.

APPENDIX 3.6- Worked example of the SHRIMP xenotime ^{206}Pb/^{238}U matrix correction technique using Excel Solver

The following procedure uses the Microsoft Excel Solver add-in to solve the linear simultaneous equations that are used to model the SHRIMP xenotime ^{206}Pb/^{238}U Matrix effect (ME).

The procedure described here requires that raw ^{206}Pb/^{238}U ratios have been calculated for the secondary standards and unknowns with reference to a primary ^{206}Pb/^{238}U calibration standard. The calibration method used to calculate the SHRIMP ^{206}Pb/^{238}U xenotime ratios and data reduction software is at the geochronologist's discretion. Additionally, U and REE concentration data for each SHRIMP spot needs to be determined. For xenotime ΣREE concentrations, EPMA (WDS) is recommended. For U concentrations, either EPMA (WDS) or SHRIMP-based relative sensitivity factors (RSF)$_{U-Ho}$ as described in Chapter 3 are recommended.

- The SHRIMP xenotime fractional ^{206}Pb/^{238}U ME is modelled by the following equation:

$$f\ ^{206}Pb/^{238}U\ ME = (\Delta U * x) + (\Delta \Sigma REE * y) \qquad (eq.\ 1)$$

Where:

- x and y are the unknown parameters or correction coefficients that are determined by Solver.
- ΔU is the wt% difference in elemental U between the averaged concentration in the primary calibration standard and secondary calibration standards and/or unknown samples.
- ΔΣREE is the wt% difference in elemental ΣREE between the averaged concentration in the primary calibration standard and secondary calibration standards and/or unknown samples.
- From equation 1, the correction factor for U (fU$_{CF}$) for example, is simply:

$$f U_{CF} = (\Delta U * x) \qquad (eq.\ 2)$$

Therefore, fU$_{CF}$ is the fractional proportion of the ^{206}Pb/^{238}U ME that has resulted from a U concentration contrast between the primary calibration standard and either secondary standard or unknown sample.

The values of the correction coefficients (x and y) are determined in a two-step process. Firstly, Excel solver estimates the values of x and y by solving the series of simultaneous equations that model the ^{206}Pb/^{238}U ME for the secondary standards.

Following this, a better determination of x and y can be made by computing a least squares solution to the problem that relies on the initial values calculated for x and y obtained in the first step.

In the following example MG1 was used as the primary calibration standard
- **MG1** electron probe WDS determined elemental U and ΣREE are 0.0991 wt% and 13.43 wt% respectively. 1σ errors are 6.05 % and 2.25 % respectively (SDOM).

Step 1:
First set out a chart as shown in Figure 1. Note that the equations in column M are set out as formulas. Cell V2 and V3 are for the solution to the correction coefficients (x and y).

name	raw Pb/U	ref. Pb/U	ΔU wt%	ΔΣREE wt%	fPb/U ME	equation (recal. fPb/U ME)	recalc. $^{206}Pb/^{238}U$	corr. Coefficient	solution
BS1-2.8	0.083117	0.082160	-0.0761	4.5270	0.0115	0	0	x	0
BS1-2.9	0.086723	0.082160	-0.0603	4.4974	0.0526	0	0	y	0
BS1-2.10	0.089830	0.082160	-0.0802	4.3639	0.0854	0	0		
BS1-3.1	0.085462	0.082160	-0.0628	4.4416	0.0386	0	0		
BS1-3.2	0.086997	0.082160	-0.0619	4.4337	0.0556	0	0		
BS1-3.3	0.086469	0.082160	-0.0473	4.5913	0.0498	0	0		
BS1-3.4	0.082617	0.082160	-0.0476	4.0914	0.0055	0	0		
BS1-3.5	0.086177	0.082160	-0.0426	4.0356	0.0466	0	0		
BS1-4.1	0.088882	0.082160	-0.0498	5.2081	0.0756	0	0		
BS1-4.2	0.084951	0.082160	-0.0380	4.6538	0.0329	0	0		
BS1-4.3	0.085656	0.082160	-0.0200	4.3395	0.0408	0	0		
BS1-4.4	0.086274	0.082160	-0.0615	5.0578	0.0477	0	0		
BS1-5.1	0.084433	0.082160	-0.0387	4.7435	0.0269	0	0		
BS1-5.2	0.084284	0.082160	-0.0631	5.1793	0.0252	0	0		
Z6413-5.1	0.204183	0.166717	1.2165	2.7897	0.1835	0	0		
Z6413-5.2	0.204357	0.166717	1.1445	2.8267	0.1842	0	0		
Z6413-5.3	0.208848	0.166717	1.4054	2.7572	0.2017	0	0		
Z6413-5.4	0.203332	0.166717	1.1929	2.7324	0.1801	0	0		
Z6413-6.1	0.206751	0.166717	1.1420	2.9042	0.1936	0	0		
Z6413-6.2	0.205761	0.166717	1.1461	2.9632	0.1898	0	0		
Z6413-6.3	0.200025	0.166717	1.0601	2.9299	0.1665	0	0		
Z6413-6.4	0.199333	0.166717	1.1125	2.8985	0.1636	0	0		
Z6413-6.5	0.207372	0.166717	1.4440	3.0659	0.1960	0	0		
Z6413-6.6	0.211118	0.166717	1.5189	2.9554	0.2103	0	0		
Z6413-7.1	0.206370	0.166717	1.2219	2.9543	0.1921	0	0		
Z6413-7.2	0.202113	0.166717	1.1824	3.0208	0.1751	0	0		

Formula annotations:

=C2*(1-M2)
=C3*(1-M3)
=C4*(1-M4)
=C5*(1-M5)
etc.

=(V2*G2)+(V3*I2)
=(V2*G3)+(V3*I3)
=(V2*G4)+(V3*I4)
=(V2*G5)+(V3*I5)
etc.

=(C2-E2)/C2
=(C3-E3)/C3
=(C4-E4)/C4
=(C5-E5)/C5
etc.

Fig. 1. Example worksheet before running Excel Solver.

Start excel solver by clicking Tools→Solver (nb. If solver does not appear on the drop down menu, then you must add it through the Tools→Add–Ins menu item). Clear the "Set Target Cell" edit box and in the "By Changing Cells" edit box select a range for the solution. Solver will calculate the best solution to the simultaneous equations by changing the values in these cells (V2 and V3). The Solver dialog box should now look like Fig. 2.
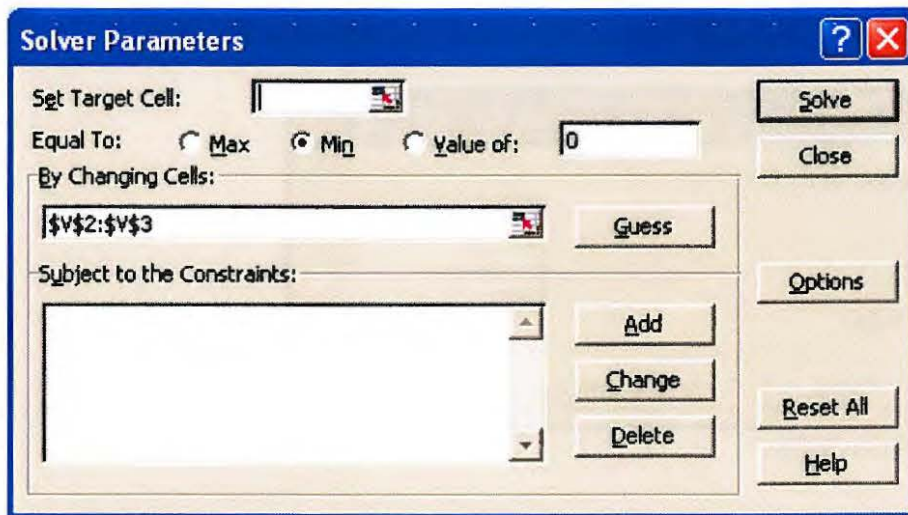
Fig. 2. Solver Parameters dialog box.

- Next set the constraints for the simultaneous equations by clicking the Add button. This step inputs the information from equation 1 into Solver. When the Add Constraint dialog box appears, fill it out as shown in Fig. 3. and click OK.
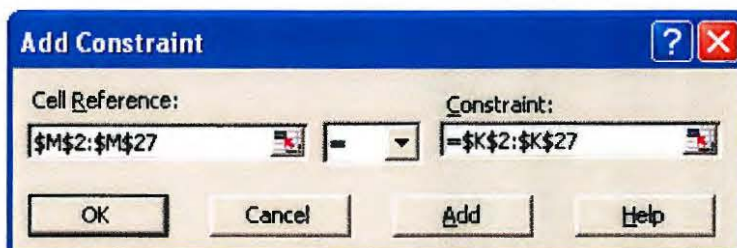
Fig3. Add Constraint dialog box.

The Solver Parameters dialog box should now look like Fig. 4.
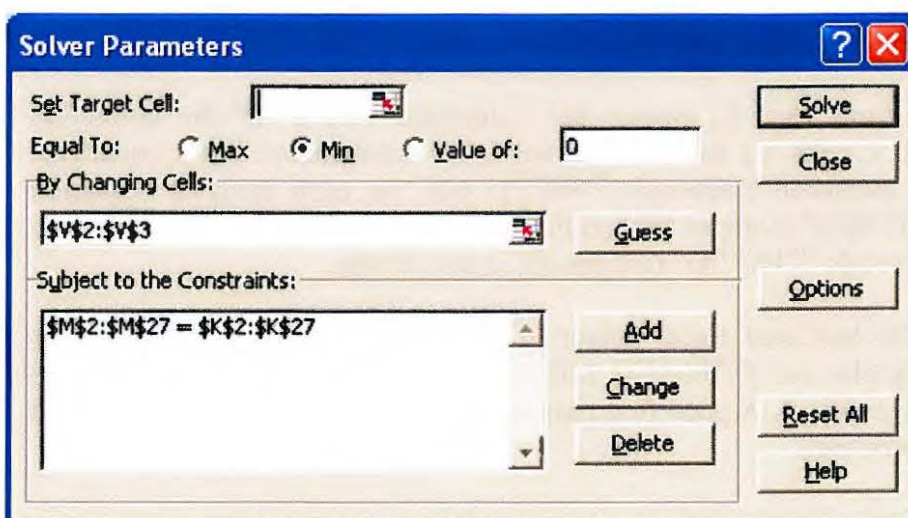
Fig. 4. Completed Solver Parameters dialog box.

Click the **Solve** button. You should now see the dialog box shown in Fig. 5.
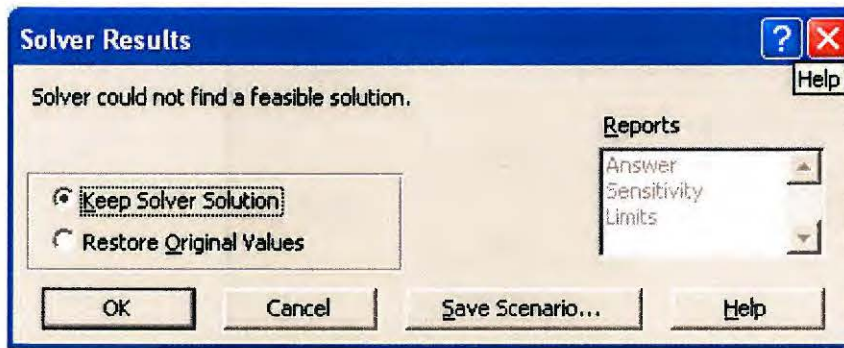
Fig. 5. Solver results dialog box.

Click on the **OK** button to keep the solution. The spreadsheet should now look like Fig. 6.

name	raw Pb/U	ref. Pb/U	ΔU wt%	ΔΣREE wt%	ƒPb/U ME	equation (recal. ƒPb/U ME)	recalc. ^{206}Pb/^{238}U		corr. Coefficient	solution
BS1-2.8	0.0831	0.082160	-0.0761	4.5270	0.0115	0.0031	0.0829		x	0.1297
BS1-2.9	0.0867	0.082160	-0.0603	4.4974	0.0526	0.0051	0.0863		y	0.0029
BS1-2.10	0.0898	0.082160	-0.0802	4.3839	0.0854	0.0022	0.0896			
BS1-3.1	0.0855	0.082160	-0.0628	4.4416	0.0386	0.0046	0.0851			
BS1-3.2	0.0870	0.082160	-0.0619	4.4337	0.0555	0.0047	0.0866			
BS1-3.3	0.0865	0.082160	-0.0473	4.5913	0.0498	0.0070	0.0859			
BS1-3.4	0.0826	0.082160	-0.0476	4.0914	0.0055	0.0055	0.0822			
BS1-3.5	0.0862	0.082160	-0.0426	4.0356	0.0466	0.0060	0.0857			
BS1-4.1	0.0889	0.082160	-0.0498	5.2081	0.0756	0.0085	0.0881			
BS1-4.2	0.0850	0.082160	-0.0360	4.6538	0.0329	0.0084	0.0842			
BS1-4.3	0.0857	0.082160	-0.0200	4.3395	0.0408	0.0098	0.0848			
BS1-4.4	0.0863	0.082160	-0.0615	5.0578	0.0477	0.0065	0.0857			
BS1-5.1	0.0844	0.082160	-0.0387	4.7435	0.0269	0.0086	0.0837			
BS1-5.2	0.0843	0.082160	-0.0631	5.1793	0.0252	0.0066	0.0837			
Z6413-5.1	0.2042	0.166717	1.2165	2.7897	0.1835	0.1658	0.1703			
Z6413-5.2	0.2044	0.166717	1.1445	2.8267	0.1842	0.1565	0.1724			
Z6413-5.3	0.2068	0.166717	1.4054	2.7572	0.1902	0.1902	0.1691			
Z6413-5.4	0.2033	0.166717	1.1929	2.7324	0.1801	0.1625	0.1703			
Z6413-6.1	0.2068	0.166717	1.1420	2.9042	0.1936	0.1564	0.1744			
Z6413-6.2	0.2058	0.166717	1.1461	2.9632	0.1898	0.1571	0.1734			
Z6413-6.3	0.2000	0.166717	1.0601	2.9299	0.1665	0.1459	0.1708			
Z6413-6.4	0.1993	0.166717	1.1125	2.8985	0.1636	0.1526	0.1689			
Z6413-6.5	0.2074	0.166717	1.4440	3.0659	0.1960	0.1960	0.1667			
Z6413-6.6	0.2111	0.166717	1.5189	2.9554	0.2103	0.2054	0.1677			
Z6413-7.1	0.2064	0.166717	1.2219	2.9543	0.1921	0.1669	0.1719			
Z6413-7.2	0.2021	0.166717	1.1824	3.0206	0.1751	0.1620	0.1694			

Fig. 6. Example worksheet after running Excel Solver (step1).

As can be seen from Fig. 6., Solver has calculated values for the correction coefficients (x and y; cells V2 and V3) that solve the simultaneous linear equations. Additionally, the estimated fractional ^{206}Pb/^{238}U ME for each analysis "equation (recalc. $ƒ^{206}$Pb/^{238}U ME)" (column M) and the ^{UΣREE}Matrix corrected ^{206}Pb/^{238}U ratio for each analysis "recalc ^{206}Pb/^{238}U" (column O) is also shown.

The above example has used Excel Solver to find a solution to the simultaneous equations that describe the $ƒ^{206}$Pb/^{238}U ME for the secondary standards BS1 and Z6413, shown in equation 1. A good first-pass estimate of the correction factors x and y has now been completed.

Step 2

In the following step, a better estimate of the correction coefficients is obtained using a least squares approach. A least squares estimation of the correction coefficients are the values that minimise the sum of squares between the measured $ƒ^{206}$Pb/^{238}U ME

for the secondary standards and the linear function used to model it (i.e. Equation 1), which in this case is "recalc $^{206}Pb/^{238}U$" (column O; Fig. 6).

In columns Q and S, type in the headings, **residual** and **res. square**, respectively. The **residual** is the difference between the measured $f^{206}Pb/^{238}U$ ME (Column K) and the linear function used to model the $^{206}Pb/^{238}U$ ME in step 1 (Column O, Fig. 6). The **res. square** column is simply the square of the values in the residual column. Lastly, define one cell as the "**target cell**" and type in the formula SUM(S2:S27). This is the sum of the square of the residuals and is the value that Solver will minimise. The spreadsheet and formulas used in each cell are shown in Fig. 7, whereas Fig. 8 shows the worksheet prior to running Excel Solver.

name	raw Pb/U	ref. Pb/U	ΔU wt%	ΔΣREE wt%	fPb/U ME	equation (recal. fPb/U ME)[1]	recalc[1] 206Pb/238U	residual	res. square	corr. Coefficient	solution
BS1-2.8	0.0831	0.082160	-0.0761	4.5270	0.0115	0.0031	0.0829			x	0.1297
BS1-2.9	0.0867	0.082160	-0.0603	4.4974	0.0526	0.0051	0.0863			y	0.0029
BS1-2.10	0.0898	0.082160	-0.0802	4.3839	0.0854	0.0022	0.0896				
BS1-3.1	0.0855	0.082160	-0.0628	4.4416	0.0386	0.0046	0.0851			=sum(S2:S27)	
BS1-3.2	0.0870	0.082160	-0.0619	4.4337	0.0556	0.0047	0.0866				
BS1-3.3	0.0865	0.082160	-0.0473	4.5913	0.0498	0.0070	0.0859			target cell	0.0000
BS1-3.4	0.0826	0.082160	-0.0476	4.0914	0.0055	0.0055	0.0822				
BS1-3.5	0.0862	0.082160	-0.0426	4.0355	0.0060	0.0060	0.0857				
BS1-4.1	0.0889	0.082160	-0.0498	5.2081	0.0756	0.0085	0.0881			=Q2^2	
BS1-4.2	0.0850	0.082160	-0.0380	4.6538	0.0329	0.0084	0.0842			=Q3^2	
BS1-4.3	0.0857	0.082160	-0.0200	4.3395	0.0408	0.0098	0.0848			=Q4^2	
BS1-4.4	0.0863	0.082160	-0.0615	5.0578	0.0477	0.0065	0.0857			=Q5^2	
BS1-5.1	0.0844	0.082160	-0.0387	4.7435	0.0269	0.0086	0.0837			=Q6^2	
BS1-5.2	0.0843	0.082160	-0.0631	5.1793	0.0252	0.0066	0.0837				
Z6413-5.1	0.2042	0.166717	1.2165	2.7897	0.1835	0.1658	0.1703				
Z6413-5.2	0.2044	0.166717	1.1445	2.8267	0.1842	0.1565	0.1724			=K2-M2	
Z6413-5.3	0.2088	0.166717	1.4054	2.7572	0.2017	0.1902	0.1691			=K3-M3	
Z6413-5.4	0.2033	0.166717	1.1929	2.7324	0.1801	0.1625	0.1703			=K4-M4	
Z6413-6.1	0.2068	0.166717	1.1420	2.9042	0.1936	0.1564	0.1744			=K5-M5	
Z6413-6.2	0.2058	0.166717	1.1461	2.9632	0.1898	0.1571	0.1734			=K6-M6	
Z6413-6.3	0.2000	0.166717	1.0601	2.9299	0.1665	0.1459	0.1708				
Z6413-6.4	0.1993	0.166717	1.1125	2.8985	0.1636	0.1526	0.1689				
Z6413-6.5	0.2074	0.166717	1.4440	3.0659	0.1960	0.1960	0.1667				
Z6413-6.6	0.2111	0.166717	1.5189	2.9554	0.2103	0.2054	0.1677				
Z6413-7.1	0.2064	0.166717	1.2219	2.9543	0.1921	0.1669	0.1719				
Z6413-7.2	0.2021	0.166717	1.1824	3.0208	0.1751	0.1620	0.1694				

Fig 7. Example worksheet showing the formulas used for each cell.

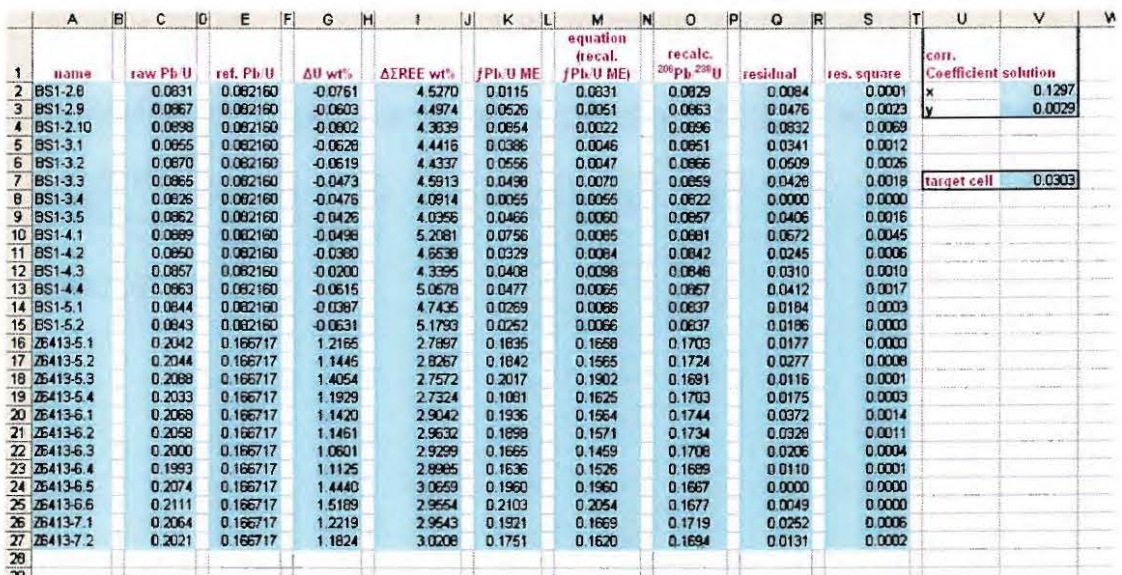| name	raw Pb/U	ref. Pb/U	ΔU wt%	ΔΣREE wt%	fPb/U ME	equation (recal. fPb/U ME)	recalc. 206Pb/238U	residual	res. square	corr. Coefficient	solution
BS1-2.8	0.0831	0.082160	-0.0761	4.5270	0.0115	0.0831	0.0829	0.0084	0.0001	x	0.1297
BS1-2.9	0.0867	0.082160	-0.0603	4.4974	0.0526	0.0051	0.0863	0.0476	0.0023	y	0.0029
BS1-2.10	0.0898	0.082160	-0.0802	4.3839	0.0854	0.0022	0.0896	0.0832	0.0069		
BS1-3.1	0.0855	0.082160	-0.0628	4.4416	0.0386	0.0046	0.0851	0.0341	0.0012		
BS1-3.2	0.0870	0.082160	-0.0619	4.4337	0.0556	0.0047	0.0866	0.0509	0.0026		
BS1-3.3	0.0865	0.082160	-0.0473	4.5913	0.0498	0.0070	0.0859	0.0428	0.0018	target cell	0.0303
BS1-3.4	0.0826	0.082160	-0.0476	4.0914	0.0055	0.0055	0.0822	0.0000	0.0000		
BS1-3.5	0.0862	0.082160	-0.0426	4.0355	0.0060	0.0060	0.0857	0.0406	0.0016		
BS1-4.1	0.0889	0.082160	-0.0498	5.2081	0.0756	0.0085	0.0881	0.0672	0.0045		
BS1-4.2	0.0850	0.082160	-0.0380	4.6538	0.0329	0.0084	0.0842	0.0245	0.0006		
BS1-4.3	0.0857	0.082160	-0.0200	4.3395	0.0408	0.0098	0.0846	0.0310	0.0010		
BS1-4.4	0.0863	0.082160	-0.0615	5.0578	0.0477	0.0065	0.0857	0.0412	0.0017		
BS1-5.1	0.0844	0.082160	-0.0387	4.7435	0.0269	0.0086	0.0837	0.0184	0.0003		
BS1-5.2	0.0843	0.082160	-0.0631	5.1793	0.0252	0.0066	0.0837	0.0186	0.0003		
Z6413-5.1	0.2042	0.166717	1.2165	2.7897	0.1835	0.1658	0.1703	0.0177	0.0003		
Z6413-5.2	0.2044	0.166717	1.1445	2.8267	0.1842	0.1565	0.1724	0.0277	0.0008		
Z6413-5.3	0.2088	0.166717	1.4054	2.7572	0.2017	0.1902	0.1691	0.0116	0.0001		
Z6413-5.4	0.2033	0.166717	1.1929	2.7324	0.1801	0.1625	0.1703	0.0175	0.0003		
Z6413-6.1	0.2068	0.166717	1.1420	2.9042	0.1936	0.1564	0.1744	0.0372	0.0014		
Z6413-6.2	0.2058	0.166717	1.1461	2.9632	0.1898	0.1571	0.1734	0.0328	0.0011		
Z6413-6.3	0.2000	0.166717	1.0601	2.9299	0.1665	0.1459	0.1708	0.0206	0.0004		
Z6413-6.4	0.1993	0.166717	1.1125	2.8985	0.1636	0.1526	0.1689	0.0110	0.0001		
Z6413-6.5	0.2074	0.166717	1.4440	3.0659	0.1960	0.1960	0.1667	0.0000	0.0000		
Z6413-6.6	0.2111	0.166717	1.5189	2.9554	0.2103	0.2054	0.1677	0.0049	0.0000		
Z6413-7.1	0.2064	0.166717	1.2219	2.9543	0.1921	0.1669	0.1719	0.0252	0.0006		
Z6413-7.2	0.2021	0.166717	1.1824	3.0208	0.1751	0.1620	0.1694	0.0131	0.0002		

Fig 8. Example worksheet before running Excel Solver (step2).

Start excel solver by clicking Tools→Solver. The Solver Parameters dialog box will again appear and be similar to Fig. 4. Highlight the "Subject to the Constraints" data

entry from step 1 and click on **delete**. The target cell for this calculation is the sum of squared residual box V7. The "By Changing Cells" edit box should not have changed. The Solver Parameters dialog box should now look similar to Fig. 9. Make sure that in the "Equal To" field, **Min** is checked. Solver will now minimise the sum of squared residuals by changing the values for the correction coefficients (x and y) that were calculated in step 1.
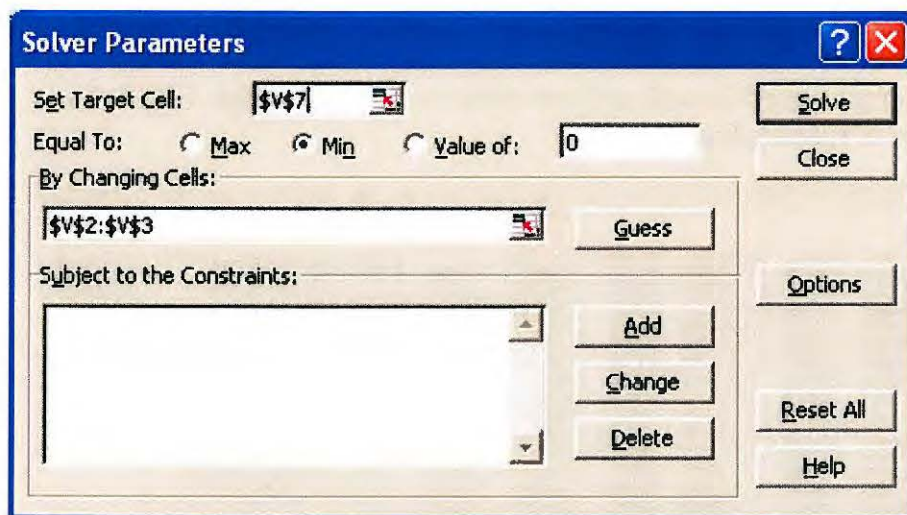

Fig. 9. Completed Solver Parameters dialog box (step 2).

Finally, click the **Solve** button and a Solver results dialog box will appear similar to Fig. 5., click **OK**.

The spreadsheet should now look like Fig. 10. Solver has recalculated the values for the correction coefficients x and y and in the process, recalculated the final $^{U\Sigma REE}$matrix corrected $^{206}Pb/^{238}U$ ratio for each of the secondary standards (Column O). The final results for the SHRIMP xenotime $^{206}Pb/^{238}U$ matrix correction procedure used in this example are shown in Fig. 11. The $^{U\Sigma REE}$matrix corrected $^{206}Pb/^{238}U$ ratios for the unknowns can now be calculated.

name	raw Pb/U	ref. Pb/U	ΔU wt%	ΔΣREE wt%	fPb/U ME	equation (recal. fPb/U ME)¹	recalc¹. $^{206}Pb/^{238}U$	residual	res. square	corr. Coefficient	solution
BS1-2.8	0.0831	0.082160	-0.0761	4.5270	0.0115	0.0394	0.0798	-0.0279	0.0008	x	0.1251
BS1-2.9	0.0867	0.082160	-0.0603	4.4974	0.0526	0.0411	0.0832	0.0115	0.0001	y	0.0108
BS1-2.10	0.0898	0.082160	-0.0802	4.3639	0.0854	0.0374	0.0865	0.0480	0.0023		
BS1-3.1	0.0855	0.082160	-0.0628	4.4416	0.0366	0.0402	0.0820	-0.0015	0.0000		
BS1-3.2	0.0870	0.082160	-0.0619	4.4337	0.0556	0.0402	0.0835	0.0154	0.0002		
BS1-3.3	0.0865	0.082160	-0.0473	4.5913	0.0498	0.0437	0.0827	0.0061	0.0000	target cell	0.0077
BS1-3.4	0.0826	0.082160	-0.0476	4.0914	0.0055	0.0383	0.0795	-0.0328	0.0011		
BS1-3.5	0.0852	0.082160	-0.0426	4.0356	0.0466	0.0383	0.0829	0.0083	0.0001		
BS1-4.1	0.0889	0.082160	-0.0498	5.2061	0.0756	0.0501	0.0844	0.0255	0.0007		
BS1-4.2	0.0850	0.082160	-0.0380	4.6538	0.0329	0.0456	0.0811	-0.0127	0.0002		
BS1-4.3	0.0857	0.082160	-0.0200	4.3395	0.0408	0.0444	0.0818	-0.0036	0.0000		
BS1-4.4	0.0863	0.082160	-0.0615	5.0578	0.0477	0.0470	0.0822	0.0007	0.0000		
BS1-5.1	0.0844	0.082160	-0.0387	4.7435	0.0289	0.0465	0.0805	-0.0195	0.0004		
BS1-5.2	0.0843	0.082160	-0.0631	5.1793	0.0252	0.0481	0.0802	-0.0229	0.0005		
Z6413-5.1	0.2042	0.166717	1.2165	2.7697	0.1835	0.1824	0.1669	0.0011	0.0000		
Z6413-5.2	0.2044	0.166717	1.1445	2.8267	0.1842	0.1738	0.1688	0.0104	0.0001		
Z6413-5.3	0.2088	0.166717	1.4054	2.7572	0.2017	0.2057	0.1659	-0.0040	0.0000		
Z6413-5.4	0.2033	0.166717	1.1929	2.7324	0.1801	0.1788	0.1670	0.0012	0.0000		
Z6413-6.1	0.2068	0.166717	1.1420	2.9042	0.1936	0.1743	0.1707	0.0193	0.0004		
Z6413-6.2	0.2058	0.166717	1.1461	2.9632	0.1898	0.1755	0.1697	0.0143	0.0002		
Z6413-6.3	0.2000	0.166717	1.0601	2.9299	0.1665	0.1844	0.1672	0.0022	0.0000		
Z6413-6.4	0.1993	0.166717	1.1125	2.8985	0.1636	0.1706	0.1653	-0.0069	0.0000		
Z6413-6.5	0.2074	0.166717	1.4440	3.0659	0.1960	0.2139	0.1630	-0.0178	0.0003		
Z6413-6.6	0.2111	0.166717	1.5169	2.9554	0.2103	0.2220	0.1642	-0.0117	0.0001		
Z6413-7.1	0.2064	0.166717	1.2219	2.9543	0.1921	0.1849	0.1682	0.0073	0.0001		
Z6413-7.2	0.2021	0.166717	1.1824	3.0208	0.1751	0.1806	0.1656	-0.0055	0.0000		

Fig. 10. Example worksheet after running Excel Solver (step2).

	A	B	C	D	E	F	G	H	I	J	K	L	M
1	name		ref. $^{206}Pb/^{238}U$ age (Ma)		raw $^{206}Pb/^{238}U$ age (Ma) ± 1(σ)			%δ[1]		U,ΣREE MC $^{206}Pb/^{238}U$ age (Ma) ± 1(σ)*			%δ[2]
2	BS1-2.8		509		515	17		1.15		495	18		-2.91
3	BS1-2.9		509		536	13		5.26		515	13		1.20
4	BS1-2.10		509		555	17		8.54		535	18		4.99
5	BS1-3.1		509		529	15		3.86		508	19		-0.16
6	BS1-3.2		509		538	15		5.56		517	16		1.60
7	BS1-3.3		509		535	12		4.98		512	13		0.64
8	BS1-3.4		509		512	13		0.55		493	13		-3.41
9	BS1-3.5		509		533	13		4.66		513	13		0.86
10	BS1-4.1		509		549	13		7.56		523	13		2.69
11	BS1-4.2		509		526	16		3.29		503	18		-1.33
12	BS1-4.3		509		530	15		4.08		507	16		-0.38
13	BS1-4.4		509		533	14		4.77		509	14		0.07
14	BS1-5.1		509		523	12		2.69		499	13		-2.05
15	BS1-5.2		509		522	13		2.52		497	15		-2.41
16	Z6413-5.1		994		1198	28		18.35		995	36		0.13
17	Z6413-5.2		994		1199	24		18.42		1006	32		1.26
18	Z6413-5.3		994		1223	24		20.17		989	36		-0.50
19	Z6413-5.4		994		1193	24		18.01		995	33		0.15
20	Z6413-6.1		994		1211	24		19.36		1016	32		2.34
21	Z6413-6.2		994		1206	24		18.98		1010	32		1.73
22	Z6413-6.3		994		1175	24		16.65		996	31		0.26
23	Z6413-6.4		994		1172	23		16.36		986	31		-0.84
24	Z6413-6.5		994		1215	24		19.60		974	36		-2.27
25	Z6413-6.6		994		1235	24		21.03		980	37		-1.51
26	Z6413-7.1		994		1209	24		19.21		1002	33		0.89
27	Z6413-7.2		994		1187	23		17.51		988	32		-0.67
28													

Fig. 11. Summary table for least squares $^{206}Pb/^{238}U$ ^{UΣREE}matrix correction technique described above. %δ[1] is the percent deviation of the raw $^{206}Pb/^{238}U$ age to its reference age. %δ[2] is the percent deviation of the ^{UΣREE}matrix corrected $^{206}Pb/^{238}U$ age to its reference age.

Errors

The errors associated with the matrix correction are four-fold. These are (1) the uncertainty associated with the calculation of the U and ΣREE correction coefficients (x and y) (2) ΔU and ΔΣREE error (3) the U and ΣREE correction error and (4) the total U-related and ΣREE-related error.

(1). Estimating the uncertainties of the least square correction coefficients (x and y)
An estimate of the uncertainty of the correction coefficients or parameters x and y, can be obtained using the jackknife method as described by Caceci (1989). The jackknife method calculates the effect that each analysis has on the uncertainty. For example, if there are n analyses in a sample, then n estimates are calculated from the sample by deleting each analysis in turn from the total sample. Finally, the uncertainty is simply the standard deviation of the mean (SDOM) or standard error of the correction coefficients x and y. Figure 12 demonstrates how to estimate the uncertainty of the correction coefficients x and y shown in Fig. 10, using the jackknife method.

	residual	res. square	corr. Coefficient	solution		name	analysis deleted	U corr. coefficient (x)	ΣREE corr. coefficient (y)
2	-0.0279	0.00078	x	0.125141		BS1-2.8	2	0.124057	0.011266
3	0.0115	0.00013	y	0.010816		BS1-2.9	3	0.125572	0.010633
4	0.0460	0.00231				BS1-2.10	4	0.126963	0.010067
5	-0.0015	0.00000				BS1-3.1	5	0.125084	0.010840
6	0.0154	0.00024				BS1-3.2	6	0.125710	0.010575
7	0.0061	0.00004	target cell	0.0077		BS1-3.3	7	0.125368	0.010717
8	-0.0328	0.00107				BS1-3.4	8	0.124060	0.011281
9	0.0083	0.00007				BS1-3.5	9	0.125409	0.010700
10	0.0255	0.00065				BS1-4.1	10	0.126235	0.010339
11	-0.0127	0.00016				BS1-4.2	11	0.124671	0.011023
12	-0.0036	0.00001				BS1-4.3	12	0.125022	0.010870
13	0.0007	0.00000				BS1-4.4	13	0.125170	0.010803
14	-0.0195	0.00038				BS1-5.1	14	0.124402	0.011142
15	-0.0229	0.00052				BS1-5.2	15	0.124143	0.011244
16	0.0011	0.00000				Z6413-5.1	16	0.125066	0.010815
17	0.0104	0.00011				Z6413-5.2	17	0.124479	0.010802
18	-0.0040	0.00002				Z6413-5.3	18	0.125486	0.010812
19	0.0012	0.00000				Z6413-5.4	19	0.125057	0.010815
20	0.0193	0.00037				Z6413-6.1	20	0.123924	0.010785
21	0.0143	0.00020				Z6413-6.2	21	0.124243	0.010790
22	0.0022	0.00000				Z6413-6.3	22	0.125020	0.010811
23	-0.0069	0.00005				Z6413-6.4	23	0.125563	0.010828
24	-0.0178	0.00032				Z6413-6.5	24	0.126711	0.010815
25	-0.0117	0.00014				Z6413-6.6	25	0.126269	0.010804
26	0.0073	0.00005				Z6413-7.1	26	0.124637	0.010807
27	-0.0055	0.00003				Z6413-7.2	27	0.125503	0.010825
29/30							standard deviation	0.0008111	0.0002577
32		SDOM = Standard deviation of mean					SDOM	0.0002	0.0001
34							% error	0.13	0.47

U correction coefficient (x) = 0.125141 ± 0.13%
ΣREE correction coefficient (y) = 0.010816 ± 0.47%

Fig. 12. Estimating uncertainties in the correction coefficients x and y using the jackknife method.

Set the sum of squared residuals cell e.g. 'target cell' to equal V7=S2+S3+S4....+S27. Delete the first analysis (S2) and use Solver to find the correction coefficients x and y for the remaining analyses. Copy and paste the values for x and y into cells AB2 and AD2 respectively. Restore the first analysis (S2) and remove the next analysis (S3) and again use Solver to find the correction coefficients. Continue to delete one analysis in turn and calculate the correction coefficients for the remaining data. Once this step is completed, calculate the SDOM for columns AB and AD. The final uncertainty is simply calculated as the percent SDOM and is shown in the box in the lower right hand corner of Fig. 12. The relatively small uncertainties calculated for the U and ΣREE correction coefficients show that the SHRIMP U-Pb xenotime and electron microprobe data for the secondary standards BS1 and Z6413 are well fitted to the simultaneous equations used to model the SHRIMP $^{206}Pb/^{238}U$ ME.

The remaining error calculations are explained using the data shown in Fig 13. This Figure shows the correction coefficients for U and ΣREE (x and y) and their uncertainties that were calculated using Solver in the previous sections (i.e. Cells C2, C3 and D2, D3; Fig. 13).

	A	B	C	D	E	F	G	H	I	J	K	L
1		corr. Coefficient	solution	% error								
2		x	0.125141	0.13								
3		y	0.010616	0.47								
6		MG1	U wt%	± % err (SDOM)	ΣREE wt%	± % err (SDOM)						
7			0.0991	6.05	13.43	2.25						
10		Z6413	raw Pb/U (Ma)	± % raw Pb/U	U wt%	± % U err (1σ)	ΣREE wt%	± % ΣREE err (1σ)	ΔU wt%	± % ΔU err 1(σ)	ΔΣREE wt%	± % ΔΣREE err (1σ)
11		Z6413-5.1	1198	2.59	1.3156	6.65	16.2197	3.55	1.2165	12.7	2.7897	5.8
13		ƒU$_{CF}$	ƒΣREE$_{CF}$									
14		0.1522	0.0302									
17		% U corr. error	% ΣREE corr. error									
18		12.70	5.82									
21		% Tot. U-related corr. Err. (1σ)	% Tot. ΣREE-related corr. Err. (1σ)									
22		1.93	0.18									
25		Final $^{U, \Sigma REE}$Matrix corrected error = √((2.59)^2+(1.93)^2+(0.18)^2)=						3.24				

Fig. 13. $^{206}Pb/^{238}U$ matrix correction error calculation spreadsheet.

(2). ΔU and ΔΣREE error

This error is simply the analytical uncertainty associated with the calculation of ΔU and ΔΣREE from electron probe (WDS) analyses. The 1(σ) % errors of the primary calibration standard are simply added to the individual 1(σ) % errors of the secondary calibration standard and unknowns. Using U as an example:

$$\% \ \Delta U \ err. = (\%U \ err.)_{PCS} + (\%U \ err.)_{SST \ and/or \ UNK}$$
i.e. J11 = (F11 + D7)

Where: PCS = primary calibration standard; SST = secondary standard and; UNK = unknown.

(3). U and ΣREE correction error

This error describes the error associated with the U and ΣREE matrix correction. The error associated with the calculation of the correction coefficients is simply added in quadrature to the ΔU and ΔΣREE errors. Using U as an example:

$$\%U \ corr. \ error = \sqrt{[(\% \ x \ err.)^2 + (\% \ \Delta U \ err.)^2]}$$
i.e. B18 = SQRT((D2)^2 + (J11)^2)

289

(4). Total U- and ΣREE-related error

This is the total error associated with the U and ΣREE $^{206}Pb/^{238}U$ matrix correction for each secondary standard and unknown analysis. It is calculated by multiplying fU_{CF} and $f\Sigma REE_{CF}$ (equation 2) by the %U corr. error and %ΣREE corr. error, respectively. Again using U as an example:

% Tot. U related corr. err. = fU_{CF} * %U corr. error
        i.e. B22 = B14 * B18

Note that the total U- and ΣREE-related error is only applied to the proportion of the $^{206}Pb/^{238}U$ ratio that has resulted from a U and ΣREE contrast with the primary calibration standard.

Finally all errors associated with the $^{206}Pb/^{238}U$ age determination are added in quadrature. These are the analytical uncertainty associated with the raw $^{206}Pb/^{238}U$ age determination, the total U-related error and the total ΣREE-related error. Therefore, the final $^{U, \Sigma REE}$matrix corrected error is:

$= \sqrt{(\pm\% \text{ raw Pb/U})^2 + (\% \text{ tot. U-related corr. err.})^2 + (\% \text{ tot. }\Sigma REE\text{-related corr. err.})^2}$

i.e. H25= SQRT((D11)^2+(B22)^2+(C22)^2)

References

Caceci, M.S. 1989. Estimating error limits in parametric curve fitting. *Analytical Chemistry*, **61**, 2324-2327.

APPENDIX 4.1- Electron microprobe settings used for monazite analysis

Detection Limits and relative errors are 1σ.
HV: 15kV
Current: 100nA
Beam focus: focussed 10μm
Cameca SX100:Research School of Earth Sciences, ANU

Element	Line	Standard	Crystal	Position	Bg 1	Bg 2	Time (s)	Det. Lim. (ppm)	% relative error (σ)
Y	Lα	YP_5O_{14}	TAP	25122	778	2000	120	143	3
Si	Kα	K412 Glas	TAP	27743	-640	580	40	82	27
P	Kα	$Ca_2P_2O_7$	TAP	23994	1900	3140	10	210	2
Ca	Kα	K412 Glas	PET	38389	-500	500	30	115	4
La	Lα	LaP_5O_{14}	PET	30475	-750	550	10	832	3
Ce	Lα	CeP_5O_{14}	PET	29286	-445	500	10	919	2
Pr	Lβ	PrP_5O_{14}	PET	25841	-280	1940	30	1480	6
Nd	Lβ	NdP_5O_{14}	PET	24811	-1020	770	10	2383	39
Sm	Lβ	SmP_5O_{14}	PET	22884	910	1	40	1887	12
Eu	Lβ	EuP_5O_{15}	LLIF	47690	-1350	560	20	758	29
Gd	Lβ	GdP_5O_{14}	LLIF	45850	-370	2000	40	1034	9
Dy	Lα	DyP_5O_{14}	LLIF	47410	380	844	30	632	19
U	Mβ	UO_2	LPET	42462	-2400	-925	120	227	12
Th	Mα	ThO_2	LPET	47292	690	1460	20	403	6

APPENDIX 4.2- Monazite standard 44069 (Aleinikoff et al. 2006) U concentration calculation

Monazite standard 44069 (Aleinikoff et al. 2006) U concentration calculation

44069 monazite WDS analyses								
oxide wt%	44069-1.1	44069-1.2	44069-1.3	44069-2.1	44069-2.2	44069-2.3	44069-3.1	44069-3.2
SiO2	0.12	0.13	0.12	0.14	0.17	0.18	0.14	0.13
CaO	0.75	0.72	0.65	0.86	0.94	1.02	1.02	0.89
P2O5	29.81	30.06	29.80	29.80	29.63	29.65	29.31	29.53
Y2O3	2.35	2.36	2.24	2.55	2.78	3.05	2.74	2.88
La2O3	12.66	12.55	12.92	12.56	11.99	11.54	12.11	11.67
Ce2O3	27.40	27.28	27.65	26.44	25.91	24.79	25.75	25.58
Pr2O3	3.91	3.89	3.85	3.78	3.61	3.63	3.59	3.74
Nd2O3	13.14	13.05	13.34	12.75	13.03	13.11	12.67	13.24
Sm2O3	2.12	2.27	2.25	2.25	2.24	2.38	2.11	2.35
Eu2O3	0.12	0.04	0.08	0.19	0.19	0.15	0.15	0.21
Gd2O3	1.79	1.81	1.78	1.86	1.99	2.22	2.01	2.07
Dy2O3	0.72	0.74	0.72	0.79	0.87	0.96	0.89	0.96
ThO2	2.65	2.52	2.34	2.88	3.41	3.51	3.17	2.89
U2O3	0.26	0.29	0.26	0.42	0.56	0.67	0.58	0.42
Total	98.19	98.13	98.35	97.58	97.72	97.42	96.70	97.01

44069 monazite WDS analyses (continued)								
oxide wt%	44069-4.1	44069-4.2	44069-5.1	44069-5.2	44069-6.1	44069-6.2	44069-7.1	44069-7.2
SiO2	0.14	0.12	0.17	0.06	0.12	0.11	0.21	0.10
CaO	0.95	0.68	0.73	0.78	1.11	0.78	1.37	0.70
P2O5	29.50	29.65	29.28	29.90	29.90	29.81	29.55	29.84
Y2O3	2.81	2.40	2.27	3.09	3.45	2.85	2.62	2.64
La2O3	12.04	12.40	12.04	11.61	11.73	12.13	11.39	12.06
Ce2O3	25.77	26.65	26.96	25.31	25.16	26.40	24.55	26.22
Pr2O3	3.66	3.77	3.91	3.78	3.58	3.79	3.54	3.71
Nd2O3	12.88	13.36	13.31	13.04	12.71	12.91	12.19	13.48
Sm2O3	2.22	2.21	2.26	2.29	2.36	2.34	2.14	2.26
Eu2O3	0.21	0.21	0.17	-0.03	0.12	0.16	0.13	0.20
Gd2O3	2.04	1.83	1.85	2.23	2.21	2.02	1.77	1.99
Dy2O3	0.81	0.70	0.67	1.05	1.05	0.90	0.79	0.75
ThO2	3.16	2.60	2.79	3.36	3.01	2.24	6.49	2.77
U2O3	0.41	0.23	0.28	0.44	0.58	0.41	0.59	0.39
Total	97.05	97.28	97.07	97.38	97.60	97.27	97.79	97.43

Average U_2O_3 =   0.4246 wt%
SDOM =   0.0347 wt%

Convert oxide to element (ppm) =   <u>3857 ± 630 ppm (2σ)</u>

APPENDIX 5.1-AGES abstract

Cross, A.J., Fletcher, I.R., Crispe, A.J., Huston, D.L. & Williams, N., 2005. New constraints on the timing of deposition and mineralisation in the Tanami Group. *Annual Geoscience Exploration Seminar (AGES) Record of Abstracts, Northern Territory Geological Survey Record* **2005-001**.

New constraints on the timing of deposition and mineralisation in the Tanami Group

[1,2]Cross, A.J., [3]Fletcher, I.R., [4]Crispe, A.J., [2]Huston, D.L. and [2]Williams, N.

[1]Research School of Earth Sciences, The Australian National University, Canberra, ACT 0200
[2]Geoscience Australia, PO Box 378, Canberra
[3]Centre for Global Metallogeny, School of Earth and Geographical Sciences, University of Western Australia, Nedlands, WA 6907, Australia
[4]Northern Territory Geological Survey, PO Box 2655, Alice Springs

Recent years have seen a sustained commitment by the Northern Territory Geological Survey and Geoscience Australia to isotopically dating the event history of the Tanami region. These studies have primarily used SHRIMP U–Pb zircon and to a lesser extent $^{40}Ar/^{39}Ar$ techniques (see Cross et al., 2003, Smith et al., 2001 and Fraser, 2002). Here we report our ongoing results and the tectonic significance of recent SHRIMP U–Pb zircon studies of two sediments and a tuffaceous unit within the Dead Bullock Formation. We also report the results of recent SHRIMP U–Pb in situ dating of ore-related hydrothermal xenotime from the Callie deposit that challenges the ca. 1720 Ma age of mineralisation suggested by Fraser (2002).

New stratigraphic constraints and tectonic interpretations

The basal Tanami Group consists of two units, the Dead Bullock Formation and conformably overlying turbidites of the Killi Killi Formation. The Dead Bullock Formation is host to the giant Callie lode Au deposit. This unit is a thick package of siltstone, carbonaceous siltstone, iron Formation and minor sandstone that is divided into the Ferdies Member (older) and Callie Member (younger).

The Killi Killi Formation is a part of a widespread northern Australian turbidite package. Four samples from this unit have remarkably similar detrital zircon age patterns. Each is dominated by a ca. 1865 Ma age mode and has a subordinate late Archaean mode at 2.5 Ga (see Cross et al. 2003). The 1865 Ma age mode coincides with peak magmatism associated with the Hooper Orogeny. The youngest zircons in the Killi Killi Formation consistently indicate a maximum depositional age of 1.84 Ga.

Recent SHRIMP U–Pb detrital zircon studies from two Ferdies Member samples from the Dead Bullock Formation show them to be markedly different to those from the overlying Killi Killi Formation. One sample is dominated by zircon 2.56–2.44 Ga old, and the other contains Archaean components with ages of 3.22, 2.77, and 2.45 Ga. These detrital zircon age components suggest a derivation from either the Pilbara Craton in Western Australia and/or the Rum Jungle region in northern Australia. The youngest zircons from the Ferdies Member imply that this unit was deposited after 2.44 Ga and possibly after 2.11 Ga. However, these detrital zircon ages may be poor estimates of the depositional age. A depositional age of 1.88 to 1.91 Ga is suggested by a possible correlation with the Saunders Creek Formation in the nearby Halls Creek Province.

The oldest well-constrained age for the Tanami Group comes from a tuff intercalated with the Callie Member. This tuff gives an age of 1838 ± 6 (95% conf.) Ma, which constrains the age of the Callie Member and provides a minimum age for the

underlying Ferdies Member. This age is similar to the Inspiration Peak Monzogranite (1844 ± 4 Ma) in the Tanami Region and bimodal volcanics of the Koongie Park Formation (1843 ± 2 Ma, Page et al., 1994) in the central zone of the Halls Creek Orogen.

Given the similarities to the Halls Creek Orogen, it is possible that the Palaeoproterozoic Tanami basin developed in response to uplift associated with the beginning of the ca. 1.88 Ga Hooper-Nimbuwah Orogeny. Initial uplift and erosion of Archaean basement rocks produced sediments now represented by the Ferdies Member of the Dead Bullock Formation. However, it was up to 40 m.y. later before the plutonic products of that magmatism were exposed, eroded and transported to form the Killi Killi Formation. A similar significant age contrast in detrital zircon between basal and overlying sediments shed from an orogen has been observed by Mclennan et. al. (2001) in the lower Palaeozoic rocks in the New England region of North America. These researchers also reported that the oldest sedimentary sequences do not record contemporaneous orogenic activity, but rather reflected older recycled continental margin rocks. Detrital zircon studies thus suggest that the first sediments shed from an emerging orogen might not record contemporaneous magmatism, but rather represent the eroded products of uplifted basement rocks.

In situ SHRIMP U–Pb dating of ore-related hydrothermal xenotime from the Callie deposit

SHRIMP U–Pb dating of ore-related hydrothermal xenotime (YPO_4) has in recent years gained credibility as a robust technique that can be used to constrain evolutionary and exploration models (Sener et al., 2003, Vielreicher et al., 2003 and references therein). The success of this technique is underpinned by the high spatial resolution and precision achievable by SHRIMP and the unique properties of xenotime which make it a good geochronometer. Advantages in using xenotime as a geochronometer include low initial Pb contents and the ability to self anneal radiation damage (Harrison et al., 2002, Fletcher et al., 2000) and a closure temperature > 750°C (Dahl, 1997). Hydothermal xenotime commonly occurs as small (<100 μm and commonly <10 μm) crystals (Vielreicher et al., 2003). The high spatial resolution of SHRIMP can target these tiny grains in polished thin sections and thus maintain the textural integrity of the analysed material.

Gold at the Callie deposit occurs within quartz veins that form sheeted sets within a D_5 structural zone, where it cuts the D_1 Dead Bullock Soak anticlinorium. In addition to gold, these veins also contain pyrite, pyrrhotite, and arsenopyrite as well as biotite, chlorite and minor carbonate gangue.

A thin section of a gold-xenotime bearing quartz vein sampled from Callie Mine drill core was cut and mounted in the surface of an epoxy disc. Following reflected- and transmitted light photography and cathodoluminescence imaging, xenotime grains were analysed for U–Pb isotopes using SHRIMP B which is housed at the Curtin University of Technology in Western Australia. The data were processed following the methods of Fletcher et al. (2000). Pb/U ratios were normalised to the MG1 xenotime standard, which has a $^{206}Pb/^{238}U$ ratio of 0.07897, equivalent to an age of 490 Ma and $^{207}Pb/^{206}Pb$ ratios were monitored using the Xeno1 standard which has a $^{207}Pb/^{206}Pb$ age of 997 Ma (Fletcher et al., 2004).

Hydrothermal xenotime occurs in the quartz veins as small (~5 to 20 µm) equant, euhedral to anhedral pale yellow-green coloured crystals. No xenotime was observed outside of the quartz vein. A SHRIMP spot of ~8 µm was used to wholly sample the xenotime grains, without overlapping onto adjacent minerals.

Seventeen SHRIMP analyses were carried out on xenotimes from within the quartz vein. Eight analyses have high common Pb contents and/or are greater than 10% discordant. These xenotimes have ambiguous compositions and the data are excluded from the pooled age calculation. The remaining concordant and near-concordant analyses combine to give a weighted mean ^{207}Pb/^{206}Pb age 1803 ± 19 Ma (95% confidence, MSWD = 0.57). This age is considered to closely represent the age of the host Au-bearing quartz vein and, by inference, the age of mineralisation at Callie.

This age is in contrast to the ca. 1720 Ma age of mineralisation interpreted from ^{40}Ar/^{39}Ar studies of hydrothermal biotite from Callie and reported by Fraser (2002). Because of the inferred robustness of the U–Pb system in xenotime, we prefer an age of ca. 1800 Ma for gold mineralisation, although the results of Fraser (2002) are at present unexplained. Our ca. 1800 Ma age is toward the younger end of the age range (1825–1790 Ma) recorded for Tanami granites. This is consistent with a genetic link between gold and granites as has been suggested elsewhere in the Tanami region by Tunks and Marsh (1998) and G. Morrison (in Smith et al., 1998).

References

Cross A.J., Claoué-Long J.C. and Crispe A.J. (2003). Summary of results. Joint NTGS-GA geochronology project: Tanami Region 2001–2002. Northern Territory Geological Survey, Record 2003-0006.

Dahl, P.S. (1997). A crystal chemical basis for Pb retention and fission-track annealing systematics in U-bearing minerals, with implications for geochronology. Earth and Planetary Science Letters, v. 150 p. 277–290.

Fletcher, I.R., McNaughton, N.J., Aleinikoff, J.A., Rasmussen, B. and Kamo, S.L. (2004). Improved calibration procedures and new standards for U–Pb and Th–Pb dating of Phanerozoic xenotime by ion microprobe. Chemical Geology, v. 209, p. 295–314.

Fletcher, I.R. Rasmussen, B., and McNaughton, N.J. (2000). SHRIMP U-Pb geochronology of authogenic xenotime and its potential for dating sedimentary basins. Australian Journal of Earth Sciences, v. 47, p. 845–859.

Fraser, G. (2002). Timing of regional tectonism and Au-mineralisation in The Tanami Region: ^{40}Ar/^{39}Ar geochronological constraints. Annual Exploration Geoscience Seminar (AGES) Record of Abstracts, Northern Territory Geological Survey Record 2002-003.

Harrison, M.T., Catlos, E.J. and Montel, J.M. (2002). U-Th-Pb dating of Phosphate Minerals, in M.J. Kohn, J. Rakovan and J.M. Hughes (editors), *PHOSPHATES Geochemical, Geobiological, and Materials Importance*. Mineralogical Society of America. Reviews in Mineralogy and Geochemistry, v. 48 p. 523–558.

McLennan, S.M., Bock, B., Compston, W., Hemming, S.R. and McDaniel, D.K. (2001). Detrital zircon geochronology of Taconian and Acadian foreland sedimentary rocks in New England. Journal of Sedimentary Research, 71, 305–317.

Page, R.W., Blake, D.H., Sun, S-s., Tyler, I.M., Griffin, T.J. and Thorne, A.M. (1994). New Geological and geochronological constraints on volcanogenic massive sulphide prospectivity near Halls Creek (WA). AGSO Research Newsletter, 20, 5–7.

Sener, A.K., Groves, D.I. and Fletcher, I.R. (2003). Timing of Gold mineralisation in the Pine Creek Orogen, Northern Territory, Australia: Its significance to the thermal-aureole gold model. Society of Geology Applied to Mineral Deposits, Conference, Athens, Greece, August 2003.

Smith, J.B. (2001). Summary of results. Joint NTGS-AGSO Age Determination Program 1999–2001. Northern Territory Geological Survey Record 2001-007.

Smith, M.E.H., Lovett, D.R., Pring, P.I. and Sando, B.G. (1998). Dead Bullock Soak gold deposits, in *Geology of Australian and Papuan New Guinean Mineral Deposits* (Eds: D A Berkmau and D H Mackenenzie), pp 449–460 (the Australasian Institute of Mining and Metallurgy: Melbourne).

Tunks, A. and Marsh, S. (1998). Gold deposits of the Tanami Corridor, in *Geology of Australian and Papuan New Guinean Mineral Deposits* (Eds: D A Berkman and D H Mackenenzie), pp 443–448 (the Australasian Institute of Mining and Metallurgy: Melbourne).

Vielreicher, N.M., Groves, D.I., Fletcher, I.R., McNaughton, N.J and Rasmussen, B. (2003). Hydrothermal Monazite and Xenotime Geochronology: A New Direction for Precise Dating of Orogenic Gold Mineralisation. Society of Economic Geologists, Newsletter, No. 53, 1, 10–16

APPENDIX 5.2-Table 1 of Sener et al. (2005)

Table 1 of:

Sener, A.K., Young, C., Groves, D.I., Krapez, B. & Fletcher, I.R. 2005. Major orogenic gold episode associated with Cordilleran-style tectonics related to the assembly of Paleoproterozoic Australia?: *Geology*, **33**, 225-228.

SHRIMP U-Pb analytical data for hydrothermal monazite from the Goodall gold deposit

Spot name	U (ppm)	Th (ppm)	Th/U	4f206 (%)	$^{207}Pb/^{206}Pb$ (±1σ %)		$^{206}Pb/^{238}U$ (±1σ %)		$^{207}Pb/^{235}U$ (±1σ %)		$^{208}Pb/^{232}Th$ (±1σ %)		Conc. (%)	$^{207}Pb/^{206}Pb$ age (Ma ± 1σ)	
Main group, excluding >1775 Ma (Shoebridge event) ages															
D.1-2	127	861	6.79	0.732	0.1059	0.0023	0.2947	0.0084	4.3020	0.1620	0.0870	0.0023	96	1730	40
D.1-3	131	748	5.70	0.785	0.1074	0.0022	0.2954	0.0076	4.3750	0.1510	0.0827	0.0024	95	1757	37
D.2-2	155	885	5.72	0.511	0.1032	0.002	0.2852	0.009	4.0570	0.1590	0.0828	0.0021	96	1682	38
H.5.3	730	233	0.32	0.438	0.1064	0.0018	0.2878	0.0081	4.2240	0.1480	0.0900	0.0049	94	1739	32
I.1-3	405	511	1.26	0.545	0.1074	0.0011	0.2922	0.0075	4.3260	0.1240	0.0814	0.0027	94	1755	18
I.1-4	337	682	2.02	0.275	0.1059	0.0014	0.3282	0.0095	4.7900	0.1580	0.0874	0.0033	106	1730	23
I.1-5	309	574	1.86	0.1	0.1054	0.0007	0.3086	0.0082	4.4850	0.1250	0.0911	0.0030	101	1722	11
J.1-4	222	396	1.78	0.528	0.1038	0.0015	0.2663	0.0079	3.8110	0.1330	0.0856	0.0032	90	1693	27
J.1-6	226	233	1.03	0.466	0.1074	0.0013	0.3073	0.0085	4.5490	0.1430	0.0913	0.0038	98	1755	22
J.1-7	507	115	0.23	0.231	0.1045	0.0007	0.2846	0.0072	4.1000	0.1110	0.0671	0.0045	95	1706	13
J.2-3	215	2343	10.92	0.214	0.1071	0.0012	0.3236	0.0088	4.7760	0.1440	0.0901	0.0025	103	1750	20
J.2-4	230	1277	5.55	0.8	0.1036	0.0016	0.2851	0.0071	3.7860	0.1240	0.0788	0.0025	90	1689	29
J.2-5	182	1770	9.71	0.514	0.1073	0.0017	0.2973	0.0082	4.3960	0.1480	0.0874	0.0025	96	1753	30
K.1-3	141	115	0.82	0.978	0.108	0.0021	0.2814	0.0082	4.1900	0.1550	0.0898	0.0047	91	1766	36
Main group >1775 Ma (Shoebridge event) ages															
D.1-1	131	757	5.79	0.362	0.1117	0.0023	0.3041	0.009	4.6850	0.1790	0.0899	0.0041	94	1826	37
D.1-4	125	723	5.79	0.375	0.109	0.0022	0.2967	0.0082	4.4590	0.1610	0.0859	0.0035	94	1783	38
D.1-5	110	744	6.77	0.263	0.1105	0.0023	0.3204	0.0104	4.8820	0.1990	0.0825	0.0031	99	1808	38
D.2-1	138	693	5.09	0.127	0.1087	0.0014	0.2888	0.0076	4.3300	0.1340	0.0859	0.0032	92	1778	24
F3-1	139	4142	29.90	0.981	0.1126	0.0025	0.2983	0.0086	4.6300	0.1780	0.0245	0.0008	91	1842	40
I.1-1	347	619	1.79	0.223	0.1094	0.0013	0.3306	0.0092	4.9860	0.1580	0.0932	0.0030	103	1789	21
I.1-2	332	497	1.50	0.102	0.1089	0.0007	0.282	0.0075	4.3840	0.1210	0.0875	0.0029	93	1781	12
J.1-5	221	209	0.95	0.496	0.1089	0.0018	0.2949	0.0085	4.4260	0.1510	0.0950	0.0043	94	1780	27
J.2-1	237	1396	5.90	0.193	0.1093	0.0012	0.2913	0.0077	4.3890	0.1310	0.0841	0.0024	92	1787	19
J.2-2	243	930	3.82	0.349	0.111	0.0016	0.295	0.0081	4.5160	0.1460	0.0856	0.0026	92	1816	28
>10 % discordant or f > 1%															
G.4-1	277	3310	11.95	1.203	0.1028	0.0023	0.2591	0.0074	3.6720	0.1420	0.0835	0.0021	89	1675	42
G.4-2	162	1820	11.25	1.662	0.1088	0.0035	0.2757	0.0074	4.1340	0.1640	0.0887	0.0027	88	1779	59
H.1-1	135	497	3.68	2.211	0.1059	0.003	0.2635	0.0078	3.8470	0.1660	0.0977	0.0035	87	1730	51
H.1-2	134	664	5.12	2.389	0.1076	0.0041	0.2707	0.0078	4.0180	0.2030	0.0894	0.0029	88	1760	70
H.1-3	2569	2777	1.08	8.995	0.0952	0.0052	0.17	0.0047	2.2310	0.1430	0.1108	0.0048	66	1532	102
H.1.4	204	1341	6.56	5.399	0.1032	0.0079	0.1431	0.0057	2.0370	0.1840	0.0918	0.0034	51	1683	141
H.1-5	131	598	4.58	3.124	0.1025	0.0044	0.2277	0.0068	3.2180	0.1780	0.0966	0.0045	78	1670	80
H.2-1	113	518	4.59	2.176	0.1071	0.0047	0.2782	0.0087	4.1090	0.2330	0.0935	0.0062	90	1751	80
H.2-2	99	470	4.75	1.729	0.1169	0.0066	0.2485	0.0089	4.0060	0.2820	0.1029	0.0066	75	1909	101
H.2-3	113	399	3.52	2.679	0.1044	0.0046	0.2335	0.0069	3.3620	0.1890	0.0999	0.0041	79	1704	82
H.2-4	131	383	2.93	2.227	0.1004	0.0039	0.2469	0.0073	3.4180	0.1750	0.0897	0.0034	87	1631	71
H.2-5	174	547	3.15	4.61	0.0927	0.0056	0.2175	0.0073	2.7810	0.2020	0.0959	0.0047	86	1482	114
H.2-6	228	461	2.02	3.196	0.1041	0.0065	0.1407	0.0052	2.0190	0.1540	0.0983	0.0047	50	1698	115
H.5-1	180	310	1.72	0.225	0.1112	0.0039	0.1626	0.0068	2.4920	0.1440	0.0529	0.0025	53	1818	64
H.5-2	205	860	3.32	3.427	0.0949	0.0038	0.1949	0.0052	2.5510	0.1300	0.0851	0.0024	75	1526	76
J.1-1	187	222	1.33	0.492	0.1091	0.0016	0.2738	0.0074	4.1170	0.1340	0.0884	0.0036	87	1785	27
J.1-2	166	157	0.94	2.22	0.0999	0.003	0.2475	0.0074	3.4090	0.1520	0.0902	0.0044	88	1622	55
J.1-3	269	233	0.87	0.411	0.1049	0.0014	0.2656	0.0082	3.8400	0.1350	0.0876	0.0035	89	1712	25
K.1-1	165	102	0.62	2.021	0.1053	0.0029	0.2493	0.007	3.6200	0.1500	0.0859	0.0052	83	1719	50
K.1-2	137	157	1.14	1.456	0.1073	0.0025	0.2727	0.0075	4.0350	0.1550	0.0913	0.0042	89	1754	43
M.1-1	49	3366	69.02	3.244	0.1042	0.0055	0.3303	0.0107	4.7440	0.3080	0.0876	0.0024	108	1700	97
Outlier in $^{207}Pb/^{206}Pb$															
H.5-4	254	286	1.13	0.218	0.0984	0.0019	0.2808	0.0088	3.6080	0.1490	0.0773	0.0054	100	1593	37

4f206 (%) is the percentage amount of common ^{206}Pb that was determined using the the ^{204}Pb correction method.